EXPERIMENTAL CHARACTERIZATION AND MODELING OF AGING-INDUCED DAMAGE IN SEMICRYSTALLINE THERMOPLASTICS

A Dissertation

by

KENNETH NOEL CUNDIFF

Submitted to the Office of Graduate and Professional Studies of
Texas A&M University
in partial fulfillment of the requirements for the degree of

DOCTOR OF PHILOSOPHY

Chair of Committee,	Amine Benzerga
Committee Members,	Darren Hartl
	Mohammad Naraghi
	Hung-Jue Sue
Head of Department,	Srinivas Rao Vadali, Interim

December 2020

Major Subject: Aerospace Engineering

ABSTRACT

Semicrystalline thermoplastics (SCTPs) are technologically important for their easy formability, high weight specific strength, and recyclability. However, certain environmental conditions, such as ultraviolet (UV) radiation, high temperatures, or moisture, initialize chemical reactions that degrade the material in a process referred to as chemical aging. Eventually, chemical aging leads to a catastrophic loss of ductility, i.e. embrittlement, often characterized a reduction of the fracture strain in uniaxial tension. Some lifetime criteria propose that embrittlement occurs at a critical molecular state achieved purely through chemical reactions. However, aging creates micromechanical damage (voids), so predictions considering only the molecular state ignore this mesoscale effect. Here, the importance of aging-induced damage to the embrittlement of SCTPs is investigated. Aging-induced damage is investigated using Polyamide-6 (PA-6) exposed to UV radiation. The effects of aging on the mechanical behavior are investigated using mechanical tests and video-based extensometry on both bulk and film specimens. Test videos also enable macroscopic observations of damage. The effects of aging on the development of micromechanical damage is evaluated using both *ex situ* and *in situ* synchrotron tomography. A viscoplastic constitutive model for a semicrystalline polymer is formulated, implemented, and calibrated to study the mechanical behavior of the bulk PA-6 material used here. Fracture by the growth and coalescence of micromechanical damage in aged and unaged PA-6 is modeled using a micromechanics-based continuum damage model. Fracture in an aged SCTP is determined to be a growth-controlled phenomenon. During loading, cracks appear on the surface of the aged material before the peak load. The density of the surface cracks increases with both strain and aging time. Additionally, *in situ* synchrotron tomography reveal that the aging-induced ductile-brittle transition coincides with a damage mechanism transition. Finally, it was found that a micromechanics-based damage model accurately predicts fracture strains of both aged and unaged material.

DEDICATION

To my parents, Kevin and Christie,

my brother, Chris,

and my wife, Natalie.

Your support is unyielding, your patience unending, and your love immeasurable.

To Granny.

You helped me over the finish line.

ACKNOWLEDGEMENTS

I am indebted to many people for their valuable contributions to this work. First and foremost, I would like to thank my advisor, Dr. Amine Benzerga, for his guidance and financial support. I benefited greatly from his clarity of thought both when teaching and forming scientific arguments. His mentorship helped me grow both as a scientist and a writer. I would also like to thank Dr. Darren Hartl, Dr. Mohammad Naraghi, and Dr. Hung-Jue Sue for serving as my committee members.

During my time as a graduate student, I have had many opportunities for scientific collaboration outside my committee. The importance of Dr. Yazid Madi's help to the experimental portion of this work (Chapters 3–5) cannot be understated. He provided to idea to use the contour tracking methodology and taught me the Python skills required to write my own contour tracking codes. He also hosted me during my stay in France during 2019, and made vital preparations for the *in situ* synchrotron tomography campaign presented in Chapter 5. Dr. Andrew King, Dr. Kamel Madi, and Maxime Pelerin also performed critical roles in carrying out the *in situ* tomography experiments at the PSICHÉ beamline of the SOLEIL synchrotron. I would also like to thank Dr. Henri Proudhoun for allowing me the use of the custom test frame, *Bulky*, which enabled the tomography to be carried out *in situ*. I gratefully acknowledge support from Dr. Thilo Morgeneyer, who provided the *ex situ* tomograms presented in Chapter 4. Dr. Georges Ayoub provided valuable guidance towards developing the semicrystalline viscoplastic polymer model introduced in Chapter 6. I would also like to thank Dr. Soondo Kweon. Although I never worked directly with him, I learned about Abaqus UMATs by studying his implementation of a macromolecular model. That knowledge was vital for writing my own UMAT of the semicrystalline polymer model presented in Chapter 6. Thank you to Xavier Colin and Mat Celina for fruitful discussions regarding the research in Chapter 3. I would also like to acknowledge Dr. Aitor Cruzado and Dr. Vikram

Kinra, both of whom I had the pleasure of working with when I was a teaching assistant. Special thanks are due to Rodney Inmon for his management of the lab in HRBB 015 and for his constant willingness to help me with the various technical problems that inevitably arise in experimental work.

I am grateful to the my fellow students and friends from Dr. Benzerga's research group. I worked closely with Ana K. Rodriguez, who was studying a research problem synergistic to mine. I thoroughly enjoyed our discussions, and they often helped me clarify my thoughts. She also helped me find many papers when I could remember what I had read, but not where I had read it. Josh Herrington provided me with his Python implementation of the damage model used in Chapter 7 and helped improve my understanding of that model. I also want to thank all my other friends from Dr. Benzerga's research group: Babak Kondori, Shamik Basu, Nithin Thomas, Mohammad Torki, Chris Greer, William Ochoa, Sahil Wajid, Basim Qamar, Vigneshwaran Radhakrishnan, and Francisco Medrano. Whether giving feedback on my presentations or advice during casual conversations, each one of them helped make this final work the best it could be.

I gratefully acknowledge financial support from the Qatar Foundation through the Qatar National Research Fund and from the Department of Aerospace Engineering at Texas A&M.

CONTRIBUTORS AND FUNDING SOURCES

Contributors

This work was supported by a dissertation committee consisting of: Amine Benzerga[a,b,c], Darren Hartl[b,c], Mohammad Naraghi[b] and, Hung-Jue Sue[d] .The following people also made contributions to this work: (1) Ana K. Rodriguez aged the PA-6 material. She also provided the the idea to to run the short study presented in Appendix G, along with the aged PE material used to conduct that study. (2) Yazid Madi, Maxime Pelerin, and Andrew King all made contributions to running experiments at the SOLEIL synchrotron and subsequent post-processing of the data produced from those experiments. Their contributions made the tomography results presented in Chapters 3 and 5 possible. (3) Additionally, Kamel Madi provided assistance that made the tomography results presented in Chapter 5 possible. (4) Thilo Morgeneyer created the *ex situ* tomograms of the round notched bars presented in Chapter 4. (5) Under my supervision, Leonardo Gasperin ran some of the mechanical tests on unaged cylindrical bars and compression pins. The results from the experiments he ran are not presented in the main text, but are included in the comprehensive database of results presented in Appendices H and I. All other work conducted for this dissertation was completed by the student independently.

Funding Sources

This research was financially supported by: (1) The Qatar Foundation through the Qatar National Research Fund (NPRP No. 7-1562-2-571). (2) The Department of Aerospace Engineering at Texas A&M, through both Research Assistantships and Teaching Assistantships (AERO 220 and AERO 304 in the Spring 2019 semester). (3) The AERO Graduate Excellence Fellowship, Fall 2019.

[a]Advisor
[b]Department of Aerospace Engineering
[c]Department of Materials Science and Engineering
[d]Department of Materials Science and Engineering, Polymer Technology Center

TABLE OF CONTENTS

Page

LIST OF FIGURES

FIGURE Page

LIST OF TABLES

TABLE Page

1. INTRODUCTION

1.1 Motivation

Thermoplastics are a versatile class of materials with a wide variety of technological applications. Some are suitable as commodity materials due to their low cost and easy formability, while others exhibit a high specific strength that makes them attractive for weight critical structures [1]. Their specific strength can be further enhanced using reinforcements to form a composite, a structural material that has attracted significant interest from the aerospace industry. Thermoplastics are also recyclable due to the low degree of crosslinking between molecular chains, which allows the material to be reformed when melted. Thermoplastics are either amorphous or semicrystalline. In semicrystalline thermoplastics, amorphous and crystalline domains coexist, with the crystalline domains increasing the strength and sometimes the chemical resistance [1]. The complicated interactions between amorphous and crystalline domains make semicrystalline thermoplastics a scientifically intriguing material for study in addition to their technological importance.

However, thermoplastics are sensitive to environmentally-induced degradation, commonly referred to as aging.[1] Aging alters several aspects of a thermoplastic's mechanical behavior, but the most critical change is typically catastrophic embrittlement that occurs after extended periods of aging. Therefore, aging compromises the long term durability of semicrystalline thermoplastics used in harsh environments. Environmental factors commonly responsible for aging are UV radiation (causes photo-oxidation), high temperature (causes thermal oxidation), and moisture (causes hydrolysis) [2,4]. These factors are ubiquitous to the point of being unavoidable and many important technologies use thermoplastics where they are subjected to such environments. For example, organic semicrystalline thin films are used in flexible solar cells, which are necessarily exposed to UV radiation [5]. UV radiation is also a

[1] In this dissertation, aging refers only to chemical aging, which may be referred to in other sources as weathering [2]. Physical aging, which is the result of free volume changes below the glass transition temperature [3], is not discussed here.

concern for low-density polyethylene (LDPE) films used as greenhouse coverings [6]. Under the hood components in automobiles, such as manifolds, are often composed of polyamides (Nylons) [1], where the high operating temperature of the engine may lead to aging. Ultra high molecular weight polyethylene (UHMWPE) is used for radiation shielding in spacecraft [7]. Amidst the recent COVID-19 pandemic, protocols to minimize the spread of the SARS-CoV-2 virus are being implemented by organizations worldwide. Since UV radiation, especially UVC (wavelength 100 nm–280 nm), is effective for inactivating viruses [8], sterilizing surfaces may help prevent the spread of viruses through means of transmission not prevented by social distancing alone. However, repeated UV sterilization might degrade the item being sterilized, particularly if the item is plastic. In many applications where aging is a concern, UV stabilizers and anti-oxidants can be added to a thermoplastic to delay aging. However, these agents are eventually consumed or lost and aging progresses as normal [2, 9].

Understanding aging is crucial for accurately predicting the lifetime of thermoplastics exposed to harsh environments. Due to the fact that aging causes embrittlement, a reduction in ultimate elongation is often used as a phenomenological lifetime criterion [6, 10]. However, aging is a complicated phenomenon that depends on physical and chemical processes [11], and predictions of embrittlement from one set of conditions may not be applicable to other environments or materials. Even when considering a single type of thermoplastic, the degree of crystallinity [4], specimen thickness [11], or initial polydispersity [12] can influence the susceptibility of the thermoplastic to aging. Developing robust, widely-applicable models of aging-induced embrittlement would reduce the need for long experimental campaigns to determine the lifetime of thermoplastic parts.

Much of the current research on the aging of thermoplastics focuses on developing kinetic models for the chemical processes that govern aging [4, 11, 13–17]. Aging results in both chain scission and crosslinking reactions [18], but chain scission often dominates [19, 20]. Current lifetime criteria propose that when chain scission reduces the molar mass below a critical value, a catastrophic decrease in ultimate elongation is observed and the polymer is

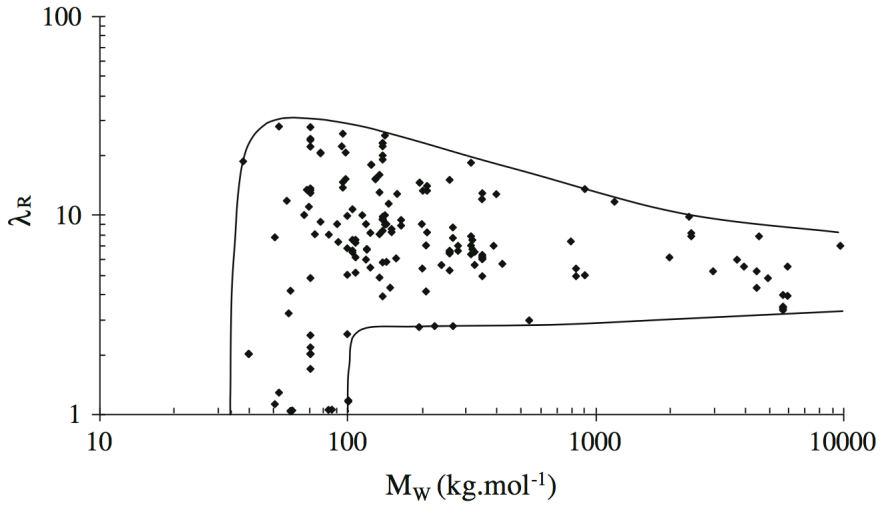

Figure 1.1: The ultimate draw ratio (λ_R) vs. molar mass (M_W) for aged and unaged PE specimens. Reprinted by permission from Springer Nature Customer Service Centre GmbH: Springer Nature [4], Copyright 2008.

considered embrittled [4, 9, 10]. However, when the ultimate draw ratio and molar mass are compared for aged and unaged PE films (see Fig. 1.1), a wide range of ductility is observed at low molar masses and exclusively high ductility is observed at high molar masses [4]. This indicates that a low molar mass is necessary but not sufficient for embrittlement, and therefore aging may cause other changes that act cooperatively with chain scission to reduce ductility.

Cavitation and crazing are important aspects of fracture in unaged polymers [21] and synchrotron tomography has revealed a detailed description of failure by void coalescence in polyamide-6 (PA-6) bars [22,23]. However, the nucleation and growth of voids caused by cavitation and crazing is affected by aging. In a study on isotactic polypropylene (iPP) loaded in tension, small angle X-ray scattering (SAXS) observations revealed that γ-irradiation changed the micromechanical deformation mechanisms, with the irradiated specimens showing more void scattering than non-irradiated specimens [24]. Additionally, aging in natural (outdoor) conditions has been observed to induce cracking in thermoplastics, both with and without an externally applied load [2, 25, 26]. In this dissertation, the term "chemical dam-

age" is used to refer to micromechanical damage (i.e. microscale voids or cracks) that forms as a result of chemical aging in the absence of an applied load. On the other hand, the term "chemo-mechanical damage" is defined as the micromechanical damage induced by a combination of chemical aging and mechanical loading. The term "aging-induced damage" is used to refer to both chemical damage and chemo-mechanical damage. In Fig. 1.1, it is shown that the molar mass alone cannot determine if the behavior will be ductile ors brittle, but the additional consideration of aging-induced damage might enable such determinations. Therefore the consideration of aging-induced damage could result in more robust lifetime criteria for aged thermoplastics.

Considerations of aging-induced embrittlement is further complicated by structural effects in bulk components. Damage from oxidative aging is typically limited to a depth of 100 µm [16, 27]. When the part is significantly thicker than this depth, aging results in a superficial embrittled layer over a core that retains its ductility. A recent study reported three different fracture behaviors in thermally oxidized PA-6 bars [28]. Each fracture behavior was characterized by different interactions between the embrittled surface and the unaged core as well as large jumps in the fracture strain.

These experimental facts make clear the need for considering mechanical damage when assessing the durability of aged semicrystalline thermoplastics. **Therefore, this dissertation aims to experimentally characterize and model the growth of aging-induced damage in semicrystalline thermoplastics. The main hypothesis of this dissertation is that aging-induced damage is an important phenomenon when evaluating the residual ductility of a semicrystalline thermoplastic.** This work takes steps towards the long term goal of developing predictive models of aging during the lifetime of a thermoplastic component. An advanced model of aging would include (1) a kinetic model predicting changes in molecular weight as a result of aging, (2) a model coupling changes in the molecular weight to changes in the constitutive thermomechanical behavior, (3) a model that predicts the nucleation of chemical damage, and (4) a damage model predicting the

nucleation and growth of chemo-mechanical damage during loading.

1.2 Objectives

As previously stated, the overall goal of this dissertation is to experimentally characterize and model the growth of aging-induced damage in semicrystalline thermoplastics. This goal is pursued by completing the following objectives:

1. Experimentally characterize the effects of aging on the mechanical behavior.
2. Investigate the effects of aging on the evolution of micromechanical damage during loading.
3. Model the intrinsic behavior of the unaged material.
4. Predict the fracture behavior of the aged material using a suitable micromechanical damage model.

To focus the scope of the research, one semicrystalline thermoplastic and one environmental factor causing aging are studied. Polyamide-6 (PA-6) is selected as the model material for semicrystalline thermoplastics, as the size of voids in PA-6 is suitable for the resolution of synchrotron tomography [23]. The relevance of synchrotron tomography to this study will be elaborated on with regards to Objective 2. PA-6 is also technologically important in its own right, due to its use in automobile parts, piping, gears, screws, and other load bearing parts [1]. The material is aged through exposure to UV radiation in air, which results in photo-oxidation. An artificial weathering machine is used to fix the spectral irradiance and wavelength of the UV light, while the degree of photo-oxidation is varied through different UV exposure times. Wavelengths in the UVA spectrum (320 nm–380 nm) are used to age the material, since this spectrum is the most relevant to natural aging at sea-level. A limited study of aging using a combination of hygrothermal and UV radiation is also conducted.

Objective 1: Experimentally characterize the effects of aging on the mechanical behavior (Chapters 3 and 4). To complete this objective, mechanical tests are

carried out on aged and unaged material. For photo-oxidation, damage is limited to a depth of approximately 100 µm due to the limited diffusibility of oxygen [27]. In thin specimens, oxygen is readily available to the entire volume, therefore oxidative damage is nominally uniform through the thickness. However, in bulk specimens, oxidative damage is limited to only the surface, otherwise known as diffusion limited oxidation (DLO) [11]. For this reason, mechanical tests are carried out on both film and bulk specimens. In the film specimens, nominally homogeneous oxidation permits insight into the effects of photo-oxidation on the intrinsic mechanical behavior. In the bulk specimens, the structural response of a brittle laminate over a ductile substrate is investigated. The former is important since many applications of thermoplastics involve parts thicker than 100 µm. The effects of aging on cylindrical bulk specimens and film specimens are presented in Chapter 3. The effects of aging on round notched specimens are presented in Chapter 4. A video-based extensometry method called contour tracking is developed to access, within limits, the true mechanical behavior, even in the presence of strong plastic localization.

Objective 2: Investigate the effects of aging on the evolution of micromechanical damage during loading (Chapters 4 and 5). This objective is completed through the use of synchrotron tomography. Synchrotron tomography has already been used to detect the growth and coalescence of voids in unaged PA-6 bars [23]. Here, it is used to observe aging-induced damage in aged PA-6. Although some preliminary observations of aging-induced damage are presented in Chapter 3, Objective 2 is primarily addressed in Chapters 4 and 5. In Chapter 4, *ex situ* synchrotron tomography is used to compare micromechanical damage in aged and unaged round notch bars loaded up to their peak force. Here, it is revealed that different damage mechanisms are responsible for failure in the aged and unaged conditions. In Chapter 5, *in situ* synchrotron tomography observations on aged films are made possible by a custom test frame [29]. The *in situ* observations reveal that the ductile-brittle transition caused by aging is accompanied by changes in the development of micromechanical damage.

Objective 3: Model the intrinsic behavior of the unaged material (Chapter 6).

A macromolecular model for amorphous polymers [30] is extended for semicrystalline polymers following a rheological model for semicrystalline polymers [31]. The resulting semicrystalline macromolecular model is implemented as an Abaqus/Standard user-defined material subroutine (UMAT). Experiments exploring the effect of temperature, strain rate, and loading mode are conducted on the unaged material. Model parameters are calibrated by optimizing finite element calculations to the nominal stress–strain data from these experiments. In this way, the intrinsic material behavior is sought using easily obtained experimental measurements, even though the presence of strong plastic localization makes deterministically accessing the intrinsic behavior from such measurements impossible. The resulting intrinsic stress–strain behavior is compared to the video-based extensometry method used in Chapter 3. The investigations of the intrinsic mechanical behavior are presented in Chapter 6.

In this objective, only the unaged mechanical behavior is studied, which is later used to approximate the mechanical behavior of aged bars. This approximation is justified because the aged surface layer (100 µm) is too thin to affect the strength of the entire volume, although the aged layer does reduce the fracture strain.

Objective 4: Predict the fracture behavior of the aged material using a suitable micromechanical damage model (Chapter 7). The final objective models aging-induced damage using a homogenization-based micromechanical damage model (i.e. a Gurson-type model [32]). The specific model used accounts for both plastic anisotropy, void shape effects, and coalescence [33–35]. The intrinsic material behavior uncovered in Objective 3 is used to generate histories of the stress triaxiality in round notched bars and to parameterize the hardening law in the damage model. The aging-induced damage observed in Objective 2 is used as a guide for the initial values of micromechanical damage variables, e.g. void volume fraction, aspect ratio, and void spacing. Then, predictions of the failure strain are compared with experimental values obtained in Objective 1. The predictions of fracture mediated by aging-induced damage are presented in Chapter 7.

This dissertation contains several novel investigations, such as:

- the first investigation of photo-oxidized semicrystalline thermoplastics including triaxiality effects,
- the first observation of aging-induced damage in a semicrystalline thermoplastic using in situ synchrotron tomography,
- the first application of a micromechanical damage model that accounts for void shape effects to agind-induced damage in semicrystalline thermoplastics.

1.3 Outline of dissertation

Prior to presenting the research produced for this dissertation, relevant background is presented in Chapter 2, each section covering material from a single topic. Section 2.1 covers cavitation in unaged semicrystalline thermoplastics. Section 2.2 presents information regarding aging and the mechanisms of aging-induced embrittlement. Section 2.3 discusses polymer constitutive models with a focus on macromolecular models. Section 2.4 provides a brief history of homogenization-based models of void growth. Original research is presented in Chapters 3–7, with each chapter primarily addressing their respective objective as defined in Section 1.2. Concluding remarks are made in Chapter 8.

A collection of appendices follow the main text of the dissertation. The appendices are of three types. The first type of appendix provides supplementary information (Appendices A, B, C, D). These appendices are provided to thoroughly document the research conducted for this dissertation without diluting the main text with minor details. The second type of appendix describes a short study (Appendices E, F, G). These appendices are short, independent reports regarding research findings that did not warrant an entire chapter. The final type of appendix serves as an experimental database (Appendices H, I, J, K). These appendices create a single location where data from all mechanical tests on a single specimen geometry can be found.

2. BACKGROUND

This chapter presents a literature review of topics relevant to the experimental characterization and modeling of aging-induced damage in semicrystalline thermoplastics. Four topics are covered, each in its own section. Section 2.1 discusses cavitation in order to build an understanding of damage mechanisms in unaged semicrystalline thermoplastics. In Section 2.2, the fundamentals of chemical aging are described, along with a discussion of whether chain scission by oxidation is homogeneous or heterogeneous. Section 2.3 describes viscoplastic constitutive models for thermoplastics and Section 2.4 describes homogenization-based micromechanical damage models that could be used to model micromechanical damage in thermoplastics, whether that damage originates from cavitation or aging.

2.1 Cavitation in semicrystalline thermoplastics

During plastic deformation, many materials accumulate damage through the nucleation and growth of voids, which are essentially inclusions with zero stiffness (i.e. "empty" volume enclosed by the matrix material). In semicrystalline thermoplastics, voids are most commonly formed through cavitation, a process where voids nucleate by the interactions of the amorphous and crystalline phases that occur during deformation [21]. Adopting the nomenclature used in the review Pawlak et al. 2014 [21], the term cavity is used here to refer to voids that form through such dual-phase interactions. Although aging promotes cavitation [2, 25], it is also widely observed in unaged semicrystalline thermoplastics [21]. In this section, a groundwork is created for upcoming discussions of aging-induced damage by first exploring existing research on cavitation in unaged semicrystalline thermoplastics.

Cavitation is an important damage mechanism in the plastic deformation of many semicrystalline thermoplastics. Voids only open under the application of a positive hydrostatic pressure, so cavitation only occurs in tension, never compression or shear [21]. Cavities form in amorphous regions trapped between crystalline regions, either in interlamellar zones [36] or at

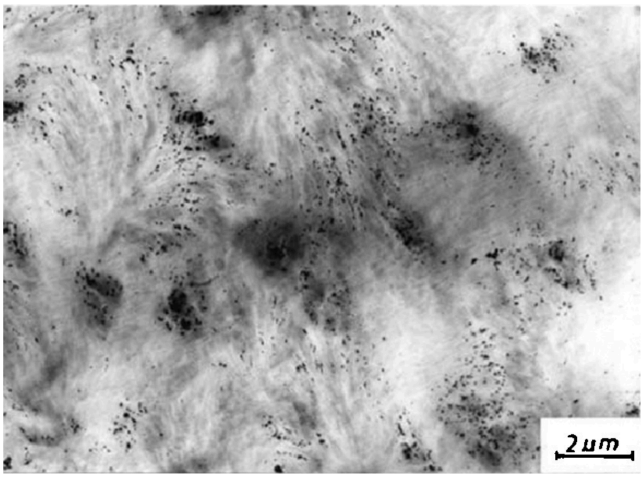

Figure 2.1: TEM image of a transverse section of PA-6 strained to a draw ratio of 2 and treated with OsO_4 and phosphotungstic acid. Image reprinted from [21] and originally appeared in [36]. Reprinted from [21], Copyright 2014, with permission from Elsevier. Reprinted with permission from [36]. Copyright 1988 American Chemical Society.

interspherulitic boundaries [36,37].[1] For this reason cavitation only occurs in semicrystalline polymers, although voids may form in amorphous polymers by other means, such as crazing [39,40]. Although a group of cavities may appear similar to a craze, cavities are distinct from crazes in that they lack internal structure [21], i.e. there are no ligaments connecting the surfaces of cavities. Cavities may have dimensions from the nanoscale to the microscale [21]. Since cavities cause abrupt spatial changes in density, they scatter light [41, 42], and this property is often used to detect cavities. For example, microsized cavities are visible to the naked eye as a whitening of the material, while nanosized cavities are detectable using small angle X-ray scattering (SAXS) [43, 44]. Since void growth causes dilatation [44, 45], cavities can also be indirectly detected by measuring the volume strain [37]. Cavities can be directly observed using transmission electron microscopy (TEM) [36], atomic force microscopy (AFM) [46], or, more recently, synchrotron tomography [22,23]. Fig. 2.1 shows an example of cavities observed by TEM and Fig. 2.2 shows an example of cavities observed by

[1]For an introduction to the concepts and terminology relevant to microstructures in semicrystalline thermoplastics, the reader is referred to Refs. [38–40].

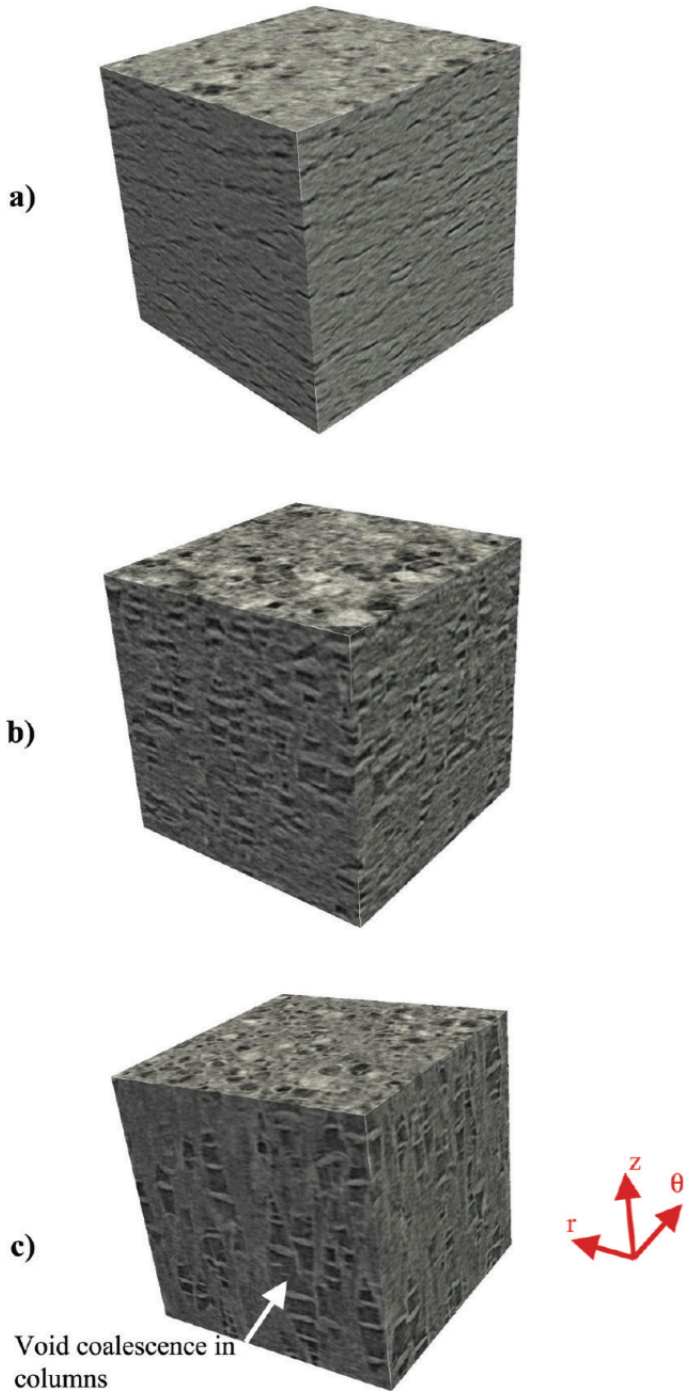

Figure 2.2: Tomograms depicting the growth of cavities in the center of a round notched bar of PA-6. The tomograms were taken at (a) the peak load, (b) after softening, and (c) prior to failure. Reprinted with permission from [23]. Copyright 2012 American Chemical Society.

synchrotron tomography.

Galeski et al. [36] studied cavitation in PA-6 using TEM by staining specimens with Osmium tetroxide (OsO_4) and phosphotungstic acid. They observed cavities, arranged in rods, concentrated at the equatorial regions of spherulites and occasionally in the polar regions of spherulites. From these observations, they proposed that cavities nucleate by a series of interactions between amorphous and crystalline features, as depicted in Fig. 2.3. Consider a spherulite under the action of a remote uniaxial load. The lamellar fans oriented at 45° to the poles experience shear as a result of the load (Fig. 2.3a). The shear stress in the 45° lamellar fans cause chain slip and stack rotation, which produces a tensile stress on the faces of equatorial lamellae and a compressive stress on the faces of polar lamellae. In addition to the stresses caused by the rotation of lamellae, the load directly produces a tensile stress along the length of the polar lamellae, and the Poisson effect produces a compressive stress along the length of the equatorial lamellae (Fig. 2.3b). The longitudinal compressive stress on the equatorial lamellae causes kinking, and the amorphous phase is opened by the tensile stress on those lamellar faces, resulting in cavitation (Fig. 2.3c). Similarly, the compressive stress on the faces of the polar lamellae create instabilities that are opened by the longitudinal tensile stress, resulting in the opening of the amorphous phase and therefore cavitation (Fig. 2.3d).

Cavities nucleate perpendicular to the loading direction as "penny-shaped" cracks [43, 44, 47]. As deformation continues, cavities elongate, eventually aligning with the principal stress [23]. Fig. 2.2 shows tomograms of the centers of PA-6 round notched bars that were interrupted at 3 stages of loading. In Fig. 2.2a, loading was interrupted at the peak stress. Here, penny-shaped cavities are observed throughout the tomogram and are oriented perpendicular to the loading direction (z-axis). In Fig. 2.2b, loading was interrupted after post-peak softening. Here cavities have elongated along the loading direction. In Fig. 2.2c, loading was interrupted prior to failure. Here, the cavities have continued to elongate and are beginning to coalesce in columns. In tomograms taken at the notch root (not shown

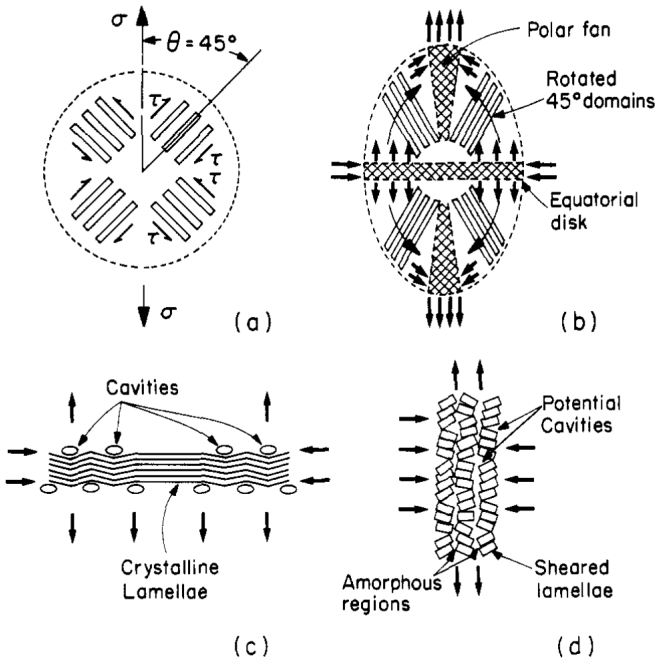

Figure 2.3: Stages of cavitation in a spherulite subjected to a remote uniaxial load. (a) Lamellar fans oriented at 45° to the poles experience a resolved shear stress that promotes chain slip and stack rotation. (b) The stack rotation produces an additional tensile stress on the faces of equatorial lamellae and a compressive stress on the faces of polar lamellae. The remote load produces a compressive stress along the length of the equatorial lamellae and tensile stress along the length of the polar lamellae. (c) The compressive stress acting along the length of the equatorial lamellae and the tensile stress acting on the faces act together to form cavities. (d) Similarly, the compressive stress on the faces of polar lamellae create instabilities that are opened by the longitudinal tensile stress, resulting in the opening of the amorphous phase and therefore cavitation. Reprinted with permission from [36]. Copyright 1988 American Chemical Society

here), cavities orient along the contours of the notch, and therefore have aligned along the direction of the principal stress, as the principal stress is aligned with the curvature of a notched bar due to the traction-free boundary condition at the surface [23].

Whether or not cavitation occurs is determined by the relative strengths of the amorphous and crystalline phases. When loading a semicrystalline thermoplastic, if the stress required to activate lamellar shear is less than the stress required for cavitation, then cavitation is not observed, since the macroscopic deformation is accommodated by the plastic deformation of the crystalline phase. On the other hand, if the stress required to activate lamellar shear is larger than the stress required for cavitation, then cavities nucleate. In other words,

$$\begin{cases} \text{for } \sigma_{\text{sh}} > \sigma_{\text{cav}}, & \text{cavitation} \\ \text{for } \sigma_{\text{sh}} < \sigma_{\text{cav}}, & \text{no cavitation,} \end{cases} \tag{2.1}$$

where σ_{sh} is the stress required to activate lamellar shear and σ_{cav} is the stress required for cavitation. Typically, thicker lamellae are stronger than thinner lamellae, as the longer crystallization time required for form thicker lamellae also results in a lower defect density [44, 48]. Therefore, thermoplastics with a high crystallinity are more likely to cavitate than thermoplastics with a low crystallinity [43, 44, 47]. The effect of the lamellar thickness, L_{c}, on σ_{sh} and σ_{cav} is plotted in Fig. 2.4. This plot can be used to determine the critical lamellar thickness, L_{cc}, where cavitation becomes favorable.

The importance of the relative strengths of each phase to cavitation was first described in Pawlak and Galeski 2005 [49]. In this study, the yield stress of several polymers was studied in uniaxial tension and plane strain compression. The significance of these two loading modes is that they are kinematically similar, except that the hydrostatic stress is negative in compression, so cavitation is suppressed. It was found that cavitating specimens exhibited a lower yield stress in tension than compression, while non-cavitating specimens exhibited similar yield stresses in both loading modes. Based on this finding, Pawlak and Galeski proposed that cavitation was determined by the competition between σ_{sh} and σ_{cav}. When

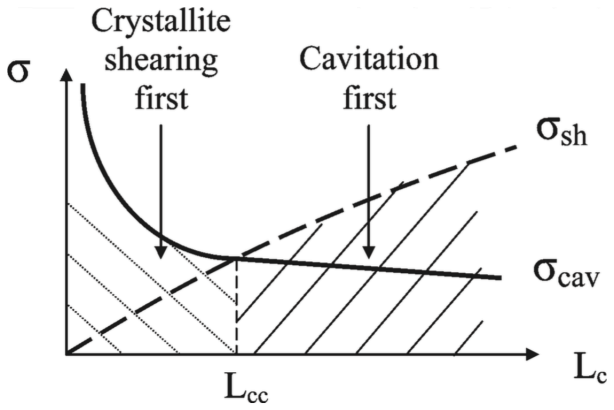

Figure 2.4: The relationship between the stress required to initiate crystal shearing, σ_{sh}, and the stress required to initiate cavitation, σ_{cav}, as a function of the lamellar thickness, L_{c}. Above the critical lamellar thickness L_{cc}, cavitation becomes favorable. Reprinted with permission from [43]. Copyright 2010 American Chemical Society.

the stress required for lamellar shear is lower than the stress required for cavitation, yield occurs at the same stress in tension and compression. However, when the stress required for lamellar shear is higher than the stress required for cavitation, different mechanisms are responsible for yield in tension and compression, resulting in different yield stresses. In tension, the stress required for cavitation is achieved and yield occurs at this stress. In compression, cavitation is not possible due to the negative hydrostatic stress, so yield occurs at the higher stress required to activate lamellar shear. This result was later reinforced through the study of cavitation in annealed high-density polyethylene (HDPE) [44]. As mentioned previously, annealing increases the thickness of the lamellae while decreasing the defect density, therefore increasing σ_{sh}. In the annealed HDPE, a 30 % volume increase during tensile drawing was observed, indicating significant cavitation. In contrast, the non-annealed specimens deformed without significant volume strain.

Cavitation is typically observed around macroscopic yield, but it was not always clear if cavitation caused yielding or if yielding caused cavitation. The question was explored in Humbert et al. 2010 [43], where cavitation was observed before macroscopic yield in some

specimens and afterwards in others. In Ref. [43], macroscopic yield is defined as the peak nominal stress. They identified three scenarios for the relationship between yielding and cavitation. In the first scenario, the stress required to activate lamellar shear is greater than the stress required to initiate cavitation, i.e. $\sigma_{\text{sh}} > \sigma_{\text{cav}}$, therefore cavitation is activated before crystal plasticity. In this scenario, cavitation occurs prior to yield and homogeneously throughout the specimen. In the second case, $\sigma_{\text{sh}} < \sigma_{\text{cav}}$, so crystal plasticity is activated first. Here, macroscopic yielding occurs first, but stress concentrations caused by lamellar deformation still eventually cause cavitation. In this scenario, cavities are nucleated only in the necked regions, since the material in the neck has yielded. In the final scenario, $\sigma_{\text{sh}} \ll \sigma_{\text{cav}}$, so the stress concentrations that occur after yield are not enough to exceed σ_{cav}. In this scenario, no cavitation occurs. Based on the experiments in Ref. [43], the scenarios presented in Eq. (2.1) are over simplified. A more accurate statement of cavitation conditions can be summarized as

$$\begin{cases} \text{for } \sigma_{\text{sh}} > \sigma_{\text{cav}}, & \text{homogeneous cavitation} \\ \text{for } \sigma_{\text{sh}} < \sigma_{\text{cav}}, & \text{cavitation in yielded material only} \\ \text{for } \sigma_{\text{sh}} \ll \sigma_{\text{cav}}, & \text{no cavitation.} \end{cases} \tag{2.2}$$

As stated previously, cavitation is only observed in tension; never in shear or compression. This is because voids open up under the application of a positive hydrostatic stress. The stress triaxiality ratio is defined as the ratio of the hydrostatic stress to the equivalent stress, therefore a higher stress triaxiality ratio, or simply triaxiality, facilitates void nucleation and growth. This behavior is general to voids in any material, not just cavities in polymers [45]. Castagnet and Debruck [37] studied the effects of triaxiality on cavitation in semicrystalline polymers by measuring the volume strain during deformation. The triaxiality was varied by using cylindrical bars and round notched bars (diabolo specimens) with different notch radii. Some bars were annealed, therefore increasing σ_{sh} and favoring the formation of voids, while

other bars were not annealed. The cylindrical annealed bars showed more volume increase, and therefore more void growth, than cylindrical non-annealed bars. For specimens with a sharper notch, and therefore a higher triaxiality, the difference in volume strain between the annealed and non-annealed specimens decreased. For the bars with the sharpest notch, annealing had no effect on the volume strain. As the triaxiality in the bar increases, the remote applied load required to initiate cavitation decreases, therefore favoring cavitation in non-annealed specimens that did not cavitate under a uniaxial stress. Laiarinandrasana et al. [23] studied cavitation in round notched bars using synchrotron tomography, where the 3D nature of a tomography permitted void volume fraction measurements throughout the volume of the specimen. They found that regions of the bar with a higher local triaxiality exhibited a higher void volume fraction compared to regions with a lower local triaxiality.

2.2 Chemical aging of thermoplastics

As with all materials, polymers are vulnerable to aging. Broadly speaking, polymers age in two ways. The first is physical aging, where a polymer below its glass transition experiences a gradual reduction of the free volume as the chains rearrange to achieve thermodynamic equilibrium [3]. Upon heating above the glass transition, the chains regain the mobility necessary to quickly achieve thermodynamic equilibrium, and physical aging is reversed. The second type of aging is chemical aging, where environmental factors initiate chemical reactions in a polymer that degrade its mechanical properties. Since chemical aging is the subject of this dissertation, the term "aging" is used here to refer exclusively to chemical aging.

There are many environmental conditions that might initiate aging, but three conditions are of primary importance: (1) Ultra-violet (UV) radiation causes photo-oxidation, (2) high temperature causes thermal oxidation, and (3) moisture causes hydrolysis [2]. After extended periods of aging, a catastrophic loss of ductility, i.e. embrittlement, occurs. In most applications, embrittlement is the most critical mechanical change induced by aging, therefore, research on aging typically focuses on predicting embrittlement. However, the effects of

aging manifest at length scales from the nanoscale to the macroscale. Due to the multiscale nature of aging, a robust understanding of aging remains elusive. Chemical reactions are the most direct effect of aging, but the causal link between chemical reactions (a nanoscale effect) and embrittlement (a macroscale effect) remains unclear.

The chemical reactions that result from aging have been extensively studied, since they are fundamental effects of aging [4, 11, 13–17]. Oxidative aging is commonly studied, since photo-oxidation and thermo-oxidation are two of the most important sources of aging, and are also mechanistically similar [27]. They are both oxidation reactions with their main difference being the source of energy that initiates and perpetuates the reaction; either photons in the case of photo-oxidation or thermal energy in the case of thermo-oxidation. Due to the importance of oxidative aging, and the abundance of information in the literature, the review here focuses on oxidative aging, although many parallels exist to other forms of (chemical) aging.

Oxidation in thermoplastics can lead to both chain scission and cross-linking reactions, however chain scission is typically dominant compared to cross-linking [20]. By definition, chain scission reduces the molecular weight of the polymer. The shorter chains have increased mobility, which may give them sufficient mobility to integrate into nearby crystals, thus increasing the crystal volume fraction [50]. The process of increasing the crystallinity through chain scission is referred to as chemi-crystallization.

Oxidation requires oxygen, therefore oxidative aging is limited by the ability of oxygen to diffuse through the volume of the polymer. Since oxygen is unable to diffuse into the more densely packed crystalline phase, oxidative degradation is confined to the amorphous domains [4, 27]. Oxygen is readily available at the surface of a polymer, but can only diffuse to a depth of approximately 100 µm [16, 27]. In specimens thicker than this, an aged surface layer forms on top of an unaged core [16, 51]. This effect is referred to as diffusion limited oxidation, or DLO [11]. One example of DLO can be found in Wei et al. 2018 [28], where 2 mm thick PA-6 specimens were aged at 180 °C. Infrared (IR) microscopy was used to measure the

thickness of the aged surface, where it was observed that the aged layer approached 130 µm after 48 h. In the case of photo-oxidation, the attenuation of photons through the material may also lead to a gradient in aging from the surface to the bulk, although the depth of damage is still approximately 100 µm [27].

Even when aging is not limited by the availability of oxygen, there is some controversy concerning whether oxidation, and therefore chain scission, occurs homogeneously or heterogeneously [4, 11]. Fayolle and co-workers have argued that chain scission is quasi-homogeneous, i.e. that given equal availability of oxygen, any chain in the amorphous phase is equally susceptible to scission by oxidation. In this framework, embrittlement occurs when some critical molecular state occurs that inhibits plastic deformation [4]. Fig. 2.5a schematically depicts the case of homogeneous oxidation. Alternatively, George and co-workers have proposed that oxidation is heterogenous, i.e. that oxidation is highly localized and spreads to nearby regions through the transfer of oxidation products [52]. In this framework, embrittlement occurs when the highly oxidized zones form cracks, and a build up of defects results in a loss of ductility [53]. Fig. 2.5b schematically depicts the case of heterogeneous oxidation.

Fayolle and co-workers have argued that oxidation causes homogeneous chain scission and that embrittlement occurs abruptly when chain scission degrades the molecular network beyond a critical state. In Fayolle et al. 2004 [10], polypropylene (PP) is thermo-oxidized at different temperatures and its molar mass and tensile properties are measured as functions of exposure time. The authors argue that chain scission is homogeneous due to the unimodal distribution of molar mass detected by size-exclusion chromatography (SEC). A sharp decrease in fracture strain was observed around a molar mass value of 210 kg/mol, regardless of the temperature used to thermo-oxidize the PP specimen. They refer to the molar mass separating ductile and brittle behavior as the critical molar mass, M_c, and because entanglements are important for activating plasticity in both semicrystalline and amorphous polymers [54], the authors speculate that M_c must be related to the molar mass between

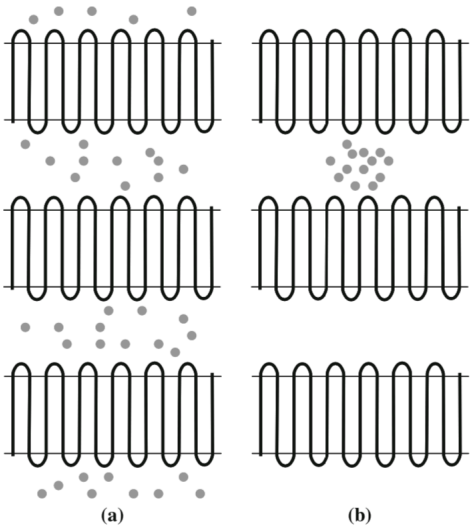

Figure 2.5: A schematic representation of two possible processes for oxidation and chain scission. (a) Homogeneous oxidation. Chain scission occurs evenly throughout the amorphous domain. (b) Heterogeneous oxidation. Chain scission is localized. Reprinted by permission from Springer Nature Customer Service Centre GmbH: Springer Nature [4], Copyright 2008.

entanglements, M_e. They therefore define $q \equiv M_c/M_e$, and observe that in amorphous polymers and semicrystalline polymers with their amorphous phase in the glassy state, $q \approx 5$, while in PP, $q \approx 60$. In Fayolle et al. 2007 [55], polyethylene (PE) is thermo-oxidized, and a similarly high value of q ($25 \leq q \leq 50$) was found through experimental observations and synthesis of data available in the literature. It was proposed that embrittlement occurs when one of two events occur: (1) the molar mass decreases below a critical value ($M_w < M_c$), representing a destruction of the entanglement network, or (2) the thickness of the interlamellar amorphous phase decreases below a critical value ($l_a < l_{a,c}$), representing a loss of amorphous phase volume fraction necessary for sustaining large deformations. These ideas were reviewed in Fayolle et al. 2008 [4], and two causal chains for embrittlement were proposed, although neither causal chain was favored as more likely. In the first causal chain, homogeneous chain scission causes a molar mass decrease, which decreases the tie molecule concentration, which inhibits plastic deformation. In the second causal chain, homogeneous chain scission causes

a molar mass decrease, which causes chemi-crystallization, which decreases the interlamellar spacing, which then inhibits plastic deformation. However, the arguments for embrittlement based on a critical molecular state ($M_w < M_c$ or $l_a < l_{a,c}$) hypothesize that aged polymers behave the same as unaged polymers with the same molecular state. When data from the literature on fracture strain vs. molar mass was collected for both aged and unaged PE (see Fig. 1.1), both ductile and brittle behavior is observed in specimens with $M_w < M_c$, while only ductile behavior is observed for $M_w > M_c$ [55]. This indicates that a critical molecular structure may be necessary for embrittlement, but is not sufficient.

On the other hand, George and Celina have argued that oxidation is heterogeneous. In one paper, they study the oxidation of PP powder and films using chemiluminescence [52]. When the PP particles were oxidized individually, a variety of induction times were observed. It was postulated that impurities in the powder resulted in less stable PP particles with shorter oxidation times. When the PP particles were oxidized in physical contact with each other, a single induction time was observed. This indicates that oxidation initiates in the least stable particles, then spreads via oxidation products to nearby particles. Similar conclusion could be drawn from the oxidation of PP films, where oxidation began in highly localized centers, then spread to nearby regions.

Aging can lead to the formation of "chemical cracks" in thermoplastics. Fig. 2.6 shows SEM micrographs of the surface of a PA-6 injection molded bar exposed to outdoor weathering for 5, 10, and 20 weeks [2]. No cracks were visible at 5 weeks, but several cracks were visible at 10 weeks. From 10 to 20 weeks, the number of cracks increased, along with the average crack size. Heterogeneous oxidation provides an intuitive explanation for the formation of chemical cracks; When the oxidized zone reaches a critical size, a crack is formed [2, 53]. However, the appearance of surface cracks does not discriminate between homogeneous of heterogeneous oxidation processes, as volume swelling [56] hardening due to crosslinking [11], and chemi-crystallization [2, 50] have also been proposed as mechanisms for crack formation in aged polymers.

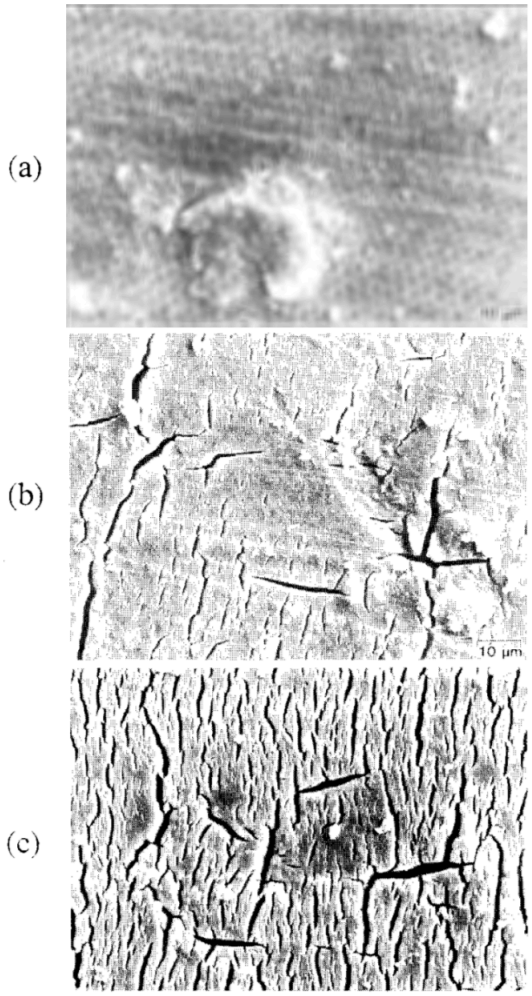

Figure 2.6: PA-6 injection molded bars exposed to outdoor conditions for (a) 5 weeks, (b) 10 weeks, and (c) 20 weeks under no load in Brisbane, Australia. Reprinted from [2].

Even when aging alone does not result in chemical cracks, the application of a mechanical load to an aged polymer may cause cracks to form. Such damage is chemo-mechanical in nature, since it requires both chemical attack and a mechanical load. However, few studies attempt to connect aging-induced embrittlement to the growth of chemo-mechanical damage. In Qayyum and White 1987 [25], thermoplastics were weathered outdoors in Saudi Arabia, then loaded until fracture. The bars were then examined using SEM, where it was determined that the aged bars fractured by the coalescence of diamond shaped cavities. Such cavities

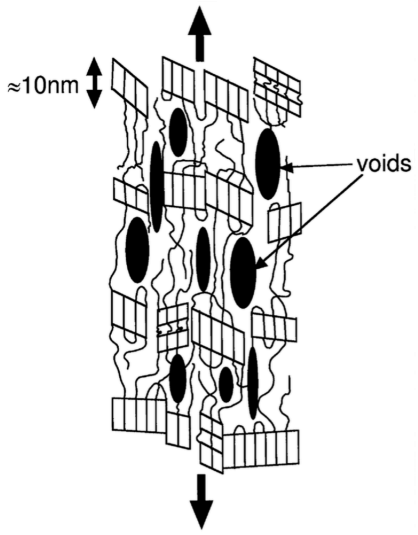

Figure 2.7: Schematic of fibrillated shear in a semicrystalline polymer. Reprinted from [24], Copyright 2000, with permission from Elsevier.

were not present in the unaged bars. It was noted that aging changed the residual stress at the surface of the bar from compressive to tensile, which likely facilitated the growth of cavities. Since the core of the specimens were unaffected by aging ($t \gg 100\,\mu m$), the growth of a single cavity was not catastrophic, as it was supported by the unaged core. This allowed many cavities to nucleate and grow before failure occurred by coalescence. Later, Zhang et al. [24] studied micromechanical deformation mechanisms in γ-irradiated isotactic polypropylene (iPP). SAXS measurements were used to reveal mechanisms such as lamellar separation, lamellar shear, fibrillation, and cavitation. In non-irradiated iPP deformed at 80 °C, lamellar separation and shear were observed, but no voids were detected. However, in iPP irradiated with 50 kGy, fibrillation was observed, which is accompanied by the formation of voids, as shown in Fig. 2.7. More recently, Wei et al. 2018 [28] studied thermo-oxidized bulk PA-6 specimens loaded to failure in tension. The surfaces of the fractured bars were then studied using SEM. Because the PA-6 specimens were thicker than depth of oxygen diffusion, DLO conditions were active, resulting in an oxidized surface and an unaged core.

They identified 3 different fracture behaviors for different levels of thermo-oxidation. In the specimens with the least oxidation, voids were observed in the necked region of the specimen and failure occurred when voids coalescence occurred. For intermediate levels of oxidation, cracks formed in the oxidized surface layer, but where arrested by the ductile core. At the onset of necking, the cracks began to propagate into the core of the specimen and fracture occurred. For the highest levels of oxidation, brittle behavior was observed. Failure occurred soon after the cracks were observed and no fibrils were found on the fracture surface of the ductile core. The results from these studies demonstrate the importance of considering mechanical damage in the deformation and fracture of aged semicrystalline thermoplastics.

2.3 Viscoplastic constitutive models for thermoplastics

Understanding and modeling the mechanical behavior of aged thermoplastics naturally requires constitutive models for pristine thermoplastics. Likewise, modeling the behavior of semicrystalline thermoplastics requires an understanding of models for amorphous thermoplastics. Thermoplastics exhibit complex behavior that can include a gradual rollover to yield, post-yield softening, and large strain hardening. These features are depicted in the representative stress–stretch curve in Fig. 2.8. Thermoplastics exhibit viscoplastic behavior, i.e. their plastic flow is affected by the strain rate and temperature. The mechanical behavior of thermoplastics is also sensitive to the molecular structure of the polymer, which includes factors such as the molecular weight, cross-linking, number of entanglements, and the presence of plasticizers. If a thermoplastic is semicrystalline, then the morphology of the crystalline phase also impacts the mechanical behavior. The wide range of factors that influence the mechanical behavior of thermoplastics poses a significant challenge to formulating constitutive models for this class of materials.

Two physically distinct resistances to plastic deformation exist in amorphous thermoplastics below their glass transition temperature [59,60]. The first resistance is the intermolecular resistance to chain rotation [60]. The physical origin of this resistance is the low free volume in glassy polymers, which causes the motion of a chain to be kinematically restricted by

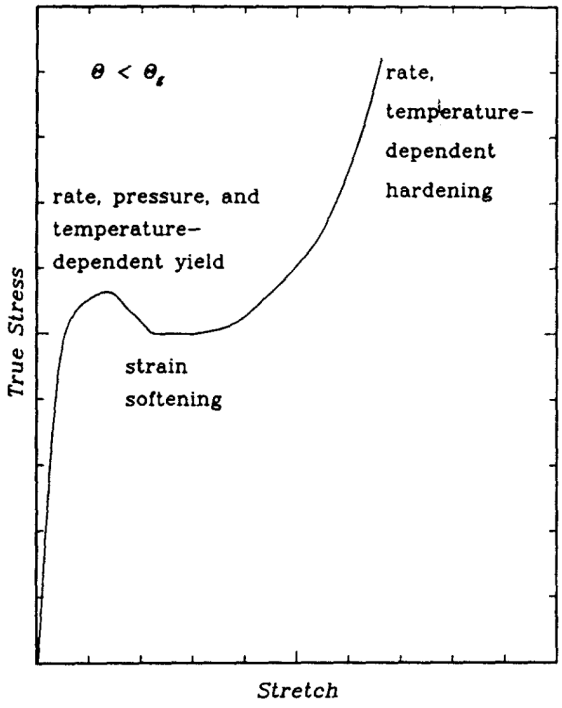

Figure 2.8: A representative stress–stretch curve for a thermoplastic below its glass transition temperature, $T < T_{\mathrm{g}}$. Reprinted from [57], Copyright 1988, with permission from Elsevier.

nearby chains. This resistance is associated with the early stages of plastic flow, such as yielding and strain softening. The second resistance is orientation hardening (i.e. network hardening or entropic hardening). At large deformations, the macromolecular network orients to resist the deformation, resulting in significant kinematic hardening. The physical entanglements responsible for connecting the macromolecular network behave like chemical crosslinks in a thermoset [59], except that entanglement slippage is possible, resulting in relaxation [31, 61]. To illustrate the contributions of these two resistances to the stress–strain behavior, Fig. 2.9 shows two representative stress–strain curves, one with both resistances and one with the orientation hardening subtracted from the overall response. Some rheological models representing these two resistances are presented in Fig. 2.10. Most physically based models for thermoplastics are based on the 1-D model from Haward and Thackray 1968 [59], in which the intermolecular resistance is modeled as an Eyring dashpot and the

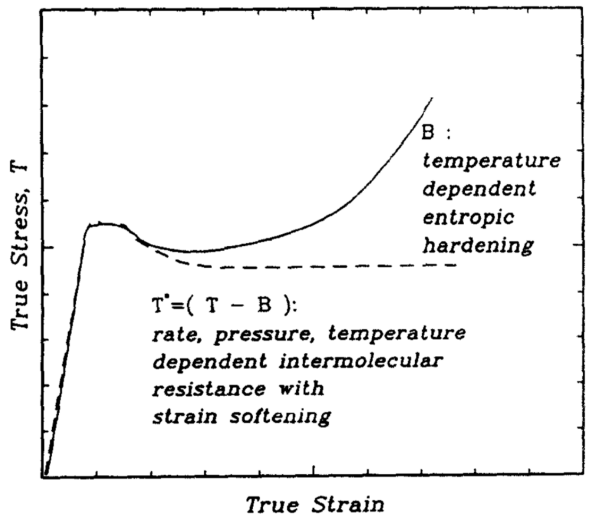

Figure 2.9: A representative stress–strain curve for a glassy thermoplastic and the resulting stress–strain curve when the orientation hardening is subtracted from the overall response. Reprinted from [57], Copyright 1988, with permission from Elsevier.

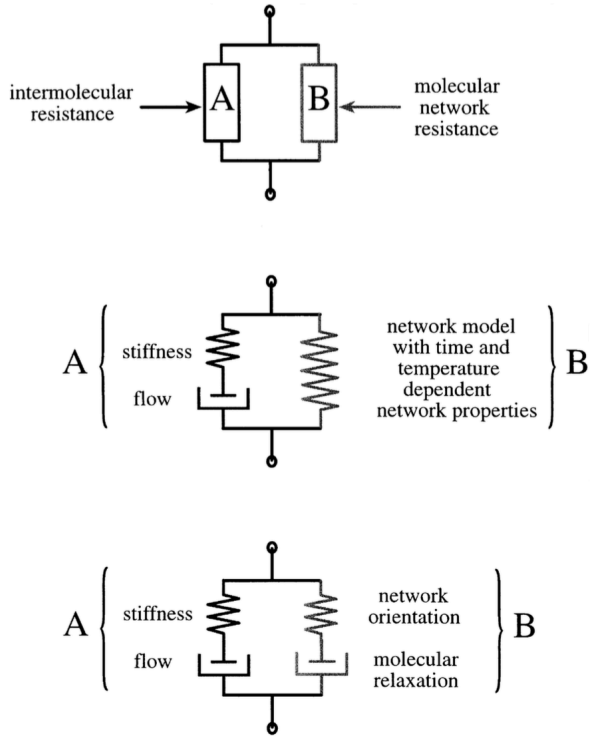

Figure 2.10: Some rheological models representing the two resistances to plastic flow in amorphous thermoplastics. Reprinted from [58], Copyright 2000, with permission from Elsevier.

network resistance is modeled by a Langevin spring. The Langevin spring is derived from rubber elasticity using non-Gaussian chains [62], and the application of rubber elasticity to thermoplastics is justified by assuming entanglements in a thermoplastic behave similarly to crosslinks in an elastomer. This model provided a physically motivated representation for the network hardening in thermoplastics. Later, Argon [60] formulated a theory for the yielding of amorphous polymers based on the thermal activation of a doubly kinked polymer chain. The resulting viscoplastic law provided a physically motivated equation for the intermolecular resistance to flow in an amorphous polymer.

The models in Haward and Thackray 1968 [59] and Argon 1973 [60] paved the way for the development of *macromolecular models*, which are a class of viscoplastic models that use the double kink molecular mechanism to model the intermolecular resistance and rubber elasticity to model the network resistance. This class of models was originally conceived for amorphous thermoplastics below their glass transition temperature [57, 59], but the concepts have also been successfully applied to thermoplastics above their glass transition [58], semicrystalline polymers [31,58,63], and thermosets [64–66]. Boyce et al. 1988 [57] developed one of the first 3D macromolecular models. They modified the viscoplastic law of Argon to include pressure sensitivity and modeled the orientation hardening using a non-Gaussian 3-chain model for rubber elasticity. Arruda and Boyce [67] later developed an 8-chain model for rubber elasticity and compared it to 3-chain and 4-chain models. They found the 8-chain model superior to the other options due to both its accuracy and its ability to predict the material response under different states of deformation without changing the model parameters. Representative volume elements for the 3, 4, and 8-chain models are depicted in Fig. 2.11. Wu and van der Giessen [68] developed a full network model for rubber elasticity and incorporated it into a macromolecular model. The full network model was computationally expensive; however, it could be accurately approximated using a linear combination of the 3-chain and 8-chain models. Later, Wu and van der Giessen [69] recast the 3-chain, 8-chain, and full network models in a co-rotational rate tangent form. However, their actual

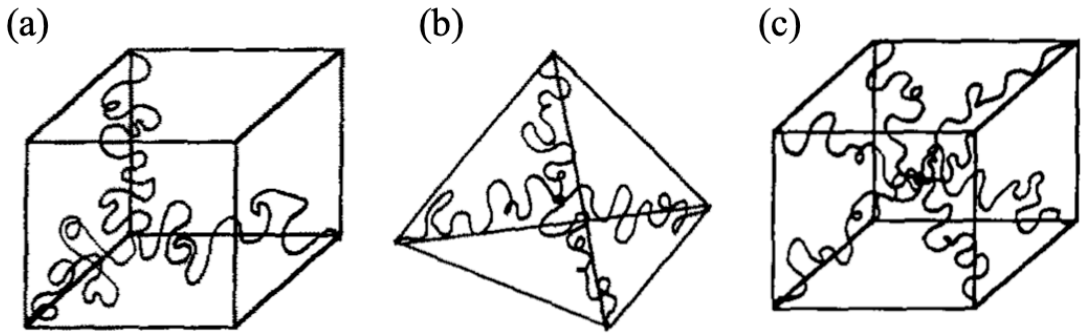

Figure 2.11: Representative volume elements for the (a) 3-chain, (b) 4-chain, and (c) 8-chain models of rubber elasticity. Reprinted from [67], Copyright 1993, with permission from Elsevier.

implementation bypassed the rate tangent evolution law for the network hardening that they formulated, leading to small errors in equilibrium. Kweon and Benzerga [30] formulated a macromolecular model employing the full network approximation, but utilized the implicit rate form proposed by Wu and van der Giessen [69]. In addition, Kweon and Benzerga used a modified evolution law for the athermal shear strength, proposed by Chowdhury et al. 2008 [70]. The modified evolution law provided a more realistic rollover to yield, as opposed to the sharp yield predicted by previous macromolecular models.

A variety of approaches have been used to model semicrystalline thermoplastics. Boyce et al. 2000 [58] proposed a model for PET above its glass transition temperature that added molecular relaxation effects, which compete with the molecular orientation predicted by the 8-chain model. Above its glass transition temperature, PET undergoes strain-induced crystallization (SIC), which was implicitly modeled in Boyce et al. 2000 by modifying the strength of the amorphous phase. They assumed that at the onset of SIC, molecular relaxation processes cease and the intermolecular resistance increases. Ahzi et al. 2003 [63] updated the model of Boyce et al. 2000 [58] by splitting the intermolecular resistance into separate resistances for the amorphous and crystalline phases. Fig. 2.12 shows one possible rheological

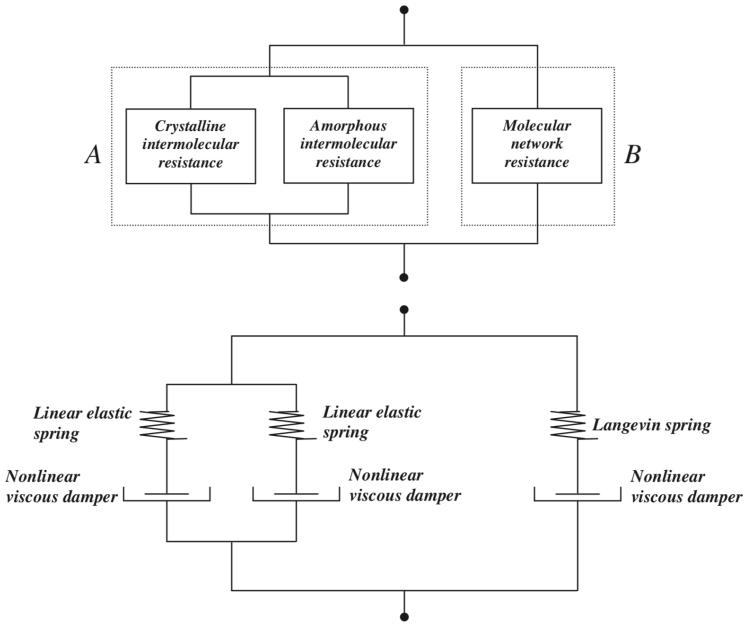

Figure 2.12: One possible rheological model for representing resistances in a semicrystalline thermoplatic. The intermolecular resistance, A, is separated into two parallel resistances representing contributions from the amorphous and crystalline phases. The network resistance, B, is in parallel with the intermolecular resistance. Reprinted from [31], Copyright 2011, with permission from Elsevier.

model for a semicrystalline thermoplastic with separate intermolecular resistances for each phase. The representation in Fig. 2.12 depicts the case where the phases are treated as parallel resistances (strain is shared, stress is additive), but Ahzi et al. 2003 [63] also explores the case where the phases are treated as resistances in series (strain is additive, stress is shared). To model SIC, Ahzi et al. 2003 [63] used a phenomenological equation derived by Doufas and co-workers [71–73] based on the non-isothermal version of the Avrami equation. Later Ayoub et al. [31, 74] would modify the models of Ahzi et al. 2003 [63] and Boyce et al. 2000 [58] to improve predictions of cyclic loading of PE. The semicrystalline models discussed so far have been rheological, in that their constitutive behavior can be represented by systems of springs and dashpots, each with their own constitutive behavior. However, another class of models, referred to as *micromechanical models*, treat the semicrystalline polymer as an aggregate

of randomly oriented composites. One such micromechanical model was proposed by van Dommelen et al. 2003 [75] based on the works of Lee et al. [76, 77]. In the model of van Dommelen et al. 2003, the two phases are treated as a layered composite. The amorphous phase is isotropically elastic with orientation hardening predicted by the 8-chain model and the crystalline phase is anisotropically elastic and flow is governed by crystallographic slip. A hybrid local-global interaction law is used to predict the macroscopic response.

2.4 Homogenization-based micromechanical damage models

Semicrystalline thermoplastics cavitate, which generates micromechanical damage in the form of voids, see Section 2.1. Additionally, aging a semicrystalline thermoplastic can either promote cavitation or directly form chemical cracks, see Section 2.2. Voids cause the apparent mechanical behavior to differ from that of the solid material. Furthermore, voids may grow or rotate during plastic deformation, further complicating the relationship between the apparent and solid mechanical behavior. After sufficient deformation, voids coalesce, initiating fracture. Therefore, constitutive models for a solid polymer alone, such as those presented in Section 2.3, may not be suitable in applications where there is significant void growth, such as in the deformation of aged semicrystalline thermoplastics.

To account for the growth of voids, constitutive models have been formulated for porous materials. One approach to the formulation of such models is to consider a representative volume element (RVE) that consists of a void embedded in a matrix. Using homogenization theory and limit analysis, an effective yield surface for the RVE is derived, and constitutive laws for the effective behavior are formulated [45]. In this way, the effective behavior of the matrix–void composite is reduced to a constitutive law that can then be applied to a material point without the need of explicitly modeling the void. Instead, the constitutive law considers a small set of state variables that characterize the average state of damage in the material. Evolution laws for these state variables are then formulated and coupled with the constitutive law for the porous media. The family of constitutive laws that follow this approach are referred to in this dissertation as homogenization-based micromechanical

damage models. They are so-named because they homogenize the effective response of an RVE containing micromechanical damage (a void) to produce a constitutive equation for the apparent mechanical behavior.

The first model of this type was formulated in Gurson 1977 [32]. Gurson considered both a spherical RVE with a spherical void and a cylindrical RVE with a cylindrical void. In both cases, a rigid–perfectly plastic matrix obeying the von Mises yield criterion was used. The yield criterion formulated in Gurson 1977 represents a rigorous upper bound. In the original Gurson model, the only microstructural variable is the void volume fraction. Later, the yield criterion was improved to better match numerical studies in [78, 79] and several other extensions and improvements have been made since then [45].

By considering spherical voids in a von Mises matrix, the Gurson model was limited to isotropic material behavior. However, two sources of anisotropy may be present in porous plastic solids [80]. The first is *plastic anisotropy*, which results from anisotropy of the matrix behavior. In metals, plastic anisotropy is typically initial to the material. However, in polymers, plastic anisotropy is induced by orientation hardening, as described in Section 2.3. The second source of anisotropy is *morphological*, which occurs by the orientation and elongation of the voids. As with plastic anisotropy, morphological anisotropy can be either initial or induced, but is typically induced in both polymers and metals [23, 80].

Plastic anisotropy was incorporated into the Gurson model in Ref. [81] and void orientation effects in Refs. [82–84]. Later, yield criteria coupling both plastic and morphological anisotropy were independently derived following a homogenization approach in Monchiet et al. 2008 [85] and Keralavarma and Benzerga 2008 [86]. Monchiet et al. 2008 derived a yield criterion by homogenizing a spheroidal RVE composed of a rigid-perfectly plastic orthotropic matrix containing a confocal spheroidal void and subjected to general loading conditions. The matrix obeyed Hill's anisotropic yield criterion [87], which is an orthotropic generalization of the von Mises yield criterion. Similarly, Keralavarma and Benzerga 2008 derived a yield criterion by homogenizing a spheroidal RVE composed of a rigid–perfectly plastic Hill-

type matrix containing a confocal spheroidal void. The yield criterion in Keralavarma and Benzerga 2008 considered only axisymmetric loading and constrained the void axis to align with a principal direction of matrix orthotropy. However, the yield criterion in Keralavarma and Benzerga 2008 produced more accurate results [80], since Monchiet et al. 2008 used a more restricted set of trial velocity fields. The evolution of microstructural variables was not studied in either Monchiet et al. 2008 or Keralavarma and Benzerga 2008.

In Keralavarma and Benzerga 2010 [33], the coupling of plastic anisotropy and void orientation was revisited. Once again, a spheroidal RVE containing a confocal spheroidal void was homogenized. The matrix material was rigid-perfectly plastic and obeyed Hill's orthotropic yield criterion. However, the derivation of the yield criterion was improved in three ways: (1) the spheroidal voids could have any orientation within the RVE, (2) the orthotropic matrix could have any orientation within the RVE, (3) the yield criterion considered any general loading of the RVE, not just axisymmetric loads. These improvements resulted in a more general and accurate yield criterion coupling plastic and morphological anisotropy. Additionally, Keralavarma and Benzerga 2010 derived evolution laws for the relevant microstructural variables: the void volume fraction, the void aspect ratio, and the void orientation.

Armed with a general yield criterion coupling plastic and morphological anisotropy, Kweon et al. 2016 [80] implemented the model of Keralavarma and Benzerga 2010 [33] as a user material subroutine (UMAT) in the finite element code Abaqus. The model was implemented in a corotational framework for compatibility with Abaqus. An isotropic hypoelastic law was incorporated. The state variables were solved for using a semi-implicit backward Newton-Raphson scheme. In order to iteratively solve for each state variable, a residual was derived from the evolution laws proposed in Ref. [33]. The one exception was the evolution of the void orientation, which was solved for explicitly. When the void orientation was solved implicitly through a residual, the resulting Jacobian matrix was overly stiff, which impeded convergence.

3. PHOTO-OXIDATION OF SEMICRYSTALLINE POLYMERS: DAMAGE NUCLEATION VERSUS GROWTH

3.1 Introduction

Oxidation-induced embrittlement of polymers is well documented [4, 11]. At fine molecular scales, oxidation induces a cascade of chain scission and crosslinking events. If the chain scission process is spatially uniform within the amorphous phase, or *homogeneous*, the residual ductility of an oxidized specimen is said to be nucleation-controlled. In this case, the oxidation-mediated ductile to brittle transition occurs abruptly (Fig. 3.1a). Arguments for a sharp transition are presented for example in [4]. On the other hand, if chain scission is *heterogeneous*, then the residual ductility is affected by the material's ability to deform while a growing density of microcracks or voids interact. In this case, the ductility is said to be growth controlled. An example of a gradual transition may be found in [11] (Fig. 3.1b).

Significant progress has been made in understanding polymer oxidation using physico-chemical analysis. However, tensile elongation is almost invariably used to assess embrittlement in polymers at macroscopic scales. Whether the residual ductility is controlled by damage nucleation or damage growth cannot be easily determined from physico-chemical characterization. In some polymers, for instance, carbonyl and vinyl growth measured by infrared spectroscopy is an indirect evidence of chain scission, but the latter is not restricted to nucleation-dominated fracture. Likewise, the evolution of crystallinity, say by scission-induced chemi-crystallization [50], does not discriminate the scale that governs damage evolution upon mechanical loading. Chemiluminescence analysis had evidenced rather heterogeneous oxidation in particulate and thin film systems [89]; yet whether the subsequent

Reprinted with permission from "Photo-oxidation of semicrystalline polymers: Damage nucleation versus growth", by K. N. Cundiff, Y. Madi, and A. A. Benzerga. *Polymer*, vol. 188, p.122090, 2020. Copyright [2020] by Elsevier [88].

The appendix appearing with the original article can be found in Appendix B of this dissertation. Where the present chapter refers to online supplementary information, refer to the online version of the original article [88].

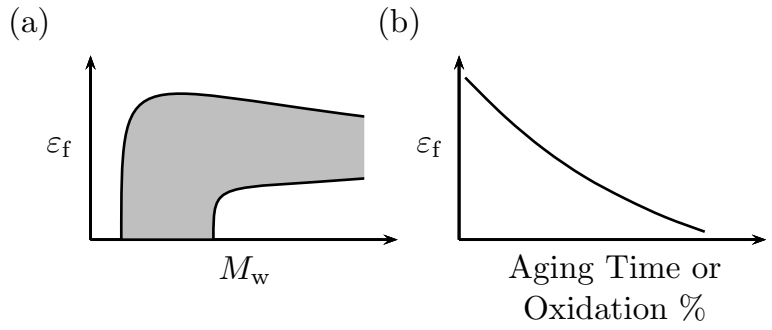

Figure 3.1: Two types of oxidative embrittlement in polymers leading to (a) sharp and (b) gradual ductile–brittle transitions.

damage nucleation is heterogeneous is debated [4]. Molar mass measurements by gel permeation chromatography have proven extremely useful in identifying a critical molar mass above which brittle fracture is not observed [55]; see Fig. 3.1a. However, not only are such measurements averages over samples but they are also strongly affected by mesoscale defects such as voids and microcracks. In fact, small angle X-ray scattering (SAXS) measurements by Zhang et al. [24] have indicated the role of voids and cavities in the deformation of irradiated isotactic polypropylene. Here again, indirect inferences neither confirm nor falsify either mechanism.

As in other damage processes, multiple length scales enter into play in oxidative embrittlement. In order to connect macroscopically measured tensile elongations with molecular-scale mechanisms, intermediate-scale observations are often appropriate, if not necessary. Interestingly, post-mortem fractography is rarely employed for oxidized polymers [11]. This is in contrast with work focused on unaged polymers [21, 23]. A noticeable exception is the extensive fractographic analyses of Qayyum and White [25] who studied several polymers that were UV-aged under natural conditions for extended periods of time.[1]

Here, we investigate the competition between damage nucleation and growth in photo-

[1]In the course of preparing this manuscript, we have come across a recent paper [28] focusing on the fracture of polyamide. Their findings will be discussed in context.

oxidized polyamide-6 (PA-6) by means of carefully instrumented tensile testing. One advantage of using PA-6 is that damage mechanisms by craze-initiated profuse cavitation are now well established in the unaged state [23]. High-resolution videos of the tests are recorded so as to correlate the evolution of surface damage with the overall mechanical response. In addition, synchrotron tomography is used to ascertain the extent of damage and its evolution over time. Also, particular attention is given to obtaining measures of (i) a true strain to fracture, and (ii) a true strain-hardening rate. The latter is key to inferring how the molar mass between entanglements evolves with oxidation, following the procedure of Séguéla [90]; also see [91].

The depth of oxidative damage can be limited by the diffusion of oxygen, as in the case of thermo- or photo-oxidation [16, 27], or can be limited by the attenuation of photons, as in the case of photo-oxidation [27]. In either scenario, the depth of oxidative damage is limited to a surface layer about 100 micrometers thick [16, 27]. To account for this, we use two types of specimens. Films are tested which are thin enough for oxidation to be considered nominally uniform. The films are used for the *in situ* synchrotron tomography experiments, and to infer the true strain hardening behavior of oxidized PA-6. Thin specimens, however, are not ideal for characterizing fracture [30]. Round smooth bars are also used in which a surface layer is oxidized. This specimen geometry allows to access a better measure of true strain to fracture and to carry out dilatation measurements so that the evolution of both ductility and dilatation with oxidation may be ascertained. Most importantly, one can observe surface cracking in real time *in situ*. Incidentally, the use of bulk specimens addresses, if only partially, the important issue of transferability of results to structural components.

3.2 Experimental

3.2.1 Material

The polymer used in all experiments is additive-free polyamide-6 (PA-6), supplied in two forms. A cast plate with thickness 0.5 in was obtained from Plastics International. Cylindrical bars with gauge length 12.70 mm and diameter 4.76 mm were machined from the plate using a lathe. In addition, PA-6 films with two thicknesses 0.06 mm and 0.10 mm were obtained from Goodfellow. The 0.06 mm film specimens had a double fillet, a total length of 75 mm, a gauge length of 6.0 mm and a gauge width of 4.0 mm. The thicker films were used in order to accommodate the custom test-frame used for *in situ* tomography; see Section 3.2.8 below. Thin 33 mm-long specimens were cut from the films using a punch. The specimens had a very shallow notch of radius 30 mm to help localize the deformation and avoid complications associated with propagating instabilities. The minimum width at the notch root was 1.3 mm. The glass transition temperature $T_g = 47\,^\circ\text{C} \pm 4\,^\circ\text{C}$ was measured on the plates using a TA Instruments Q20 DSC.

3.2.2 Aging

The cylindrical bars and films were aged in a QUV Accelerated Weathering Tester by exposure to UV radiation for 48, 96, and 192 h. The aging took place at a temperature of 60 °C, in ambient humidity, and a UV spectral irradiance of $1.55\,\text{W/m}^2\text{/nm}$ with an approximate wavelength of 340 nm. To evenly irradiate the cylindrical specimens, they were rotated by 120° every 8 h. Each 120° section of the lateral surface was aged for the full nominal aging time. Both faces of the 0.1 mm films were exposed to UV radiation. They were flipped every 8 h during aging. Aging conditions are referred to by the nominal duration of UV exposure in hours appended to "UV" (UV48, UV96, UV192).

3.2.3 Conditioning

PA-6 is a hygroscopic thermoplastic [92] in that it absorbs moisture from the air even at ambient temperature and relative humidity. Water acts as a plasticizer in the polymer.

Therefore, as the moisture content of the material increases, the glass transition temperature decreases and thus the material behaves as if the temperature had been increased [93]. In order to regulate the amount of moisture contained in the test specimens, they were conditioned in a Napco model 5831 vacuum oven fitted with a Welch-Ilmvac Duoseal 1400B-01 pump at 80 °C for 72 h prior to testing. This procedure evaporates moisture from the specimen without inducing thermal oxidation.

3.2.4 Differential scanning calorimetry

Differential scanning calorimetry (DSC) was used to characterize the crystallinity of the aged and unaged 0.06 mm-thick film material. Tests were carried out using a PerkinElmer Pyris 1 DSC under the flow of nitrogen gas to prevent oxidative degradation. The samples were heated from 25 °C to 230 °C at a rate of 5 °C/ min. The melting enthalpy of 100 % crystalline PA-6 was assumed to be 190 J/g [94, 95]. At least three samples were used for each measurement.

3.2.5 Mechanical testing

The specimens were tested on an MTS Insight Electromechanical Testing System that was operated in displacement control mode. The tests were conducted at room temperature (24 °C) with a nominal strain rate of 10^{-3} /s. A 30 kN load cell was used for the bulk specimens and a 1 kN load cell was used for the 0.06 mm-thick film specimens. A custom-made loading device was used for the 0.10 mm films, as described in Section 3.2.8.

3.2.6 Extensometry

In this study, nominal force–displacement data is presented using F/A_0 and δ/L_0, where F is the force measured by the load cell, δ is the crosshead displacement, L_0 is the initial gauge length of the specimen, and A_0 is the initial cross-sectional area.

Polymers that undergo large deformations will exhibit plastic instabilities that obscure the intrinsic material response. In tension, the plastic instabilities manifest as necking. As a result, care is required to determine an appropriate metrology for specimen deformation.

Contact strain gauges may lead to premature failure in polymers via the formation of stress concentrations [96], therefore non-contact methods are necessary for accessing, within limits, the intrinsic material behavior. Poulain et al. demonstrate that the intrinsic true stress–strain behavior of a polymer can be approximated by measuring the circumference of a circular specimen using videos, which they refer to as video-based radial extensometry (VRE) [97]. The true strain is approximated as

$$\varepsilon = \ln\left(\frac{A_0}{A}\right) = 2\ln\left(\frac{\Phi_0}{\Phi}\right), \tag{3.1}$$

and the true axial stress as

$$\sigma = \frac{F}{A} = \frac{4F}{\pi\Phi^2}, \tag{3.2}$$

where A is the cross-sectional area, Φ is the diameter, F is the remote applied force, and a subscript 0 denotes values in the undeformed state. Eq. (3.1) is an approximation because it assumes that the deformation is incompressible, the deformation is homogenous in the radial direction, and also that the material is transversely isotropic. Eq. (3.2) only provides the true axial stress, which corresponds to the true stress before the neck forms and after the neck is fully drawn. While the neck is forming, the stress state becomes triaxial and Eq. (3.2) is no longer a valid calculation for the true stress, at least until the neck front is far enough from the minimum diameter that the local stress-state becomes uniaxial again.

For the bulk specimens tested in this study, the true stress–strain behavior was approximated using contour tracking, which is similar to VRE when the specimen cross-section is circular. During testing, *in situ* pictures of the specimen were taken. After the test, these images were processed by a script that identifies specimen contours and then finds the minimum distance between them. The minimum distance between the contours is taken to be the minimum diameter of the cross-section. Assuming the cross-section remains circular, the true strain was calculated using Eq. (3.1) and the diameter measurements output from the script. The true stress was calculated using Eq. (3.2), load measurements from the load cell,

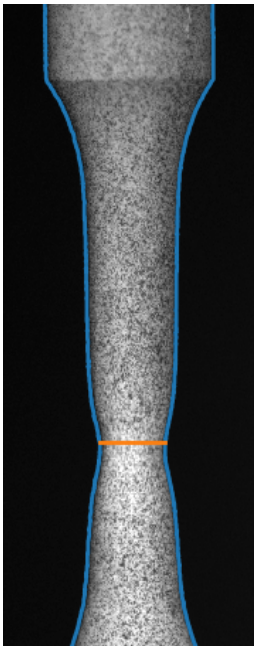

Figure 3.2: Image processed by the contour tracking method. The blue lines are drawn on the edges of the specimen and the orange line is drawn across the shortest distance between the specimen edges. The minimum distance between the edges is assumed to represent the diameter of a circular cross-section.

and the diameter measurements output from the script. Fig. 3.2 shows an example of an image processed by the contour tracking script implemented in this study.

This methodology is also adapted for use with the film specimens. The distance between the contours of the specimen were still identified using image processing, but the distance was assumed to represent the film width. Since the material is treated as transversely isotropic, it was assumed that the thickness contracts by the same ratio as the width. For the films, the true strain was then calculated using

$$\varepsilon = 2 \ln \left(\frac{W_0}{W} \right), \tag{3.3}$$

and the true stress was calculated using

$$\sigma = \frac{F}{A} = \frac{F}{A_0 \left(\frac{W}{W_0}\right)^2}, \tag{3.4}$$

where W is the width of the specimen, F is the force measured by the load cell, and a subscript 0 represents quantities in the undeformed state.[2]

3.2.7 Plastic dilatation analysis

Cavitation plays an important role in the deformation and fracture of PA-6 [22, 23]. Although plastic deformation of PA-6 is incompressible locally, the growth of voids will result in global dilatation for the specimen. This calls into question the applicability of Eq. (3.1), which is a global measure of deformation that assumes incompressibility. Therefore, a speckle pattern was applied to select bulk specimens to facilitate analysis by both digital image correlation (DIC) and contour tracking methodologies. Point-wise Hencky strains along the loading direction were measured using DIC. Using the strains calculated from the DIC and contour tracking methods, an approximation of the plastic volume strain was calculated. The volume strain then provides insight into the significance of void growth for a given specimen.

Without assuming incompressibility, the diameter measurements from contour tracking were used to calculate the lateral strains and the axial strain was measured using DIC. Therefore, the total dilatation was calculated as

$$\varepsilon_{kk} = \varepsilon^{\mathrm{DIC}} + 2 \ln \left(\frac{\Phi}{\Phi_0} \right), \tag{3.5}$$

where ε_{kk} represents the trace of the strain tensor, $\varepsilon^{\mathrm{DIC}}$ is the axial Hencky strain measured by DIC, Φ_0 is the initial diameter, and Φ is the current diameter as measured by contour tracking. The elastic dilatation was calculated using linear elasticity, assuming a completely uniaxial stress state, although this assumption is briefly invalid in the transient state when

[2]To calculate the true strain in the film, Eq. (3.3) assumes a state of plane stress and also that the lateral strains are equal, i.e. $W/W_0 = t/t_0$. This is in addition to the three assumptions listed for Eq. (3.1).

the neck is forming. The plastic dilatation was calculated by subtracting the total dilatation from the elastic dilatation,

$$\varepsilon_{kk}^{\mathrm{p}} = \varepsilon_{kk} - \sigma\frac{1-2\nu}{E}, \tag{3.6}$$

where $\varepsilon_{kk}^{\mathrm{p}}$ represents the trace of the plastic strain tensor, σ is the true axial stress calculated in Eq. (3.2), E is the elastic modulus, and ν is Poisson's ratio. The elastic modulus is estimated as 2000 MPa and the Poisson's ratio is estimated as 0.4. Assuming the plastic dilatation is due to void growth, the void volume fraction can be obtained by integrating the plastic dilatation with respect to time according to

$$\frac{\Delta f}{\Delta t} = (1-f)\frac{\Delta\varepsilon_{kk}^{\mathrm{p}}}{\Delta t}, \tag{3.7}$$

where f is the void volume fraction and Δt is the time step between measurements. Thus, if the initial void volume fraction can be estimated (see e.g. [22]) then one may estimate the void volume fraction in the course of deformation. Otherwise, one may access the ratio f/f_0.

3.2.8 Synchrotron tomography

Microscopic observations of damage nucleation and growth were made *in situ* using high-resolution tomography at the PSICHÉ beamline of the SOLEIL synchrotron in France. To this end, several 0.1 mm film specimens were irradiated for 96 h and conditioned, as previously described. They were then stored in a desiccant for transport to the synchrotron.

A custom-made tensile machine with a 445 N load cell was mounted on the rotation stage of the beamline [29]. Some preliminary tests were carried out prior to observation. Subsequently, a thin specimen was loaded at a constant displacement rate of 10^{-2} mm/s. X-ray micro-tomography scans were composed of 1500 equally-spaced projections. Contrast was obtained by coherent X-rays according to the Beer-Lambert's absorption law using a monochromatic extended parallel beam and a peak energy set to 25.515 keV. An exposure time of 0.2 s was used, resulting in a total acquisition time of about 442 s. The crosshead displacement of the tensile machine was paused for 120 s prior to starting the scan and then

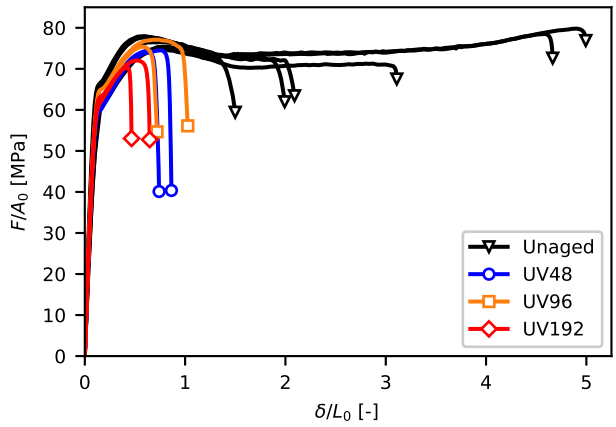

Figure 3.3: Nominal response of photo-oxidized and unaged PA-6 cylindrical bars tested in tension at room temperature (24 °C) and a nominal strain rate of 10^{-3} /s.

remained stationary during the scan. The images were recorded on a high-resolution detector to a 2084×2048 pixel camera, giving an effective pixel size of 0.65 µm. A total of 8 scans were recorded in this study. Both X-ray absorption projections before reconstruction and 3D reconstructed volumes (tomograms) have been used to better understand the effects of aging on the mechanisms of failure.

3.3 Results

3.3.1 Mechanical behavior

Fig. 3.3 presents the nominal stress–strain responses for photo-oxidized (aged) and unaged PA-6 cylindrical bars. Regardless of the aging condition, the mechanical response of each specimen follows approximately the same path up to an abrupt load drop, which corresponds to the initiation of a macroscopic crack. For simplicity, the initiation of the macrocrack that ultimately causes fracture will be referred to as "crack initiation". As will be demonstrated later, many sub-critical cracks form during loading prior to the load drop. The departure from the initial linear response is referred to here as the yield point. Following yield, hardening is observed up to the peak load, which marks the initiation of necking [98].

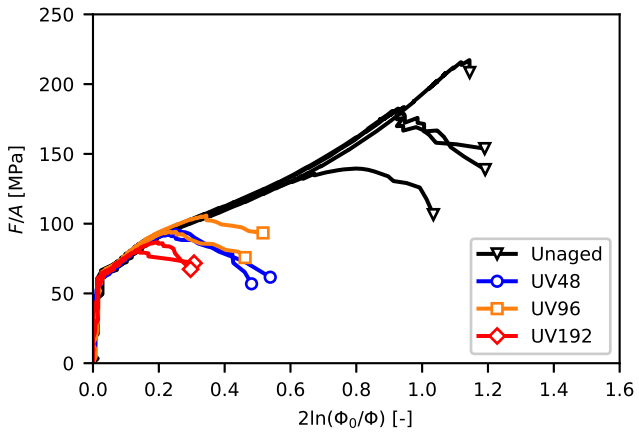

Figure 3.4: True response of photo-oxidized and unaged PA-6 cylindrical bars tested in tension at room temperature (24 °C) and a nominal strain rate of 10^{-3} /s.

After the peak load, the curve exhibits a load drop as the cross-sectional area of the neck decreases. Note that the strain to failure has a much wider scatter in the unaged specimens. Further details will be given in Section 3.3.4.

Fig. 3.4 presents the true stress–strain responses, as determined by contour tracking, for the bulk specimens. Some early tests were conducted without cameras; they are not represented in Fig. 3.4. Specifically, the two unaged specimens with the highest strain to crack initiation in Fig. 3.3 are not included in Fig. 3.4. As with the nominal response, the true stress–strain curves are similar until crack initiation, with failure taking place significantly sooner for photo-oxidized specimens than for unaged ones. Unlike the nominal (specimen-level) response, the true stress–strain response exhibits continuous (apparent) strain hardening beyond yield.

It should be noted that the formation of a neck induces a triaxial stress state so that Eq. (3.2) inevitably overestimates the (effective) true stress in the material. The stress is overestimated until the neck front has travelled sufficiently far away from the minimum section, at which point the uniaxial true stress once again becomes an accurate measure of the effective true stress. Therefore, intrinsic post-yield softening might be masked during

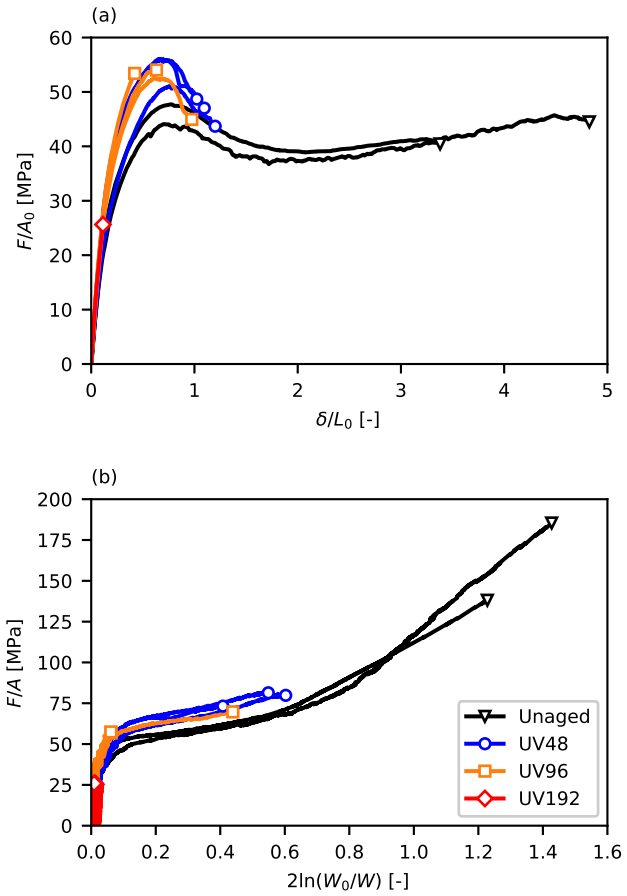

Figure 3.5: (a) Nominal and (b) true mechanical response of photo-oxidized and unaged PA-6 films tested at room temperature (24 °C) and a nominal strain rate of 10^{-3} /s.

the transient triaxial stress state.

Crack initiation manifests on the true stress–strain curve as a "tail" that departs from the general path initially followed by all specimens. After crack initiation, the reduction in distance between the contours is no longer a result of straining, but instead a result of crack propagation into the core of the specimen. In this case, Eq. (3.1) is no longer a valid strain calculation. Only a portion of each "tail" is shown in Fig. 3.4 to facilitate the identification of crack initiation and to demonstrate the gradual nature of cracking in these specimens.

The nominal responses of the film specimens are presented in Fig. 3.5a. Unlike the bulk specimens, there is no clear limit of proportionality for the films. Instead, there is a gradual

rollover to the maximum load. Only the unaged films exhibit large enough strains for post-peak hardening to manifest on the nominal responses. The UV48 films fracture after the peak load whereas the UV192 film fractures while still exhibiting an approximately linear response. The situation is intermediate for the UV96 films. Only one mechanical test on a UV192 film is reported; other realizations broke at the grips or during handling due to extreme brittleness.

A key observation in Fig. 3.5a is that, unlike the bulk specimens, the strength of the film specimens is affected by photo-oxidation. There is strengthening at low UV doses (UV48) followed by weakening. This effect of aging on flow strength is somewhat counter-intuitive.

The true mechanical behavior of the films is presented in Fig. 3.5b. Once again, no intrinsic softening is observed post-yield, although that does not preclude its existence given that a transient triaxial stress state will lead to a brief overestimation of the true stress. Most importantly, apart from the brittle UV192 condition, all film specimens exhibit significant strain hardening. This could not be ascertained based on the nominal responses of Fig. 3.5a.

3.3.2 Strain to crack initiation

Fig. 3.6 shows the strain to crack initiation (or simply strain to failure, ε_f) in bulk (Fig. 3.6a) and film (Fig. 3.6b) specimens. The insets only plot data on aged specimens. The strain to failure decreases, as expected, with increasing UV exposure. A sharp decrease is observed from the unaged condition to the UV48 condition. After this initial sharp decrease, the strain to failure continues to gradually decrease with increasing UV aging.

In the films, the decrease in ε_f after 48 h of aging is steeper than in bulk specimens, as can be seen by comparing the slopes in Figs. 3.6a and 3.6b. Photo-oxidation of the bulk specimen results in a "composite" specimen consisting of a brittle skin over a ductile substrate. Even after the brittle skin cracks, the ductile core sustains further deformation without catastrophic failure. The brittle films have no such support, so crack growth is fatal much earlier. For the UV192 film, fracture is nearly immediate.

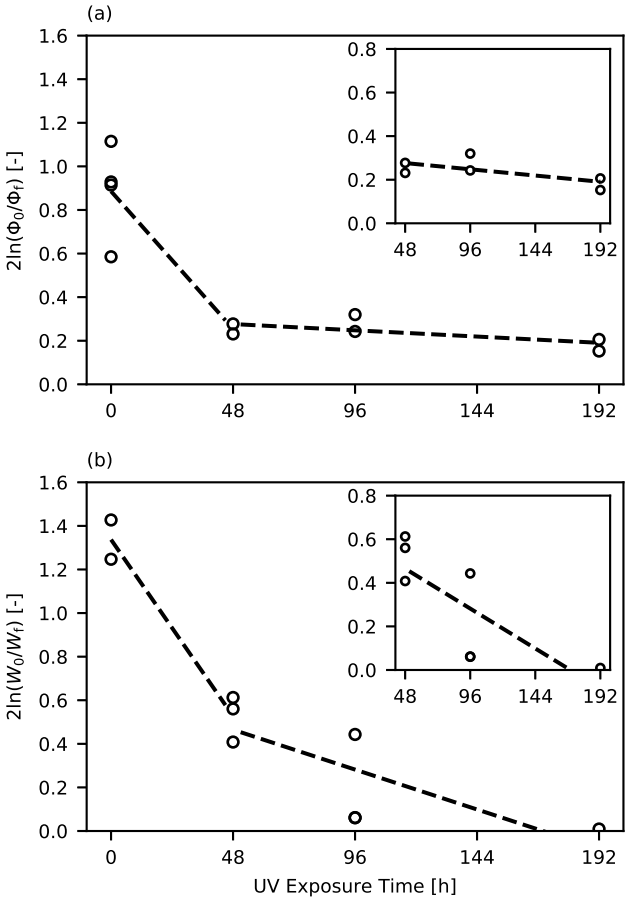

Figure 3.6: Effect of photo-oxidation on the strain to failure of PA-6 (a) cylindrical bars and (b) films. The insets exclude unaged data points to better compare trends among the aged specimens. Linear fits of the data are included to guide the eye.

3.3.3 Strength and molar mass between entanglements

Fig. 3.7 summarizes the effects of photo-oxidation on strength and strain hardening in both bulk and film specimens. To assess changes in strength with aging, the yield stress, defined as the limit of proportionality, is used for bulk specimens, while the stress at the maximum load is used for the film specimens. The key trends are insensitive to the precise definition.

Because of the limited depth of the oxidation layer in a bulk specimen, no effect of photo-oxidation is likely to be detected, Fig. 3.7a. Therefore, the average load bearing capability

of the volume is unchanged.

On the other hand, the strength of the films is clearly affected by photo-oxidation, Fig. 3.7b. Since the specimen thickness is below 100 µm, the entire volume of the film is nominally oxidized during aging. The inset in Fig. 3.7b plots the crystallinity of the films against the duration of UV exposure. An increase in strength is observed from the unaged condition to UV48. The inset reveals that chemi-crystallization is responsible for at least a portion of the strengthening. However, other physico-chemical mechanisms, such as cross-linking, may play a role as well [11]. A slight decrease in strength is observed from UV48 films to UV96 films, while the crystallinity at these conditions is essentially constant. For this aging interval, the loss of strength may be due to some combination of aging-induced microcracks and chain scission. From UV96 to UV192, a significant loss of (apparent) strength occurs. For all film conditions other than UV192, the maximum force corresponds to the onset of necking and changes in strength represent changes in the stress at which necking is induced. For the UV192 films, the load never reaches the stress required for necking, and therefore the reduction in strength is due to catastrophic embrittlement. A reduction in crystallinity is also observed from UV96 to UV192 films. This indicates that at extremely long durations of aging, the crystalline phase has a limited vulnerability to oxidative attack; see Fig. B.1 in Appendix B for typical thermograms from the film specimens.

The molar mass between entanglements, M_e, can be approximated from the strain hardening of a semicrystalline polymer [90]. By assuming ideal network behavior in the amorphous phase and also that plastic deformation in the crystalline phase occurs at a constant stress, the strain hardening can be described by the stress–stretch relationship of a rubber network,

$$\sigma = \frac{\rho R T}{M_e} \left(\lambda^2 - \lambda^{-1} \right), \tag{3.8}$$

where σ is the true stress, ρ the density of the amorphous phase, R the gas constant, T the temperature, and λ the stretch. Such analysis is only possible for films. Analyzing

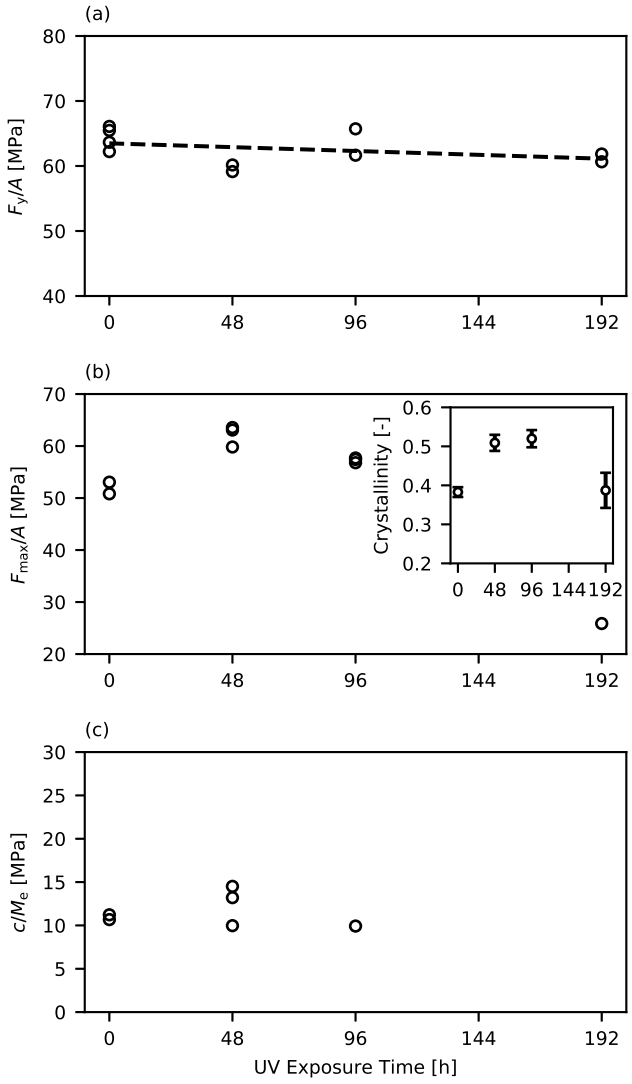

Figure 3.7: Effect of photo-oxidation on (a) the yield stress of bulk PA-6; (b) the true stress at maximum load and crystallinity (inset) of PA-6 films; and (c) the molecular weight between entanglements, M_e (see text for details).

the effects of aging on M_e using the strain hardening is inappropriate for bulk specimens, since their overall strength is not affected by aging, due to the limited depth of oxidative damage. However, the films are thin enough for nominally constant degradation across the thickness. Also, the same analysis cannot be used to make inferences for the UV192 film, since it fractured before the onset of strain hardening.

In Fig. 3.7c, the slope of F/A vs. $(\lambda^2 - \lambda^{-1})$ is used to estimate relative changes in M_e based on Eq. (3.8). The slope is fit for data between the peak force and $\lambda = 2$. Data above $\lambda = 2$ is ignored because the unaged specimens see a change in slope around this stretch, and the aged specimens fracture before this stretch.[3] The plot of F/A vs. $\lambda^2 - \lambda^{-1}$ is presented in Fig. B.2 in Appendix B.

The estimation yields values for M_e that are around 250 g/mol, which is approximately twice the monomer molar mass of PA-6, 113.16 g/mol. The calculated values of M_e are too low as result of the high post-yield hardening slopes ($\frac{\rho RT}{M_e} \approx 15$ MPa). In the influential model of Haward and Thackray [59], the resistances to deformation in a thermoplastic below T_g are categorized into two parts. The first is an intermolecular resistance due to segment rotation, modeled with a viscous component, and the second is the entropic network resistance, modeled with rubber elasticity [57, 59]. The approximation in Eq. (3.8) assumes that the network resistance is the only source of hardening and neglects an important component of resistance for $T < T_g$. In other words, an unrealistically over-entangled network is calculated by trying to predict the hardening of a glassy polymer using rubber elasticity alone. In spite of that, the normalized values in Fig. 3.7c still provide relative information about the post-yield hardening. There are unaged, UV48, and UV96 realizations all with the same hardening rate, but with decreasing ductility (Fig. 3.6b). Even without accessing the true values for M_e, the post-yield hardening rate is due, in part, to the entanglement network. That embrittlement occurs without a reduction in the hardening rate hints that the destruc-

[3] A minor corrigendum to [88] is presented here. The text should have been: "The slope is fit for data between the peak force and $\lambda^2 - \lambda^{-1} = 2$. Data above $\lambda^2 - \lambda^{-1} = 2$ is ignored because the unaged specimens see a change in slope around this stretch, and the aged specimens fracture before this stretch."

tion of the entanglement network is not solely responsible for aging-induced embrittlement.

3.3.4 Macroscopic damage observations

Figs. 3.8 and 3.9 illustrate how physical events in the bulk tests correspond across the test images, the nominal response curves (Fig. 3.3), and the true response curves (Fig. 3.4). The initial undeformed image is presented in each case. Videos of the tests with animated stress–strain curves are available in the online supplementary material (see Vids. B.1 and B.2 for videos of Fig. 3.8 and Fig. 3.9, respectively).

In unaged specimens, a constant load is eventually reached after necking and the neck is cold-drawn in a steady-state. During this time, the neck front moves along the axis of the specimen. Material on either side of the front maintains an approximately constant diameter and nearly all the deformation occurs via the movement of the front [98]. Once the neck is fully drawn along the gauge length of the specimen, the material may exhibit specimen-level hardening. At any point in this process, crack initiation may occur, marked by an abrupt decrease in load and a departure from the stress–strain path generally followed by the specimens, see Fig. 3.3.

Fig. 3.8 shows images from a tensile test on a cylindrical bar of unaged PA-6 that failed after its neck propagated across nearly the entire gauge length of the specimen. The first event identified is yield (Image 1). Here, yielding is roughly defined as a departure from the initial linear behavior in both the nominal and true stress–strain curves. The next event identified is when the specimen reaches its peak nominal stress (Image 2). This point corresponds to an inflection point in the true stress–strain curve. Image 2 in Fig. 3.8 reveals that deformation is still homogenous up to this point, but necking initiates shortly thereafter. Past its peak, the nominal stress decreases until a steady-state is achieved, also referred to as cold-drawing, which is the next event identified (Image 3). Image 3 in Fig. 3.8 reveals that the neck forms in between the peak stress and cold-drawing. The final stage (Image 4) corresponds the the last image taken before fracture. For the specimen depicted, the neck propagated across the majority of the gauge section. In other unaged bars, different amounts

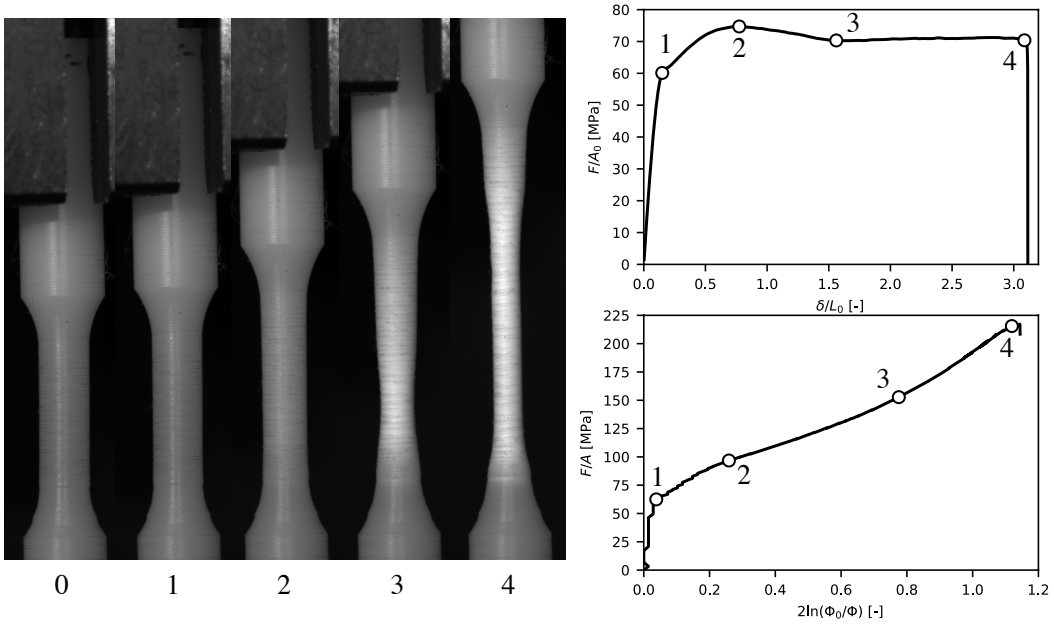

Figure 3.8: Images from a test on a cylindrical bar of unaged PA-6. The images are labelled to identify their locations on the nominal and true stress–strain curves. The images correspond to (0) the undeformed specimen, (1) yield, (2) the nominal peak stress and the initiation of necking, (3) the beginning of cold-drawing, and (4) the final image taken during the test. Full videos of the test can be found online in the supplementary material (see Vid. B.1).

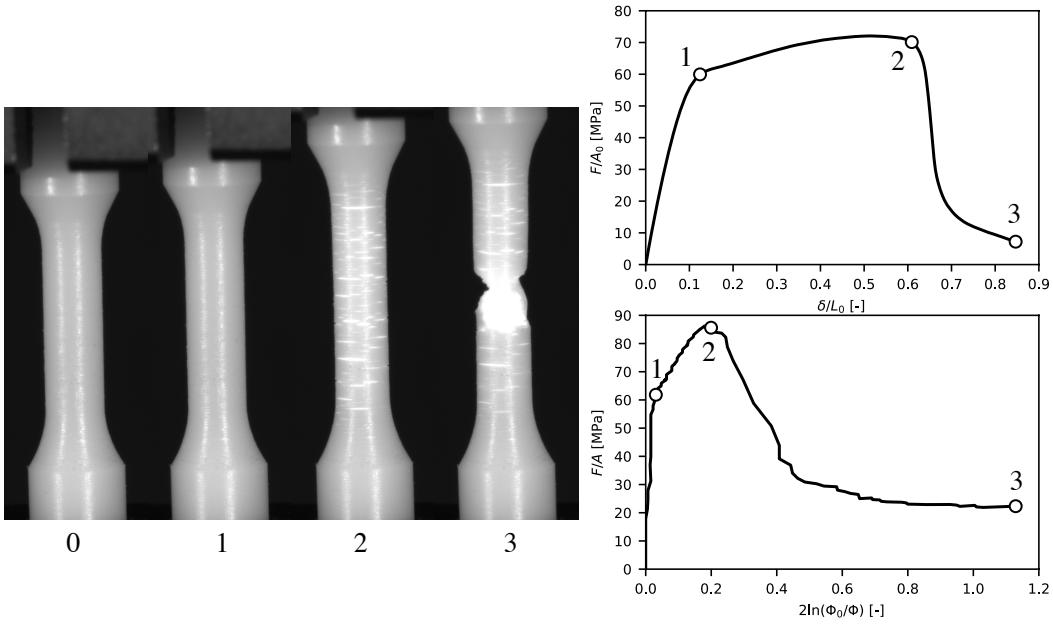

Figure 3.9: Images from a test on a cylindrical bar of PA-6 aged for 192 h. The images are labelled to identify their locations on the nominal and true stress–strain curves. The images correspond to (0) undeformed, (1) yield, (2) crack initiation, and (3) final image taken during the test. Full videos of the tests can be found online in the supplementary material (see Vid. B.2).

of neck propagation were responsible for the large differences in the strain to crack initiation.

In the unaged specimens, the strain to failure exhibits a wide scatter. The scatter is likely affected by pre-existing defects that are activated when the neck front passes over them, initiating failure and preventing any further drawing of the neck [19]. If the neck initiates near such a defect, then the axial elongation is limited. For the unaged specimen with the lowest strain to failure, Fig. 3.3, the neck has formed very near such a defect; therefore, the specimen breaks before the neck fully develops. In the case shown in Fig. 3.8, the neck forms and propagates across most of the gauge length before fracture occurs. In the specimen with the highest strain to failure, also shown above in Fig. 3.3, the neck actually reaches one loading end causing an apparent hardening after the steady state. Several unaged specimens fractured during the formation or drawing of the neck. In these cases, the fracture occurs near the edge of the propagating neck. This difference in the circumstances of fracture is responsible for the wide scatter of strain to failure in the unaged specimens.

It is worth emphasizing that the formation of the neck induces a transient triaxial stress state. Therefore, F/A does not represent the true stress during the transient. At the start of cold-drawing, the neck has reached its minimum radius and begins to propagate across the gauge section. As the neck fronts move away from each other, some region of the specimen will become cylindrical again and the stress state returns to a uniaxial one. At any point during deformation, the specimen might form a crack or otherwise lose its integrity, which manifests on the nominal stress–strain curve as a sharp decrease in stress shortly followed by failure of the specimen.

For the photo-oxidized specimens, damage in the form of profuse cracking occurs before any localized necking. Fig. 3.9 shows selected images from a test on a cylindrical bar aged for 192 h. Small cracks begin to form well before the peak nominal stress is reached and profuse cracking on the surface is evident at (macro) crack initiation (see Image 2 from Fig. 3.9). After crack initiation, the crack travels into the unaged bulk, which still retains a significant amount of ductility, as demonstrated by the long "tail" on the nominal and true stress–strain

curves in Fig. 3.9. Recall that the diameter-based strain measured beyond crack initiation is not an actual measurement of the true strain; the contours of the specimen become closer because cracks are moving into the bulk, not because the diameter is contracting from strain.

Unlike in Fig. 3.4, the stress–strain plot in Fig. 3.9 retains data points well beyond crack initiation. Although these points do not accurately represent the true response, they do illustrate the gradual nature of failure in these specimens.

In the photo-oxidized specimens, crack initiation occurs at various points between yield to just after the peak stress. Therefore the photo-oxidized specimens fail before significant strain localization has occurred. The pre-existing defects that cause the scatter in the unaged bars are not activated by the strains at which the aged bars fracture. Therefore, less scatter is observed in the aged bars. The scatter in the strain to failure for a single aging condition can be inferred from the full set of aged data. For example, the UV192 bars give a lower bound for the strain to crack initiation in all other aged bars. Similarly, a UV96 bar has the highest strain to crack initiation and provides an upper bound for UV96 and UV48 aged bars.

Fig. 3.10 shows images of aged cylindrical bars at crack initiation (load drop). Surface crack density clearly increases with the extent of photo-oxidation. Test videos (see Vids. B.3, B.4, and B.2 for UV48, UV96, and UV192 videos, respectively) indicate that the surface cracks become visible before (macro) crack initiation, and grow larger with increasing strain. When specimens were painted with a speckle pattern for DIC analysis, the paint obscured the microcracking until the critical cracks responsible for failure opened up.

Strain measurements from contour tracking and DIC were combined in some tests to estimate the plastic dilatation during tensile testing of bulk specimens and then the plastic dilatation was integrated to estimate the void volume fraction (see Eqs. (3.6) and (3.7)). The relationship between plastic dilatation and strain is approximately linear, with a slope that changes with UV exposure time, as shown in Fig. 3.11a. The linear fits for the unaged, UV48, and UV96 bars all show approximately the same slope, while the fit for UV192 has a

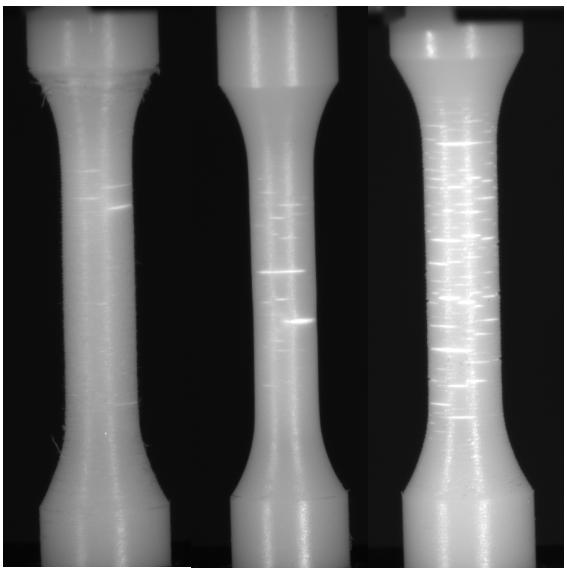

(a) (b) (c)

Figure 3.10: Test images at crack initiation of PA-6 cylindrical specimens photo-oxidized for (a) 48 h, (b) 96 h, and (c) 192 h. Full videos of the tests can be found online in the supplementary material (see Vids. B.3, B.4, and B.2 for (a), (b), and (c), respectively).

higher slope. This is due to the profuse cracking on the surface induced by photo-oxidation as revealed in Fig. 3.10. Surface cracks open during loading, leading to an increase in the void volume fraction of the material.

Assuming that all plastic dilatation is due to cavitation or microcracking, it is possible to estimate the ratio of current to initial void volume fractions using Eq. (3.7). The results are summarized in Fig. 3.11b, which shows an increase by up to a factor of 15 in unaged specimens and by at least a factor of 4 in the most aged specimens. Using an estimate of the initial void volume fraction, $f_0 = 0.01$, based on measurements reported in [22], the porosity in the unaged specimens may reach 15 %. Although the rate of plastic dilatation is greater in the UV192 specimens, the much higher strains achieved by the less oxidized specimens ultimately results in a higher void volume fraction.

In the unaged case, the dilatation is due to cavitation, as seen in the tomography observations of Laiarinandrasana et al. [22, 23]. In the aged bars, the dilatation must be due to a

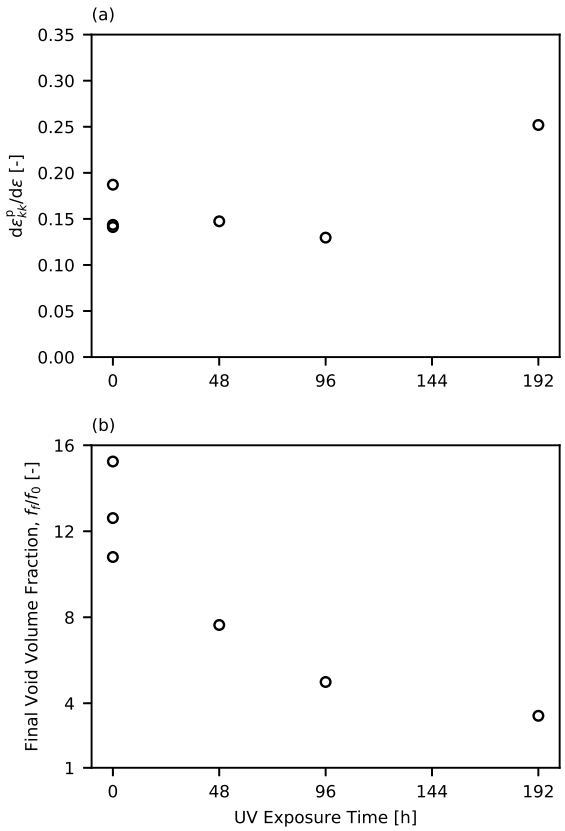

Figure 3.11: (a) Plastic dilatation rate, i.e. dilatation $\varepsilon^{\mathrm{p}}_{kk}$ per unit strain, versus UV exposure time for PA-6 cylindrical bars tested in tension. (b) Estimated final void volume fraction divided by its initial value versus UV exposure time.

combination of cavitation and the growth of aging-induced damage, with the latter becoming more dominant at longer aging times.

3.3.5 Microscopic damage observations

The synchrotron tomography observations on films, as described in Section 3.2.8, are now presented. Fig. 3.12 shows the force–displacement curve during the *in situ* tomography experiment. In order to take a tomography scan, it was necessary to pause the loading, during which time the specimen relaxes somewhat. The locations of scans presented in the main text of this paper are marked on Fig. 3.12. Additionally, all points where loading was resumed are marked. The jagged character of the force–displacement response between

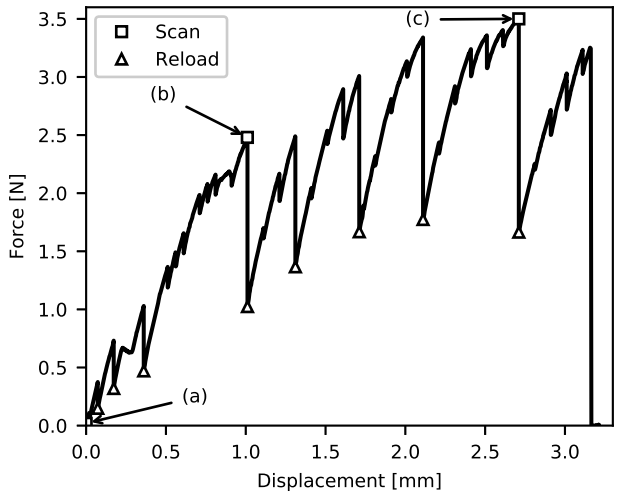

Figure 3.12: Force–displacement curve during *in situ* synchrotron tomography observations of a PA-6 film exposed to UV radiation on both faces for 96 h. The locations of scans presented in Figs. 3.13 and 3.14 are marked along with locations where loading was resumed.

loading and scanning points is due to the sensitivity of the load cell used and the jerky character of plastic flow.

In what follows, two types of images are shown. The first corresponds to X-ray absorption projections of the film. When such images are presented on paper (necessarily 2D), it must be emphasized that features throughout the volume are visible. The second type of images are strictly 2D cross-sections of a 3D reconstruction of a given scan. Often, it is desirable to obtain both types of images for a complete appreciation of the extent of damage.

Fig. 3.13 presents X-ray absorption projections of the width plane. Prior to loading (Fig. 3.13a), there is no visible damage at the microscale. At stage (b) (see Fig. 3.12), damage is clearly visible, Fig. 3.13b. The width plane reveals several long thin cracks that span the entire width of the film accompanied by shorter cracks throughout the length. Most cracks are oriented perpendicular to the load; however, a few cracks are smoothly curved (see top portion of Fig. 3.13b). Fig. 3.13c shows the final set of absorption projections prior to fracture. At this stage, profuse cracking is seen in the film. Many cracks span the

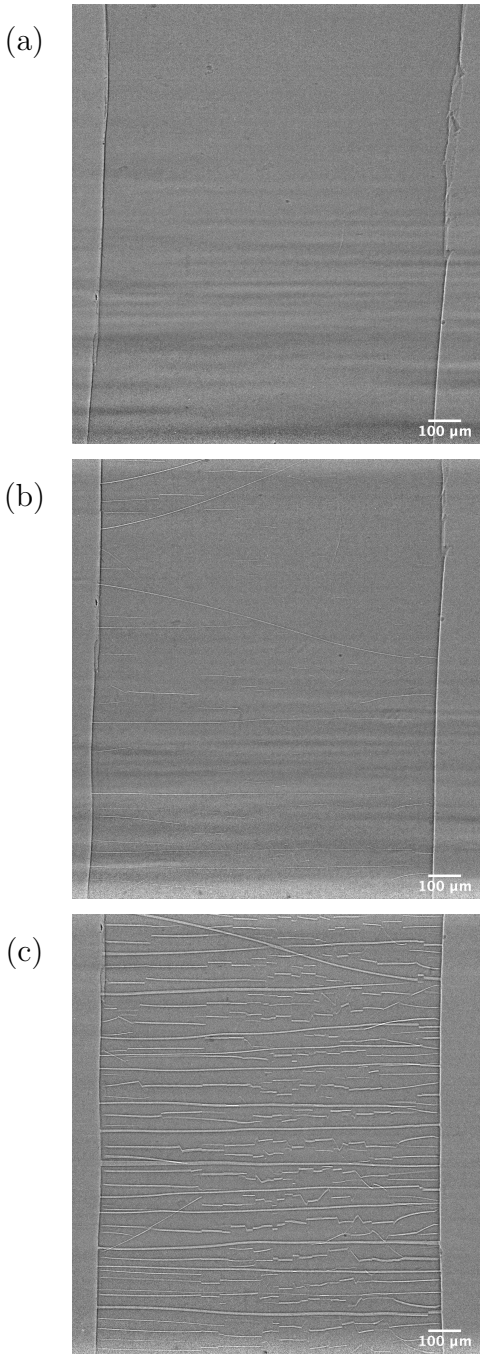

Figure 3.13: X-ray absorption projections from the width plane of a PA-6 film exposed to UV radiation on both faces for 96 h. (a) State of the material prior to loading. (b) First scan where damage is clearly visible. (c) Final scan prior to failure. A video is available in the online supplementary material (Vid. B.5).

entire width; yet, the specimen still had some residual stress-bearing capacity (see Fig. 3.12). Some cracks are straight while others show a "zig-zag" pattern, indicating that many shorter cracks have formed at slightly different heights and then linked up. Also, only one of the three curved cracks previously seen in Fig. 3.13b is now partly visible in Fig. 3.13c because they fall outside the field of view after stretching.

Fig. 3.14 presents the X-ray absorption projections of the thickness plane corresponding to the images in Fig. 3.13. The thickness view reveals that the cracks are confined to the surfaces of the film where photo-oxidative degradation is highest due to the limited diffusion of oxygen. Although damage becomes clearly visible at approximately 70% of the maximum load, some damage is faintly visible as early as 30% of the maximum load (see Vids. B.5 and B.6 in the online supplementary material).

The side view in Fig. 3.14 shows that the damage has propagated from the irradiated surfaces into the core, but no damage nucleates in the center of the film. Therefore, even in this relatively thin specimen, there is a gradient in photo-oxidative damage from the surface to the bulk. Upon continued loading, the microcracks blunt into the more ductile core.

By inspecting the 3D reconstruction of the scans, a clearer picture of the microscale damage can be inferred. For the sake of brevity, we focus here on the final scan and examine two cross-sections, at the front and the back of the film.

On the front face (Fig. 3.15a), a network of mostly parallel cracks run through the width of the film. Keeping in mind that the image is a 2D cross-section, each crack appears as a set of black lines and a gray core: the distance between the black lines represents the crack opening while the gray core shows the core of the specimen (recall that the cracks do not cut through the thickness, as shown in Fig. 3.14).

On the other hand, the "zig-zag" cracks are confined near the back face, as clearly seen in Fig. 3.15b. Zooming into the images online, a complex network of microcracks appears to have formed. In particular, it is difficult to reconstruct the full genesis of the pattern. It suffices to state that multiple micro-shear bands form. These could have either formed

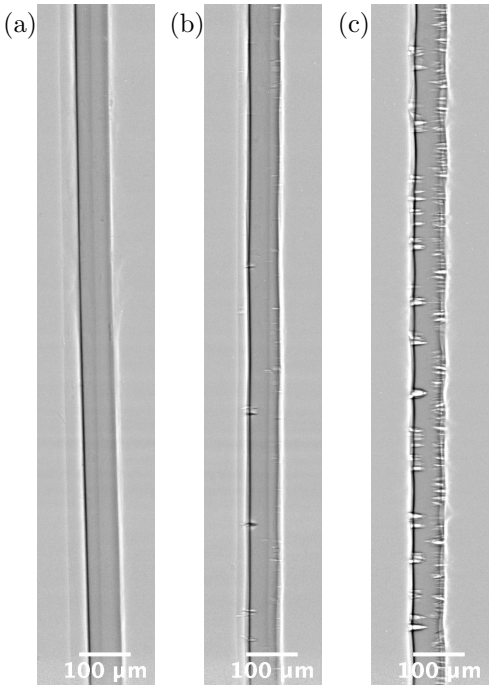

Figure 3.14: X-ray absorption projections from the thickness plane of a PA-6 film exposed to UV radiation on both faces for 96 h. (a) State of the material prior to loading. (b) First scan where damage is clearly visible. (c) Final scan prior to failure. A video is available in the online supplementary material (Vid. B.6).

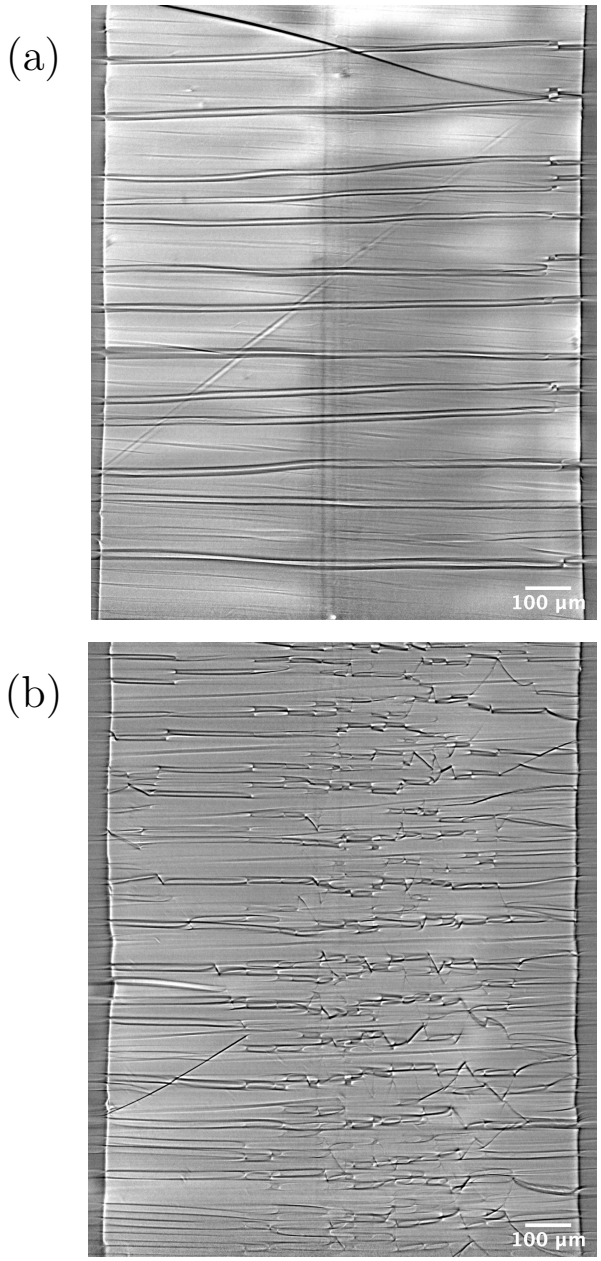

Figure 3.15: Cross-sections of the 3D reconstruction of the final scan prior to failure showing the width plane of a PA-6 film exposed to UV radiation on both faces for 96 h. (a) Front face; (b) back face.

prior to cracking, such as those running across the width, or subsequent to the formation of microcracks at differing heights of the film. It remains that the cracking pattern is quite asymmetrical between the two faces of the film. The asymmetrical development of damage is evident from the thickness view of Fig. 3.14 as well. The left edge of Fig. 3.14c reveals a few larger cracks, while the right edge reveals numerous smaller cracks. This asymmetrical cracking pattern may be due to the history of aging (material on one side must have been aged first); but it is also likely that the asymmetric pattern results from a change in the mechanical state of one face once cracking has begun on the other face.

3.4 Discussion

In the study of oxidative embrittlement of thermoplastics, chemo-mechanical aspects are inevitably intertwined. For ductility to decrease, changes to the internal state must occur, which lead to abrupt or gradual damage progression. For ductility to be severely compromised, cracks must be generated without any remote load, and that requires a "chemical" stress, to be further elucidated below. In recent years, chemical-kinetic models have been developed which connect the concentration of chain scissions to other reaction products that are accessible to quantitative measurement by physico-chemical analytical techniques [4,15]. Chemical-kinetic models shed light on the process of oxidation-induced damage nucleation. However, they alone cannot explain whether embrittlement is abrupt or gradual (Fig. 3.1) for the latter distinction depends on whether the damage process is nucleation- or growth-controlled and a nucleation model is not discriminant in this regard.

Assume, for instance, that the control volume is thin enough for oxidation to be nominally uniform. Chemical-kinetic models provide rate equations for chain scissions (Fig. 3.16a) but do not explain how such scission events give way to microcracks (Fig. 3.16b). It may be argued that, at least for the purpose of understanding the mechanical degradation of polymers, it is the stage depicted in Fig. 3.16b that may refer to damage nucleation. In this sense, mechanism-based damage nucleation models are still lacking, let alone models for microcrack interaction and eventual blunting, Fig. 3.16c.

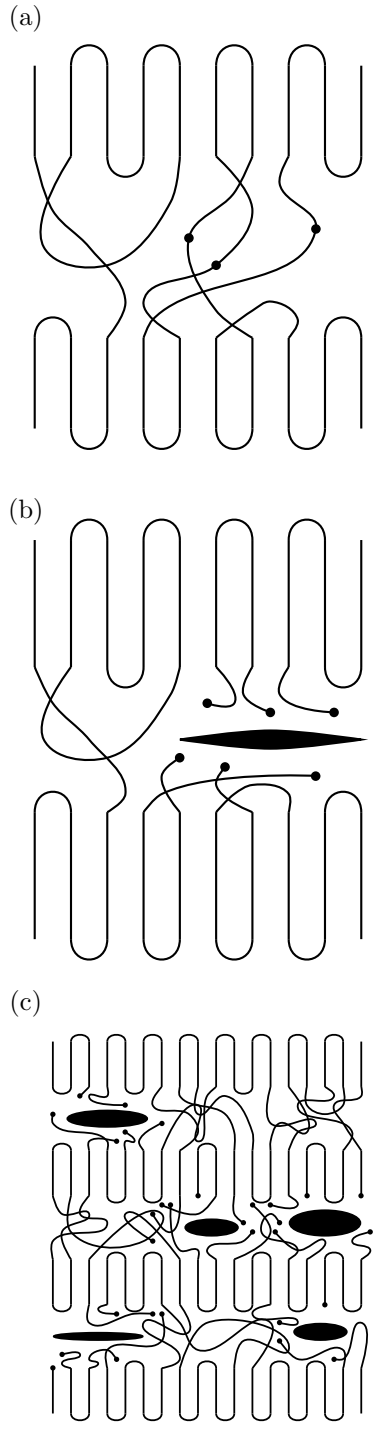

Figure 3.16: (a) Chain scission in interlamellar space. (b) Microcrack formation. Chemicrystallization may also reduce the interlamellar spacing. (c) Heterogeneous oxidation implies dissipation due to microcrack blunting and interaction is dominant.

In many applications, ductile polymers are used in bulk form. The question of how superficial embrittlement affects the integrity of a component or structure is of paramount importance. How do the brittle superficial cracks interact with the ductile core? What is a good characterization measure of the fracture resistance of the layer-core composite? To our knowledge, the chemo-mechanics of polymer degradation by oxidation is largely unaddressed in the literature.

One issue that is often debated is whether chain scission is homogeneous or heterogeneous with the presumed consequence of abrupt versus gradual ductile to brittle transition, respectively, Fig. 3.1. The question is difficult to settle because chain scission is a nanoscale phenomenon. One argument in favor of heterogeneous chain scission that emerges from our experiments is the insensitivity of the (true) strain hardening rate of oxidized films to UV dose, Fig. 3.7c. The procedure of Séguéla [90, 91] allows one to connect the strain hardening rate with the molar mass between entanglements (M_e) so that a change in one implies a change in the other. Although the analysis of post-yield strain hardening cannot predict absolute values of M_e when $T < T_g$, relative changes in the hardening can be used to draw inferences about changes in M_e. Since heterogeneous chain scission is characterized by localized oxidative attack, the constancy of M_e with UV radiation dose is expected. Fig. 3.7c reveals no change in the post-yield hardening for aging times up to 96 h, while reductions in ductility occur at both 48 h and 96 h of UV exposure, Fig. 3.6b. The reduction of ductility without a reduction in the molar mass between entanglements is a strong indicator that homogeneous chain scission is not solely responsible for embrittlement of the films studied here.

Lifetime criteria for aged thermoplastics commonly assume that homogeneous chain scission is the dominant mechanism during aging. However, if ductility is controlled by the molar mass, then aged and unaged polymers with the same molar mass should exhibit the same strain to failure. It is seen in Fig. 3.1 (based on Fig. 2 from [4]) that brittle behavior is not observed above a critical molar mass, but specimens below the critical value can exhibit

both ductile and brittle behavior. Although it is clear that the molecular state plays an important role in determining ductility, other factors must also be relevant to explain these differences.

Regardless of whether chain scission is homogeneous or heterogeneous, one finding from the present investigation is that damage nucleation itself is heterogeneous. Following along the lines above, damage nucleation refers here to the formation of microcracks, as sketched in Fig. 3.16b. Cracking becomes visible well before the peak load and the surface density of cracks increases with both strain and oxidation levels, Fig. 3.10 (Also see Vids. B.3, B.4, and B.2 in the online supplementary material). Heterogeneous damage initiation is also apparent at the microscale based on synchrotron tomography, Figs. 3.13 and 3.14.

The fact that cracks are observed well before the maximum load is amenable to two interpretations. It is possible that microcracks of the type sketched in Fig. 3.16b result from photo-oxidation then open up when a mechanical stress is applied. It is also possible that the cracks nucleated only after loading. That superficial microcracks can be induced by photo-oxidation is documented [25, 28]. In a companion study on low-density polyethylene, cracks were observed prior to loading in scanning electron microscopy [99]. Tomography observations reported here reveal no damage at the microscale prior to loading. However, damage is clearly visible at one-third of the ultimate axial elongation and some damage is faintly visible at one-sixth of the ultimate axial elongation. However, the two interpretations are not exclusive of one another. There is likely a transition between a microcrack-free oxidized state to an oxidation-induced cracked state depending on the radiation dose.

This transition may be elucidated further by invoking the notion of "chemical stress", that is a residual stress induced by the inward thickening of an oxidized layer (shown white in the sketch of Fig. 3.17a) atop a pristine core (gray). To appreciate the buildup and potential role of the chemical stress, assume that at some instant t, oxygen has diffused inward to a thickness $h(t)$. In some polymers, the superficial oxidized layer changes color so that its current thickness $h(t)$ may be ascertained [100]. Typical penetration depths are of the order

of 100 µm [27]. The superficial layer acts as a process zone for the cascade of chemical reactions that are well described by chemical-kinetic models [4, 15]. Since these reactions are dense within the process zone, we postulate that they would induce a volume change (or swelling) should the deformation be unconstrained. But since the superficial layer is tied to the pristine core, a biaxial stress state arises in the superficial layer. Another possible origin for the residual stress lies in chemical potential gradients associated with oxygen diffusion or density gradients induced by oxidation, either directly by chain scission itself [101] or by chemi-crystallization [102]. At present, it is not possible to ascertain the physical origin of the residual stress, but since it must be related to chemical aspects of oxidation, we call it the chemical stress.

Having so posed the problem, the latter reduces to a mixed mode cracking problem in a system defined by a brittle film constrained by a ductile substrate. The cracking of such systems is often discussed in the context of thermal stresses, as pioneered by Hutchinson and Suo [103] but their treatment is far more general. For our purposes here, various cracking patterns are catalogued based on a dimensionless parameter, Z, defined such that the energy release rate is given by

$$G = Z\sigma_{\text{chem}}^2 h/E_{\text{s}}, \tag{3.9}$$

where σ_{chem} is the chemical stress, h is the thickness of the superficial layer, and E_{s} its elastic modulus. Figs. 3.17a and 3.17b depict two crack patterns that seem especially relevant to oxidative embrittlement. Fig. 3.17a depicts surface cracking ($Z = 3.951$). Surface cracks are initiated from defects in the material, but the cracks are stable and lack the necessary stress to propagate. Fig. 3.17b depicts channeling ($Z = 1.976$), where the stress is sufficient to propagate the crack until an edge or another channel is reached. As shown in Fig. 3.17d, a channeling crack consumes the full thickness of the superficial layer. The process is unstable and can lead to the pattern shown in Fig. 3.17b. Here, we observed surface cracks but no patterned channeling in cylindrical specimens, Fig. 3.10, at least at the resolution of our observations. However, Rodriguez et al. [100] observed surface cracks as well as channeling

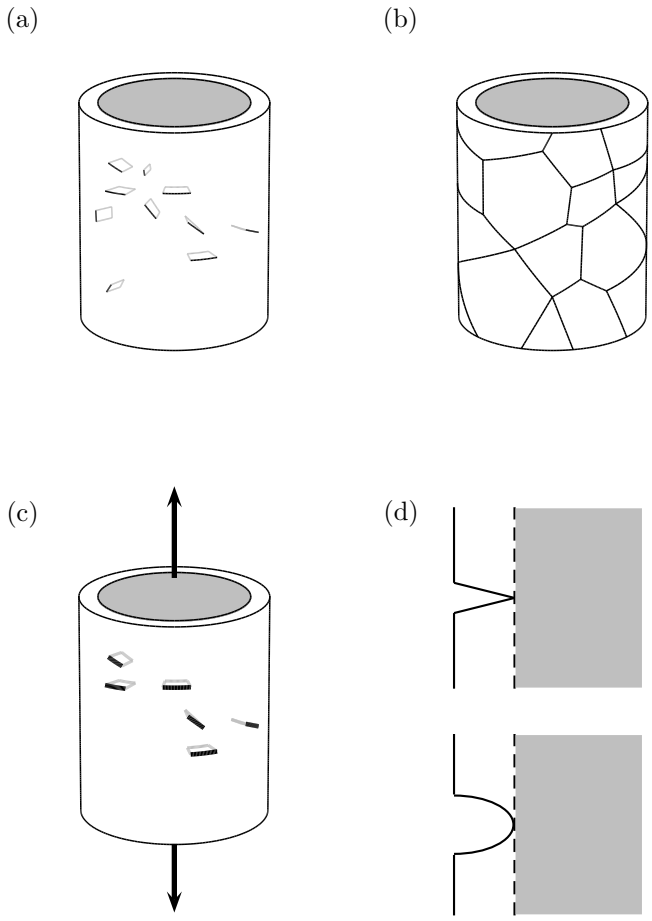

Figure 3.17: Potential cracking patterns in bulk oxidized polymer cylinders. (a) Slit cracks in oxidized layer. (b) Channeling. (c) Opening of subset of slit cracks in tension. (d) Side view of slit crack and its blunting.

depending on oxidation level. In films, it is unclear whether surface cracks consume the entire thickness of the oxidation layer. However, a combination of channeling and surface cracking is likely to have occurred, Fig. 3.15b.

The chemical stress may or may not be sufficient for cracking. This depends on the fracture resistance Γ of the superficial layer, at fixed layer thickness (or oxidation depth). One key difference between oxidative embrittlement and the mixed mode cracking treatment by Hutchinson and Suo is that, in a given oxidation program, the thickness of the layer is an increasing function of time with an eventual saturation $h_{\max}$ set by diffusion-limited

oxidation. Thus, at fixed Γ, which is a characteristic of the polymer, an increasing layer thickness increases the driving force per Eq. (3.9). Another way to employ this equation is to derive estimates for the chemical stress assuming that the critical thickness is known. Indeed, the latter can be estimated from direct observations of cracking or the lack thereof or with the aid of oxidation models. The required chemical stress for a given crack pattern can be expressed in terms of the critical thickness of the oxidized layer by rearranging Eq. (3.9):

$$\sigma_{\mathrm{chem}} = \sqrt{\frac{\Gamma E_{\mathrm{s}}}{Z h_{\mathrm{c}}}}, \tag{3.10}$$

With some estimates for material properties ($E_{\mathrm{s}} = 2000\,\mathrm{MPa}$ based on experiments presented here and $\Gamma = 5\,\mathrm{kJ/m^2}$ [39]) and assuming $h_{\mathrm{c}} = 100\,\mu\mathrm{m}$ [16, 28], the critical chemical stress is 159 MPa for surface cracking and 225 MPa for channeling. Lower estimates would be obtained for LDPE. These values seem plausible, as they are large enough (in comparison with the flow stresses measured) to induce cracking.

When the chemical stress is not large enough to induce cracking then superposition of a mechanical stress would lead to microcrack nucleation in an otherwise weakened bulk polymer. The fact that the crack density increases with strain suggests that microcrack nucleation is heterogeneous enough to warrant a growth-controlled damage process. The fact that it increases with UV dose suggests that the transition is gradual, which is consistent with a growth-controlled phenomenon.

The process of UV exposure is transversely isotropic in the sense that photo-oxidation has no preferential orientation with respect to the specimen surface, although there is clearly a gradient from the surface to the bulk. Despite this, all oxidation-induced damage reported here is oriented perpendicular to the load. In general, three possible sources of orientation can be envisioned. First, a chemical stress is induced by oxidation, but the stress is insufficient to produce cracking. After the superposition of a mechanical load, a preferential orientation is introduced and cracks nucleate perpendicular to the applied load. Given that no damage

is observed prior to loading at macro- or microscales, this is the likely scenario for the results reported here. In the second scenario, the chemical stress is sufficient to produce an array of randomly oriented cracks, Fig. 3.17a. After the application of a load, only a subset of cracks are activated on the basis of their orientation, Fig. 3.17c. In the final scenario, the processing conditions of the oxidized polymer might result in a preferential orientation for crack formation. In Rodriguez et al. [99], oriented surface cracks are observed in highly aged films specimens prior to loading, while randomly oriented cracks are observed on the surface of bulk specimens. These differences are likely due to different processing conditions. There are also other reports in the literature of the orientation of oxidation-induced damage being affected by processing conditions [102].

The results presented here also have applicability to the fracture of bulk components subjected to oxidation by their service environment. Synchrotron tomography observations of unaged PA-6 by Laiarinandrasna et al. [22, 23] reveal penny shaped cavities that elongate during loading and eventually cause failure by coalescence. The cavities show the greatest volume change at the center of the bars, where the triaxiality is highest. It is presumed that the dilatation measured here in the unaged specimens in Fig. 3.11 is due to this damage mechanism. For the UV48 and UV96 bars, the rate of dilatation is nearly identical to that of the unaged bars, indicating that cavitation at the center is still an important mechanism, even while these aged conditions are seen to fracture from the growth of surface cracks. There must necessarily be a transition from fracture mediated by cavitation at the core to fracture mediated by oxidation-induced damage at the surface. Even when fracture in a bulk thermoplastic is mediated by surface damage, several transitions in how that surface damage evolves have been reported in a recent study by Wei et al. [28]. At the lowest oxidation levels, fracture by the coalescence of surface voids is observed in a necked region. As the surface is increasingly oxidized, crack grow until they are arrested by the unaged core. As strain localization begins, cracks are reactivated and propagate through the core, leading to fracture. At the highest level of oxidation, surface cracks, once activated, immediately

travel through the unaged core and result in fracture. Each of these three fracture behaviors is marked by an abrupt decrease in the strain to failure, although changes in strain to failure are artificially abrupt when comparing the axial elongation in a specimen showing extensive necking and a specimen that fractured during neck formation, such as from an unaged condition to a condition with low amounts of oxidation.

3.5 Conclusion

The processes of damage nucleation and growth have been studied in photo-oxidized PA-6 by means of tensile testing and synchrotron tomography observations. The main findings are:

- The molar mass between entanglements is unaffected by oxidation, thus likely implying heterogeneous chain scission. Regardless, oxidation-induced damage is shown to be heterogeneous and the fracture process is controlled by the growth of damage.

- At the macroscale, surface cracks became visible well before the maximum load. The surface crack density was found to increase with increasing oxidation rate and with increasing strain.

- The microscale tomography observations reveal no oxidation-induced damage prior to loading, but damage becomes clearly visible long before the maximum load. Damage in the film appears in the form of both short surface cracks and channels that span the entire width of the film.

- The concept of a chemical stress is invoked to connect chemical changes to macroscopic embrittlement. In this framework, oxidation leads to changes in the volume of a superficial degraded layer restricted from deformation by the unaged core. This induces a biaxial chemical stress that increases as the thickness of the degraded layer increases. The chemical stress may then lead to cracking in the absence of an applied load or with the superposition of some mechanical stress.

- In this way, the fracture of an aged thermoplastic is generally a growth-controlled phenomenon driven by a cascade of events across many scales. These events begin with chemical changes at the nanoscale, followed by the nucleation of cracks due to a buildup of chemical stress at the microscale, eventually culminating in microcrack interaction causing material separation and fracture at the macroscale.

4. ROUND NOTCHED BAR EXPERIMENTS

4.1 Introduction

Chapter 3 investigated the deformation and fracture of aged and unaged cylindrical bars of PA-6. In the unaged condition, the cylindrical bars exhibited a high level of ductility. The specimens underwent neck formation, neck stabilization, neck propagation, and finally fracture at true strains of around 100 %. Additionally, estimates of the plastic dilatation hinted that significant void growth occurred during deformation, which is in accord with other studies that have shown significant cavitation[1] in unaged cylindrical PA-6 bars [22, 49]. However, when the cylindrical bars were UV-aged, the ductility was catastrophically reduced. UV aging causes photo-oxidation, the depth of which is limited by the diffusion of oxygen into the specimen. In thermoplastics, this depth is on the order of 100 µm [16, 27, 28]. The cylindrical bars have a diameter much larger than the depth of oxidative damage, but the ductility was still reduced by the introduction of surface cracks in the aged layer. Upon loading, these surface cracks grow, and eventually propagate into the unaged core. Specimens with higher UV exposure times exhibited a greater density of surface cracks immediately prior to fracture. Therefore, in both the unaged and the aged conditions, the cylindrical bars likely fractured by the growth of microscale damage; the unaged specimens fracture from cavitation [22], while the aged specimens fracture from aging-induced cracks [88].

The stress triaxiality ratio, or simply the triaxiality, is defined as the ratio of the mean normal stress (i.e. the hydrostatic stress) to the equivalent stress;

$$\mathcal{T} = \frac{\sigma_{\mathrm{m}}}{\sigma_{\mathrm{eqv}}}, \tag{4.1}$$

[1] The terminology of Pawlak et al. 2014 [21] is adopted here. The term cavitation is used here to mean a specific mechanism of void formation in semicrystalline thermoplastics that arises from a competition of the strengths of the amorphous and crystalline phases. For more information, see Section 2.1.

$$\sigma_{\mathrm{m}} = \frac{1}{3}\operatorname{tr}\boldsymbol{\sigma}, \quad \sigma_{\mathrm{eqv}} = \sqrt{\frac{3}{2}\boldsymbol{\sigma}' : \boldsymbol{\sigma}'}, \quad \boldsymbol{\sigma}' = \boldsymbol{\sigma} - \sigma_{\mathrm{m}}\boldsymbol{I}, \tag{4.2}$$

where $\boldsymbol{I}$ is the second order isotropic tensor. The triaxiality is an important driving factor for void growth [45]. Given that both unaged and aged cylindrical bars in Chapter 3 fractured from void growth (cavities in the unaged case and cracks in the aged case), a complete characterization of the mechanical behavior in the unaged and aged condition should explore the effects of triaxiality on fracture. However, directly applying a multiaxial stress state to an experimental specimen is not practical. Instead, round notched bars are typically used to investigate the effects triaxiality on deformation and fracture [45]. In a round notched bar, the curvature of the specimen induces a triaxial stress state when the bar is uniaxially loaded. This triaxiality remains roughly constant throughout deformation, so long as the notch geometry is not significantly deformed. Additionally, the triaxiality can be controlled by using specimens with different ratios of the notch radii to the minimum section diameter [104]. These features make round notched bars ideal constant-$\mathcal{T}$ specimens [35,45]. Round notched bars have been used to study cavitation in semicrystalline thermoplastics [23, 37, 105–107], but, to the author's knowledge, have not been used to study damage mechanisms in aged semicrystalline thermoplastics.

This Chapter studies the deformation and fracture of unaged and aged round notched bars of PA-6. The primary objectives of this chapter are to characterize the effects of triaxiality and aging on the mechanical behavior and the development of micromechanical damage. The effects of triaxiality are explored through the use of specimens with different notch geometries. The effects of temperature are also briefly explored. Mechanical tests are used to characterize the fracture strain. Video-based extensometry is used to approximate the amount of plastic dilatation, and therefore the amount of void growth in the specimen. Finally, *ex situ* synchrotron tomography is used to characterize the micromechanical damage in an unaged and aged round notched bar. All of the specimens studied here are *bulk* specimens. The term bulk is used here to describe specimens with a characteristic width

much greater than the nominal depth of oxidative aging, 100 µm. Bulk specimens are useful to study, since many structural components composed of thermoplastics have thicknesses greater than 100 µm. The use of bulk specimens in this study is also a matter of practicality; it would be difficult to machine round notched bar specimens with a radius on the order of 100 µm.

Thus far, aging has only been explored using UV radiation, which induces photo-oxidation [27]. In this chapter, some specimens are exposed to combined hygrothermal and UV aging. This type of aging regimen is chosen to simulate the operating conditions of thermoplastics used in outdoor applications, where significant humidity may exist. Moisture can exacerbate UV aging [27], but can also induce hydrolysis, which leads to chain scission [14, 108].

The outline of this chapter is as follows. Section 4.2 describes the methodology, and Section 4.3 presents the results. A brief discussion of the results is given in Section 4.4, and Section 4.5 summarizes the conclusions.

4.2 Experimental

4.2.1 Material

Additive-free bulk PA-6 was obtained from Plastics International in the form of a cast plate with thickness 0.5 in (12.7 mm). The same cast plate from Chapter 3 was used here. The crystallinity and glass transition temperature of the as-received material were determined by differential scanning calorimetry (DSC) using a TA Instruments Q20 DSC. The crystal mass fraction was calculated as 38 % ± 1 %, assuming that the melting enthalpy of 100 % crystalline PA-6 is 190 J/g. This approximation assumes that multiple crystalline forms of PA-6 are present in the DSC sample [94, 95]. The glass transition temperature was measured as $T_g = 47\,^\circ\text{C} \pm 4\,^\circ\text{C}$. In the as-received material, no glass transition is apparent, since the presence of the crystalline phase suppresses the appearance of the transition in DSC measurements. By heating the material above the crystal melting temperature ($T_{cm} \approx 220\,^\circ\text{C}$) then rapidly quenching, the crystallinity is reduced and the glass transition becomes apparent.

4.2.2 Specimen geometry

Two types of round notched bars were machined from the PA-6 plate using a lathe. The first was a shallow notch specimen, which had a notch radius of 3.90 mm, a notch root diameter of 3.90 mm, and a notch shoulder diameter of 7.00 mm. The second was a sharp notch specimen, which had a notch radius of 1.17 mm, a notch root diameter of 5.85 mm, and a notch shoulder diameter 10.50 mm. A larger notch root diameter and notch shoulder diameter were used for the sharp notch specimen to facilitate video-based extensometry methods. Detailed drawings of these two specimen geometries are shown in Fig. A.1.

During the deformation of a round notched bar, the stress triaxiality is approximately constant, making these specimens ideal for experiments studying the effects of stress triaxiality on fracture [45]. In this work, the round notched bars are designated as RNζ specimens, following the nomenclature used in Kondori and Benzerga 2014 [109]. RN stands for "round notch" (as opposed to PN for a "plane notch") and ζ is the notch severity parameter. The notch severity parameter is defined as

$$\zeta = 10\frac{R_0}{\Phi_0}, \tag{4.3}$$

where R is the notch radius, Φ is the notch root diameter, and the subscript zero indicates the dimensions are measured in the undeformed state. A lower value of ζ corresponds to a higher level of stress triaxiality [110]. The shallow notch specimen has a notch severity of $\zeta = 10$, and is therefore designated as an RN10 specimen. The sharp notch specimen has a notch severity of $\zeta = 2$, and is therefore designated as an RN2 specimen. As R_0 approaches infinity, the specimen geometry approaches a cylindrical bar. In this sense, the cylindrical bars studied in Chapter 3 can be thought of as RN∞ specimens. Using the Bridgman formula [104, 105], the stress triaxiality at the center of an RN bar can be approximated as

$$\mathcal{T}_0 = \frac{1}{3} + \ln\left(1 + \frac{5}{2\zeta}\right). \tag{4.4}$$

Table 4.1: Nominal stress triaxiality at the center of bulk specimens.

Specimen Geometry	$\mathcal{T}_0$
Cylindrical (RN∞)	0.33
RN10	0.56
RN2	1.14

During deformation, R and Φ may change significantly, leading to changes in the stress triaxiality. Additionally, there are gradients in the triaxiality throughout the volume of the specimen, with the highest value realized in center. For this reason, the stress triaxiality calculated from Eq. (4.4) is only the nominal value for the specimen, and is denoted as $\mathcal{T}_0$ to acknowledge the limitations of Eq. (4.4). Table 4.1 lists the bulk specimens used in the present chapter and Chapter 3 along with their nominal stress triaxiality values.

4.2.3 Aging

Two categories of aging regimens were used: UV only and combined UV and hygrothermal aging. Specimens aged under the UV only regimens were aged in a QUV Accelerated Weathering Tester using a spectral irradiance of $1.55\,\mathrm{W/m^2/nm}$ and an approximate wavelength of 340 nm. The aging occurred at a temperature of 60 °C and at ambient humidity. Nominal exposure times from 48 to 192 hours were used. To evenly irradiate the specimens, they were periodically rotated by 120° every 8 h. Each 120° section of the lateral surface was aged for the full nominal aging time. This is the same aging procedure employed for the cylindrical bars in Chapter 3.

Some specimens were aged under a combination of UV and hygrothermal conditions in order to simulate the natural conditions of hot and humid environments. These specimens were aged by alternating between the UV exposure as previously described and hygrothermal exposure. The hygrothermal exposure also took place in the QUV Accelerated Weathering Tester, but the UV lamps were turned off. During hygrothermal aging, the temperature

Table 4.2: Summary of aging regimens for bulk specimens.

Label	UV Exposure, per 120° (h)	Hygrothermal Exposure (h)
Unaged	0	0
UV48	48	0
UV96	96	0
UV192	192	0
HUV48	48	24
HUV96	96	48
HUV192	192	96

was kept at 60 °C, but the relative humidity was increased to 100 %. After every 8 h of UV exposure, there were 4 h of hygrothermal exposure. Then the specimen was rotated by 120° and this process was repeated until each 120° section of the lateral surface area was aged for the full nominal aging time.

Table 4.2 summarizes the aging regimens used. In this dissertation, aging conditions are referred to by their labels as listed in Table 4.2. The labels refer to the type of aging, either UV or HUV (for hygrothermal and UV aging), and the nominal duration of UV exposure in hours. Each HUV condition has a corresponding UV condition with the same duration of UV exposure, but with additional hygrothermal aging.

Supplementary experiments on cylindrical bars and films subjected to UV and HUV aging reveal that the additional hygrothermal aging has a negligible impact on ductility compared to UV aging. For example, a UV48 specimen and an HUV48 specimen will exhibit approximately the same fracture strain. More details on UV versus HUV aging can be found in Appendix F.

4.2.4 Conditioning

Even in ambient conditions, PA-6 absorbs moisture from the air, which acts as a plasticizer, altering its mechanical behavior [1, 93, 111]. In order to control the moisture content

in the specimens, they were dried in a vacuum oven immediately prior to testing. This procedure is referred to as a conditioning treatment. During conditioning, the temperature was controlled using a Napco model 5831 vacuum oven and the vacuum was maintained using a Welch-Ilmvac Duoseal 1400B-01 pump. The specimens were conditioned for 72 h at a temperature of 80 °C. The round notched specimens in this chapter were dried following the same conditioning procedure used for the cylindrical bars in Chapter 3.

The impact of moisture absorbed during ambient conditions on the mechanical behavior of PA-6 RN10 bars is studied in Appendix E. The experimental observations reported there illustrate the importance of conditioning the specimens.

4.2.5 Mechanical testing

The specimens were tested on an MTS Insight Electromechanical Testing System that was operated in displacement control mode. A 30 kN load cell was used to measure the force. The specimens were loaded at a nominal strain rate of $\dot{\delta}/L_0 = 10^{-3}$ /s, where δ is the motion of the MTS crosshead and L_0 is the initial notch height of the bar. Tests were conducted at room temperature (24 °C), 0 °C, and 60 °C. For tests not at room temperature, a custom temperature chamber was used. The temperature chamber is heated using a built in oven and cooled using an attached reservoir of liquid nitrogen.

4.2.6 Extensometry

The contour tracking method presented in Chapter 3 is again employed here to access the true strain in the round notched bars. Contour tracking is a video-based extensometry method that tracks the lateral contractions of the specimen at its narrowest point, then uses this measurement to calculate the true strain in the specimen assuming (1) incompressible deformation, (2) no lateral strain gradients, and (3) the material is transversely isotropic. Using this method, the true strain in a round specimen is given by

$$\varepsilon = 2 \ln \left(\frac{\Phi_0}{\Phi} \right), \tag{4.5}$$

where Φ is the current diameter of the notch root and Φ_0 is its value in the undeformed state. The round notch causes a triaxial stress state, so the true stress in the notch is not equal to the applied load divided by the current cross-sectional area, $\sigma_{\text{eqv}} \neq F/A$. If the current notch curvature is measured in addition to the current cross-sectional area, it is possible to calculate the true (equivalent) stress in a round notched bar [112]. However, no attempt is made here to calculate the true stress. The nominal stress is therefore used when discussing the mechanical behavior of the round notched bars and is given by

$$\sigma^{\text{nom}} = \frac{F}{A_0}, \tag{4.6}$$

where F is the force measured by the load cell and A_0 is the initial cross-sectional area at the notch root.

Due to the difficulty of obtaining clear images through the window of the temperature chamber, contour tracking was not used for tests studying the effects of temperature. Additionally, some early tests on aged bars were conducted without contour tracking. Instead, a laser extensometer was used to measure the nominal strain, calculated as

$$\varepsilon^{\text{nom}} = \frac{\Delta L}{L_0}, \tag{4.7}$$

where ΔL is the notch opening displacement as measured by the laser extensometer and L_0 is the initial notch height.

4.2.7 Plastic dilatation analysis

In Chapter 3, strain measurements from DIC and contour tracking were combined to estimate the plastic dilatation in the cylindrical bars. The plastic dilatation was then integrated to estimate the evolution of the void volume fraction during loading. Those calculations, presented in Eqs. (3.5)–(3.7), are expanded here for applicability to round notched bars.

As with the cylindrical bars, the total dilatation is given by the sum of the axial (Hencky)

strain, as measured by DIC, and twice the lateral strain, as calculated by contour tracking,

$$\varepsilon_{kk} = \varepsilon^{\mathrm{DIC}} + 2\ln\left(\frac{\Phi}{\Phi_0}\right). \tag{4.8}$$

It is assumed that the total strain can be additively decomposed into elastic and plastic components. The components of the stress tensor are approximated to calculate the elastic dilatation. The stress state at the center of a round bar loaded in tension is axisymmetric. When the stress tensor is coordinatized using the orthonormal triad $\hat{\boldsymbol{e}}_i$, where $\hat{\boldsymbol{e}}_2$ points along the loading axis,

$$[\boldsymbol{\sigma}] = \begin{bmatrix} \sigma_{11} & 0 & 0 \\ 0 & \sigma_{22} & 0 \\ 0 & 0 & \sigma_{11} \end{bmatrix}, \quad \sigma_{22} > 0, \quad \sigma_{11} > 0, \quad \frac{\sigma_{11}}{\sigma_{22}} < 1, \tag{4.9}$$

where σ_{22} is the axial stress and σ_{11} is the radial stress. The scalar θ is defined as the ratio of the radial stress to the axial stress and depends on the stress triaxiality. Assuming that the stress triaxiality is constant and equal to the nominal value calculated using the Bridgman formula, Eq. (4.4), the stress ratio is given by

$$\theta = \frac{\sigma_{11}}{\sigma_{22}} = \frac{3\mathcal{T}_0 - 1}{3\mathcal{T}_0 + 2}. \tag{4.10}$$

The axial stress is assumed to be equal to the remote applied stress,

$$\sigma_{22} = \frac{F}{A}, \tag{4.11}$$

where F is the force measured by the load cell and A is current cross-sectional area of the notch root measured by contour tracking. If the elastic strain is approximated using Hooke's

law, then the elastic dilatation is given by

$$\varepsilon_{kk}^{\mathrm{e}} = \frac{1}{E}\left[\sigma_{22} - \nu\left(2\sigma_{11}\right)\right] + \frac{2}{E}\left[\sigma_{11} - \nu\left(\sigma_{22} + \sigma_{11}\right)\right], \tag{4.12}$$

where E and ν are the elastic modulus and Poisson's ratio, approximated here as 2000 MPa and 0.4 respectively. The plastic dilatation is calculated by subtracting the elastic dilatation from the total dilatation,

$$\varepsilon_{kk}^{\mathrm{p}} = \varepsilon_{kk} - \varepsilon_{kk}^{\mathrm{e}}. \tag{4.13}$$

The plastic dilatation is then integrated in time to approximate the void volume fraction,

$$\frac{\Delta f}{\Delta t} = (1 - f)\,\frac{\Delta \varepsilon_{kk}^{\mathrm{p}}}{\Delta t}. \tag{4.14}$$

The void volume fraction of one unaged RN10 bar and one UV192 RN10 bar were analyzed and compared to the results from the cylindrical bars presented in Chapter 3.

4.2.8 Synchrotron tomography

Microscopic observations of damage were made *ex situ* using syncrhotron tomography at the PSICHÉ beamline of the SOLEIL synchrotron in France. One unaged RN10 and one HUV192 RN10 bar were studied. The specimens were mechanically tested using the procedures described in this section, but mechanical loading was stopped at the maximum load and the specimens were unloaded. The specimens were then transported to SOLEIL for study. The images were recorded on a high-resolution detector to a 2084×2048 pixel camera, using an effective pixel size of 0.65 µm. The resulting tomograms contain a $2048 \times 2048 \times 2048$ array of voxels. Each voxel is a cube with a side length of 0.65 µm.

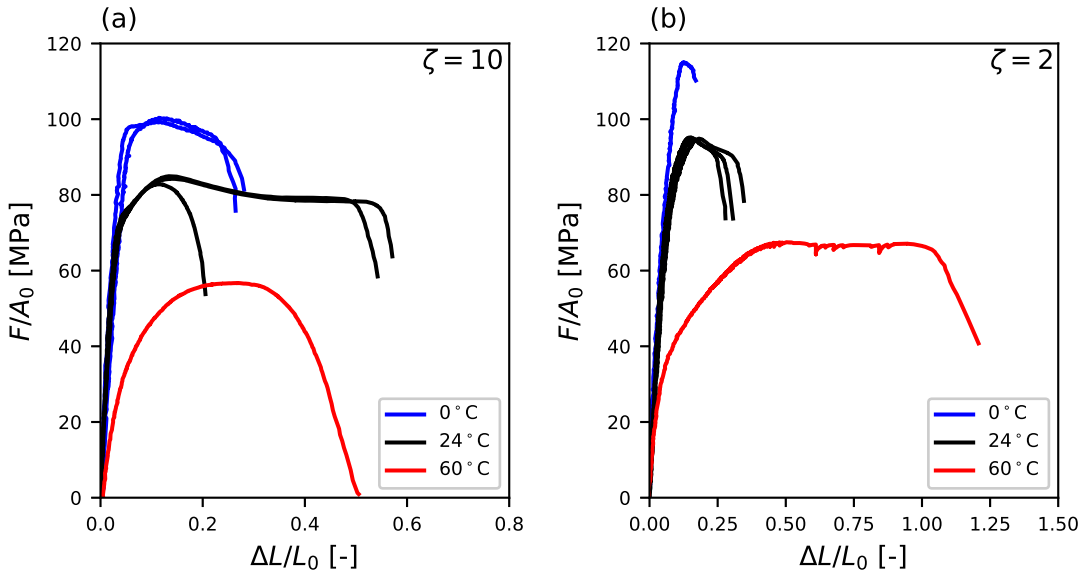

Figure 4.1: Nominal stress–strain curves for unaged round notched bars tested at different temperatures. (a) RN10 bars. (b) RN2 bars.

4.3 Results

4.3.1 Effect of temperature

Fig. 4.1 shows the effect of temperature on the nominal stress–strain behavior of PA-6 round notched bars. Only tests on unaged bars are shown. Results from RN10 bars are shown in Fig. 4.1a, while results from RN2 bars are shown in Fig. 4.1b. For specimens tested below $T_g = 47\,°C$, the stress–strain curves show an initial linear region that gradually rolls-over to a peak nominal stress. After the peak nominal stress, the stress decreases. In most cases, fracture occurs while the stress is decreasing, which is evidenced by a knee in the curve followed by an abrupt decrease in the stress. This knee coincides with crack initiation and the nominal strain at which the knee occurs is referred to as the nominal fracture strain. For two of the RN10 bars tested at 24 °C, a stress plateau occurs before crack initiation.

For specimens tested above $T_g = 47\,°C$, the stress–strain curve is noticeably different. The initial response is not linear. Instead, the slope of the curve gradually decreases until a

stress plateau is reached. Instead of a well-defined peak nominal stress, the maximum stress occurs somewhere along the stress plateau. Crack initiation occurs after the stress plateau. In tests above T_g, the post-knee stress decrease is more gradual than in tests below T_g.

For a given notch severity parameter, ζ, increasing the temperature causes the nominal fracture strain to increase and the peak nominal stress to decrease. This is the expected effect of temperature on the strength and ductility of thermoplastic round notched bars [105]. Fig. 4.1 also shows that decreasing ζ (and therefore increasing $\mathcal{T}_0$) increases the peak nominal stress and decreases the nominal fracture strain, which is the expected trend [105]. However, the trends with test temperature and the notch severity parameter are not followed by the test on an RN10 bar at 60 °C. Given the low number of experimental realizations at 60 °C, this is likely an artifact arising from experimental scatter. For example, compare to the scatter in the nominal fracture strain for RN10 bars deformed at room temperature. Round notched bars of PVDF were deformed at different temperatures in Ref. [105], where it was reported that deformation at lower temperatures resulted in less cavitation.

4.3.2 Effect of aging

4.3.2.1 Mechanical behavior and fracture strain

The effect of aging on the nominal stress–strain behavior of round notched PA-6 bars is presented in Fig. 4.2, where the mechanical behavior of both unaged and UV192 aged bars are displayed. Results from RN10 bars are shown in Fig. 4.2a, while results from RN2 bars are shown in Fig. 4.2b. As previously described, the unaged bars exhibit a peak nominal stress, a decrease in the nominal stress, a stress plateau, and finally crack initiation, indicated by a knee in the curve. On the other hand, the UV-aged bars do not exhibit a stress plateau, and crack initiation appears to coincide with the peak nominal stress.

UV aging reduces the nominal fracture strain and the peak nominal stress. Only a superficial surface layer of the bar is affected by UV aging, since the diffusion of oxygen limits the depth of oxidation to approximately 100 µm [16, 27, 28]. In the aged layer, microcracks

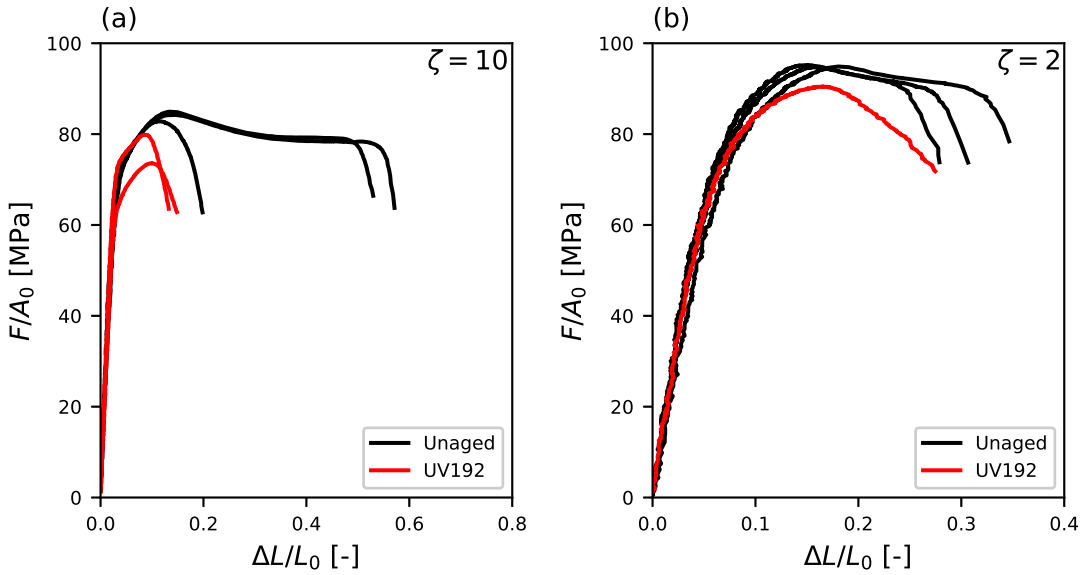

Figure 4.2: Nominal stress–strain curves for unaged and aged round notched bars tested at room temperature (24 °C). (a) RN10 bars. (b) RN2 bars.

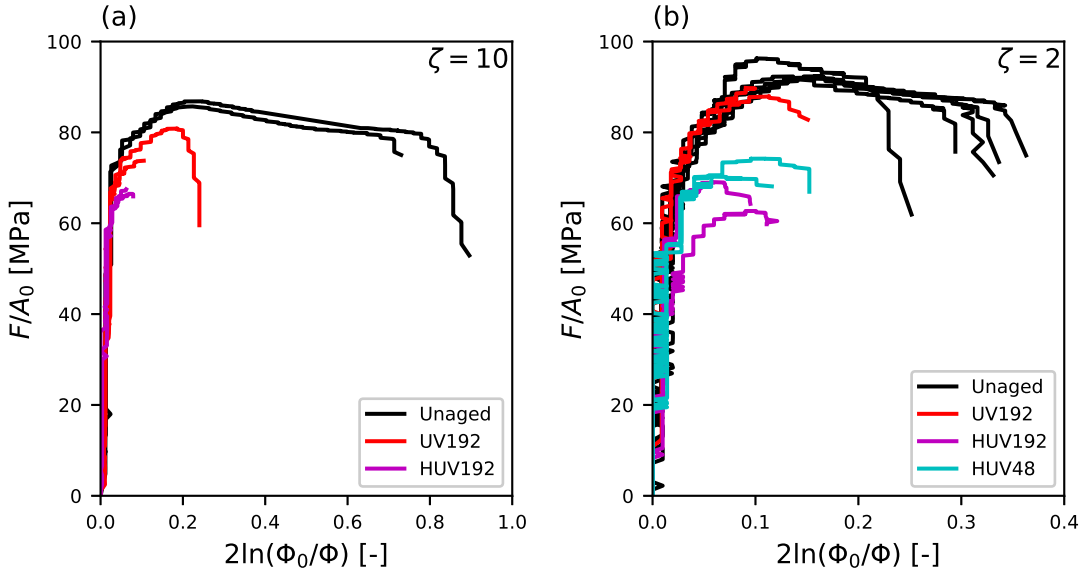

Figure 4.3: Nominal stress–true strain curves for unaged and aged round notched bars tested at room temperature (24 °C). (a) RN10 bars. (b) RN2 bars.

nucleate and grow during loading. Even after the microcracks becomes visible, the applied load continues to increase for a while [88]. Therefore, in the aged bars, the term "crack-initiation" is somewhat misleading, as a population of microcracks exists prior to the knee in the stress–strain curve. However, the microcracks eventually coalesce and grow to form a critical "macrocrack" that leads to failure, causing a knee in the stress–strain curve. This macrocrack is the crack to that is referred to by the term crack initiation. The growth of these microcracks is the mechanism that reduces the fracture strain in the aged specimens [88]. It should be noted that the reduction of the nominal fracture strain by UV aging is more pronounced in the RN10 bar than in the RN2 bar. The microcracks are also responsible for the reduced peak nominal stress. Since the depth of oxidation is much smaller than the radius of the specimens, the effect of UV aging on the average strength of the volume is negligible. Therefore, when the stress–strain curve of the UV-aged bar deviates from the curve of the unaged bar, it is because cracks have begun propagating into the unaged core, reducing the strength of the specimen. At (macro-)crack initiation, the reduction in strength associated with fracture causes a local maximum in the nominal stress–strain curve. Crack initiation in the UV-aged bars occurs at a lower strain than the peak nominal stress in the aged bars, so crack initiation is the cause of the peak nominal stress in the UV-aged bars.

Fig. 4.3 shows the effect of UV aging on the mechanical behavior of round notched bars, except the stress–strain curves use the true strain, as measured by contour tracking. Additionally, Fig. 4.3 shows results from specimens subjected to combined hygrothermal and UV (HUV) aging. Results from RN10 bars are presented in Fig. 4.3a, while results from RN2 bars are presented in Fig. 4.3b. The stress–strain curves in Fig. 4.3 are somewhat jagged due to the resolution of the contour tracking setup used here. The quality of the curves could be improved by using either a higher resolution camera or by placing the camera as close to the specimens as possible without their gauge section extending outside the field-of-view.[2]

[2] Most bulk specimens were tested using the same experimental setup, so the camera was placed in the same location for the cylindrical bars from Chapter 3 as it was for the round notched bars in this chapter. For the round notched bars, this was an inefficient use of the camera's field-of-view, since they have a much shorter gauge section than the cylindrical bar. For the stress–strain curves presented in Fig. 4.7, the camera

With regard to the mechanical behavior of the unaged and UV192 bars, the observations from the nominal stress–strain curves (Fig. 4.2) still hold true when examinging the nominal stress–true strain curves (Fig. 4.3). In the unaged bars, the mechanical behavior is initially linear, followed by a rollover to the peak stress, a stress decrease, a stress plateau, and then crack initiation. In the UV-aged bars, the mechanical behavior is mostly coincident with the unaged behavior until crack initiation or damage otherwise reduces the strength of the specimen. As with the nominal fracture strain, UV aging reduces the true fracture strain. The effect of UV aging on the true fracture strain is more pronounced in the RN10 bars than the RN2 bars. In the UV-aged bars, the peak nominal stress coincides with crack initiation, resulting in a lower peak nominal stress than in the unaged bars.

Fig. 4.3 includes results from HUV-aged specimens, which were not present in Fig. 4.2. HUV-aged and UV-aged specimens with the same UV exposure (e.g. UV192 versus HUV192 aging), exhibit similar fracture strains. This indicates that the additional hydrolysis induced by hygrothermal aging is insignificant compared to the photo-oxidation induced by the UV aging. Therefore, the extent of aging in the conditions presented here is effectively measured using the UV exposure time alone. This observation is also supported by the data in Appendix F, where the effects of HUV aging are more thoroughly studied. However, this does not imply that PA-6 is impervious to hygrothermal aging. HUV aging does reduce the strength of the bars, in contrast to UV aging, which does not affect the strength of the bars until crack initiation. During the hygrothermal cycles, the increased relative humidity and temperature increases the diffusion of water into the specimen, which acts as a plasticizer in PA-6, reducing the strength of the bar [93, 111]. Therefore, this reduction in strength is not an effect of hydrolytic aging. For the unaged and UV-aged bars, a 72 h conditioning treatment was sufficient to remove moisture from the specimens, but this conditioning treatment is too short for the increased moisture content absorbed during the hygrothermal cycles. Experiments in Appendix F reveal that the loss of strength due to HUV aging is

was placed much closer to the RN10 bars. Accordingly, the true strain measurements are less noisy.

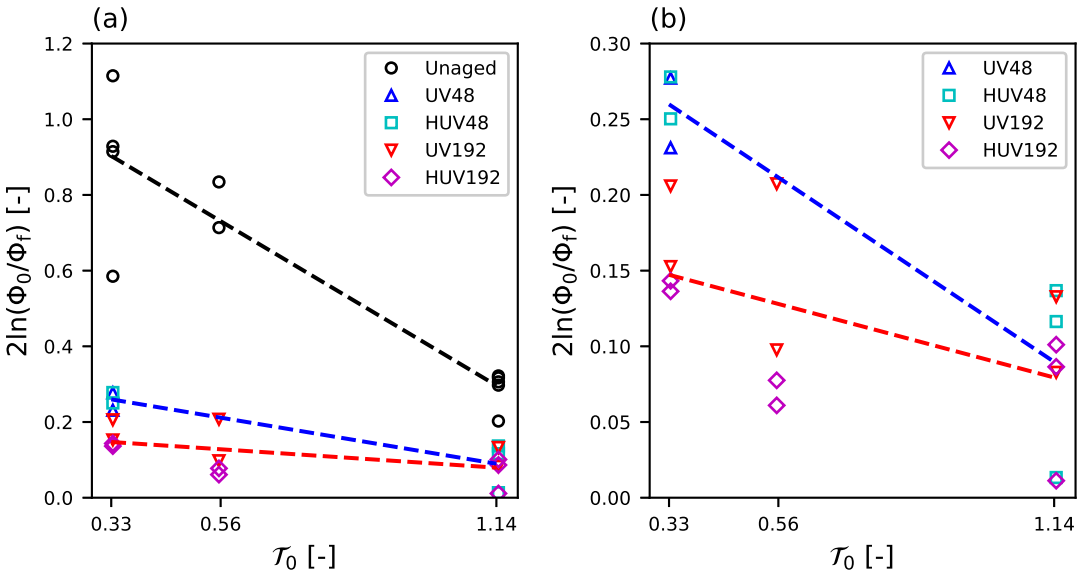

Figure 4.4: The effect of aging and nominal stress triaxiality on the strain to failure of bulk PA-6 specimens. The nominal stress triaxiality is calculated at the center of the bar using the Bridgman formula, Eq. (4.4) [104]. Linear fits are plotted using dashed lines, and are included to guide the eye. The black dashed line is fit to unaged data points. The blue dashed line is fit to UV48 and HUV48 data points. The red dashed line is fit to UV192 and HUV192 data points. (a) Unaged and aged data. (b) Aged data only.

reversed when the specimens are conditioned for 144 h. This confirms that loss of strength due to HUV aging shown in Fig. 4.3 is a result of plasticization by absorbed water and not hydrolytic degradation.

Fig. 4.4 plots the true fracture strain, $2\ln(\Phi_0/\Phi_f)$, against the nominal stress triaxiality, $\mathcal{T}_0$, for unaged and aged bulk PA-6 specimens. To increase the range of triaxiality explored, Fig. 4.4 also includes results imported from Chapters 3 and Appendix F on cylindrical bars. Although the resolution of contour tracking introduces a large uncertainty to the measurements of the true fracture strain, that uncertainty is still much smaller than the experimental scatter observed in Fig. 4.4. In Fig. 4.4a, both unaged and aged results are shown. In Fig. 4.4b, only aged results are shown. Linear fits to the data are plotted to help visualize trends, although the actual relationship between triaxiality and the true

fracture strain is not expected to be linear. The black dashed line is fit to data from unaged specimens. Since the additional hygrothermal aging component of the HUV aging regimen had no apparent effect on the fracture strain, data for corresponding UV and HUV aging conditions are combined when plotting the linear fits. The blue dashed line is fit to data from both UV48 and HUV48 aged specimens. The red dashed line is fit to data from both UV192 and HUV192 aged specimens. Although linear fits combine data from UV and HUV-aged specimens, UV and HUV data points are still plotted using separate symbols in Fig. 4.4.

In the unaged bars, increasing the nominal stress triaxiality greatly reduces the true fracture strain. This is expected, as increasing the stress triaxiality typically leads to increased void growth, and therefore a lower fracture strain [23,45]. However, aging reduces the impact of triaxiality on the true fracture strain. The slopes of the linear fits in Fig. 4.4 clearly show this trend; as the UV exposure time increases, the slopes of the linear fits decrease. This is rationalized based on the expected damage mechanism leading to failure in the different aging conditions. In the aged bars, fracture initiates from cracks on the surface that are induced by UV aging. However, the stress triaxiality at the surface of a round notched bar is less than the triaxiality at the center [23, 104], due to the traction-free boundary condition. The triaxiality at the surface still increases with decreasing ζ, but the change is less pronounced than at the notch center. Therefore, the stress triaxiality driving fracture in the aged bars is less than the nominal triaxiality used to plot data in Fig. 4.4. Even beyond the minimum UV exposure time, the impact of triaxiality on the fracture strain continues to decrease with increasing aging times, e.g. the slope of the UV48 and HUV48 fit is greater than the slope of the UV192 and HUV192 fit. Since these conditions presumably fracture from aging-induced damage at the surface, the triaxiality driving fracture is the same. Therefore, the loss of sensitivity of the fracture strain to the triaxiality is possibly a result of changes to the state of damage at the surface that occurs between 48 hours of UV exposure and 192 hours.

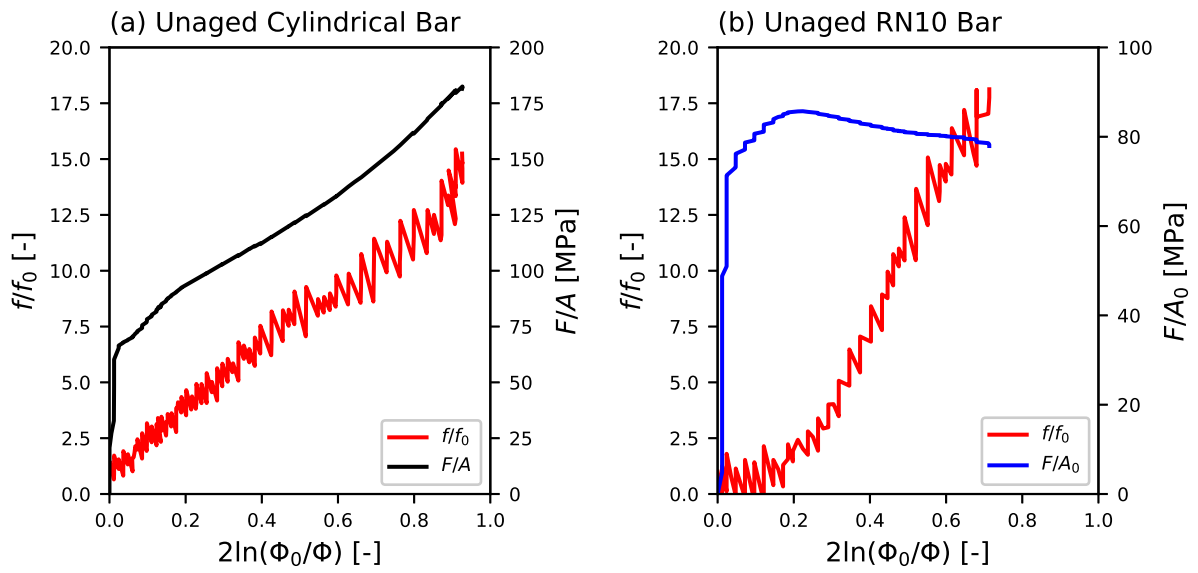

Figure 4.5: The evolution of the void volume fraction for (a) an unaged cylindrical bar and (b) an unaged RN10 bar. In both (a) and (b), the mechanical behavior is plotted on a secondary ordinate for context.

4.3.2.2 Evolution of the void volume fraction

In Chapter 3, the void volume fraction of smooth round bars was approximated through a combination of axial strain measurements (by DIC) and lateral strain measurements (by contour tracking). Eqs. (4.8)–(4.14) expand that analysis for applicability to round notched bars. In addition to the specimens analyzed in Chapter 3, two round notched bars are analyzed: an unaged RN10 bar and a UV192 aged RN10 bar. The results from this analysis are presented in Figs. 4.5 and 4.6.

Fig. 4.5 shows the evolution of the normalized void volume fraction with the true strain for an unaged cylindrical bar (Fig. 4.5a) and an unaged RN10 bar (Fig. 4.5b). The stress is plotted on a secondary ordinate in Fig. 4.5 to provide context for the evolution of the void volume fraction. The true stress (F/A) is shown for the cylindrical bar, while the nominal stress (F/A_0) is shown for the RN10 bar. Although the data is noisy, the cylindrical bar depicts an approximately linear increase in the void volume fraction with strain. In the RN10

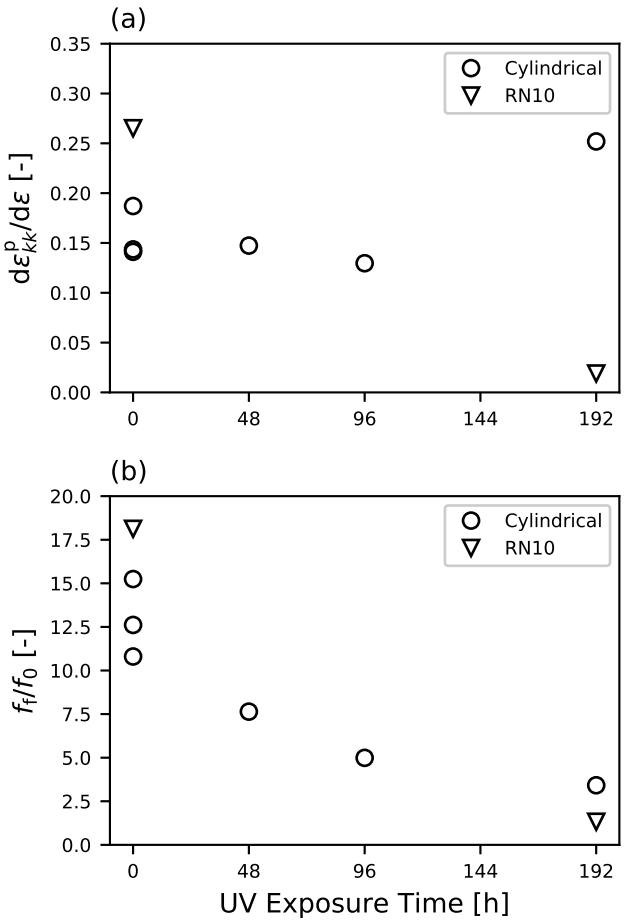

Figure 4.6: (a) The average plastic dilatation rate, i.e. $\varepsilon^{\mathrm{p}}_{kk}$ per unit true strain, versus UV exposure time for PA-6 cylindrical and RN10 bars tested in tension. (b) The estimated final void volume fraction divided by its initial value versus UV exposure time.

bar, the rate of void growth increases after the peak nominal stress. The RN10 bar exhibits a higher final void volume fraction than the cylindrical bar. In Ref. [22], cryofractography determined that the initial void volume fraction in PA-6 was approximately 1 %. Given this initiation void volume fraction, the analysis in Fig. 4.5 predicts an extremely high final porosity at crack initiation.

The dilatation analysis results from Chapter 3 and the results from two RN10 bars studied in the present chapter are aggregated in Fig. 4.6. In Fig. 4.6a, the average rate of plastic dilatation with respect to the true strain, $\mathrm{d}\varepsilon^{\mathrm{p}}_{kk}/\mathrm{d}\varepsilon$, is presented as a measure of the rate of

void growth. For the unaged specimens, the RN10 bar has a higher rate of void growth than the cylindrical bars, due to the higher nominal triaxiality in the RN10 bar. However, this is not true for the UV192 specimens, where the cylindrical bar shows a higher rate of void growth. For the UV192 cylindrical bar, profuse cracking is observed over the gauge section prior to fracture. This profuse cracking increases the measured void volume fraction. The minimum section in an RN10 bar is infinitesimally small (at least, in a perfect specimen), so surface cracking is more localized. This results in a lower measured dilatation. Fig. 4.6b shows the normalized final void volume fraction in the cylindrical and RN10 specimens. As expected, the unaged RN10 bar exhibits a much higher final void volume fraction than the unaged cylindrical bars due to the higher stress triaxiality in the RN10 bars. The RN10 bar subjected to UV192 aging shows a lower final void volume fraction than the UV192 cylindrical bar.

4.3.2.3 Synchrotron tomography

In order to study micromechanical damage in the unaged and aged round notched bars, two RN10 bars were scanned *ex situ* using synchrotron tomography. One unaged bar and one bar subjected to HUV192 aging were studied. The bars were loaded to their peak nominal stress, unloaded, and then sent to the SOLEIL synchrotron to be scanned. The mechanical behavior of the two bars is presented in Fig. 4.7. In the unaged bar, significant ductility is expected beyond the peak nominal stress, as the unaged RN10 bars have fracture strains around $2\ln(\Phi_0/\Phi_f) \approx 0.8$, see Fig. 4.4. On the other hand, for the aged RN10 bars, the peak stress coincided with crack initiation, so fracture was imminent in the interrupted HUV192 aged RN10 bar in Fig. 4.7. In Fig. 4.7, the HUV192 aged bar has a lower strength than the unaged bar. Again, this is a result of hygrothermal aging increasing the diffusion of moisture into the PA-6, which acts as a plasticizer [93, 111]. The reduced strength is not a consequence of hydrolytic aging, as it is reversible after drying. For more details about the effects of HUV aging regimens studied in this dissertation, see Appendix F.

For each RN10 bar, two tomograms were made: one at the center of the notch and one

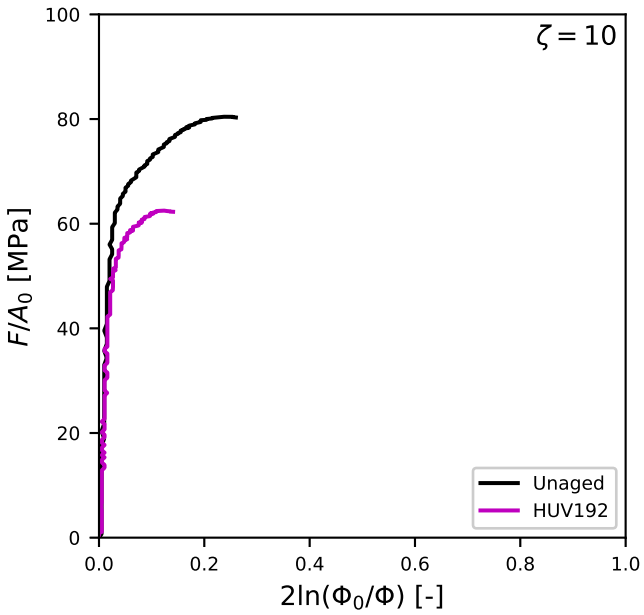

Figure 4.7: Nominal stress–true strain curves for an unaged RN10 bar and an HUV192 aged RN10 bar tested at room temperature (24 °C). The bars were loaded up to the peak nominal stress, unloaded, and inspected using *ex situ* synchrotron tomography.

at the surface of the notch root. The 3D scans are cylindrical with a height and diameter of 1331.2 µm. The scans, which are 3D, are presented here in 2D slices.

Fig. 4.8 depicts slices of the tomogram from the notch centers of the RN10 bars. Slices from the unaged bar are depicted in Figs. 4.8a,c, and slices from the HUV192 aged bar are depicted in Figs. 4.8b,d. Slices cut normal to the loading axis (i.e. in the $\hat{\boldsymbol{e}}_3$-$\hat{\boldsymbol{e}}_1$–plane) are shown in Figs. 4.8a,b. These slices show the "top view" of the tomogram, since their viewpoint is along the loading axis. Slices cut along the loading axis (i.e. in the $\hat{\boldsymbol{e}}_1$-$\hat{\boldsymbol{e}}_2$–plane) are shown in Figs. 4.8c,d. These slices show the "side view". The circular rings visible in the top views and the patterns down the centers of the side views are artifacts from constructing the tomogram. In the images of the unaged bar (Figs. 4.8a,c), cavities are visible as black spots on the image. The cavities are approximately circular in the top view, but are flat in the side view, indicating that their 3D-shape is that of a penny-shaped crack. Ref. [23] also reported penny-shaped cracks in a round notched PA-6 bar loaded up to the peak nominal

stress. However, no cavities are visible in the HUV192 bar, see Figs. 4.8b,d.

Fig. 4.9 depicts slices of the tomograms from the notch root surfaces of the RN10 bars. Figs. 4.9a,c show slices of the unaged bar and Figs. 4.9b,d show slices from the HUV192 aged bar. Figs. 4.9a,c show a top view of the tomogram (slices in the $\hat{\boldsymbol{e}}_3$-$\hat{\boldsymbol{e}}_1$–plane). and Figs. 4.9b,d show a side of the tomogram (looking in the $\hat{\boldsymbol{e}}_3$ direction). Since the notch root surface is curved, the side view is created by taking a curved slice from the top view and projecting that slice onto a flat image. The curved line used to create the projected side views are drawn in yellow in Figs. 4.9a,b. In the side view of the tomogram from the unaged bar (Fig. 4.9c), cavities are arranged in several horizontal lines. Other slices from the tomogram (not shown here) reveal that these lines of cavities form behind surface imperfections. Significant surface roughness is visible in the top view of the tomogram of the unaged bar (Fig. 4.9). Despite the surface roughness of the unaged bar scanned here, cavitation at the notch root surface is still less severe than cavitation at the notch center. In the HUV192 aged bar, an extensive network of cracks are visible (Fig. 4.9d). Some cracks are small and isolated, but many have linked up to form long, branching crack patterns. Some cracks are oriented perpendicular to the load and others are oriented parallel to the load, but the perpendicular cracks have opened more.

4.4 Discussion

The tomogram slices in Figs. 4.8 and 4.9 illustrate the different types of micromechanical in the unaged and aged bars. In the unaged bars, fracture is mediated by cavitation at the center of the bar, where the stress triaxiality is highest, see Fig. 4.8. In the aged bars, fracture is mediated by aging-induced damage at the surface, where the oxidative degradation is most severe, see Fig. 4.9. In Fig. 4.4, it was observed that at higher aging times, the true fracture strain became less sensitive to the notch severity parameter, ζ, of the specimen. This trend is concordant with the observations of damage from the tomogram slices in Figs. 4.8 and 4.9. The triaxiality at the center of a round notched bar is strongly sensitive to the notch severity parameter. Since the unaged bars fracture from cavitation at the center, the true fracture

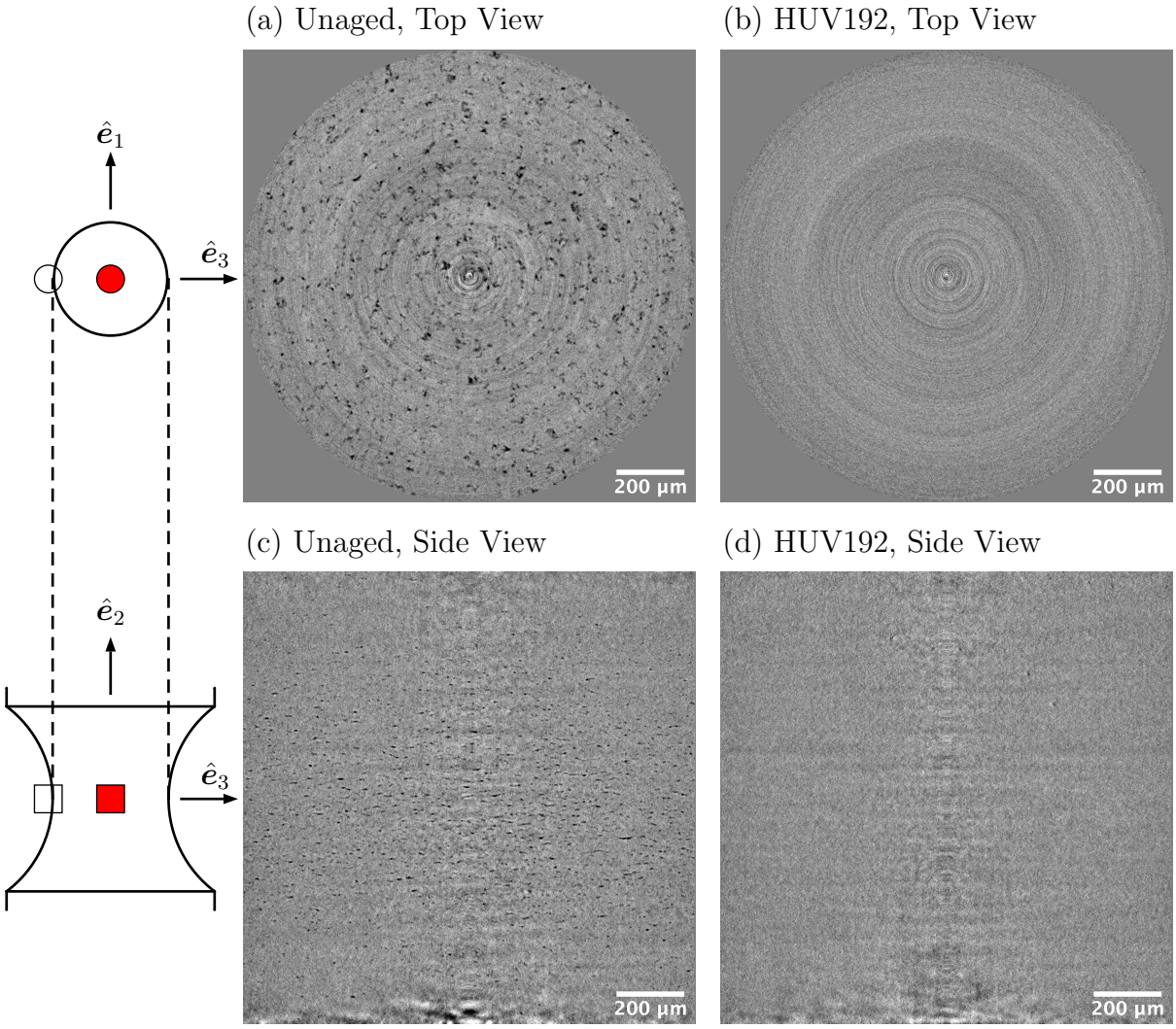

Figure 4.8: Slices from tomograms taken from the notch center of (a,c) an unaged RN10 bar and (b,d) an HUV 192 aged RN10 bar. Both RN10 bars were scanned *ex situ* after loading to the peak nominal stress. (a,b) Slices cut normal to the loading axis, i.e. in the $\hat{\boldsymbol{e}}_3$-$\hat{\boldsymbol{e}}_1$–plane. (c,d) Slices cut along the loading axis i.e. in the $\hat{\boldsymbol{e}}_1$-$\hat{\boldsymbol{e}}_2$–plane.

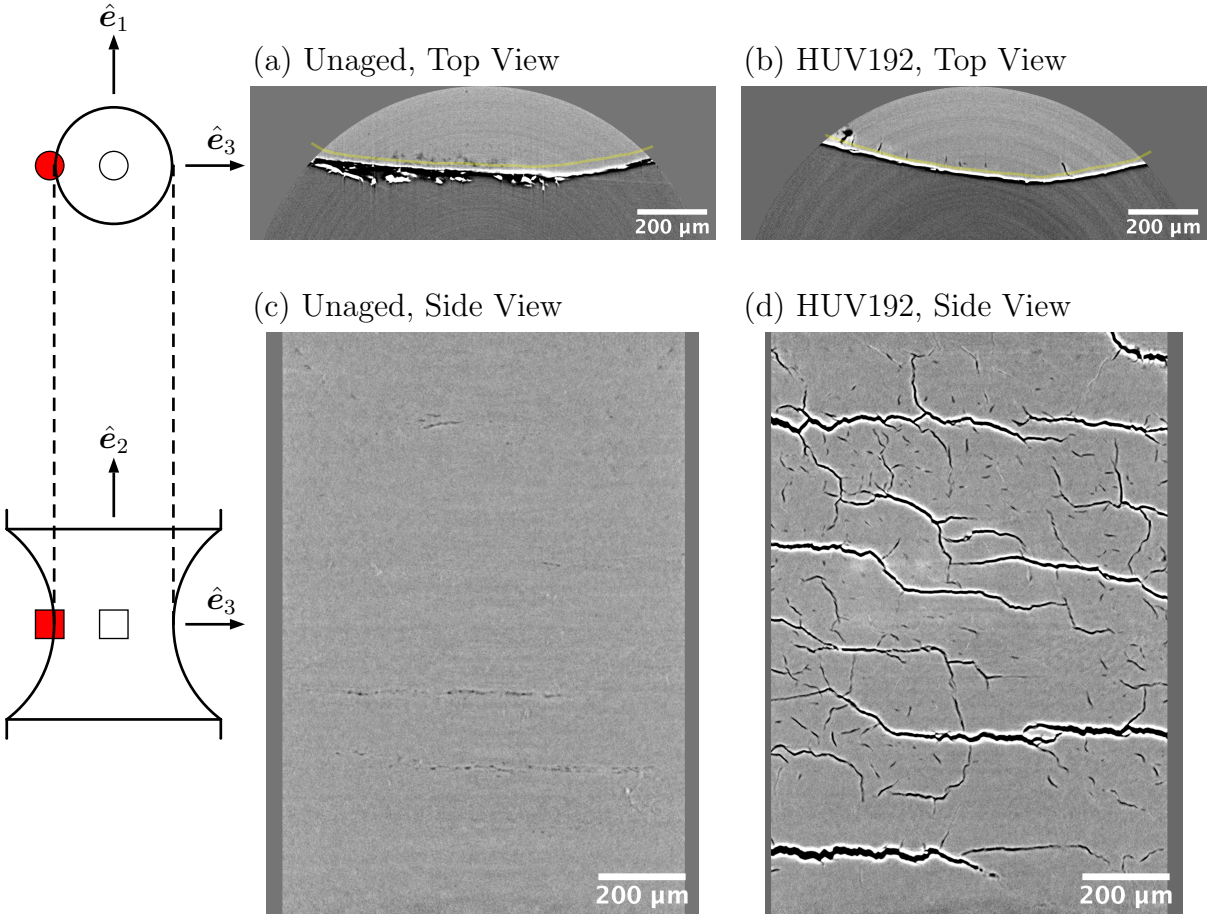

Figure 4.9: Slices from tomograms taken from the notch root surface of (a,c) an unaged RN10 bar and (b,d) an HUV 192 aged RN10 bar. Both RN10 bars were scanned *ex situ* after loading to the peak nominal stress. (a,b) Slices cut normal to the loading axis, i.e. in the $\hat{e}_3$-$\hat{e}_1$–plane. (c,d) Slices cut from the yellow lines in (a) and (b) and projected onto a flat image looking along the $\hat{e}_3$ direction.

strain is then also strongly sensitive to the notch severity parameter. On the other hand, the triaxiality at the surface is weakly sensitive to the notch severity parameter, since the traction free boundary condition limits the triaxiality. Even though the triaxiality at the surface is lower, the damage induced by aging is severe enough to govern fracture. However, there must be some critical UV aging time[3] where fracture transitions from being mediated by cavitation at the center to being mediated by aging-induced damage at the surface. This critical UV aging time is expected to increase with decreasing notch severity parameter, since for lower values of ζ, cavitation is more severe, so more extensive aging-induced damage is required for the transition to surface mediated fracture. For a bulk specimen aged below the critical UV aging time, the mechanical behavior and fracture strain may even be indistinguishable from those of an unaged specimen, since, in this case, the aging-induced damage is not the mechanism responsible for fracture, and the relatively shallow depth of oxidative degradation does not affect the average strength of the volume of the specimen. The UV48 and HUV48 aging conditions use the shortest UV exposure times studied here. Based on the data in Fig. 4.4, these aging conditions appear to be above the critical exposure time for all values of the notch severity parameter studied here.

4.5 Conclusion

This chapter investigated the mechanical behavior of and micromechanical damage in round notched bars of PA-6 loaded in tension. The effect of triaxiality was explored by varying the notch severity of the bar. In addition to the triaxiality, the effect of temperature and aging were studied. The expected effect of temperature on a viscoplastic material was observed; increasing the temperature decreased the strength and increased the fracture strain. Two types of aging conditions were explored: UV aging and combined UV and hygrothermal aging. It was found that the additional hygrothermal component of the combined aging regimen had no impact on the fracture strain, therefore aging was effectively measured by the UV exposure time alone. However, hygrothermal aging did reduce the strength of the PA-6

[3]Or more generally, some critical aging dose.

bars by increasing the amount of moisture that diffused into the material. The rate of void growth was estimated by measuring the plastic dilatation using axial strain measurements from digital image correlation and lateral strain measurements from contour tracking. As expected, it was found that the rate of void growth was higher in an unaged RN10 bar than an unaged cylindrical bar. The micromechanical damage in an unaged RN10 bar and an aged RN10 bar were investigated by *ex situ* synchrotron tomography.

The main finding of this chapter is that UV aging in bulk round notched bars causes a transition from fracture mediated by cavitation at the center of the notch to fracture mediated by aging-induced damage at the surface of the notch root. In the unaged bars, fracture occurs by cavitation at the center of the notch, where the triaxiality is highest. The triaxiality at the center is strongly sensitive to the notch severity, so the fracture strains are similarly sensitive to the notch severity. In the aged bars, fracture occurs by aging-induced damage that accumulates at the surface of the bar. At the notch surface, the traction free boundary condition limits the triaxiality, so the fracture strain is only weakly sensitive to the notch severity. For an aged bulk thermoplastic, these two micromechanical damage mechanisms are therefore in competition to determine the fracture strain: cavitation at a location with high triaxiality versus aging-induced damage at a location with low triaxiality.

5. THE EFFECTS OF PHOTO-OXIDATION ON THE EVOLUTION OF MICROMECHANICAL DAMAGE DURING THE LOADING OF FILMS

5.1 Introduction

So far in this dissertation, the experimental investigations of aged PA-6 have focused on bulk specimens, where the specimen thickness is much greater than the typical depth of oxidative damage [16, 27, 28]. In aged bulk specimens, fracture is a structural process; cracks in the aged layer grow, and eventually propagate into the unaged core. Additionally, Chapter 4 revealed that fracture in aged bulk specimens involves a competition between cavitation in the unaged core and cracks in the surface layer. The structural interactions leading to fracture in the bulk bars motivate the study of film specimens, where the thickness allows for nominally homogeneous oxidation. As a first-order approximation, the aged film can be studied as a substitute for the aged layer of a bulk bar. However, the film is not attached to the unaged core, making it a simpler system to study.

Photo-oxidation [27], and aging in general [4, 11], induces a ductile-brittle transition in thermoplastics. However, the UV exposure times studied in Chapters 3 and 4 age the material well into the brittle regime. Although aging abruptly decreases the fracture strain, it is possible for specimens to exhibit intermediate amounts of ductility within a narrow band of aging times [10, 28]. In Fayolle et al. 2004 [10], the plot of the uniaxial fracture strain with aging time in polypropylene films has a backwards "S" shape. The fracture strain gradually decreases with aging in the ductile region, drops abruptly at a ductile-brittle transition, and then continues to gradually decrease after the transition. Similar trends are observed in Wei et al. 2018 [28] for bulk PA-6 specimens, where three different types of fracture behavior are separated by three abrupt drops in the fracture strain with respect to aging time. Each type of fracture behavior in Ref. [28] is characterized by different interactions between the aged surface and the unaged bulk. It would therefore be interesting to study the active damage

mechanisms in films across the ductile-brittle transition, which motivates using shorter aging times than what was used in Chapters 3 and 4.

In this chapter, synchrotron tomography is used to characterize micromechanical damage in aged PA-6 films. The tomography scans are made *in situ* while applying a mechanical load, which has been made possible by a custom test frame that can be mounted to the synchrotron hutch [29]. Studying the damage *in situ* will be especially useful for future modeling efforts in Chapter 7, where state variables in a damage model will be calibrated based on the morphology of damage observed during loading. To identify priority aging conditions for study at the synchrotron, uniaxial tensile loading is used to characterize the effects of low aging doses on the mechanical behavior. The aging conditions closest to the ductile-brittle transition are identified using the true uniaxial fracture strain. Efforts at the synchrotron prioritize the films nearest to the transition.

The outline of this chapter is as follows. Section 5.2 describes the methodology, and Section 5.3 presents the results. A brief discussion of the results is given in Section 5.4, and Section 5.5 summarizes the conclusions.

5.2 Experimental

5.2.1 Material and aging

Additive-free films with thickness 0.1 mm were obtained from Goodfellow. While some films were tested without aging, others were aged in a QUV Accelerated Weathering Tester by exposure to UV radiation. The UV aging procedure took place at a temperature of 60 °C and at the ambient humidity of the laboratory. UVA lamps were used, which produced UV radiation with a spectral irradiance of $1.55\,\mathrm{W/m^2/nm}$ and an approximate wavelength of 340 nm. Nominal aging times of 12 h, 24 h, and 48 h were used, referred to as UV12, UV24, and UV48 aging conditions, respectively. In air, UV radiation initiates photo-oxidation in thermoplastics [27]. In thermoplastics, the depth of oxidation is limited by the diffusion of oxygen into the thickness. This depth is typically on the order of 100 µm [16, 27, 28]. Since

the films used here have a thickness on the same order as the depth of oxidation, they were flipped during aging to ensure that both sides were irradiated evenly. Therefore, both sides of the 0.1 mm film were exposed to UV radiation for the full nominal aging time.

5.2.2 Conditioning

PA-6 is hygroscopic, so it absorbs moisture from the air at ambient temperatures and relative humidities [93]. Since the moisture content affects the mechanical behavior of the material [93, 111], a conditioning procedure was used to dry the films prior to any experiments. All films were conditioned in a vacuum oven at a temperature of 80 °C for at least 24 h prior to any mechanical testing. The use of a vacuum oven prevents thermal oxidation of the material while drying. For specimens studied using tomography, the specimens were stored in a desiccant for approximately 48 h during transport to the synchrotron.

5.2.3 Specimen geometry

After aging and conditioning, specimens were cut from the films using a custom punch. The specimen geometry was designed for compatibility with a custom test frame used for *in situ* synchrotron tomography [29]. The specimens had a gauge length of 23 mm with two 5 mm tabs used for gripping. The gauge section had a very shallow notch of radius 30 mm to help localize the deformation and damage. At the minimum cross-section, the width of the specimen was 1.3 mm.

5.2.4 Mechanical testing

To identify the most critical aging conditions to study at the synchrotron, the mechanical behavior of the films was characterized through uniaxial tensile tests. These mechanical tests were carried out at room temperature with a constant displacement rate of $\dot{\delta} = 2.8\,\text{mm/min} = 0.047\,\text{mm/s}$. The deformation was measured using both the crosshead displacement and contour tracking, which was described in Chapter 3. Contour tracking analyzes videos of the mechanical test to determine the width of the specimen throughout the history of the experiment [88]. Even after strain localization causes an axial gradient in

the strain field, the true strain was calculated from the width following

$$\varepsilon = 2 \ln \left(\frac{W_0}{W} \right), \tag{5.1}$$

where W_0 is the initial width of the specimen and W is the current width. Eq. (5.1) assumes that (1) the deformation is incompressible, (2) the material is transversely isotropic, (3) there are no lateral strain gradients [97], (4) a plane stress state, and (5) the lateral strains are equal, i.e. $W/W_0 = t/t_0$ [88]. Assuming that the deformation is transversely isotropic and that $W/W_0 = t/t_0$, the true axial stress was calculated as

$$\sigma = \frac{F}{A} = \frac{F}{A_0 \left(\frac{W}{W_0} \right)^2}, \tag{5.2}$$

where F is the force measured by the load cell, A_0 is the initial cross-sectional area, and A is the current cross-sectional area.

5.2.5 Synchrotron tomography

Microscopic observations of aging-induced damage were made *in situ* using tomography at the PSICHÉ beamline of the SOLEIL synchrotron in France. The specimens were loaded in a custom test frame with a 445 N load cell mounted on the rotation stage of the beamline. Details of the custom test frame can be found in Ref. [29].[1] The films were loaded at a rate of $\dot{\delta} = 0.006\,\text{mm/s}$. Prior to making a tomogram (a 3D reconstructed volume), the films were unloaded by 0.05 mm, and then the displacement was held constant while the specimen relaxed. X-ray micro-tomography scans were composed of 750 equally-spaced projections. Contrast was obtained by coherent X-rays according to the Beer-Lambert's absorption law using a monochromatic extended parallel beam and a peak energy set to 25.515 keV. An exposure time of 50 ms was used, resulting in a total acquisition time of about 37.5 s. The crosshead displacement of the tensile machine was paused prior to starting the

[1] This is not the same test frame described in Section 5.2.4.

scan and then remained stationary during the scan. The final tomograms were composed of a $1024 \times 1024 \times 1024$ array of voxels, where each voxel is a cube with side length 1.73 µm. A small number of tomograms were taken at a lower resolution, using 375 equally-spaced projections, an exposure time of 10 ms, a total acquisition time of 3.75 s, a size of $512 \times 512 \times 512$ voxels, with a voxel side length of 3.47 µm. Tomograms are presented in this chapter using 2D slices from the 3D volume.

5.3 Results

5.3.1 Mechanical behavior

Fig. 5.1 presents the mechanical behavior of film specimens loaded in uniaxial tension using a displacement rate of $\dot{\delta} = 0.047\,\text{mm/s}$. The nominal mechanical behavior (nominal stress–displacement curve) is shown in Fig. 5.1a, and the true axial mechanical behavior (true axial stress–true strain curve) is shown in Fig. 5.1b. Only one representative curve for each aging condition is shown.

Consider the nominal mechanical behavior of the unaged film. The nominal stress rises before it gradually rolls-over to the peak stress, associated with the onset of strain localization. Afterwards, the stress decreases, followed by a gradual, but linear increase of the stress. This post-peak hardening is associated with neck stabilization and propogation [98, 113]. Even after the test frame reached its maximum crosshead displacement, the unaged film did not fracture, therefore the fracture strain of the unaged film was inaccessible. For the true mechanical behavior of the unaged film, the true axial stress increases monotonically with the true strain; no softening occurs at any point. Three different regions on the true axial stress–strain curve are apparent. First, the response is relatively stiff. Eventually, the stiff response rolls-over into a second region where the hardening is approximately linear, but at a lower slope than the first region. The transition from the first region to the second region is roughly defined here as yield. The second region ends when the hardening slope increases, indicating the onset of large-strain network hardening [57]. Vid. 5.1 shows a test video of

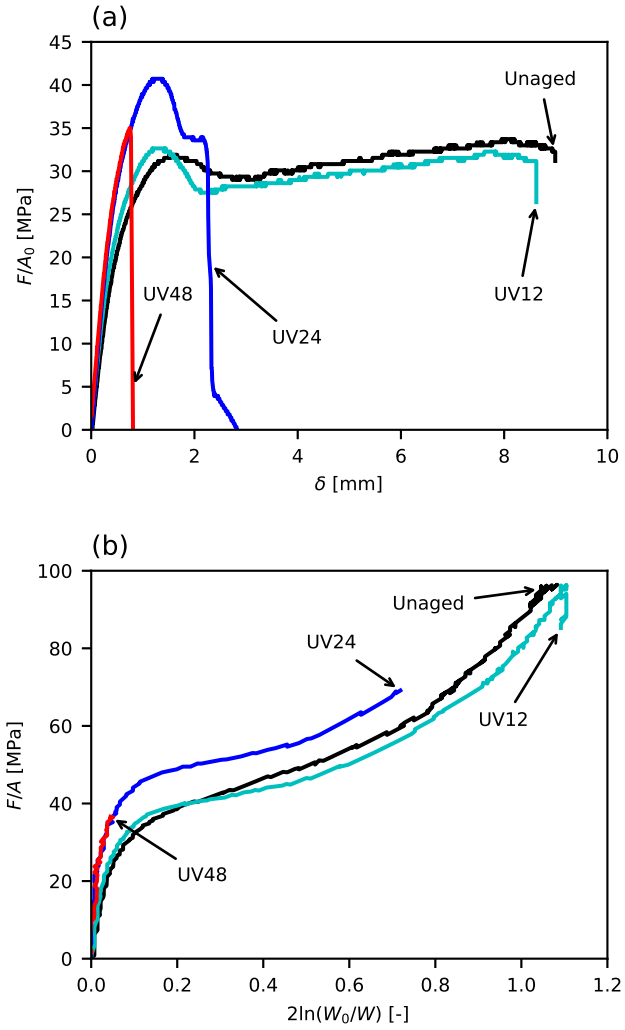

Figure 5.1: The (a) nominal and (b) true axial mechanical behavior of unaged and photo-oxidized PA-6 films. These tests use a displacement rate of $\dot{\delta} = 0.047\,\text{mm/s}$. See Vids. 5.1, 5.2, 5.3, and 5.4 for test videos and animated stress–strain plots of the unaged, UV12, UV24, and UV48 films shown here.

the unaged film, along with animated plots for the nominal and true mechanical behavior.[2]

The nominal mechanical behavior of the UV12 film is similar to that of the unaged film, but with two key differences: (1) the peak nominal stress is slightly increased by UV aging and (2) the post-peak stress decrease is increased by UV aging. The increased peak stress manifests on the true axial stress–strain curve as a slightly increased yield stress. It was observed in Chapter 3 and Ref. [99] that small amounts of UV aging had a strengthening effect on thermoplastic films. This strengthening effect has been attributed to chemi-crystallization [99], see also Fig. 3.7b. The increased post-peak stress decrease manifests on the true axial stress–strain curve as slightly decreased post-yield hardening, see how the UV12 curve crosses the unaged curve in Fig. 5.1b. This could be the result of chain scission, which decreases the concentration of entanglements, which decreases the strain hardening of the macromolecular network [4, 88, 90]. In Chapter 3, the post-yield strain hardening was relatively insensitive to UV aging, see Fig. 3.7c. However, a different grade of film was used for the experiments in Chapter 3. As with the unaged film, the UV12 film does not fracture at the maximum crosshead displacement of the test frame. Vid. 5.2 shows a test video of the UV12 film, along with animated plots for the nominal and true mechanical behavior.

In the nominal mechanical behavior of the UV24 film, there is also an initially stiff response that rolls-over to the peak nominal stress. The initial stiffness and peak stress are significantly higher than for the UV12 film. Again, this is most likely a result of further chemi-crystallization [99], see also Fig. 3.7b. As with the other films, the nominal stress decreases after the peak, which is associated with strain localization [98]. Although the UV24 film has a higher peak nominal stress, the post-peak stress decreases is approximately the same size in the UV24 and UV12 films. Since these two curves show a similar post-peak nominal stress decrease, their true axial stress–strain curves are approximately parallel after yield. After the nominal stress decrease, there is a short plateau followed by an abrupt drop in the load, which coincides with fracture. Data beyond the load drop is removed from the

[2] Email `kncundiff.dissertationquestions@gmail.com` to request video files.

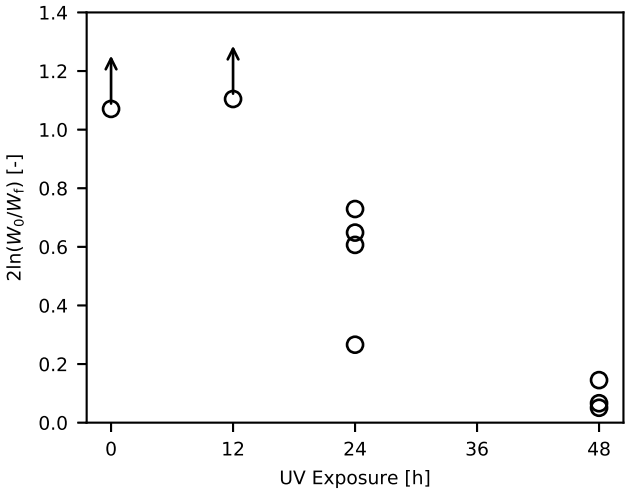

Figure 5.2: True fracture strains for unaged and photo-oxidized PA-6 films.

true axial stress–strain curves, since contour tracking can no longer measure the true strain beyond this point. Therefore, the maximum true strain for the UV24 film in Fig. 5.1b is defined as the true fracture strain. Vid. 5.3 shows a test video of the UV24 film, along with animated plots for the nominal and true mechanical behavior. The UV48 film fractures before yield. However, prior to fracture, the nominal and true axial mechanical behavior of the UV48 film is identical to those of the UV24 film. Vid. 5.4 shows a test video of the UV48 film, along with animated plots for the nominal and true mechanical behavior.

Fig. 5.2 plots the true fracture strain versus UV exposure time for all films tested here. The unaged and UV12 films did not fracture, so their maximum strains are plotted with an upward-pointing arrow to indicate the plotted values are only a lower bound. The fracture strains for the UV24 films are significantly lower than the lower bounds for the unaged and UV12 films. Additionally, there is significant scatter in the fracture strains of the UV24 films. The UV48 films all fracture at low true strains, with minimal scatter in the measurements. In thermoplastics, aging eventually causes a ductile-brittle transition [4, 55]. The fracture strains in Fig. 5.2 indicate that the UV12 films are on the ductile side of the transition and the UV48 films are on the brittle side. The UV24 films appear to lie on or near the

transition. In order to study the damage mechanisms across the ductile-brittle transition, the UV24 and UV48 films were prioritized for study at the synchrotron.

5.3.2 Macroscale damage

The test videos recorded for contour tracking also enabled macroscopic observations of damage. Fig. 5.3 shows images from mechanical tests conducted at $\dot{\delta} = 0.047\,\mathrm{mm/s}$. Figs. 5.3a,b show the unaged and UV12 films at their maximum strains. At this stage, the necks have stabilized and spread across most of gauge section. Since the maximum displacement of the crosshead was insufficient to fracture these films, the remaining ductility is unknown. No macroscopic damage is clearly visible for either the unaged or UV12 films. Fig. 5.3c shows an image of the UV24 film taken at its fracture strain, $2\ln(W_0/W_\mathrm{f}) = 0.73$. Here, a neck has formed, but significant neck propagation has not yet occurred. In the necked region, two large holes are visible. In Vid. 5.3, these two holes can be traced back to white spots that appear at a true strain of approximately $2\ln(W_0/W) \approx 0.1$.[3] Vid. 5.3 also reveals that fracture occurs when the ligament separating the edge of the specimen from the outermost hole breaks. Fig. 5.3d shows the image of UV48 film taken at its fracture strain, $2\ln(W_0/W_\mathrm{f}) = 0.05$. No visible strain localization occurs in the UV48 film, which is expected, since it fractures the peak nominal stress, see Fig. 5.1a. No holes are visible immediately prior to fracture in the UV48 film. Instead, cracks appear, which are visible as white lines running perpendicular to the loading axis. In Fig. 5.3d, there is a large crack towards the bottom of the image that spans nearly the entire width. Vid. 5.4 shows that the film fractures along this crack. The images in Fig. 5.3 indicate that the damage mechanisms leading to fracture change significantly across the ductile-brittle transition (UV24 to UV48). This gives further importance to focusing on the UV24 and UV48 films at the synchrotron.

[3] Email `kncundiff.dissertationquestions@gmail.com` to request video files.

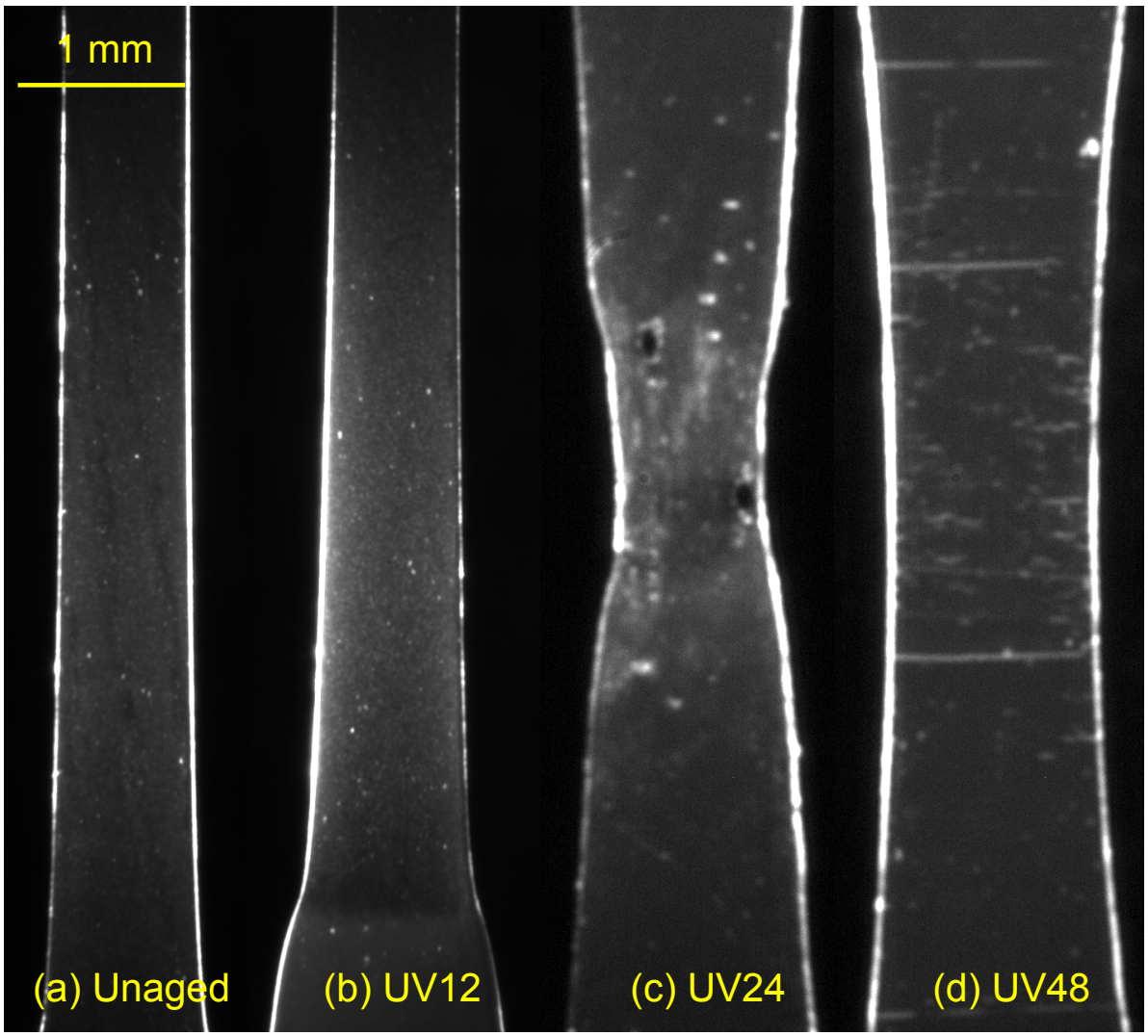

Figure 5.3: Images of (a) an unaged film at its maximum strain, (b) a UV12 film at its maximum strain, (c) a UV24 film at its fracture strain, (d) a UV48 film at its fracture strain. See Vids. 5.1, 5.2, 5.3, and 5.4 for test videos and animated stress–strain plots of the unaged, UV12, UV24, and UV48 films shown here.

5.3.3 Microscale damage

Synchrotron tomography was used to investigate, *in situ*, micromechanical damage in the films. Loading was paused to perform the scans that were used to construct the tomograms. Here, the 2D slices from the tomograms are presented in Figs. 5.4–5.8. The slices are taken from the surfaces and edges of the films, where the damage is concentrated. Only tomogram slices from UV24 and UV48 films are shown here. For the equipment and settings used in this study, no micromechanical damage was visible in the unaged and UV12 films.

Fig. 5.4 shows tomogram slices from the front face of a UV24 film. The nominal stress–displacement curve is shown in Fig. 5.4a. The marked points represent when the loading was paused to scan the film. Tomogram slices are presented in Figs. 5.4b–f. No damage is initially visible in the specimen, see Fig. 5.4b. As discussed in Chapter 3, there are two possibilities for the apparent absence of damage [88, 99]. One possibility is that chemical cracks form during aging without a mechanical load, in which case damage is initial to the material, but is below the resolution of the tomogram. The other possibility is that the damage nucleates after the superposition of a chemical stress and a mechanical load, in which case the damage is chemo-mechanical in nature [88, 99]. After loading, cracks appear all over the surface of the film, see Fig. 5.4c. As loading progresses, the cracks primarily grow by elongating in the direction of the load, although the cracks seen here remain oblate, see Figs. 5.4d,f. Eventually, the cracks coalesce, leading to failure. In the tomogram taken immediately prior to fracture, Fig. 5.4f, multiple cracks coalesced to form a single large crack. After the tomogram in Fig. 5.4f was taken, fracture occurred immediately after attempting to resume loading. Vid. 5.5 shows 3D views of the tomograms corresponding to Figs. 5.4d–f.[4] Fig. 5.5 shows tomogram slices from the right edge of the film in Fig. 5.4. Here, it is seen that the cracks do not extend through the thickness of the film. This was also observed previously in Chapter 3, see Fig. 3.14. Even though the thickness of the film is equal to the nominal depth of oxidation, there is still a significant gradient of aging-induced damage from

[4] Email `kncundiff.dissertationquestions@gmail.com` to request video files.

the surface to the bulk.

Tomogram slices from the front face of another UV24 film are shown in Fig. 5.6. The nominal stress–displacement curve is shown in Fig. 5.6a, and tomogram slices are presented in Fig. 5.6b–e. These tomograms show cracks first appearing near the edges of the film, see Fig. 5.6b. Cracks appear in the center at higher deformation levels, but the density of damage remains highest at the edges, see Figs. 5.6c,d. In the final tomogram taken before fracture, Fig. 5.6e, a large crack has opened up on the right edge of the film. This crack is presumably the cause of failure. Near the critical crack, several other cracks have elongated to have nearly circular cross-sections. Additionally, shear bands between several of the cracks in this area are visible. The tomographic investigations in Fig. 5.6 shows that cracks in a UV24 film can elongate significantly during loading. This finding at the microscale is consistent with the macroscale observations in Fig. 5.3, where fracture occurred by the growth of two circular holes in the film.

Tomogram slices from the front face of a UV48 film are presented in Fig. 5.7. Again, the nominal stress–displacement curve is shown in Fig. 5.7a, and tomogram slices are presented in Fig. 5.7b–g. Tomogram slices from the right edges of the same UV48 film are presented in Fig. 5.8. The growth of damage in the UV48 film shares four similarities with the growth of damage in the UV24 film. (1) No cracks are initially visible in the UV48 film, see Fig. 5.7b. (2) Cracks first appear at the edges of the specimen, while cracks at the center the surface appear later, see Figs. 5.7c–f. (3) Throughout loading, the density of cracks remains greater at the edges than the center, see Figs. 5.7f,g. (4) Cracks form on the surface, and do not extend all the way through the thickness, see Fig. 5.8. However, there are several differences between the evolution of damage in the UV48 film and the UV24 film. For one, cracks appear much earlier in the UV48 films, compare Fig. 5.7f ($\delta = 0.65\,\mathrm{mm}$) to Fig. 5.6b ($\delta = 0.77\,\mathrm{mm}$). In UV48 films, cracks open up during loading, but do no significantly elongate as in the UV24 films. The cracks in the UV48 films primarily grow laterally. Eventually, the cracks link up laterally until a series of linked cracks spans nearly the entire face of the specimen.

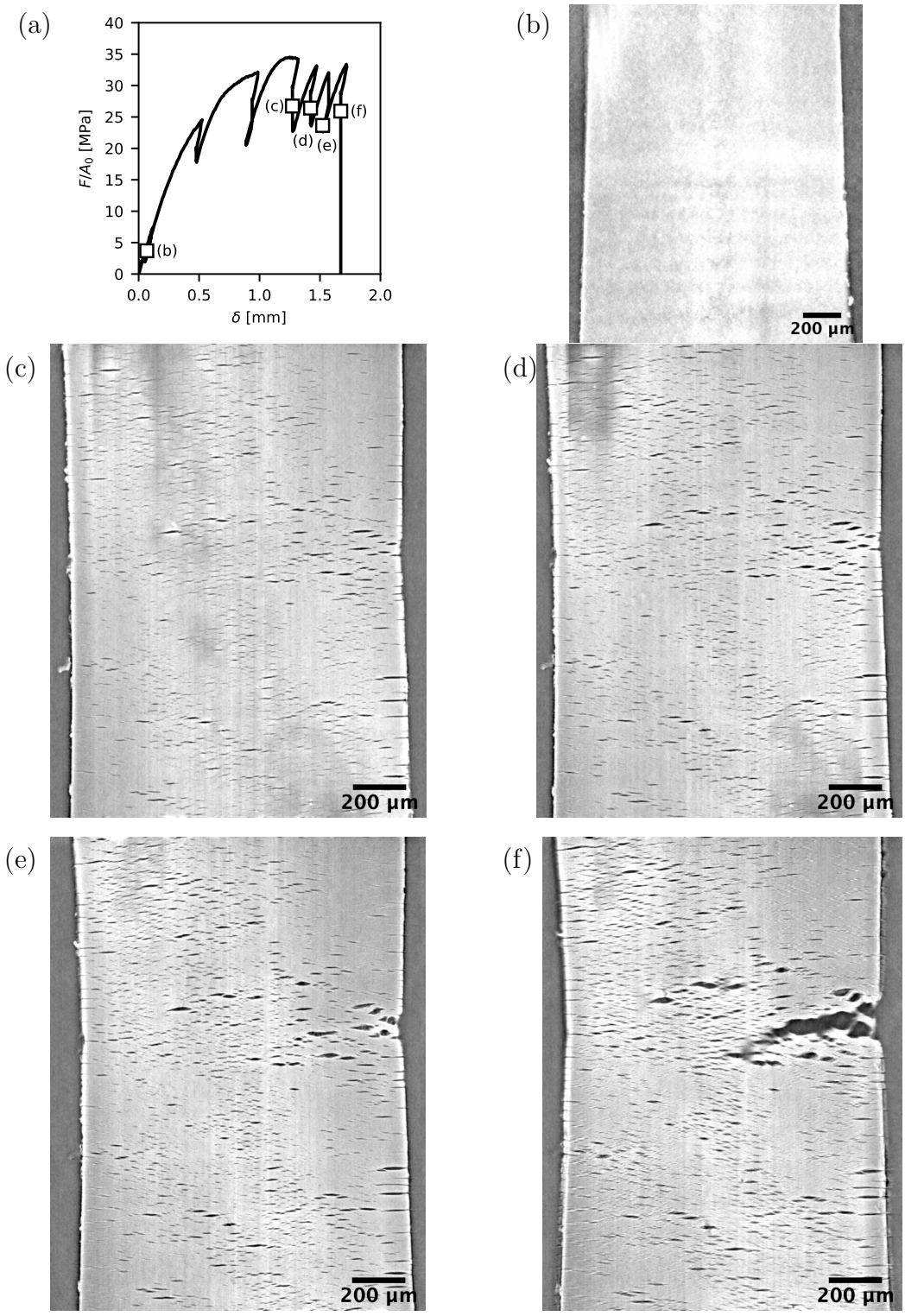

Figure 5.4: Slices from *in situ* tomograms taken throughout the loading of a UV24 film. The slices show the front face of the film. (a) The nominal stress–displacement curve. Slices from tomograms taken at the surface of the film at crosshead displacements of (b) $\delta = 0.07\,\text{mm}$, (c) $\delta = 1.27\,\text{mm}$, (d) $\delta = 1.42\,\text{mm}$, (e) $\delta = 1.52\,\text{mm}$, and (f) $\delta = 1.67\,\text{mm}$.

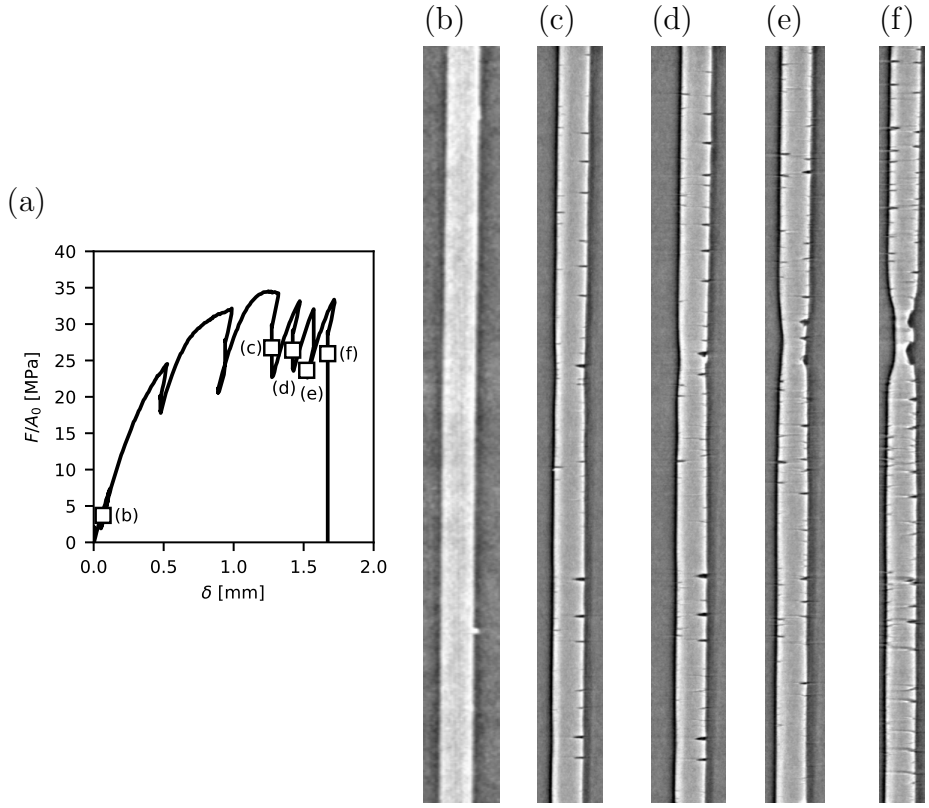

Figure 5.5: Tomogram slices showing the right edge of the specimen shown in Fig. 5.4. The right sides of the images shown here correspond to the faces shown in Fig. 5.4. (a) The nominal stress–displacement curve. Slices from tomograms taken at the surface of the film at crosshead displacements of (b) $\delta = 0.07\,\mathrm{mm}$, (c) $\delta = 1.27\,\mathrm{mm}$, (d) $\delta = 1.42\,\mathrm{mm}$, (e) $\delta = 1.52\,\mathrm{mm}$, and (f) $\delta = 1.67\,\mathrm{mm}$. For scale, the initial nominal thickness of the film was $0.1\,\mathrm{mm}$.

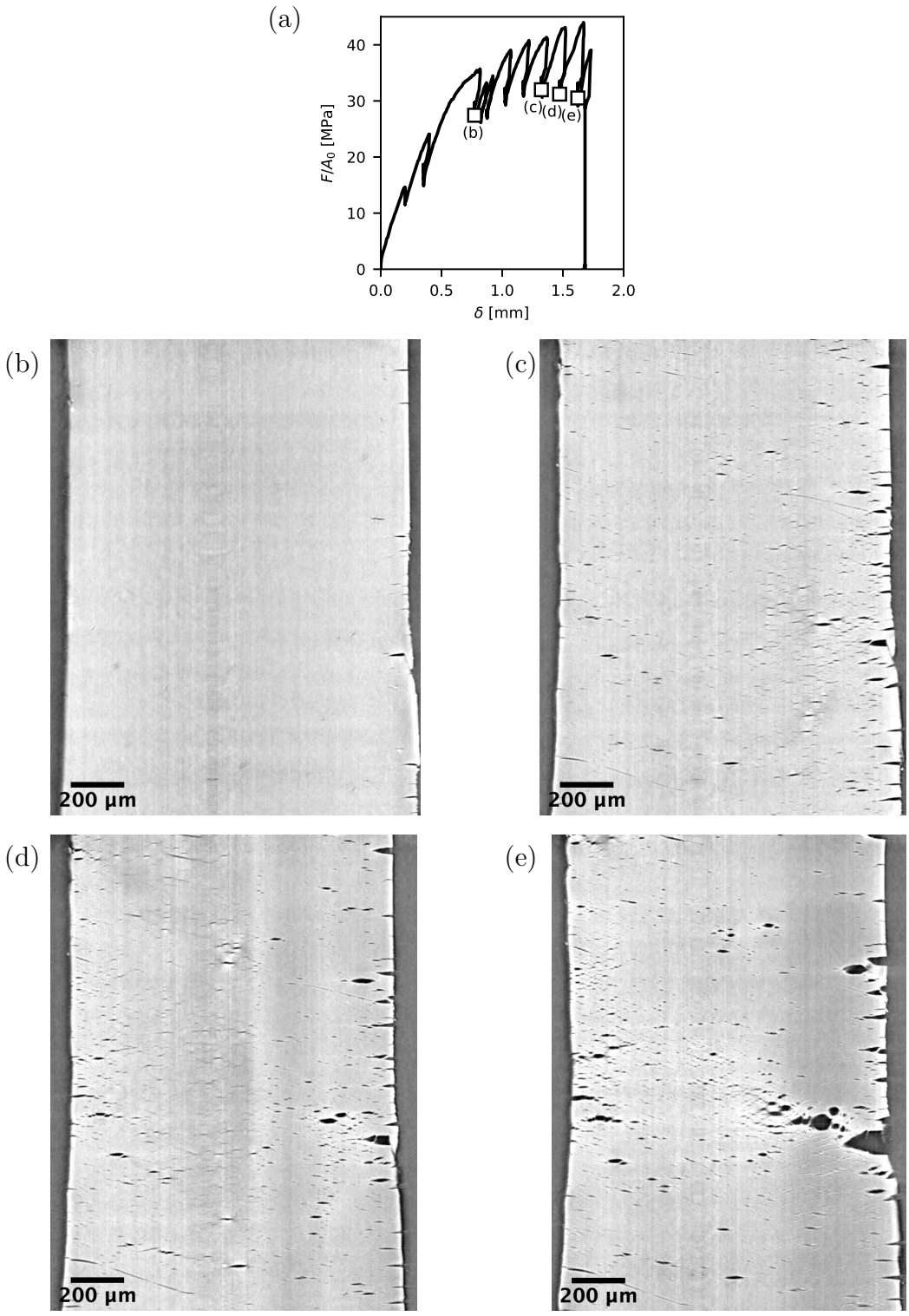

Figure 5.6: Slices from *in situ* tomograms taken throughout the loading of a UV24 film. The slices show the front face of the film. (a) The nominal stress–displacement curve. Slices from tomograms taken at the surface of the film at crosshead displacements of (b) $\delta = 0.77\,\mathrm{mm}$, (c) $\delta = 1.32\,\mathrm{mm}$, (d) $\delta = 1.47\,\mathrm{mm}$, and (e) $\delta = 1.62\,\mathrm{mm}$.

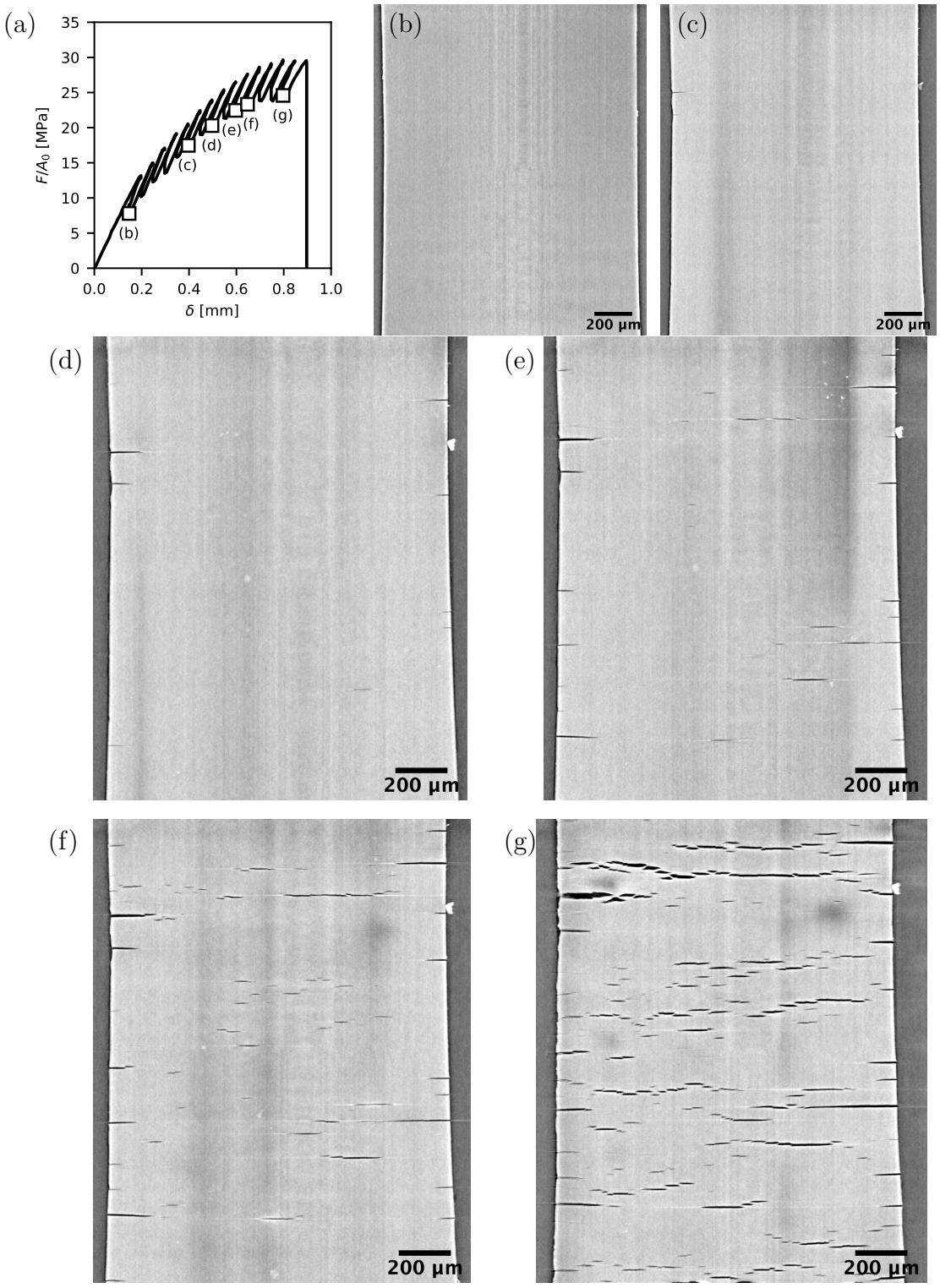

Figure 5.7: Slices from *in situ* tomograms taken throughout the loading of a UV48 film. The slices show the front face of the film. (a) The nominal stress–displacement curve. Slices from tomograms taken at the surface of the film at crosshead displacements of (b) $\delta = 0.15\,\text{mm}$, (c) $\delta = 0.40\,\text{mm}$, (d) $\delta = 0.50\,\text{mm}$, (e) $\delta = 0.60\,\text{mm}$, (f) $\delta = 0.65\,\text{mm}$, and (g) $\delta = 0.80\,\text{mm}$.

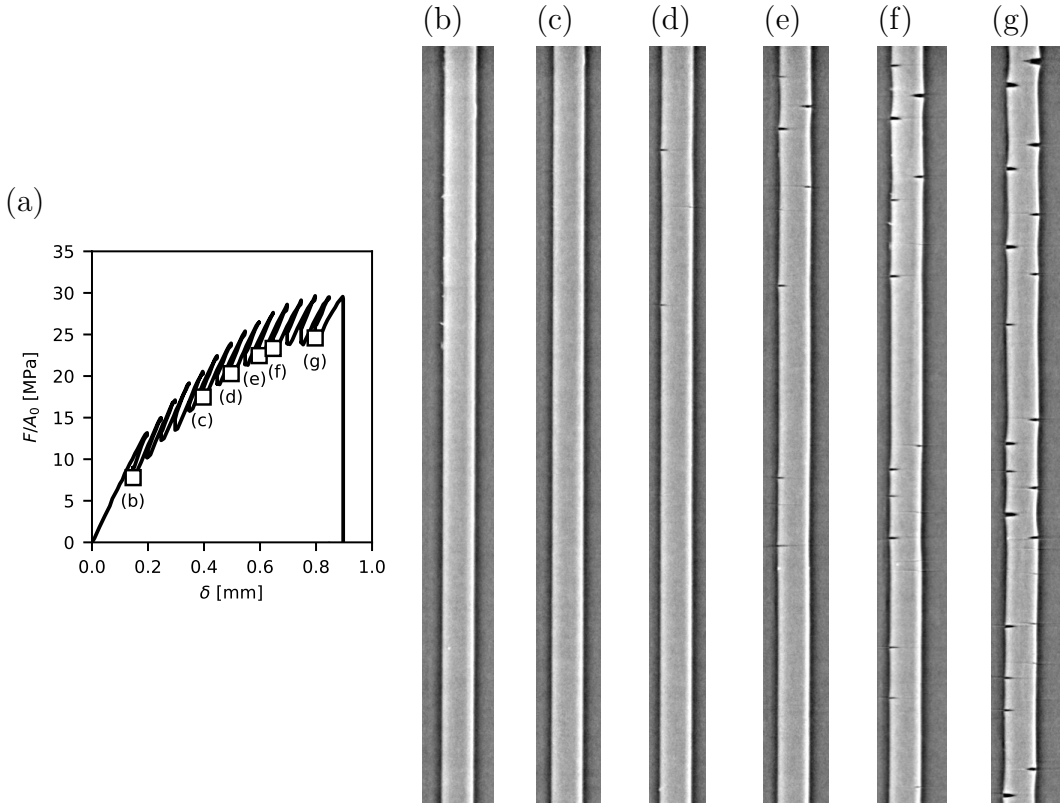

Figure 5.8: Tomogram slices showing the right edge of the specimen shown in Fig. 5.7. The right sides of the images shown here correspond to the faces shown in Fig. 5.7. (a) The nominal stress–displacement curve. Slices from tomograms taken at the surface of the film at crosshead displacements of (b) $\delta = 0.15\,\mathrm{mm}$, (c) $\delta = 0.40\,\mathrm{mm}$, (d) $\delta = 0.50\,\mathrm{mm}$, (e) $\delta = 0.60\,\mathrm{mm}$, (f) $\delta = 0.65\,\mathrm{mm}$, and (g) $\delta = 0.80\,\mathrm{mm}$. For scale, the initial nominal thickness of the film was 0.1 mm.

Presumably, this is the mechanism that leads to fracture, which is also what was inferred from macroscopic observations in Fig. 5.3d. A second series of tomograms from a different UV48 film, not shown here, confirm the repeatability of the observations in Fig. 5.7.

5.4 Discussion

Aging causes a ductile-brittle transition in thermoplastics [4, 11]. The transition is often characterized by a reduction in the fracture strain for specimens tested in uniaxial tension. Fayolle et al. have shown that this reduction in the fracture strain occurs abruptly [10,19,55], and have proposed that it occurs when oxidation-induced chain scission reduces the molar mass below a critical value. However, this approach neglects mesoscale phenomenon, such as cracks [25] and cavities [99] that form after aging. Such micromechanical damage has been referred to in this dissertation collectively as "aging-induced damage". In Chapter 3 [88], it was shown that aging-induced damage nucleates on the surface of aged bars well before the maximum load. These cracks grew as the loading progressed until a critical crack propagated into the core of the specimen and caused fracture. This finding, along with others from Chapter 3 hinted that embrittlement was the result of aging-induced damage.

However, the aging conditions studied in Chapter 3 were all well beyond the ductile-brittle transition. The transition was captured here, as the UV12 films still exhibited ductile behavior (high uniaxial fracture strain), the UV48 films exhibited brittle behavior (low uniaxial fracture strain), and the UV24 films exhibited an intermediate behavior. With the transition from high fracture strain to low fracture strain, a damage mechanism transition was also observed. In both the UV24 and UV48 conditions, aging-induced damage appeared over the surface of the specimen. However, this damage developed very differently in the two cases. In the UV24 films, cracks become visible only after loading. These cracks elongated during loading, and eventually coalesced into large voids that caused fracture. In the UV48 films, cracks become visible at lower levels of deformation. These cracks did not significantly elongate, but instead grew laterally until a network of cracks were connected across most of the width of the specimen. The importance of aging-induced damage in semicrystalline ther-

moplastics is further emphasized by the fact that a damage mechanism transition coincides with the ductile-brittle transition.

If fracture in an aged semicrystalline thermoplastic is mediated by aging-induced damage, then an appropriate micromechanics-based continuum damage model should be capable of predicting fracture strains. In Chapter 7, a Gurson-type model [32] will be used to model fracture in aged and unaged PA-6. For Gurson-type [32] damage models, such as the Keralavarma-Benzerga model [33, 34, 80], state variables are calibrated to represent the average morphology of voids in a material. The voids of the aged material will be calibrated to represent aging-induced damage. The work in this chapter and Chapter 4 have built a database of tomographic observations that can be used to quantitatively characterize the damage in aged PA-6.

Films were used in this research to study specimens that were homogeneously oxidized. Since oxygen only diffuses to a depth of 100 µm in a thermoplastic [16,27,28], bulk specimens show a large amount of aging-induced damage at the surface, but none at the center [28, 88], see also Chapter 4. However, in these films that had an initial thickness of 100 µm, a gradient in aging-induced damage was still observed from the surface to the center; the cracks visible in the surface do not extend into the center of the film, see Figs. 5.5 and 5.8. Additionally, on the surface of the specimens, a gradient in damage was observed from the edges to the center, where the density of damage is highest at the edge. Although the thickness of the films used here is approximately equal to the depth of oxidation, oxygen is still more readily available at the surface of the film than the center. Fayolle et al. 2004 utilized FTIR to confirm the homogeneity of oxidation through the thickness of polypropylene films [10]. In future work, it would be interesting to perform a similar analysis to compare the homogeneity of oxidation to the distribution of damage in the films.

5.5 Conclusion

Micromechanical damage that developed in UV-irradiated PA-6 during mechanical loading was studied using *in situ* synchrotron tomography. A preliminary mechanical charac-

terization determined that 24 hours of UV radiation induced a ductile-brittle transition, characterized by a large decrease in the fracture strain. The tomograms of the mechanically loaded films revealed that the ductile-brittle transition coincided with a damage mechanism transition. After 24 hours of aging, the films exhibited an intermediate level of ductility; these films existed near or on the ductile-brittle transition. In films aged for 24 hours, cracks appeared after loading began. During loading, these cracks elongated, with some attaining approximately circular cross-sections. Immediately prior to fracture, elongated cracks began coalescing into larger voids. Films aged for 48 hours exhibited brittle behavior. In films aged for 48 hours, cracks appeared after loading began, but at earlier levels of deformation. These cracks did not significantly elongate, but instead grew laterally across the face of the specimen. Immediatley prior to fracture, cracks spanned nearly the entire width of the specimen. In both films aged for 24 hours and films aged for 48 hours, damage was not homogenous. Cracks formed on the faces of the film, but not in the center of the thickness. Additionally, the crack density was greater at the edges of the faces than the centers of the faces. No damage was visible in the films aged for less than 24 hours, which was due to the maximum displacement of the test frame and the extremely high ductility of the films with low amounts of UV exposure.

The coincidence of the aging-induced ductile-brittle transition with the damage mechanism transition provides further evidence that micromechanical damage plays an important role in the embrittlement of aged semicrystalline thermoplastics. In Chapter 7, a micromechanics-based continuum damage model will be used to predict fracture in aged and unaged PA-6. Two ingredients are needed for this modeling task. First, state variables in the damage model need to be calibrated to represent the average void morphology. The tomograms from this chapter, along with those in Chapter 4, will be useful for quantitatively characterizing the morphology of micromechanical damage in unaged and aged PA-6. Second, the constitutive behavior of the dense material needs to be defined. This ingredient is addressed in the next chapter (Chapter 6).

6. MODELING THE THERMOMECHANICAL BEHAVIOR

6.1 Introduction

With the experimental characterization of aging presented in Chapters 3–5, a foundation has been prepared to begin modeling aging-induced damage in semicrystalline thermoplastics. The final objective of this dissertation is to predict fracture in aged semicrystalline thermoplastics using a micromechanical damage model. A constitutive description of the damaged material necessarily requires a constitutive description of the undamaged (dense) material. Therefore, the present chapter seeks to identify the constitutive behavior, or the "intrinsic behavior", of the undamaged material.

At the nanoscale, plastic deformation of a polymer is heterogeneous, as the deformation is accommodated by the motion of macromolecular chains. However, at the continuum scale, plastic deformation can be considered homogeneous, and it is at this scale that the notion of the "intrinsic" mechanical behavior is defined. When a volume of material at the continuum scale is deformed homogeneously, the resulting mechanical behavior can be considered intrinsic to the material. When formulating a constitutive model for use with finite elements, the goal is to represent the intrinsic behavior.

However, identification of the intrinsic mechanical behavior of a polymer is a challenging task. First, it is not trivial to homogeneously deform a polymer, and therefore not trivial to measure the true stress and true strain during an experiment. At large strains, plastic instabilities, such as necking or barreling, develop in test specimens to create a highly non-uniform strain field. After the onset of a plastic instability, the nominal strain, $\Delta L/L_0$, measures only the average axial deformation over a specimen experiencing a wide range of strains. Additionally, the large strains achieved during barreling and necking result in significant changes in the cross-sectional area, such that the nominal stress, F/A_0, deviates significantly from the true axial stress, F/A. Therefore, it is impossible to access the true

stress–strain curve using the nominal stress–strain curve alone; the nominal stress–strain curve is produced from a complicated coupling of the intrinsic (constitutive) behavior and specimen-level structural effects. Second, plastic instabilities also make it difficult to control the true strain rate. As the strain localizes due to a plastic instability, the specimen experiences true strain rates that vary with both position and time. For example, when a neck is formed, the true strain rate in the neck dramatically increases and can vary at a single point by an order of magnitude [114]. After the neck stabilizes, the strain rate at the site of neck initiation decreases, and the true strain rate is highest at the propagating neck fronts [115]. Polymers are viscoplastic, therefore changes in strain rate affect their strength, making the intrinsic behavior even more elusive.

Many approaches to accessing the intrinsic behavior after the onset of necking or barreling have been explored in the literature. One seemingly simple solution would be the use of a radial extensometer to measure the local strain at the site of neck initiation, as such methods have been employed for metals that undergo necking [109]. However, contact strain gauges may lead to premature fracture in polymers [96]. For this reason, non-contact, video-based extensometry is attractive for mechanical tests on polymeric specimens.

One video-based extensometry method accesses the minimum specimen width by analyzing images of the specimen during testing. Then, the true axial strain is calculated from the true lateral strain measured in the test images and the true axial stress is calculated by dividing the applied load by the current minimum cross-sectional area. One example of this method can be found in G'Sell et al. 1992 [112]. There, the true strain was calculated from images in real-time so that a closed loop system could be implemented to control the true strain rate in the neck. The speed of analysis required for real-time strain calculation was possible due to the use of an hourglass specimen, as the neck location was known *a priori*, therefore the video system only needs to calculate the width at the known location. However, curvature of the specimen, either induced by necking or initial to the specimen geometry, gives rise to a triaxial stress state. When the stress state is triaxial, the true

axial stress (F/A) is greater than the true (equivalent) stress (σ_{eqv}), but the former is easily obtained from the video-based width measurements. To account for differences in the axial and effective stresses, G'Sell et al. 1992 [112] also obtain the local curvature from test images. Given the local curvature, the minimum width, and the remote applied load, the true effective stress in the neck can be calculated [104]. The contour tracking method employed in Chapters 3–5 calculates the true axial stress using the instantaneous specimen width measured from a test image. However, unlike in G'Sell et al. 1992 [112], the images are analyzed in post-processing, since the use of un-notched specimens makes it impossible to determine the location of neck initiation *a priori*. Without calculating the strains in real-time, the true strain rate could be not be controlled. Additionally, the local curvature was not extracted from the images, so only the true axial stress was calculated.

While measuring the specimen width is convenient for axial loading, it is less useful for other loading paths such as shear. Marker tracking is another form of video-based extensometry where markers are painted onto the specimen surface and the true strain is calculated from their motion. This method was applied for both tension and shear tests in Mohanraj et al. 2006 [116]. However, if the spacing of the markers is greater than the size of the plastic localization, then measurements from this method fail to decouple structural effects from the intrinsic mechanical behavior [97].

Digital image correlation (DIC) is a widely used technique that is conceptually similar to marker tracking. In DIC, a speckle pattern is applied over the entire surface of the specimen. For a given image, the deformation of the speckle pattern is calculated by comparing the current image to a reference image. In this way, the strain field over the visible surface of the specimen is computed. Since DIC only measures strains of the specimen surface, the true stress is not directly measured, but instead approximated using assumptions about the local stress state. In Parsons et al. 2004 [114], DIC was used to study the intrinsic behavior of polycarbonate (PC). To account for the wide variations in the true strain rate in the necked region, a composite intrinsic stress–strain curve was constructed from the

true stress–strain measurements provided by DIC. Each point on the stress–strain curve was chosen from a location experiencing the targeted true strain rate. When only one camera is used for DIC, the specimen surface must be flat and strain can only be measured in the plane of the surface. By adding a second camera with a different perspective, 3D-DIC is possible, capable of measuring out-of-plane strains, such as in the study of necking in HDPE by Farge et al. [115]. One disadvantage of DIC is that the painted speckle pattern may obscure valuable information on the specimen surface. For example, the cracks visible in Fig. 3.10 were not visible when using DIC. Another issue with DIC encountered in Chapter 3 is that the speckle pattern sometimes becomes too deformed for successful comparison to the reference image.

While these video-based extensometry methods have many strengths, they are far more complicated than measurements used to create nominal (engineering) stress–strain curves. It would therefore be advantageous to develop methods of accessing the intrinsic mechanical behavior using easily obtained nominal measurements of stress and strain. As mentioned previously, nominal measurements alone are insufficient for accessing the true stress–strain curve after a plastic instability. However, if the nominal stress–strain curve from a mechanical test was accurately reproduced from a finite element model of the experimental specimen and an appropriately calibrated constitutive law, then the calibrated constitutive law could be taken as an approximate representation of the intrinsic mechanical behavior. Since the true stress–strain curve is not known, model parameters could not be extracted directly from the experimental data. However, the constitutive law could be calibrated by optimizing its parameters to produce a good match between the simulated and experimental nominal stress–strain curves. In this way, the nominal stress–strain curve is supplemented with a finite element model and an appropriate constitutive law to make accessing the intrinsic mechanical behavior possible.

This chapter accesses the intrinsic mechanical behavior of PA-6 through inverse parameter identification, an approach that combines experiments and simulations. Nominal stress–

strain curves are produced from experiments using only the crosshead displacement and a load cell. Then, the specimen geometry is modeled using a finite element model employing a viscoplastic semicrystalline polymer constitutive model to govern the stress–strain relations. The constitutive model is calibrated by optimizing its parameters so that the finite element model produces a nominal stress–strain curve equivalent to the experimental one. The resulting set of constitutive model parameters are then taken to represent the intrinsic mechanical behavior. In this way, the intrinsic mechanical behavior is uncovered without sophisticated or laborious experimental techniques. This procedure for determining the model parameters is referred to here as "inverse parameter identification", since the observed nominal mechanical behavior (the effect) is used to identify the intrinsic mechanical behavior (the cause). The model parameters, parameter constraints, and nominal mechanical behavior constitute the "inverse problem". This is not the first work to utilize inverse methods for model calibration [117–119]. Inverse methods have been used to study barreling in the compression of high-temperature steel [119], and also to calibrate constitutive models for thermoplastics [118, 120].

One previously mentioned difficulty in experimentally obtaining the intrinsic mechanical behavior is the wide variations in true strain rate that occurs during necking and neck propagation. The method explored here has a unique advantage with regard to this problem. If plastic instabilities are accurately represented in the finite element model, then changes in the local true strain rate will naturally emerge in the simulation. By appropriately calibrating the rate and temperature sensitivity of the constitutive model, the effect of variations in strain rate during necking are explicitly accounted for. In order to calibrate the rate and temperature sensitivity, the experimental database must include experiments on specimens loaded under different rates and temperatures. However, this increases the computational cost of optimization, since it requires that multiple simulations using different temperatures and loading rates are run at each iteration, and hundreds of iterations may be necessary for convergence. The use of PA-6 is advantageous in this regard, as its deformation in

compression is approximately homogeneous, which therefore can be modeled using a single element. The temperature and rate sensitivity of the viscoplastic constitutive model is therefore calibrated from compression experiments in order to reduce the computational expense of running multiple simulations per iteration. Asymmetrical mechanical behavior in tension and compression still requires the modeling of tensile tests, where a more accurate finite element model is employed in order to accurately capture plastic localization.

The viscoplastic constitutive model calibrated in this chapter will be useful for modeling aging-induced damage in Chapter 7 in two key ways. First, the calibrated constitutive model will be used in finite element models of round notched bars to predict local loading paths at critical locations in the bar. These loading paths will then be imported into a micromechanics-based continuum damage model whose constitutive relations are integrated at a material point. Second, the intrinsic mechanical behavior uncovered here will be used to inform the hardening law within the damage model. With regard to these two uses, two approximations are made regarding the calibration of the viscoplastic model. First, the effects of micromechanical damage on the strength of the material are not explicitly considered. In other words, the viscoplastic model employed here assumes that the material is completely dense, i.e. free of voids or microcracks. This approximation is further discussed in Section 6.10 of this chapter. The second approximation is that the strength of the material is not altered by aging. In other words, the primary effect of aging is the introduction of aging-induced damage that reduces the fracture strain of the material. Because of this approximation, only the intrinsic behavior of unaged PA-6 is studied in the present chapter. A full discussion of this approximation is delayed until Chapter 7.

The outline of this chapter is as follows. Sections 6.2–6.6 thoroughly describe the approach used for inverse parameter identification. Section 6.2 shows the experimental data available for calibration and validation. Section 6.3 presents the finite element models used to simulate the experimental specimens. Section 6.4 describes the macromolecular semicrystalline polymer constitutive model formulated for this work and Section 6.5 describes its

implementation. In Section 6.6, the inverse problem is defined. First, the model parameters entering into the constitutive model are reiterated. Next, some parameters are assigned values from deterministic calibrations, while others are assigned values from simplifying assumptions and approximations. In Section 6.7, the parameters controlling the rate and temperature sensitivity are calibrated from compression tests. In Section 6.8, the intrinsic mechanical behavior is identified through calibration to a tensile test on a cylindrical bar. In Section 6.9, the calibrated model is used to perform finite element simulations of round notched (RN) bars loaded in tension. These RN bar simulations are then compared to experimental results to validate the calibration of the constitutive model. Section 6.10 presents a discussion of the inverse parameter identification method and the results generated here, and concluding remarks are made in Section 6.11.

6.2 Experimental data

Parameters for a viscoplastic polymer model are calibrated by fitting simulated nominal stress–strain curves to experimental curves produced from mechanical tests on PA-6. This section briefly describes the experimental data used for calibration and validation. Tests under a variety of stress states are required for calibration, since the strength of cavitating polymers is sensitive to the hydrostatic pressure [49, 97]. To explore the effect of the hydrostatic pressure, the experimental data considered in this chapter includes tests on pins loaded in compression, as well as cylindrical bars and round notched bars loaded in tension. Since PA-6 is viscoplastic, it is also necessary to explore loading under different temperatures and strain rates. A large experimental database exploring the effects of pressure, temperature, and strain rate has been generated, but only select experiments are used in this chapter. Only relevant methodological details and results are presented here. The complete methodologies and experimental databases are presented in Appendix I for compression pins, Appendix H for cylindrical bars, and Chapter 4 for round notched bars.

6.2.1 Compression pins

Compression tests were conducted on cylindrical pins of PA-6 with a height and diameter of 9.53 mm (0.375 in). The pins were loaded at a various nominal strain rates, defined as $\left|\dot{\delta}\right| / L_0$, where $\dot{\delta}$ is the speed of the crosshead, and L_0 is the initial height of the pin. A temperature chamber was used to control the temperature at which the experiment occurred, T. For tests at room temperature, $T = 24\,^{\circ}\mathrm{C} \pm 1\,^{\circ}\mathrm{C}$, the temperature chamber was not used. The PA-6 pins did not fracture in compression. Instead, they flattened until the applied force reached the load cell limit (21.4 kN). After compression, the pins exhibited a limited amount of barreling, as seen in Fig. 6.1. The effect of barreling in compression was less pronounced than the effect of necking in tension. Therefore, barreling is ignored, and the true stress and strain are calculated from the nominal stress and strain by approximating the deformation to be homogeneous and incompressible. The true (logarithmic[1]) strain is calculated as

$$\varepsilon = \left| \ln\left(1 - \frac{|\delta|}{L_0}\right) \right|, \tag{6.1}$$

and the true stress as

$$\sigma = \frac{|F|}{A_0}\left(1 - \frac{|\delta|}{L_0}\right), \tag{6.2}$$

where L_0 and A_0 are the initial height and cross-sectional area of the compression pin, δ is the displacement of the test frame's crosshead, and F is the force measured by the load cell.

Table 6.1 shows the test matrix of compression experiments used for calibration and validation of the viscoplastic model. Both the calibration and validation experimental sets include tests at different nominal strain rates and temperatures. Conditions at temperatures above $T_g \approx 47\,^{\circ}\mathrm{C}$ (see Appendices H or I) are omitted from calibration since the viscoplastic model is not intended to model temperature effects across thermodynamic transitions.

[1]While other strain measures could have been chosen, any strain measure is useful for making comparisons between experiments and simulations. In the context of this chapter, the important feature of Eqs. (6.1) and (6.2) is that the only *in situ* measurements they require are the crosshead displacement, δ, and the force measured by the load cell, F.

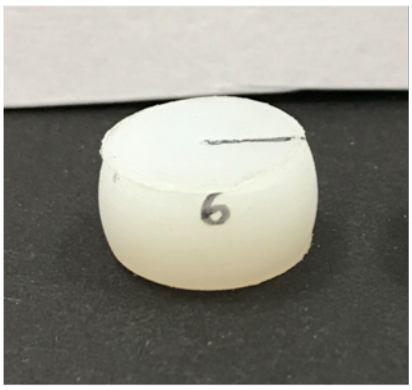

Figure 6.1: A PA-6 compression pin after loading to 21.4 kN. The effect of barreling in compression was less pronounced than the effect of necking in tension. Therefore barreling is ignored.

Table 6.1: Test matrix of compression experiments used for calibration and validation. Conditions marked with a "C" are used for calibration. Conditions marked with a "V" are used for validation.

Compression Pins Unaged		$T < T_g$			$T > T_g$
		−30 °C	0 °C	24 °C	60 °C
$\left\|\dot{\delta}\right\| / L_0$	10^{-1} /s	V		C	
	10^{-3} /s	C	C	C	V
	10^{-5} /s				

Nevertheless, comparisons are still made to data above T_g to test the limits of the calibrated constitutive model.

Fig. 6.2 shows the true stress–strain data for compression experiments. Fig. 6.2a shows data from tests using a nominal strain rate of $\left|\dot{\delta}\right| / L_0 = 10^{-3}$ /s. Fig. 6.2b shows data from tests using a nominal strain rate of $\left|\dot{\delta}\right| / L_0 = 10^{-1}$ /s. The test conducted at $T = 24\,°\text{C}$ and $\left|\dot{\delta}\right| / L_0 = 10^{-3}$ /s is also plotted in Fig. 6.2b to facilitate comparisons between the two plots.

Fig. 6.2 reveals the expected effect of strain rate and temperature on the yield stress; increasing the strain rate or decreasing the temperature increases the yield stress. However, tests at $\left|\dot{\delta}\right| / L_0 = 10^{-1}$ /s show significant post-yield softening that causes the stress–strain

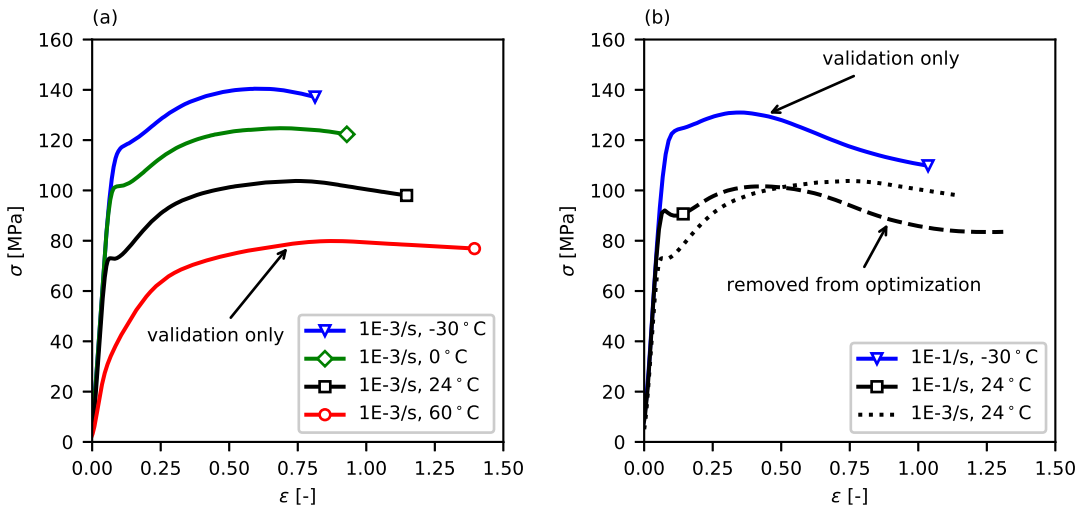

Figure 6.2: The experimental true stress–strain curves for PA-6 pins loaded in compression at nominal strain rates of (a) $\left|\dot{\delta}\right| / L_0 = 10^{-3}\,/\mathrm{s}$ and (b) $\left|\dot{\delta}\right| / L_0 = 10^{-1}\,/\mathrm{s}$. A reference test from (a) using the loading condition $T = 24\,^{\circ}\mathrm{C}$ and $\left|\dot{\delta}\right| / L_0 = 10^{-3}\,/\mathrm{s}$ is plotted in (b) with a dotted line to facilitate comparisons between (a) and (b). Data ignored during optimization is indicated by a dashed line.

curve to eventually drop below stress–strain curves for tests at the same temperature but lower strain rates. This is an effect of thermal softening, which occurs when a portion of the plastic work is converted into heat, raising the temperature of the specimen [121, 122]. For convenience, this effect is referred to within this chapter as self-heating [112]. For tests using a sufficiently slow strain rate, the conversion of plastic work into thermal energy is offset by conduction and convection. Therefore, deformation at sufficiently low strain rates is approximately isothermal. In polymers, the deformation can no longer be approximated as isothermal around strain rates of $10^{-2}\,/\mathrm{s}$ or greater [122, 123]. On the other hand, if the strain rate is sufficiently fast, then conduction and convection are negligible compared to the rate of plastic work converted into heat. Therefore, deformation at sufficiently high strain rates is approximately adiabatic. The effects of thermal softening can be quantified and modeled [64, 122, 124], but an isothermal model is implemented in this chapter to facilitate

a study of specimen-level structural effects, see the discussion in Section 6.10. Since the model implemented here is isothermal, it is incapable of predicting the thermal softening that occurs in the tests at nominal strain rates of $\left|\dot{\delta}\right| / L_0 = 10^{-1}\,/\text{s}$. Therefore, data for calibration is restricted to $\varepsilon \leq 0.15$ in tests using a nominal strain rate of $\left|\dot{\delta}\right| / L_0 = 10^{-1}\,/\text{s}$. This strain level corresponds to just after yield, at which point heat generated by plastic work is assumed to still be negligible.

6.2.2 Cylindrical bars

Tension tests were conducted on PA-6 cylindrical bars with gauge length 12.70 mm and diameter 4.76 mm. The cylindrical bars were loaded at a various nominal strain rates, defined as $\dot{\delta}/L_0$, where $\dot{\delta}$ is the speed of the crosshead, and L_0 is the initial gauge length of the bar. A temperature chamber was used to control the temperature at which the experiment occurred, T. For tests at room temperature, $T = 24\,^{\circ}\text{C} \pm 1\,^{\circ}\text{C}$, the temperature chamber was not used. The nominal stress and strain are calculated from the crosshead displacement, δ; the force from the load cell, F; the initial gauge length, L_0, and the initial cross-sectional area, A_0;

$$\varepsilon^{\text{nom}} = \frac{\delta}{L_0}, \quad \sigma^{\text{nom}} = \frac{F}{A_0}. \tag{6.3}$$

Unlike the compression tests, the cylindrical bars experience significant strain localization. At the peak load, neck initiation occurs as strains localize in the neck. The strain continues to localize in the neck during the load drop. Once the stress plateau is reached, the neck begins to propagate. During this time, axial elongation occurs primarily by the propagation of the neck. While the strain field is heterogeneous, the true strain cannot be obtained from axial measurements. To address this issue, a method referred to in this dissertation as contour tracking was introduced in Chapter 3. In contour tracking, images from test videos are processed to detect the specimen edges (contours). The minimum distance between the contours is determined, and taken to correspond to the minimum diameter of the specimen. In this way, lateral deformations and the minimum cross-sectional area are

Table 6.2: Test matrix of tensile experiments on cylindrical bars used for calibration and validation. Conditions marked with a "C" are used for calibration. Conditions marked with a "V" are used for validation.

Cylindrical Bars Unaged		$T < T_g$			$T > T_g$
		$-30\,°C$	$0\,°C$	$24\,°C$	$60\,°C$
$\dot{\delta}/L_0$	$10^{-1}\,/s$		V	V	V
	$10^{-3}\,/s$		V	C	
	$10^{-5}\,/s$			V	

measured *in situ*. By assuming that deformation is incompressible and radially homogeneous, as well as assuming a transversely isotropic material behavior, the true (logarithmic) strain in a given test image can be calculated as

$$\varepsilon = 2 \ln \left(\frac{\Phi_0}{\Phi} \right), \tag{6.4}$$

where Φ_0 is the initial diameter and Φ is the current diameter. The true axial stress is calculated as

$$\sigma = \frac{F}{A} = \frac{4F}{\pi \Phi^2}, \tag{6.5}$$

where F is the force measured by the load cell. As discussed in Chapter 3, Eq. (6.5) is only a measure of the true *axial* stress. When necking initiates, the stress state becomes triaxial, during which time Eq. (6.5) overestimates the true stress. However, once the neck front travels sufficiently far from the minimum cross-section, the local geometry is once again approximately cylindrical and a uniaxial stress state returns.

Despite the availability of approximate true stress–strain data, only the nominal stress–strain data is used for calibration. After calibration, the final parameter set is used to compare the intrinsic stress–strain behavior to the approximate true stress–strain behavior measured by contour tracking. This comparison is made to assess the accuracy of contour tracking.

Table 6.2 shows a test matrix of the tension experiments on cylindrical bars used in this chapter. Only a single tensile loading condition ($T = 24\,^{\circ}\text{C}$, $\dot{\delta}/L_0 = 10^{-3}\,/\text{s}$) is used for optimization. Since finite element models of homogeneous deformation are less computationally expensive than finite element models capturing plastic localization, data from compression tests are exclusively relied upon to optimize the temperature and rate sensitivity. This avoids running the more expensive cylindrical bar finite element model multiple times during a single iteration of the optimization algorithm. Many of the conditions in Table 6.2 were carried out at a strain rate of $\dot{\delta}/L_0 = 10^{-1}\,/\text{s}$. As with the tests in compression, these tests exhibit self-heating leading to thermal softening.

Fig. 6.3 shows the nominal stress–strain data for tension experiments on cylindrical bars. Fig. 6.3a shows tests conducted at room temperature ($T = 24\,^{\circ}\text{C}$). The stress–strain curve from the realization using a strain rate of $\dot{\delta}/L_0 = 10^{-1}\,/\text{s}$ crosses the stress–strain curves of other realizations at the same temperature but lower strain rates. Again, the load drop that results in crossing stress–strain curves is an effect of self-heating, and not an intrinsic effect of strain rate. Fig. 6.3b shows tension tests conducted at $T = 0\,^{\circ}\text{C}$ and Fig. 6.3c shows tension tests conducted at $T = 60\,^{\circ}\text{C}$. In Fig. 6.3b,c, data from the experiment using the loading conditions $T = 24\,^{\circ}\text{C}$ and $\dot{\delta}/L_0 = 10^{-3}\,/\text{s}$ is included for reference. Fig. 6.4 shows the true axial stress–true strain curve calculated by contour tracking for the experiment using the loading conditions $T = 24\,^{\circ}\text{C}$ and $\dot{\delta}/L_0 = 10^{-3}\,/\text{s}$.

6.2.3 Round notched bars

Tension tests were conducted on PA-6 round notched (RN) bars. The stress triaxiality in a round notched bar is approximately constant during its deformation, making it a useful tool for exploring the effect of the stress state [35, 45]. Two different specimen geometries were employed. The first was an RN10 bar with a notch radius of 3.90 mm, a notch root diameter of 3.90 mm, and a notch shoulder diameter of 7.00 mm. The second was an RN2 bar with a notch radius of 1.17 mm, a notch root diameter of 5.85 mm, and a notch shoulder diameter 10.50 mm. The round notched bar nomenclature used in this dissertation is defined

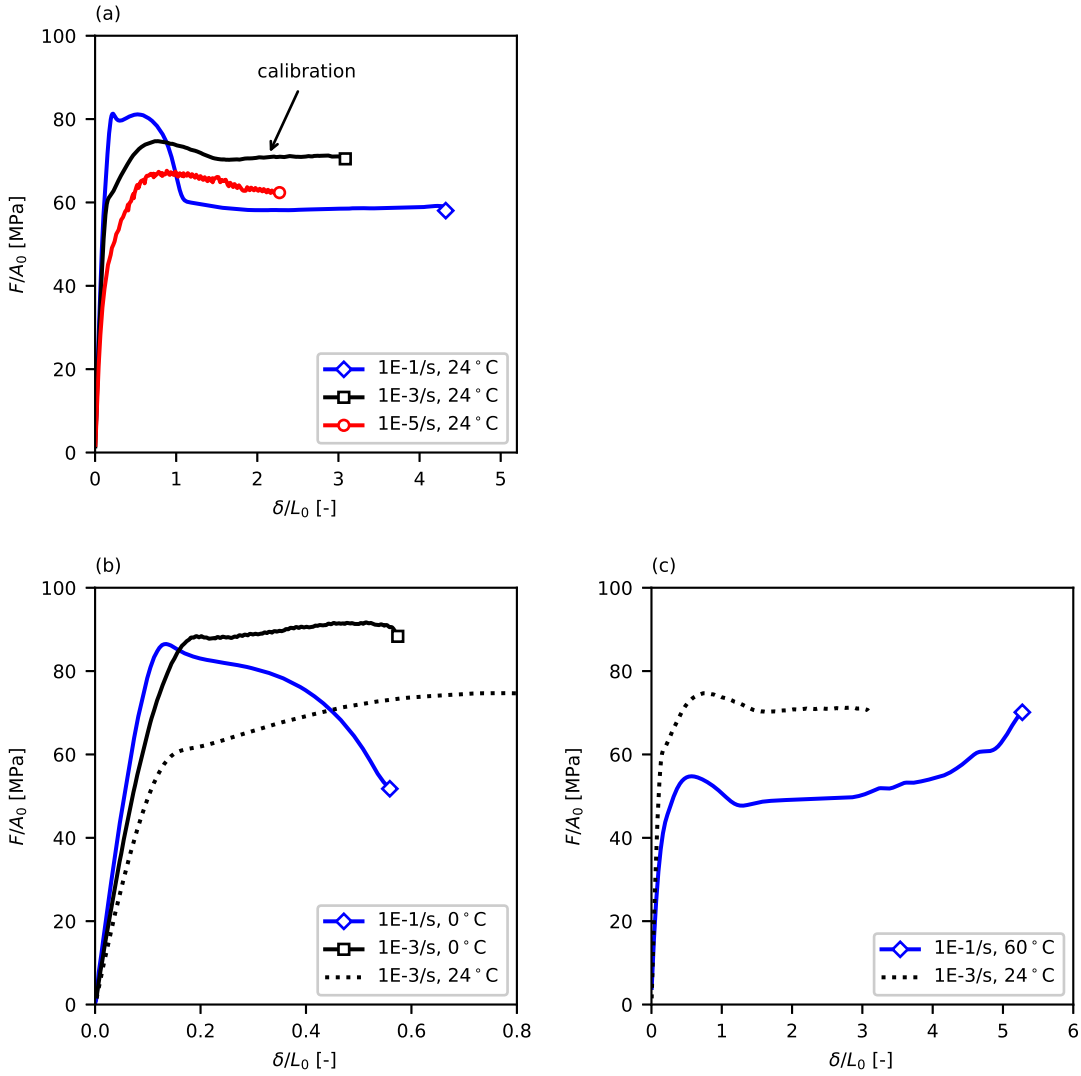

Figure 6.3: The experimental nominal stress–strain curves for PA-6 cylindrical bars loaded in tension at temperatures of (a) $T = 24\,^{\circ}\mathrm{C}$, (b) $T = 0\,^{\circ}\mathrm{C}$, and (c) $T = 60\,^{\circ}\mathrm{C}$. A reference test from (a) using the loading condition $T = 24\,^{\circ}\mathrm{C}$ and $\dot{\delta}/L_0 = 10^{-3}\,/\mathrm{s}$ is plotted in (b) and (c) with a dotted line to facilitate comparisons between (a), (b), and (c).

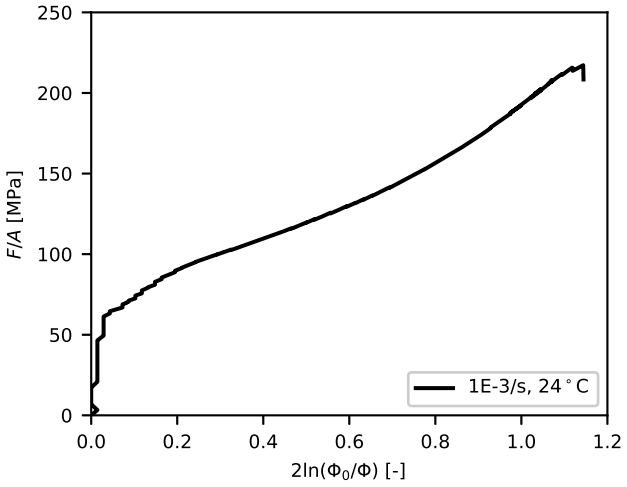

Figure 6.4: The true axial stress and true strain, as calculated by contour tracking, for a PA-6 cylindrical bar tested in tension at $T = 24\,^{\circ}\mathrm{C}$ and $\dot{\delta}/L_0 = 10^{-3}\,/\mathrm{s}$.

in Chapter 4. For drawings of the round notched bar geometry, refer to Appendix A. The RN bars were loaded at room temperature ($T = 24\,^{\circ}\mathrm{C} \pm 1\,^{\circ}\mathrm{C}$) using a nominal strain rate of $\dot{\delta}/L_0 = 10^{-3}\,/\mathrm{s}$, where L_0 is the initial height of the notch. As with the cylindrical bars, the true strain in the RN bars is measured by contour tracking, see Eq. (6.4). The nominal stress, F/A_0, is used when presenting the mechanical behavior of RN bars.

Tables 6.3 and 6.4 show the test matrices of the RN10 and RN2 bar experiments used in this chapter. Only a single experiment for each geometry is used here, and these experiments are reserved to validate the final calibration. The mechanical behavior of the RN bars is shown in Fig. 6.5.

6.3 Finite element models

Finite element calculations have been carried out in Abaqus/Standard, Version 6.14 [125]. Finite element models were created for each experimental specimen: the compression pin, the cylindrical bar, the RN10 bar, and the RN2 bar. This section describes these finite element models. After the viscoplastic polymer constitutive model was calibrated, the intrinsic mechanical behavior was studied using a single element, free from structural effects. The

Table 6.3: Test matrix of tensile experiments on RN10 bars used for validation. Conditions marked with a "V" are used for validation. No experiments on RN10 bars were used for calibration.

RN10 Bars Unaged		Temperature, $T < T_g$ $-30\,°C$	$0\,°C$	$24\,°C$	$T > T_g$ $60\,°C$
$\dot{\delta}/L_0$	$10^{-1}\,/s$				
	$10^{-3}\,/s$			V	
	$10^{-5}\,/s$				

Table 6.4: Test matrix of tensile experiments on RN2 bars used for validation. Conditions marked with a "V" are used for validation. No experiments on RN2 bars were used for calibration.

RN2 Bars Unaged		Temperature, $T < T_g$ $-30\,°C$	$0\,°C$	$24\,°C$	$T > T_g$ $60\,°C$
$\dot{\delta}/L_0$	$10^{-1}\,/s$				
	$10^{-3}\,/s$			V	
	$10^{-5}\,/s$				

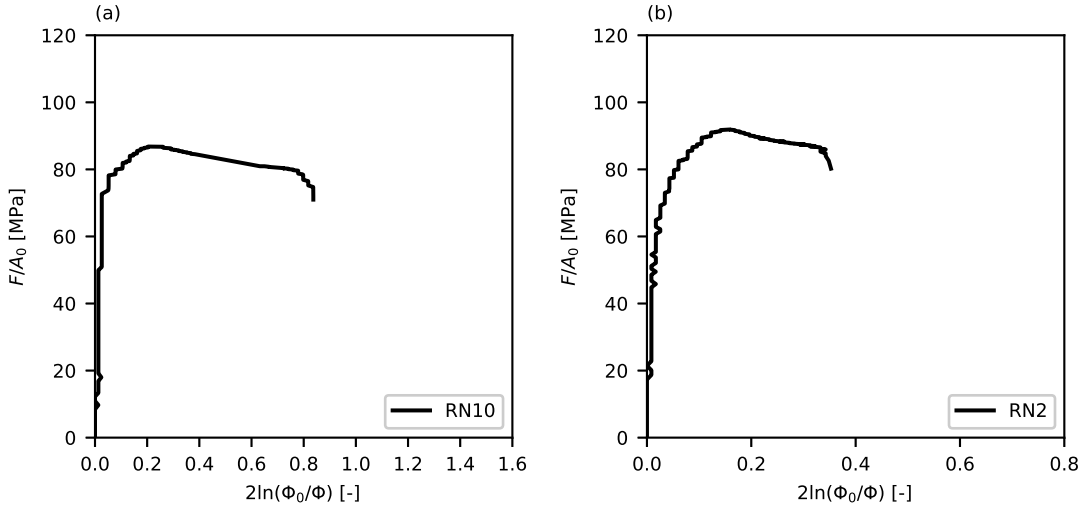

Figure 6.5: The experimental mechanical behavior for PA-6 round notched bars tested in tension at $T = 24\,°C$ and $\dot{\delta}/L_0 = 10^{-3}\,/s$. (a) The RN10 bar results. (b) The RN2 bar results.

boundary conditions applied to the single element to study the intrinsic behavior are also described in this section.

6.3.1 Compression pin model

Since the limited barreling exhibited by the compression pins is ignored (see Fig. 6.1), the deformation is approximated to be homogeneous, i.e. the effect of the specimen geometry on the mechanical behavior is neglected. Therefore, the compression pins are modeled using a single C3D8 element. The element is cubic with an initial length of $L_0 = 1$. First-order, fully-integrated elements are acceptable for modeling approximately incompressible deformation, as they are not as prone to volume locking as second-order, fully-integrated elements. Symmetry boundary conditions are applied to the $-x$, $-y$, and $-z$-faces. A constant displacement rate, $\dot{\delta}$, is applied to the $+y$-face.

6.3.2 Cylindrical bar model

An axisymmetric model is employed to model the tensile experiments on cylindrical bars. The boundary conditions and finite element mesh for the cylindrical bar are shown in Fig. 6.6. A symmetry condition is applied at the center of the model (zx-plane symmetry applied to the $-y$-face), so that only one-half of the specimen geometry is explicitly modeled. A constant displacement rate, $\dot{\delta}/2$, is applied to the top of the model ($+y$-face). Since a symmetry boundary condition is applied such that only half of the specimen is modeled, a displacement rate of $\dot{\delta}/2$ in the finite element model is equivalent to a displacement rate of $\dot{\delta}$ in the experiments. The mesh consists of 1241 nodes connected by 384 CAX8R elements. Reduced integration was used because second-order, fully-integrated elements (e.g. CAX8 elements), are susceptible to volume locking in problems when the deformation is approximately incompressible. The mesh is finest in the gauge section, which consists of a 12 by 24 grid of elements. This mesh was selected after a mesh convergence study.

The outputs from the model are designed to reflect the physical measurements from the experiments in Section 6.2. The crosshead displacement, δ, is simulated by measuring the

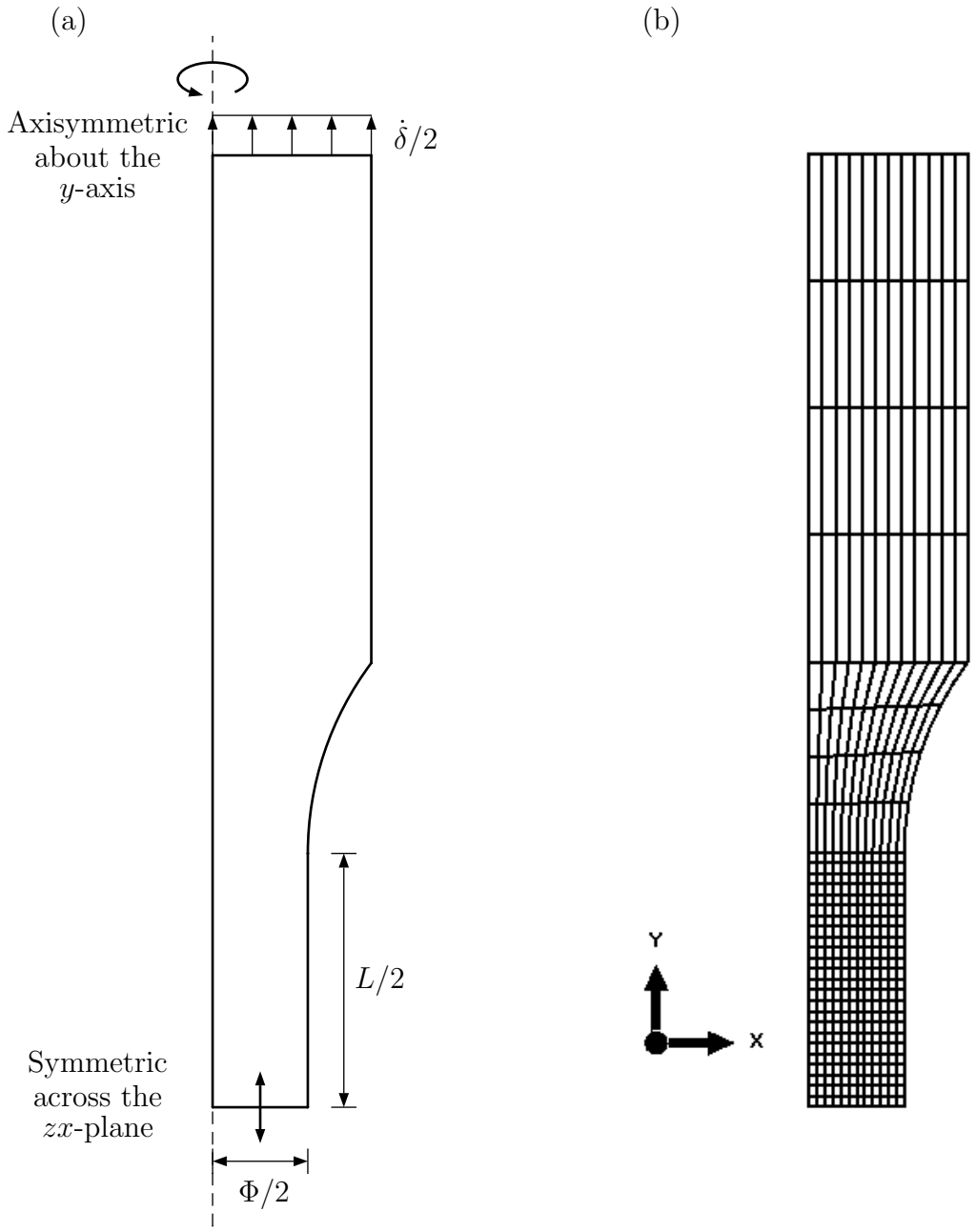

Figure 6.6: (a) Boundary conditions applied to the cylindrical bar model. (b) Finite element mesh of the cylindrical bar model.

displacement of the top face (y-face) of the model in the y-direction. Since a symmetry boundary condition is applied such that only half of the specimen is modeled, when the top face displaces by $\delta/2$, it corresponds to a displacement of δ in an experiment. The applied load, F, is measured by summing the reaction forces from all nodes across the center of the specimen, which is the $-y$-face in the symmetric model. The nominal stress and strain are calculated using Eq. (6.3), just as in the experiments. Therefore, the nominal stress–strain curve output from simulations is prone to the same weakness as in experiments; the nominal strain includes deformation of the both the grip and gauge section. For this reason, the grip length of the model is half that in the experimental specimen (see Fig. A.1 for a drawing of the experimental specimen). This represents the portion of the physical specimen that is clamped inside the grip of the test frame. Contour tracking measurements are also simulated by the model output. The radius of specimen is measured at the center (along the $-y$-face) to calculate the diameter, Φ, and the cross-sectional area, A. The stress and strain from simulated contour tracking are calculated using Eqs. (6.4) and (6.5).

6.3.3 Round notched bar models

Axisymmetric models are employed to model the tensile experiments on round notched bars. The boundary conditions and finite element meshes for the RN10 and RN2 bar are shown in Figs. 6.7 and 6.8. For both the RN10 and RN2 models, a symmetry condition is applied at the center of the model (zx-plane symmetry applied to the $-y$-face), so that only one-half of the specimen geometry is explicitly modeled. A constant displacement rate of $\dot{\delta}/2$ is applied to the top of the specimen ($+y$-face). The RN10 model mesh consists of 9817 nodes connected by 3168 CAX8R elements. The RN2 model mesh consists of 10201 nodes connected by 3312 CAX8R elements. As with the cylindrical bar, only half of the grip length is modeled, accounting for the portion of the experimental specimen clamped by the MTS grips.

The outputs from the model are designed to reflect the physical measurements from the experiments in Section 6.2. As with the cylindrical bar model, the crosshead displacement,

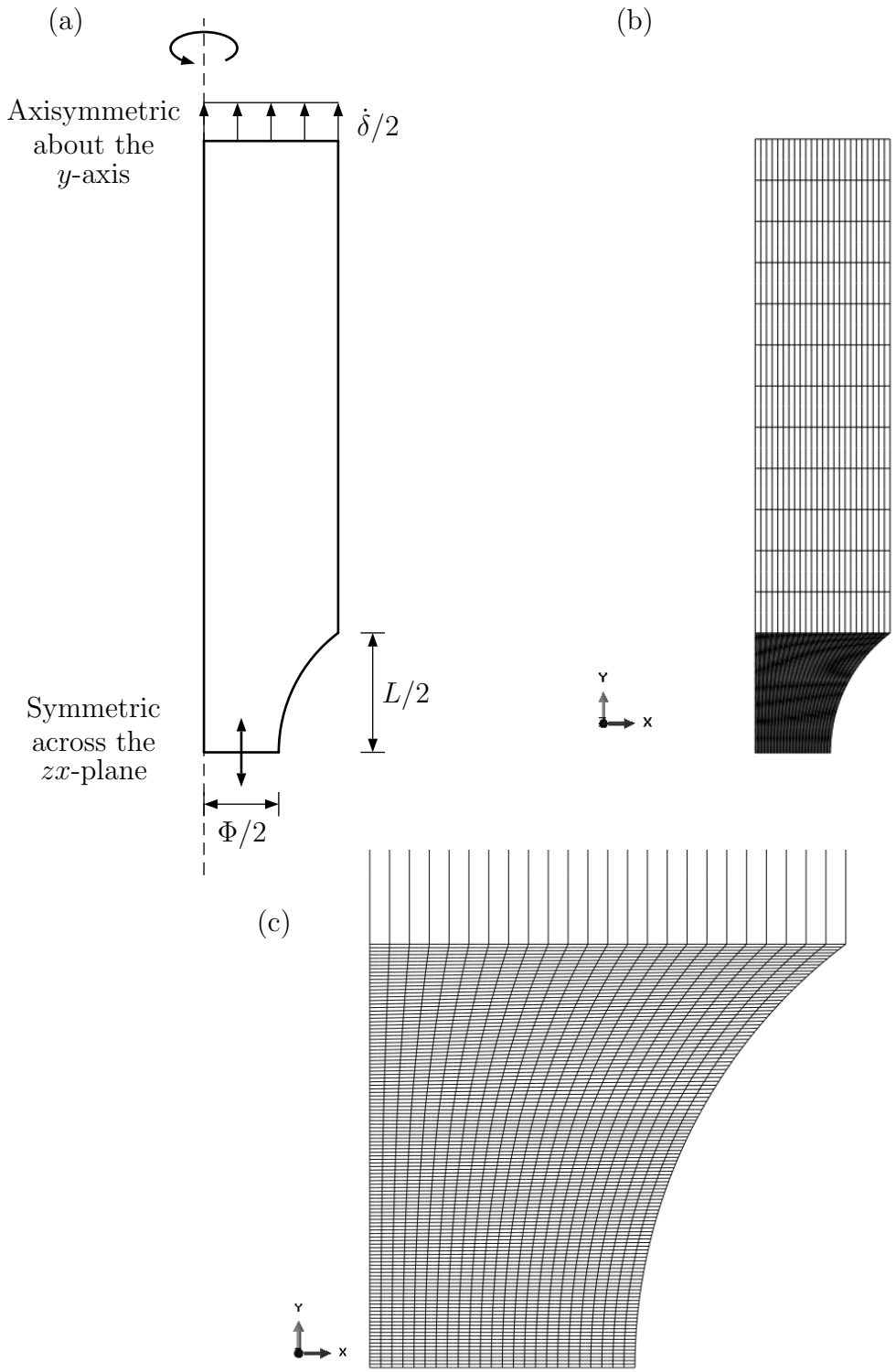

Figure 6.7: (a) Boundary conditions applied to the RN10 bar model. (b) Finite element mesh of the RN10 bar model. (c) A zoomed-in view of the mesh in the notch.

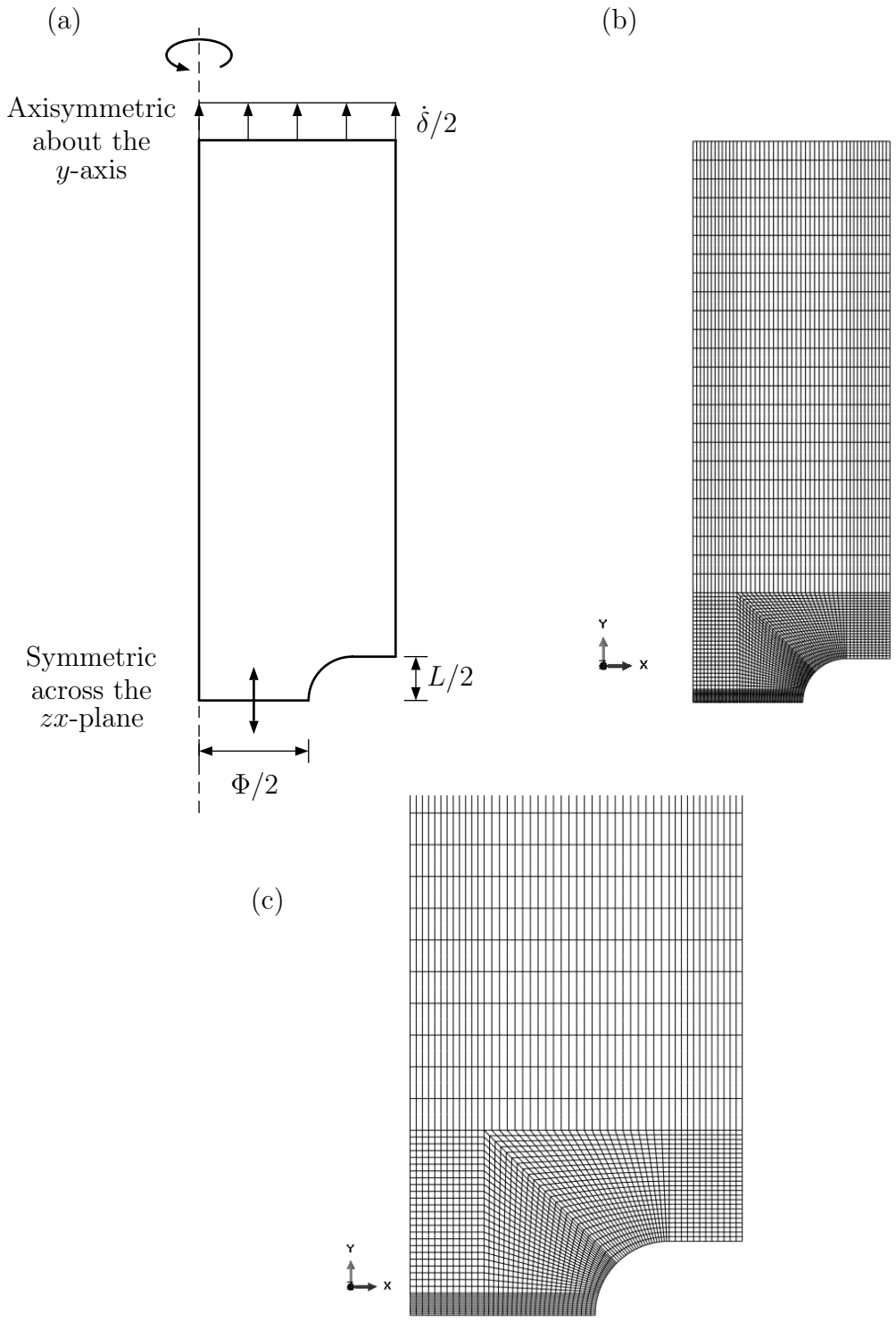

Figure 6.8: (a) Boundary conditions applied to the RN2 bar model. (b) Finite element mesh of the RN2 bar model. (c) A zoomed-in view of the mesh in the notch.

δ, is calculated from the displacement of the top face of the model in the y-direction, and the force is calculated by summing the reaction forces in all the nodes across the center of the specimen, the $-y$-face of the model. The nominal stress is calculated using F/A_0 and the true strain is calculated from the reduction in diameter using Eq. (6.4).

6.3.4 Finite element model for studying the intrinsic mechanical behavior

Once the constitutive law is calibrated, the intrinsic mechanical behavior is studied using a single C3D8 element. The element is cubic with an initial length of $L_0 = 1$. Symmetry boundary conditions are applied to the $-x$, $-y$, and $-z$-faces. A constant true strain rate is applied to the $+y$-face using the displacement function

$$\delta(t) = L_0 \left(e^{\dot{\varepsilon}_{22} t} - 1 \right), \tag{6.6}$$

where t is the time and $\dot{\varepsilon}_{22}$ is the applied constant true strain rate.

6.4 Constitutive model formulation

A macromolecular model is employed to represent the mechanical behavior of PA-6. The macromolecular model for amorphous polymers implemented by Kweon and Benzerga [30] is extended here for semicrystalline polymers. The extension follows the semicrystalline polymer model of Ayoub et al. 2011 [31].

Thermoplastics possess two physcially distinct resistances to large deformation: (1) the intermolecular resistance and (2) the network resistances [59, 60]. Following the model of Ayoub et al. 2011 [31], the intermolecular resistance in this model is composed of two parallel resistances representing contributions from the amorphous and crystalline phases. The intermolecular resistance in each phase is modeled using a hypoelastic law and a viscoplastic law sensitive to strain rate, temperature, and pressure. The crystal volume fraction is free to evolve based on the phenomenological equation for strain-induced crystallization used in Ahzi et al. 2003 [63]. The network resistance, introduced as a back stress in the flow rule of both phases, is modeled using the full network model [68] approximated by a linear com-

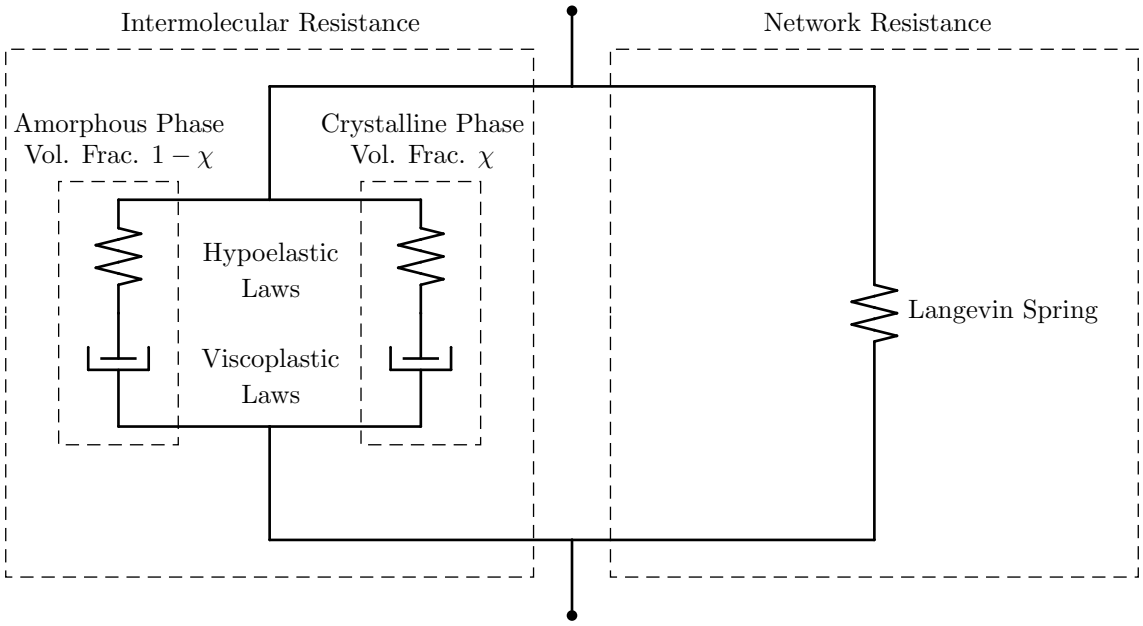

Figure 6.9: Rheological representation of the semicrystalline macromolecular model.

bination of the 3-chain [57] and 8-chain [67] models of rubber elasticity. In thermoplastics, the macromolecular network is not chemically linked as in a thermoset, but is instead connected through physical entanglements. At long timescales, disentanglement is possible, and is sometimes modeled by adding relaxation mechanisms to the network resistance [31, 61]. Disentanglement is neglected in this model. See Fig. 6.9 for a rheological representation of the model.

The model implemented here applies the network resistance to both the amorphous and crystalline phases, despite the fact that the 3-chain and 8-chain models are derived by sampling configurations of amorphous chains (see Fig. 2.11 for the representative volume elements of the 3-chain and 8-chain models). However, the 8-chain model has been applied to highly crystalline thermoplastics [31, 63]. At large strains, crystalline lamella unfold and reorient to form a fibrillar structure [126], similar to the orientation of amorphous chains. Although models of rubber elasticity are still inappropriate for the crystalline phase at small

strains, the network resistance at this stage is small relative to the crystalline intermolecular resistance.

6.4.1 Notation

For clarity, the notational conventions used to describe the model formulation (Section 6.4) and implementation (Section 6.5) are described here. Bold faced symbols represent second order tensors (e.g. $\boldsymbol{Z}$) and double struck symbols represent fourth order tensors (e.g. $\mathbb{Z}$). A symbol enclosed in brackets represents a matrix (e.g. $[Z]$). Unit vectors are written in boldface with a circumflex (e.g. $\hat{\boldsymbol{e}}_1$), and a set of basis vectors is denoted using curled brackets (e.g. $\{\hat{\boldsymbol{e}}_i\}$). For any symmetric, second order tensor $\boldsymbol{A}$, the symbols $\boldsymbol{A}'$ and A_m denote the deviatoric and mean normal parts of the tensor, defined as

$$\boldsymbol{A}' = \boldsymbol{A} - A_\mathrm{m}\boldsymbol{I}, \quad A_\mathrm{m} = \frac{1}{3}\operatorname{tr}\boldsymbol{A}, \tag{6.7}$$

where $\boldsymbol{I}$ is the second order identity tensor.

The Einstein summation convention is used for italicized lowercase indices, but not for italicized uppercase indices. The following notation is used for tensor and matrix operations:

- the transpose, $\left(\boldsymbol{Z}^\top\right)_{ij} = (\boldsymbol{Z})_{ji}$ or $\left(\mathbb{Z}^\top\right)_{ijkl} = (\mathbb{Z})_{klij}$,
- the inner product, $(\boldsymbol{Z}\cdot\boldsymbol{Y})_{ij} = Z_{im}Y_{mj}$,
- the double inner product, $\boldsymbol{Z}:\boldsymbol{Y} = Z_{mn}Y_{mn}$, or $(\mathbb{Z}:\boldsymbol{Y})_{ij} = Z_{ijmn}Y_{mn}$, or $(\mathbb{Z}:\mathbb{Y})_{ijkl} = Z_{ijmn}Y_{mnkl}$,
- the outer product, $(\boldsymbol{Z}\otimes\boldsymbol{Y})_{ijkl} = Z_{ij}Y_{kl}$,
- the operation $(\boldsymbol{Z}\odot\boldsymbol{Y})_{ijkl} = Z_{ik}Y_{jl}$, which is useful for defining fourth order rotation matrices in direct notation.

The coordinatization of a generic tensor $\boldsymbol{Z}$ into a basis $\{\hat{\boldsymbol{e}}_i\}$ is noted as ${}^{\{\hat{\boldsymbol{e}}_i\}}[\boldsymbol{Z}]$ [127]. In other words, ${}^{\{\hat{\boldsymbol{e}}_i\}}[\boldsymbol{Z}]$ is a matrix of the components of $\boldsymbol{Z}$ in the basis of $\{\hat{\boldsymbol{e}}_i\}$. For a second

order tensor, $\boldsymbol{Z} = {}^{\{\hat{\boldsymbol{e}}_i\}}[\boldsymbol{Z}]\, \hat{\boldsymbol{e}}_i \otimes \hat{\boldsymbol{e}}_j$. For a fourth order tensor, $\mathbb{Z} = {}^{\{\hat{\boldsymbol{e}}_i\}}[\mathbb{Z}]\, \hat{\boldsymbol{e}}_i \otimes \hat{\boldsymbol{e}}_j \otimes \hat{\boldsymbol{e}}_k \otimes \hat{\boldsymbol{e}}_l$.

The non-italicized subscript "a" denotes a quantity belonging to the amorphous phase, and the non-italicized subscript "c" denotes a quantity belonging to the crystalline phase. The subscript π is used as an index for either phase (i.e. $\pi = \mathrm{a}$ or c).

6.4.2 Kinematics and mixture rule for stresses

The intermolecular forces in the amorphous and crystalline phases are treated as parallel resistances, therefore the velocity gradients in both phases are equal;

$$\boldsymbol{L}_{\mathrm{a}} = \boldsymbol{L}_{\mathrm{c}} = \boldsymbol{L}. \tag{6.8}$$

The velocity gradient is additively decomposed into a symmetric and a skew symmetric part, known as the rate of deformation tensor and the spin tensor, respectively. This decomposition is unique; therefore the rate of deformation and spin tensors in each phase must also be equal;

$$\boldsymbol{D}_{\mathrm{a}} = \boldsymbol{D}_{\mathrm{c}} = \boldsymbol{D}, \quad \boldsymbol{W}_{\mathrm{a}} = \boldsymbol{W}_{\mathrm{c}} = \boldsymbol{W}. \tag{6.9}$$

It is assumed that the rate of deformation tensor in each phase can be additively decomposed into an elastic and a plastic part;

$$\boldsymbol{D} = \boldsymbol{D}_{\mathrm{a}}^{\mathrm{e}} + \boldsymbol{D}_{\mathrm{a}}^{\mathrm{p}}, \tag{6.10}$$

$$\boldsymbol{D} = \boldsymbol{D}_{\mathrm{c}}^{\mathrm{e}} + \boldsymbol{D}_{\mathrm{c}}^{\mathrm{p}}. \tag{6.11}$$

This decomposition is not unique; in general $\boldsymbol{D}_{\mathrm{a}}^{\mathrm{e}} \neq \boldsymbol{D}_{\mathrm{c}}^{\mathrm{e}}$ and $\boldsymbol{D}_{\mathrm{a}}^{\mathrm{p}} \neq \boldsymbol{D}_{\mathrm{c}}^{\mathrm{p}}$.

As a consequence of treating the phases as parallel resistances, the Cauchy stress tensors of each phase are added together in a modified mixture rule. The rule, as in the model of Ayoub et al. [31], is

$$\boldsymbol{\sigma} = \chi^{\gamma} \boldsymbol{\sigma}_{\mathrm{c}} + (1 - \chi)^{\gamma}\, \boldsymbol{\sigma}_{\mathrm{a}}, \tag{6.12}$$

where $\boldsymbol{\sigma}$ represents the total Cauchy stress tensor, $\boldsymbol{\sigma}_{\mathrm{a}}$ and $\boldsymbol{\sigma}_{\mathrm{c}}$ represent the Cauchy stress tensors in the amorphous and crystalline phases, χ represents the crystal volume fraction, and γ is a fitting parameter introduced to account for interactions between the amorphous and crystalline phases.

6.4.3 Intermolecular resistance

The elastic part of the rate of deformation tensor in each phase is governed by a hypoelastic law,

$$\boldsymbol{D}_{\pi}^{\mathrm{e}} = \mathbb{C}_{\pi}^{-1} : \overset{\triangledown}{\boldsymbol{\sigma}}_{\pi}, \tag{6.13}$$

where $\mathbb{C}_{\pi}$ is the isotropic stiffness tensor and $\overset{\triangledown}{\boldsymbol{\sigma}}_{\pi}$ is the Jaumann stress rate, defined by

$$\overset{\triangledown}{\boldsymbol{\sigma}}_{\pi} = \dot{\boldsymbol{\sigma}}_{\pi} + \boldsymbol{\sigma}_{\pi} \cdot \boldsymbol{W} - \boldsymbol{W} \cdot \boldsymbol{\sigma}_{\pi}. \tag{6.14}$$

The plastic part of the rate of deformation tensor is given by the flow rule,

$$\boldsymbol{D}_{\pi}^{\mathrm{p}} = \frac{3\dot{\bar{\varepsilon}}_{\pi}^{\mathrm{p}}}{2\bar{\sigma}_{\pi}} \left(\boldsymbol{\sigma}'_{\pi} - \boldsymbol{b}'\right), \tag{6.15}$$

where $\dot{\bar{\varepsilon}}_{\pi}^{\mathrm{p}}$ is defined as

$$\dot{\bar{\varepsilon}}_{\pi}^{\mathrm{p}} = \sqrt{\frac{2}{3}\boldsymbol{D}_{\pi}^{\mathrm{p}} : \boldsymbol{D}_{\pi}^{\mathrm{p}}}, \tag{6.16}$$

$\bar{\sigma}_{\pi}$ is the equivalent driving stress, defined as

$$\bar{\sigma}_{\pi} = \sqrt{\frac{3}{2}\left(\boldsymbol{\sigma}'_{\pi} - \boldsymbol{b}'\right) : \left(\boldsymbol{\sigma}'_{\pi} - \boldsymbol{b}'\right)}, \tag{6.17}$$

$\boldsymbol{\sigma}'_{\pi}$ is the deviatoric Cauchy stress tensor, and $\boldsymbol{b}'$ is the deviatoric part of the back stress tensor, which represents the orientation hardening. A description of the evolution of $\boldsymbol{b}$ is postponed until Section 6.4.4.

The magnitude of the plastic rate of deformation in both phases is calculated from the

temperature, strain rate, and pressure-sensitive viscoplastic law

$$\dot{\bar{\varepsilon}}_{\pi}^{\mathrm{p}} = \dot{\varepsilon}_0 \exp\left[-\frac{\mathcal{A}_{\pi}\left(s_{\pi} - 3\alpha_{\pi}\sigma_{\pi,\mathrm{m}}\right)}{T}\left(1 - \left(\frac{\bar{\sigma}_{\pi}}{s_{\pi} - 3\alpha_{\pi}\sigma_{\pi,\mathrm{m}}}\right)^{m_{\pi}}\right)\right], \tag{6.18}$$

where $\dot{\varepsilon}_0$ and $\mathcal{A}_{\pi}$ are material parameters that control the rate and temperature sensitivity, α_{π} is a material parameter that controls the pressure sensitivity, s_{π} is the athermal shear strength, $\sigma_{\pi,\mathrm{m}}$ is the mean normal Cauchy stress, T is the absolute temperature, and m_{π} is an exponent that also controls the temperature and rate sensitivity. The exponent m_{a} was derived to be 5/6 in Argon 1973 [60], but was taken as a material parameter in Kweon and Benzerga 2013 [30]. Although this viscoplastic law was derived from a model of an amorphous polymer chain [60], it has the form of an Arrhenius-type equation. The plastic flow in the crystalline phase is assumed to be primarily due to crystallographic slip [128], which is also a thermally activated process commonly modeled by the Arrhenius equation. Therefore, the form of this viscoplastic law is assumed to be capable of appropriately modeling plastic flow in the crystalline phase [63].

The athermal shear strength, s_{π}, evolves to capture the intrinsic softening and hardening that occurs in polymers at low strains. It essentially controls the strength of the intermolecular resistance. The original evolution law used by Boyce et al. 1988 [57] results in a sharp yield point, which is rarely observed in polymers. A modified evolution law presented by Chowdhury et al. 2008 [70] allows for a more gradual rollover to yield. The modified evolution law for the athermal shear strength, implemented here, is given by

$$\dot{s}_{\pi} = H_{1,\pi}\left(\bar{\varepsilon}_{\pi}^{\mathrm{p}}\right)\left(1 - \frac{s_{\pi}}{s_{1,\pi}}\right)\dot{\bar{\varepsilon}}_{\pi}^{\mathrm{p}} + H_{2,\pi}\left(\bar{\varepsilon}_{\pi}^{\mathrm{p}}\right)\left(1 - \frac{s_{\pi}}{s_{2,\pi}}\right)\dot{\bar{\varepsilon}}_{\pi}^{\mathrm{p}}, \tag{6.19}$$

$$H_{1,\pi}\left(\bar{\varepsilon}_{\pi}^{\mathrm{p}}\right) = -h_{1,\pi}\left[\tanh\left(\frac{\bar{\varepsilon}_{\pi}^{\mathrm{p}} - \bar{\varepsilon}_{\pi}^{\mathrm{w}}}{f_{\pi}\bar{\varepsilon}_{\pi}^{\mathrm{w}}}\right) - 1\right], \tag{6.20}$$

$$H_{2,\pi}\left(\bar{\varepsilon}_{\pi}^{\mathrm{p}}\right) = h_{2,\pi}\left[\tanh\left(\frac{\bar{\varepsilon}_{\pi}^{\mathrm{p}} - \bar{\varepsilon}_{\pi}^{\mathrm{w}}}{f_{\pi}\bar{\varepsilon}_{\pi}^{\mathrm{w}}}\right) + 1\right], \tag{6.21}$$

$$\bar{\varepsilon}_{\pi}^{\mathrm{p}}(t) = \int_0^t \dot{\bar{\varepsilon}}_{\pi}^{\mathrm{p}}\,\mathrm{d}\tau, \tag{6.22}$$

where $s_{1,\pi}$ and $s_{2,\pi}$ are adjustable parameters related to the peak and saturation strength, $h_{1,\pi}$ is related to the slope of the rise to the initial peak strength, $h_{2,\pi}$ is the decreasing slope past the peak strength, f_{π} is a parameter related to the width of the peak, and $\bar{\varepsilon}_{\pi}^{\mathrm{w}}$ is a parameter related to the location of the peak.

In some situations, large deformations may favor crystallization, referred to as strain-induced crystallization. In this model, the crystalline volume fraction is free to evolve according to a phenomenological equation first derived by Doufas et al. [72, 73] and later modified by Ahzi et al. [63]. The evolution law for the crystallinity is given by

$$\dot{\chi} = \phi_{\infty}\left\{\frac{\dot{\bar{\varepsilon}}^{\mathrm{tot}}}{\dot{\varepsilon}_0^{\mathrm{tot}}} n K_{\mathrm{av}}(T)\left[-\ln\left(1 - \frac{\chi}{\phi_{\infty}}\right)\right]^{(n-1)/n}\left(1 - \frac{\chi}{\phi_{\infty}}\right)\exp\left(\zeta\frac{\mathrm{tr}\,\boldsymbol{\sigma}}{\mu_{\mathrm{eff}}}\right)\right\}, \tag{6.23}$$

where ϕ_{∞} is the maximum possible crystallinity for the polymer, n is the Avrami exponent, $K_{\mathrm{av}}(T)$ is the transformation rate function for the polymer, ζ is a dimensionless material parameter related to the pressure sensitivity, $\dot{\bar{\varepsilon}}^{\mathrm{tot}}$ is the effective total strain rate, defined as

$$\dot{\bar{\varepsilon}}^{\mathrm{tot}} = \sqrt{\frac{2}{3}\boldsymbol{D} : \boldsymbol{D}}, \tag{6.24}$$

$\dot{\varepsilon}_0^{\mathrm{tot}}$ is a reference strain rate, and μ_{eff} is the effective shear modulus of the combined phases, given by the same mixture rule governing the Cauchy stress,

$$\mu_{\mathrm{eff}} = \chi^{\gamma}\mu_{\mathrm{c}} + (1 - \chi)^{\gamma}\,\mu_{\mathrm{a}}. \tag{6.25}$$

6.4.4 Network resistance

Wu and van der Giessen [68] derived a full network model for rubber elasticity and found that it could be conveniently approximated through a linear combination of the 3-chain [57] and 8-chain [67] models previously proposed. Later, they rederived the back stress evolution in a rate tangent form [69] as

$$\overset{\triangledown}{\boldsymbol{b}} = \mathbb{R} : \boldsymbol{D}, \tag{6.26}$$

$$\mathbb{R} = (1-\kappa)\,\mathbb{R}^{3-\mathrm{ch}} + \kappa \mathbb{R}^{8-\mathrm{ch}}, \quad \kappa = 0.85\frac{\bar{\lambda}}{\sqrt{N}}, \tag{6.27}$$

where $\mathbb{R}^{3-\mathrm{ch}}$ and $\mathbb{R}^{8-\mathrm{ch}}$ are the back stress moduli for the 3-chain and 8-chain models, N is the average number of links between entanglements, and $\bar{\lambda}$ is the maximum principal stretch calculated from the left Cauchy-Green tensor, $\boldsymbol{B} = \boldsymbol{F} \cdot \boldsymbol{F}^{\top}$. Although the back stress tensor should evolve according to the accumulated plastic deformation [57], it is assumed here that the elastic deformations are small compared to the plastic deformations and therefore the difference between using $\overset{\triangledown}{\boldsymbol{b}} = \mathbb{R} : \boldsymbol{D}$ and $\overset{\triangledown}{\boldsymbol{b}}_{\pi} = \mathbb{R} : \boldsymbol{D}^{\mathrm{p}}_{\pi}$ is not significant [69]. This decision was made to avoid the need for separate back stresses in each phase. The components of $\mathbb{R}^{8-\mathrm{ch}}$, expressed in the material frame, $\{\hat{\boldsymbol{e}}_i\}$, can be written as

$$R^{8-\mathrm{ch}}_{ijkl} = \frac{1}{3}C^{\mathrm{R}}\sqrt{N}\left[\left(\frac{\xi_{\mathrm{c}}}{\sqrt{N}} - \frac{\beta_{\mathrm{c}}}{\lambda_{\mathrm{c}}}\right)\frac{B_{ij}B_{kl}}{B_{mm}} + \frac{\beta_{\mathrm{c}}}{\lambda_{\mathrm{c}}}\left(\delta_{ik}B_{jl} + B_{ik}\delta_{jl}\right)\right], \tag{6.28}$$

$$\lambda_{\mathrm{c}}^2 = \frac{1}{3}\operatorname{tr}\boldsymbol{B}, \quad \beta_{\mathrm{c}} = \mathcal{L}^{-1}\left(\frac{\lambda_{\mathrm{c}}}{\sqrt{N}}\right), \quad \xi_{\mathrm{c}} = \frac{\beta_{\mathrm{c}}^2}{1 - \beta_{\mathrm{c}}^2 \operatorname{csch}^2 \beta_{\mathrm{c}}}, \tag{6.29}$$

where C^{R} is the rubbery modulus, δ_{ij} is the Kronecker delta, and $\mathcal{L}(x) = \coth(x) - \frac{1}{x}$ is the Langevin function, whose inverse is approximated in this model by a Padé approximation. The Padé approximation used here is

$$\mathcal{L}^{-1}(x) = 3x + \frac{9}{5}x^3 + \frac{297}{175}x^5 + \frac{1539}{875}x^7. \tag{6.30}$$

The form of $\mathbb{R}^{3-\mathrm{ch}}$ does not lend itself to an easy tensorial representation. The components of $\mathbb{R}^{3-\mathrm{ch}}$ are calculated from the principal stretches and expressed using the basis in which the components of $\boldsymbol{B}$ form a diagonal matrix, referred to here as the principal frame of $\boldsymbol{B}$, the basis of which is denoted as $\{\hat{\boldsymbol{p}}_i\}$. The components of $\mathbb{R}^{3-\mathrm{ch}}$, expressed in the principal frame of $\boldsymbol{B}$, $\{\hat{\boldsymbol{p}}_i\}$, can be written as

$$R^{3-\mathrm{ch}}_{IJKL} = \begin{cases} \dfrac{1}{6}C^{\mathrm{R}}\sqrt{N}\lambda_I^2\left(\dfrac{\xi_I}{\sqrt{N}}+\dfrac{\beta_I}{\lambda_I}\right)(\delta_{IK}\delta_{JL}+\delta_{JK}\delta_{IL}) & \text{if } \lambda_I = \lambda_J \\ \dfrac{1}{6}C^{\mathrm{R}}\sqrt{N}\dfrac{\lambda_I^2+\lambda_J^2}{\lambda_I^2-\lambda_J^2}(\lambda_I\beta_I-\lambda_J\beta_J)(\delta_{IK}\delta_{JL}+\delta_{JK}\delta_{IL}) & \text{if } \lambda_I \neq \lambda_J \end{cases} \tag{6.31}$$

$$\beta_I = \mathcal{L}^{-1}\left(\frac{\lambda_I}{\sqrt{N}}\right), \quad \xi_I = \frac{\beta_I^2}{1-\beta_I^2\,\mathrm{csch}^2\,\beta_I}. \tag{6.32}$$

6.5 Constitutive model implementation

The constitutive model in Section 6.4 has been implemented as an Abaqus/Standard user-defined material subroutine (UMAT). The model uses a corotational formulation for compatibility with Abaqus. In a corotational formulation, constitutive equations are expressed in a rotated configuration obtained from a transformation by $\boldsymbol{R}^*$, where $\boldsymbol{R}^*$ is the rotation tensor obtained from the polar decomposition of the incremental deformation gradient,

$$\Delta\boldsymbol{F} = \boldsymbol{R}^* \cdot \boldsymbol{U}^*. \tag{6.33}$$

Tensorial quantities are transformed into the rotated configuration according to

$$\tilde{\boldsymbol{Z}} = \boldsymbol{R}^* \cdot \boldsymbol{Z} \cdot \boldsymbol{R}^{*\top}, \tag{6.34}$$

Where $\boldsymbol{Z}$ is a generic second order tensor and the over-tilde ($\tilde{\boldsymbol{Z}}$) represents quantities transformed into the rotated configuration. This preserves incremental objectivity in that it is equivalent to to using the Jaumann rate, Eq. (6.14). Therefore, the actual Jaumann rate is

not calculated. For example, Eq. (6.13) becomes

$$\tilde{\boldsymbol{D}}_{\pi}^{\mathrm{e}} = \mathbb{C}_{\pi}^{-1} : \dot{\tilde{\boldsymbol{\sigma}}}_{\pi}. \tag{6.35}$$

Notice that $\mathbb{C}$ is not rotated, as it is an isotropic tensor.[2]

The computation of the back stress modulus $\mathbb{R}$ requires special attention. The components of $\mathbb{R}^{8-\mathrm{ch}}$ are expressed in the basis $\{\hat{\boldsymbol{e}}_i\}$ using the components of $\boldsymbol{B} = \boldsymbol{F} \cdot \boldsymbol{F}^{\top}$ see Eqs. (6.28) and (6.29). In the UMAT, $\boldsymbol{F}$ is taken at the end of the time step, therefore the components of $\mathbb{R}^{8-\mathrm{ch}}$ are already expressed in the rotated configuration and do not need to be rotated by $\boldsymbol{R}^{*}$, i.e. $\{\hat{\boldsymbol{e}}_i\}$ is the basis of the rotated configuration. However, the components of $\mathbb{R}^{3-\mathrm{ch}}$ are calculated from the principal stretches and expressed in the principal frame of $\boldsymbol{B}$, which uses the basis $\{\hat{\boldsymbol{p}}_i\}$, see Eqs. (6.31) and (6.32). In order to represent the components of $\mathbb{R}^{3-\mathrm{ch}}$ in the basis $\{\hat{\boldsymbol{e}}_i\}$, they are rotated following the transformation rule for a fourth order tensor, which can be written as

$${}^{\{\hat{\boldsymbol{e}}\}}\left[\tilde{\mathbb{R}}^{3-\mathrm{ch}}\right] = ([\boldsymbol{V}] \odot [\boldsymbol{V}]) : {}^{\{\hat{\boldsymbol{p}}\}}\left[\tilde{\mathbb{R}}^{3-\mathrm{ch}}\right] : ([\boldsymbol{V}] \odot [\boldsymbol{V}])^{\top}, \tag{6.36}$$

where $[\boldsymbol{V}]$ is the matrix of the eigenvectors of $\boldsymbol{B}$ (the columns of $[\boldsymbol{V}]$ are the eigenvectors of $\boldsymbol{B}$). After transforming the components of $\mathbb{R}^{3-\mathrm{ch}}$ into the basis $\{\hat{\boldsymbol{e}}_i\}$, ${}^{\{\hat{\boldsymbol{e}}\}}\left[\tilde{\mathbb{R}}^{8-\mathrm{ch}}\right]$ and ${}^{\{\hat{\boldsymbol{e}}\}}\left[\tilde{\mathbb{R}}^{3-\mathrm{ch}}\right]$ are added together following Eq. (6.27).

A Newton-Raphson procedure is used to solve for the state variables at the current time increment. The rotated state variables are collected in a vector set,

$$[X] = \left[\tilde{\boldsymbol{\sigma}}'_{\mathrm{a}},\ \tilde{\boldsymbol{\sigma}}'_{\mathrm{c}},\ \tilde{\boldsymbol{b}}',\ \tilde{b}_{\mathrm{m}},\ \tilde{\sigma}_{\mathrm{a,m}},\ \tilde{\sigma}_{\mathrm{c,m}},\ s_{\mathrm{a}},\ s_{\mathrm{c}},\ \chi\right]^{\top}. \tag{6.37}$$

[2]It has recently been brought to my attention that the evolution of the back stress in Eq. (6.26) does not uphold objectivity. This was not an issue in Ref. [69] where a convected representation of finite plasticity was used; it is, however, an issue within a corotational formulation. Although this needs to be addressed in future versions of the model, the loss of objectivity will not significantly impact the results presented here, as the calculations primarily involve stretching with very little rotation.

The volumetric-deviatoric decomposition is applied to tensors to facilitate convergence [30]. The system of equations is solved using an implicit backward Euler scheme. For example, the athermal shear strength in the amorphous phase is integrated using,

$$s_{\mathrm{a}}(t+\Delta t) = s_{\mathrm{a}}(t) + \Delta t \dot{s}_{\mathrm{a}}(t+\Delta t, [X]), \tag{6.38}$$

where t is the time at the start of the step and Δt is the time step. The residual on s_{a} is then calculated as

$$R_{s_{\mathrm{a}}} = \frac{s_{\mathrm{a}}(t+\Delta t) - s_{\mathrm{a}}(t)}{\Delta t} - \dot{s}_{\mathrm{a}}(t+\Delta t, [X]), \tag{6.39}$$

and the evolution equation, Eq. (6.19), is used to evaluate $\dot{s}_{\mathrm{a}}(t+\Delta t, [X])$. The residuals are collected in a vector set

$$[R] = \left[\boldsymbol{R}_{\tilde{\boldsymbol{\sigma}}'_{\mathrm{a}}},\ \boldsymbol{R}_{\tilde{\boldsymbol{\sigma}}'_{\mathrm{c}}},\ \boldsymbol{R}_{\tilde{\boldsymbol{b}}'},\ R_{\tilde{b}_{\mathrm{m}}},\ R_{\tilde{\sigma}_{\mathrm{a,m}}},\ R_{\tilde{\sigma}_{\mathrm{c,m}}},\ R_{s_{\mathrm{a}}},\ R_{s_{\mathrm{c}}},\ R_{\chi}\right]^{\top}. \tag{6.40}$$

The expression of each residual is:

$$\boldsymbol{R}_{\tilde{\boldsymbol{\sigma}}'_{\mathrm{a}}} = \left(\frac{1}{2\mu_{\mathrm{a}}}\right)\frac{\tilde{\boldsymbol{\sigma}}'_{\mathrm{a}} - (\tilde{\boldsymbol{\sigma}}'_{\mathrm{a}})_0}{\Delta t} + \frac{3\dot{\tilde{\varepsilon}}^{\mathrm{p}}_{\mathrm{a}}}{2\tilde{\bar{\sigma}}_{\mathrm{a}}}\left(\tilde{\boldsymbol{\sigma}}'_{\mathrm{a}} - \tilde{\boldsymbol{b}}'\right) - \tilde{\boldsymbol{D}}', \tag{6.41}$$

$$\boldsymbol{R}_{\tilde{\boldsymbol{\sigma}}'_{\mathrm{c}}} = \left(\frac{1}{2\mu_{\mathrm{c}}}\right)\frac{\tilde{\boldsymbol{\sigma}}'_{\mathrm{c}} - (\tilde{\boldsymbol{\sigma}}'_{\mathrm{c}})_0}{\Delta t} + \frac{3\dot{\tilde{\varepsilon}}^{\mathrm{p}}_{\mathrm{c}}}{2\tilde{\bar{\sigma}}_{\mathrm{c}}}\left(\tilde{\boldsymbol{\sigma}}'_{\mathrm{c}} - \tilde{\boldsymbol{b}}'\right) - \tilde{\boldsymbol{D}}', \tag{6.42}$$

$$\boldsymbol{R}_{\tilde{\boldsymbol{b}}'} = \frac{\tilde{\boldsymbol{b}}' - \left(\tilde{\boldsymbol{b}}'\right)_0}{\Delta t} - \mathbb{J} : \tilde{\mathbb{R}} : \tilde{\boldsymbol{D}}, \tag{6.43}$$

$$R_{\tilde{b}_{\mathrm{m}}} = \frac{\tilde{b}_{\mathrm{m}} - \left(\tilde{b}_{\mathrm{m}}\right)_0}{\Delta t} - \frac{1}{3}\boldsymbol{I} : \tilde{\mathbb{R}} : \tilde{\boldsymbol{D}}, \tag{6.44}$$

$$R_{\tilde{\sigma}_{\mathrm{a,m}}} = \frac{\tilde{\sigma}_{\mathrm{a,m}} - (\tilde{\sigma}_{\mathrm{a,m}})_0}{\Delta t} - K_{\mathrm{a}}\,\mathrm{tr}\,\tilde{\boldsymbol{D}}, \tag{6.45}$$

$$R_{\tilde{\sigma}_{\mathrm{c,m}}} = \frac{\tilde{\sigma}_{\mathrm{c,m}} - (\tilde{\sigma}_{\mathrm{c,m}})_0}{\Delta t} - K_{\mathrm{c}}\,\mathrm{tr}\,\tilde{\boldsymbol{D}}, \tag{6.46}$$

$$R_{s_\mathrm{a}} = \frac{s_\mathrm{a} - (s_\mathrm{a})_0}{\Delta t} - H_{1,\mathrm{a}} \left(1 - \frac{s_\mathrm{a}}{s_{1,\mathrm{a}}}\right) \tilde{\dot{\varepsilon}}^\mathrm{p}_\mathrm{a} - H_{2,\mathrm{a}} \left(1 - \frac{s_\mathrm{a}}{s_{2,\mathrm{a}}}\right) \tilde{\dot{\varepsilon}}^\mathrm{p}_\mathrm{a}, \tag{6.47}$$

$$R_{s_\mathrm{c}} = \frac{s_\mathrm{c} - (s_\mathrm{c})_0}{\Delta t} - H_{1,\mathrm{c}} \left(1 - \frac{s_\mathrm{c}}{s_{1,\mathrm{c}}}\right) \tilde{\dot{\varepsilon}}^\mathrm{p}_\mathrm{c} - H_{2,\mathrm{a}} \left(1 - \frac{s_\mathrm{c}}{s_{2,\mathrm{c}}}\right) \tilde{\dot{\varepsilon}}^\mathrm{p}_\mathrm{c}, \tag{6.48}$$

$$R_\chi = \frac{\chi - (\chi)_0}{\Delta t} - \phi_\infty \left\{ \frac{\tilde{\dot{\varepsilon}}^\mathrm{tot}}{\dot{\varepsilon}^\mathrm{tot}_0} n K_\mathrm{av}(T) \left[-\ln\left(1 - \frac{\chi}{\phi_\infty}\right)\right]^{(n-1)/n} \left(1 - \frac{\chi}{\phi_\infty}\right) \right. \tag{6.49}$$

$$\left. \exp\left[\frac{3\zeta\left(\chi^\gamma \tilde{\sigma}_\mathrm{c,m} + (1-\chi)^\gamma \tilde{\sigma}_\mathrm{a,m}\right)}{\chi^\gamma \mu_\mathrm{c} + (1-\chi)^\gamma \mu_\mathrm{a}}\right] \right\}.$$

In the above expressions, μ_a, μ_c are the shear moduli, K_a, K_c are the bulk moduli, $\boldsymbol{I}$ is the second order identity tensor, and $\mathbb{J}$ is the fourth-order deviatoric projector, i.e. $J_{ijkl} = \frac{1}{2}\left(\delta_{ik}\delta_{jl} + \delta_{il}\delta_{jk}\right) - \frac{1}{3}\delta_{ij}\delta_{kl}$. The values of the state variables at the start the time increment are denoted using a subscript 0.

The Newton-Raphson method is used to iteratively solve Eqs. (6.41)–(6.49) for $[R] = [0]$:

$$[X]^{i+1} = [X]^i - \left[\frac{\partial [R]}{\partial [X]}\right]^{-1} [R], \tag{6.50}$$

where i is the iteration count within the current time step. The Jacobian matrix, $\left[\frac{\partial [R]}{\partial [X]}\right]$ must be evaluated. Its terms are given in Section C.1.

To facilitate convergence, the consistent tangent matrix is calculated and returned to the finite element solver,

$$\tilde{\mathbb{L}} = \frac{1}{\Delta t}\left(\frac{\partial \tilde{\boldsymbol{\sigma}}'}{\partial \tilde{\boldsymbol{D}}} + \boldsymbol{I} \otimes \frac{\partial \tilde{\sigma}_\mathrm{m}}{\partial \tilde{\boldsymbol{D}}}\right). \tag{6.51}$$

The derivatives $\frac{\partial \tilde{\boldsymbol{\sigma}}'}{\partial \tilde{\boldsymbol{D}}}$ and $\frac{\partial \tilde{\sigma}_\mathrm{m}}{\partial \tilde{\boldsymbol{D}}}$ are calculated from $\frac{\partial [X]}{\partial \tilde{\boldsymbol{D}}}$, which itself is calculated by

$$\left[\frac{\partial [X]}{\partial \tilde{\boldsymbol{D}}}\right] = -\left[\frac{\partial [R]}{\partial [X]}\right]^{-1} \left[\frac{\partial [R]}{\partial \tilde{\boldsymbol{D}}}\right]. \tag{6.52}$$

The components of $\left[\frac{\partial [R]}{\partial \tilde{\boldsymbol{D}}}\right]$ are given in Section C.2.

6.6 Inverse problem definition

Optimization is the process of determining values for a set of parameters that minimizes some function, referred to as the objective function. The objective function itself may be a weighted sum of other functions. For example, an objective function $G(x_i)$ with q parameters $(i = 1,\ 2, ...,\ q)$ might be defined by the weighted sum of r different constituent objective functions, $g_j(x_i)$ $(j = 1,\ 2, ...,\ r)$,

$$G(x_i) = \sum_{j=1}^{r} w_j g_j(x_i), \tag{6.53}$$

where w_j is the weight of g_j. In the context of model calibration, optimization can be used to select model parameters that create the best fit between the model output and an experimental data set. In this case, each objective function represents the difference between experimental data from one set of conditions and corresponding model data. The total objective function then represents the best fit across all experiments, with the possibility of giving more important experimental conditions a higher weight during optimization.

In this chapter, the semicrystalline macromolecular model is calibrated using optimization. Optimization is carried out using the optimization module of Z-set [129, 130]. The Nelder-Mead optimization algorithm [131] is used. Although the classic Nelder-Mead algorithm does not support parameter constraints, constraints are supported in the Z-set implementation through a basic penalty technique [129].

During each iteration of the optimization algorithm, some constitutive behavior is assumed, defined by a set of model parameters. That assumed constitutive behavior is then used to simulate the mechanical behavior of one or more specimens. The constitutive behavior that produces the best fit to the specimen-level response is assumed to be the correct intrinsic mechanical behavior of the actual material. This method is therefore referred to as "inverse parameter identification", since it starts from the effects of a phenomenon (the specimen-level response of the experiment) to determine the cause (the intrinsic mechani-

cal behavior). In this section, the inverse problem is defined, which consists of the model parameters, constraints on those parameters, and the experimental data from the specimen-level response. The experimental data has already been described in Section 6.2, so the present section is concerned with defining the parameters and their constraints. Many parameters enter into model described in Section 6.4, so it is desirable to reduce the parameter space explored during optimization. Some parameters are assigned values from deterministic calibration, while simplifying approximations are used to assign values to others.

This section is divided into three parts. In Section 6.6.1, all model parameters are summarized. In Section 6.6.2, the space of free parameters is reduced through a combination of simplifying approximations and deterministic calibration. In Section 6.6.3, the inverse problem definition is summarized by listing the free parameters and parameter constraints.

6.6.1 Summary of model parameters

Table 6.5 summarizes all of the model parameters introduced in Section 6.4. The parameters $s_{\mathrm{a},0}$, $s_{\mathrm{c},0}$, and χ_0 are somewhat different than the other parameters in that they are initial values of the state variables s_{a}, s_{c}, and χ. The parameterization of the model is such that multiple parameter sets might produce the same mechanical behavior, i.e. no unique solution is guaranteed to exist to this inverse problem.

6.6.2 Parameter reduction

Given the large number of parameters in Table 6.5, it is advantageous to simplify the inverse problem by fixing some parameters. In the sections that follow, the number of free parameters are reduced through a combination of simplifying approximation and deterministic calibration.

Table 6.5: List of parameters for the macromolecular semicrystalline polymer model.

UMAT Var.	Param.	Units	Description
PROPS(1)	E_{a}	MPa	Young's modulus, amorphous
PROPS(2)	E_{c}	MPa	Young's modulus, crystalline
PROPS(3)	ν_{a}	–	Poisson's ratio, amorphous
PROPS(4)	ν_{c}	–	Poisson's ratio, crystalline
PROPS(5)	C^{R}	MPa	Rubbery modulus
PROPS(6)	N	–	Average number of links between entanglements
PROPS(7)	$\dot{\varepsilon}_0$	1/s	Reference strain rate
PROPS(8)	$\mathcal{A}_{\mathrm{a}}$	K/MPa	Temperature and rate sensitivity, amorphous
PROPS(9)	$\mathcal{A}_{\mathrm{c}}$	K/MPa	Temperature and rate sensitivity, crystalline
PROPS(10)	α_{a}	–	Pressure sensitivity, amorphous
PROPS(11)	α_{c}	–	Pressure sensitivity, crystalline
PROPS(12)	$s_{1,\mathrm{a}}$	MPa	Peak strength, amorphous
PROPS(13)	$s_{1,\mathrm{c}}$	MPa	Peak strength, crystalline
PROPS(14)	$s_{2,\mathrm{a}}$	MPa	Saturation strength, amorphous
PROPS(15)	$s_{2,\mathrm{c}}$	MPa	Saturation strength, crystalline
PROPS(16)	$h_{1,\mathrm{a}}$	MPa	Slope to peak strength, amorphous
PROPS(17)	$h_{1,\mathrm{c}}$	MPa	Slope to peak strength, crystalline
PROPS(18)	$h_{2,\mathrm{a}}$	MPa	Slope from peak to saturation strength, amorphous
PROPS(19)	$h_{2,\mathrm{c}}$	MPa	Slope from peak to saturation strength, crystalline
PROPS(20)	$\bar{\varepsilon}_{\mathrm{a}}^{\mathrm{w}}$	–	Location of peak strength, amorphous
PROPS(21)	$\bar{\varepsilon}_{\mathrm{c}}^{\mathrm{w}}$	–	Location of peak strength, crystalline
PROPS(22)	f_{a}	–	Width of peak, amorphous
PROPS(23)	f_{c}	–	Width of peak, crystalline
PROPS(24)	m_{a}	–	Temperature and rate sensitivity, amorphous
PROPS(25)	m_{c}	–	Temperature and rate sensitivity, crystalline
PROPS(26)	γ	–	Interaction exponent in mixture rule
PROPS(27)	ϕ_∞	–	Maximum crystallinity
PROPS(28)	n	–	Avrami exponent in crystal evolution law
PROPS(29)	$\dot{\varepsilon}_0^{\mathrm{tot}}$	1/s	Reference strain rate in crystal evolution law
PROPS(30)	ζ	–	Pressure sensitivity in crystal evolution law
STATEV(4)	$s_{\mathrm{a},0}$	MPa	Initial value of s_{a}
STATEV(5)	$s_{\mathrm{c},0}$	MPa	Initial value of s_{c}
STATEV(6)	χ_0	–	Initial value of crystal volume fraction

6.6.2.1 *Crystallinity*

The crystallinity of the PA-6 plate was determined to be 38 % by DSC analysis (see Chapter 4).[3] Therefore,

$$\chi_0 = 0.38. \tag{6.54}$$

The crystalline phase of PA-6 is polymorphic. It exhibits a stable monoclinic α-phase, a metastable monoclinic or pseudo-hexagonal γ-phase, and a mesomorphic β-phase, which is often ignored due to being difficult to distinguish from the amorphous phase [133]. When PA-6 is strained, changes in the crystalline structure occur [134, 135]. In one study, PA-6 strained beyond necking exhibited transitions from γ-phase to α-phase and also transitions from the amorphous phase to the α-phase. The amorphous phase to α-phase transformation resulted in a 7 % increase in the total crystallinity [135]. It is assumed here that increases in the strength at large strains due to strain-induced crystallization are negligible compared to increases in the strength due to orientation hardening. Therefore, strain-induced crystallization is neglected by setting the Avrami exponent in Eq. (6.23) to zero;

$$n = 0. \tag{6.55}$$

When strain-induced crystallization is neglected, the following parameters in Eq. (6.23) are made irrelevant, so are set to either unity or zero as appropriate;

$$\phi_\infty = 1, \quad \dot{\varepsilon}_0^{\text{tot}} = 1\,/\text{s}, \quad \zeta = 0. \tag{6.56}$$

The stresses in the amorphous and crystalline phases are added together using a simple

[3] DSC measurements produce the crystal mass fraction, while the model requires the crystal volume fraction. This distinction escaped my notice until after performing all calculations. Assuming a crystalline density of $1.23\,\text{g/cm}^3$ and an amorphous density of $1.09\,\text{g/cm}^3$ [132], the crystal volume fraction is actually 35 %. This error is of the same order of magnitude as variations in the crystallinity measured by DSC.

mixture rule without making use of the phenomenological fitting exponent in Eq. (6.12), i.e.

$$\gamma = 1. \tag{6.57}$$

6.6.2.2 Intermolecular resistance of the crystalline phase

The crystalline phase is treated as an elastic–perfectly viscoplastic resistance, following the assumptions in Seguela and Rietsch 1988 [90]. By setting $\dot{s}_{\mathrm{c}} = 0$, the intermolecular resistance in the crystalline phase is constant. However, the crystalline flow stress is still dependent on the temperature and rate through the parameters $\mathcal{A}_{\mathrm{c}}$, $\dot{\varepsilon}_0$, and m_{c}. Additionally, the crystalline flow stress is increased by orientation hardening.

To fix $\dot{s}_{\mathrm{c}} = 0$,

$$h_{1,\mathrm{c}} = 0, \quad h_{2,\mathrm{c}} = 0. \tag{6.58}$$

With s_{c} held constant, the following parameters become irrelevant and are arbitrarily assigned values of unity,

$$s_{1,\mathrm{c}} = 1\,\mathrm{MPa}, \quad s_{2,\mathrm{c}} = 1\,\mathrm{MPa}, \quad \bar{\varepsilon}_{\mathrm{c}}^{\mathrm{w}} = 1, \quad f_{\mathrm{c}} = 1. \tag{6.59}$$

However, several of the experiments in Figs. 6.2 and 6.3 exhibit a double yield, which has been previously observed in PA-6 [136]. Fully utilizing the parameters governing the evolution of both s_{a} and s_{c} may allow for a richer modeling of double yield in PA-6. However, double yielding behavior is neglected here for two reasons. First, the "bend" in the stress–strain curve following the first yield is small, so post-yield behavior can be adequately modeled using an evolving s_{a} and a fixed s_{c}. Second, double yielding is a result of complex interactions between the specimen geometry, microstructure, and temperature and rate dependence of both phases [137,138]. The experimental database generated here is not suitable for thorough investigations on the effects of crystallinity on the mechanical behavior, and so it is convenient to make simplifications regarding the crystalline phase. However, with the

appropriate experimental database, this model could be useful for exploring the double yield behavior of PA-6.

6.6.2.3 Intermolecular resistance of the amorphous phase

The width of the peak in strength, f_{a}, is of secondary importance [66]. Therefore, f_{a} is fixed;

$$f_{\mathrm{a}} = 0.3. \tag{6.60}$$

All other variables related to the intermolecular resistance of the amorphous phase are left as free parameters during optimization. During optimization, the peak width can be controlled second-hand through $h_{1,\mathrm{a}}$ and $h_{2,\mathrm{a}}$.

6.6.2.4 Temperature and rate sensitivity

Although the crystalline and amorphous phases are not equally sensitive to strain rate and temperature [21, 139], an accurate apportioning of viscoplastic effects between the two phases is not attempted here. Instead, the aggregate effect of strain rate and temperature is considered for the particular crystal volume fraction used here ($\chi = 0.38$). Therefore, parameters governing rate and temperature dependence are combined to apply to both phases;

$$\mathcal{A}_{\pi} = \mathcal{A}_{\mathrm{a}} = \mathcal{A}_{\mathrm{c}}, \tag{6.61}$$

$$m_{\pi} = m_{\mathrm{a}} = m_{\mathrm{c}}. \tag{6.62}$$

6.6.2.5 Pressure sensitivity

The strength of polymers is sensitive to the hydrostatic pressure, which is accounted for in the model through the parameter α_{π} that enters into the viscoplastic law in Eq. (6.18). In Pawlak and Galeski 2005 [49], PA-6 and several other thermoplastics were loaded in tension and channel die compression. In cavitating polymers, the yield stress was reduced in tension, due to the formation of cavities in the presence of a positive hydrostatic pressure. Since cavities form in the amorphous domains of PA-6 [36], the pressure sensitivity in PA-6

is assumed here to be primarily caused by the amorphous phase. Therefore,

$$\alpha_{\mathrm{c}} = 0. \tag{6.63}$$

The value of α_{a} is calibrated following a procedure similar to that used in Poulain et al. 2014 [66]. By comparing the yield stress in tension and compression, the pressure sensitivity in the amorphous phase is determined to be

$$\alpha_{\mathrm{a}} = 0.087. \tag{6.64}$$

6.6.2.6 Elastic constants

For the compression test conducted at $T = 24\,^{\circ}\mathrm{C}$ and $\left|\dot{\delta}\right| / L_0 = 10^{-3}\,/\mathrm{s}$ in Fig. 6.2, the initial linear response has a slope of approximately 1550 MPa. This value is assumed to correspond to the effective Young's modulus, and is within the range of Young's moduli found in the literature for PA-6 and PA-6,6 [1, 39, 140]. To ensure that the crystalline phase is stiffer than the amorphous phase, the ratio of the crystalline modulus to the amorphous modulus is arbitrarily set to two. For an effective modulus of $E_{\mathrm{eff}} = 1550\,\mathrm{MPa}$, a crystal volume fraction of $\chi_0 = 0.38$ (see Eq. (6.54)), and $E_{\mathrm{c}}/E_{\mathrm{a}} = 2$,

$$E_{\mathrm{a}} = 1123\,\mathrm{MPa}, \quad E_{\mathrm{c}} = 2246\,\mathrm{MPa}. \tag{6.65}$$

The Poisson's ratio in both phases was approximated as 0.4 based on values found in the literature [1, 140];

$$\nu_{\mathrm{a}} = \nu_{\mathrm{c}} = 0.4. \tag{6.66}$$

6.6.2.7 Summary of fixed parameters

Table 6.6 lists the values of all fixed parameters as described in Sections 6.6.2.1–6.6.2.6.

Table 6.6: List of fixed model parameters and their values.

Param.	Value	Units
E_a	1123	MPa
E_c	2246	MPa
ν_a	0.4	–
ν_c	0.4	–
α_a	0.087	–
α_c	0	–
$s_{1,\mathrm{c}}$	1	MPa
$s_{2,\mathrm{c}}$	1	MPa
$h_{1,\mathrm{c}}$	0	MPa
$h_{2,\mathrm{c}}$	0	MPa
$\bar{\varepsilon}_\mathrm{c}^\mathrm{w}$	1	–
f_a	0.3	–
f_c	1	–
γ	1	–
ϕ_∞	1	–
n	0	–
$\dot{\varepsilon}_0^\mathrm{tot}$	1	1/s
ζ	0	–
χ_0	0.38	–

Table 6.7: List of free model parameters.

Param.	Units	Description
C^R	MPa	Rubbery modulus
N	–	Average number of links between entanglements
$\dot{\varepsilon}_0$	1/s	Reference strain rate
$\mathcal{A}_\pi$	K/MPa	Temperature and rate sensitivity, amorphous and crystalline
$s_{1,\mathrm{a}}$	MPa	Peak strength, amorphous
$s_{2,\mathrm{a}}$	MPa	Saturation strength, amorphous
$h_{1,\mathrm{a}}$	MPa	Slope to peak strength, amorphous
$h_{2,\mathrm{a}}$	MPa	Slope from peak to saturation strength, amorphous
$\bar{\varepsilon}_\mathrm{a}^\mathrm{w}$	–	Location of peak strength, amorphous
m_π	–	Temperature and rate sensitivity, amorphous and crystalline
$s_{\mathrm{a},0}$	MPa	Initial value of s_a
$s_{\mathrm{c},0}$	MPa	Constant value of s_c

6.6.3 Adjustable parameters and their constraints

After fixing several parameters as described in Section 6.6.2, there are twelve free parameters used for calibration by optimization. The free parameters are listed in Table 6.7. These parameters are subject to three constraints. The first constraint,

$$s_{\mathrm{a},0} < s_{1,\mathrm{a}}, \tag{6.67}$$

is imposed because the model implementation experiences convergence issues when this constraint is not satisfied. The second and third constraints,

$$s_{1,\mathrm{a}} < s_{\mathrm{c},0} \tag{6.68}$$

$$s_{2,\mathrm{a}} < s_{\mathrm{c},0}, \tag{6.69}$$

are imposed to ensure that the crystalline phase is always stronger than the amorphous phase.

Even with the dramatically reduced set of adjustable parameters, there is still no guarantee of a unique solution to the inverse problem.

6.7 Calibration of temperature and strain rate sensitivity

The parameters governing the temperature and rate sensitivity ($\dot{\varepsilon}_0$, $\mathcal{A}_\pi$, and m_π) were calibrated by optimizing all free model parameters (see Table 6.7) to fit the response of the compression pin model (see Section 6.3.1) to the experimental response of PA-6 compression pins (see Section 6.2.1). Four different loading conditions were used during optimization:

- $T = -30\,^{\circ}\mathrm{C}$, $\left|\dot{\delta}\right| / L_0 = 10^{-3}\,/\mathrm{s}$
- $T = 0\,^{\circ}\mathrm{C}$, $\left|\dot{\delta}\right| / L_0 = 10^{-3}\,/\mathrm{s}$
- $T = 24\,^{\circ}\mathrm{C}$, $\left|\dot{\delta}\right| / L_0 = 10^{-3}\,/\mathrm{s}$
- $T = 24\,^{\circ}\mathrm{C}$, $\left|\dot{\delta}\right| / L_0 = 10^{-1}\,/\mathrm{s}$

The experimental results for these loading conditions can be found in Fig. 6.2.

Calibrating the temperature and rate sensitivity requires experimental data from multiple loading conditions. For calibration by optimization, each of those loading conditions were evaluated at each iteration of the optimization algorithm. The use of PA-6 compression pins was ideal in this regard. Since the deformation of the pins is approximately homogeneous, they are effectively modeled using a single element. This greatly reduces the computational expense of running the compression pin model, which in turn facilitates the evaluation of multiple loading conditions at each iteration.

Prior to optimization, initial parameters were chosen following the calibration procedure described in Poulain et al. 2014 [66]. Although the model used here is similar to the one in Ref. [66], the model in Ref. [66] is for an amorphous polymer and the present model is for a semicrystalline polymer. Therefore, the calibration procedure required some modification. Where the procedure in Ref. [66] was not applicable to the current model, the procedure was either modified or parameters were manually adjusted to generate reasonable initial conditions.

After setting the initial conditions, optimization commenced by applying the Nelder-Mead algorithm in Z-set using all four compressive loading conditions. The resulting set of model parameters accurately reproduced the temperature and rate sensitivity, and also accurately reproduced the mechanical response up to the yield stress. However, there was still significant room for improvement regarding the post-yield behavior. Therefore, two more executions of the Nelder-Mead algorithm were used. In the second and third executions of the Nelder-Mead algorithm, the parameters governing temperature and rate sensitivity were fixed ($\dot{\varepsilon}_0$, $\mathcal{A}_\pi$, and m_π) and the parameters governing the yield stress were fixed ($s_{\mathrm{a},0}$ and $s_{\mathrm{c},0}$). Additionally, the objective function of only a single loading condition was considered ($T = 24\,^{\circ}\mathrm{C}$, $\left|\dot{\delta}\right| / L_0 = 10^{-3}\,/\mathrm{s}$). Despite considering the objective function of a single loading condition, the sum of all four objective functions decreased. This indicates that the temperature and rate sensitivity were well calibrated after the first optimization run. It also

demonstrates that if the temperature and strain rate sensitivity are properly calibrated, then only one loading condition needs to be considered during optimization.

Further details of the optimization process are described in Tables 6.8–6.10. In these tables, each execution of the optimization algorithm is referred to as a "stage". Table 6.8 shows an overview of all three stages of optimization using compressive loading conditions, including the loading conditions used during each stage, the initial simplex length used by the algorithm, and the number of iterations.

Table 6.9 shows the evaluation of the objective functions for each loading condition at the end of of each optimization stage using compressive loading conditions. The relative weight of each loading condition is also shown. The weight of the loading condition using the faster strain rate ($T = 24\,^{\circ}\mathrm{C}$, $\left|\dot{\delta}\right| / L_0 = 10^{-1}\,/\mathrm{s}$) was increased for two reasons. First, it was the only loading condition not using a nominal strain rate of $10^{-3}\,/\mathrm{s}$, so was especially important for capturing the rate sensitivity. Second, at this condition, thermal softening begins to occur after yield as a result of self-heating. Given that the model implemented here does not account for the conversion of plastic work into heat, data significantly beyond yield was not useable for optimization, and the shorter length of the curve resulted in an objective function that was artificially lower than the objective functions for other loading conditions. Although optimization at stages 2 and 3 only considered a single objective function, the objective function for all four conditions were evaluated to demonstrate that improvements in one loading condition lead to improvements in the sum of all loading conditions when the parameters governing temperature and rate sensitivity are appropriately calibrated. Finally, Table 6.10 shows the values of the parameters at the end of each optimization stage using the compressive loading conditions.

After one optimization stage considering all four loading conditions and two optimization stages considering only a single condition, the mechanical behavior in compression showed good agreement between the model and experiments, as shown in Fig. 6.10. Fig. 6.10a shows loading conditions using a nominal strain rate of $\left|\dot{\delta}\right| / L_0 = 10^{-3}\,/\mathrm{s}$, including one condition

Table 6.8: Overview of all three stages of optimization using compressive loading conditions.

	Loading Conditions Used					
Stage	$-30\,^{\circ}\mathrm{C}$ $10^{-3}\,/\mathrm{s}$	$0\,^{\circ}\mathrm{C}$ $10^{-3}\,/\mathrm{s}$	$24\,^{\circ}\mathrm{C}$ $10^{-3}\,/\mathrm{s}$	$24\,^{\circ}\mathrm{C}$ $10^{-1}\,/\mathrm{s}$	Initial Simplex Length	Iterations
1	✓	✓	✓	✓	1.00	228
2			✓		1.00	142
3			✓		1.00	100

Table 6.9: Evaluation of the objective functions for each loading condition at the end of each optimization stage using compressive loading conditions.

		Objective Function			
Loading Condition	Weight	Initial	Stage 1	Stage 2	Stage 3
$-30\,^{\circ}\mathrm{C}$, $10^{-3}\,/\mathrm{s}$	1	4.43×10^{3}	6.77×10^{0}	6.27×10^{1}	5.16×10^{1}
$0\,^{\circ}\mathrm{C}$, $10^{-3}\,/\mathrm{s}$	1	4.79×10^{3}	8.25×10^{1}	8.01×10^{0}	1.37×10^{1}
$24\,^{\circ}\mathrm{C}$, $10^{-3}\,/\mathrm{s}$	1	9.52×10^{3}	1.93×10^{2}	2.53×10^{0}	1.29×10^{0}
$24\,^{\circ}\mathrm{C}$, $10^{-1}\,/\mathrm{s}$	8	4.41×10^{3}	7.00×10^{1}	1.05×10^{2}	7.85×10^{1}
	Sum:	2.31×10^{4}	3.52×10^{2}	1.79×10^{2}	1.45×10^{2}

Table 6.10: Values of the parameters at the end of each optimization stage using the compressive loading conditions. The symbol "–" indicates the parameter was fixed at the value found from the previous stage. The upper and lower bounds for each parameter are also displayed.

Param.	Units	Min.	Max.	Initial	Stage 1	Stage 2	Stage 3
C^{R}	MPa	0	50	24.00	19.11	5.784	5.434
N	–	1	50	28.00	33.99	33.23	31.45
$\dot{\varepsilon}_0$	1/s	$\exp(-10)$	$\exp(100)$	$\exp(36.84)$	$\exp(55.65)$	–	–
$\mathcal{A}_\pi$	K/MPa	1	1000	58.00	73.26	–	–
$s_{1,\mathrm{a}}$	MPa	1	1000	358.4	334.3	378.0	380.2
$s_{2,\mathrm{a}}$	MPa	1	1000	353.0	309.5	340.7	338.6
$h_{1,\mathrm{a}}$	MPa	100	10 000	3975	4936	1409	1088
$h_{2,\mathrm{a}}$	MPa	100	10 000	2805	3789	4094	3951
$\bar{\varepsilon}_{\mathrm{a}}^{\mathrm{w}}$	–	0.001	2	0.3200	0.4064	0.932	0.9538
m_π	–	0.01	10	0.833	0.7290	–	–
$s_{\mathrm{a},0}$	MPa	1	1000	263.5	329.2	–	–
$s_{\mathrm{c},0}$	MPa	1	1000	411.7	408.3	–	–

at $T = 60\,^{\circ}\mathrm{C}$ that was not evaluated during optimization. For $T = 60\,^{\circ}\mathrm{C}$, the experimental behavior does not show a sharp yield point as in the other conditions. However, the simulated behavior at $T = 60\,^{\circ}\mathrm{C}$ exhibits the same sharp yield point that is predicted by the model at other temperatures. The disappearance of the sharp yield is likely because $60\,^{\circ}\mathrm{C} > T_{\mathrm{g}}$ for PA-6. The intermolecular resistance due to segment rotation is largely responsible for yielding in polymers below their glass transition temperature [59, 60]. However, for $T > T_{\mathrm{g}}$, large increases in the free volume dramatically reduce the intermolecular resistance. The present model does not consider changes in the intermolecular resistance across T_{g}, so this behavior cannot be accurately represented. Despite this, the flow stress at $T = 60\,^{\circ}\mathrm{C}$ is accurately predicted by the model. It is conceivable that the flow properties might be governed by the crystalline phase or the rubbery network, both of which are still active for $T > T_{\mathrm{g}}$.

Fig. 6.10b shows loading conditions using a nominal strain rate of $\left|\dot{\delta}\right| / L_0 = 10^{-1}\,/\mathrm{s}$, including one condition at $T = -30\,^{\circ}\mathrm{C}$ that was not evaluated during optimization. In the experiments using this strain rate, the conversion of plastic work into heat is not offset by conduction and convection, resulting in thermal softening beyond yield [112]. Since the model implementation is isothermal, it cannot predict thermal softening as a result of self-heating. Therefore good agreement between the simulations and the experiments are only expected up to yield. For this reason, the simulated responses in Fig. 6.10 are only plotted until slightly after yield ($\varepsilon < 0.15$). Although the model accurately represents yield at $T = 24\,^{\circ}\mathrm{C}$, its prediction for yield at $T = -30\,^{\circ}\mathrm{C}$ is approximately 10 MPa too high.

None of the experiments depicted in Fig. 6.10 exhibit the large-strain hardening behavior characteristic of polymers. For this reason, the calibration of C^{R} and N produced from optimizing to this data should be viewed with skepticism. The apparent absence of orientation hardening means that the mechanical behavior is entirely governed by the intermolecular resistances, s_{a} and s_{c}. Physically speaking, the intermolecular resistance should only be dominant at small strains, and evolving s_{a} and s_{c} at large strains is an abusive use of these state variables. Therefore, this physical basis for the model equations is not applicable for

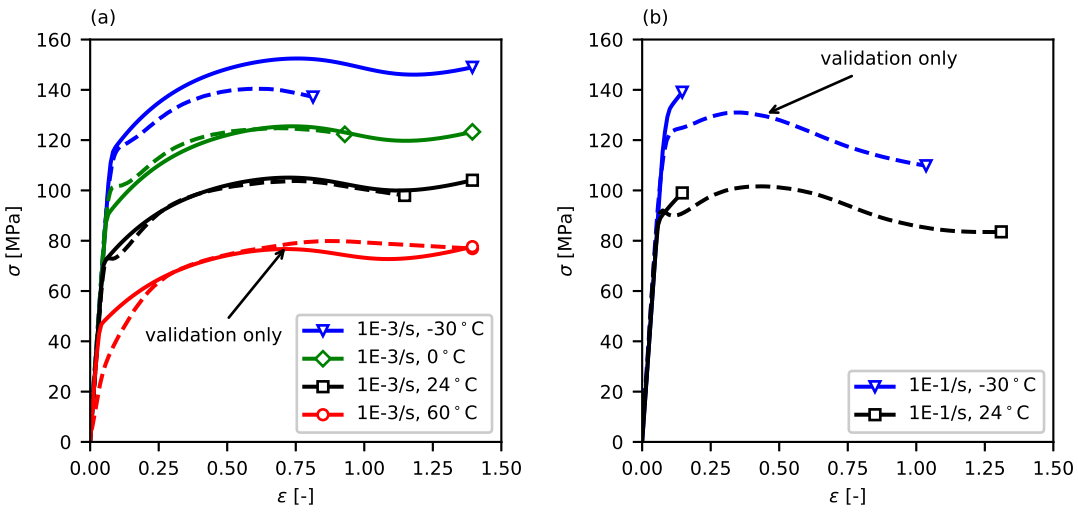

Figure 6.10: Simulated (solid lines) and experimental (dashed lines) true stress–strain curves for PA-6 pins loaded in compression. (a) Tests using a nominal strain rate of $\left|\dot{\delta}\right| / L_0 = 10^{-3}\,/\mathrm{s}$ (b) Tests using a nominal strain rate of $\left|\dot{\delta}\right| / L_0 = 10^{-1}\,/\mathrm{s}$. The simulated behavior uses parameter values determined after three stages of optimization, see Stage 3 parameter values in Table 6.10.

the fit found here, although Fig. 6.10 indicates that the model produces a good fit from a phenomenological standpoint.

6.8 Determination of the intrinsic mechanical behavior

The intrinsic mechanical behavior is identified by optimizing parameters of the constitutive model so the simulated nominal stress–strain curve of the cylindrical bar finite-element model matches the experimental nominal stress–strain curve. The assumption is that if the simulated and experimental nominal responses are in agreement, then the constitutive behavior described by the optimized parameters accurately represents the intrinsic behavior of the physical material. The parameter values determined from optimizing the compression pin model were used as the initial values for optimizing the cylindrical bar model. Since the temperature and rate sensitivity were accurately calibrated from multiple loading conditions on compression pins, only a single loading condition ($T = 24\,^{\circ}\mathrm{C}$, $\dot{\delta}/L_0 = 10^{-3}\,/\mathrm{s}$) was consid-

ered with the cylindrical bar. Therefore, the parameters governing the rate and temperature sensitivity ($\dot{\varepsilon}_0$, $\mathcal{A}_\pi$, and m_π) were kept fixed. As previously stated, it is advantageous to consider only a single loading condition during optimization of the cylindrical bar model, since its computational expense is greater than the compression pin model.

The Nelder-Mead optimization algorithm was applied three times. Each execution of the algorithm used an initial simplex length that was one-half of the previous initial simplex length. Nelder-Mead searches beyond the third yielded only marginal improvements of the objective function.

Details of the optimization method used with regards to the cylindrical bar model are presented in Tables 6.11–6.13. As in the previous section, each execution of the Nelder-Mead algorithm is referred to as a stage. Stages in these tables are numbered as 4–6, continuing the numbering used in Section 6.7. Table 6.11 shows an overview of all three stages of optimization using the cylindrical bar model, including the initial simplex length and the number of iterations at each stage. Table 6.12 shows the value of the objective function for the cylindrical bar model after each stage. Table 6.13 shows the value of the parameters after each stage.

The calibrated parameters produce good agreement between the simulated and experimental nominal stress–strain curve for the loading condition considered during optimization, $T = 24\,^{\circ}\mathrm{C}$, $\dot{\delta}/L_0 = 10^{-3}\,/\mathrm{s}$. Fig. 6.11 compares the simulated and experimental nominal stress–strain curves at all loading conditions where experimental data is available. Figs. 6.11a,c,d compare experimental data to data generated by the cylindrical bar finite element model (see Section 6.3.2), while Fig. 6.11b compares experimental data to data generated by a single element loaded at a constant true strain rate (see Section 6.3.4).

Fig. 6.11a compares simulated and experimental results for loading conditions at $T = 24\,^{\circ}\mathrm{C}$. For the conditions using a nominal strain rates of $\dot{\delta}/L_0 = 10^{-3}\,/\mathrm{s}$ and $\dot{\delta}/L_0 = 10^{-5}\,/\mathrm{s}$, the simulated behavior is in good agreement with the experimental behavior. For $\dot{\delta}/L_0 = 10^{-1}\,/\mathrm{s}$, the simulated behavior yields near the same nominal stress as in the experiment,

Table 6.11: Overview of all three stages of optimization using the cylindrical bar model.

Stage	Loading Conditions Used 24 °C, 10^{-3} /s	Initial Simplex Length	Iterations
4	✓	1.00	191
5	✓	0.50	110
6	✓	0.25	254

Table 6.12: Evaluation of the objective function for the cylindrical bar model at the end of of each optimization stage.

		Objective Function			
Loading Condition	Weight	Initial	Stage 4	Stage 5	Stage 6
24 °C, 10^{-3} /s	1	1.89×10^{2}	2.91×10^{0}	9.63×10^{-1}	4.36×10^{-1}

Table 6.13: Values of the parameters at the end of each optimization stage using the cylindrical bar model. The symbol "–" indicates the parameter was fixed at the value from the previous stage. The upper and lower bounds for each parameter are also displayed.

Param.	Units	Min.	Max.	Initial (Stage 3)	Stage 4	Stage 5	Stage 6
C^{R}	MPa	0	50	5.434	8.898	12.69	12.11
N	–	1	200	31.45	53.05	57.47	59.63
$\dot{\varepsilon}_0$	1/s	–	–	exp(55.65)	–	–	–
$\mathcal{A}_\pi$	K/MPa	–	–	73.26	–	–	–
$s_{1,\mathrm{a}}$	MPa	1	1000	380.2	398.5	399.9	406.6
$s_{2,\mathrm{a}}$	MPa	1	1000	338.6	422.4	402.4	406.6
$h_{1,\mathrm{a}}$	MPa	100	10 000	1088	649.5	753.3	980.9
$h_{2,\mathrm{a}}$	MPa	100	10 000	3951	5749	5956	6141
$\bar{\varepsilon}_{\mathrm{a}}^{\mathrm{w}}$	–	0.001	4	0.9538	0.8841	0.9148	0.9359
m_π	–	–	–	0.7290	–	–	–
$s_{\mathrm{a},0}$	MPa	1	1000	329.2	292.2	320.2	316.3
$s_{\mathrm{c},0}$	MPa	1	1000	408.3	459.2	412.7	406.7

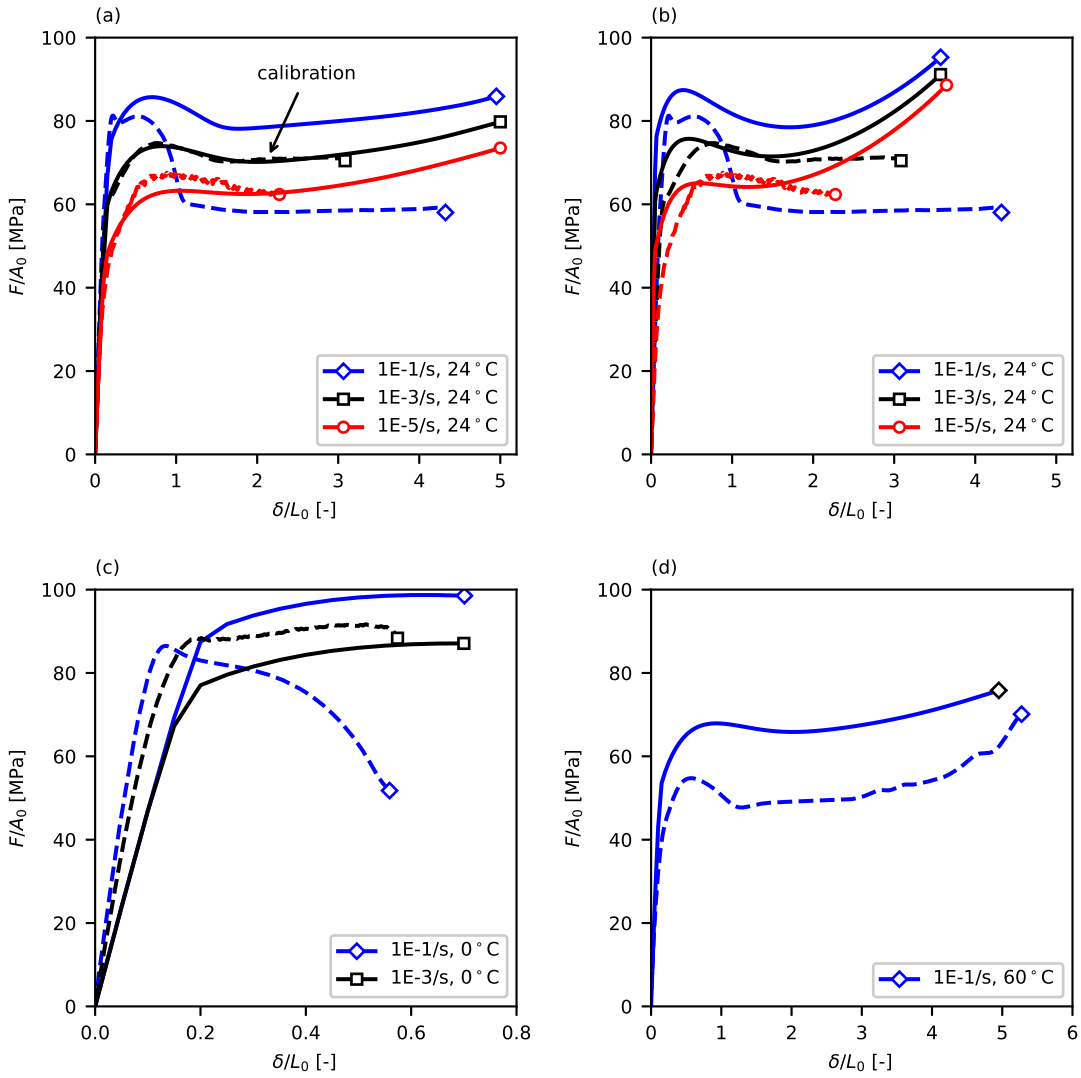

Figure 6.11: Simulated (solid lines) and experimental (dashed lines) nominal stress–strain curves for PA-6 cylindrical bars tested in tension. The simulated behavior uses the calibrated model parameter, see Stage 6 parameter values in Table 6.13. (a) $T = 24\,°\text{C}$, simulated results are generated from the cylindrical bar model. (b) $T = 24\,°\text{C}$, simulated results are generated from a single element (i.e. no structural effects). (c) $T = 0\,°\text{C}$, simulated results are generated from the cylindrical bar model. (d) $T = 60\,°\text{C}$, simulated results are generated from the cylindrical bar model.

but the simulated response maintains a higher stress level beyond yield. As mentioned previously, the source of this difference is self-heating, which typically occurs in polymers at strain rates above 10^{-2} /s [122, 123]. The model accurately predicts the trend that the post-peak (nominal) stress decrease is greater at higher strain rates. The post-peak stress decrease is also greater at lower temperatures, see Figs. 6.11c,d. Since necking is the result of a local minimum in the nominal stress–strain curve [98], these results indicate that necking is more severe at higher strain rates and lower temperatures. To explore this result further, Fig. 6.11b compares simulated and experimental nominal stress–strain curves for loading conditions at $T = 24\,^{\circ}\mathrm{C}$, except that the simulated results are produced from the deformation of a single element. As with the results produced from the cylindrical bar model, the nominal stress–strain curve of the single element shows a post-peak stress decrease that becomes more pronounced as the strain rate decreases. The post-peak nominal stress decrease in the single element also becomes more pronounced as the temperature decreases, although this is not shown in Fig. 6.11b. Since the sensitivity of the post-peak stress decrease to strain rate and temperature is reproduced in a single element, this effect is a consequence of the constitutive behavior. Therefore, the sensitivity of necking to strain rate and temperature is a consequence of the constitutive behavior. Although the trend regarding the post-peak stress decrease is similar between a single element and the cylindrical bar models, there are still large differences between their nominal stress–strain curves. For instance, there is no stress plateau in the single element response, since no neck propagation occurs in a single element. This highlights the importance of considering structural effects produced by the specimen geometry.

Fig. 6.11c compares simulated and experimental results for loading conditions at $T = 0\,^{\circ}\mathrm{C}$. With respect to the yield stress and the flow stress, the simulated data matches the experimental data reasonably well, although the fit is not as close as for conditions at $T = 24\,^{\circ}\mathrm{C}$ in Fig. 6.11a. However, at $T = 0\,^{\circ}\mathrm{C}$, the stiffness of the model is noticeably lower than what is experimentally observed. Polymers exhibit viscoelastic behavior; their elastic

properties are functions of strain rate and temperature [40]. However, the model implemented here utilizes a constant Young's modulus that has been calibrated to loading at $T = 24\,^{\circ}\mathrm{C}$ and $\dot{\delta}/L_0 = 10^{-3}\,/\mathrm{s}$. At $T = 0\,^{\circ}\mathrm{C}$, the temperature decrease has increased the Young's modulus in the experiment, but the Young's modulus in the model remains unchanged. A more accurate model formulation would use a stiffness tensor that was a function of the strain rate and temperature. However, given the magnitude of the elastic strains compared to the total strains, using constant elastic properties is an adequate approximation for this application. Fig. 6.11d compares the simulated and experimental response for a single loading condition at $T = 60\,^{\circ}\mathrm{C}$. Here, the model predicts a higher yield and flow stress than what is observed experimentally. At $T = 60\,^{\circ}\mathrm{C}$, the material is above its glass transition temperature, $T > T_{\mathrm{g}}$. Therefore, a large increase in the free volume occurs in the physical material, which significantly decreases the intermolecular resistance. However, the constitutive model applied here does not consider changes in the intermolecular resistance across T_{g}, and so the model over-predicts yield. Once again, self-heating is likely responsible for the over-prediction of the flow stress, since the model used here does not account for the conversion of plastic work into heat. Despite these discrepancies, the slopes of the simulated and experimental curves match at large strains, which provides additional confidence in the calibration of the parameters governing orientation hardening, C^{R} and N.

At this point, it has been mentioned multiple times that self-heating causes thermal softening in experiments loaded at $\dot{\delta}/L_0 = 10^{-1}\,/\mathrm{s}$, but since the model is isothermal, it does not predict the temperature increase due to self-heating. However, by comparing the experimental results to the results from the isothermal model, it is possible to estimate the experimental temperature increase due to self-heating. Consider the post-peak minimum (nominal) stress in the cylindrical bar using the loading conditions $T = 24\,^{\circ}\mathrm{C}$ and $\dot{\delta}/L_0 = 10^{-1}\,/\mathrm{s}$, see Fig. 6.11a. In the isothermal model, the minimum stress is approximately 80 MPa, while it is approximately 60 MPa in the experiment. The viscoplastic law in

Eq. (6.18) can be rearranged into an expression for the flow stress, $\bar{\sigma}$,

$$\bar{\sigma} = (s - 3\alpha\sigma_{\mathrm{m}}) \left[1 + \frac{T}{\mathcal{A}\,(s - 3\alpha\sigma_{\mathrm{m}})} \ln\left(\frac{\dot{\bar{\varepsilon}}^{\mathrm{p}}}{\dot{\varepsilon}_0} \right) \right]^{1/m} . \tag{6.70}$$

To simplify the analysis, the dual-phase nature of the model is ignored, and only a single value for the athermal shear strength is utilized. In the isothermal case, $\bar{\sigma}$, T, and $\dot{\bar{\varepsilon}}^{\mathrm{p}}$, are all known, and so the value of $(s - 3\alpha\sigma_{\mathrm{m}})$ can be determined using Eq. 6.70. Using the calibrated parameters in Table 6.13, a temperature of $T = 24\,^{\circ}\mathrm{C}$, and an effective plastic strain rate of $\dot{\bar{\varepsilon}}^{\mathrm{p}} = 10^{-1}\,/\mathrm{s}$, it can be shown that $\bar{\sigma} = 80\,\mathrm{MPa}$ when $(s - 3\alpha\sigma_{\mathrm{m}}) = 375\,\mathrm{MPa}$. Then, assuming that $(s - 3\alpha\sigma_{\mathrm{m}}) = 375\,\mathrm{MPa}$ at the post-peak minimum stress in the experiment, the temperature required to produce $\bar{\sigma} = 80\,\mathrm{MPa}$ can be calculated. Using the calibrated parameters in Table 6.13, a pressure adjusted athermal shear strength of $(s - 3\alpha\sigma_{\mathrm{m}}) = 375\,\mathrm{MPa}$, and an effective plastic strain rate of $\dot{\bar{\varepsilon}}^{\mathrm{p}} = 10^{-1}\,/\mathrm{s}$, it can be shown that $\bar{\sigma} = 60\,\mathrm{MPa}$ when $T = 51\,^{\circ}\mathrm{C}$. Therefore, a temperature increase of approximately $27\,^{\circ}\mathrm{C}$ occurs as a result of self-heating. Based on the literature data aggregated in Ref. [124], a temperature increase between $20\,^{\circ}\mathrm{C}$–$40\,^{\circ}\mathrm{C}$ is typical for polymers loaded at $\dot{\bar{\varepsilon}} = 10^{-1}\,/\mathrm{s}$.

In Chapter 3, the true axial stress–strain curve was approximated through contour tracking, which measures the true strain through *in situ* measurements of the diameter and calculates the true axial stress by dividing the net force by the current cross-sectional area. In Fig. 6.12, the simulated and experimental stress–strain curves generated from diameter measurements of the cylindrical bar specimen and finite element model are compared, revealing excellent agreement. The objective function used during optimization only considered axial deformation (the nominal stress–strain curve), therefore, the agreement between the diameter-based stress–strain curves in Fig. 6.12 has emerged from optimization without being explicitly sought. This indicates that the structural effect of necking has been accurately captured in the finite element model.

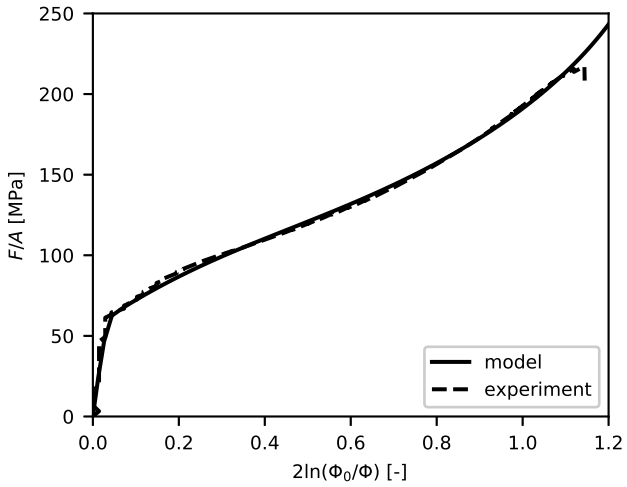

Figure 6.12: Experimental and simulated true axial stress and true strain, as calculated by contour tracking, for a PA-6 cylindrical bar tested in tension at $T = 24\,^{\circ}\mathrm{C}$ and $\dot{\delta}/L_0 = 10^{-3}\,/\mathrm{s}$. The simulated behavior uses the calibrated model parameters, see Stage 6 parameter values in Table 6.13.

6.9 Assessment of the calibration

The calibration is assessed by comparing the simulated and experimental mechanical behavior of round notched bars. Fig. 6.13 compares the mechanical response produced from the RN10 and RN2 finite element models described in Section 6.3.3 to the experimental data in Fig. 6.5. In Fig. 6.13a, the simulated and experimental data for the RN10 bar are compared. The model produces excellent agreement with the experiment for the entire strain range achieved prior to fracture in the experiment. The maximum difference in the nominal stress is around 5 MPa and occurs after the peak nominal stress at a strain of approximately $2\ln(\Phi_0/\Phi) \approx 0.50$. The peak nominal stress is approximately $F/A_0 \approx 85\,\mathrm{MPa}$ in both the model and experiment, although its location is slightly delayed in the model, occurring at $2\ln(\Phi_0/\Phi) \approx 0.4$, compared to its experimental occurrence at $2\ln(\Phi_0/\Phi) \approx 0.3$ In Fig. 6.13b, the simulated and experimental data for the RN2 are compared. The model briefly produces a good match to the experimental data, but begins to deviate around a

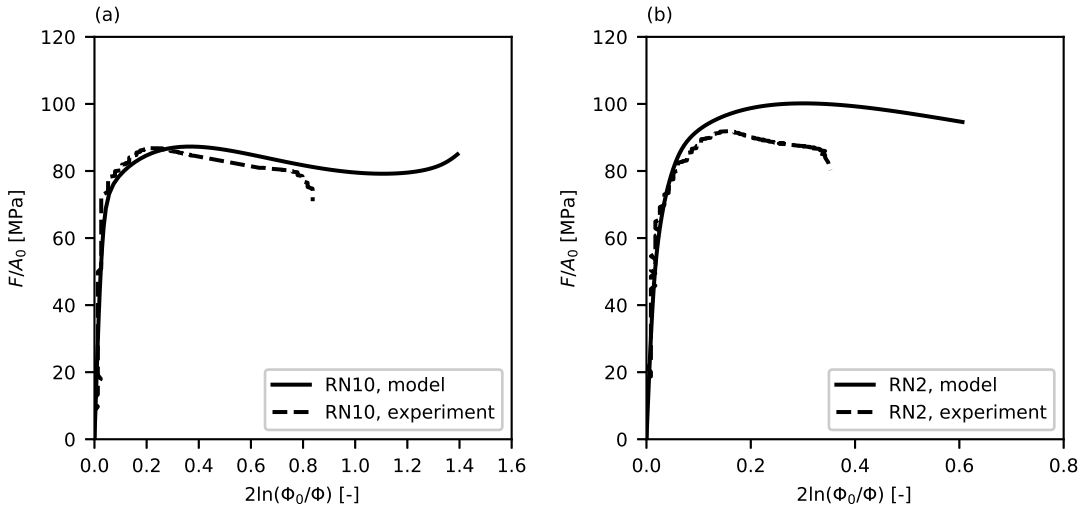

Figure 6.13: Experimental and simulated mechanical behavior for PA-6 round notched bars tested in tension at $T = 24\,^{\circ}\mathrm{C}$ and $\dot{\delta}/L_0 = 10^{-3}\,/\mathrm{s}$. The simulated behavior uses the calibrated model parameter, see Stage 6 parameter values in Table 6.13. (a) The RN10 bar results. (b) The RN2 bar results.

strain of $2\ln(\Phi_0/\Phi) \approx 0.10$. Afterwards, the model predicts a higher stress than what is observed experimentally. The maximum difference in the nominal stress is approximately 15 MPa. In the experiment, the peak nominal stress is $F/A_0 \approx 90\,\mathrm{MPa}$ and occurs at a strain of $2\ln(\Phi_0/\Phi) \approx 0.15$. However, in the model, the peak nominal stress is $F/A_0 \approx 100\,\mathrm{MPa}$ and occurs at a strain of $2\ln(\Phi_0/\Phi) \approx 0.30$. Overall, the round notched bar models show acceptable agreement with experimental data, although at higher triaxialities, the model predicts a behavior that is slightly stronger than what is experimentally observed.

6.10 Discussion

The discussion is divided into two sections. In Section 6.10.1, the effect of strain rate and temperature on necking is explored. In Section 6.10.2, the inverse parameter identification method used here is assessed.

6.10.1 Effect of strain rate and temperature on necking

Using the calibrated parameters, the putatively intrinsic behavior is studied by loading a single element at a constant true strain rate. This enables observations of the intrinsic behavior without the presence of structural effects that cloud experimental observations. The intrinsic mechanical behavior is plotted for a variety of drawing temperatures and true strain rates in Figs. 6.14a,c,e. The nominal stress–strain behavior of the cylindrical bar model is plotted for the same drawing temperatures and nominal strain rates in Fig. 6.14b,d,f. For the intrinsic behavior, changes in the temperature and strain rate shift the stress–strain curve, with no discernible changes to its overall shape. However, for the nominal stress–strain curves, changes in temperature and strain rate both shift the curve and change its shape. Specifically, increasing the strain rate or decreasing the temperature results in a larger and more distinct peak in the nominal stress–strain curve. Since the neck forms during the post-peak stress decrease in the nominal stress–strain curve, the model reveals that necking is more severe at higher strain rates and lower temperatures. This effect has already been reported in experiments [115, 141] and simulations [113, 142]. For some conditions using both a low nominal strain rate and a high temperature, the local maximum disappears completely, indicating that that no necking occurs. The effects of temperature and strain rate on the severity of necking are also evident by inspecting the model geometry throughout the simulation. In Fig. 6.15, the model geometry for three loading conditions are displayed. One condition shows extremely localized necking (Fig. 6.15a), one shows homogeneous deformation within the gauge section (Fig. 6.15c), and one condition is intermediate (Fig. 6.15b). For the case with very localized necking and the intermediate case, the model geometry is displayed at the local minimum after the maximum load. This point on the nominal stress–strain curve corresponds to the occurrence of neck stabilization, i.e. the point at which necking is the most localized prior to steady-state drawing of the neck. Since the condition exhibiting homogeneous deformation does not exhibit a stress decrease, the model geometry half-way through the simulation is arbitrarily chosen for display. Fig. 6.15 makes

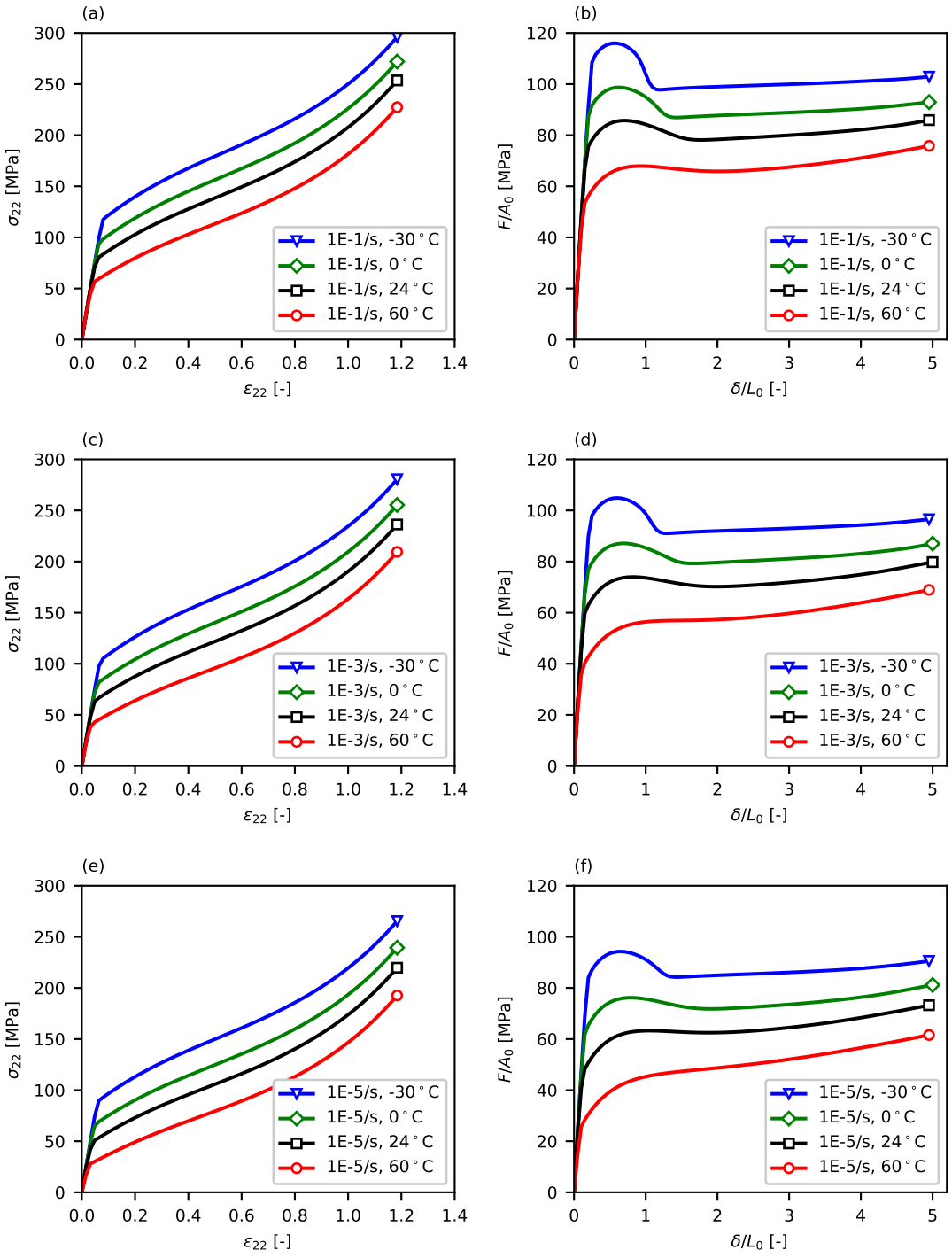

Figure 6.14: (a,c,e) Intrinsic true stress–strain curves of PA-6 loaded in tension, as determined by loading a single element using the calibrated parameters in Table 6.13. (b,d,f) Simulated nominal stress–strain curves using calibrated parameters with the cylindrical bar finite element model. (a) $\dot{\varepsilon}_{22} = 10^{-1}$ /s, (b) $\dot{\delta}/L_0 = 10^{-1}$ /s, (c) $\dot{\varepsilon}_{22} = 10^{-3}$ /s, (d) $\dot{\delta}/L_0 = 10^{-3}$ /s, (e) $\dot{\varepsilon}_{22} = 10^{-5}$ /s, (f) $\dot{\delta}/L_0 = 10^{-5}$ /s.

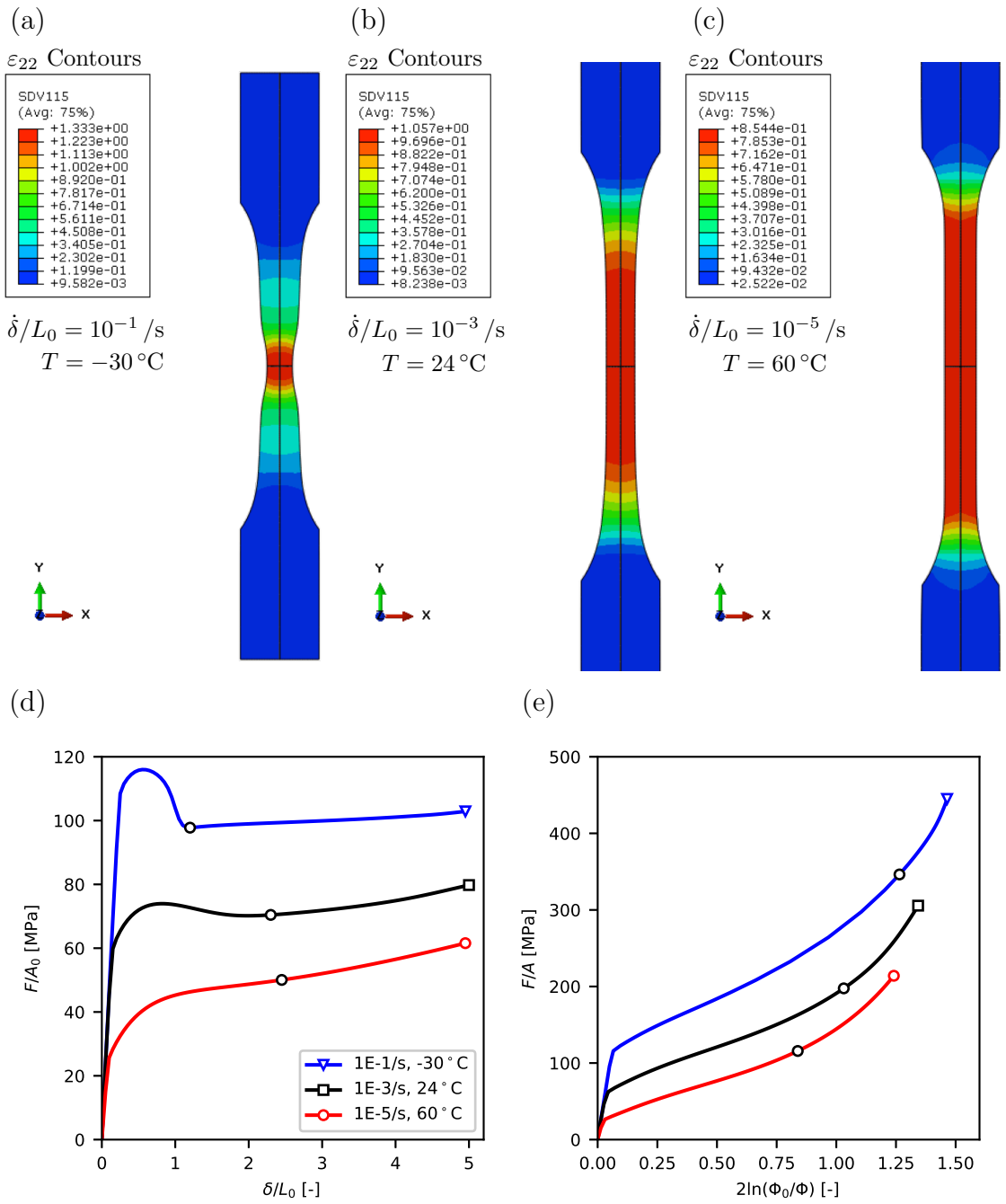

Figure 6.15: Model geometry with contours of axial strain (ε_{22}) for three different loading conditions showing different necking behaviors. (a) A case showing very localized necking. (b) A case showing an intermediate amount of necking. (c) A case showing no necking, i.e. homogeneous deformation. (d) Nominal stress–strain state of the model geometry displayed in (a)–(c). (e) True axial stress–strain state of the model geometry displayed in (a)–(c). See Vids. 6.1, 6.2, 6.3 for animations of contour plots.

clear what was inferred from the nominal stress–strain curves in Fig. 6.14; necking becomes more diffuse at higher temperatures and lower strain rates. Animations of the model geometry along with animated stress–strain curves for the three conditions in Fig. 6.15 can be found in Vids. 6.1, 6.2, 6.3.[4]

A local maximum in the nominal stress–strain curve is necessary for necking [98], and the depth of the post-peak stress decrease controls how localized necking becomes before neck stabilization. Therefore, to understand why necking is more pronounced at higher strain rates and lower temperatures, it is useful to study the nominal stress–strain curves from single elements. Figs. 6.16a,c,e present "intrinsic" nominal stress–strain curves using the calibrated model parameters and various loading conditions. The nominal stress–strain curve is referred to as intrinsic in that it is produced from the deformation of a single element and is therefore not altered by structural artifacts. In Figs. 6.16b,d,f nominal stress–strain curves produced from the cylindrical bar model are presented again. The shapes of the nominal stress–strain curves vary significantly between the single element response and the structural response. However, the nominal stress–strain curves for the single element and the cylindrical bar model show the same trend regarding the post-peak stress decrease: it becomes larger at higher strain rates and lower temperatures. At sufficiently low strain rates or high temperatures, the local minimum disappears completely. Since the sensitivity of the post-peak (nominal) stress decrease manifests in the mechanical behavior of a single element, the severity of necking is coupled to the strain rate and temperature through the constitutive law.

To study the effects of strain rate and temperature on the post-peak stress decrease, consider the viscoplastic law, Eq. (6.18), for the amorphous phase. Since the calibration procedure used here has assumed that $\dot{s}_{\mathrm{c}} = 0$, the amorphous viscoplastic law must be the source of the post-peak stress decrease. The strength of intermolecular amorphous resistance, $\bar{\sigma}_{\mathrm{a}}$, increases with the athermal shear strength, s_{a}, although an increase in the hydrostatic

[4] Email `kncundiff.dissertationquestions@gmail.com` to request video files.

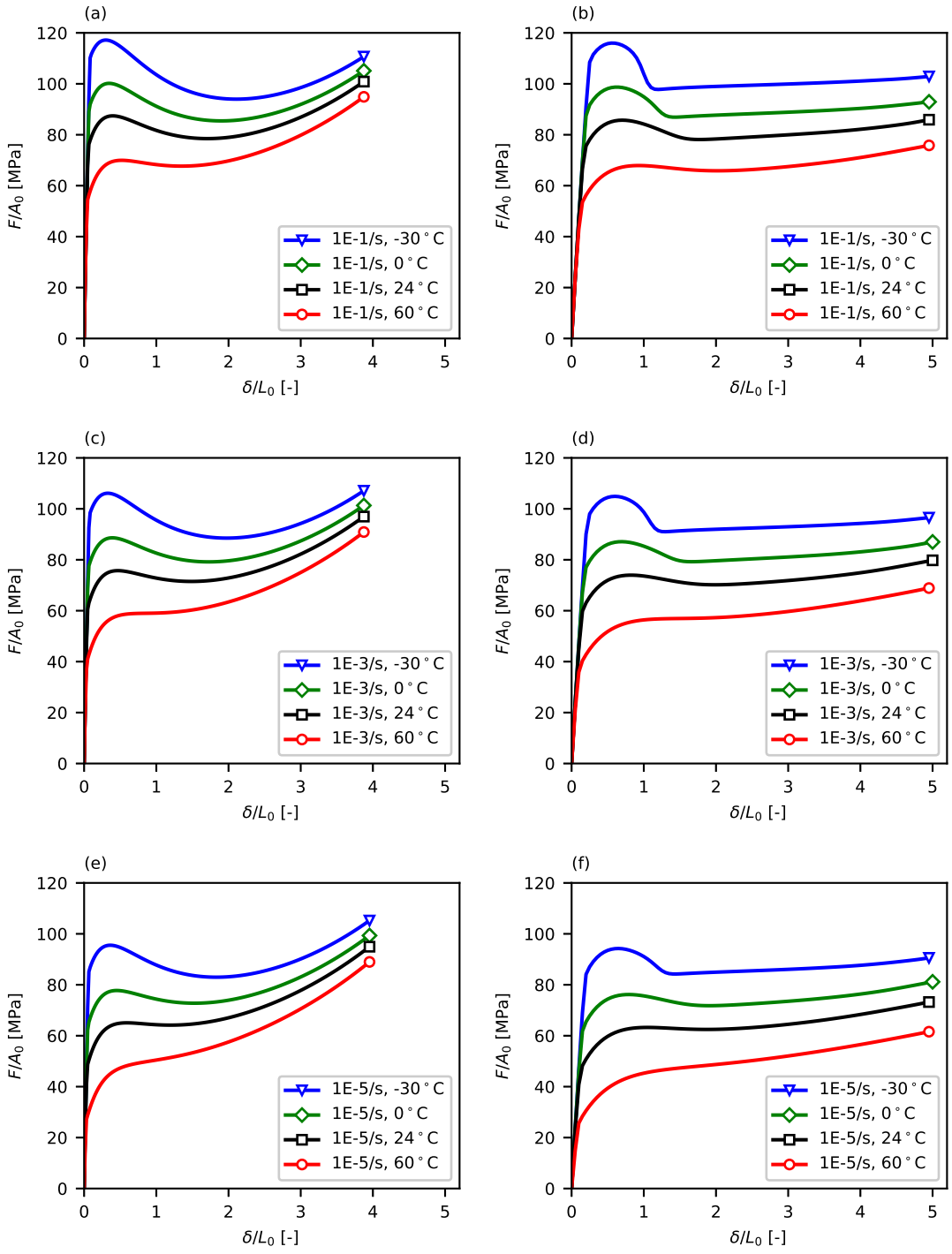

Figure 6.16: (a,c,e) Nominal stress–strain curves of PA-6 loaded in tension, as determined by loading a single element using the calibrated parameters in Table 6.13. (b,d,f) Simulated nominal stress–strain curves using calibrated parameters with the cylindrical bar finite element model. (a) $\dot{\varepsilon}_{22} = 10^{-1}$ /s, (b) $\dot{\delta}/L_0 = 10^{-1}$ /s, (c) $\dot{\varepsilon}_{22} = 10^{-3}$ /s, (d) $\dot{\delta}/L_0 = 10^{-3}$ /s, (e) $\dot{\varepsilon}_{22} = 10^{-5}$ /s, (f) $\dot{\delta}/L_0 = 10^{-5}$ /s.

pressure, $\sigma_{\mathrm{a,m}}$, reduces $\bar{\sigma}_{\mathrm{a}}$ through the term $s_{\mathrm{a}} - 3\alpha_{\mathrm{a}}\sigma_{\mathrm{a,m}}$. Therefore, the pressure-adjusted athermal shear strength is introduced as

$$s_{\mathrm{a}}^{*} = s_{\mathrm{a}} - 3\alpha_{\mathrm{a}}\sigma_{\mathrm{a,m}}. \tag{6.71}$$

In order to decrease the strength, $\bar{\sigma}_{\mathrm{a}}$, the pressure adjusted athermal shear strength, s_{a}^{*}, must also decrease. The amorphous viscoplastic law can be rearranged into an expression for $\bar{\sigma}_{\mathrm{a}}$ in terms of the pressure-adjusted athermal shear strength,

$$\bar{\sigma}_{\mathrm{a}} = s_{\mathrm{a}}^{*}\left[1 + \frac{T}{\mathcal{A}_{\mathrm{a}} s_{\mathrm{a}}^{*}} \ln\left(\frac{\dot{\bar{\varepsilon}}_{\mathrm{a}}^{\mathrm{p}}}{\dot{\varepsilon}_{0}}\right)\right]^{\frac{1}{m_{\mathrm{a}}}}. \tag{6.72}$$

For the calibrated parameters used here, the history for $s_{\mathrm{a}}^{*}(\bar{\varepsilon}_{\mathrm{a}}^{\mathrm{p}})$ is nearly independent of T and $\dot{\bar{\varepsilon}}_{\mathrm{a}}^{\mathrm{p}}$. However, a single function for $s_{\mathrm{a}}^{*}(\bar{\varepsilon}_{\mathrm{a}}^{\mathrm{p}})$ can produce dramatically different histories for $\bar{\sigma}_{\mathrm{a}}(\bar{\varepsilon}_{\mathrm{a}}^{\mathrm{p}})$, depending on the values of T and $\dot{\bar{\varepsilon}}_{\mathrm{a}}^{\mathrm{p}}$. To illustrate this point, Fig. 6.17a plots $\bar{\sigma}_{\mathrm{a}}$ versus s_{a}^{*} for the three different loading conditions investigated in Fig. 6.15. Now, consider the derivative of $\bar{\sigma}_{\mathrm{a}}$ with respect to s_{a}^{*},

$$\frac{\partial \bar{\sigma}_{\mathrm{a}}}{\partial s_{\mathrm{a}}^{*}} = \left[1 + \frac{T}{\mathcal{A}_{\mathrm{a}} s_{\mathrm{a}}^{*}} \ln\left(\frac{\dot{\bar{\varepsilon}}_{\mathrm{a}}^{\mathrm{p}}}{\dot{\varepsilon}_{0}}\right)\right]^{\frac{1}{m_{\mathrm{a}}}} - \frac{T}{\mathcal{A}_{\mathrm{a}} m_{\mathrm{a}} s_{\mathrm{a}}^{*}} \ln\left(\frac{\dot{\bar{\varepsilon}}_{\mathrm{a}}^{\mathrm{p}}}{\dot{\varepsilon}_{0}}\right)\left[1 + \frac{T}{\mathcal{A}_{\mathrm{a}} s_{\mathrm{a}}^{*}} \ln\left(\frac{\dot{\bar{\varepsilon}}_{\mathrm{a}}^{\mathrm{p}}}{\dot{\varepsilon}_{0}}\right)\right]^{\frac{1-m_{\mathrm{a}}}{m_{\mathrm{a}}}}. \tag{6.73}$$

Eq. (6.73) is plotted in Fig. 6.17b for the three different loading conditions investigated in Fig. 6.15. Fig. 6.17b reveals that $\frac{\partial \bar{\sigma}_{\mathrm{a}}}{\partial s_{\mathrm{a}}^{*}}$ increases with increasing strain rate or decreasing temperature. Therefore, for the same decrease in s_{a}^{*}, loading conditions at higher strain rates and lower temperatures experience a larger decrease in $\bar{\sigma}_{\mathrm{a}}$, resulting in a larger stress decrease in the nominal stress–strain curve, and therefore more severe necking.

For the calibrated parameters in Table 6.13, the peak strength and the saturation strength are equal, $s_{1,\mathrm{a}} = s_{2,\mathrm{a}}$. Therefore, $s_{\mathrm{a}}(\bar{\varepsilon}_{\mathrm{a}}^{\mathrm{p}})$ monotonically increases from $s_{\mathrm{a},0}$ to $s_{1,\mathrm{a}}$, and then remains constant. However, as the load increases, $\sigma_{\mathrm{a,m}}$ increases as well. Therefore, $s_{\mathrm{a}}(\bar{\varepsilon}_{\mathrm{a}}^{\mathrm{p}})$ works to increase $s_{\mathrm{a}}^{*}(\bar{\varepsilon}_{\mathrm{a}}^{\mathrm{p}})$, while $\sigma_{\mathrm{a,m}}$ works to decrease it. Once $s_{\mathrm{a}}(\bar{\varepsilon}_{\mathrm{a}}^{\mathrm{p}})$ reaches its saturation

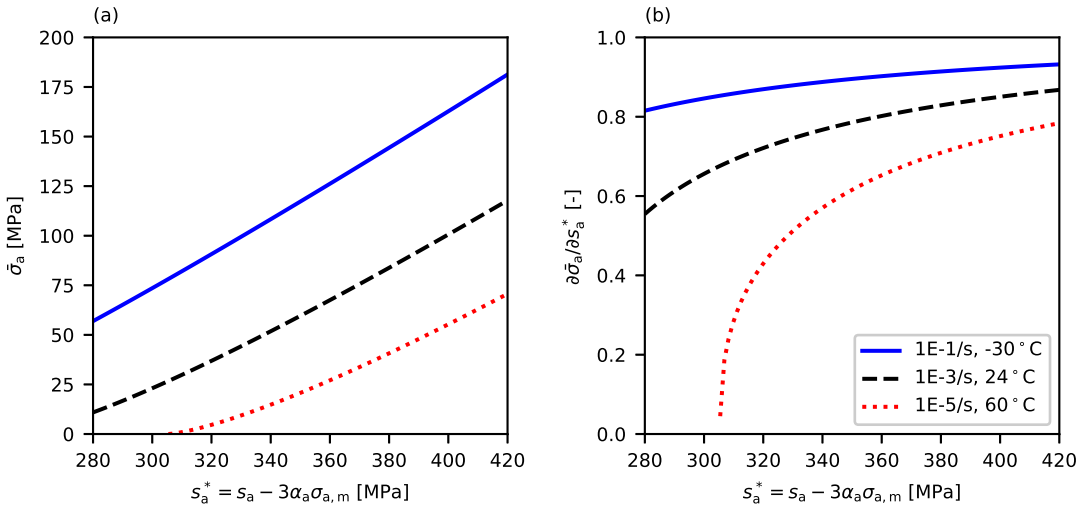

Figure 6.17: (a) The intermolecular strength of the amorphous phase, $\bar{\sigma}_a$ versus the pressure adjusted athermal shear strength of the amorphous phase, s_a^*, see Eq. (6.72). (b) $\frac{\partial\bar{\sigma}_a}{\partial s_a^*}$ versus s_a^*, see Eq. (6.73). Both equations use the calibrated model parameters in Table 6.13.

value, $s_a(\bar{\varepsilon}_a^p) = s_{2,a}$, then $s_a^*(\bar{\varepsilon}_a^p)$ will decrease through the increases in $\sigma_{a,m}$. In most cases, this results in a decrease in the nominal stress. Eventually, the orientation hardening, $\boldsymbol{b}$, begins to dominate the mechanical behavior, which increases the flow stress of the material. When the increase in the nominal flow stress due orientation hardening is greater than the decrease in the nominal flow stress due to decreasing $s_a^*(\bar{\varepsilon}_a^p)$, then hardening resumes, a local minimum in the nominal stress occurs, and the neck stabilizes. For lower strain rates and higher temperatures, the value of $\bar{\sigma}_a$ is lower, so the orientation hardening becomes the dominant effect in the nominal stress–strain curve sooner, therefore, the local minimum occurs at an earlier nominal strain level, see Fig. 6.16. For sufficiently low strain rates or high temperatures, the orientation hardening becomes the dominant effect before $s_a^*(\bar{\varepsilon}_a^p)$ begins to decrease. When this occurs, no local minimum is observed in the nominal stress–strain curve, and therefore no necking occurs. It should be noted that, regardless whether the *nominal* stress–strain curve has a local minimum, the *true* stress–strain curve monotonically increases in all cases studied here, see Fig. 6.14a,c,e.

From this analysis, it has been determined that larger decreases in the function $s_{\mathrm{a}}^{*}(\bar{\varepsilon}_{\mathrm{a}}^{\mathrm{p}})$ results in necking behavior that is more sensitive to strain rate and temperature, provided that the decrease in $s_{\mathrm{a}}^{*}(\bar{\varepsilon}_{\mathrm{a}}^{\mathrm{p}})$ occurs before orientation hardening becomes the dominant component of the nominal mechanical behavior. The most straightforward way to increase the post-peak dip of $s_{\mathrm{a}}^{*}(\bar{\varepsilon}_{\mathrm{a}}^{\mathrm{p}})$ is to increase $s_{1,\mathrm{a}} - s_{2,\mathrm{a}}$. For tensile loading, increasing α_{a} also causes larger decreases in $s_{\mathrm{a}}^{*}(\bar{\varepsilon}_{\mathrm{a}}^{\mathrm{p}})$ through the development of a hydrostatic pressure, $\sigma_{\mathrm{a,m}}$. Of course, the range of $s_{\mathrm{c}}^{*}(\bar{\varepsilon}_{\mathrm{c}}^{\mathrm{p}})$ will also affect the sensitivity of necking to strain rate and temperature, but $s_{\mathrm{c}}^{*}(\bar{\varepsilon}_{\mathrm{c}}^{\mathrm{p}})$ is assumed constant in this study for the reasons presented in Sections 6.6.2.2 and 6.6.2.5. This discussion also makes it clear that there are many different parameter sets could produce the same mechanical behavior. For the final calibrated parameters, a decrease in $s_{\mathrm{a}}^{*}(\bar{\varepsilon}_{\mathrm{a}}^{\mathrm{p}})$ is achieved through the pressure sensitivity, α_{a}, even while the saturation and peak values of s_{a} are the same, $s_{1,\mathrm{a}} = s_{2,\mathrm{a}}$. The same $s_{\mathrm{a}}^{*}(\bar{\varepsilon}_{\mathrm{a}}^{\mathrm{p}})$ could be achieved by decreasing α_{a} while also lowering $s_{2,\mathrm{a}}$. It is likely that many other combinations of the parameters $s_{1,\mathrm{a}}$, $s_{2,\mathrm{a}}$, $h_{1,\mathrm{a}}$, $h_{2,\mathrm{a}}$, $\bar{\varepsilon}_{\mathrm{a}}^{\mathrm{w}}$, f_{a}, and α_{a} could all produce identical or similar histories for $s_{\mathrm{a}}^{*}(\bar{\varepsilon}_{\mathrm{a}}^{\mathrm{p}})$.

6.10.2 Assessment of inverse parameter identification method

When studying the mechanical behavior of polymers, decoupling the intrinsic mechanical behavior from structural effects, such as necking, poses a challenge. Here, the problem is studied by constructing a finite element model of the specimen and then employing a constitutive model for a viscoplastic polymer to govern the stress–strain behavior. By calibrating the parameters of the constitutive model such that the finite element specimen replicates the experimentally measured nominal stress–strain curve, the intrinsic and structural effects are decoupled. Structural effects are easily studied through the finite element model geometry while the intrinsic effects are studied through the mechanical behavior produced by the calibrated constitutive law. While this method requires a significant modeling effort, its key advantage compared to other methods is that it requires only the simplest of mechanical measurements, i.e. the nominal stress–strain curve. In this study, the mechanical behavior of a cylindrical bar of PA-6 was accessed using the calibrated parameters presented in

Table 6.13. In this section, the strengths and weaknesses of the method are assessed and comments are made about the specific calibration produced here for PA-6.

Necking during the loading of polymers introduces several structural effects that must be considered when probing the intrinsic mechanical behavior. The primary effect introduced is a heterogeneous strain field over the specimen. This effect is typically overcome through the use of video-based extensometry capable of producing local strain measurements. Here, the effect is accounted for through the geometry of the finite element model, which, if properly constructed, exhibits a strain field equivalent to the experimental strain field. However, two secondary effects are introduced by necking which are not accounted for using local strain measurements alone, but are automatically accounted for here. These two effects are (1) differences between the true axial stress and true equivalent stress and (2) variations in the strain rate throughout the gauge length of the specimen. Neither of these effects are considered in the contour tracking method introduced in Chapter 3.

When a neck forms, a triaxial stress state develops in the necked region [112]. When the lateral stresses are no longer negligible, the equivalent stress is less than the axial stress, i.e.

$$\sigma_{\text{eqv}} < F/A, \quad \sigma_{\text{eqv}} = \sqrt{\frac{3}{2}\boldsymbol{\sigma}' : \boldsymbol{\sigma}'}. \tag{6.74}$$

To illustrate the importance of this effect, Fig. 6.18 compares the true axial stress–strain curve for the cylindrical bar finite element model to the intrinsic stress–strain curve for a single element model (i.e. a model without structural effects). The true axial stress is calculated from the reaction force in the center of the bar divided by the current cross-sectional area (F/A). The strain used along with the true axial stress is the true global strain, calculated from the reduction of the specimen diameter ($2\ln(\Phi_0/\Phi)$). These definitions of the specimen level stress and strain are equivalent to the definitions used for contour tracking in Eqs. (6.4) and (6.5). Since necking becomes more severe at lower temperatures and higher strain rates, different loading conditions are used to control the severity of necking

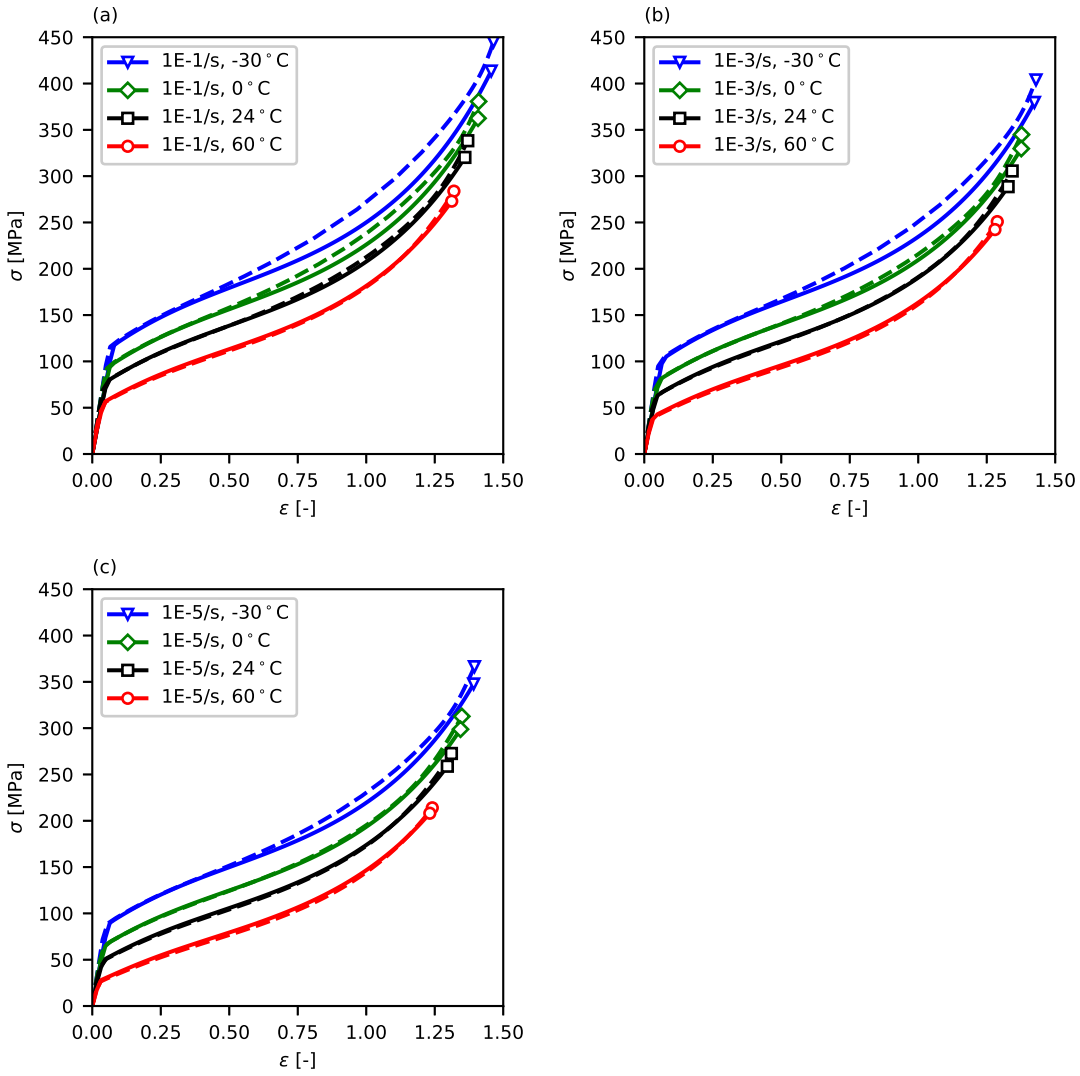

Figure 6.18: The true axial stress–strain curves ($\varepsilon = 2\ln(\Phi_0/\Phi)$ versus $\sigma = F/A$, dashed lines) for the cylindrical bar finite element model compared to the intrinsic stress–strain curves ($\varepsilon = \varepsilon_{22}$ versus $\sigma = \sigma_{22}$, solid lines) produced from the loading of a single element at a constant true strain rate. Different loading rates and temperatures are explored for each model. As the amount of necking increases (by loading at a lower temperature or higher strain rate), the difference between the axial and intrinsic stress–strain curves increases.

experienced in the cylindrical bar model. For the simulation using the highest temperature and lowest strain rate ($T = 60\,^{\circ}\mathrm{C}$, $\dot{\delta}/L_0 = 10^{-5}\,/\mathrm{s}$), the deformation occurs without necking and the true axial stress–strain curve is identical to the intrinsic stress–strain curve. As the amount of necking increases (i.e. decreasing temperature and increasing strain rate), the difference between the axial stress–strain curve and the intrinsic stress–strain curve increases. The stress–strain curves begin to differ at the onset of necking, see Vid. 6.1.

In order for a heterogeneous strain field to develop from an initially uniform strain field, differences in the local true strain rate must emerge. In Parsons et al. 2004 [114], DIC measurements of necking in PC revealed that the local strain rate can vary by as much as an order of magnitude. Since polymers are viscoplastic, large changes in the local strain rate result in changes in the local strength. In G'Sell et al. 1992 [112], the true strain rate is controlled by developing a closed-loop video-based extensometry software that calculates the true strain in real-time. In Parsons et al. 2004 [114], a composite stress–strain curve for a constant true strain rate is constructed from various material points that experience the target true strain rate at different times. In the method employed here, strain rate variations emerge naturally from the finite element model, and then the corresponding changes in strength are automatically accounted for through the viscoplastic constitutive model. Fig. 6.19, shows contours of the effective plastic strain rate in the amorphous phase, $\dot{\bar{\varepsilon}}^{\mathrm{p}}_{\mathrm{a}}$, at three different times during the loading of the cylindrical bar model.[5] The loading condition used in Fig. 6.19 is $T = -30\,^{\circ}\mathrm{C}$ and $\dot{\delta}/L_0 = 10^{-1}\,/\mathrm{s}$, where the neck severity is highest for the conditions studied here. In Fig. 6.19a, the neck is still forming. Accordingly, the strain rate is highest in the center of the neck. In Fig. 6.19b, the neck has stabilized. While the strain rate is still higher in the center of the neck than the rest of the gauge section, the strain rate is highest at the neck fronts. In Fig. 6.19c, the neck has propagated away from the center of the bar. Here, the strain rate is highest at the neck fronts while the strain rate is equally low in front of and

[5] Although $\dot{\varepsilon} \neq \dot{\bar{\varepsilon}}^{\mathrm{p}}_{\mathrm{a}} \neq \dot{\bar{\varepsilon}}^{\mathrm{p}}_{\mathrm{c}}$, these values are all approximately equal. In Fig. 6.19, the variable $\dot{\bar{\varepsilon}}^{\mathrm{p}}_{\mathrm{a}}$ is chosen as a proxy for the true strain rate, since its magnitude is directly responsible for changes in the strength of the amorphous phase, $\bar{\sigma}_{\mathrm{a}}$.

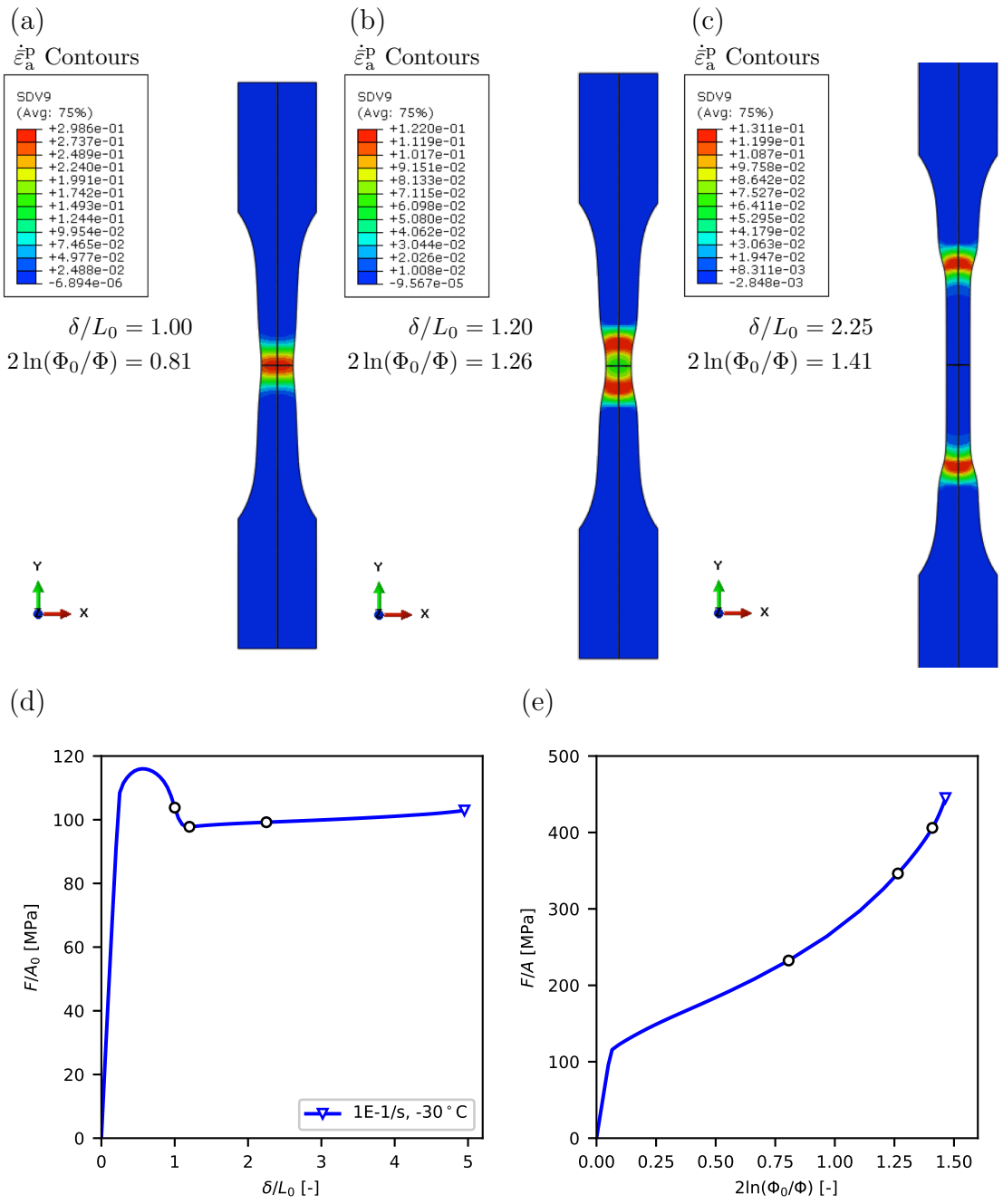

Figure 6.19: (a)–(c) Contours of $\dot{\varepsilon}_a^p$ over the surface of the cylindrical bar finite element model for global true strains, $2\ln(\Phi_0/\Phi)$, of (a) 0.81, (b) 1.26, and (c) 1.41. The simulation uses the loading condition $T = -30\,^\circ\mathrm{C}$ and $\dot{\delta}/L_0 = 10^{-1}\,/\mathrm{s}$. (d) The nominal stress–strain curve of the cylindrical bar model with the locations of the contour images marked on the curve. (e) The true axial stress–strain curve of the cylindrical bar model with the locations of the contour images marked on the curve. See Vid. 6.4 for an animation of the $\dot{\varepsilon}_a^p$ contours over the entire loading history.

behind the neck fronts. At all three stages of deformation presented in Fig. 6.19, the local strain rate across the specimen varies by an order of magnitude, similar to the findings in Ref. [114]. Vid. 6.4 shows a video of the contours of $\dot{\varepsilon}_{\mathrm{a}}^{\mathrm{p}}$ along with animated stress–strain plots.[6]

Although the method applied here has many strengths, some weaknesses have become evident from discussions in previous sections. For one, the model implementation used here does not account for the conversion of plastic work into heat. Therefore, thermal softening that occurs in experiments at high strain rates ($\gtrsim 10^{-2}$ /s), cannot be accounted for. However, using an isothermal approach allowed for an exploration of the sensitivity of necking to temperature and strain rate. Another weakness previously mentioned is the lack of a unique solution to the inverse problem, given the large number of parameters entering into the constitutive model. Therefore, the calibrated parameter set might vary dramatically depending on the constraints and assumptions imposed on the parameters during optimization.

One weakness of the chosen constitutive model is the inability to accurately predict the mechanical behavior in both tension and compression using the same material parameters. The intrinsic behavior in tension (i.e. using the Stage 6 parameters in Table 6.13) and compression (i.e. using the Stage 3 parameters in Table 6.10) are compared in Fig. 6.20 by loading a single element at a constant true strain rate. Significant hardening is observed in tension, while very little hardening is observed in compression. Physically, this is presumably related to differences in the evolution of the network hardening in tension and compression. In the constitutive model, orientation hardening is captured through the network resistance described in Section 6.4.4. This asymmetrical hardening calls for a more careful study of orientation hardening in the compressive loading of PA-6.

It is a well established fact that PA-6 undergoes cavitation when subjected to a positive hydrostatic pressure [21], and fracture in unaged PA-6 occurs by the growth and coalescence

[6] Email `kncundiff.dissertationquestions@gmail.com` to request video files.

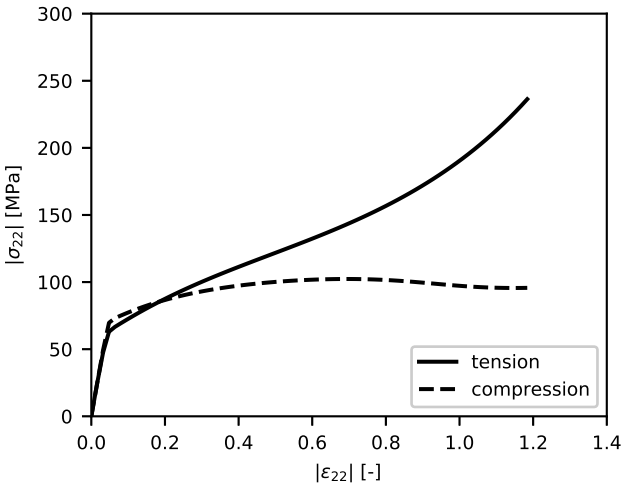

Figure 6.20: The intrinsic mechanical behavior in tension and compression, using the Stage 6 parameters in Table 6.13 for tension and the Stage 3 parameters in Table 6.10 for compression.

of voids [22, 23]. An increasing void volume fraction will naturally decrease the apparent strength of a material, yet the constitutive model chosen here neglects the presence of voids in the material. Although recent work has been conducted to develop constitutive models for the growth of anisotropic voids in a viscoplastic polymeric matrix [107], work towards this goal is relatively new. In Chapter 3, the dilatation of cylindrical bar specimens was studied and used to approximate the void volume fraction, see Fig. 3.11. These measurements indicate that the cylindrical specimens achieve void volume fractions as high as 15 %. Since the viscoplastic constitutive model employed here neglects damage, the intrinsic response produced from calibration is actually an average behavior of the matrix with voids. Therefore, the mechanical behavior of the solid matrix must be stronger than what is predicted here.

Although the constitutive model is capable of accurately representing the specimen-level mechanical behavior of PA-6, there is no guarantee that the model parameters in Table 6.13 are uniquely capable of representing the experimental behavior. In fact, since only one value of the crystal volume fraction, χ, was explored, the apportionment of strength between the crystalline and amorphous phases is somewhat arbitrary. To expand on this point, identical

stress–strain curves could be produced for a single value of χ by lowering $s_{\mathrm{a}}(\bar{\varepsilon}_{\mathrm{a}}^{\mathrm{p}})$ while proportionally increasing $s_{\mathrm{c}}(\bar{\varepsilon}_{\mathrm{c}}^{\mathrm{p}})$. In order to accurately apportion the strength between the two phases, the experimental data set used for calibration would need to explore the effect of the crystal volume fraction. However, no such tests were conducted in this dissertation, since exploring the effects of strain rate, temperature, loading mode, and aging already resulted in an extremely large test matrix. Many of the features of the viscoplastic law were not fully utilized for the crystalline phase, and a fuller utilization of these features could have been realized from an experimental database exploring the effects of crystallinity. First, the temperature and rate sensitivity of each phase was treated as being equal, although this not true in general [21, 139]. Second, it was assumed that the crystalline phase deforms at constant stress, i.e. $s_{\mathrm{c}}(\bar{\varepsilon}_{\mathrm{c}}^{\mathrm{p}}) = s_{\mathrm{c},0}$. Using a more sophisticated function for $s_{\mathrm{c}}(\bar{\varepsilon}_{\mathrm{c}}^{\mathrm{p}})$ would enable the modeling of a broader range of mechanical behaviors. For example, double yielding is a phenomenon observed in PA-6 [136–138] as well as other semicrystalline polymers [115]. The double yield phenomenon is a result of two thermally activated rate processes [138] and depends on the crystal volume fraction of the polymer [137]. Since the constitutive model developed here takes into account the amorphous and crystalline phases, and yielding is governed by two separate Arrhenius-type (i.e. thermally activated) viscoplastic laws, this model is possibly well suited for studying double yielding in semicrystalline polymers. Since the phenomenon of double yielding is also the result of a coupling of specimen-level effects with the intrinsic behavior [138], it would be especially interesting to use the inverse parameter identification method explored here to study double yielding.

6.11 Conclusion

In this chapter, a method for using the nominal stress–strain curve to access the true stress–strain curve, even after the onset of necking, was explored. The method is referred to here as "inverse parameter identification" and combines simple experimental techniques with finite element modeling. The method consists of the following steps:

1. Create a finite element model to simulate the conditions of the experiment.

2. Inform the mechanical behavior of the finite element model with an appropriate constitutive law.

3. Calibrate the constitutive law by optimizing its parameters until the nominal stress–strain curve from the finite element model matches the experimental curve.

4. Once there is good agreement between the simulated and experimental stress–strain curves, it is assumed that the calibrated constitutive law accurately represents the intrinsic mechanical behavior of the experiment. Now the constitutive law can be used to study the intrinsic mechanical behavior, free from structural effects such as necking.

This method was used here to access the intrinsic mechanical behavior of PA-6 in tension. The constitutive law used in the finite element model was a macromolecular model for a semicrystalline polymer, which was developed and implemented as an Abaqus user material subroutine. Its formulation and implementation were based on a previous macromolecular constitutive law for an amorphous polymer [30]. Although the goal was to study the tensile behavior of PA-6 after the onset of necking, tests in compression were used to calibrate parameters governing the temperature and strain rate sensitivity of PA-6. Compression tests were advantageous in this regard since their deformation was approximately homogeneous, allowing multiple executions of the model at various temperatures and strain rates with minimal computational expense. However, the amount of network hardening in tension and compression showed large differences which the model was not able to capture.

The model parameters were calibrated to produce excellent agreement between the simulated and experimental nominal stress–strain curve. From the calibration, which used axial measurements of deformation (i.e. only the nominal strain), excellent agreement emerged between the simulated and experimental measurements of the lateral specimen deformation, therefore, the calibrated model accurately simulated necking. The calibration was also assessed using finite element simulations of round notched bars, which produced good agreement with experimental results.

Simulations conducted here revealed that necking is sensitive to strain rate and temperature. At higher strain rates and lower temperatures, necking becomes more severe, i.e. more localized. At sufficiently low strain rates and high temperatures, no necking occurs. This effect has been observed in both experiments [115,141] and models [113,142]. Here, the sensitivity of necking to strain rate and temperature is a direct result of the chosen viscoplastic law.

There are two main strengths of the inverse parameter identification method. First, this method requires only the nominal stress–strain curve, which is trivial to produce from any test frame. Second, geometric effects induced by necking are automatically decoupled from the intrinsic behavior of the material. Specifically, the following geometric effects are automatically accounted for using this method:

- a heterogeneous strain field induced by necking,
- order of magnitude variations in the local true strain rate,
- differences between the true axial stress, F/A, and the true equivalent stress σ_{eqv} that emerge as a result of the triaxial stress state induced by necking.

While these effects are automatically accounted for here, they are laborious to account for using experimental techniques alone.

Four areas for improvement in the method implemented here are also identified. (1) The model implementation is isothermal, limiting its ability to study the mechanical response at strain rates above 10^{-2} /s, where the conversion of plastic work into heat causes thermal softening. (2) The constitutive model was unable to account for the observed asymmetry in tension and compression. (3) The constitutive model implemented here is capable of a much richer modeling of the effects of crystallinity than what was attempted. However, a richer constitutive description of the crystalline phase would have required a significantly larger experimental database that explored the effects of crystallinity in addition to the already explored effects of temperature, strain rate, and pressure. (4) Given the large number of

parameters in the constitutive model, no unique solution to the inverse problem exists. Therefore, the final calibrated parameters are sensitive to the constraints and assumptions imposed on the parameters during calibration.

7. MODELING AGING-INDUCED DAMAGE

7.1 Introduction

Semicrystalline thermoplastic components designed for long-term use commonly experience chemical degradation, referred to here as aging. The most common causes of aging are UV radiation, high temperatures, and moisture [2], which cause photo-oxidation [18, 99], thermo-oxidation [15, 143], and hydrolysis [14, 108], respectively. While these factors are a concern for almost any long-term application, some applications require exposure to especially harsh environments that exacerbate aging, e.g. greenhouse coverings, pipes transporting hot fluids, and car engine components. Aging causes both chain scission and cross-linking, although chain scission is typically dominant when oxygen is present [99]. This causes the average molar mass of the material to decrease [55]. Eventually, aging leads to a catastrophic loss of ductility, which is often characterized by an abrupt decrease in the engineering fracture strain [19].

Several studies have found that when aging-induced chain scission reduces the (weight average) molar mass below a critical value, M_c, an abrupt and catastrophic reduction in the engineering fracture strain is observed [4, 55]. These studies proposed that embrittlement occurred by either the destruction of the entanglement network or by chemi-crystallization reducing the volume fraction of the amorphous phase [4]. If embrittlement occurs below a critical molar mass, then thermoplastics with the same molar mass should exhibit the same residual ductility, regardless of if they have been aged or not. In Refs. [4, 55], data from the literature was gathered to plot the ultimate draw ratio against the weight average molar mass for aged and unaged polyethylene (PE) (The plot is reproduced in Fig. 1.1). The data revealed that when the molar mass was above a critical value, only ductile behavior was observed. However, below the critical molar mass, both ductile and brittle behavior occurred, indicating that the molar mass is not sufficient for determining when embrittlement occurs.

In Chapter 3, mechanical tests on UV-aged PA-6 were conducted, where videos of mechanical tests on bulk specimens as well as tomograms of film specimens revealed the appearance and growth of surface cracks prior to the peak load. This evidence was used to argue that aging-induced embrittlement in semicrystalline thermoplastics was growth-controlled, meaning that the residual ductility was controlled by the growth of aging-induced damage. This conclusion was further supported by the tomography evidence presented in Chapters 4 and 5, as well as other studies of fracture in aged semicrystalline thermoplastics [28, 99]. In Chapter 3, a chemical stress model was proposed to explain the nucleation of aging-induced damage. As the photo-oxidized layer thickens inwardly from the surface, a kinematic mismatch occurs between the aged skin and the core, which is offset by a chemical stress in the surface layer. For sufficiently large aging doses, the chemical stress is high enough to form cracks without the application of mechanical force [99]. These cracks can be referred to as "chemical cracks", since they form after chemical aging absent from a mechanical load. On the other hand, the chemical stress may not be sufficient to cause cracking after aging, but cracks may from after the addition of a mechanical load. In this case, the damage is "chemo-mechanical". Aging also promotes cavitation in semicrystalline thermoplastics that do not cavitate in the unaged condition [99]. This chemically-induced cavitation can also be considered chemo-mechanical damage. Regardless of the specific mechanism leading to aging-induced damage, these results indicate that aging-induced embrittlement is likely a consequence of aging-induced damage. Therefore, aging-induced damage is potentially a mesoscale effect that connects chemical effects at the nanoscale and embrittlement at the macroscale.

If embrittlement is a consequence of aging-induced damage at the microscale, then micromechanics-based continuum damage models should be capable of predicting the residual ductility in aged semicrystalline thermoplastics. One approach to modeling damage is the continuum damage mechanics approach, where damage is modeled within the thermodynamic framework of irreversible processes [107]. This approach has been recently applied to

study cavitation in PA-6 [107]. However, this approach treats damage as a phenomenological effect, and therefore it is not straightforward to compare the modeled state of damage to the microstructure in the real material. The Gurson model represents another approach to modeling micromechanical damage [32]. The Gurson model uses homogenization theory and limit analysis to derive constitutive equations for a spherical RVE composed of a von Mises matrix with an embedded, spherical void. In the Gurson model, the microstructural state of the material is represented by a state variable, the void volume fraction. Such an approach makes it easy to compare the modeled microstructural state to an experimental microstructural state. Many improved models for void growth have since been formulated using homogenization theory and limit analysis to derive constitutive equations for more general RVEs [45]. One such Gurson-type models is the Keralavarma-Benzerga model [33,34,80], which homogenizes a spheroidal RVE composed of an (orthotropic) Hill-type matrix with an embedded, misaligned, spheroidal void. In addition to the void volume fraction, the Keralavarma-Benzerga model uses the void aspect ratio and void orientation as state variables, enabling a richer representation of the microstructure of the porous material.

In this chapter, a Gurson-type micromechanics-based continuum damage model is applied to predict fracture in unaged and aged semicrystalline thermoplastics. Specifically, unaged PA-6 and PA-6 subjected to UV aging are modeled, so the experimental evidence in Chapters 3–5 can be drawn upon for calibration and validation. In the unaged material, the state variables characterizing the microstructure are calibrated to represent cavities. This approach is expected to successfully predict fracture, as it is well known that PA-6 fractures due to the growth and coalesence of cavities [21–23, 106]. In the aged material, the state variables are calibrated to represent aging-induced damage. If fracture in an aged semicrystalline thermoplastic is growth controlled, then the micromechanical damage model model should produce accurate predictions of the fracture strain.

Fracture in two different round notched bar geometries are modeled to test the predictive ability of the damage model across different stress triaxiality ratios. The stress triaxiality

ratio, defined as the ratio of the hydrostatic stress to the mean normal stress, is an important factor for void growth [45]. Round notched bars are ideal for exploring triaxiality effects, since they experience an approximately constant triaxiality [45]. However, since the damage model employed here does not include certain features of polymeric deformation, the viscoplastic polymer model developed and calibrated in Chapter 6 is employed to create finite element models of the round notched bars. Using these finite element models, each round notched bar boundary value problem is reduced to a problem at a critical material point where fracture is expected to initiate. Without structural effects in the simulation, the importance of polymer-specific constitutive equations is reduced, and the mechanical behavior can be accurately represented by the damage model using a hardening law calibrated to the mechanical behavior at the material point. In the unaged material, the modeled material point is the center of the notch, where the stress triaxiality is highest. In the aged material, the modeled material point is the surface of the notch root, where the aging-induced damage is most severe. The choice of the notch root surface as the point where fracture initiates is supported by the investigations in Chapters 3 and 4.

In the modeling approach used here, the effect of UV aging on the mechanical behavior of PA-6 is neglected. The finite element models used to reduce the structural calculation to a material point employ the calibrated polymer constitutive model developed in Chapter 6. This calibration was fit using mechanical data from unaged PA-6, but UV aging is known to change the strength of the material [99] (see also Figs. 3.5, 5.1). This approximation is made for two reasons. First, this chapter studies fracture in round notched bars, which have radii much larger than the nominal depth of oxidative damage (100 µm) [16, 27, 28]. Therefore, while aging may increase the strength of the superficial surface layer, the change in strength is not detectable at the specimen level. Second, neglecting the effect of aging on the mechanical behavior is equivalent to making the approximation that the only change incurred by aging is the introduction of aging-induced damage. Therefore, if the damage model successfully predicts the fracture strain of the aged material, then it can be concluded

that aging-induced damage is sufficient for explaining embrittlement.

The outline of this Chapter is as follows. In Section 7.2, the experimental fracture strains from aged and unaged round notched bars are presented. The database of tomograms available to characterize the microstructure is also described. In Section 7.3, the formulation of the Gurson-type micromechanics-based continuum damage model is presented. In Section 7.4, the modeling approach is briefly summarized. Sections 7.5–7.7 describe how the model is calibrated. In Section 7.5, finite element calculations on round notched bars using the viscoplastic polymer model are used to reduce each boundary value problem to a critical material point. In Section 7.6, the hardening law in the damage model is calibrated using the stress–strain path experienced by the critical point in the finite element calculations. In Section 7.7, tomography from Chapters 4 and 5 are used to characterize the morphology of damage in the both the unaged and aged material. The characterization of the morphology is used to calibrate the micromechanical damage variables in the model. In Section 7.8, the results from the damage model calculations are shown. In Section 7.9, the significance of the results is discussed, and concluding remarks are made in Section 7.10.

7.2 Experimental data

In this chapter, a micromechanics-based continuum damage model is applied to predict the fracture strains of aged and unaged PA-6 round notched bars. Broadly speaking, two categories of experimental data are necessary for this modeling task. First, fracture strains from mechanical tests are needed to validate the model predictions. This data is imported from the mechanical tests on PA-6 round notched bars in Chapter 4. Second, an experimental characterization of the state of damage in both the aged and unaged material is required to determine initial values of model parameters related to micromechanical damage. To this end, tomographic observations are imported from Chapters 4 and 5. The constitutive behavior of the dense material has already been calibrated in Chapter 6, so no experimental stress–strain curves are required for model calibration.

In Chapter 4, mechanical tests on aged and unaged round notched bars of PA-6 were

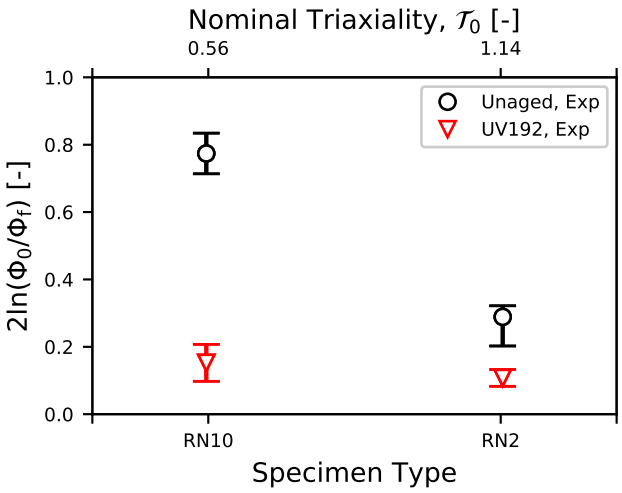

Figure 7.1: Specimen-level fracture strain versus nominal triaxiality for aged and unaged round notched bars of PA-6.

conducted. The fracture strains from these experiments are used here to validate model predictions. Two different notched bar geometries are studied here: an RN10 bar and an RN2 bar. The nominal stress triaxiality at the center of a round notched bar, $\mathcal{T}_0$, can be calculated using Eq. (4.4). For the RN10 bar, $\mathcal{T}_0 = 0.56$, and for the RN2 bar, $\mathcal{T}_0 = 1.14$. Two different aging conditions are studied here: unaged PA-6 and PA-6 exposed to UV radiation for 192 hours, referred to here as the UV192 aging condition. For a full description of the experimental methodology of the round notched bars, see Section 4.2. In Fig. 7.1, the average fracture strains for aged and unaged round notched bars are plotted versus the nominal stress triaxiality associated with the specimen geometry. The error-bars in Fig. 7.1 are associated with the minimum and maximum fracture strains for a given condition. For the complete data set of fracture strains, see Fig. 4.4. The strain is measured using contour tracking, a video-based extensometry method that tracks the minimum diameter of the specimen *in situ*. The strain is calculated as

$$\varepsilon = 2\ln\left(\frac{\Phi_0}{\Phi}\right), \tag{7.1}$$

where Φ_0 is the initial diameter of the specimen and Φ is the current diameter. The subscript "f" is used to denote the value of a quantity at fracture, e.g. when fracture occurs, $\Phi = \Phi_f$. Eq. (7.1) is a specimen-level measurement of strain; the strain in Eq. (7.1) is calculated from the minimum diameter of the specimen, and therefore represents an average strain over the minimum section. In Section 7.5, finite element modeling is used to associate specimen-level strains to local strains at critical locations.

For the unaged bars in Fig. 7.1, the fracture strain is significantly higher in the RN10 bar than the RN2 bar. This is because the triaxiality in the RN2 bar is higher, resulting in greater void growth, thereby reducing the ductility. For the unaged bars, fracture initiates in the center of the notch, as this is the location with the highest triaxiality. For the aged bars, the fracture strain is similar for both the RN10 and the RN2 bar. Since the depth of oxidation in thermoplastics is limited to approximately 100 µm [16, 27, 28], the surface of the bar is degraded while the core retains it ductility. Therefore, fracture initiates at the surface of the notch root. Since the traction free boundary condition at the surface limits the stress triaxiality, the stress triaxiality changes less between the surfaces of the RN10 and RN2 bars than it does between the centers. Therefore, the fracture strain becomes less sensitive to the specimen geometry after aging, see Chapter 4.

Tomograms are used to characterize the morphology of damage, which are then used to calibrate the microstructural variables in the damage model. A significant database of tomograms on aged and unaged PA-6 was developed in Chapters 4 and 5. Relavent tomograms appear in Figs. 4.8, 4.9, 5.4, 5.6, and 5.7. For brevity, these figures are not repeated here. Instead, tomograms are presented in the following sections as they become relevant to calibration.

7.3 Micromechanics-based continuum damage model

A Gurson-type [32] micromechanics-based continuum damage model is employed to evaluate the role of aging-induced damage in the fracture of aged PA-6. The chosen model derives constitutive equations for a material with voids by homogenizing a representative

volume element (RVE) composed of a rigid–Hill plastic (orthotropic) matrix containing an arbitrarily oriented spheroidal void [33, 34]. In the application of this model to aged PA-6, the voids represent aging-induced damage [88]. Two scenarios are possible for the formation of aging-induced damage. In the first, the chemical cracks forms during aging, prior to the application of a load. In the second, aging creates a chemical stress or promotes cavitation. When loading begins, chemo-mechanical damage forms from a combination of chemical and mechanical effects [99]. However, the model implementation used here does not consider void nucleation. It is assumed that all voids are either initial to the material, or nucleate prior to yield. The damage model is also applied to study fracture in PA-6, where fracture by void growth and coalescence is known to occur in round notched bars [21, 23].

The plastic deformation in the model is controlled by a yield criterion for an anisotropic materials with arbitrarily oriented, anisotropic voids [33, 34]. In addition to the stress state, the yield criterion is a function of several microstructural damage variables that characterize, on average, the population of voids in the material. An evolution law is associated with each microstructural damage variable, allowing the voids to grow, distort, or rotate during plastic deformation. Since plastic deformation in the model is associated with the evolution of the damage variables, the yield criterion is also referred to as a "void growth criterion". Failure is determined by the onset of coalescence, as predicted by the void coalescence criterion originally formulated by Benzerga and Leblond [144] and later modified with heuristic parameters by Torki et al. [145]. The yield stress of the matrix evolves using a phenomenological hardening law. Although the original model [33, 34] assumes that the matrix behavior is rigid–plastic, elasticity has been incorporated using a hypoelastic law [35, 80].

The model implementation used here considers only a single material point subjected to axisymmetric loading, following the methodology of a similar study by Kondori and Benzerga [35]. A more general implementation, suitable for finite-element analysis, is described in Ref. [80].

As a reminder regarding notation, for any symmetric, second order tensor, $\boldsymbol{Z}$, the devi-

atoric tensor of $\boldsymbol{Z}$ is denoted as $\boldsymbol{Z}'$ and the mean normal component is denoted as Z_{m};

$$\boldsymbol{Z}' = \boldsymbol{Z} - Z_{\mathrm{m}}, \quad Z_{\mathrm{m}} = \frac{1}{3}\,\mathrm{tr}\,\boldsymbol{Z}. \tag{7.2}$$

7.3.1 Representative volume element and definitions of microstructural damage variables

Prior to a full description of the constitutive equations, a qualitative understanding of the model is first presented by describing the general RVE of the original model, the simplified RVE considered here, and the definitions of the microstructural damage variables. The RVE considered here is a cylinder with an embedded, coaxial, spheroidal void. The RVE of the original model [33, 34] allows for an orthotropic matrix, arbitrarily aligned voids, and arbitrary loading conditions. The original RVE is most conveniently analyzed using three different coordinate systems: (1) the principal axes of loading, $\hat{\boldsymbol{e}}_i$; (2) the void axis, $\hat{\boldsymbol{n}}_2$, and two orthogonal base vectors in the transverse plane to form the triad $\hat{\boldsymbol{n}}_i$; (3) and the principal directions of orthotropy, $\hat{\boldsymbol{m}}_i$. The general RVE and the three coordinate systems are depicted in Fig. 7.2a.

The analysis conducted here uses three approximations that simplify the constitutive equations. These approximations permit a simpler RVE than what is depicted in Fig. 7.2a. First, the loading is restricted to be axisymmetric with a constant stress triaxiality. The model is applied here to study the deformation and fracture of round notched bars, which experience an axisymmetric stress state. Also, during the deformation of notched bars, the stress triaxiality ratio remains approximately constant [146]. Therefore, the stress tensor is represented as

$$\boldsymbol{\sigma} = \sigma_{22}\left(\hat{\boldsymbol{e}}_2 \otimes \hat{\boldsymbol{e}}_2\right) + \sigma_{11}\left(\hat{\boldsymbol{e}}_1 \otimes \hat{\boldsymbol{e}}_1 + \hat{\boldsymbol{e}}_3 \otimes \hat{\boldsymbol{e}}_3\right), \tag{7.3}$$

where σ_{22} is the major axial stress and σ_{11} is the lateral stress ($\sigma_{11} = \sigma_{33}$). Since the stress

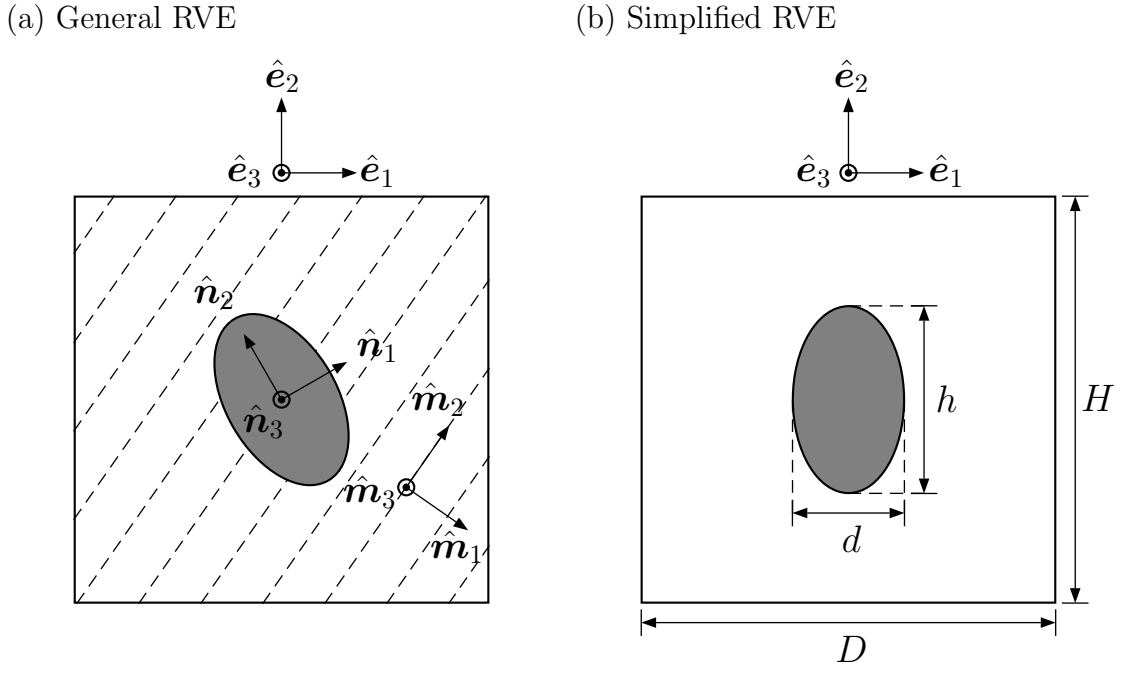

Figure 7.2: (a) The general RVE for the original model [33, 34]. Coordinate systems are defined for the axes of loading, $\hat{\boldsymbol{e}}_i$; the triad defined by the void axis, $\hat{\boldsymbol{n}}_i$; and principal directions of orthotropy, $\hat{\boldsymbol{m}}_i$. (b) The simplified RVE considered here. The void axis is aligned with the principal direction of loading and the matrix is isotropic, therefore $\hat{\boldsymbol{e}}_i$ is sufficient to describe the RVE.

triaxiality ratio, $\mathcal{T}$, is constant, the ratio of σ_{22} and σ_{11} is also constant,

$$\mathcal{T} = \frac{\frac{1}{3}\operatorname{tr}\boldsymbol{\sigma}}{\sqrt{\frac{3}{2}\boldsymbol{\sigma}' : \boldsymbol{\sigma}'}} = \frac{\frac{1}{3}\left(2\sigma_{11} + \sigma_{22}\right)}{|\sigma_{22} - \sigma_{11}|} \quad \rightarrow \quad \frac{\sigma_{11}}{\sigma_{22}} = \frac{3\mathcal{T} - 1}{3\mathcal{T} + 2}. \tag{7.4}$$

Second, the voids are assumed to be aligned with the major axial stress, obviating the need for $\hat{\boldsymbol{n}}_i$ and any evolution equations regarding the orientation of the void axis. When cavities nucleate in unaged PA-6, they initially appear as penny-shaped cracks perpendicular to the load. As deformation continues, they elongate, but remain aligned with the principal stress [22, 23]. Similarly, the tomographic investigations of aging-induced damage presented in Chapters 3 and 5 reveal that aging-indcuced damage also nucleates as cracks perpendicular

to the load. For highly aged PA-6 (UV48 and higher), specimens fracture before the voids can elongate, see Figs. 3.13 and 5.7, but for lower amounts of aging, the void can elongate to become nearly circular, see Fig. 5.6. In all of the cases studied here, the voids are initially aligned with the loading axis and remain aligned with the loading axis during deformation. Finally, any anisotropy in the matrix is neglected, so that $\hat{\boldsymbol{m}}_i$ is no longer needed. Although polymers are anisotropic, their anisotropy is induced by the orientation of the molecular network. This kind of anisotropy is not easily described by the Hill yield criterion. Therefore, the strength along the direction of major axial stress is represented through a hardening law, while anisotropy is neglected. The RVE that emerges from these three simplifications is represented in Fig. 7.2b.

The microstructural damage variables are defined using the dimensions of the void and the shape of the RVE in Fig. 7.2b. The void volume fraction, f, is the ratio of the volume of the void to the total volume of the RVE. The void aspect ratio, w, is the ratio of the void height, h, to the void width, d. The void is prolate when $w > 1$, oblate when $w < 1$, and spherical when $w = 1$. The void spacing ratio (or RVE aspect ratio), λ, is the ratio of the axial void spacing, H, and the lateral void spacing, D. The void ligament ratio, ξ, is the ratio of the void width, d, to the lateral void spacing, D. In general, the void axis, $\hat{\boldsymbol{n}}_2$, is also a microstructural variable, but here is assumed to be constant and coincident with $\hat{\boldsymbol{e}}_2$. Voids in a real material will exhibit a distribution of these parameters, but here a single value is used to represent the average of the distribution. In summary, there are four microstructural damage state variables used for this analysis and their definitions are

$$f = \frac{V_{\text{void}}}{V_{\text{RVE}}}, \quad w = \frac{h}{d}, \quad \lambda = \frac{H}{D}, \quad \xi = \frac{d}{D}. \tag{7.5}$$

However, only three of these variables are independent. Evolution equations are formulated for f, w, and λ, but ξ is calculated from the other three using the equation for a ligament

in a cylindrical RVE with a spheroidal void [35],

$$\xi = \left(\frac{3f\lambda}{2w}\right)^{1/3}. \tag{7.6}$$

7.3.2 Model formulation

The following model formulation describes an isotropic material with a population of aligned voids, subjected to axisymmetric loading. It is assumed that the voids are always aligned with the major axial stress. The rate of deformation tensor is additively decomposed into an elastic part and a plastic part,

$$\boldsymbol{D} = \boldsymbol{D}^{\mathrm{e}} + \boldsymbol{D}^{\mathrm{p}}. \tag{7.7}$$

The elastic part of the rate of deformation tensor is governed by a hypoelastic law,

$$\boldsymbol{D}^{\mathrm{e}} = \mathbb{C}^{-1} : \overset{\nabla}{\boldsymbol{\sigma}}, \tag{7.8}$$

where $\mathbb{C}$ is the isotropic tensor of the elastic modulus and $\overset{\nabla}{\boldsymbol{\sigma}}$ denotes the Jaumann stress rate, as defined in Eq. (6.14). The isotropic tensor of the elastic modulus, $\mathbb{C}$, is defined by any two elastic constants. Here, damaged elastic constants are used that account for the void volume fraction,

$$\mu_{\mathrm{dmg}} = \frac{(1-f)\,\mu}{1 + 6f\left(\frac{K+2\mu}{9K+8\mu}\right)}, \quad K_{\mathrm{dmg}} = \frac{4\mu K\,(1-2f)}{4\mu + 3fK}, \tag{7.9}$$

where μ and K are the shear and bulk moduli of the solid matrix, and μ_{dmg} and K_{dmg} are the effective shear and bulk modulus of the RVE with a void volume fraction of f.

The plastic part of the rate of deformation tensor is calculated from normality to the yield surface $\Psi^{\mathrm{VG}}(\boldsymbol{\sigma}; f, w) = 0$,

$$\boldsymbol{D}^{\mathrm{p}} = \Lambda \frac{\partial \Psi^{\mathrm{VG}}}{\partial \boldsymbol{\sigma}}, \tag{7.10}$$

where Λ is the plastic multiplier. The yield criterion, referred to here as the void growth criterion, was originally derived in Ref. [33]. In addition to the stress, the void growth criterion depends on the void volume fraction and the void aspect ratio,

$$\Psi^{\mathrm{VG}}\left(\boldsymbol{\sigma}; f, w\right) = C\frac{\sigma_q^2}{\bar{\sigma}^2} + 2q_w\left(g+1\right)\left(g+f\right)\cosh\left(\kappa\frac{\sigma_h}{\bar{\sigma}}\right) - \left(g+1\right)^2 - q_w^2\left(g+f\right)^2. \quad (7.11)$$

The flow stress of the matrix is represented by $\bar{\sigma}$. The void growth acceleration factor, q_w, is a heuristic parameter introduced to improve agreement between the void growth criterion and unit cell calculations [34]. The void growth acceleration factor is a function of the void shape and is taken here to be

$$q_w = 1 + \frac{w}{1+w^2}. \quad (7.12)$$

The stress tensor enters into Eq. (7.11) through the terms σ_q and σ_h, which are defined as

$$\sigma_q^2 = \frac{3}{2}\boldsymbol{\sigma} : \mathbb{H} : \boldsymbol{\sigma}, \quad (7.13)$$

$$\sigma_h = \boldsymbol{\sigma} : \boldsymbol{X}. \quad (7.14)$$

In the original model [33,34], the matrix anisotropy enters into Eq. (7.11) through $\mathbb{H}$. Here, the anisotropy is neglected so that

$$\mathbb{H} = \mathbb{J} + \eta\left(\boldsymbol{X}\otimes\boldsymbol{Q} + \boldsymbol{Q}\otimes\boldsymbol{X}\right), \quad (7.15)$$

where $\mathbb{J}$ is the fourth-order deviatoric projector ($J_{ijkl} = \frac{1}{2}\left(\delta_{ik}\delta_{jl} + \delta_{il}\delta_{jk}\right) - \frac{1}{3}\delta_{ij}\delta_{kl}$), $\boldsymbol{Q}$ and $\boldsymbol{X}$ are transversely isotropic tensors, and $\otimes$ signifies the dyadic product ($\left(\boldsymbol{X}\otimes\boldsymbol{Q}\right)_{ijkl} = X_{ij}Q_{kl}$). The expressions for $\boldsymbol{Q}$ and $\boldsymbol{X}$ are

$$\boldsymbol{Q} = -\frac{1}{2}\left(\hat{\boldsymbol{e}}_1\otimes\hat{\boldsymbol{e}}_1 + \hat{\boldsymbol{e}}_3\otimes\hat{\boldsymbol{e}}_3\right) + \hat{\boldsymbol{e}}_2\otimes\hat{\boldsymbol{e}}_2, \quad (7.16)$$

$$\boldsymbol{X} = \alpha_2\left(\hat{\boldsymbol{e}}_1\otimes\hat{\boldsymbol{e}}_1 + \hat{\boldsymbol{e}}_3\otimes\hat{\boldsymbol{e}}_3\right) + \left(1-2\alpha_2\right)\hat{\boldsymbol{e}}_2\otimes\hat{\boldsymbol{e}}_2, \quad (7.17)$$

where $\hat{\boldsymbol{e}}_2$ is the void axis, here assumed to aligned with the major axial stress, and $\hat{\boldsymbol{e}}_1$ and $\hat{\boldsymbol{e}}_3$ form an orthonormal triad with $\hat{\boldsymbol{e}}_2$, see Fig. 7.2b. The parameters C, g, κ, η, and α_2 are functions of f and w. Their expressions are given in Appendix D. For axisymmetric loading, voids aligned with the major stress, and an isotropic matrix, the expressions for σ_q and σ_h in Eqs. (7.13) and (7.14) reduce to

$$\sigma_q^2 = (\sigma_{22} - \sigma_{11})^2 + 3\eta\sigma_h (\sigma_{22} - \sigma_{11}), \tag{7.18}$$

$$\sigma_h = 2\alpha_2\sigma_{11} + (1 - 2\alpha_2)\sigma_{22}. \tag{7.19}$$

Fracture is controlled by the void coalescence criterion developed by Benzerga and Leblond [144]. This coalescence criterion is a function of the stress, the void aspect ratio, and the void ligament ratio; $\Psi^{\mathrm{VC}}(\boldsymbol{\sigma}; w, \xi)$. Once the onset of coalescence occurs, i.e. $\Psi^{\mathrm{VC}}(\boldsymbol{\sigma}; w, \xi) \geq 0$, the simulation of loading is stopped and the final strain is recorded as the fracture strain. The expression for the void coalescence criterion is

$$\begin{aligned}\Psi^{\mathrm{VC}}(\boldsymbol{\sigma}; w, \xi) =& \frac{|\hat{\boldsymbol{e}}_2 \cdot \boldsymbol{\sigma} \cdot \hat{\boldsymbol{e}}_2|}{\bar{\sigma}} - \frac{b}{\sqrt{3}}\left[2 - \sqrt{1+3\xi^4} + \ln\left(\frac{1+\sqrt{1+3\xi^4}}{3\xi^2}\right)\right] \\ &+ \frac{t}{3\sqrt{3}}\left[\frac{\xi^3 - 3\xi + 2}{\xi w}\right].\end{aligned} \tag{7.20}$$

The parameters t and b were introduced by Torki et al. [145] to improve comparisons to finite element unit cell calculations for the case of penny shaped cracks. The parameter t is a function of w and ξ, as well as two additional parameters, t_0 and t_1,

$$t = \frac{(t_0 + t_1\xi)\, w}{1 + (t_0 + t_1\xi)\, w}\xi. \tag{7.21}$$

The values of b, t_0, and t_1 were calibrated in Torki et al. 2015 through comparison to finite

element unit cell calculations. The calibrated values are

$$b = 0.9, \quad t_0 = -0.84, \quad t_1 = 12.9. \tag{7.22}$$

Evolution laws are formulated for the microstructural damage variables f, w, and λ. The void volume fraction evolves assuming that the matrix is plastically incompressible,

$$\dot{f} = (1 - f)\,\mathrm{tr}\,\boldsymbol{D}^{\mathrm{p}}. \tag{7.23}$$

The void aspect ratio evolves according to [80]

$$\dot{w} = \boldsymbol{Q} : \left\{ kw \left[(1 + k_f k_w k_{\mathcal{T}})\,\boldsymbol{D}^{\mathrm{p}} + \left(\frac{1}{f}\boldsymbol{X}^{v} - \boldsymbol{X} \right) \mathrm{tr}\,\boldsymbol{D}^{\mathrm{p}} \right] \right\}. \tag{7.24}$$

The heuristic parameters k_f, k_w, and $k_{\mathcal{T}}$ correct mismatches between model predictions and finite element unit cell calculations that arise from the effect of the void volume fraction, void shape, and stress triaxiality, respectively. The expressions for k_f, k_w, and $k_{\mathcal{T}}$ are

$$k_f = \left(1 - \sqrt{f}\right)^2, \tag{7.25}$$

$$k_w = \frac{9}{2}\frac{\alpha_1 - \alpha_1^{\mathrm{G}}}{1 - 3\alpha_1}, \tag{7.26}$$

$$k_{\mathcal{T}} = \begin{cases} 1 - \frac{\mathcal{T}^2 + \mathcal{T}^4}{9} & \text{for } \varsigma = +1 \\ 1 - \frac{\mathcal{T}^2 + \mathcal{T}^4}{18} & \text{for } \varsigma = -1 \end{cases}, \quad \varsigma = \mathrm{sgn}\left(\sigma_{\mathrm{m}}\sigma'_{22}\right), \tag{7.27}$$

where ς is related to the third stress invariant. The second order tensor $\boldsymbol{X}^{v}$ is defined similarly to $\boldsymbol{X}$, except that α_2 is replaced with α_1;

$$\boldsymbol{X}^{v} = \alpha_1 \left(\hat{\boldsymbol{e}}_1 \otimes \hat{\boldsymbol{e}}_1 + \hat{\boldsymbol{e}}_3 \otimes \hat{\boldsymbol{e}}_3\right) + (1 - 2\alpha_1)\,\hat{\boldsymbol{e}}_2 \otimes \hat{\boldsymbol{e}}_2. \tag{7.28}$$

The parameters α_1 and α_1^{G} are functions of f and w, and their expressions are given in

Appendix D. The parameter k was introduced in Kondori and Benzerga 2017 [35] as an adjustable parameter for fitting experimental data. Here, k is referred to as the "void opening factor", since it directly influences the rate at which the void aspect ratio increases. For axisymmetric loading, voids aligned with the major axial stress, and an isotropic matrix, Eq. (7.24) reduces to

$$\dot{w} = \frac{3}{2} k w \left(1 + k_f k_w k_{\mathcal{T}}\right) \left(\hat{\boldsymbol{e}}_2 \cdot \boldsymbol{D}^{\mathrm{p}'} \cdot \hat{\boldsymbol{e}}_2\right) + k w \left(\frac{1 - 3\alpha_1}{f} + 3\alpha_2 - 1\right) \operatorname{tr} \boldsymbol{D}^{\mathrm{p}}. \tag{7.29}$$

The evolution of the void spacing ratio is given by [35]

$$\dot{\lambda} = \frac{3}{2} \lambda D^{\mathrm{p}}_{\mathrm{eqv}}, \tag{7.30}$$

$$D^{\mathrm{p}}_{\mathrm{eqv}} = \sqrt{\frac{2}{3} \boldsymbol{D}^{\mathrm{p}'} : \boldsymbol{D}^{\mathrm{p}'}}. \tag{7.31}$$

No evolution equation is formulated for ξ, which is instead updated using Eq. (7.6).

The effective plastic strain, $\bar{\varepsilon}^{\mathrm{p}}$, is updated by calculating the effective plastic strain rate, $\dot{\bar{\varepsilon}}^{\mathrm{p}}$, from the expression for the plastic dissipation,

$$(1 - f)\, \bar{\sigma} \dot{\bar{\varepsilon}}^{\mathrm{p}} = \boldsymbol{\sigma} : \boldsymbol{D}^{\mathrm{p}}. \tag{7.32}$$

Then, the flow stress of the matrix hardens with the effective plastic strain according to a power law,

$$\bar{\sigma} = K \left(\bar{\varepsilon}_0 + \bar{\varepsilon}^{\mathrm{p}}\right)^n. \tag{7.33}$$

Nine model parameters require calibration. Five parameters determine the mechanical behavior of the dense matrix: Two elastic constants to define $\mathbb{C}$ and three constants to define the hardening law. Three parameters define the initial state of microstructural damage. The last parameter requiring calibration is the void opening parameter, k. In addition to these parameters, the loading path is specified through a single constant value: the stress

Table 7.1: Model inputs.

Param.	Units	Type	Description
E	MPa	Elastic constant	Young's modulus
ν	–	Elastic constant	Poisson's ratio
K	MPa	Hardening law constant	Hardening law factor
$\bar{\varepsilon}_0$	–	Hardening law constant	Hardening law offset
n	–	Hardening law constant	Hardening law exponent
f_0	–	Initial value of damage variable	Initial void volume fraction
w_0	–	Initial value of damage variable	Initial void aspect ratio
λ_0	–	Initial value of damage variable	Initial void spacing ratio
k	–	Adjustable parameter	Void opening factor
$\mathcal{T}$	–	Loading	Constant stress triaxiality ratio

triaxiality. In total, the model requires ten values as inputs. These ten inputs are listed in Table 7.1.

7.4 Modeling approach

The damage model is applied to predict the fracture strain in aged and unaged round notched bars of PA-6. In total, four conditions are studied. Two specimen geometries are used (an RN10 bar and an RN2 bar), and two aging conditions are used (unaged and UV192). The different specimen geometries are used to explore the effect of the stress state on fracture, as void growth is sensitive to the stress triaxiality [45]. The unaged condition is studied as a control; it is already known that fracture in unaged PA-6 occurs by the coalescence of cavities [23], so the damage model should produce accurate predictions of the fracture strain. The aged condition is used to assess the role of aging-induced damage in catastrophic embrittlement after extended periods of aging. If fracture strains for the aged condition are accurately predicted by the damage model, then the assertion that embrittlement is caused by aging-induced damage is supported.

Polymers are viscoplastic, meaning their plastic deformation is rate and temperature dependent. When a polymer is deformed, variations in the local strain rate emerge as a result

of structural effects [112, 114]. At a given instant in time, the local strain rates throughout the volume may vary by as much as an order of magnitude [114] (see also Fig. 6.19). Therefore, a constitutive model that considers the strain rate sensitivity of a polymer is essential to structural calculations. However, the damage model presented in Section 7.3 is not viscoplastic, and also lacks other features common to polymer constitutive models, making it not ideal for structural calculations of polymeric specimens. Although it would be desirable to reformulate the model for polymeric materials, such a reformulation is not a trivial task. Therefore, the constitutive equations of the damage model are only integrated for a single material point, and the polymer constitutive model presented in Chapter 6 is used to bridge the gap between the structural response of the specimen and the material point modeled by the damage model.

In Chapter 6, finite element models employing a viscoplastic semicrystalline polymer constitutive model were used to simulate the loading of an RN10 bar and an RN2 bar. In those simulations, the polymer model was calibrated to represent the mechanical behavior of the unaged bulk PA-6 material used throughout this dissertation. Those finite element simulations are used here to extract the stress–strain history and stress state at critical locations, i.e. locations where fracture initiates. The damage model is then applied to predict the local fracture strains at these critical locations. In an unaged round notched bar, the stress triaxiality is highest in the notch center, resulting in more void growth. Therefore, the notch center is the critical location in the unaged round notched bars. In an aged round notched bar, oxidation is limited to a superficial layer on the surface [16, 28], and fracture initiates from the aging-induced damage in this surface layer [88]. Therefore, the surface of the notch root is the critical location in the aged round notched bars. In Fig. 7.3, the four critical locations studied in this chapter are labeled on drawings of the RN10 bar and the RN2 bar. For each critical location, three key pieces of information are determined using the round notched bar finite element models from Chapter 6. (1) The local fracture strain is determined by extracting the strain from the element at the critical location when the finite

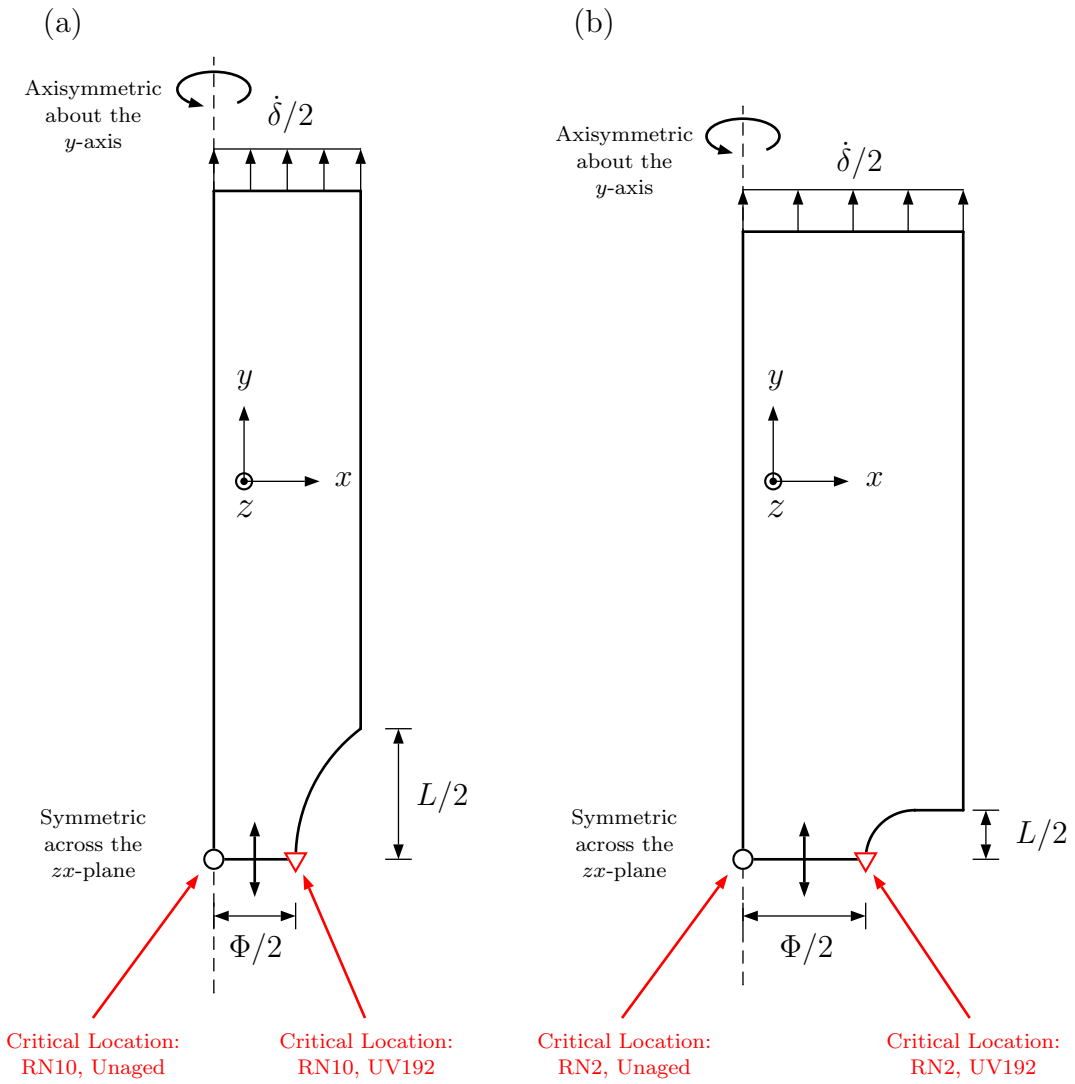

Figure 7.3: Drawings of the round notched bar geometries with critical locations labelled. (a) The RN10 bar. (b) The RN2 bar.

element model reaches the average specimen-level fracture strain, which was determined experimentally and shown in Fig. 7.1. This local fracture strain serves to validate the fracture strain calculated by the damage model. (2) A constant triaxiality is supplied to the damage model, which is determined by averaging the triaxiality over the strain history at the critical location. The average begins immediately after loading starts and ends at the local fracture strain for that critical location. This triaxiality is one of the ten model inputs in Table 7.1. (3) The mechanical behavior is extracted from the critical location to calibrate the parameters entering into the hardening law in Eq. (7.33). Section 7.5 describes in detail how items (1) and (2) are determined. Section 7.6 describes in detail how item (3) is determined.

For a given specimen geometry, the same finite element calculation is used to characterize the critical points in the aged and the unaged material, the only difference in the location from the model where the characterization is extracted. Even though the finite element analysis of the round notched bars uses the polymer model calibrated to the *unaged* material, the results are applied to study both the *aged and unaged* conditions. Since the depth of oxidation is limited to a superficial layer [27], the strength of the specimen is unaffected by aging [88]. Therefore, the mechanical response of the unaged specimen can serve as an approximation for the mechanical response of the aged specimen. In essence, this procedure neglects the effect of aging on the mechanical behavior, and therefore assumes that the only effect of aging is the accumulation of aging-induced damage.

Once the boundary value problems are reduced to problems at critical points, the initial state of damage is characterized for both the unaged and aged material. For both aging conditions, initial values of the microstructural damage variables, see Eq. (7.5), are approximated using the synchrotron tomography observations first presented in Chapters 4 and 5. In this approach, it is assumed that all damage is ether initial to the material, or nucleates prior to yield. Since the size of the initial voids is below the resolution of the tomograms [106], the work here is not suitable for differentiating between damage that nucleates after the application of a load and damage that is initial to the material but grows above the tomogram

resolution after the application of a load.

7.5 Determination of local fracture strains and critical loading paths

The damage model implementation used here integrates the constitutive relations in Section 7.3 for a single material point subjected to an axisymmetric load with a constant stress triaxiality. Therefore, a structural analysis of the round notched bar specimens is not attempted using the damage model. Instead, the model is applied to study critical locations in the bars, i.e. the locations at which fracture initiates. In the unaged bars, the critical location is at the center of the notch, as this is the location with the highest stress triaxiality [23]. In the aged bars, the critical location is at the surface of the notch root, since this is where oxidation-induced damage is concentrated [88] (see also Fig. 4.9). In order to reduce the specimen-level boundary value problem to a single material point, finite element calculations are consulted. As an approximation, it is assumed that aging does not effect the constitutive behavior of the polymer, but only reduces the fracture strain through the accumulation of aging-induced damage at the surface of the specimen. Therefore, the finite element calculations on an RN10 and RN2 bar from Section 6.9 are used for both the aged and the unaged cases. These finite element calculations use the semicrystalline polymer model calibrated to the mechanical behavior of the unaged bulk PA-6 used throughout this dissertation. In this section, two key pieces of information are extracted from the critical locations: (1) the local fracture strain when the specimen-level strain of the finite element model matches the experimentally determined, specimen-level fracture strains (experimental fracture strains are shown in Fig. 7.1) and (2) the average triaxiality at the critical locations.

Since the damage model is applied to analyze a single material point, it predicts the local fracture strains, not the specimen-level fracture strains shown in Fig. 7.1. Therefore, the round notched bar finite element models are used to determine the local fracture strains. When the finite element model reaches the experimentally determined, average specimen-level fracture strain, the local strain is extracted from the element at the critical location. This local strain is assumed to correspond to the local fracture strain. For each finite element

model (RN10 and RN2), two local fracture strains are extracted. The local fracture strain at the notch center when the specimen reaches the unaged specimen-level fracture strain, and the local fracture strain at the notch root surface when the specimen reaches the aged specimen-level fracture strain. For convenience, the local strains are reported using the equivalent strain, ε_{eqv}, defined as

$$\varepsilon_{\text{eqv}} = \sqrt{\frac{2}{3}\boldsymbol{\varepsilon}' : \boldsymbol{\varepsilon}'}, \quad \boldsymbol{\varepsilon}(t) = \int_0^t \boldsymbol{D}(\tau)\,\mathrm{d}\tau. \tag{7.34}$$

For axisymmetric loading

$$\varepsilon_{\text{eqv}} = \frac{2}{3}\left|\varepsilon_{22} - \varepsilon_{11}\right|. \tag{7.35}$$

The local fracture strain is then denoted as $\varepsilon_{\text{eqv,f}}$. The uncertainty in the local fracture strain is quantified by extracting the local fracture strains at the minimum and maximum specimen-level fracture strains.

An axisymmetric loading path with a constant stress triaxiality ratio is used by the damage model. Therefore, the model loading path is fully specified by a single constant scalar, the stress triaxiality, $\mathcal{T}$. The stress triaxiality history is extracted from critical locations in the round notched bar finite element models using the calibrated semicrystalline polymer model. The triaxiality history is recorded as a function of the equivalent strain, $\mathcal{T}(\varepsilon_{\text{eqv}})$. To reduce the function $\mathcal{T}(\varepsilon_{\text{eqv}})$ to a constant, an average is calculated. For each condition (RN10 bar or RN2 bar; unaged or aged), the average of $\mathcal{T}(\varepsilon_{\text{eqv}})$ is calculated at the relevant critical location over an interval of the equivalent strain,

$$\mathcal{T}_{\text{ave}} = \frac{1}{\varepsilon_{\text{eqv,f}} - \varepsilon_{\text{eqv},0^+}} \int_{\varepsilon_{\text{eqv},0^+}}^{\varepsilon_{\text{eqv,f}}} \mathcal{T}(\varepsilon_{\text{eqv}})\,\mathrm{d}\varepsilon_{\text{eqv}}. \tag{7.36}$$

The average starts at the local equivalent strain immediately after loading begins, denoted as $\varepsilon_{\text{eqv},0^+}$ and the average ends at the local equivalent fracture strain, $\varepsilon_{\text{eqv,f}}$.

The procedure for determining $\varepsilon_{\text{eqv,f}}$ and $\mathcal{T}_{\text{ave}}$ is graphically represented in Fig. 7.4 for the

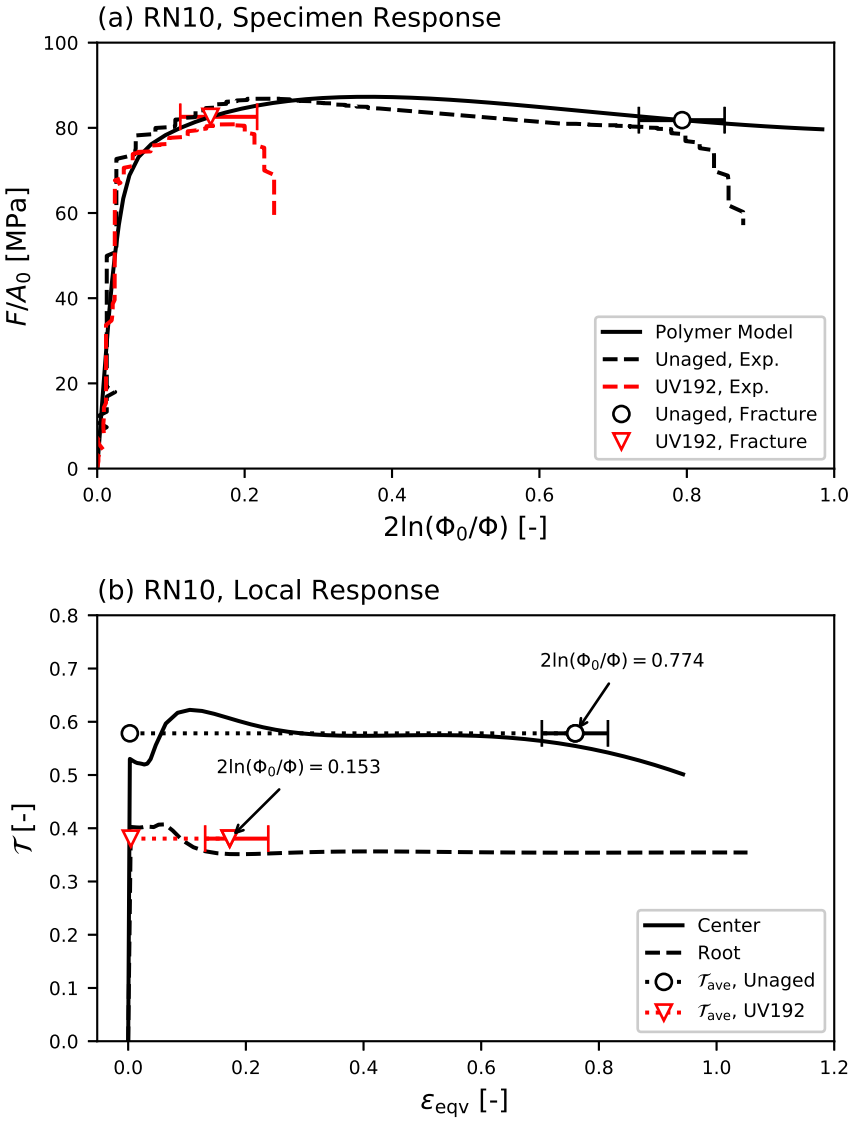

Figure 7.4: (a) The specimen-level stress–strain curve for the RN10 finite element model using the semicrystalline polymer constitutive model (solid black line). Characteristic experimental stress–strain curves are also presented for the aged (dashed red line) and unaged (dashed black line) cases. Average experimental fracture strains are marked for the unaged and aged cases, with uncertainty bars representing the minimum and maximum values of the specimen-level fracture strains. (b) The local stress triaxiality ratio versus the equivalent strain at the notch center (solid line) and notch root surface (dashed line). The average stress triaxiality ratio is marked for the unaged case (black dotted line) and the aged case (red dotted line). The lines for the average triaxiality end at the local fracture strain for that condition. Error bars represent minimum and maximum values of the local fracture strains.

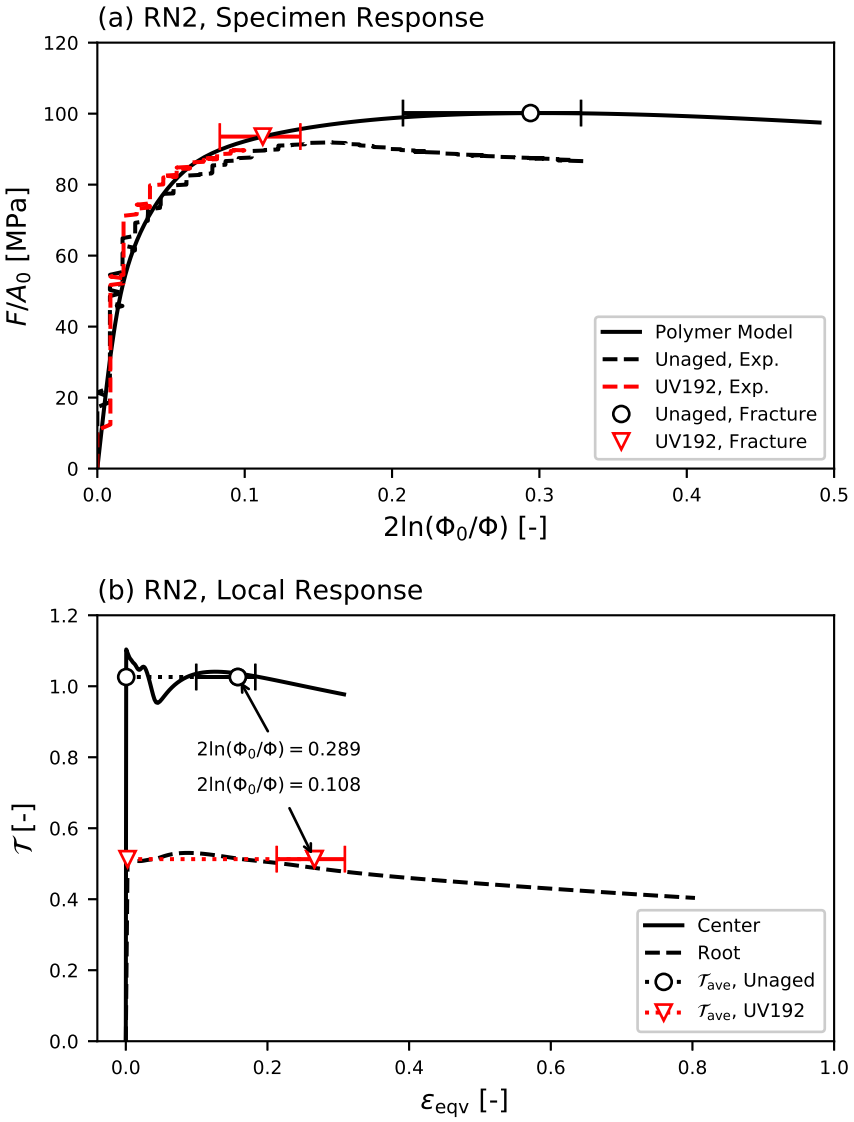

Figure 7.5: (a) The specimen-level stress–strain curve for the RN2 finite element model using the semicrystalline polymer constitutive model (solid black line). Characteristic experimental stress–strain curves are also presented for the aged (dashed red line) and unaged (dashed black line) cases. Average experimental fracture strains are marked for the unaged and aged cases, with uncertainty bars representing the minimum and maximum values of the specimen-level fracture strains. (b) The local stress triaxiality ratio versus the equivalent strain at the notch center (solid line) and notch root surface (dashed line). The average stress triaxiality ratio is marked for the unaged case (black dotted line) and the aged case (red dotted line). The lines for the average triaxiality end at the local fracture strain for that condition. Error bars represent minimum and maximum values of the local fracture strains.

Table 7.2: The experimental specimen-level fracture strain, $2\ln(\Phi_0/\Phi_f)$; local equivalent fracture strain at the critical location, $\varepsilon_{eqv,f}$; and the average local triaxiality at the critical location, $\mathcal{T}_{ave}$.

Specimen Type	Aging Cond.	$2\ln(\Phi_0/\Phi_f)$	$\varepsilon_{eqv,f}$	$\mathcal{T}_{ave}$
RN10	Unaged	0.774	0.760	0.578
RN10	UV192	0.153	0.173	0.381
RN2	Unaged	0.289	0.158	1.026
RN2	UV192	0.108	0.266	0.513

aged and unaged RN10 cases. In Fig. 7.4a, the specimen-level response of the RN10 bar finite element model is plotted. Representative experimental curves for the specimen-level response are also plotted for the aged and unaged conditions. Experimental, specimen-level fracture strains are marked on the simulated curve, both for the aged and unaged conditions. The data point represents the average experimental, specimen-level fracture strains. The error bars represent the minimum and maximum experimental, specimen-level fracture strains. In Fig. 7.4b, the triaxiality is plotted as a function of the equivalent strain for the notch center and notch root surface, the critical locations for the unaged case and aged case, respectively. For each critical location, the average triaxiality is plotted as a straight line, which begins at $\varepsilon_{eqv,0^+}$ and ends at $\varepsilon_{eqv,f}$. Similarly, Fig. 7.5 graphically represents the procedure for determining $\varepsilon_{eqv,f}$ and $\mathcal{T}_{ave}$ for the aged and unaged RN2 cases. Comparing Figs. 7.4 and 7.5 reveals that the triaxiality at the notch center of the RN2 bar is significantly higher than at the notch center of the RN10 bar. On the other hand, the triaxiality at the notch root surface is similar in both the RN10 and the RN2 bars.

Animated contours of ε_{eqv} and $\mathcal{T}$ for the RN10 bar finite element model using the semicrystalline polymer constitutive model are available in Vids. 7.1 and 7.2. Contour plots for the RN2 bar finite element model are available in Vids. 7.3 and 7.4.[1]

Table 7.2 lists the specimen-level fracture strain, $2\ln(\Phi_0/\Phi_f)$; the local equivalent fracture

[1] Email `kncundiff.dissertationquestions@gmail.com` to request video files.

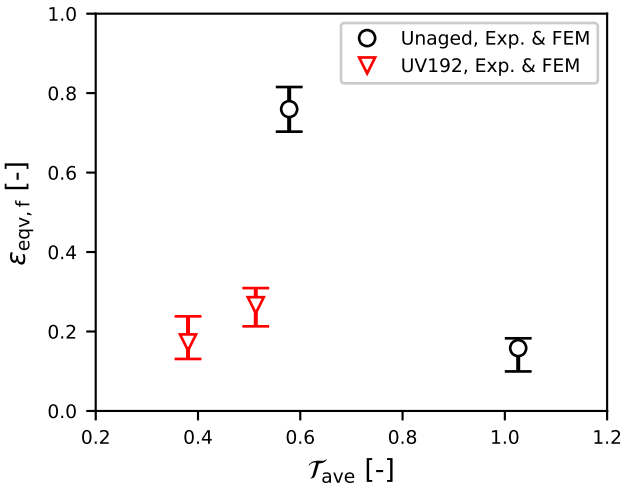

Figure 7.6: The local equivalent fracture strain versus the average stress triaxiality. The values are determined from a combination of experimental data and finite element simulations.

strain, $\varepsilon_{\text{eqv,f}}$; and the average triaxiality, $\mathcal{T}_{\text{ave}}$, for all four loading conditions studied in this chapter. The local equivalent fracture strains at critical locations are plotted against the average triaxiality in Fig. 7.6. The data in Fig. 7.6 serves validate the damage model analysis presented in Section 7.8. The average local fracture strain increases from the aged RN10 case to the aged RN2 case. However, it is unexpected for the local fracture strain to increase with increasing triaxiality. This is likely an artifact arising from the build-up of errors across the multiple stages used to determine ε_{f}. In fact, the error bars for ε_{f} on the aged RN10 and RN2 cases do overlap somewhat. One possible explanation is the different rates of straining at the notch root surfaces in the RN10 and RN2 bars. For the same increment in the global strain, the local strain increases at the notch root surface faster in the RN2 bar compared to the RN10 bar. This creates higher uncertainty when using the method described here to convert a global strain in an RN2 bar to a local strain at the notch root surface.

7.6 Calibration of the mechanical behavior of the dense material

The mechanical behavior of the dense material is governed by two elastic constants and three parameters entering into the hardening law, Eq. (7.33). The elastic constants were cali-

brated to the values used for the semicrystalline polymer constitutive model, $E = 1550\,\text{MPa}$ and $\nu = 0.4$, see Section 6.6.2.6. The plastic behavior of the dense material follows the von Mises yield criterion with isotropic hardening governed by the power hardening law in Eq. (7.33).

The hardening law parameters were calibrated to the effective stress–strain behavior at critical locations in the finite element simulations of the round notch bars presented in Chapter 6. The effective strain has already been defined in Eq (7.34). The effective stress (i.e. the von Mises stress) is defined as

$$\sigma_{\text{eqv}} = \sqrt{\frac{3}{2}\boldsymbol{\sigma}' : \boldsymbol{\sigma}'}. \tag{7.37}$$

For axisymmetric loading

$$\sigma_{\text{eqv}} = |\sigma_{22} - \sigma_{11}|\,. \tag{7.38}$$

The polymer constitutive model is affected by both the strain rate and hydrostatic pressure, so the effective stress–strain path is different at each critical location. However, for the calibration produced in Chapter 6, the effective stress–strain behavior is not significantly different at each critical location. Therefore, the hardening law parameters for all conditions are calibrated using the effective stress–strain behavior at the notch center of the RN10 finite element model. The notch center of the RN10 bar was chosen since this condition exhibits the highest $\varepsilon_{\text{eqv,f}}$, so an accurate calibration for this condition is valid over the ranges of strains experienced in other conditions.

The hardening law parameters were calibrated through optimization. By setting the void volume fraction to a negligibly small value, the damage model simulates the stress–strain response of the dense material. The effective stress–strain behavior of the dense material is then compared to the effective stress–strain data extracted from the notch center of the RN10 bar finite element model. Accordingly, a triaxiality of $\mathcal{T} = 0.578$ was used by the damage model when executing the optimization, see Table 7.2. The calibration considers data on

Table 7.3: Calibrated parameters governing the mechanical behavior of the dense material.

Param.	Value	Units	Type	Description
E	1550	MPa	Elastic constant	Young's modulus
ν	0.4	–	Elastic constant	Poisson's ratio
K	162.	MPa	Hardening law constant	Hardening law factor
$\bar{\varepsilon}_0$	0.234	–	Hardening law constant	Hardening law offset
n	0.633	–	Hardening law constant	Hardening law exponent

the interval $0 < \varepsilon_{\text{eqv}} < 0.8$, which ensures that the hardening law is well calibrated for the range of ε_{eqv} expected in the damage calculations. Optimization was conducted using the Levenberg–Marquardt algorithm in Z-set. After 37 iterations, the algorithm converged. The calibrated parameters governing the mechanical behavior of the dense material are listed in Table 7.3. In Fig. 7.7, the effective stress–strain behavior of the dense material is compared to the effective stress–strain data extracted from the RN10 bar finite element model at the notch center (i.e. the target data during calibration).

For the interval of ε_{eqv} investigated here, Fig. 7.7 shows good agreement between the calibrated hardening law and the local stress–strain history predicted by the polymer model. However, for larger strains, the hardening law is not suitable for predicting the orientation hardening that occurs in the polymer model. Specifically, the rate of hardening in the polymer model will begin to increase after $\varepsilon_{\text{eqv}} = 0.8$, while the rate of hardening will decrease for the power law. Since $\varepsilon_{\text{eqv,f}} < 0.8$ at the critical location for all cases, the fit produced by the parameters in Table 7.3 is acceptable for studying fracture for the conditions listed in Table 7.2.

7.7 Calibration of initial values for microstructural damage variables

This section describes how the initial values for the microstructural damage variables are calibrated. This goal is achieved by analyzing the tomograms originally presented in Chapters 4 and 5. In Section 7.7.1, the initial state of damage in the unaged material is

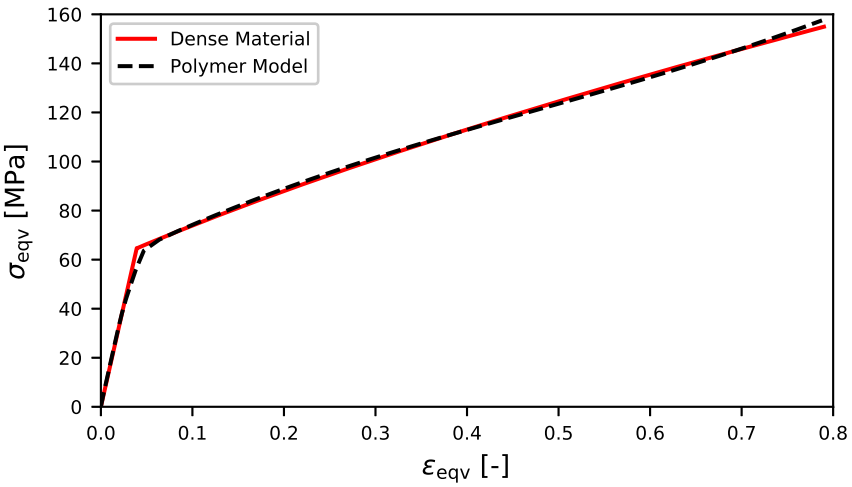

Figure 7.7: The effective stress–strain behavior of the dense material using the calibrated parameters in Table 7.3 compared to the effective stress–strain behavior produced from the semicrystalline polymer constitutive model. The damage model used a constant triaxiality of $\mathcal{T} = 0.578$. The effective stress–strain curve from the polymer constitutive model was extracted from the notch center of the RN10 bar finite element simulations conducted in Chapter 6.

characterized. In Section 7.7.2, the initial state of damage in the aged material is characterized. The final state of damage in the aged material is also characterized, and is used to validate the final state of damage predicted by the model.

7.7.1 Unaged material

The initial state of damage in the unaged material is characterized using the *ex situ* tomograms of an RN10 bar that were first shown in Chapter 4. These tomograms were generated after loading an unaged RN10 bar to the peak force, unloading, and then scanning the bar. The tomogram from the notch center is analyzed, given that this is critical location in the unaged bars. To simplify the analysis, only a 2D slice of the 3D tomogram is analyzed. Fig. 7.8 shows the chosen slice from a tomogram used to characterize the initial state of damage in the unaged material. This tomogram slice originally appeared in Fig. 4.8. In Fig. 7.8, voids are visible as black spots spread throughout the image. Artifacts from the

method of creating the tomogram appear at the middle of the bottom edge of the slice. A gradient in damage is visible, with a higher concentration of voids appearing in the center, where the triaxiality is highest [23]. Since the damage model analysis is local in nature, only the region with the highest concentration of voids is used to characterize the state of damage. The chosen region of interest is bounded by a yellow rectangle in Fig. 7.8. Since the RN10 bar was loaded up to the peak force before scanning to create Fig. 7.8, it does not truly depict an *initial* state of damage. However, the peak force is still early in the deformation of an unaged RN10 bar, and therefore is used as an approximation of the initial state. Using a tomogram of an RN10 bar loaded up the peak force is also convenient for making comparisons to the tomographic observations of cavitation in unaged PA-6 made by Laiarinandrasana et al. [23, 106]. In these works, tomograms at the earliest stages studied are made from scanning an RN11.4 bar of PA-6 loaded up to the peak force, which is referred to as "Sample A" in Refs. [23, 106].

Using Fiji (Fiji is just imageJ), the tomogram slice in Fig. 7.8 was analyzed to determine the values of the microstructural damage variables at the peak force. A particle analysis was conducted to determine the void volume fraction, f, the average void height, h, and the average void diameter, d. From the voids identified by the particle analysis, the image is then segmented into Set Voronoi cells.[2] The Set Voronoi cells are then analyzed to determine the average vertical and lateral void spacings, H and D. The analyzed region of interest is presented in Fig. 7.9. The voids are marked using magenta and red, while the boundaries of the Set Voronoi cells are marked in black. The background of the tomogram slice is removed to make the void shapes and cell boundaries clearer.

In total, 775 voids were identified by the particle analysis. Their average height was $h = 3.771\,\mu\text{m}$ and their average diameter was $d = 7.077\,\mu\text{m}$, giving a void aspect ratio of $w = 0.533$. The particle analysis also measured the void area fraction to be $3.392\,\%$. Since the tomogram slice is taken as a representative sample of the full 3D volume, it is

[2] A Set Voronoi partition is a generalization of a Voronoi tessellation for non-circular particles [147].

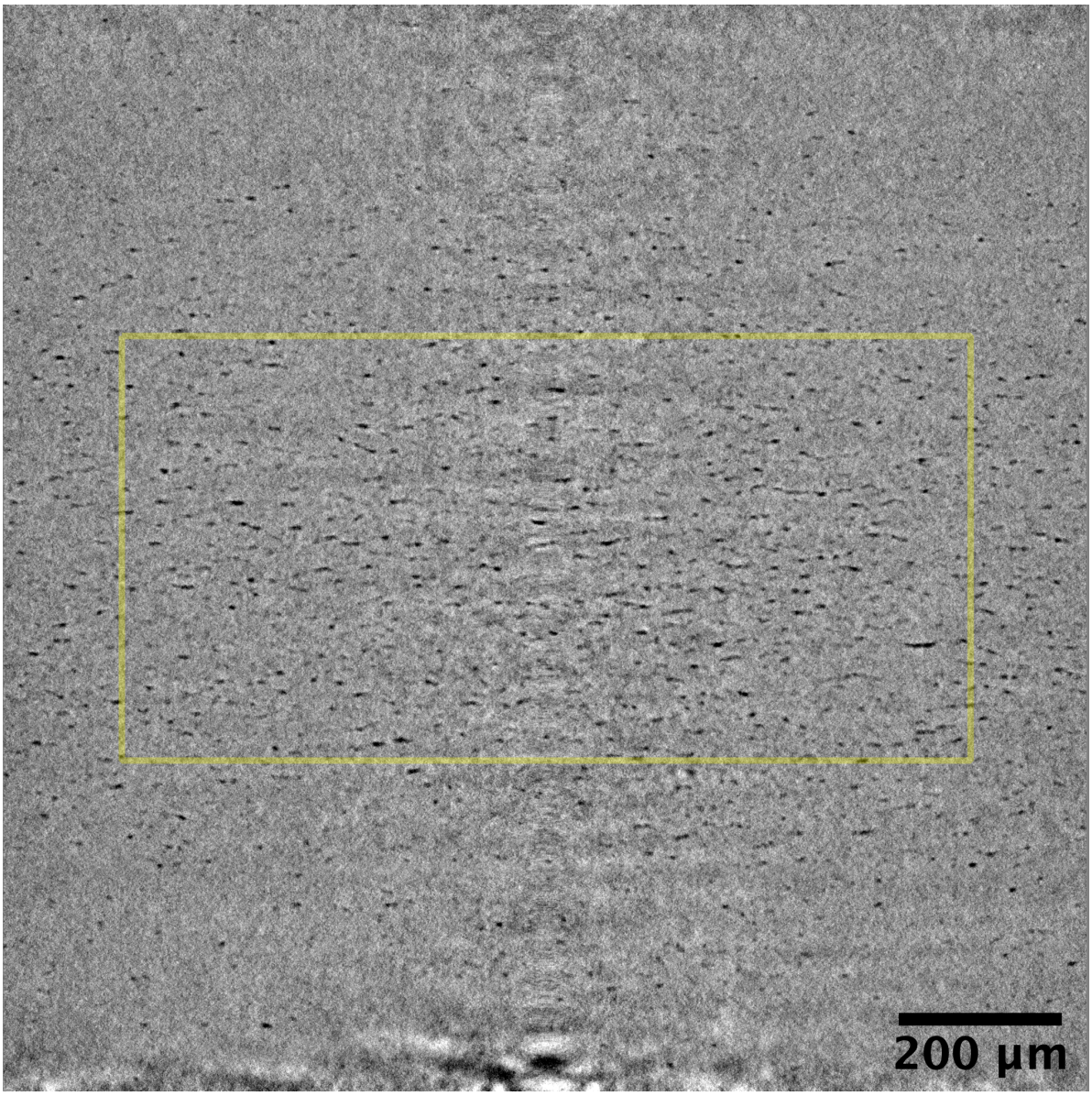

Figure 7.8: Tomogram slice from the center of an unaged RN10 bar of PA-6. The tomogram was taken *ex situ* after loading to the peak force. This image originally appeared in Fig. 4.8. The area bounded by the yellow rectangle constitutes the region of interest used to characterize the initial state of damage in the unaged material. The loading direction in the image is vertical.

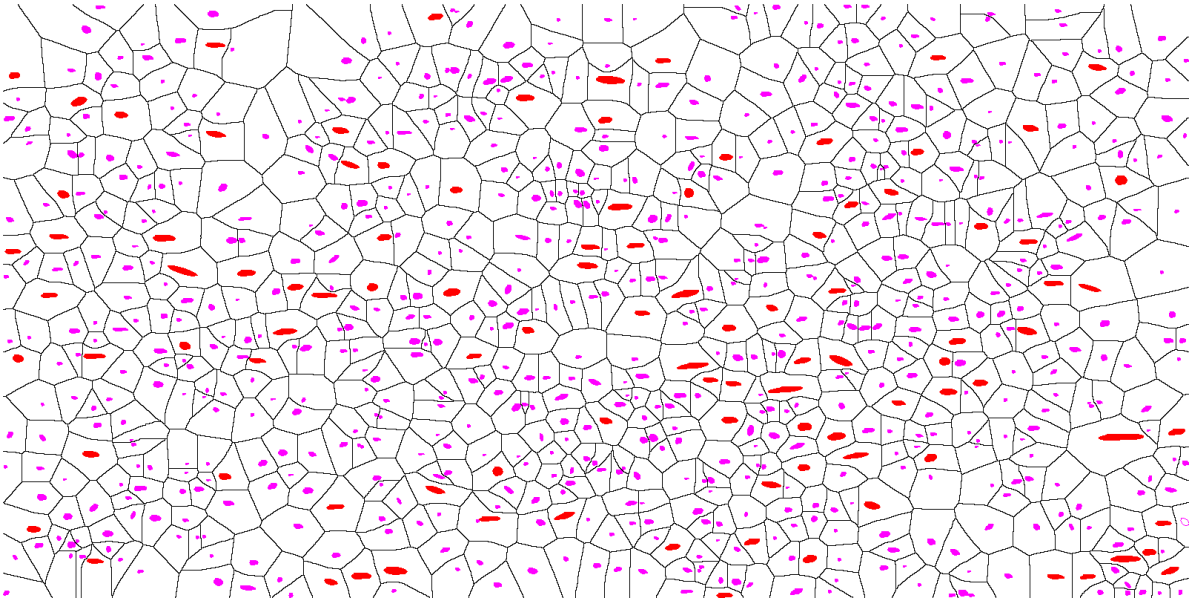

Figure 7.9: Analyzed region of interest used to characterize the initial state of damage in the unaged material. The 102 largest voids are marked in red. The remaining voids are marked in magenta. The Set Voronoi cell boundaries generated from the voids are drawn in black.

assumed that the void area fraction of a slice corresponds to the void volume fraction, f. Void measurements determined by the particle analysis are recorded in Table 7.4. The average values of h and d agree reasonably well to the average void dimensions reported in Laiarinandrasana et al. 2016 [106], which studied an RN11.4 bar of PA-6 loaded up to the peak force, referred to as "Sample A". In Sample A, the voids had an average height of 1.75 µm and an average diameter of 5.25 µm [106].

Although the void aspect ratio calculated from the full void population is $w = 0.533$, larger voids in the population tended to be more more oblate than smaller voids, see Fig. 7.9. Since larger voids are more likely to limit the ductility than smaller voids, the particle analysis was repeated considering only the 102 largest voids.[3] These voids are highlighted in red in Fig. 7.9. The results from the particle analysis of the 102 largest voids are presented in Table 7.5. The average void height was 5.402 µm, not significantly larger than the average height found from the full void population. However, the average void diameter was

[3]There was a three-way tie for the 100th largest void.

Table 7.4: Average void dimensions and void volume fraction in the region of interest used to characterize the *initial* state of damage in the *unaged* material.

Param.	Average	Standard Deviation	Units
h	3.771	1.212	µm
d	7.077	4.308	µm
$w = h/d$	0.533		–
f	0.03392		–

Table 7.5: Average dimensions and volume fraction of the 102 largest voids in the region of interest used to characterize the *initial* state of damage in the *unaged* material.

Param.	Average	Standard Deviation	Units
h	5.402	0.869	µm
d	15.179	4.969	µm
$w = h/d$	0.356		–
f	0.01198		–

15.179 µm, giving a void aspect ratio of $w = 0.356$. The 102 largest voids also occupied an area fraction of 1.198 %.

The unaged region of interest was partitioned into Set Voronoi cells using the voids identified in the particle analysis. The boundaries of the Set Voronoi cells are drawn with black lines in Fig. 7.9. The mean linear intercept method was used to determine the average cell height, H, and diameter, D. The mean linear intercept analysis determined the average cell dimensions to be $H = 20.562\,\mu\text{m}$ and $D = 21.304\,\mu\text{m}$, giving a cell aspect ratio of $\lambda = 0.965$. The results from the mean linear intercept analysis are presented in Table 7.6.

The results from the particle analysis of the largest voids in Table 7.5 and the results from the mean linear intercept method in Table 7.6 are used to estimate initial values for the microstructural damage variables in the unaged material. Upper and lower bounds for each variable are also estimated and used to calculate the uncertainty in the predictions of $\varepsilon_{\text{eqv,f}}$ for

Table 7.6: Average vertical and lateral lengths of Set Voronoi cells in the region of interest used to characterize the *initial* state of damage in the *unaged* material.

Param.	Average	Standard Deviation	Units
H	20.562	2.816	µm
D	21.304	0.999	µm
$\lambda = H/D$	0.965		–

each condition. While the analysis of the entire void population determined the void volume fraction to be $f = 3.392\,\%$, this value may be too high, since it is based on the analysis of a tomogram taken after loading the specimen to the peak force. In Laiarinandrasana et al. 2010 [22], cryofractography was used to measure the void volume fraction of undeformed, unaged, PA-6. They reported initial void volume fractions between $1\,\%$ and $2\,\%$. Therefore $f_0 = 0.015$ is used for the unaged material, with $f_0^- = 0.01$ and $f_0^+ = 0.02$ used for the upper and lower bounds. It is assumed that the void aspect ratio, w, and cell aspect ratio, λ, are not significantly distorted by loading to the peak force. Therefore, the analysis of the specimen loaded to the peak force is used as an approximation of the initial state of damage. The initial void aspect ratio is approximated to be $w_0 = 0.356$, following the particle analysis results presented in Table 7.5. The upper and lower bounds of w_0 are approximated using the standard deviations of h and d. For the lower bound,

$$w_0^- = \min\left(\frac{h^-}{d}, \frac{h}{d^+}\right), \quad h^- = h - h_{\text{std}}, \quad d^+ = d + d_{\text{std}}, \tag{7.39}$$

where the subscript "std" denotes the standard deviation of a quantity. Similarly,

$$w_0^+ = \max\left(\frac{h^+}{d}, \frac{h}{d^-}\right), \quad h^+ = h + h_{\text{std}}, \quad d^- = d - d_{\text{std}}. \tag{7.40}$$

The initial cell aspect ratio is approximated to be $\lambda_0 = 0.965$, following the mean linear intercept analysis results presented in Table 7.6. The upper and lower bounds of λ_0 are

Table 7.7: Calibrated *initial* values of microstructural damage variables for the *unaged* material.

Param.	Lower bound	Baseline value	Upper bound
f_0	0.01	0.015	0.02
w_0	0.268	0.356	0.529
λ_0	0.833	0.965	1.097
ξ_0	0.344	0.394	0.433

calculated from H, H_{std}, D, D_{std} using the same method as for w_0. The value of ξ_0 is dependent on the other three damage variables, according to Eq. (7.6).

The chosen initial values, along with their estimated upper and lower bounds, are listed in Table 7.7. For a given condition, the baseline prediction of $\varepsilon_{\text{eqv,f}}$ is made by running the damage model with the baseline values in Table 7.7. The upper and lower bounds of $\varepsilon_{\text{eqv,f}}$ are calculated by running the damage model multiple times, each time perturbing one of the independent damage variables (f_0, w_0, λ_0) to either its upper or lower bound. The upper and lower bounds of ξ_0 presented in Table 7.7 are the minimum and maximum initial value of ξ_0 found when conducting the uncertainty analysis.

7.7.2 Aged material

An aged (HUV192) RN10 bar of PA-6 was also loaded up to the peak force and scanned *ex situ* by synchrotron tomography. This scan revealed extensive cracking at the surface of the notch root, but no cavitation in the notch center, see Figs. 4.8 and 4.9. However, at the peak force, the aged bar was close to fracture, making it impossible to analyze the current state of damage to make approximations about the initial state of damage. Therefore, the *in situ* tomograms from UV48 aged PA-6 films ($t = 0.1\,\text{mm}$) were used to characterize the initial state of damage for the aged material. These scans were originally presented in Fig. 5.7. The aging-induced damage in these films is used as an approximate representation of the aging-induced damage at the surface of the UV192 round notched bars. Although the films

are not as highly aged as the UV192 round notched bars, they are aged beyond the damage mechanism transition discussed in Chapter 5, making them an acceptable representation of the damage in the UV192 condition.[4] The crystalline morphology of polymers is strongly affected by its processing and thermal history [39], so the bulk and film materials are likely to have very different crystalline structures. Since the crystalline phase plays an important role in cavitation [21], the different crystalline morphologies in the bulk and films specimens might also impact the formation of aging-induced damage. In this study, the effect of the crystalline morphology on the development of aging-induced damage is neglected, so that the aged film is used as an approximate representation of the aged surface of the bulk material. However, the effect of the crystalline morphology on aging-induced damage is worth investigating in future work.

The tomogram slices used to characterize the state of damage in the aged material are presented in Fig. 7.10. Once again, the analysis is simplified by analyzing 2D slices from the tomograms. The tomogram slices in Fig. 7.10 are taken from the surface of the films, where the damage is most severe. In the tomogram of the undeformed UV48 film (not shown here), no damage is visible. This is either because chemical cracks initial to the material are below the resolution of the tomogram, or the damage is primarily chemo-mechanical in nature and nucleates at a later stage of deformation. Regardless, the initial state of damage cannot be characterized from the tomogram of the undeformed film. Figs. 7.10a,b show two consecutive tomogram slices, with a region of interest bounded by a yellow box. In Fig. 7.10a, the region of interest is essentially free of damage. In Fig. 7.10b, multiple cracks appear in the region of interest. Either the cracks in Fig. 7.10b have very recently grown above the resolution of the tomogram, or they nucleated in this state, as the deformation between Fig. 7.10a and Fig. 7.10b is small, see Fig. 7.10d. Therefore, the region of interest in Fig. 7.10b is used to characterize the initial state of damage in the aged material. Fig. 7.10c shows a slice from the

[4] As a reminder, the damage mechanism transition discussed in Chapter 5 occurs between the UV24 and UV48 aging conditions. In the UV24 aged films, voids are initially oblate, but elongate upon loading, with some even achieving a circular cross-section. For the UV48 films, the voids remain oblate throughout loading, propagating laterally across the face of the specimen like cracks.

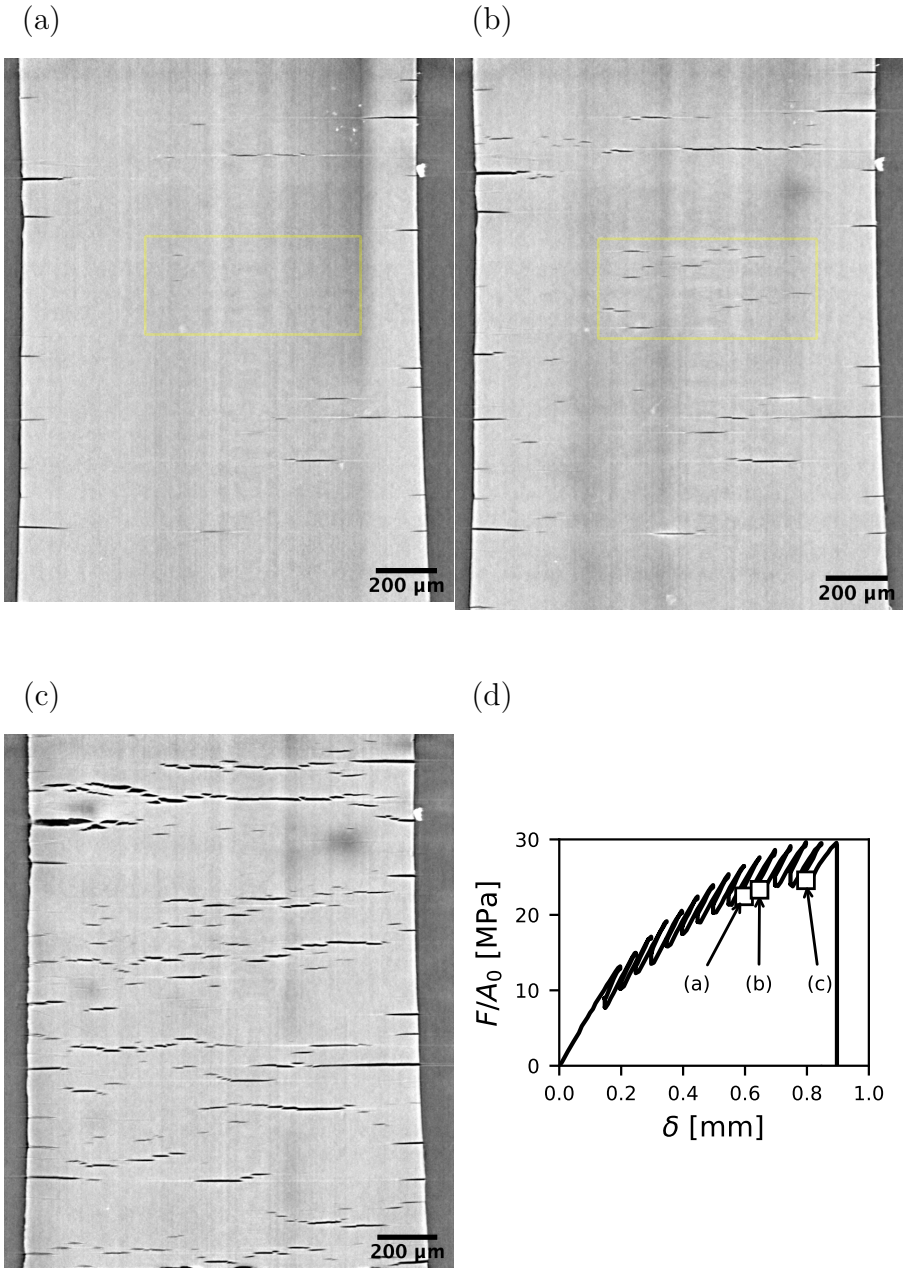

Figure 7.10: Tomogram slices from the surface of a UV48 aged PA-6 film ($t = 0.1\,\mathrm{mm}$). These images originally appeared in Fig. 5.7. The tomograms were taken *in situ*. For each tomogram slice, the loading direction is vertical. (a) Slice from a tomogram where the region of interest (bounded by the yellow rectangle) has almost no visible damage. (b) Slice from the tomogram immediately after (a). Damage has become visible in the region of interest. The region of interest in (b) is used to characterize the initial state of damage in the aged material. (c) A slice from the final tomogram taken before fracture. This slice is used to characterize the final state of damage in the aged material. (d) The load–displacement curve for the UV48 aged film, with the coordinates of (a), (b), and (c) marked.

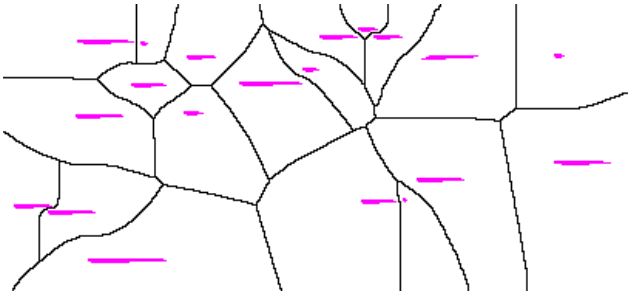

Figure 7.11: Analyzed region of interest used to characterize the initial state of damage in the aged material. Voids are marked in magenta. The Set Voronoi cell boundaries generated from the voids are drawn in black.

final tomogram taken before the film fractured. This image was analyzed to characterize the final state of damage in the aged material. The characterization of the final state of damage is useful for validating the final values of the microstructural damage variables predicted by the model. Fig. 7.10d shows the load–displacement curve for the UV48 film. The locations of the tomogram slices in Fig. 7.10a,b,c are marked in Fig. 7.10d. The serrated shape of the curve is due to the unloading and relaxing that occurs when preparing the film for a tomogram, which is not generated instantaneously.

Images of the aged material were analyzed using the same methodology applied to the images of the unaged material. A Fiji particle analysis was conducted to measure the average void dimensions and the void volume fraction. Set Voronoi cells were generated from the identified particles and used to measure the cell height and width. The analyzed region of interest used to characterize the *initial* state of damage in the aged material is presented in Fig. 7.11. The analyzed image used to characterize the *final* state of damage in the aged material is presented in Fig. 7.12.

The results of the particle analysis of the initial and final states of damage in the aged material are shown in Tables 7.8 and 7.9. In the image used to characterize the initial state, the average void height is $h_0 = 4.376\,\mu\text{m}$, and the average void diameter is $d_0 = 40.961\,\mu\text{m}$, giving an initial void aspect ratio of $w_0 = 0.107$. In the final state of damage, the average

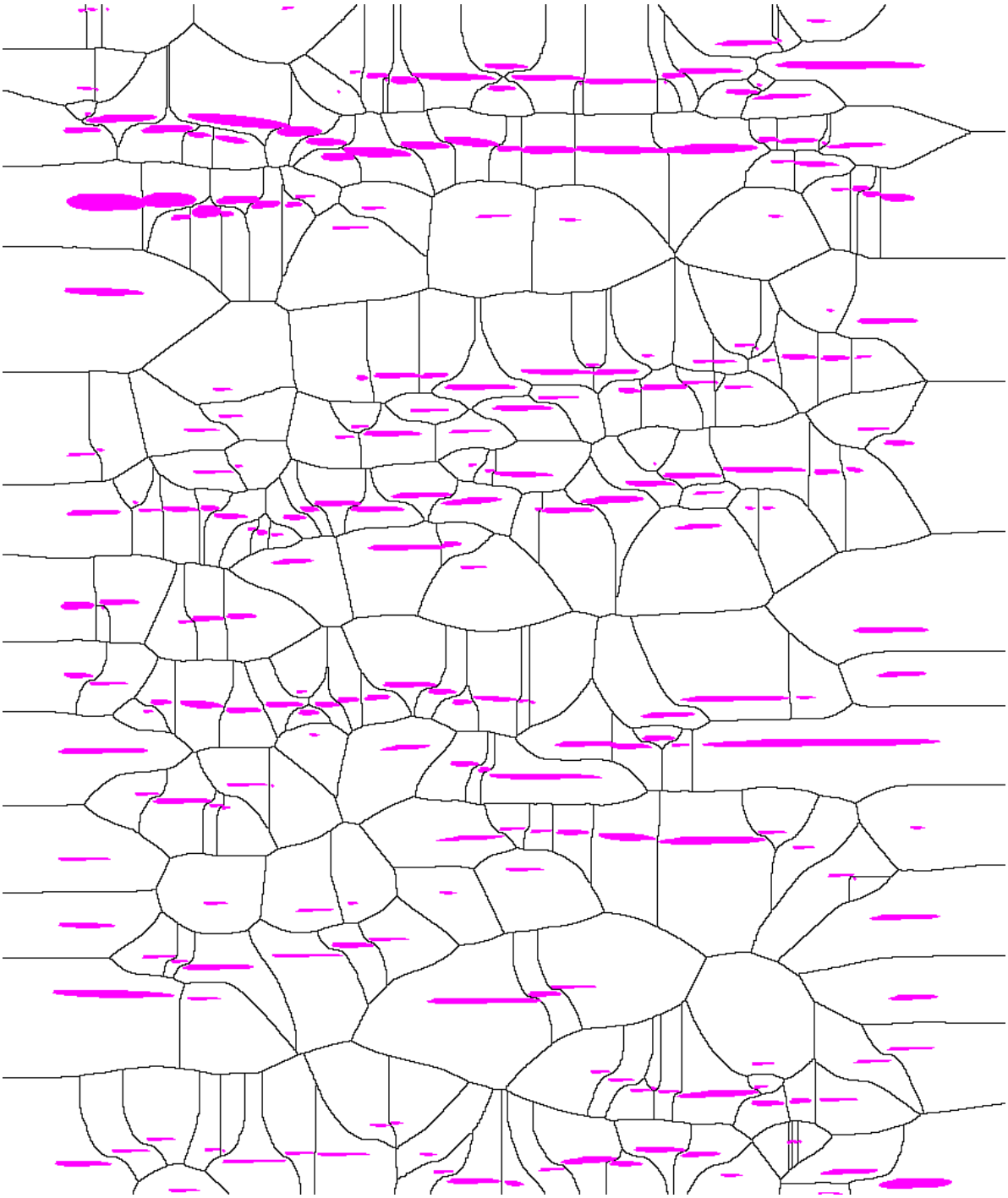

Figure 7.12: Analyzed region of interest used to characterize the final state of damage in the aged material. Voids are marked in magenta. The Set Voronoi cell boundaries generated from the voids are drawn in black.

height has increased by 2.440 µm and the average diameter by 11.403 µm, giving a final void aspect ratio of $w_f = 0.130$. For the aged material, the voids start as oblate cracks, and remain oblate during loading. For a given condition, all voids have similar heights, as evidenced by the small standard deviation of h in both the initial and final void populations. However, the standard deviation of the void diameter is extremely large. In the initial state, the void volume fraction is $f_0 = 1.409\,\%$, which is within the range of initial void volume fractions for PA-6 observed in Ref. [22]. In the final state, the void volume fraction increases to $f_f = 3.417\,\%$.

The results of the mean linear intercept analysis of the initial and final states of damage in the aged material are shown in Tables 7.10 and 7.11. For the initial state of damage, the average cell height is $H_0 = 97.313\,\mu m$, and the average cell diameter is $D_0 = 95.871\,\mu m$, giving a cell aspect ratio of $\lambda_0 = 1.015$. Due to the small number of voids observed in the region of interest, see Fig. 7.11, the uncertainty of the mean linear intercept analysis is high, as evidenced by the high standard deviations of the average cell dimensions. For the mean linear intercept analysis of the final state of damage in the aged material, a more statistically significant sample size is available. For the final state of damage, the average cell height is $H_f = 82.070\,\mu m$, and the average cell diameter is $D_f = 70.150\,\mu m$, giving a cell aspect ratio of $\lambda_f = 1.170$. The average cell dimensions are smaller for the final state than for the initial state. indicating that the number of visible cracks increases between the initial and final state. This may be due to crack nucleation or cracks growing above the resolution of the tomogram. However, the average cell aspect ratio increases (elongates) with increasing deformation, which is the expected trend.

The microstructural damage variables characterizing the initial state of damage in the aged material, along with estimated upper and lower bounds, are summarized in Table 7.12. The value of f_0 from the particle analysis (Table 7.8) is used. The upper and lower bounds of f_0 are estimated as 1 % and 2 %, following the cryofractographic analysis of Ref. [22]. The value of w_0 from the particle analysis is used. The lower bound for w_0 is estimated following

Table 7.8: Average void dimensions and void volume fraction in the region of interest used to characterize the *initial* state of damage in the *aged* material.

Param.	Average	Standard Deviation	Units
h_0	4.376	1.158	µm
d_0	40.961	22.406	µm
$w_0 = h_0/d_0$	0.107		–
f_0	0.01409		–

Table 7.9: Average void dimensions and void volume fraction in the region of interest used to characterize the *final* state of damage in the *aged* material.

Param.	Average	Standard Deviation	Units
h_f	6.816	3.257	µm
d_f	52.364	41.809	µm
$w_\mathrm{f} = h_\mathrm{f}/d_\mathrm{f}$	0.130		–
f_f	0.03417		–

Table 7.10: Average vertical and lateral lengths of Set Voronoi cells in the region of interest used to characterize the *initial* state of damage in the *aged* material.

Param.	Average	Standard Deviation	Units
H_0	97.313	72.188	µm
D_0	95.871	21.639	µm
$\lambda_0 = H_0/D_0$	1.015		–

Table 7.11: Average vertical and lateral lengths of Set Voronoi cells in the region of interest used to characterize the *final* state of damage in the *aged* material.

Param.	Average	Standard Deviation	Units
H_f	82.070	10.26	µm
D_f	70.150	16.60	µm
$\lambda_\mathrm{f} = H_\mathrm{f}/D_\mathrm{f}$	1.170		–

Table 7.12: Calibrated *initial* values of microstructural damage variables for the *aged* material.

Param.	Lower bound	Baseline value	Upper bound
f_0	0.01	0.01409	0.02
w_0	0.069	0.107	0.130
λ_0	0.744	1.015	1.768
ξ_0	0.522	0.585	0.704

Table 7.13: Calibrated *final* values of microstructural damage variables for the *aged* material.

Param.	Lower bound	Baseline value	Upper bound
f_f		0.03417	
w_f	0.068	0.130	0.646
λ_f	0.946	1.170	1.533
ξ_f	0.453	0.773	0.959

the same procedure used for the unaged material. However, the upper bound, w_0^+, is taken as the void aspect ratio of the final state of damage in the material, i.e. $w_0^+ = w_\mathrm{f}$. The value of λ_0 from the mean linear intercept analysis (Table 7.8) is used. The upper and lower bounds for λ_0 are calculated following the same method used with the unaged material, with one modification. Since the sample size is too small for an accurate mean linear analysis, the standard deviations of H_0 and D_0 are extremely large, such that $H_0 - H_{0,\mathrm{std}}$ and $D_0 - D_{0,\mathrm{std}}$ are lower than the minimum measured values from the analysis. Therefore, $H_{0,\mathrm{min}}$ and $D_{0,\mathrm{min}}$ are used as the lower bounds for H_0 and D_0 when calculating the upper and lower bounds of λ_0. As with the unaged material, ξ_0 is calculated from Eq. 7.6, and its upper and lower bounds are calculated from the minimum and maximum values of ξ_0 used when analyzing the uncertainty in $\varepsilon_{\mathrm{eqv,f}}$.

The microstructural damage variables characterizing the final state of damage in the aged material, along with estimated upper and lower bounds, are summarized in Table 7.13. The

baseline values are taken directly from Tables 7.9 and 7.11, and the upper and lower bounds are calculated following the same methodology used for the unaged material.

7.8 Results

The damage model is used to predict the local fracture strain, $\varepsilon_{\text{eqv,f}}$, in aged and unaged round notched bars of PA-6. Four loading cases are studied; two specimen geometries, RN2 and RN10 bars, and two aging conditions, unaged and UV192. The constitutive equations in the damage model are only integrated at a single material point. The location of that point is chosen to represent the location in the round notched bar where fracture is most likely to occur. In the unaged bars, this is at the center of the notch, where the triaxiality and void growth are highest. In the aged bars, this is at the surface of the notch root, where the oxidation-induced damage is greatest. The average triaxiality for each case, $\mathcal{T}$, along with the local fracture strains, were determined from a combination of experiments and finite element simulations employing the calibrated viscoplastic polymer model from Chapter 6. The average triaxiality and local fracture strain for each of the four cases are listed in Table 7.2. The parameters governing the mechanical behavior of the dense material were determined by curve fitting to the local stress–strain response predicted by the viscoplastic polymer model. The parameters governing the mechanical behavior of the dense material are listed in Table 7.3. Finally, the initial values of the microstructural damage variables were experimentally determined for both the unaged case and aged case, and are listed in Tables 7.7 and 7.12, respectively. In Tables 7.2, 7.3, 7.7, and 7.12, nine of the ten model inputs listed in Table 7.1 have been determined for each of the four cases. The final model input is the void opening factor, k. The default value of $k = 1.0$, i.e. no modification to the void aspect ratio evolution equation, is initially used for all four cases.

In Fig. 7.13a, model predictions of $\varepsilon_{\text{eqv,f}}$ using $k = 1.0$ are compared to the values determined through a combination of experiments and finite element modeling.[5] For the

[5] Although the results used for validation were obtained through a combination of experiments and finite element modeling, they are henceforth referred to as experimental results for simplicity.

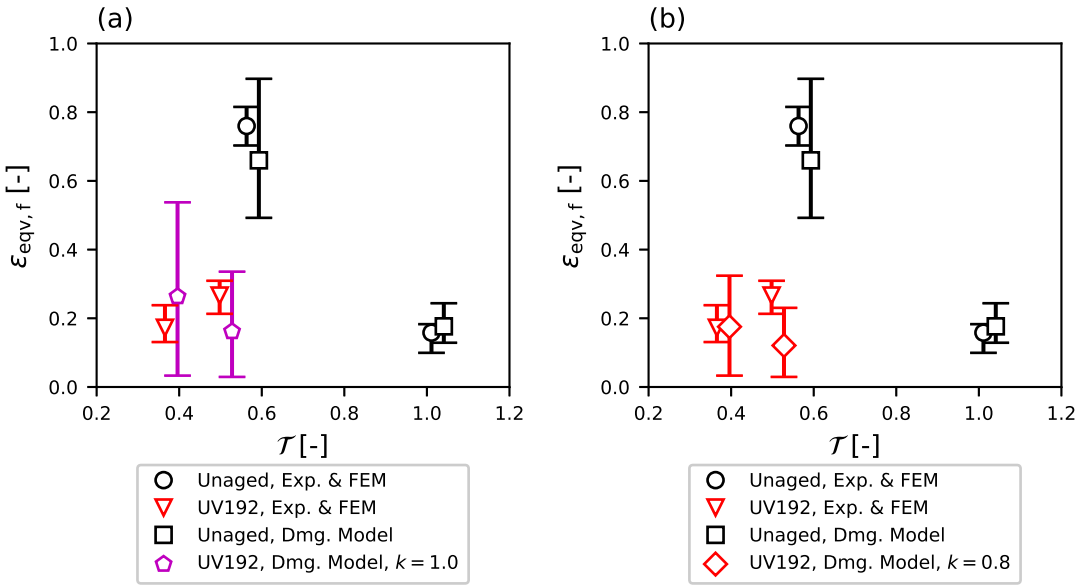

Figure 7.13: Damage model predictions of the local fracture strain, $\varepsilon_{\text{eqv,f}}$, for round notched bars of PA-6 compared to predictions of the local fracture strain determined from a combination of experiments and finite element modeling. Small horizontal offsets are applied to data points for clarity, see Table 7.2 for the actual values of $\mathcal{T}$. The predictions of $\varepsilon_{\text{eqv,f}}$ for the unaged cases are repeated in both (a) and (b). (a) Predictions of $\varepsilon_{\text{eqv,f}}$ for the aged cases when using a void opening factor of $k = 1.0$. (b) Predictions of $\varepsilon_{\text{eqv,f}}$ for the aged cases when using a void opening factor of $k = 0.8$.

unaged cases, the model predictions of $\varepsilon_{\text{eqv,f}}$ show good agreement with the experimental data, especially for the RN2 case ($\mathcal{T} = 1.026$). Although the baseline value of $\varepsilon_{\text{eqv,f}}$ predicted for the unaged RN10 case ($\mathcal{T} = 0.578$) is slightly lower than the experimental value, the error bars in the model predictions encompass the observed range of experimental data. For the unaged RN10 case, the upper and lower limits of $\varepsilon_{\text{eqv,f}}$ are due to the upper and lower limits of w_0, indicating that fracture at medium triaxialities is very sensitive to the void aspect ratio. On the other hand, for the unaged RN2 case, the upper and lower limits of $\varepsilon_{\text{eqv,f}}$ are due to the lower and upper limits of f_0. For the aged cases in Fig. 7.13a, the model prediction of $\varepsilon_{\text{eqv,f}}$ for the RN10 bar ($\mathcal{T} = 0.381$) is slightly above the experimental value, while the model prediction for the aged RN2 bar ($\mathcal{T} = 0.513$) is slightly below the experimental value. However, the uncertainty in the aged model predictions are extremely

high, such that the uncertainty in the model predictions encompasses the experimentally observed range for $\varepsilon_{\text{eqv,f}}$. The high amount of uncertainty is due to the wide range of the upper and lower bounds of λ_0, and the wide uncertainty in λ_0 is due to applying the mean linear intercept method to an area with a small number of cracks. Therefore, more data for characterizing the average cell spacing in the aged material would reduce the uncertainty in the model predictions.

In Fig. 7.13b, model predictions of $\varepsilon_{\text{eqv,f}}$ are compared to the experimentally determined values, except the results from the aged cases are updated to use a void opening factor of $k = 0.8$. For $k = 0.8$, the prediction of $\varepsilon_{\text{eqv,f}}$ for the aged RN10 case is extremely close to the experimentally determined value. Also, the prediction of $\varepsilon_{\text{eqv,f}}$ for the aged RN2 case is moved further away from the experimental value, but the upper bound of the model prediction still overlaps with the lower bound of the experimental data. For both aged cases, using $k = 0.8$ reduces the uncertainty in the predictions of $\varepsilon_{\text{eqv,f}}$.

More compelling evidence for using $k = 0.8$ with the aged material is uncovered by studying the evolution of the microstructural damage variables predicted by the model. Fig. 7.14 compares the evolution of the microstructural damage variables for the aged cases using $k = 1.0$ and $k = 0.8$. By definition, decreasing k decreases $\dot{w}$, see Fig. 7.14b. However, Figs. 7.14a,d reveal that decreasing k increases $\dot{f}$ and $\dot{\xi}$, ultimately leading to a lower $\varepsilon_{\text{eqv,f}}$. However, $\dot{\lambda}$ is unaffected by changes in k, see Fig. 7.14c. By comparing the final values of the microstructural damage variables to the experimental final values determined by analyzing Fig. 7.12 (see Table 7.13 for values), the case for using $k = 0.8$ for the aged material is strengthened. In the experiment used to characterize the final state of damage in the aged material, the film has a very shallow notch and is subjected to a uniaxial load. Therefore, the stress triaxiality leading to the final state of damage in Fig. 7.12 is expected to be around 1/3. For the aged RN10 case, $\mathcal{T} = 0.381$, making it the most appropriate case for comparing the modeled final values to the available experimental data. Table 7.14 compares the final values of the microstructural damage variables determined experimentally, predicted by the

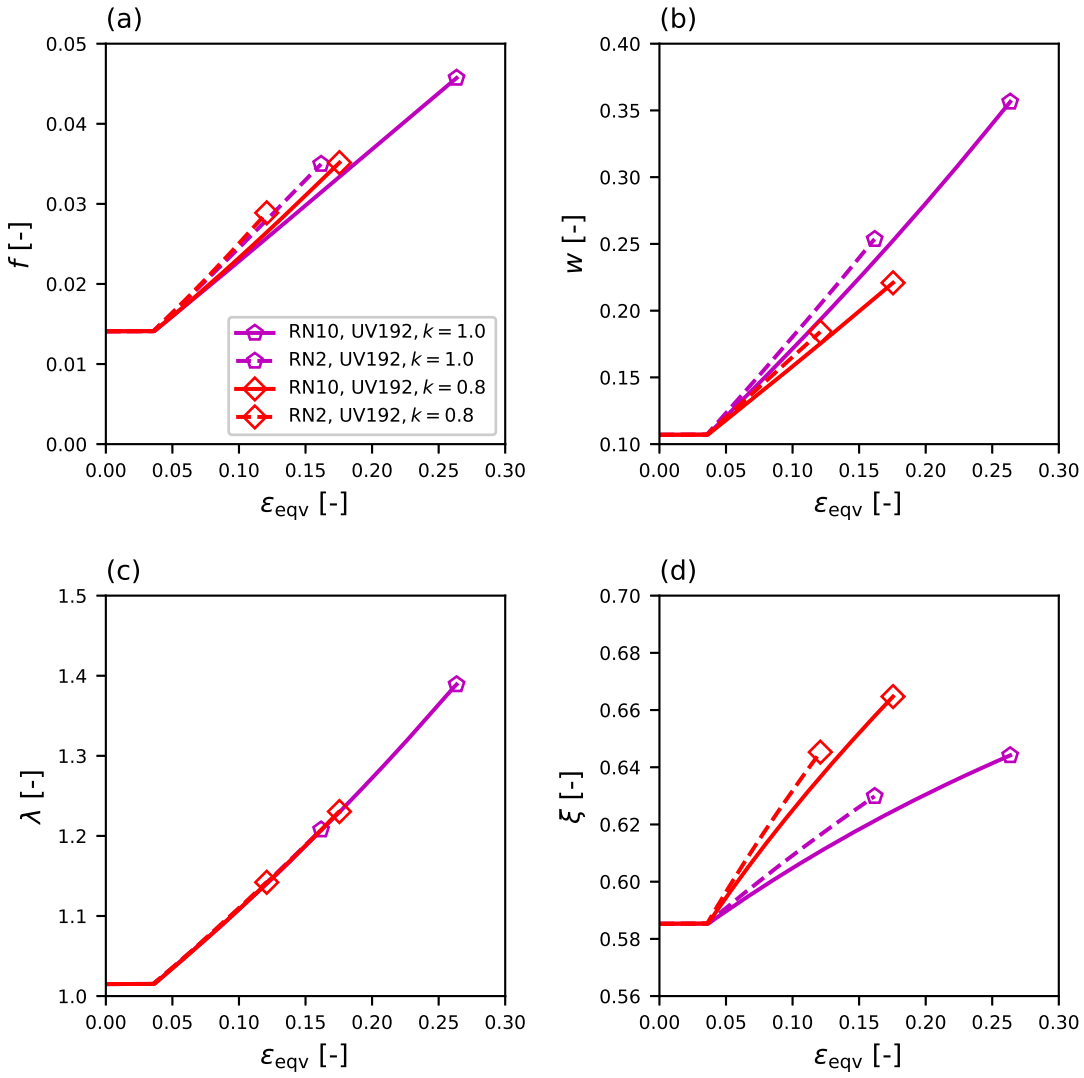

Figure 7.14: The damage model predictions for the evolution of the microstructural damage variables in the aged cases for a void opening factor of $k = 1.0$ and $k = 0.8$. (a) The void volume fraction, f. (b) The void aspect ratio, w. (c) The void spacing ratio, λ. (d) The void ligament ratio, ξ.

Table 7.14: Final values of the microstructural damage variables determined from the analysis of Fig. 7.12 compared to final values determined by the damage model using a void opening factor of $k = 0.8$ and $k = 1.0$.

Param.	Experimental (Fig. 7.12)	UV192, RN10 ($\mathcal{T} = 0.381$) $k = 0.8$	$k = 1.0$
f_f	0.03417	0.03515	0.04572
w_f	0.130	0.221	0.356
λ_f	1.170	1.230	1.389
ξ_f	0.773	0.665	0.644

model using $k = 0.8$, and predicted by the model using $k = 1.0$. For all four damage variables, the final values predicted using $k = 0.8$ are closer to the experimental values than those predicted using $k = 1.0$. For f_f and λ_f, the error between the model predictions with $k = 0.8$ and the experimental values is below 10 %. From this analysis, it is concluded that using $k = 0.8$ improves the model predictions, both with regards to $\varepsilon_{\mathrm{eqv,f}}$ and the evolution of the damage variables. For the unaged material, the void opening factor is maintained at $k = 1.0$.

With calibrated void opening factors of $k = 1.0$ for the unaged material and $k = 0.8$ for the aged material, Fig. 7.13b represents the final results for using the micromechanics-based continuum damage model to predict fracture in aged and unaged round notched bars of PA-6. The effective stress–strain curves for the four cases studied here are plotted in Fig. 7.15. The micromechanical damage has only a minor effect of the mechanical behavior. Both aged cases and the unaged RN2 case have a slightly reduced strength compared to the unaged RN10 case. The evolution of the of the microstructural damage variables for the four cases studied here are plotted in Fig. 7.16. For the two aged cases and the unaged RN2 case, the evolution of f follows a similar path, ending with fracture at a void volume fraction between 3 % and 4 %. For the unaged RN10 case, $\dot{f}$ is lower, but the local fracture strain is higher, resulting in a higher final void volume fraction, around 7 %. In Chapter 4, contour tracking

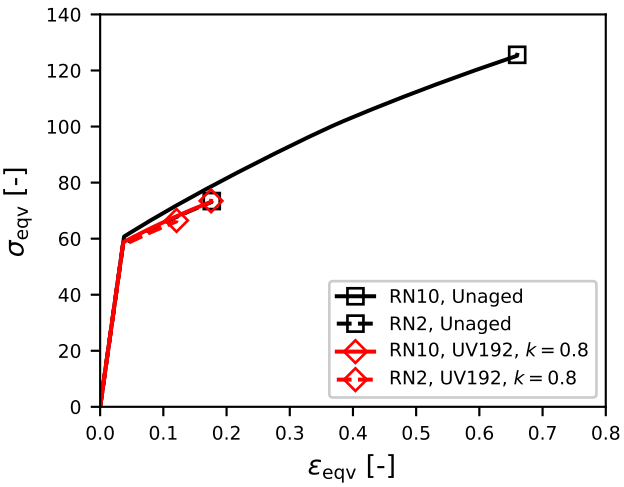

Figure 7.15: The mechanical behavior, as predicted by the damage model, for the four cases studied here. Aged cases use a void opening factor of $k = 0.8$.

and DIC were combined to estimate the dilatation in an unaged RN10 bar, which was then integrated to estimate the void volume fraction, see Fig. 4.5b. This method determined the final void volume fraction to be around 17.5 %, a much higher final value than what is predicted by the damage model. The value predicted by the model, $f_f \approx 7\,\%$, appears to be more reasonable. Of all the initial values of the microstructural damage variables, w_0 is the most different between the unaged and the aged conditions. For the unaged conditions, the evolution of w follows a similar path until fracture occurs in the RN2 case, at which point the RN10 condition still has significant ductility. In the unaged RN2 case, fracture occurs while the voids are still oblate ($w < 1$). On the other hand, the voids become prolate for the unaged RN10 case. For the aged cases, the voids remain extremely oblate, partly due to their small initial value and the use of $k < 1$. In both the aged and the unaged material, $\lambda_0 \approx 1$, indicating that the voids are, on average, isotropically spaced. Since $\dot{\lambda}$ depends only on λ and $D^{\mathrm{p}}_{\mathrm{eqv}}$, see Eq. (7.30), the evolution of λ with respect to $\varepsilon_{\mathrm{eqv}}$ is similar in all four cases. The initial value of of the void ligament ratio is much higher in the aged material than the unaged material, which is a direct result of the highly oblate voids in the aged material.

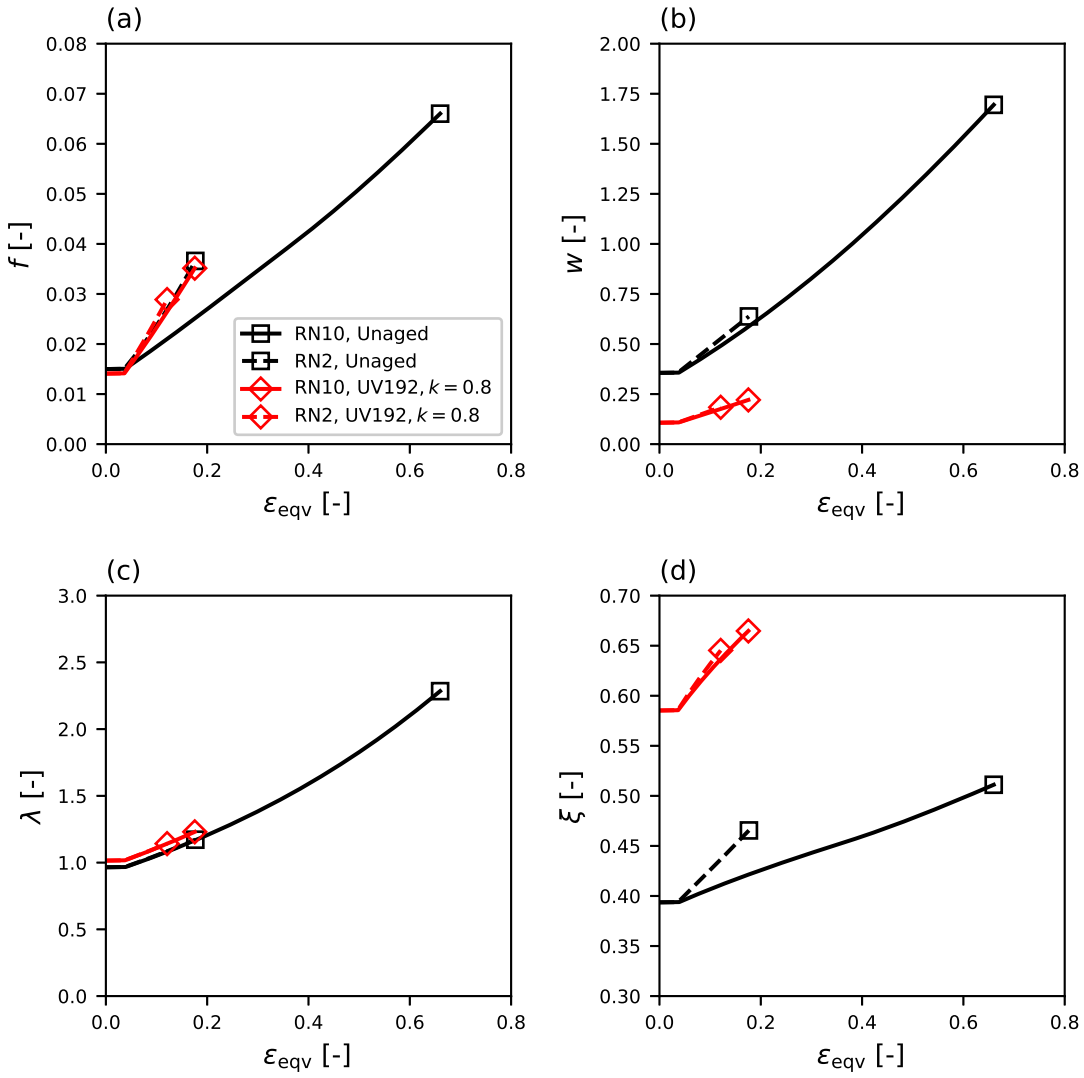

Figure 7.16: The evolution of the microstructural damage variables, as predicted by the damage model, for the four cases studied here. Aged cases use a void opening factor of $k = 0.8$. (a) The void volume fraction, f. (b) The void aspect ratio, w. (c) The void spacing ratio, λ. (d) The void ligament ratio, ξ.

Since the coalescence criterion, Eq. (7.20), is strongly influenced by ξ, the high initial value of ξ in the aged material is responsible for the significantly reduced ductility. For the unaged cases, $\dot{\xi}$ is higher in the RN2 case, leading to a significantly lower local fracture strain. Since the evolution of w is similar between the unaged RN10 and RN2 cases, a higher $\dot{\xi}$ in the unaged RN2 case is a consequence of a higher $\dot{f}$, which itself a consequence of the increased triaxiality applied when simulating the unaged RN2 case.

7.9 Discussion

The results in the previous section show that the micromechanics-based continuum damage model is capable of accurately predicting fracture strains in both aged and unaged round notched bars of PA-6. This result is not surprising for the unaged material, where the micromechanical damage variables are calibrated to represent cavities. Although not all semicrystalline thermoplastics cavitate in the unaged condition [49], PA-6 is known to cavitate, and thorough tomographic investigations by Laiarinandrasana et al. have revealed that fracture in PA-6 is due to the growth and coalescence of cavities [22,23,106]. Therefore, a void growth model is an appropriate tool for predicting fracture in unaged PA-6 and other cavitating semicrystalline thermoplastics. In the aged material, the micromechanical damage variables are calibrated to represent cracks that form as a results of aging, i.e. aging-induced damage. Therefore, the ability of the damage model to accurately predict fracture in the aged material supports the main hypothesis of this dissertation: that aging-induced damage is an important phenomenon when evaluating the residual ductility of (chemically) aged semicrystalline thermoplastics. To the author's knowledge, this is the first instance where a micromechanical damage model has been used to predict fracture in an aged semicrystalline thermoplastic.

Some studies have argued that aging-induced embrittlement in thermoplastics is a direct result of chain scission reducing the molar mass below a critical value [4, 55]. Such an approach to aging-induced embrittlement uses nanoscale measurements (the molar mass) to determine macroscale effects (fracture), which alludes to questions regarding the importance

of mesoscale phenomenon. The experimental evidence collected in Chapter 3 hinted that fracture in aged PA-6 is a growth-controlled process. When aged PA-6 specimens were loaded, cracks became visible at the microscale and macroscale, and, as loading progressed, fracture occurred by the growth of these cracks. Chapters 4 and 5 provided further experimental evidence that fracture in aged PA-6 is a growth-controlled process. By using a micromechanics-based continuum damage model to predict fracture in an aged semicrystalline thermoplastic, a possible causal link between aging-induced damage and embrittlement is established.

One approximation employed here is that the only consequence of aging is a change in the initial state of damage, i.e. the same mechanical behavior was used for the dense material of unaged and aged material. However, this approximation is useful in that it further demonstrates that aging-induced embrittlement is, to first order, a consequence of aging-induced damage, instead of changes to the mechanical behavior that result from changes to the molar mass.

Although the work presented here shows that fracture in aged PA-6 is directly caused by aging-induced damage, it cannot explain the causal link between the chemical changes induced by aging and the development of aging-induced damage. However, this relationship was explored in Rodriguez et al. 2020 [99], where the effect of UV aging on low-density polyethylene (LDPE) was characterized using chemical and mechanical techniques, as well as scanning electron microscopy (SEM). In Ref. [99], "chemical cracks" were seen to form on aged films that were never loaded. As in Chapter 3, a chemical residual stress model was invoked in Ref. [99] to explain the formation of cracks in the absence of an applied load. Ref. [99] also revealed that photo-oxidation promoted cavitation in LDPE, which was rationalized on the basis that cavitation is a competition between the strengths of the amorphous and crystalline phases [43]. Photo-oxidation promotes chemi-crystallization, presumably increasing the strength required to activate plastic deformation in the crystalline phase [99]. Photo-oxidation also primarily attacks the amorphous region of a semicrystalline thermoplastic [4], lowering the strength required for cavitation. The net result of these

two effects is that cavitation becomes more favorable after aging. Therefore, two possible mechanisms for the formation of chemo-mechanical damage can be identified. First, aging could favor cavitation following the mechanism previously discussed. Second, cracks could form from the superposition of a chemical stress and a mechanical stress, as discussed in Chapter 3. As a first approach to modeling the growth of micromechanical damage in an aged semicrystalline thermoplastic, the methodology used here approximated that all damage was either initial to the material or nucleated prior to yielding, i.e. nucleation was not modeled. However, the results from Ref. [99] highlight the complexity of actual situation. A more advanced approach would initialize the micromechanical damage variables based on chemical cracks and would also include nucleation models for chemo-mechanical damage. Predictions of the initial state of chemical damage could be facilitated by linking kinetic models to predictions of the chemical stress. Similarly, models for the nucleation of chemo-mechanical damage could be informed by the chemical stress model and models for cavitation.

For simulating fracture of the aged material, all model parameters were calibrated using experimental data: either the mechanical behavior of the unaged material or tomographic observations of aging-induced damage. The one exception to this is the void opening factor, k, which was reduced from $k = 1.0$ to $k = 0.8$ in the aged cases on the basis that doing so improved the results produced by the model. However, the tomographic observations in Chapter 5 provide a physical basis for reducing the rate of void opening in highly aged PA-6. Fig. 7.17a shows a slice from the last *in situ* tomogram made before fracture of a UV24 aged PA-6 film, and Fig. 7.17b shows a slice from the last *in situ* tomogram made before fracture of a UV48 aged PA-6 film. Load–displacement curves for the mechanical loading of the UV24 and UV48 films are shown in Fig. 7.17c. In both the UV24 and the UV48 films, the voids initiate as oblate cracks, see Fig. 5.6 and Fig. 5.7. Prior to fracture in the UV24 aged film (Fig. 7.17a), the voids have elongated. Although none become prolate, some achieve approximately circular profiles in the plane of the tomogram slice. However, the voids in the UV48 aged film remain extremely oblate throughout loading. Rather than elongating, these

(a) UV24

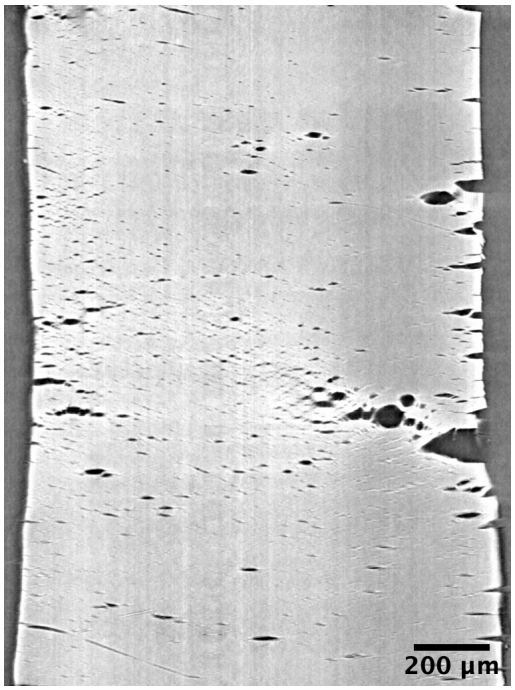

(b) UV48

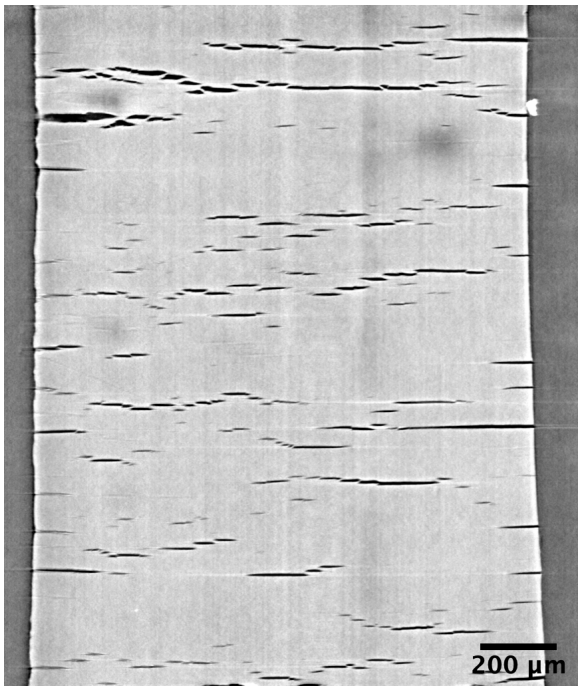

(c)

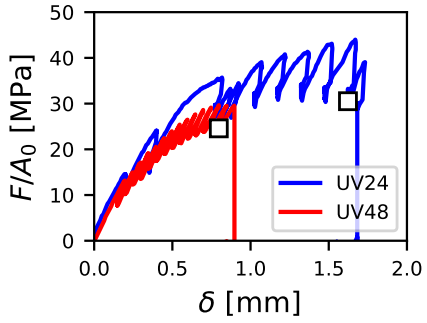

Figure 7.17: Slices from the last *in situ* tomograms before fracture in aged PA-6 films. (a) UV24 aged film at $\delta = 1.62\,\text{mm}$, see Fig. 5.6. (b) UV48 aged film $\delta = 0.80\,\text{mm}$, see Fig. 5.7. (c) Load–displacement curves for the mechanical loading of the UV24 aged film (blue line) and the UV48 aged film (red line). The moments where the final tomograms were taken are marked with white squares.

voids tend to grow laterally. This provides a physical basis for reducing the void opening factor when simulating the growth of damage in the highly aged material studied here. In Figs. 7.17a,b, the tomograms are taken at different levels of displacement, $\delta = 1.62\,\text{mm}$ for the UV24 aged film and $\delta = 0.80\,\text{mm}$ for the UV48 aged film. However, if the tomogram slice of the UV48 aged film was compared to a tomogram slice from the UV24 film at a similar displacement level, very little damage would be visible in the UV24 aged film (for example, see Fig. 5.6). For this reason, comparing films exposed to different UV doses at the same displacement is not appropriate, as a higher UV dose facilitates greater aging-induced damage. However, when tomograms from UV24 and UV48 aged films are compared at any stage beyond when damage initially becomes visible, it is clear that the average void aspect ratio in the UV24 aged film is higher. Therefore, the specific tomograms selected to justify reducing k in the highly aged material is not important.

This work demonstrates proof-of-concept that a micromechanics-based continuum damage model can be successfully applied to predict fracture in an aged semicrystalline thermoplastic. However, the approach applied is preliminary, in that many estimations and approximations were necessary to calibrate the model. It would be desirable to improve this approach in future work. The damage model employed here was formulated fo use with porous metallic materials [33–35, 80]. Therefore, many features of polymeric behavior are not accounted for in the model, such as polymeric viscoplastic laws [60] and entropic hardening due to the orientation of the macromolecular network [57]. In this study, the lack of these features required a two-stage modeling approach. In the first step, finite element calculations of the experimental specimen using a viscoplastic polymer model were necessary to characterize the mechanical behavior at a single critical point. In the second step, the damage model was applied to predict fracture, but only at the critical material point in the structure. Improving the formulation of the model to account for polymer-specific behaviors would enable accurate models of polymeric structures, thus eliminating the need for a two-stage modeling approach. In Ref. [107], a finite element model for a polymer with

voids was developed. However, the specific damage parameters in the model are not directly comparable physical measurements of voids. It was also assumed here that aging does not effect the mechanical behavior of the dense material. While this assumption was useful for demonstrating the importance of aging-induced damage to fracture, in reality, aging leads to a transient strengthening of the material and an increase in the strain hardening [99], see also Figs. 3.5 and 5.1. As mentioned previously, another area for future work is the development of models that predict the initial state of damage and the rate of damage nucleation during loading as a function of the aging exposure time. Such an effort would elucidate the connection between nanoscale effects induced directly by aging and the microscale effects directly responsible for embrittlement.

7.10 Conclusion

In this chapter, a Gurson-type micromechanics-based continuum damage model accounting for anisotropic voids was applied to predict fracture in photo-oxidized (i.e. UV-aged) and unaged round notched bars of PA-6. In the unaged material, the micromechanical damage represents cavities that are typically observed in the deformation of unaged PA-6. In the aged material, the micromechanical damage represents chemical cracks (voids that form during stress-free oxidation) and chemo-mechanical damage (voids that form from the superposition of a chemical and a mechanical stress). For both the unaged and aged material, the fracture strains predicted by the damage model show good agreement with the experimentally determined fracture strains. Accurate predictions of fracture are expected for the unaged material, as it has already been demonstrated that void growth and coalescence are important phenomena in the deformation and fracture of unaged PA-6, as well as several other semicrystalline thermoplastics. On the other hand, accurate predictions of fracture for the aged material demonstrates that aging-induced embrittlement is a consequence of microscale damage induced by aging, rather than changes to the mechanical behavior caused by chain scission. This is the first instance (to the author's knowledge), where a Gurson-type model is used to predict fracture in an aged semicrystalline thermoplastic.

This preliminary work demonstrates the proof-of-concept that aging-induced damage is the direct cause of aging-induced embrittlement. However, three key areas of improvement to this modeling approach have been identified. First, a damage model that specifically accounts for the features of polymeric constitutive behavior, such as a polymeric viscoplastic law and orientation hardening, should be developed. Second, the effects of aging on the mechanical behavior of the polymer should be characterized, modeled, and linked to the kinetics of aging, as aging is known to have a transient strengthening effect on polymers. Third, predictive models that correlate the aging dose with the initial state of damage in the material, along with the nucleation of chemo-mechanical damage during loading should be developed. This improvement would reduce uncertainty in the damage model predictions, but would also help to establish a causal link between chemical aging and the development of aging-induced damage. With such models, the effects of aging could be predicted across multiple scales, from chemical reactions fundamental to aging, to macroscale embrittlement of polymeric structures.

8. CONCLUSIONS

This dissertation has explored the embrittlement caused by chemical aging in semicrystalline thermoplastics. The research here has focused on polyamide-6 (PA-6) aged by exposure to UV radiation in air, which leads to photo-oxidation. Previous approaches to this problem have focused on the chemical aspects of aging, and propose that embrittlement occurs when oxidation-mediated chain scission reduces the molar mass below a critical value. However, this approach connects nanoscale causes (chain scission) to macroscale effects (embrittlement), while ignoring the mesoscale (micromechanical damage induced by aging). The research presented here demonstrates the importance of mesoscale phenomena to predicting embrittlement in semicrystalline thermoplastics. The following conclusions are drawn from the research presented in this dissertation.

- Fracture of an aged thermoplastic is a growth-controlled phenomenon. In aged cylindrical bars, no damage was visible at the macroscale prior to loading. In aged films, damage was also not visible at the microscale prior to loading. However, in both bars and films, surface cracks appeared after loading, but well before the maximum force. The number and size of cracks increased with the strain. Specimens aged for longer times also showed an increased number of surface cracks. The concept of a chemical stress was invoked to explain the nucleation of cracks on the surface of an aged specimen, even in the absence of any applied loads. (Chapter 3)

- In aged round notched bars, fracture is determined by a competition between surface cracks induced by aging and cavitation in the bulk. At the center of the bar, the high stress triaxiality favors cavitation. On the other hand, aging causes cracks to form on the surface, irrespective of the triaxiality. If the bar is sufficiently large, these two populations of void-like defects do not significantly interact, so only the critical damage mechanism determines fracture. Which mechanism is dominant is affected by

the exposure time and also the notch bar geometry, which is used to indirectly vary the stress state. (Chapter 4)

- The ductile-brittle transition coincides with a damage mechanism transition. The transition was best analyzed using films specimens, where the gradient of damage from the surface to the center is minimized. In films aged near to the ductile-brittle transition, cracks appear on the faces of the films after loading. As loading continues, these cracks open along the loading axis and blunt, with some attaining a well-blunted profile on the face of the film. Eventually, these blunted microcracks coalesce, leading to fracture. In films aged beyond the ductile-brittle transition, cracks appear at much lower loads. These cracks do not significantly open or blunt during loading. Instead, they primarily grow laterally, linking up with nearby cracks. Fracture occurs when cracks have linked up across the width of the specimen face. In both the ductile and brittle regimes, damage was found to be diffuse. (Chapter 5)

- Fracture in an aged semicrystalline thermoplastic can be predicted using a micromechanics-based continuum damage model. A Gurson-type damage model was applied to predict fracture strains in unaged and aged round notched bars of PA-6. The initial values of the microstructural damage variables in the model were chosen to represent the average morphology of cavities in the unaged material and aging-induced damage in the aged material. By accounting for void shape effects, cavities and microcracks were therefore modeled using a single framework. For both the aged and unaged material, the determination of the initial microstructural damage variables was made possible by synchrotron tomography observations of appropriate specimens. The damage model accurately predicted the fracture strains in both the unaged and aged conditions, albeit using a single adjustable parameter. This demonstrates a causal link between embrittlement caused by aging and micromechanical damage. (Chapter 7)

In addition to the above conclusions regarding aging-induced damage, a viscoplastic con-

stitutive model for a semicrystalline thermoplastic was formulated and implemented as a tool for studying the mechanical behavior of the dense material. The viscoplastic constitutive model was used to identify the intrinsic mechanical behavior using only the nominal mechanical behavior, even after the onset of necking. (Chapter 6)

Although this research has specifically studied PA-6 aged by UV radiation, the conclusions are likely also valid for other semicrystalline thermoplastics and other aging conditions. It would be interesting for future work to thoroughly investigate the transferability of these results. Unaged PA-6 cavitates, which occurs by interactions between the amorphous and crystalline phases [21]. Generally, a weaker amorphous phase or a stronger crystalline phase favors cavitation [43]. On the other hand, some polymers, such as LDPE, do not cavitate in the unaged condition [47]. However, recent work [99, 148] has shown cavitation in UV-aged LDPE. Therefore, it seems that aging-induced damage is relevant to fracture in both cavitating and non-cavitating semicrystalline thermoplastics. Semicrystalline thermoplastics can also be categorized based on the state of the amorphous phase at room temperature. For example, in PA-6, the amorphous phase is glassy at room temperature, but the amorphous phase of PE is rubbery. Studies by Fayolle et al. reported that embrittlement occurred at different ratios of the molar mass to the molar mass between entanglements, M_c/M_e, for these two classes of polymers [4, 10, 55]. Furthermore, future work could investigate how aging-induced damage manifests and develops in amorphous thermoplastics or thermosets.

Another open question regarding aging is the link between nanoscale chemical reactions and the microscale damage studied here, as it is not precisely known how such damage forms from aging. Understanding this link could allow the development of chemical kinetic models [14, 15] that link aging conditions to the nucleation and growth of damage. This in turn would enable a more robust characterization of the initial state of damage in the aged material, which is essential for predicting fracture using a micromechanics-based damage model. Additionally, exploring the link between chemistry, mechanical stresses, and micromechanical damage might produce nucleation laws that could be incorporated into damage

models. Eventually, a model that integrated effects across all relevant scales could enable robust lifetime predictions for aged thermoplastics. Such a model would take the environmental conditions and mechanical loads as inputs to predict chemical reactions in the polymer and the nucleation and growth of micromechanical damage, then use these predictions to determine the lifetime of a polymeric component.

REFERENCES

[1] M. Biron, *Thermoplastics and Thermoplastic Composites*. Butterworth-Heinemann, first ed., 2007.

[2] G. A. George, "Weathering of polymers," *Mater. Forum*, vol. 19, pp. 145–161, 1995.

[3] L. C. E. Struik, "Physical aging in plastics and other glassy materials," *Pol. Eng. Sci.*, vol. 17, no. 3, pp. 165–173, 1977.

[4] B. Fayolle, E. Richaud, X. Colin, and J. Verdu, "Review: Degradation-induced embrittlement in semi-crystalline polymers having their amorphous phase in rubbery state," *J. Mater. Sci.*, vol. 43, no. 22, pp. 6999–7012, 2008.

[5] B. Zhao and M. A. Zikry, "Oxidation-induced failure in semi-crystalline organic thin films," *Int. J. Solids Struct.*, vol. 109, pp. 72–83, 2017.

[6] D. Briassoulis, A. Aristopoulou, M. Bonora, and I. Verlodt, "Degradation characterisation of agricultural low-density polyethylene films," *Biosyst. Eng.*, vol. 88, no. 2, pp. 131–143, 2004.

[7] C. S. Cummings, E. M. Lucas, J. A. Marro, T. M. Kieu, and J. D. DesJardins, "The effects of proton radiation on UHMWPE material properties for space flight and medical applications," *Adv. Space Res.*, vol. 48, no. 10, pp. 1572–1577, 2011.

[8] C. D. Lytle and J.-L. Sagripanti, "Predicted inactivation of viruses of relevance to biodefense by solar radiation," *J. Virol.*, vol. 79, no. 22, pp. 14244–14252, 2005.

[9] O. Okamba-Diogo, E. Richaud, J. Verdu, F. Fernagut, J. Guilment, and B. Fayolle, "Investigation of polyamide 11 embrittlement during oxidative degradation," *Polymer*, vol. 82, pp. 49–56, 2016.

[10] B. Fayolle, L. Audouin, and J. Verdu, "A critical molar mass separating the ductile and brittle regimes as revealed by thermal oxidation in polypropylene," *Polymer*, vol. 45, no. 12, pp. 4323–4330, 2004.

[11] M. C. Celina, "Review of polymer oxidation and its relationship with materials performance and lifetime prediction," *Polym. Degrad. Stab.*, vol. 98, no. 12, pp. 2419–2429, 2013.

[12] A. F. Reano, A. Guinault, E. Richaud, and B. Fayolle, "Polyethylene loss of ductility during oxidation: Effect of initial molar mass distribution," *Polym. Degrad. Stab.*, vol. 149, pp. 78–84, 2018.

[13] M. Celina, E. Linde, D. Brunson, A. Quintana, and N. Giron, "Overview of accelerated aging and polymer degradation kinetics for combined radiation-thermal environments," *Polym. Degrad. Stab.*, vol. 166, pp. 353–378, 2019.

[14] C. El-Mazry, O. Correc, and X. Colin, "A new kinetic model for predicting polyamide 6-6 hydrolysis and its mechanical embrittlement," *Polym. Degrad. Stab.*, vol. 97, no. 6, pp. 1049–1059, 2012.

[15] C. El-Mazry, M. B. Hassine, O. Correc, and X. Colin, "Thermal oxidation kinetics of additive free polyamide 6-6," *Polym. Degrad. Stab.*, vol. 98, no. 1, pp. 22–36, 2013.

[16] P. Gijsman, W. Dong, A. Quintana, and M. C. Celina, "Influence of temperature and stabilization on oxygen diffusion limited oxidation profiles of polyamide 6," *Polym. Degrad. Stab.*, vol. 130, pp. 83–96, 2016.

[17] O. Okamba-Diogo, E. Richaud, J. Verdu, F. Fernagut, J. Guilment, and B. Fayolle, "Molecular and macromolecular structure changes in polyamide 11 during thermal oxidation — Kinetic modeling," *Polym. Degrad. Stab.*, vol. 120, pp. 76–87, 2015.

[18] J. F. Rabek, *Polymer Photodegradation: Mechanisms and Experimental Methods*. Springer Netherlands, first ed., 1995.

[19] B. Fayolle, L. Audouin, and J. Verdu, "Oxidation induced embrittlement in polypropylene — A tensile testing study," *Polym. Degrad. Stab.*, vol. 70, no. 3, pp. 333–340, 2000.

[20] O. Okamba-Diogo, E. Richaud, J. Verdu, F. Fernagut, J. Guilment, and B. Fayolle, "Molecular and macromolecular structure changes in polyamide 11 during thermal oxidation," *Polym. Degrad. Stab.*, vol. 108, pp. 123–132, 2014.

[21] A. Pawlak, A. Galeski, and A. Rozanski, "Cavitation during deformation of semicrystalline polymers," *Prog. Polym. Sci.*, vol. 39, no. 5, pp. 921–958, 2014.

[22] L. Laiarinandrasana, T. F. Morgeneyer, H. Proudhon, and C. Regrain, "Damage of semicrystalline polyamide 6 assessed by 3D X-ray tomography: From microstructural evolution to constitutive modeling," *J. Polym. Sci., Part B: Polym. Phys.*, vol. 48, no. 13, pp. 1516–1525, 2010.

[23] L. Laiarinandrasana, T. F. Morgeneyer, H. Proudhon, F. N'guyen, and E. Maire, "Effect of multiaxial stress state on morphology and spatial distribution of voids in deformed semicrystalline polymer assessed by X-ray tomography," *Macromolecules*, vol. 45, no. 11, pp. 4658–4668, 2012.

[24] X. C. Zhang, M. F. Butler, and R. E. Cameron, "The ductile–brittle transition of irradiated isotactic polypropylene studied using simultaneous small angle X-ray scattering and tensile deformation," *Polymer*, vol. 41, no. 10, pp. 3797–3807, 2000.

[25] M. M. Qayyum and J. R. White, "Plastic fracture in weathered polymers," *Polymer*, vol. 28, no. 3, pp. 469–476, 1987.

[26] G. A. George and M. S. O'Shea, "Environmental degradation of nylon 6 under mechanical load," *Mater. Forum*, vol. 13, pp. 11–20, 1989.

[27] J. F. Rabek, *Photodegradation of Polymers: Physical Characteristics and Applications*. Springer, first ed., 1996.

[28] X.-F. Wei, K. J. Kallio, S. Bruder, M. Bellander, H.-H. Kausch, U. W. Gedde, and M. S. Hedenqvist, "Diffusion-limited oxidation of polyamide: Three stages of fracture behavior," *Polym. Degrad. Stab.*, vol. 154, pp. 73–83, 2018.

[29] M. Pelerin, A. King, L. Laiarinandrasana, and H. Proudhon, "Development of a versatile mechanical testing device for in situ synchrotron tomography and diffraction experiments," *Integr. Mater. Manuf. Innov.*, vol. 8, pp. 378–387, Sep 2019.

[30] S. Kweon and A. A. Benzerga, "On the localization of plastic flow in glassy polymers," *Eur. J. Mech. A. Solids*, vol. 39, pp. 251–267, 2013.

[31] G. Ayoub, F. Zaïri, C. Fréderix, J. M. Gloaguen, M. Naït-Abdelaziz, R. Séguéla, and J. M. Lefebvre, "Effects of crystal content on the mechanical behaviour of polyethylene under finite strains: Experiments and constitutive modelling," *Int. J. Plasticity*, vol. 27, no. 4, pp. 492–511, 2011.

[32] A. L. Gurson, "Continuum theory of ductile rupture by void nucleation and growth: Part I—yield criteria and flow rules for porous ductile media," *J. Eng. Mater. Technol.*, vol. 99, no. 1, pp. 2–15, 1977.

[33] S. M. Keralavarma and A. A. Benzerga, "A constitutive model for plastically anisotropic solids with non-spherical voids," *J. Mech. Phys. Solids*, vol. 58, no. 6, pp. 874–901, 2010.

[34] S. M. Keralavarma and A. A. Benzerga, "Numerical assessment of an anisotropic porous metal plasticity model," *Mech. Mater.*, vol. 90, pp. 212–228, 2015. Proceedings of the IUTAM Symposium on Micromechanics of Defects in Solids.

[35] B. Kondori and A. A. Benzerga, "Modeling damage accumulation to fracture in a magnesium-rare earth alloy," *Acta Mater.*, vol. 124, pp. 225–236, 2017.

[36] A. Galeski, A. S. Argon, and R. E. Cohen, "Changes in the morphology of bulk spherulitic nylon 6 due to plastic deformation," *Macromolecules*, vol. 21, no. 9, pp. 2761–2770, 1988.

[37] S. Castagnet and Y. Deburck, "Relative influence of microstructure and macroscopic triaxiality on cavitation damage in a semi-crystalline polymer," *Mater. Sci. Eng., A*, vol. 448, no. 1, pp. 56–66, 2007.

[38] C. G'Sell and A. Dahoun, "Evolution of microstructure in semi-crystalline polymers under large plastic deformation," *Mater. Sci. Eng., A*, vol. 175, no. 1, pp. 183–199, 1994.

[39] H. H. Kausch, *Polymer Fracture*. Springer-Verlag Berlin Heidelberg, 2nd ed., 1987.

[40] I. M. Ward and J. Sweeney, *An Introduction to the Mechanical Properties of Solid Polymers*. John Wiley & Sons, 2nd ed., 2004.

[41] K. D. Pae, H.-C. Chu, J. K. Lee, and J.-H. Kim, "Healing of stress-whitening in polyethylene and polypropylene at or below room temperature," *Pol. Eng. Sci.*, vol. 40, no. 8, pp. 1783–1795, 2000.

[42] J. K. Lee, J. H. Kim, H.-C. Chu, and K. D. Pae, "Macroscopic observation of healing process in stress-whitened polypropylene under hydrostatic pressure," *PES*, vol. 42, no. 12, pp. 2351–2360, 2002.

[43] S. Humbert, O. Lame, J. M. Chenal, C. Rochas, and G. Vigier, "New insight on initiation of cavitation in semicrystalline polymers: In-situ SAXS measurements," *Macromolecules*, vol. 43, no. 17, pp. 7212–7221, 2010.

[44] A. Pawlak and A. Galeski, "Cavitation during tensile drawing of annealed high density polyethylene," *Polymer*, vol. 51, no. 24, pp. 5771–5779, 2010.

[45] A. A. Benzerga and J.-B. Leblond, "Ductile fracture by void growth to coalescence," *Adv. Appl. Mech.*, vol. 44, pp. 169–305, 2010.

[46] C. Thomas, V. Ferreiro, G. Coulon, and R. Séguéla, "In situ AFM investigation of crazing in polybutene spherulites under tensile drawing," *Polymer*, vol. 48, no. 20, pp. 6041–6048, 2007.

[47] A. Pawlak, "Cavitation during tensile deformation of high-density polyethylene," *Polymer*, vol. 48, no. 5, pp. 1397–1409, 2007.

[48] A. Galeski, "Strength and toughness of crystalline polymer systems," *Prog. Polym. Sci.*, vol. 28, no. 12, pp. 1643–1699, 2003.

[49] A. Pawlak and A. Galeski, "Plastic deformation of crystalline polymers: The role of cavitation and crystal plasticity," *Macromolecules*, vol. 38, no. 23, pp. 9688–9697, 2005.

[50] M. S. Rabello and J. R. White, "Crystallization and melting behaviour of photodegraded polypropylene — I. Chemi-crystallization," *Polymer*, vol. 38, no. 26, pp. 6379–6387, 1997.

[51] K. T. Gillen and R. L. Clough, "Rigorous experimental confirmation of a theoretical model for diffusion-limited oxidation," *Polymer*, vol. 33, no. 20, pp. 4358–4365, 1992.

[52] M. C. Celina, G. A. George, and N. C. Billingham, "Physical spreading of oxidation in solid polypropylene as studied by chemiluminescence," *Polym. Degrad. Stab.*, vol. 42, no. 3, pp. 335–344, 1993.

[53] M. C. Celina and G. A. George, "A heterogeneous model for the thermal oxidation of solid polypropylene from chemiluminescence analysis," *Polym. Degrad. Stab.*, vol. 40, no. 3, pp. 323–335, 1993.

[54] H. R. Brown, "A molecular interpretation of the toughness of glassy polymers," *Macromolecules*, vol. 24, no. 10, pp. 2752–2756, 1991.

[55] B. Fayolle, X. Colin, L. Audouin, and J. Verdu, "Mechanism of degradation induced embrittlement in polyethylene," *Polym. Degrad. Stab.*, vol. 92, no. 2, pp. 231–238, 2007.

[56] X. Colin, A. Mavel, C. Marais, and J. Verdu, "Interaction between cracking and oxidation in organic matrix composites," *J. Compos. Mater.*, vol. 39, no. 15, pp. 1371–1389, 2005.

[57] M. C. Boyce, D. M. Parks, and A. S. Argon, "Large inelastic deformation of glassy polymers. Part I: Rate dependent constitutive model," *Mech. Mater.*, vol. 7, no. 1, pp. 15–33, 1988.

[58] M. C. Boyce, S. Socrate, and P. G. Llana, "Constitutive model for the finite deformation stress-strain behavior of poly(ethylene terephthalate) above the glass transition," *Polymer*, vol. 41, no. 6, pp. 2183–2201, 2000.

[59] R. N. Haward and G. Thackray, "The use of a mathematical model to describe isothermal stress-strain curves in glassy thermoplastics," *Proc. R. Soc. London, Ser. A*, vol. 302, no. 1471, pp. 453–472, 1968.

[60] A. S. Argon, "A theory for the low-temperature plastic deformation of glassy polymers," *Phil. Mag.*, vol. 28, no. 4, pp. 839–865, 1973.

[61] P. J. Dooling, C. P. Buckley, S. Rostami, and N. Zahlan, "Hot-drawing of poly(methyl methacrylate) and simulation using a glass–rubber constitutive model," *Polymer*, vol. 43, no. 8, pp. 2451–2465, 2002.

[62] L. R. G. Treloar, *The physics of rubber elasticity.* Clarendon, Oxford, 3rd ed., 1975.

[63] S. Ahzi, A. Makradi, R. V. Gregory, and D. D. Edie, "Modeling of deformation behavior and strain-induced crystallization in poly(ethylene terephthalate) above the glass transition temperature," *Mech. Mater.*, vol. 35, no. 12, pp. 1139–1148, 2003.

[64] X. Poulain, *On the Thermomechanical Behavior of Epoxy Polymers: Experiments and Modeling.* PhD thesis, Texas A&M University, College Station, TX, December 2010.

[65] A. de Castro, "Contribution to the study of fracture in amorphous polymers: Experiments and modeling," Master's thesis, Texas A&M University, College Station, TX, December 2010.

[66] X. Poulain, A. A. Benzerga, and R. K. Goldberg, "Finite-strain elasto-viscoplastic behavior of an epoxy resin: Experiments and modeling in the glassy regime," *Int. J. Plasticity*, vol. 62, pp. 138–161, 2014.

[67] E. Arruda and M. C. Boyce, "A three-dimensional constitutive model of the large stretch behavior of rubber elastic materials," *J. Mech. Phys. Solids*, vol. 41, no. 2, pp. 389–412, 1993.

[68] P. D. Wu and E. van der Giessen, "On improved network models for rubber elasticity and their applications to orientation hardening in glassy polymers," *J. Mech. Phys. Solids*, vol. 41, no. 3, pp. 427–456, 1993.

[69] P. D. Wu and E. van der Giessen, "Computational aspects of localized deformations in amorphous glassy polymers," *Eur. J. Mech. A. Solids*, vol. 15, no. 5, pp. 799–823, 1996.

[70] K. A. Chowdhury, R. Talreja, and A. A. Benzerga, "Effects of manufacturing-induced voids on local failure in polymer-based composites," *J. Eng. Mater. Technol.*, vol. 130, pp. 021010–1–9, 04 2008.

[71] I. S. Dairanieh, A. J. McHugh, and A. K. Doufas, "Phenomenological model for flow-induced crystallization," *ANTEC Conf. Proc.*, vol. 1, pp. 212–216, 1998.

[72] A. K. Doufas, I. S. Dairanieh, and A. J. McHugh, "A continuum model for flow-induced crystallization of polymer melts," *J. Rheol.*, vol. 43, no. 1, pp. 85–109, 1999.

[73] A. K. Doufas, A. J. McHugh, and C. Miller, "Simulation of melt spinning including flow-induced crystallization Part I. Model development and predictions," *J. Non-Newton. Fluid Mech.*, vol. 92, no. 1, pp. 27–66, 2000.

[74] G. Ayoub, F. Zaïri, C. Fréderix, J. M. Gloaguen, M. Naït-Abdelaziz, R. Séguéla, and J. M. Lefebvre, "Modelling finite deformation stress-strain response during loading-unloading of polyethylene over a wide range of crystallinities," *Procedia Eng.*, vol. 2, no. 1, pp. 977–984, 2010.

[75] J. A. W. van Dommelen, D. M. Parks, M. C. Boyce, W. A. M. Brekelmans, and F. P. T. Baaijens, "Micromechanical modeling of the elasto-viscoplastic behavior of semi-crystalline polymers," *J. Mech. Phys. Solids*, vol. 51, no. 3, pp. 519–541, 2003.

[76] B. J. Lee, D. M. Parks, and S. Ahzi, "Micromechanical modeling of large plastic deformation and texture evolution in semi-crystalline polymers," *J. Mech. Phys. Solids*, vol. 41, no. 10, pp. 1651–1687, 1993.

[77] B. J. Lee, A. S. Argon, D. M. Parks, S. Ahzi, and Z. Bartczak, "Simulation of large strain plastic deformation and texture evolution in high density polyethylene," *Polymer*, vol. 34, no. 17, pp. 3555–3575, 1993.

[78] V. Tvergaard, "Influence of voids on shear band instabilities under plane strain conditions," *Int. J. Frac.*, vol. 17, no. 4, pp. 389–407, 1981.

[79] V. Tvergaard and A. Needleman, "Analysis of the cup-cone fracture in a round tensile bar," *Acta metall.*, vol. 32, no. 1, pp. 157–169, 1984.

[80] S. Kweon, B. Sagsoy, and A. A. Benzerga, "Constitutive relations and their time integration for anisotropic elasto-plastic porous materials," *Comput. Methods Appl. Mech. Eng.*, vol. 310, pp. 495–534, 2016.

[81] A. A. Benzerga and J. Besson, "Plastic potentials for anisotropic porous solids," *Eur. J. Mech. A. Solids*, vol. 20, no. 3, pp. 397–434, 2001.

[82] M. Gologanu, J.-B. Leblond, and J. Devaux, "Approximate models for ductile metals containing non-spherical voids—Case of axisymmetric prolate ellipsoidal cavities," *J. Mech. Phys. Solids*, vol. 41, no. 11, pp. 1723–1754, 1993.

[83] M. Gologanu, J.-B. Leblond, and J. Devaux, "Approximate models for ductile metals containing nonspherical voids—Case of axisymmetric oblate ellipsoidal cavities," *J. Eng. Mater. Technol.*, vol. 116, no. 3, pp. 290–297, 1994.

[84] M. Gărăjeu, J. C. Michel, and P. Suquet, "A micromechanical approach of damage in viscoplastic materials by evolution in size, shape and distribution of voids," *Comput. Methods Appl. Mech. Eng.*, vol. 183, no. 3, pp. 223–246, 2000.

[85] V. Monchiet, O. Cazacu, E. Charkaluk, and D. Kondo, "Macroscopic yield criteria for plastic anisotropic materials containing spheroidal voids," *Int. J. Plasticity*, vol. 24, no. 7, pp. 1158–1189, 2008.

[86] S. M. Keralavarma and A. A. Benzerga, "An approximate yield criterion for anisotropic porous media," *C. R. Mecanique*, vol. 336, no. 9, pp. 685–692, 2008.

[87] R. Hill, "A theory of the yielding and plastic flow of anisotropic metals," *Proc. R. Soc. London, Ser. A*, vol. 193, no. 1003, pp. 281–297, 1948.

[88] K. N. Cundiff, Y. Madi, and A. A. Benzerga, "Photo-oxidation of semicrystalline polymers: Damage nucleation versus growth," *Polymer*, vol. 188, p. 122090, 2020.

[89] M. C. Celina and G. A. George, "Heterogeneous and homogeneous kinetic analyses of the thermal oxidation of polypropylene," *Polym. Degrad. Stab.*, vol. 50, no. 1, pp. 89–99, 1995.

[90] R. Séguéla and F. Rietsch, "Molecular topology in ethylene copolymers studied by means of mechanical testing," *J. Mater. Sci.*, vol. 23, no. 2, pp. 415–421, 1988.

[91] P. J. Mills, J. N. Hay, and R. N. Hayward, "The post-yield behaviour of low-density polyethylenes — Part 1: Strain hardening," *J. Mater. Sci.*, vol. 20, no. 2, pp. 501–507, 1985.

[92] N. Jia, H. A. Fraenkel, and V. A. Kagan, "Effects of moisture conditioning methods on mechanical properties of injection molded nylon 6," *J. Reinf. Plast. Compos.*, vol. 23, no. 7, pp. 729–737, 2004.

[93] M. I. Kohan, *Nylon Plastics*. John Wiley & Sons, 1973.

[94] I. Campoy, M. A. Gómez, and C. Marco, "Structure and thermal properties of blends of nylon 6 and a liquid crystal copolyester," *Polymer*, vol. 39, no. 25, pp. 6279–6288, 1998.

[95] Q. Wu and L. A. B. Xiaohui Liu, "An unusual crystallization behavior in polyamide 6/montmorillonite nanocomposites," *Macromol. Rapid Commun.*, vol. 22, no. 17, pp. 1438–1440, 2001.

[96] R. K. Goldberg, G. D. Roberts, and A. Gilat, "Implementation of an associative flow rule including hydrostatic stress effects into the high strain rate deformation analysis of polymer matrix composites," *J. of Aerosp Eng.*, vol. 18, no. 1, pp. 18–27, 2005.

[97] X. Poulain, L. W. Kohlman, W. Binienda, G. D. Roberts, R. K. Goldberg, and A. A. Benzerga, "Determination of the intrinsic behavior of polymers using digital image correlation combined with video-monitored testing," *Int. J. Solids Struct.*, vol. 50, no. 11–12, pp. 1869–1878, 2013.

[98] J. W. Hutchinson and K. W. Neale, "Neck propagation," *J. Mech. Phys. Solids*, vol. 31, no. 5, pp. 405–426, 1983.

[99] A. K. Rodriguez, B. Mansoor, G. Ayoub, X. Colin, and A. A. Benzerga, "Effect of UV-aging on the mechanical and fracture behavior of low density polyethylene," *Polym. Degrad. Stab.*, vol. 180, p. 109185, 2020.

[100] A. K. Rodriguez, B. Mansoor, and A. A. Benzerga, "Oxidation induced stiffening versus weakening in semicrystalline polymers," *In preparation*, 2020.

[101] I. Yakimets, D. Lai, and M. Guigon, "Effect of photo-oxidation cracks on behaviour of thick polypropylene samples," *Polym. Degrad. Stab.*, vol. 86, no. 1, pp. 59–67, 2004.

[102] M. S. Rabello and J. R. White, "The role of physical structure and morphology in the photodegradation behaviour of polypropylene," *Polym. Degrad. Stab.*, vol. 56, no. 1, pp. 55–73, 1997.

[103] J. W. Hutchinson and Z. Suo, "Mixed mode cracking in layered materials," *Adv. Appl. Mech.*, vol. 29, pp. 63–191, 1991.

[104] P. W. Bridgman, *Studies in Large Plastic Flow and Fracture*. Harvard University Press, second ed., 1964.

[105] L. Laiarinandrasana, J. Besson, M. Lafarge, and G. Hochstetter, "Temperature dependent mechanical behaviour of PVDF: Experiments and numerical modelling," *Int. J. Plasticity*, vol. 25, no. 7, pp. 1301–1324, 2009.

[106] L. Laiarinandrasana, O. Klinkova, F. Nguyen, H. Proudhon, T. F. Morgeneyer, and W. Ludwig, "Three dimensional quantification of anisotropic void evolution in deformed semi-crystalline polyamide 6," *Int. J. Plasticity*, vol. 83, pp. 19–36, 2016.

[107] W. Ayadi, L. Laiarinandrasana, and K. Saï, "Anisotropic (continuum damage mechanics)-based multi-mechanism model for semi-crystalline polymer," *Int. J. Damage Mech.*, vol. 27, no. 3, pp. 357–386, 2018.

[108] B. Jacques, M. Werth, I. Merdas, F. Thominette, and J. Verdu, "Hydrolytic ageing of polyamide 11. 1. Hydrolysis kinetics in water," *Polymer*, vol. 43, no. 24, pp. 6439–6447, 2002.

[109] B. Kondori and A. A. Benzerga, "Effect of stress triaxiality on the flow and fracture of Mg alloy AZ31," *Metall. Mater. Trans. A*, vol. 45, no. 8, pp. 3292–3307, 2014.

[110] A. A. Benzerga, J. Besson, and A. Pineau, "Anisotropic ductile fracture: Part II: Theory," *Acta Mater.*, vol. 52, no. 15, pp. 4639–4650, 2004.

[111] A. Rozanski and A. Galeski, "Plastic yielding of semicrystalline polymers affected by amorphous phase," *Int. J. Plasticity*, vol. 41, pp. 14–29, 2013.

[112] C. G'Sell, J. M. Hiver, A. Dahoun, and A. Souahi, "Video-controlled tensile testing of polymers and metals beyond the necking point," *J. Mater. Sci.*, vol. 27, no. 18, pp. 5031–5039, 1992.

[113] H. X. Li and C. P. Buckley, "Evolution of strain localization in glassy polymers: A numerical study," *Int. J. Solids Struct.*, vol. 46, no. 7, pp. 1607–1623, 2009.

[114] E. Parsons, M. C. Boyce, and D. M. Parks, "An experimental investigation of the large-strain tensile behavior of neat and rubber-toughened polycarbonate," *Polymer*, vol. 45, no. 8, pp. 2665–2684, 2004.

[115] L. Farge, S. André, and J. Boisse, "Use of digital image correlation to study the effect of temperature on the development of plastic instabilities in a semi-crystalline polymer," *Polymer*, vol. 153, pp. 295–304, 2018.

[116] J. Mohanraj, D. C. Barton, I. M. Ward, A. Dahoun, J. M. Hiver, and C. G'Sell, "Plastic deformation and damage of polyoxymethylene in the large strain range at elevated temperatures," *Polymer*, vol. 47, no. 16, pp. 5852–5861, 2006.

[117] S. Cooreman, D. Lecompte, H. Sol, J. Vantomme, and D. Debruyne, "Elasto-plastic material parameter identification by inverse methods: Calculation of the sensitivity matrix," *Int. J. Solids Struct.*, vol. 44, no. 13, pp. 4329–4341, 2007.

[118] M. Polanco-Loria, H. Daiyan, and F. Grytten, "Material parameters identification: An inverse modeling methodology applicable for thermoplastic materials," *Pol. Eng. Sci.*, vol. 52, no. 2, pp. 438–448, 2012.

[119] X. Wang, H. Li, K. Chandrashekhara, S. A. Rummel, S. Lekakh, D. C. V. Aken], and R. J. O'Malley, "Inverse finite element modeling of the barreling effect on experimental stress-strain curve for high temperature steel compression test," *J. Mater. Process. Technol.*, vol. 243, pp. 465–473, 2017.

[120] Y. Tomita, T. Adachi, and P. S. Sik, "Computational simulation of three-dimensional neck propagation in polymeric specimens under tension and hybrid identification of constitutive equation," *Int. J. Mech. Sci.*, vol. 39, no. 8, pp. 913–923, 1997.

[121] D. Rittel, "On the conversion of plastic work to heat during high strain rate deformation of glassy polymers," *Mech. Mater.*, vol. 31, no. 2, pp. 131–139, 1999.

[122] E. M. Arruda, M. C. Boyce, and R. Jayachandran, "Effects of strain rate, temperature and thermomechanical coupling on the finite strain deformation of glassy polymers," *Mech. Mater.*, vol. 19, no. 2, pp. 193–212, 1995.

[123] A. Marquez-Lucero, C. G'Sell, and K. Neale, "Experimental investigation of neck propagation in polymers," *Polymer*, vol. 30, no. 4, pp. 636 – 642, 1989.

[124] G. Shao, S. Zhu, Y. Wang, and Q. Zhao, "An internal state variable thermodynamic model for determining the Taylor-Quinney coefficient of glassy polymers," *Int. J. Mech. Sci.*, vol. 126, pp. 261–269, 2017.

[125] *Abaqus Analysis User's Guide, Version 6.14*. United States, 2014.

[126] A. Peterlin, "Molecular model of drawing polyethylene and polypropylene," *J. Mater. Sci.*, vol. 6, no. 6, pp. 490–508, 1971.

[127] J. E. Hurtado, *Kinematic and Kinetic Principles*. Lulu.com, 2016.

[128] L. Lin and A. S. Argon, "Structure and plastic deformation of polyethylene," *J. Mater. Sci.*, vol. 29, no. 2, pp. 294–323, 1994.

[129] Transvalor S. A., France, *Z-set Materials Manual Version 9.0*.

[130] J. Besson and R. Foerch, "Large scale object-oriented finite element code design," *Comput. Methods Appl. Mech. Eng.*, vol. 142, no. 1, pp. 165–187, 1997.

[131] J. A. Nelder and R. Mead, "A simplex method for function minimization," *Comput. J.*, vol. 7, no. 4, pp. 308–313, 1965.

[132] T. D. Fornes and D. R. Paul, "Crystallization behavior of nylon 6 nanocomposites," *Polymer*, vol. 44, no. 14, pp. 3945–3961, 2003.

[133] R. Séguéla, "On the strain-induced crystalline phase changes in semi-crystalline polymers: Mechanisms and incidence on the mechanical properties," *J. Macromol. Sci., Part C: Polym. Rev.*, vol. 45, no. 3, pp. 263–287, 2005.

[134] V. Miri, O. Persyn, R. Séguéla, and J. M. Lefebvre, "On the deformation induced order–ĂŞdisorder transitions in the crystalline phase of polyamide 6," *Eur. Polym. J.*, vol. 47, no. 1, pp. 88–97, 2011.

[135] M. A. Guseva, V. A. Gerasin, B. F. Shklyaruk, and V. A. Dubinskiy, "Relation between thermal effects and structural changes under deformation of thermoplastics," *Polymer*, vol. 144, pp. 18–32, 2018.

[136] G.-F. Shan, W. Yang, B.-H. Xie, Z.-M. Li, J. Chen, and M.-B. Yang, "Double yielding behaviors of polyamide 6 and glass bead filled polyamide 6 composites," *Polym. Test.*, vol. 24, no. 6, pp. 704–711, 2005.

[137] G.-F. Shan, W. Yang, M.-B. Yang, B.-H. Xie, Z. ming Li, and J.-M. Feng, "Effect of crystallinity level on the double yielding behavior of polyamide 6," *Polym. Test.*, vol. 25, no. 4, pp. 452–459, 2006.

[138] G.-F. Shan, W. Yang, M.-B. Yang, B.-H. Xie, J.-M. Feng, and Q. Fu, "Effect of temperature and strain rate on the tensile deformation of polyamide 6," *Polymer*, vol. 48, no. 10, pp. 2958–2968, 2007.

[139] A. Pawlak and A. Galeski, "Cavitation and morphological changes in polypropylene deformed at elevated temperatures," *J. Polym. Sci., Part B: Polym. Phys.*, vol. 48, no. 12, pp. 1271–1280, 2010.

[140] C. Regrain, L. Laiarinandrasana, S. Toillon, and K. Saï, "Multi-mechanism models for semi-crystalline polymer: Constitutive relations and finite element implementation," *Int. J. Plasticity*, vol. 25, no. 7, pp. 1253–1279, 2009.

[141] R. Séguéla, "On the natural draw ratio of semi-crystalline polymers: Review of the mechanical, physical and molecular aspects," *Macromol. Mater. Eng.*, vol. 292, no. 3, pp. 235–244, 2007.

[142] H. X. Li and C. P. Buckley, "Necking in glassy polymers: Effects of intrinsic anisotropy and structural evolution kinetics in their viscoplastic flow," *Int. J. Plasticity*, vol. 26, no. 12, pp. 1726–1745, 2010.

[143] W. Dong and P. Gijsman, "Influence of temperature on the thermo-oxidative degradation of polyamide 6 films," *Polym. Degrad. Stab.*, vol. 95, no. 6, pp. 1054–1062, 2010.

[144] A. A. Benzerga and J.-B. Leblond, "Effective yield criterion accounting for microvoid coalescence," *J. Appl. Mech.*, vol. 81, no. 3, pp. 031009–1–7, 2014. 031009.

[145] M. E. Torki, A. A. Benzerga, and J.-B. Leblond, "On void coalescence under combined tension and shear," *J. Appl. Mech.*, vol. 82, no. 7, pp. 071005–1–15, 2015. 071005.

[146] A. Pineau, A. A. Benzerga, and T. Pardoen, "Failure of metals I: Brittle and ductile fracture," *Acta Mater.*, vol. 107, pp. 424 – 483, 2016.

[147] F. M. Schaller, S. C. Kapfer, M. E. Evans, M. J. Hoffmann, T. Aste, M. Saadatfar, K. Mecke, G. W. Delaney, and G. E. Schröder-Turk, "Set Voronoi diagrams of 3D assemblies of aspherical particles," *Phil. Mag.*, vol. 93, no. 31–33, pp. 3993–4017, 2013.

[148] A. K. Rodriguez, *Characterization and Thermo-Mechanical Modeling of UV-Aged Semi-Crystalline Polymers*. PhD thesis, Texas A&M University, College Station, TX, December 2020.

[149] R. J. Hernandez, "Effect of water vapor on the transport properties of oxygen through polyamide packaging materials," *J. Food. Eng.*, vol. 22, no. 1, pp. 495–507, 1994.

[150] ASTM G154-12a, "Standard practice for operating fluorescent ultraviolet (UV) lamp apparatus for exposure of nonmetallic materials," standard, ASTM International, West Conshohocken, PA, December 2012.

[151] G. A. George and M. S. O'Shea, "The effect of morphology on the environmental degradation of nylon 6 under tensile load," *Polym. Degrad. Stab.*, vol. 28, no. 3, pp. 289–310, 1990.

INTRODUCTION TO THE APPENDICES

In addition to exploring aging-induced damage in semicrystalline thermoplastics, I wanted this dissertation to document, as completely as possible, all the work I did during my Ph.D.. However, research is often nonlinear, so a significant portion of the work was not needed in the main text of the dissertation. In order to create a full record of my Ph.D. research, and to document supporting details from the main text of secondary importance, a series of appendices have been written. These appendices are grouped into three categories: (1) supplementary information (Appendices A–D), (2) short studies (Appendices E–G), and (3) experimental databases (Appendices H–K).

Appendices A–D provide supporting information to the main text. Appendix A shows drawings of the experimental specimens used in this work. Appendix B reprints the Appendix from Ref. [88], which was the publication reprinted in this dissertation as Chapter 3. Appendix C enumerates the terms of the Jacobian matrix for the viscoplastic semicrystalline polymer constitutive model that was described in Chapter 6. It also shows the equation used to calculate the consistent tangent matrix. Appendix D lists parameters entering into the micromechanics-based continuum damage model presented in Chapter 7. This information already described in both Refs. [34] and [80], but was included here anyway to provide a complete and independent description of the model.

Appendices E–G are reports over short studies that did not warrant inclusion in the main text. Appendix E reports the mechanical behavior of dried and undried RN10 bars of PA-6. In this way, the effects of moisture on the mechanical behavior of PA-6 is explored. Appendix F reports on the effects of combined hygrothermal and UV aging (HUV aging) on the mechanical behavior of PA-6. In general, the additional hygrothermal component of aging was found to have a negligible impact the chemical aging of PA-6, so experiments on specimens subjected to this type of aging were removed from the main text wherever

possible. Appendix G reports on the anisotropoic behavior of UV-aged LDPE films. These experiments were done in collaboration with Ana K. Rodriguez.

Appendices H–K serve as databases for experimental results from specimens of a single geometry. Appendix H documents all stress–strain curves for cylindrical tension specimens. Additionally, different extensometry methods are discussed. Appendix I documents all stress–strain curves for compression pins. Additionally, the effect of aging on PA-6 loaded in compression is presented, since aged compression pins are not discussed in the main text. Appendix J documents all stress–strain curves for PA-6 films with a thickness of 0.060 mm. Appendix K documents all stress–strain curves for PA-6 films with a thickness of 0.01 mm.

APPENDIX A. SUPPLEMENTARY INFORMATION: SPECIMEN GEOMETRIES

Several types of specimens for mechanical testing are described in Chapters 3–7. For brevity, detailed drawings of the specimens were omitted from those chapters, but have been included here.

Fig. A.1 shows drawings of the bulk specimens used in this dissertation. From left to right, the specimens are referred to as a cylindrical bar (or smooth round bar), an RN10 bar, an RN2 bar, and a compression pin. Refer to Section 4.2 for details of notched bar nomenclature. The specimens depicted in Fig. A.1 were machined from a 0.5 in thick cast plate of PA-6 obtained from Plastics International.

The bulk specimens appear in the following chapters:

- The cylindrical bars are referenced in Chapters 3, 4, and 6, as well as Appendices B, F and H.
- The RN10 and RN2 bars are referenced in Chapters 4, 6, and 7, as well as Appendix E.
- The compression pins are referenced in Chapter 6 and Appendix I.

Fig. A.2 shows drawings of the film specimen used for mechanical tests without synchrotron tomography. Specimens of this type were cut from a PA-6 film of thickness 0.060 mm obtained from Goodfellow. Film specimens using this geometry appear in Chapter 3 as well as Appendices B, F and J. Additionally, the PE specimens studied in Appendix G use this specimen geometry.

Fig. A.3 shows drawings of the film specimen used for experiments using *in situ* synchrotron tomography. These specimens were specifically designed for compatibility with the test frame *Bulky* [29]. Specimens of this type were cut from a PA-6 film of thickness 0.100 mm obtained from Goodfellow. Film specimens using this geometry appear in Chapter 3 and 5, as well as Appendices B and K.

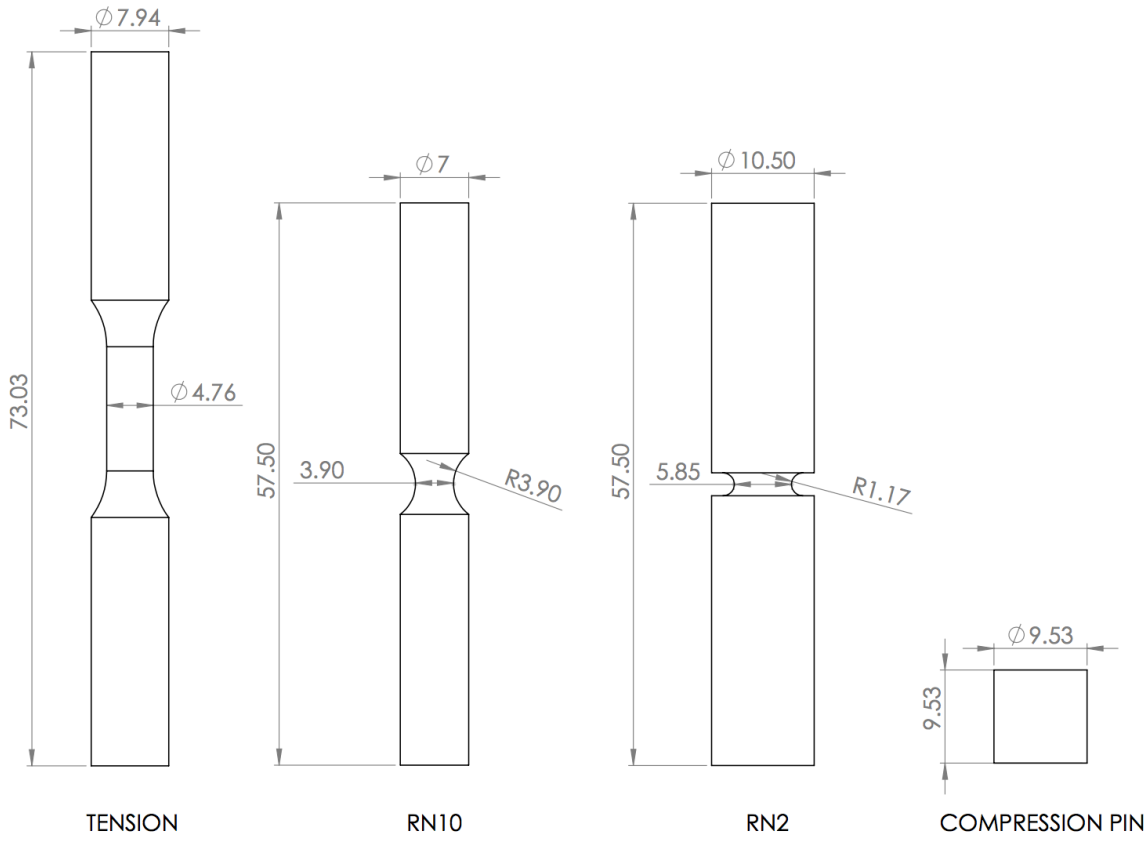

Figure A.1: Drawings of bulk specimens. These specimens were machined from a cast plate of PA-6. From left to right, a cylindrical bar (or smooth round bar), an RN10 bar, an RN2 bar, and a cylindrical compression pin. Dimensions are in mm.

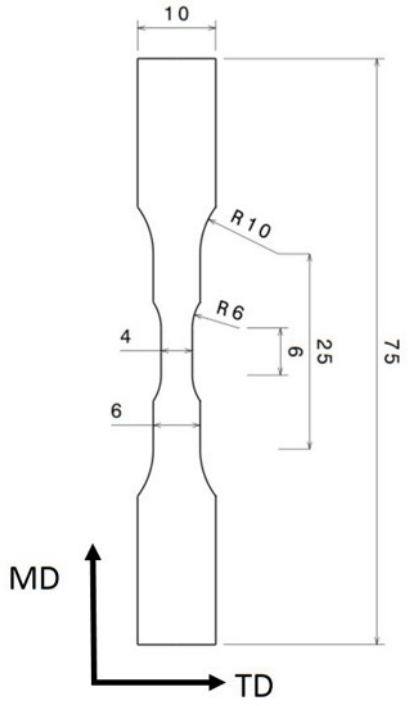

Figure A.2: Drawing of a film specimen used for mechanical testing. Film specimens using this geometry were cut from a film with thickness 0.060 mm. MD stands for mold direction and TD stands for transverse direction. These abbreviations denote the orientation of the specimen relative to the film from which it was cut. Dimensions are in mm.

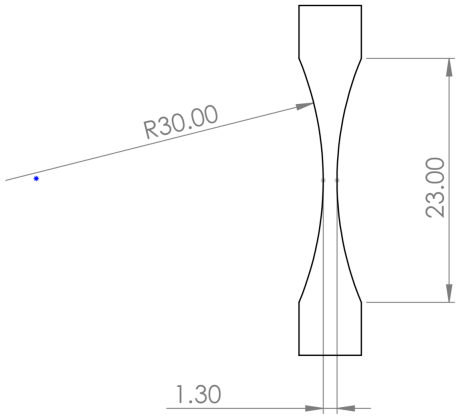

Figure A.3: Drawing of the film specimen used for *in situ* synchrotron tomography experiments. Film specimens using this geometry were cut from a film with thickness 0.100 mm. Dimensions are in mm.

Thermograms from the DSC analysis used to determine the crystallinity of unaged and photo-oxidized 0.06 mm-thick films are shown in Fig. B.1. As the film is subjected to more aging, the melting peaks become broader, possibly indicating a wider range of lamellar thicknesses.

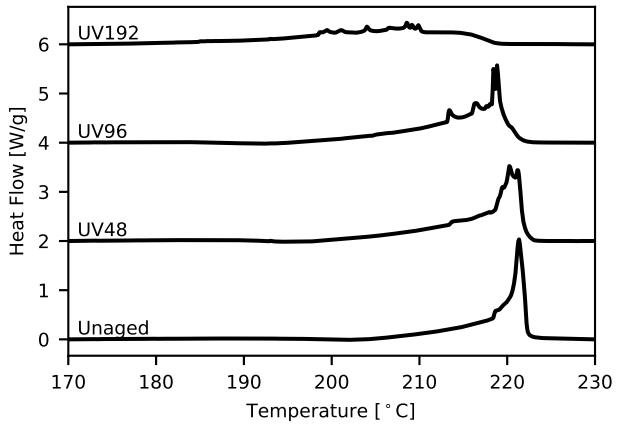

Figure B.1: Thermograms of photo-oxidized and unaged PA-6 films (endothermic up). Curves are shifted vertically for ease of comparison.

Reprinted with permission from "Photo-oxidation of semicrystalline polymers: Damage nucleation versus growth", by K. N. Cundiff, Y. Madi, and A. A. Benzerga. *Polymer*, vol. 188, p.122090, 2020. Copyright [2020] by Elsevier [88].

Where the present appendix refers to online supplementary information, refer to the online version of the original article [88].

In Fig. B.2, the true axial stress, F/A is plotted against $\lambda^2 - \lambda^{-1}$. The stretch, λ, is calculated from the true strain as determined by contour tracking, i.e.

$$\lambda = 1 + \varepsilon = 1 + 2 \ln W_0/W \tag{B.1}$$

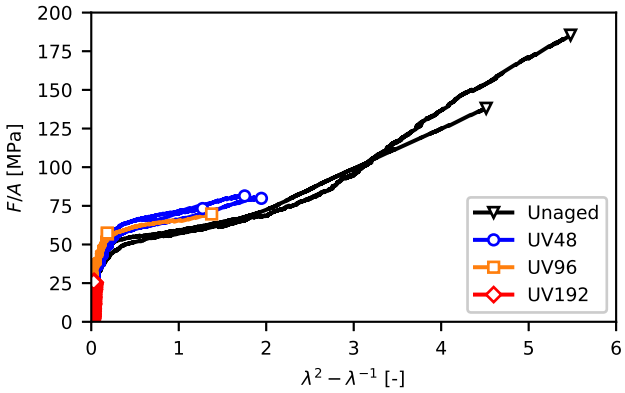

Figure B.2: The stress–stretch response, as calculated by contour tracking, of photo-oxidized and unaged PA-6 films tested at room temperature (24 °C) and with a nominal strain rate of 10^{-3} /s.

Videos of mechanical tests on cylindrical bars with animated nominal and true stress–strain curves are included in the online material. Videos are included for the loading of an unaged bar (Vid. B.1), a UV192 bar (Vid. B.2), a UV48 bar (Vid. B.3), and a UV96 bar (Vid. B.4).

All X-ray absorption projections from synchrotron tomography are presented as videos and available online. Vid. B.5 presents projections from the width plane of the specimen and Vid. B.6 presents projections from the thickness plane. The force and time at which the scans were taken is presented in Fig. B.3.

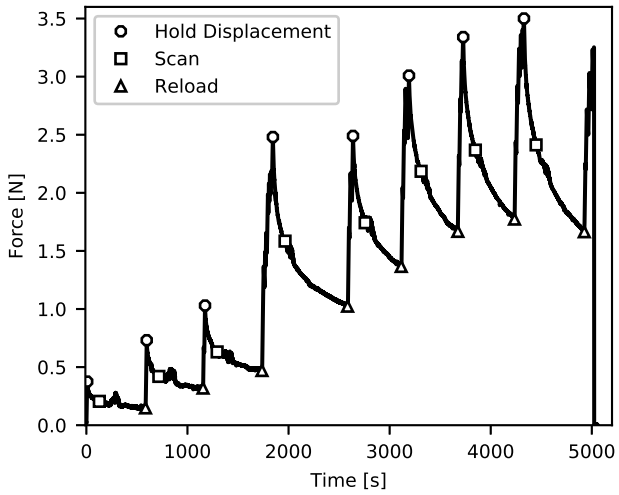

Figure B.3: Load versus time for the *in situ* synchrotron tomography tensile testing of the irradiated PA-6 film of Fig. 3.12.

APPENDIX C. SUPPLEMENTARY INFORMATION: IMPLEMENTATION OF THE SEMICRYSTALLINE MACROMOLECULAR MODEL

The material in this appendix contains supplementary information for Section 6.5, which covers the implementation of the semicrystalline macromolecular model. First, the components of the Jacobian matrix, $\left[\frac{\partial[R]}{\partial[X]}\right]$, are presented in Section C.1. Second, a more complete expression for the consistent tangent matrix, $\mathbb{L}$, is given in Section C.2, along with components of the matrix $\left[\frac{\partial[R]}{\partial\tilde{\boldsymbol{D}}}\right]$, which is used to calculate $\mathbb{L}$.

Some definitions for mathematical symbols used in this appendix:

- δ_{ij} is the Kronecker delta, $\delta_{ij} = 1$ for $i = j$ and $\delta_{ij} = 0$ for $i \neq j$.
- $\mathbb{J}$ is the fourth-order deviatoric projector, $J_{ijkl} = \frac{1}{2}\left(\delta_{ik}\delta_{jl} + \delta_{il}\delta_{jk}\right) - \frac{1}{3}\delta_{ij}\delta_{kl}$
- $\mathbb{O}$ is the fourth-order zero tensor, $O_{ijkl} = 0$
- $\boldsymbol{I}$ is the second-order identity tensor, $I_{ij} = \delta_{ij}$
- $\mathbf{0}$ is the second-order zero tensor, $0_{ij} = 0$
- $\otimes$ denotes the dyadic product, $(\boldsymbol{A} \otimes \boldsymbol{B})_{ijkl} = A_{ij}B_{kl}$.

C.1 Calculation of the Jacobian matrix

The Newton-Raphson method is used to iteratively solve Eqs. (6.41)–(6.49) for $[R] = [0]$:

$$[X]^{i+1} = [X]^{i} - \left[\frac{\partial\,[R]}{\partial\,[X]}\right]^{-1}[R]\,, \tag{C.1}$$

where i is the increment number. The Jacobian matrix, $\left[\frac{\partial[R]}{\partial[X]}\right]$ must be evaluated. Its terms are given below.

Derivatives of $R_{\tilde{\boldsymbol{\sigma}}'_{\mathrm{a}}}$

$$\frac{\partial R_{\tilde{\boldsymbol{\sigma}}'_{\mathrm{a}}}}{\partial \tilde{\boldsymbol{\sigma}}'_{\mathrm{a}}} = \left(\frac{1}{2\mu_{\mathrm{a}}\Delta t} + \frac{3\tilde{\dot{\varepsilon}}^{\mathrm{p}}_{\mathrm{a}}}{2\tilde{\bar{\sigma}}_{\mathrm{a}}}\right)\mathbb{J} + \left(\frac{3}{2\tilde{\bar{\sigma}}_{\mathrm{a}}}\right)^2 \left(\frac{\partial \tilde{\dot{\varepsilon}}^{\mathrm{p}}_{\mathrm{a}}}{\partial \tilde{\bar{\sigma}}_{\mathrm{a}}} - \frac{\tilde{\dot{\varepsilon}}^{\mathrm{p}}_{\mathrm{a}}}{\tilde{\bar{\sigma}}_{\mathrm{a}}}\right)\left(\tilde{\boldsymbol{\sigma}}'_{\mathrm{a}} - \tilde{\boldsymbol{b}}'\right) \otimes \left(\tilde{\boldsymbol{\sigma}}'_{\mathrm{a}} - \tilde{\boldsymbol{b}}'\right) \tag{C.2}$$

$$\frac{\partial R_{\tilde{\boldsymbol{\sigma}}'_{\mathrm{a}}}}{\partial \tilde{\boldsymbol{\sigma}}'_{\mathrm{c}}} = \mathbb{O} \tag{C.3}$$

$$\frac{\partial R_{\tilde{\boldsymbol{\sigma}}'_{\mathrm{a}}}}{\partial \tilde{\boldsymbol{b}}'} = \left(\frac{3}{2\tilde{\bar{\sigma}}_{\mathrm{a}}}\right)^2 \left(-\frac{\partial \tilde{\dot{\varepsilon}}^{\mathrm{p}}_{\mathrm{a}}}{\partial \tilde{\bar{\sigma}}_{\mathrm{a}}} + \frac{\tilde{\dot{\varepsilon}}^{\mathrm{p}}_{\mathrm{a}}}{\tilde{\bar{\sigma}}_{\mathrm{a}}}\right)\left(\tilde{\boldsymbol{\sigma}}'_{\mathrm{a}} - \tilde{\boldsymbol{b}}'\right) \otimes \left(\tilde{\boldsymbol{\sigma}}'_{\mathrm{a}} - \tilde{\boldsymbol{b}}'\right) - \left(\frac{3\tilde{\dot{\varepsilon}}^{\mathrm{p}}_{\mathrm{a}}}{\tilde{\bar{\sigma}}_{\mathrm{a}}}\right)\mathbb{J} \tag{C.4}$$

$$\frac{\partial R_{\tilde{\boldsymbol{\sigma}}'_{\mathrm{a}}}}{\partial \tilde{b}_{\mathrm{m}}} = \mathbf{0} \tag{C.5}$$

$$\frac{\partial R_{\tilde{\boldsymbol{\sigma}}'_{\mathrm{a}}}}{\partial \tilde{\sigma}_{\mathrm{a,m}}} = \frac{3}{2\tilde{\bar{\sigma}}_{\mathrm{a}}}\left(\frac{\partial \tilde{\dot{\varepsilon}}^{\mathrm{p}}_{\mathrm{a}}}{\partial \tilde{\sigma}_{\mathrm{a,m}}}\right)\left(\tilde{\boldsymbol{\sigma}}'_{\mathrm{a}} - \tilde{\boldsymbol{b}}'\right) \tag{C.6}$$

$$\frac{\partial R_{\tilde{\boldsymbol{\sigma}}'_{\mathrm{a}}}}{\partial \tilde{\sigma}_{\mathrm{c,m}}} = \mathbf{0} \tag{C.7}$$

$$\frac{\partial R_{\tilde{\boldsymbol{\sigma}}'_{\mathrm{a}}}}{\partial s_{\mathrm{a}}} = \frac{3}{2\tilde{\bar{\sigma}}_{\mathrm{a}}}\left(\frac{\partial \tilde{\dot{\varepsilon}}^{\mathrm{p}}_{\mathrm{a}}}{\partial s_{\mathrm{a}}}\right)\left(\tilde{\boldsymbol{\sigma}}'_{\mathrm{a}} - \tilde{\boldsymbol{b}}'\right) \tag{C.8}$$

$$\frac{\partial R_{\tilde{\boldsymbol{\sigma}}'_{\mathrm{a}}}}{\partial s_{\mathrm{c}}} = \mathbf{0} \tag{C.9}$$

$$\frac{\partial R_{\tilde{\boldsymbol{\sigma}}'_{\mathrm{a}}}}{\partial \chi} = \mathbf{0} \tag{C.10}$$

Derivatives of $R_{\tilde{\boldsymbol{\sigma}}'_{\mathrm{c}}}$

$$\frac{\partial R_{\tilde{\boldsymbol{\sigma}}'_{\mathrm{c}}}}{\partial \tilde{\boldsymbol{\sigma}}'_{\mathrm{a}}} = \mathbb{O} \tag{C.11}$$

$$\frac{\partial R_{\tilde{\boldsymbol{\sigma}}'_{\mathrm{c}}}}{\partial \tilde{\boldsymbol{\sigma}}'_{\mathrm{c}}} = \left(\frac{1}{2\mu_{\mathrm{c}}\Delta t} + \frac{3\tilde{\dot{\varepsilon}}^{\mathrm{p}}_{\mathrm{c}}}{2\tilde{\bar{\sigma}}_{\mathrm{c}}}\right)\mathbb{J} + \left(\frac{3}{2\tilde{\bar{\sigma}}_{\mathrm{c}}}\right)^2 \left(\frac{\partial \tilde{\dot{\varepsilon}}^{\mathrm{p}}_{\mathrm{c}}}{\partial \tilde{\bar{\sigma}}_{\mathrm{c}}} - \frac{\tilde{\dot{\varepsilon}}^{\mathrm{p}}_{\mathrm{c}}}{\tilde{\bar{\sigma}}_{\mathrm{c}}}\right)\left(\tilde{\boldsymbol{\sigma}}'_{\mathrm{c}} - \tilde{\boldsymbol{b}}'\right) \otimes \left(\tilde{\boldsymbol{\sigma}}'_{\mathrm{c}} - \tilde{\boldsymbol{b}}'\right) \tag{C.12}$$

$$\frac{\partial R_{\tilde{\boldsymbol{\sigma}}'_{\mathrm{c}}}}{\partial \tilde{\boldsymbol{b}}'} = \left(\frac{3}{2\tilde{\bar{\sigma}}_{\mathrm{c}}}\right)^2 \left(-\frac{\partial \tilde{\dot{\varepsilon}}^{\mathrm{p}}_{\mathrm{c}}}{\partial \tilde{\bar{\sigma}}_{\mathrm{c}}} + \frac{\tilde{\dot{\varepsilon}}^{\mathrm{p}}_{\mathrm{c}}}{\tilde{\bar{\sigma}}_{\mathrm{c}}}\right)\left(\tilde{\boldsymbol{\sigma}}'_{\mathrm{c}} - \tilde{\boldsymbol{b}}'\right) \otimes \left(\tilde{\boldsymbol{\sigma}}'_{\mathrm{c}} - \tilde{\boldsymbol{b}}'\right) - \left(\frac{3\tilde{\dot{\varepsilon}}^{\mathrm{p}}_{\mathrm{c}}}{\tilde{\bar{\sigma}}_{\mathrm{c}}}\right)\mathbb{J} \tag{C.13}$$

$$\frac{\partial R_{\tilde{\boldsymbol{\sigma}}'_{\mathrm{c}}}}{\partial \tilde{b}_{\mathrm{m}}} = \mathbf{0} \tag{C.14}$$

$$\frac{\partial R_{\tilde{\boldsymbol{\sigma}}'_{\mathrm{c}}}}{\partial \tilde{\sigma}_{\mathrm{a,m}}} = \mathbf{0} \tag{C.15}$$

$$\frac{\partial R_{\tilde{\boldsymbol{\sigma}}'_{\mathrm{c}}}}{\partial \tilde{\sigma}_{\mathrm{c,m}}} = \frac{3}{2\tilde{\bar{\sigma}}_{\mathrm{c}}} \left(\frac{\partial \tilde{\dot{\bar{\varepsilon}}}^{\mathrm{p}}_{\mathrm{c}}}{\partial \tilde{\sigma}_{\mathrm{c,m}}} \right) \left(\tilde{\boldsymbol{\sigma}}'_{\mathrm{c}} - \tilde{\boldsymbol{b}}' \right) \tag{C.16}$$

$$\frac{\partial R_{\tilde{\boldsymbol{\sigma}}'_{\mathrm{c}}}}{\partial s_{\mathrm{a}}} = \mathbf{0} \tag{C.17}$$

$$\frac{\partial R_{\tilde{\boldsymbol{\sigma}}'_{\mathrm{c}}}}{\partial s_{\mathrm{c}}} = \frac{3}{2\tilde{\bar{\sigma}}_{\mathrm{c}}} \left(\frac{\partial \tilde{\dot{\bar{\varepsilon}}}^{\mathrm{p}}_{\mathrm{c}}}{\partial s_{\mathrm{c}}} \right) \left(\tilde{\boldsymbol{\sigma}}'_{\mathrm{c}} - \tilde{\boldsymbol{b}}' \right) \tag{C.18}$$

$$\frac{\partial R_{\tilde{\boldsymbol{\sigma}}'_{\mathrm{c}}}}{\partial \chi} = \mathbf{0} \tag{C.19}$$

Derivatives of $R_{\tilde{\boldsymbol{b}}'}$

$$\frac{\partial R_{\tilde{\boldsymbol{b}}'}}{\partial \tilde{\boldsymbol{\sigma}}'_{\mathrm{a}}} = \mathbb{O} \tag{C.20}$$

$$\frac{\partial R_{\tilde{\boldsymbol{b}}'}}{\partial \tilde{\boldsymbol{\sigma}}'_{\mathrm{c}}} = \mathbb{O} \tag{C.21}$$

$$\frac{\partial R_{\tilde{\boldsymbol{b}}'}}{\partial \tilde{\boldsymbol{b}}'} = \frac{1}{\Delta t} \mathbb{J} \tag{C.22}$$

$$\frac{\partial R_{\tilde{\boldsymbol{b}}'}}{\partial \tilde{b}_{\mathrm{m}}} = \mathbf{0} \tag{C.23}$$

$$\frac{\partial R_{\tilde{\boldsymbol{b}}'}}{\partial \tilde{\sigma}_{\mathrm{a,m}}} = \mathbf{0} \tag{C.24}$$

$$\frac{\partial R_{\tilde{\boldsymbol{b}}'}}{\partial \tilde{\sigma}_{\mathrm{c,m}}} = \mathbf{0} \tag{C.25}$$

$$\frac{\partial R_{\tilde{\boldsymbol{b}}'}}{\partial s_{\mathrm{a}}} = \mathbf{0} \tag{C.26}$$

$$\frac{\partial R_{\tilde{\boldsymbol{b}}'}}{\partial s_{\mathrm{c}}} = \mathbf{0} \tag{C.27}$$

$$\frac{\partial R_{\tilde{\boldsymbol{b}}'}}{\partial \chi} = \mathbf{0} \tag{C.28}$$

Derivatives of $R_{\tilde{b}_\mathrm{m}}$

$$\frac{\partial R_{\tilde{b}_\mathrm{m}}}{\partial \tilde{\boldsymbol{\sigma}}'_\mathrm{a}} = \mathbf{0} \tag{C.29}$$

$$\frac{\partial R_{\tilde{b}_\mathrm{m}}}{\partial \tilde{\boldsymbol{\sigma}}'_\mathrm{c}} = \mathbf{0} \tag{C.30}$$

$$\frac{\partial R_{\tilde{b}_\mathrm{m}}}{\partial \tilde{\boldsymbol{b}}'} = \mathbf{0} \tag{C.31}$$

$$\frac{\partial R_{\tilde{b}_\mathrm{m}}}{\partial \tilde{b}_\mathrm{m}} = \frac{1}{\Delta t} \tag{C.32}$$

$$\frac{\partial R_{\tilde{b}_\mathrm{m}}}{\partial \tilde{\sigma}_\mathrm{a,m}} = 0 \tag{C.33}$$

$$\frac{\partial R_{\tilde{b}_\mathrm{m}}}{\partial \tilde{\sigma}_\mathrm{c,m}} = 0 \tag{C.34}$$

$$\frac{\partial R_{\tilde{b}_\mathrm{m}}}{\partial s_\mathrm{a}} = 0 \tag{C.35}$$

$$\frac{\partial R_{\tilde{b}_\mathrm{m}}}{\partial s_\mathrm{c}} = 0 \tag{C.36}$$

$$\frac{\partial R_{\tilde{b}_\mathrm{m}}}{\partial \chi} = 0 \tag{C.37}$$

Derivatives of $R_{\tilde{\sigma}_\mathrm{a,m}}$

$$\frac{\partial R_{\tilde{\sigma}_\mathrm{a,m}}}{\partial \tilde{\boldsymbol{\sigma}}'_\mathrm{a}} = \mathbf{0} \tag{C.38}$$

$$\frac{\partial R_{\tilde{\sigma}_\mathrm{a,m}}}{\partial \tilde{\boldsymbol{\sigma}}'_\mathrm{c}} = \mathbf{0} \tag{C.39}$$

$$\frac{\partial R_{\tilde{\sigma}_\mathrm{a,m}}}{\partial \tilde{\boldsymbol{b}}'} = \mathbf{0} \tag{C.40}$$

$$\frac{\partial R_{\tilde{\sigma}_\mathrm{a,m}}}{\partial \tilde{b}_\mathrm{m}} = 0 \tag{C.41}$$

$$\frac{\partial R_{\tilde{\sigma}_\mathrm{a,m}}}{\partial \tilde{\sigma}_\mathrm{a,m}} = \frac{1}{\Delta t} \tag{C.42}$$

$$\frac{\partial R_{\tilde{\sigma}_{\mathrm{a,m}}}}{\partial \tilde{\sigma}_{\mathrm{c,m}}} = 0 \tag{C.43}$$

$$\frac{\partial R_{\tilde{\sigma}_{\mathrm{a,m}}}}{\partial s_{\mathrm{a}}} = 0 \tag{C.44}$$

$$\frac{\partial R_{\tilde{\sigma}_{\mathrm{a,m}}}}{\partial s_{\mathrm{c}}} = 0 \tag{C.45}$$

$$\frac{\partial R_{\tilde{\sigma}_{\mathrm{a,m}}}}{\partial \chi} = 0 \tag{C.46}$$

Derivatives of $R_{\tilde{\sigma}_{\mathrm{c,m}}}$

$$\frac{\partial R_{\tilde{\sigma}_{\mathrm{c,m}}}}{\partial \tilde{\boldsymbol{\sigma}}'_{\mathrm{a}}} = \mathbf{0} \tag{C.47}$$

$$\frac{\partial R_{\tilde{\sigma}_{\mathrm{c,m}}}}{\partial \tilde{\boldsymbol{\sigma}}'_{\mathrm{c}}} = \mathbf{0} \tag{C.48}$$

$$\frac{\partial R_{\tilde{\sigma}_{\mathrm{c,m}}}}{\partial \tilde{\boldsymbol{b}}'} = \mathbf{0} \tag{C.49}$$

$$\frac{\partial R_{\tilde{\sigma}_{\mathrm{c,m}}}}{\partial \tilde{b}_{\mathrm{m}}} = 0 \tag{C.50}$$

$$\frac{\partial R_{\tilde{\sigma}_{\mathrm{c,m}}}}{\partial \tilde{\sigma}_{\mathrm{a,m}}} = 0 \tag{C.51}$$

$$\frac{\partial R_{\tilde{\sigma}_{\mathrm{c,m}}}}{\partial \tilde{\sigma}_{\mathrm{c,m}}} = \frac{1}{\Delta t} \tag{C.52}$$

$$\frac{\partial R_{\tilde{\sigma}_{\mathrm{c,m}}}}{\partial s_{\mathrm{a}}} = 0 \tag{C.53}$$

$$\frac{\partial R_{\tilde{\sigma}_{\mathrm{c,m}}}}{\partial s_{\mathrm{c}}} = 0 \tag{C.54}$$

$$\frac{\partial R_{\tilde{\sigma}_{\mathrm{c,m}}}}{\partial \chi} = 0 \tag{C.55}$$

Derivatives of R_{s_a}

$$\frac{\partial R_{s_\mathrm{a}}}{\partial \tilde{\boldsymbol{\sigma}}'_\mathrm{a}} = -\left[\frac{\partial H_{1,\mathrm{a}}}{\partial \tilde{\boldsymbol{\sigma}}'_\mathrm{a}}\left(1-\frac{s_\mathrm{a}}{s_{1,\mathrm{a}}}\right)+\frac{\partial H_{2,\mathrm{a}}}{\partial \tilde{\boldsymbol{\sigma}}'_\mathrm{a}}\left(1-\frac{s_\mathrm{a}}{s_{2,\mathrm{a}}}\right)\right]\tilde{\dot{\varepsilon}}^\mathrm{p}_\mathrm{a} \tag{C.56}$$

$$-\left[H_{1,\mathrm{a}}\left(1-\frac{s_\mathrm{a}}{s_{1,\mathrm{a}}}\right)+H_{2,\mathrm{a}}\left(1-\frac{s_\mathrm{a}}{s_{2,\mathrm{a}}}\right)\right]\frac{\partial \tilde{\dot{\varepsilon}}^\mathrm{p}_\mathrm{a}}{\partial \tilde{\boldsymbol{\sigma}}'_\mathrm{a}}$$

$$\frac{\partial R_{s_\mathrm{a}}}{\partial \tilde{\boldsymbol{\sigma}}'_\mathrm{c}} = \mathbf{0} \tag{C.57}$$

$$\frac{\partial R_{s_\mathrm{a}}}{\partial \tilde{\boldsymbol{b}}'} = -\left[\frac{\partial H_{1,\mathrm{a}}}{\partial \tilde{\boldsymbol{b}}'}\left(1-\frac{s_\mathrm{a}}{s_{1,\mathrm{a}}}\right)+\frac{\partial H_{2,\mathrm{a}}}{\partial \tilde{\boldsymbol{b}}'}\left(1-\frac{s_\mathrm{a}}{s_{2,\mathrm{a}}}\right)\right]\tilde{\dot{\varepsilon}}^\mathrm{p}_\mathrm{a} \tag{C.58}$$

$$-\left[H_{1,\mathrm{a}}\left(1-\frac{s_\mathrm{a}}{s_{1,\mathrm{a}}}\right)+H_{2,\mathrm{a}}\left(1-\frac{s_\mathrm{a}}{s_{2,\mathrm{a}}}\right)\right]\frac{\partial \tilde{\dot{\varepsilon}}^\mathrm{p}_\mathrm{a}}{\partial \tilde{\boldsymbol{b}}'}$$

$$\frac{\partial R_{s_\mathrm{a}}}{\partial \tilde{b}_\mathrm{m}} = 0 \tag{C.59}$$

$$\frac{\partial R_{s_\mathrm{a}}}{\partial \tilde{\sigma}_{\mathrm{a,m}}} = -\left[\frac{\partial H_{1,\mathrm{a}}}{\partial \tilde{\sigma}_{\mathrm{a,m}}}\left(1-\frac{s_\mathrm{a}}{s_{1,\mathrm{a}}}\right)+\frac{\partial H_{2,\mathrm{a}}}{\partial \tilde{\sigma}_{\mathrm{a,m}}}\left(1-\frac{s_\mathrm{a}}{s_{2,\mathrm{a}}}\right)\right]\tilde{\dot{\varepsilon}}^\mathrm{p}_\mathrm{a} \tag{C.60}$$

$$-\left[H_{1,\mathrm{a}}\left(1-\frac{s_\mathrm{a}}{s_{1,\mathrm{a}}}\right)+H_{2,\mathrm{a}}\left(1-\frac{s_\mathrm{a}}{s_{2,\mathrm{a}}}\right)\right]\frac{\partial \tilde{\dot{\varepsilon}}^\mathrm{p}_\mathrm{a}}{\partial \tilde{\sigma}_{\mathrm{a,m}}}$$

$$\frac{\partial R_{s_\mathrm{a}}}{\partial \tilde{\sigma}_{\mathrm{c,m}}} = 0 \tag{C.61}$$

$$\frac{\partial R_{s_\mathrm{a}}}{\partial s_\mathrm{a}} = \frac{1}{\Delta t} - \left[\frac{\partial H_{1,\mathrm{a}}}{\partial s_\mathrm{a}}\left(1-\frac{s_\mathrm{a}}{s_{1,\mathrm{a}}}\right)+\frac{\partial H_{2,\mathrm{a}}}{\partial s_\mathrm{a}}\left(1-\frac{s_\mathrm{a}}{s_{2,\mathrm{a}}}\right)-\frac{H_{1,\mathrm{a}}}{s_{1,\mathrm{a}}}-\frac{H_{2,\mathrm{a}}}{s_{2,\mathrm{a}}}\right]\tilde{\dot{\varepsilon}}^\mathrm{p}_\mathrm{a} \tag{C.62}$$

$$-\left[H_{1,\mathrm{a}}\left(1-\frac{s_\mathrm{a}}{s_{1,\mathrm{a}}}\right)+H_{2,\mathrm{a}}\left(1-\frac{s_\mathrm{a}}{s_{2,\mathrm{a}}}\right)\right]\frac{\partial \tilde{\dot{\varepsilon}}^\mathrm{p}_\mathrm{a}}{\partial s_\mathrm{a}}$$

$$\frac{\partial R_{s_\mathrm{a}}}{\partial s_\mathrm{c}} = 0 \tag{C.63}$$

$$\frac{\partial R_{s_\mathrm{a}}}{\partial \chi} = 0 \tag{C.64}$$

Derivatives of R_{s_c}

$$\frac{\partial R_{s_\mathrm{c}}}{\partial \tilde{\boldsymbol{\sigma}}'_\mathrm{a}} = \mathbf{0} \tag{C.65}$$

$$\begin{aligned}\frac{\partial R_{s_\mathrm{c}}}{\partial \tilde{\boldsymbol{\sigma}}'_\mathrm{c}} = &- \left[\frac{\partial H_{1,\mathrm{c}}}{\partial \tilde{\boldsymbol{\sigma}}'_\mathrm{c}}\left(1 - \frac{s_\mathrm{c}}{s_{1,\mathrm{c}}}\right) + \frac{\partial H_{2,\mathrm{c}}}{\partial \tilde{\boldsymbol{\sigma}}'_\mathrm{c}}\left(1 - \frac{s_\mathrm{c}}{s_{2,\mathrm{c}}}\right)\right]\tilde{\dot{\varepsilon}}^\mathrm{p}_\mathrm{c} \\ &- \left[H_{1,\mathrm{c}}\left(1 - \frac{s_\mathrm{c}}{s_{1,\mathrm{c}}}\right) + H_{2,\mathrm{c}}\left(1 - \frac{s_\mathrm{c}}{s_{2,\mathrm{c}}}\right)\right]\frac{\partial \tilde{\dot{\varepsilon}}^\mathrm{p}_\mathrm{c}}{\partial \tilde{\boldsymbol{\sigma}}'_\mathrm{c}}\end{aligned} \tag{C.66}$$

$$\begin{aligned}\frac{\partial R_{s_\mathrm{c}}}{\partial \tilde{\boldsymbol{b}}'} = &- \left[\frac{\partial H_{1,\mathrm{c}}}{\partial \tilde{\boldsymbol{b}}'}\left(1 - \frac{s_\mathrm{c}}{s_{1,\mathrm{c}}}\right) + \frac{\partial H_{2,\mathrm{c}}}{\partial \tilde{\boldsymbol{b}}'}\left(1 - \frac{s_\mathrm{c}}{s_{2,\mathrm{c}}}\right)\right]\tilde{\dot{\varepsilon}}^\mathrm{p}_\mathrm{c} \\ &- \left[H_{1,\mathrm{c}}\left(1 - \frac{s_\mathrm{c}}{s_{1,\mathrm{c}}}\right) + H_{2,\mathrm{c}}\left(1 - \frac{s_\mathrm{c}}{s_{2,\mathrm{c}}}\right)\right]\frac{\partial \tilde{\dot{\varepsilon}}^\mathrm{p}_\mathrm{c}}{\partial \tilde{\boldsymbol{b}}'}\end{aligned} \tag{C.67}$$

$$\frac{\partial R_{s_\mathrm{c}}}{\partial \tilde{b}_\mathrm{m}} = 0 \tag{C.68}$$

$$\frac{\partial R_{s_\mathrm{c}}}{\partial \tilde{\sigma}_{\mathrm{a,m}}} = 0 \tag{C.69}$$

$$\begin{aligned}\frac{\partial R_{s_\mathrm{c}}}{\partial \tilde{\sigma}_{\mathrm{c,m}}} = &- \left[\frac{\partial H_{1,\mathrm{c}}}{\partial \tilde{\sigma}_{\mathrm{c,m}}}\left(1 - \frac{s_\mathrm{c}}{s_{1,\mathrm{c}}}\right) + \frac{\partial H_{2,\mathrm{c}}}{\partial \tilde{\sigma}_{\mathrm{c,m}}}\left(1 - \frac{s_\mathrm{c}}{s_{2,\mathrm{c}}}\right)\right]\tilde{\dot{\varepsilon}}^\mathrm{p}_\mathrm{c} \\ &- \left[H_{1,\mathrm{c}}\left(1 - \frac{s_\mathrm{c}}{s_{1,\mathrm{c}}}\right) + H_{2,\mathrm{c}}\left(1 - \frac{s_\mathrm{c}}{s_{2,\mathrm{c}}}\right)\right]\frac{\partial \tilde{\dot{\varepsilon}}^\mathrm{p}_\mathrm{c}}{\partial \tilde{\sigma}_{\mathrm{c,m}}}\end{aligned} \tag{C.70}$$

$$\frac{\partial R_{s_\mathrm{c}}}{\partial s_\mathrm{a}} = 0 \tag{C.71}$$

$$\frac{\partial R_{s_\mathrm{c}}}{\partial s_\mathrm{c}} = \frac{1}{\Delta t} - \left[\frac{\partial H_{1,\mathrm{c}}}{\partial s_\mathrm{c}}\left(1 - \frac{s_\mathrm{c}}{s_{1,\mathrm{c}}}\right) + \frac{\partial H_{2,\mathrm{c}}}{\partial s_\mathrm{c}}\left(1 - \frac{s_\mathrm{c}}{s_{2,\mathrm{c}}}\right) - \frac{H_{1,\mathrm{c}}}{s_{1,\mathrm{c}}} - \frac{H_{2,\mathrm{c}}}{s_{2,\mathrm{c}}}\right]\tilde{\dot{\bar{\varepsilon}}}^{\mathrm{p}}_{\mathrm{c}} - \left[H_{1,\mathrm{c}}\left(1 - \frac{s_\mathrm{c}}{s_{1,\mathrm{c}}}\right) + H_{2,\mathrm{c}}\left(1 - \frac{s_\mathrm{c}}{s_{2,\mathrm{c}}}\right)\right]\frac{\partial \tilde{\dot{\bar{\varepsilon}}}^{\mathrm{p}}_{\mathrm{c}}}{\partial s_\mathrm{c}} \tag{C.72}$$

$$\frac{\partial R_{s_\mathrm{c}}}{\partial \chi} = 0 \tag{C.73}$$

Derivatives of R_χ

$$\frac{\partial R_\chi}{\partial \tilde{\boldsymbol{\sigma}}'_\mathrm{a}} = \mathbf{0} \tag{C.74}$$

$$\frac{\partial R_\chi}{\partial \tilde{\boldsymbol{\sigma}}'_\mathrm{c}} = \mathbf{0} \tag{C.75}$$

$$\frac{\partial R_\chi}{\partial \tilde{\boldsymbol{b}}'} = \mathbf{0} \tag{C.76}$$

$$\frac{\partial R_\chi}{\partial \tilde{b}_\mathrm{m}} = 0 \tag{C.77}$$

$$\frac{\partial R_\chi}{\partial \tilde{\sigma}_{\mathrm{a,m}}} = \phi_\infty \left\{ \frac{\tilde{\dot{\bar{\varepsilon}}}^{\mathrm{tot}}}{\dot{\varepsilon}_0^{\mathrm{tot}}} n K_{\mathrm{av}}(T) \left[-\ln\left(1 - \frac{\chi}{\phi_\infty}\right)\right]^{(n-1)/n} \left(1 - \frac{\chi}{\phi_\infty}\right) \left[\frac{3\zeta\left(1-\chi\right)^\gamma}{\chi^\gamma \mu_\mathrm{c} + \left(1-\chi\right)^\gamma \mu_\mathrm{a}}\right] \exp\left[\frac{3\zeta\left(\chi^\gamma \tilde{\sigma}_{\mathrm{c,m}} + \left(1-\chi\right)^\gamma \tilde{\sigma}_{\mathrm{a,m}}\right)}{\chi^\gamma \mu_\mathrm{c} + \left(1-\chi\right)^\gamma \mu_\mathrm{a}}\right]\right\} \tag{C.78}$$

$$\frac{\partial R_\chi}{\partial \tilde{\sigma}_{\mathrm{c,m}}} = \phi_\infty \left\{ \frac{\tilde{\dot{\bar{\varepsilon}}}^{\mathrm{tot}}}{\dot{\varepsilon}_0^{\mathrm{tot}}} n K_{\mathrm{av}}(T) \left[-\ln\left(1 - \frac{\chi}{\phi_\infty}\right)\right]^{(n-1)/n} \left(1 - \frac{\chi}{\phi_\infty}\right) \left[\frac{3\zeta\chi^\gamma}{\chi^\gamma \mu_\mathrm{c} + \left(1-\chi\right)^\gamma \mu_\mathrm{a}}\right] \exp\left[\frac{3\zeta\left(\chi^\gamma \tilde{\sigma}_{\mathrm{c,m}} + \left(1-\chi\right)^\gamma \tilde{\sigma}_{\mathrm{a,m}}\right)}{\chi^\gamma \mu_\mathrm{c} + \left(1-\chi\right)^\gamma \mu_\mathrm{a}}\right]\right\} \tag{C.79}$$

$$\frac{\partial R_\chi}{\partial s_\mathrm{a}} = 0 \tag{C.80}$$

$$\frac{\partial R_\chi}{\partial s_\mathrm{c}} = 0 \tag{C.81}$$

The derivative $\frac{\partial R_\chi}{\partial \chi}$ is expressed here in several parts.

$$\frac{\partial R_\chi}{\partial \chi} = \frac{1}{\Delta t} - \mathcal{C} e^w \left[u \frac{\partial v}{\partial \chi} + v \frac{\partial u}{\partial \chi} + uv \frac{\partial w}{\partial \chi} \right] \tag{C.82}$$

$$\mathcal{C} = \phi_\infty \frac{\tilde{\dot{\varepsilon}}^{\text{tot}}}{\dot{\varepsilon}_0^{\text{tot}}} n K_{\text{av}}(T) \tag{C.83}$$

$$u = 1 - \frac{\chi}{\phi_\infty} \tag{C.84}$$

$$v = \left[-\ln\left(1 - \frac{\chi}{\phi_\infty}\right) \right]^{(n-1)/n} \tag{C.85}$$

$$w = \frac{3\zeta \left(\chi^\gamma \tilde{\sigma}_{\text{c,m}} + (1-\chi)^\gamma \tilde{\sigma}_{\text{a,m}} \right)}{\chi^\gamma \mu_{\text{c}} + (1-\chi)^\gamma \mu_{\text{a}}} \tag{C.86}$$

$$\frac{\partial u}{\partial \chi} = -\frac{1}{\phi_\infty} \tag{C.87}$$

$$\frac{\partial v}{\partial \chi} = \frac{n-1}{n\left(\phi_\infty - \chi\right)} \left[-\ln\left(1 - \frac{\chi}{\phi_\infty}\right) \right]^{-1/n} \tag{C.88}$$

$$\frac{\partial w}{\partial \chi} = \frac{\frac{\partial g}{\partial \chi} h - \frac{\partial h}{\partial \chi} g}{h^2} \tag{C.89}$$

$$g = 3\zeta \left(\chi^\gamma \tilde{\sigma}_{\text{c,m}} + (1-\chi)^\gamma \tilde{\sigma}_{\text{a,m}} \right) \tag{C.90}$$

$$h = \chi^\gamma \mu_{\text{c}} + (1-\chi)^\gamma \mu_{\text{a}} \tag{C.91}$$

$$\frac{\partial g}{\partial \chi} = 3\zeta\gamma \left(\chi^{\gamma-1} \tilde{\sigma}_{\text{c,m}} - (1-\chi)^{\gamma-1} \tilde{\sigma}_{\text{a,m}} \right) \tag{C.92}$$

$$\frac{\partial h}{\partial \chi} = \gamma \left(\chi^{\gamma-1} \mu_{\text{c}} - (1-\chi)^{\gamma-1} \mu_{\text{a}} \right) \tag{C.93}$$

The above equations make use of the following derivatives,

$$\frac{\partial \tilde{\bar{\sigma}}_\pi}{\partial \tilde{\boldsymbol{\sigma}}'_\pi} = \frac{3}{2\tilde{\bar{\sigma}}_\pi} \left(\tilde{\boldsymbol{\sigma}}'_\pi - \tilde{\boldsymbol{b}}' \right), \quad \pi = \text{a, c} \tag{C.94}$$

$$\frac{\partial \tilde{\bar{\sigma}}_\pi}{\partial \tilde{\boldsymbol{b}}'} = -\frac{3}{2\tilde{\bar{\sigma}}_\pi}\left(\tilde{\boldsymbol{\sigma}}'_\pi - \tilde{\boldsymbol{b}}'\right) \tag{C.95}$$

$$\frac{\partial \tilde{\dot{\bar{\varepsilon}}}^{\mathrm{p}}_\pi}{\partial \tilde{\bar{\sigma}}_\pi} = \frac{\tilde{\dot{\bar{\varepsilon}}}^{\mathrm{p}}_\pi}{}\left(\frac{\mathcal{A}_\pi m_\pi}{T}\right)\left(\frac{\tilde{\bar{\sigma}}_\pi}{s_\pi - 3\alpha_\pi \tilde{\sigma}_{\pi,\mathrm{m}}}\right)^{m_\pi - 1} \tag{C.96}$$

$$\frac{\partial \tilde{\dot{\bar{\varepsilon}}}^{\mathrm{p}}_\pi}{\partial \tilde{\sigma}_{\pi,\mathrm{m}}} = \left(\frac{3\mathcal{A}_\pi \alpha_\pi}{T}\right)\tilde{\dot{\bar{\varepsilon}}}^{\mathrm{p}}_\pi\left[1 + \left(\frac{\tilde{\bar{\sigma}}_\pi}{s_\pi - 3\alpha_\pi \tilde{\sigma}_{\pi,\mathrm{m}}}\right)^{m_\pi}(m_\pi - 1)\right] \tag{C.97}$$

$$\frac{\partial \tilde{\dot{\bar{\varepsilon}}}^{\mathrm{p}}_\pi}{\partial s_\pi} = \left(-\frac{\mathcal{A}_\pi}{T}\right)\tilde{\dot{\bar{\varepsilon}}}^{\mathrm{p}}_\pi\left[1 + \left(\frac{\tilde{\bar{\sigma}}_\pi}{s_\pi - 3\alpha_\pi \tilde{\sigma}_{\pi,\mathrm{m}}}\right)^{m_\pi}(m_\pi - 1)\right] \tag{C.98}$$

$$\frac{\partial H_{1,\pi}}{\partial \tilde{\bar{\varepsilon}}^{\mathrm{p}}_\pi} = \frac{-h_{1,\pi}\Delta t}{f_\pi \bar{\varepsilon}^{\mathrm{w}}_\pi}\operatorname{sech}^2\left(\frac{\tilde{\bar{\varepsilon}}^{\mathrm{p}}_\pi - \bar{\varepsilon}^{\mathrm{w}}_\pi}{f_\pi \bar{\varepsilon}^{\mathrm{w}}_\pi}\right) \tag{C.99}$$

$$\frac{\partial H_{2,\pi}}{\partial \tilde{\bar{\varepsilon}}^{\mathrm{p}}_\pi} = \frac{h_{2,\pi}\Delta t}{f_\pi \bar{\varepsilon}^{\mathrm{w}}_\pi}\operatorname{sech}^2\left(\frac{\tilde{\bar{\varepsilon}}^{\mathrm{p}}_\pi - \bar{\varepsilon}^{\mathrm{w}}_\pi}{f_\pi \bar{\varepsilon}^{\mathrm{w}}_\pi}\right) \tag{C.100}$$

$$\frac{\partial \tilde{\dot{\bar{\varepsilon}}}^{\mathrm{p}}_\pi}{\partial \tilde{\boldsymbol{\sigma}}'_\pi} = \left(\frac{\partial \tilde{\dot{\bar{\varepsilon}}}^{\mathrm{p}}_\pi}{\partial \tilde{\bar{\sigma}}_\pi}\right)\left(\frac{\partial \tilde{\bar{\sigma}}_\pi}{\partial \tilde{\boldsymbol{\sigma}}'_\pi}\right), \qquad \frac{\partial \tilde{\dot{\bar{\varepsilon}}}^{\mathrm{p}}_\pi}{\partial \tilde{\boldsymbol{b}}'} = \left(\frac{\partial \tilde{\dot{\bar{\varepsilon}}}^{\mathrm{p}}_\pi}{\partial \tilde{\bar{\sigma}}_\pi}\right)\left(\frac{\partial \tilde{\bar{\sigma}}_\pi}{\partial \tilde{\boldsymbol{b}}'}\right) \tag{C.101}$$

$$\frac{\partial H_{1,\pi}}{\partial \tilde{\boldsymbol{\sigma}}'_\pi} = \left(\frac{\partial H_{1,\pi}}{\partial \tilde{\dot{\bar{\varepsilon}}}^{\mathrm{p}}_\pi}\right)\left(\frac{\partial \tilde{\dot{\bar{\varepsilon}}}^{\mathrm{p}}_\pi}{\partial \tilde{\boldsymbol{\sigma}}'_\pi}\right), \qquad \frac{\partial H_{2,\pi}}{\partial \tilde{\boldsymbol{\sigma}}'_\pi} = \left(\frac{\partial H_{2,\pi}}{\partial \tilde{\dot{\bar{\varepsilon}}}^{\mathrm{p}}_\pi}\right)\left(\frac{\partial \tilde{\dot{\bar{\varepsilon}}}^{\mathrm{p}}_\pi}{\partial \tilde{\boldsymbol{\sigma}}'_\pi}\right) \tag{C.102}$$

$$\frac{\partial H_{1,\pi}}{\partial \tilde{\boldsymbol{b}}'} = \left(\frac{\partial H_{1,\pi}}{\partial \tilde{\dot{\bar{\varepsilon}}}^{\mathrm{p}}_\pi}\right)\left(\frac{\partial \tilde{\dot{\bar{\varepsilon}}}^{\mathrm{p}}_\pi}{\partial \tilde{\boldsymbol{b}}'}\right), \qquad \frac{\partial H_{2,\pi}}{\partial \tilde{\boldsymbol{b}}'} = \left(\frac{\partial H_{2,\pi}}{\partial \tilde{\dot{\bar{\varepsilon}}}^{\mathrm{p}}_\pi}\right)\left(\frac{\partial \tilde{\dot{\bar{\varepsilon}}}^{\mathrm{p}}_\pi}{\partial \tilde{\boldsymbol{b}}'}\right) \tag{C.103}$$

$$\frac{\partial H_{1,\pi}}{\partial \tilde{\sigma}_{\pi,\mathrm{m}}} = \left(\frac{\partial H_{1,\pi}}{\partial \tilde{\dot{\bar{\varepsilon}}}^{\mathrm{p}}_\pi}\right)\left(\frac{\partial \tilde{\dot{\bar{\varepsilon}}}^{\mathrm{p}}_\pi}{\partial \tilde{\sigma}_{\pi,\mathrm{m}}}\right), \qquad \frac{\partial H_{2,\pi}}{\partial \tilde{\sigma}_{\pi,\mathrm{m}}} = \left(\frac{\partial H_{2,\pi}}{\partial \tilde{\dot{\bar{\varepsilon}}}^{\mathrm{p}}_\pi}\right)\left(\frac{\partial \tilde{\dot{\bar{\varepsilon}}}^{\mathrm{p}}_\pi}{\partial \tilde{\sigma}_{\pi,\mathrm{m}}}\right) \tag{C.104}$$

$$\frac{\partial H_{1,\pi}}{\partial s_\pi} = \left(\frac{\partial H_{1,\pi}}{\partial \tilde{\dot{\bar{\varepsilon}}}^{\mathrm{p}}_\pi}\right)\left(\frac{\partial \tilde{\dot{\bar{\varepsilon}}}^{\mathrm{p}}_\pi}{\partial s_\pi}\right), \qquad \frac{\partial H_{2,\pi}}{\partial s_\pi} = \left(\frac{\partial H_{2,\pi}}{\partial \tilde{\dot{\bar{\varepsilon}}}^{\mathrm{p}}_\pi}\right)\left(\frac{\partial \tilde{\dot{\bar{\varepsilon}}}^{\mathrm{p}}_\pi}{\partial s_\pi}\right) \tag{C.105}$$

C.2 Calculation of the consistent tangent matrix

The UMAT calculates the consistent tangent matrix, $\mathbb{L}$, and returns it to Abaqus to aid convergence. The expression for $\mathbb{L}$ is

$$\tilde{\mathbb{L}} = \frac{1}{\Delta t}\left(\frac{\partial \tilde{\boldsymbol{\sigma}}'}{\partial \tilde{\boldsymbol{D}}} + \boldsymbol{I} \otimes \frac{\partial \tilde{\sigma}_{\mathrm{m}}}{\partial \tilde{\boldsymbol{D}}}\right). \tag{C.106}$$

To express $\mathbb{L}$ in terms of state variables, the mixture rule for stresses in Eq. (6.12) must be substituted into Eq. (C.106). The resulting expression is

$$\begin{aligned}\tilde{\mathbb{L}} = \frac{1}{\Delta t}\Bigg\{&\left[\chi^{\gamma}\frac{\partial \tilde{\boldsymbol{\sigma}}'_{\mathrm{c}}}{\partial \tilde{\boldsymbol{D}}} + (1-\chi)^{\gamma}\frac{\partial \tilde{\boldsymbol{\sigma}}'_{\mathrm{a}}}{\partial \tilde{\boldsymbol{D}}}\right] + \boldsymbol{I} \otimes \left[\chi^{\gamma}\frac{\partial \tilde{\sigma}_{\mathrm{c,m}}}{\partial \tilde{\boldsymbol{D}}} + (1-\chi)^{\gamma}\frac{\partial \tilde{\sigma}_{\mathrm{a,m}}}{\partial \tilde{\boldsymbol{D}}}\right] \\ &+\gamma\left[\chi^{\gamma-1}\left(\tilde{\boldsymbol{\sigma}}'_{\mathrm{c}} + \tilde{\sigma}_{\mathrm{c,m}}\boldsymbol{I}\right) - (1-\chi)^{\gamma-1}\left(\tilde{\boldsymbol{\sigma}}'_{\mathrm{a}} + \tilde{\sigma}_{\mathrm{a,m}}\boldsymbol{I}\right)\right] \otimes \frac{\partial \chi}{\partial \tilde{\boldsymbol{D}}}\Bigg\}.\end{aligned} \tag{C.107}$$

The derivatives in $\frac{\partial \tilde{\boldsymbol{\sigma}}'_{\pi}}{\partial \tilde{\boldsymbol{D}}}$, $\frac{\partial \tilde{\sigma}_{\pi,\mathrm{m}}}{\partial \tilde{\boldsymbol{D}}}$, and $\frac{\partial \chi}{\partial \tilde{\boldsymbol{D}}}$ in Eq. (C.107) are extracted from $\left[\frac{\partial [X]}{\partial \tilde{\boldsymbol{D}}}\right]$, itself calculated using the Jacobian,

$$\left[\frac{\partial [X]}{\partial \tilde{\boldsymbol{D}}}\right] = -\left[\frac{\partial [R]}{\partial [X]}\right]^{-1}\left[\frac{\partial [R]}{\partial \tilde{\boldsymbol{D}}}\right]. \tag{C.108}$$

. The components of $\left[\frac{\partial [R]}{\partial \tilde{\boldsymbol{D}}}\right]$ are as follows:

$$\frac{\partial \boldsymbol{R}_{\tilde{\boldsymbol{\sigma}}'_{\mathrm{a}}}}{\partial \tilde{\boldsymbol{D}}} = -\mathbb{J}, \qquad \frac{\partial \boldsymbol{R}_{\tilde{\boldsymbol{\sigma}}'_{\mathrm{c}}}}{\partial \tilde{\boldsymbol{D}}} = -\mathbb{J}, \tag{C.109}$$

$$\frac{\partial \boldsymbol{R}_{\tilde{\boldsymbol{b}}'}}{\partial \tilde{\boldsymbol{D}}} = -\mathbb{J} : \tilde{\mathbb{R}}, \qquad \frac{\partial \boldsymbol{R}_{\tilde{b}_{\mathrm{m}}}}{\partial \tilde{\boldsymbol{D}}} = -\frac{1}{3}\boldsymbol{I} : \tilde{\mathbb{R}}, \tag{C.110}$$

$$\frac{\partial \boldsymbol{R}_{\tilde{\sigma}_{\mathrm{a,m}}}}{\partial \tilde{\boldsymbol{D}}} = -K_{\mathrm{a}}\boldsymbol{I}, \qquad \frac{\partial \boldsymbol{R}_{\tilde{\sigma}_{\mathrm{c,m}}}}{\partial \tilde{\boldsymbol{D}}} = -K_{\mathrm{c}}\boldsymbol{I}, \tag{C.111}$$

$$\frac{\partial \boldsymbol{R}_{s_{\mathrm{a}}}}{\partial \tilde{\boldsymbol{D}}} = \boldsymbol{0}, \qquad \frac{\partial \boldsymbol{R}_{s_{\mathrm{c}}}}{\partial \tilde{\boldsymbol{D}}} = \boldsymbol{0}, \tag{C.112}$$

$$\frac{\partial R_\chi}{\partial \tilde{\boldsymbol{D}}} = -\frac{2\phi_\infty}{3\tilde{\dot{\varepsilon}}^{\mathrm{tot}}}\tilde{\boldsymbol{D}}\left\{\frac{1}{\dot{\varepsilon}_0^{\mathrm{tot}}} n K_{\mathrm{av}}(T)\left[-\ln\left(1-\frac{\chi}{\phi_\infty}\right)\right]^{(n-1)/n}\left(1-\frac{\chi}{\phi_\infty}\right)\right. \tag{C.113}$$

$$\left.\exp\left[\frac{3\zeta\left(\chi^\gamma\tilde{\sigma}_{\mathrm{c,m}}+(1-\chi)^\gamma\,\tilde{\sigma}_{\mathrm{a,m}}\right)}{\chi^\gamma\mu_{\mathrm{c}}+(1-\chi)^\gamma\,\mu_{\mathrm{a}}}\right]\right\}.$$

APPENDIX D. SUPPLEMENTARY INFORMATION: DAMAGE MODEL PARAMETERS

This appendix provides expressions for parameters from the micromechanics-based continuum damage model presented in Section 7.3. The parameters C, g, κ, η, and α_2 enter into the void growth criterion, Eq. (7.11). The parameters α_1 and α_1^{G} enter into the evolution equation for the void aspect ratio, Eq. (7.24). The expressions for many of these parameters change depending on if the void is oblate or prolate. When writing expressions that depend on the void form, the following shorthand is adopted,

$$\begin{cases} \text{for } w > 1, & \text{Prolate void, (p)} \\ \text{for } w = 1, & \text{Spherical void, (s)} \\ \text{for } w < 1, & \text{Oblate void, (o).} \end{cases} \tag{D.1}$$

It is sufficient to define the parameters for prolate and oblate cases only. The parameter value for the spherical case is calculated by taking the limit as $w \to 1$. However, for the convenience of the reader, the expressions that depend on the void form explicitly give values for the spherical case. The parameter definitions presented here neglect matrix anisotropy. For more general definitions that include anisotropy, refer to Ref. [34] or Ref. [80].[1]

The "secondary-porosity", g, is non-zero only for oblate voids,

$$g = \begin{cases} 0, & \text{(p, s)} \\ \frac{e_2^3}{\sqrt{1-e_2^2}}, & \text{(o).} \end{cases} \tag{D.2}$$

The original model derives its constitutive equations from a spheroidal representative volume element (RVE) with an embedded, confocal, spheroidal void [33, 34]. Accordingly, e_1 is the

[1] While Ref. [34] provides useful intuitive explanations for the meaning of these parameters, it also contains a typographical error. Therefore, Ref. [80] is also recommended.

eccentricity of the spheroidal void, while e_2 is the eccentricity of the spheroidal RVE. The expression for e_1 is

$$e_1^2 = \begin{cases} 1 - \frac{1}{w^2}, & \text{(p)} \\ 0, & \text{(s)} \\ 1 - w^2, & \text{(o)}. \end{cases} \tag{D.3}$$

The eccentricity of the RVE, e_2, is an implicit function of e_1, f, and w

$$\frac{(1-e_2^2)^a}{e_2^3} = \frac{1}{f}\frac{(1-e_1^2)^a}{e_1^3}, \quad a = \begin{cases} 1, & \text{(p)} \\ 1/2, & \text{(o)}. \end{cases} \tag{D.4}$$

For a spherical void, $e_2 = 0$.

The parameter κ is a measure of the pressure dependency of the void growth criterion, Eq. (7.11). It is given by

$$\kappa = \begin{cases} \frac{3}{2}\left[1 + \frac{1}{4\ln f}\ln\left(\frac{1-e_2^2}{1-e_1^2}\right)\right]^{-1/2}, & \text{(p)} \\ \frac{3}{2}, & \text{(s)} \\ \frac{3}{2}\left[\frac{\left(g_f - g_1\right) + \frac{4}{5}\left(g_f^{5/2} - g_1^{5/2}\right) - \frac{3}{5}\left(g_f^5 - g_1^5\right)}{\ln\left(\frac{g_f}{g_1}\right)}\right], & \text{(o)}, \end{cases} \tag{D.5}$$

where

$$g_f = \frac{g}{g+f}, \quad g_1 = \frac{g}{g+1}. \tag{D.6}$$

The values of α_1 and α_1^{G} depend on the eccentricity of the spheroidal void, while the value of α_2 depends on the eccentricity of the spheroidal RVE;

$$\alpha_1 = \begin{cases} \left[e_1 - (1-e_1^2)\operatorname{arctanh} e_1\right] / \left(2e_1^3\right), & \text{(p)} \\ \frac{1}{3}, & \text{(s)} \\ \left[-e_1\left(1-e_1^2\right) + \sqrt{1-e_1^2}\arcsin e_1\right] / \left(2e_1^3\right), & \text{(o)}, \end{cases} \tag{D.7}$$

$$\alpha_1^{\mathrm{G}} = \begin{cases} \frac{1}{3-e_1^2}, & \text{(p)} \\ \frac{1}{3}, & \text{(s)} \\ \frac{1-e_1^2}{3-2e_1^2}, & \text{(o)}, \end{cases} \tag{D.8}$$

$$\alpha_2 = \begin{cases} \frac{\left(1+e_2^2\right)}{\left(1+e_2^2\right)^2+2\left(1-e_2^2\right)}, & \text{(p)} \\ \frac{1}{3}, & \text{(s)} \\ \frac{\left(1-e_2^2\right)\left(1-2e_2^2\right)}{\left(1-2e_2^2\right)^2+2\left(1-e_2^2\right)}, & \text{(o)}. \end{cases} \tag{D.9}$$

Note that, for a spherical void, $\alpha_2 = 1/3$, therefore σ_h reduces to the mean normal stress, $\sigma_{\mathrm{m}} = (1/3)\,\mathrm{tr}\,\boldsymbol{\sigma}$, see Eqs. (7.14) or (7.19).

Finally, the parameters η and C are given by

$$\eta = -\frac{2}{3}\frac{\kappa Q^* (g+1)(g+f)\sinh(\kappa H^*)}{(g+1)^2+(g+f)^2+(g+1)(g+f)\left[\kappa H^*\sinh(\kappa H^*)-2\cosh(\kappa H^*)\right]}, \tag{D.10}$$

$$C = -\frac{2}{3}\frac{\kappa (g+1)(g+f)\sinh(\kappa H^*)}{\left(Q^*+\frac{3}{2}\eta H^*\right)\eta}, \tag{D.11}$$

where

$$H^* = 2(\alpha_1-\alpha_2), \quad Q^* = 1-f. \tag{D.12}$$

For a spherical void, $\eta = 0$, therefore σ_q reduces to the von Mises equivalent stress, $\sigma_{\mathrm{eqv}} = \sqrt{(3/2)\boldsymbol{\sigma}' : \boldsymbol{\sigma}'}$, see Eqs. (7.13) and (7.18). For a spherical void, $C = 1$.

APPENDIX E. HYGROSCOPIC NATURE OF POLYAMIDE-6

PA-6 is a hygroscopic material, meaning that it absorbs moisture from the air even at ambient temperatures and humidities [1]. The absorbed moisture acts as a plasticizer within the material and therefore decreases the strength and increases the ductility [93]. While preparing the experimental campaigns presented in the body of this text, preliminary mechanical tests on PA-6 were carried out without appropriately controlling for moisture uptake, leading to variable results under nominally constant test conditions.

The preliminary tests used RN10 specimens (see Section 4.2.2 and Appendix A) and the notch opening displacement was measured using a laser extensometer. The same specimen nomenclature and testing procedure from Section 4.2 was executed here, except the conditioning treatment described in Section 4.2.4 was not applied to specimens unless otherwise noted. The specimens studied here were machined from a different cast plate than all other bulk specimens studied in this dissertation. However, both plates shared the same supplier, product number, and geometry.

When the cast PA-6 plate was received, it was stored in a cabinet with a tray of calcium sulfate ($CaSO_4$) desiccant. After the RN10 bars were machined from the plate, they were stored in the same cabinet with the desiccant. When the desiccant changed colors, indicating a significant absorption of moisture, the desiccant was replaced. The humidity in the laboratory was typically measured as $60\,\% \pm 5\,\%$, although measurements as low as $50\,\% \pm 5\,\%$ and as high as $70\,\% \pm 5\,\%$ were recorded.

In Fig. E.1, the blue and red curves depict the nominal stress-strain response of tests on RN10 specimens conducted without any conditioning treatment. The figure legend indicates how many days passed between receipt of the raw material and the test date of the specimen, i.e. how long the material was stored in the laboratory. Otherwise, the tests represented by the red and blue curves experienced the same testing conditions. When the material spent more time in storage, the strength decreased and the ductility increased, symptoms consistent

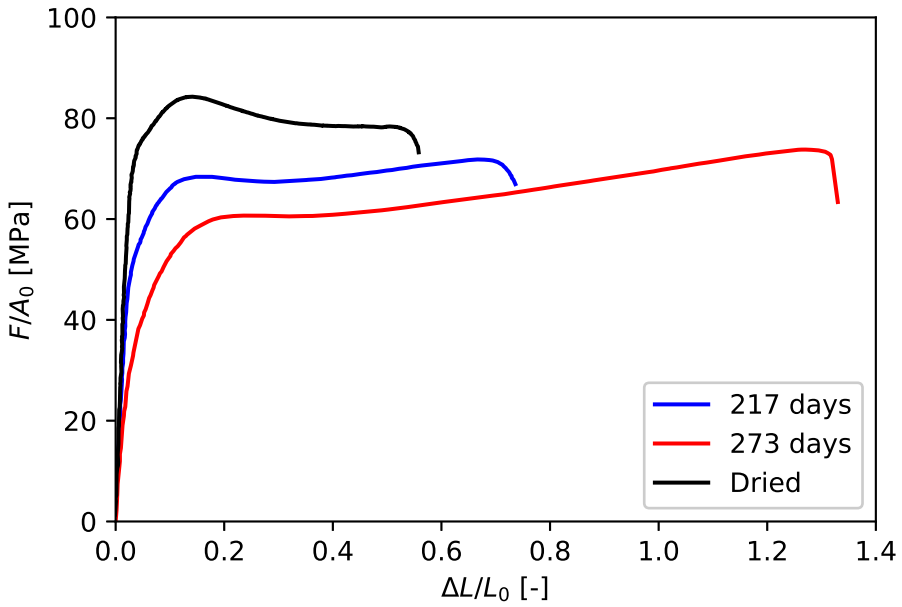

Figure E.1: Notch opening displacement of unaged PA-6 RN10 bars that were loaded in tension at room temperature (24 °C) and with a nominal strain rate of 10^{-3} /s. The mechanical behavior of bars tested a variable number of days after receipt of the raw material are compared to the mechanical behavior of a bar that was dried in a vacuum at 80 °C for 72 h.

with plasticization by water. To verify that this effect was a result of water plasticization, a specimen was dried in a vacuum oven at 80 °C for 72 h and then tested immediately upon removal from the oven. The mechanical response of the specimen tested after drying is represented by the black curve in Fig. E.1. The reversal of moisture plasticization is evidenced by the increase in strength and reduction in ductility.

Rozanski and Galeski studied the effects of plasticization by water on the strength of PA-6 [111]. They found that water was absorbed exclusively by the amorphous phase, which caused swelling. The swollen amorphous phase exerted a stress on the crystalline phase, therefore reducing the remote applied load necessary to induce yielding in the crystalline phase. This explains the reduction in strength caused by absorbed moisture in PA-6.

Rozanski and Galeski also found that low molecular weight penetrants, such as water in PA-6 or chloroform in PP, suppressed cavitation [111], which might be responsible for the

increase in ductility observed in Fig. E.1 when specimens are not dried. In fact, when the specimens were not dried, the material was ductile enough that the RN10 notch became completely smooth prior to failure. Fig. E.2 compares an undeformed RN10 bar to an RN10 bar that was loaded and then unloaded immediately prior to fracture and an RN10 bar loaded to fracture. Both of the deformed bars in Fig. E.2 were tested 217 days after receipt of the raw material. In both cases, the notch become cylindrical during loading. Notched bar specimens are used to induce a triaxial stress state [45]. Sharper notches result in a higher triaxiality, which favors void growth [45]. An RN10 bar has an initial triaxiality of 0.56 at the center of the bar, while a cylindrical bar has an initial triaxiality of 1/3 (see Table 4.1). If the notch geometry deforms from an RN10 notch to a cylinder (i.e. RN∞), then the stress triaxiality will decrease from 0.56 to 1/3. Therefore, the cavitation in the plasticized bars is reduced by both the absorbed moisture and by large changes in specimen geometry that reduce the stress triaxiality. For this reason, it would be interesting to study the effects of moisture and notch geometry on cavitation in polyamide-6.

These experiments revealed two important facts. (1) Even when the PA-6 is stored with a desiccant, moisture uptake is still significant enough to change the mechanical properties. This results in a mechanical response that varies with storage time. (2) Drying the material in a vacuum oven reverses this effect. Therefore, conditioning the specimens at 80 °C in a vacuum oven for 72 h immediately prior to testing became standard procedure for all subsequent tests on PA-6. It was necessary to dry the specimens in a vacuum to prevent thermal-oxidation.

This conditioning procedure proved sufficient for standardizing the behavior of both bulk and film specimens that were either unaged or subjected to UV exposure, i.e. the mechanical behavior of the tests no longer varied with specimen storage time. However, combined hygrothermal and UV aging conditions were later introduced to the experimental campaign. Hygrothermal aging exposed the material to high levels of humidity at elevated temperatures and therefore required a re-evaluation of the implemented conditioning treatment. The

Figure E.2: (Left) An undeformed RN10 bar used in preliminary studies. (Middle) An RN10 bar of PA-6 loaded and interrupted immediately prior to fracture. (Right) An RN10 bar of PA-6 loaded to fracture. Both tests were carried out at room temperature (24 °C), with a nominal strain rate of 10^{-3} /s, and 217 days after receipt of the raw material.

effects of combined hygrothermal and UV aging with regards to moisture uptake and failure strain are studied in Appendix F.

APPENDIX F. COMBINED HYGROTHERMAL AND UV AGING

F.1 Introduction

Aging regimens that consisted of hygrothermal and UV aging components, abbreviated here as HUV aging, were studied in an experimental campaign conducted concurrently with the experiments presented in Chapters 3 and 4. HUV aging conditions were introduced to simulate natural aging conditions in outdoor environments. Polyamides are sensitive to moisture in two key ways. First, moisture may induce hydrolysis, a chemical reaction that results in chain scission and eventually catastrophic embrittlement [14]. Hydrolysis and photo-oxidation are similar in that they are both forms of chemical aging. Second, polyamides can absorb moisture from their environment, which occurs because PA-6 is hygroscopic. The absorbed water acts as a plasticizer, decreasing the strength and increasing the ductility [93]. Thermoplastics in general are affected by hydrolysis, but not all thermoplastics are hygroscopic. It is not the intent of this dissertation to study the hygroscopic nature of PA-6 or plasticization by water, therefore these effects are controlled by conditioning the specimens in a vacuum oven immediately prior to loading. This procedure removes the moisture from the specimens and reverses plasticization caused by water (see Appendix E).

During HUV aging regimens applied here, the material is exposed to UV radiation for several hours at ambient humidity and then exposed to an environment with no UV and 100 % relative humidity for several hours. The UV and hygrothermal exposure alternates until the prescribed aging times are completed. Each HUV aging regimen has a corresponding UV only regimen with exactly the same amount of UV exposure time. Therefore, by comparing the effects of an HUV aging regimen to effects of the corresponding UV aging regimen, the impact of hygrothermal aging can be assessed. Hygrothermal aging can induce hydrolysis, but might also affect photo-oxidation, as moisture absorbed during hygrothermal aging might impact the availability of oxygen to the material [149].

The purpose of this appendix is to demonstrate that the chemical aging induced by hygrothermal aging is negligible compared to the chemical aging induced by UV exposure. It should be emphasized that these results should not be interpreted to mean that hygrothermal aging is irrelevant in general, simply that it is irrelevant for the specific conditions studied in this work.

The outline of this appendix is as follows. In Section F.2, the experimental procedures are described. The procedures are mostly described through references to other chapters, but details especially pertinent to the discussion here are reiterated. In Section F.3, the effects of HUV aging on PA-6 cylindrical bars are shown. In Section F.4, the effects of HUV aging on PA-6 films are shown. The conclusions from these experiments are then summarized in Section F.5.

F.2 Experimental procedures

Mechanical tests on HUV-aged bulk and film specimens presented here follow the same procedures described in Section 3.2. However, no description of HUV aging is given in Section 3.2. The HUV aging procedure is described for bulk specimens in Section 4.2, but not for films. Therefore, the UV and HUV aging procedures are described here for both bulk and film specimens.

Two categories of aging regimens were used: UV only and combined UV and hygrothermal aging. Specimens aged under the UV only regimens were aged in an accelerated weathering machine using UVA lamps with a spectral irradiance of $1.55\,\mathrm{W/m^2/nm}$ and an approximate wavelength of 340 nm. The temperature in the weathering machine was 60 °C and the humidity was ambient. Nominal UV exposure times from 48 to 240 hours were used. To evenly irradiate the lateral surface of the bulk specimens, they were periodically rotated by 120°. Each 120° section of the lateral surface was aged for the full nominal aging time. The film specimens have a thickness less than the typical depth of oxidation, so there was no need to rotate or flip them during UV exposure. Some specimens were aged under a combination of UV and hygrothermal conditions in order to simulate the natural outdoor conditions. These

specimens were aged by alternating between the UV exposure as previously described and hygrothermal exposure without UV radiation at 100% relative humidity and at a temperature of 60 °C. In the bulk specimens, for every 24 hours of nominal UV exposure, there were 12 hours of hygrothermal exposure. In the film specimens, for every 24 hours of UV exposure, there were 4 hours of hygrothermal exposure. The different ratios of UV to hygrothermal exposure is a result of needing to expose each 120° section of the bulk specimens to the full nominal UV exposure time while concurrently aging both bulk and film specimens. The hygrothermal aging conditions are loosely based on ASTM G154-12a [150].

Table F.1 summarizes the aging regimens used for the bulk specimens and Table F.2 summarize the aging regimens used for the film specimens. Aging conditions are referred to by their labels as listed in Tables F.1 and F.2. The labels refer to the type of aging, either UV or HUV (for hygrothermal and UV aging), and the duration of UV exposure in hours. Each HUV condition has a corresponding UV condition with the same duration of UV exposure, but with additional hygrothermal aging. It should be noted that the same HUV aging label has a different meaning for bulk and film specimens, as they use different ratios of UV exposure time to hygrothermal aging time.

The conditioning procedures used to remove moisture in the specimen are pertinent to the discussion of hygrothermal aging and so are also reiterated here. PA-6 is a hygroscopic and absorbs moisture even at ambient temperatures and humidities. As shown in Appendix E, sufficient moisture is absorbed at ambient conditions to influence the mechanical behavior of the material. To prevent changes in mechanical behavior with storage time, each specimen was conditioned (dried) in a vacuum oven for 72 hours at 80 °C immediately prior to mechanical testing.

F.3 Cylindrical bars

Fig. F.1 shows the nominal and true stress-strain curves for aged PA-6 cylindrical bars. The plots are grouped to easily compare UV and HUV aging conditions with the same duration of UV exposure. As the UV exposure time increases, the difference in strength

Table F.1: Summary of aging regimens for bulk specimens.

Label	UV Exposure, per 120° (hrs)	Hygrothermal Exposure (hrs)
Unaged	0	0
UV48	48	0
UV96	96	0
UV192	192	0
HUV48	48	24
HUV96	96	48
HUV192	192	96

Table F.2: Summary of aging regimens for film specimens.

Label	UV Exposure (hrs)	Hygrothermal Exposure (hrs)
Unaged	0	0
UV48	48	0
UV96	96	0
UV192	192	0
UV240	240	0
HUV48	48	8
HUV96	96	16

between the UV and HUV-aged bars increases. The strength in UV-aged bars is constant (see Chapter 3 for details), while the the strength in the HUV-aged bars decreases. For example, for UV48 and HUV48 aged bars, no meaningful difference between strength is observed, while the HUV192 aged bar has a yield stress approximately 10 MPa lower than the yield stress of the UV192 aged bar.

The reduction in strength with an increasing duration of hygrothermal aging is consistent with plasticization by water, indicating that the conditioning treatment of 72 hours may be too short to dry PA-6 subjected to hygrothermal aging. The elevated temperature and humidity will accelerate moisture absorption, but the duration of the conditioning treatment was chosen for specimens only exposed to ambient humidity. To investigate this explanation, the weight of an unaged specimen and an HUV192 aged specimen were tracked during a 120 hour conditioning treatment (using a vacuum oven at 80 °C). The percent reduction in weight versus conditioning time is plotted in Fig. F.2. It is assumed that reductions in weight are due to the removal of moisture, and therefore the efficacy of the conditioning treatment can be assessed. For the unaged specimen, only minor changes in weight are observed after 72 hours, indicating that this length of time is sufficient to dry the material. For the HUV192 specimen, weight loss steadily continues from 72 hours to 120 hours. This confirms that after 72 hours, the HUV192 specimens have not been sufficiently dried.

Fig. F.2 confirms that the HUV-aged specimens are not sufficiently dried after 72 hours of conditioning, but it remains to be demonstrated that the excess moisture is responsible for the reduction in strength observed in Fig. F.1. To confirm this, cylindrical bars subjected to HUV aging were conditioned for 144 hours (standard conditioning time is 72 hours) and then mechanically loaded. Fig. F.3 compares the results of the tests using an extended conditioning treatment to tests using the standard treatment. When the conditioning treatment is extended to 144 hours, no differences in strength are observed between specimens subjected to UV or HUV aging. Therefore, the loss of strength seen in the bulk HUV-aged specimens in Fig. F.1 is confirmed to be an effect of water plasticization and 144 hours of conditioning

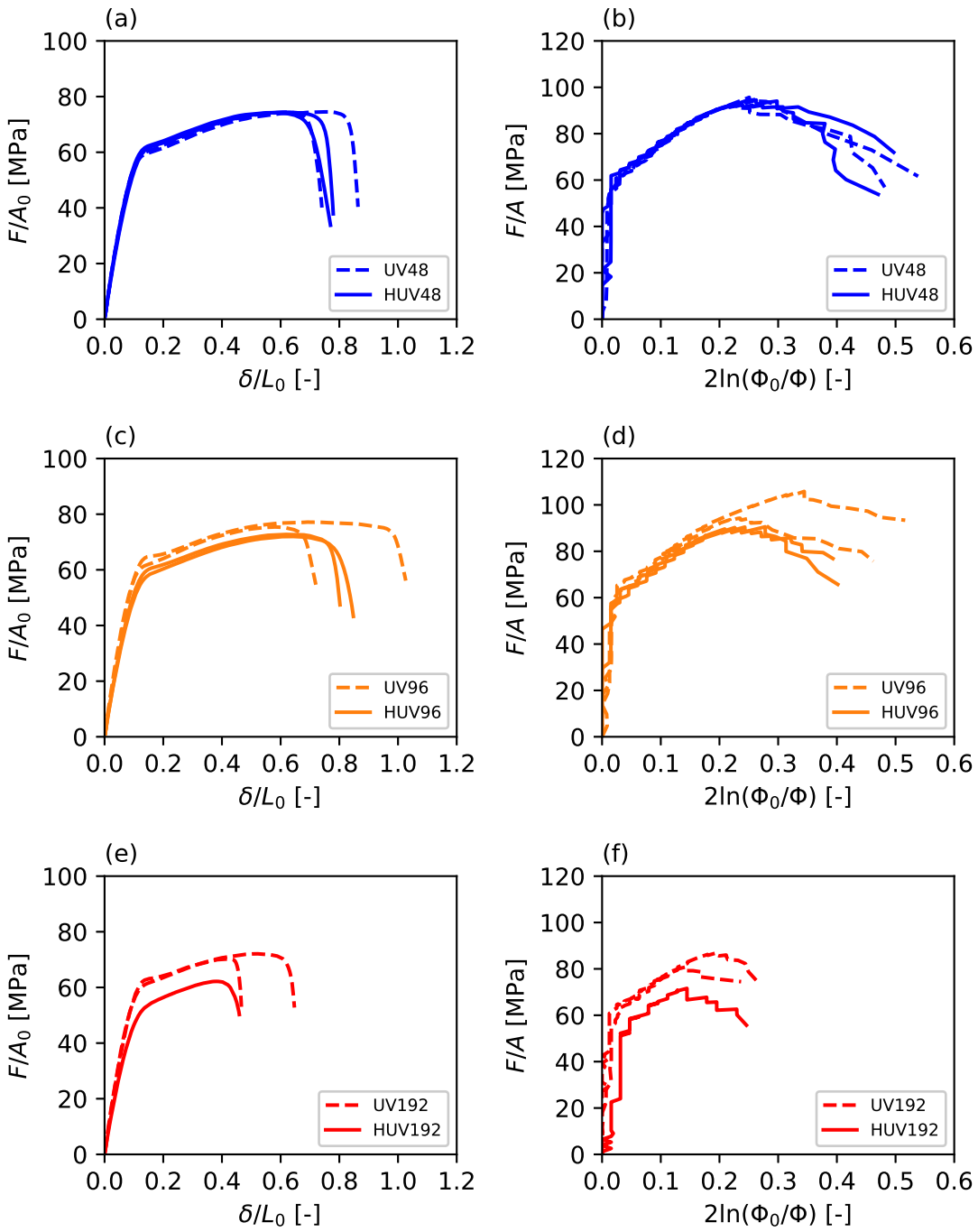

Figure F.1: The mechanical response of PA-6 cylindrical specimens subjected to UV and HUV aging and tested in tension at room temperature (24 °C) and with a nominal strain rate of 10^{-3} /s. The nominal mechanical response is shown in the left column (a,c,e) and the true mechanical response is shown in the right column (b,d,f). Results are grouped in rows by UV exposure time: (a,b) UV48 and HUV48, (c,d) UV96 and HUV96, (e,f) UV192 and HUV192.

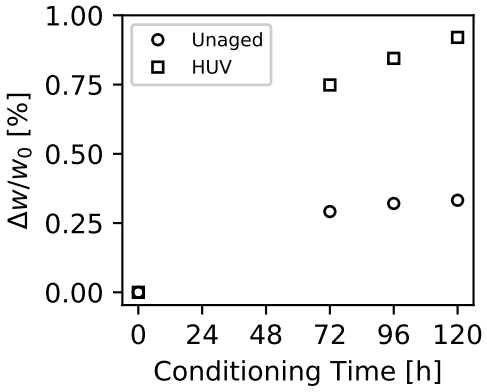

Figure F.2: The percent reduction in weight versus conditioning (drying) time for an unaged specimen and an HUV192 specimen. Conditioning took place in a vacuum oven at 80 °C.

is shown to be sufficient for drying bulk HUV-aged specimens.

The effects of HUV aging and the duration of the conditioning treatment are summarized by Fig. F.4, which shows the yield stress versus UV exposure time. Data from unaged, UV-aged, and HUV-aged specimens all using the 72 hour conditioning treatment are plotted alongside data from HUV-aged specimens subjected to 144 hours of conditioning. As expected, no changes in the yield stress should occur with UV aging due to the superficial depth of the oxidized layer, as described in Chapter 3. For the HUV-aged bars using the standard conditioning time, a steady decrease in the yield stress is seen with increased aging, which is caused by the additional moisture absorbed at the elevated temperature and humidity during hygrothermal aging. When the HUV-aged bars are dried for 144 hours, the additional moisture is removed and no effect of hygrothermal aging on strength is observed.

Discussion thus far has focused on changes in strength that occur with hygrothermal aging, but it is also of interest to examine if hygrothermal aging has any effect on ductility. Fig. F.5 shows the strain to failure in UV and HUV-aged bars. Comparing the UV condition to the HUV condition with extended drying (dry HUV) allows an assessment of ductility without the effects of hygroscopic plasticization. For both UV and dry HUV, fracture occurs at similar strains. Therefore, any chemical aging induced or accelerated by the hygrothermal

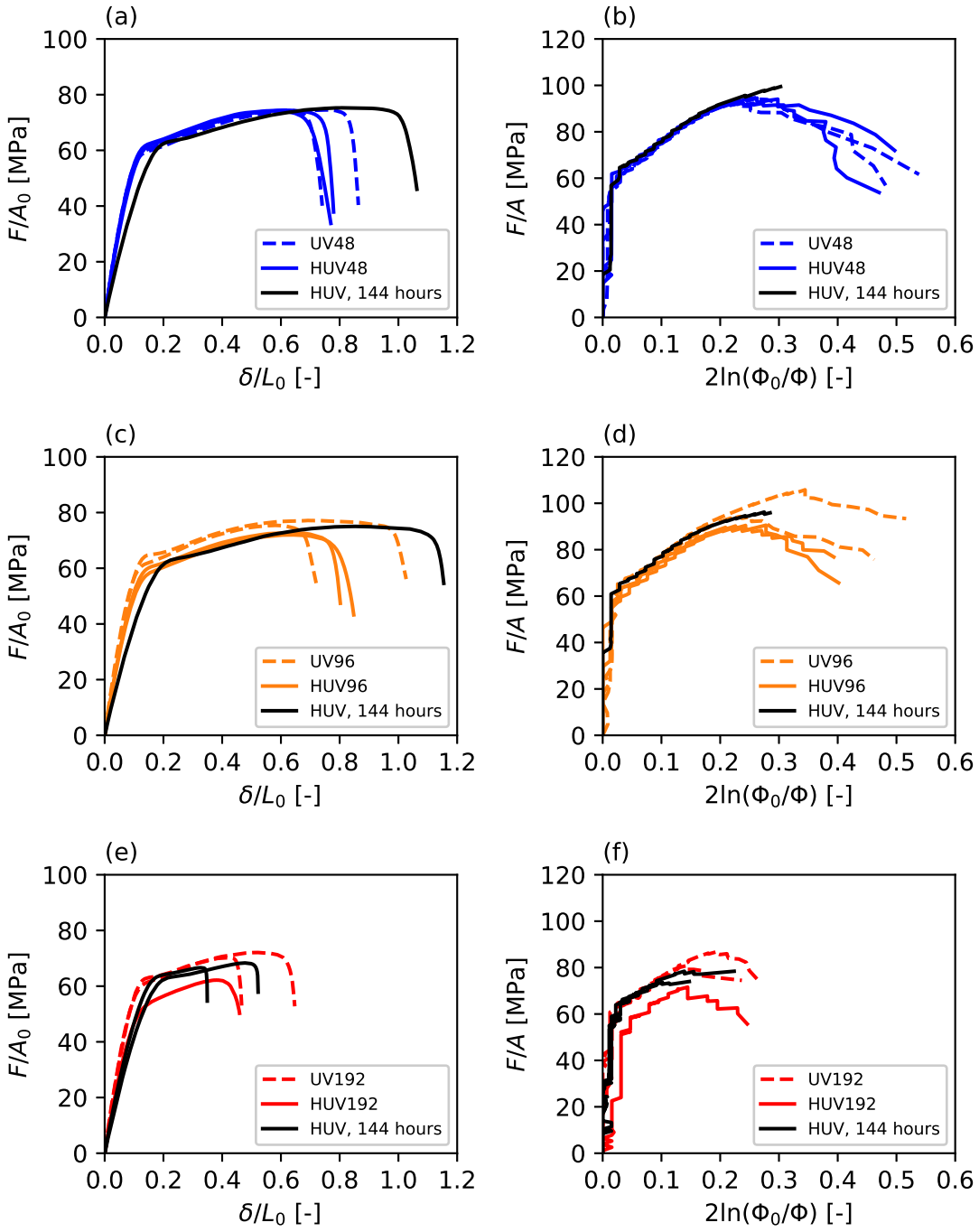

Figure F.3: The mechanical response of PA-6 cylindrical specimens subjected to a standard conditioning treatment are repeated from Fig. F.1, but also shown are the mechanical response of specimens subjected to HUV aging and conditioned for 144 hours.

component of HUV aging is insignificant compared to the photo-oxidation caused by the UV aging component.

The bars subjected to HUV aging but insufficiently dried (wet HUV) also exhibit fracture strains similar to the UV-aged bars, but the wet HUV bars fracture at a lower load (see Fig. F.1). Since fracture is ultimately driven by forces, this is a surprising result. However, a study by Rozanski and Galeski provides an explanation for this observation [111]. They found that when PA-6 specimens were dried with their ends fixed, a residual stress developed in the specimen. This residual stress was equal to the decrease in strength observed when moisture is absorbed by a dry specimen. They concluded that moisture is absorbed into the amorphous phase of PA-6 and exerts an internal stress on the crystalline lamella. Therefore, although the wet HUV-aged bars fracture at a lower applied load than the UV-aged bars, the internal stresses at fracture must be similar due to the additional internal stress caused by absorbed moisture.

F.4 Films

The effects of HUV aging on PA-6 films was also investigated. The nominal and true stress-strain curves for UV48 aged films and HUV48 aged films are shown in Fig. F.6. The nominal and true stress-strain curves for UV96 films and HUV96 aged films are similarly presented in Fig. F.7. Three different nominal strain rates were used to collect data on the effect of strain rate on the strength of PA-6, although the effects of strain rate are not discussed here. Nevertheless, the tests at different strain rates are presented to expand the data available for drawing conclusions about the effects of hygrothermal aging on PA-6 films.

No differences between the UV and HUV conditions can be seen from the stress-strain curves. Unlike the bulk bars, the films are thin enough that the additional moisture absorbed during hygrothermal aging is removed using the standard (72 hour) conditioning procedure.

The true stress at the maximum force is plotted against strain rate for UV48 and HUV48 aged films in Fig. F.8 and for UV96 and HUV96 aged films in Fig. F.9. Hygrothermal aging has no effect on the strength of the film specimens. Some UV96 and HUV96 films exhibit

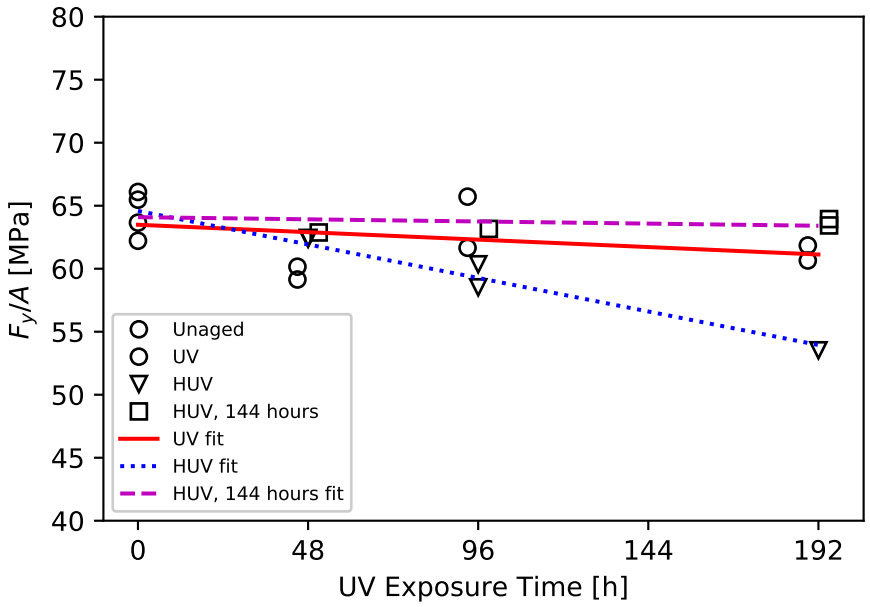

Figure F.4: The true yield stress of cylindrical PA-6 bars versus their UV exposure time for unaged bars conditioned for 72 hours, UV-aged bars conditioned for 72 hours, HUV-aged bars conditioned for 72 hours, and HUV-aged bars conditioned for 144 hours.

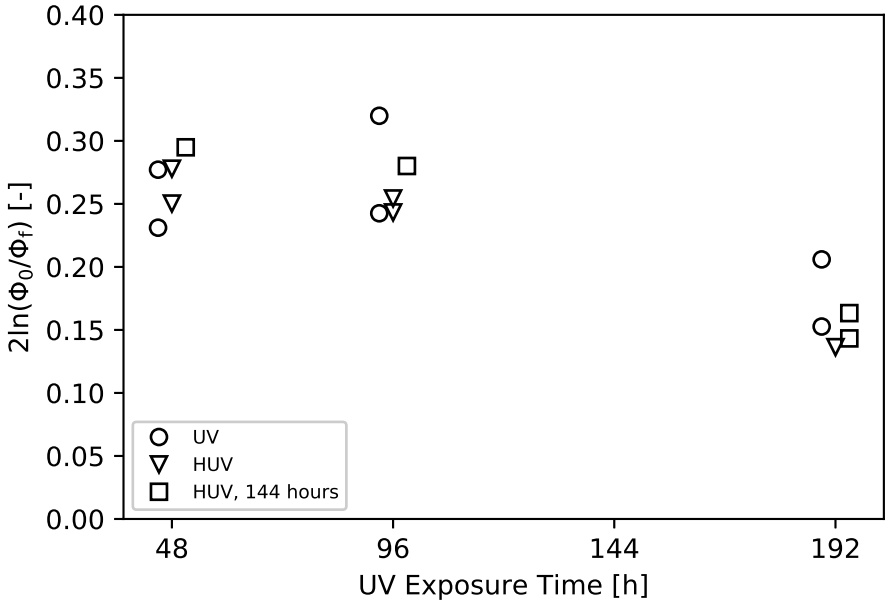

Figure F.5: The true strain to failure of cylindrical PA-6 bars versus their UV exposure time for specimens subjected to UV aging, HUV aging, and HUV aging with an extended conditioning treatment (144 hours).

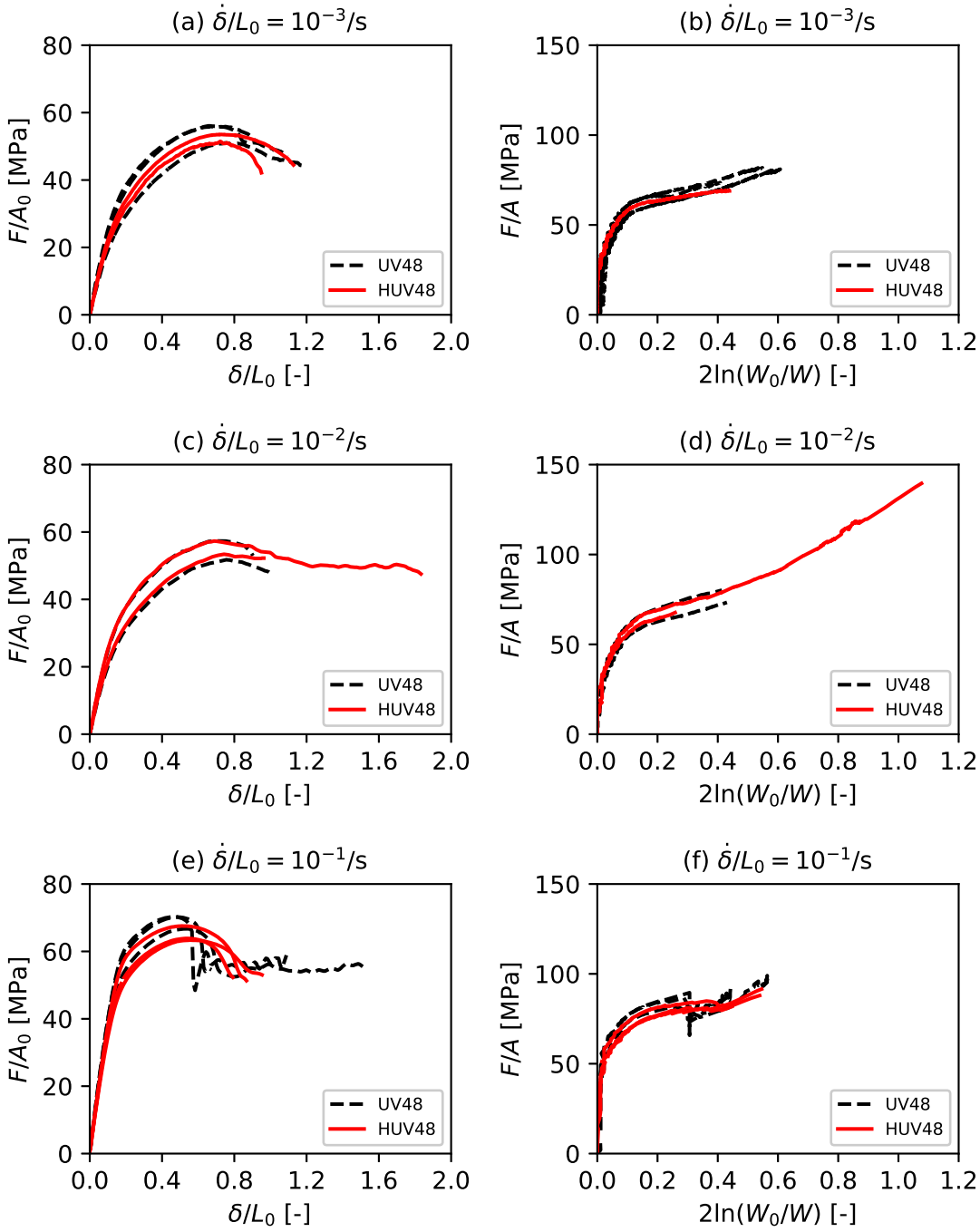

Figure F.6: The mechanical response of PA-6 films subjected to UV48 and HUV48 aging. The nominal mechanical response is shown in the left column (a,c,e) and the true mechanical response is shown in the right column (b,d,f). Results are grouped in rows by nominal strain rate: (a,b) $\dot{\delta}/L_0 = 10^{-3}$ /s, (c,d) $\dot{\delta}/L_0 = 10^{-2}$ /s, (e,f) $\dot{\delta}/L_0 = 10^{-1}$ /s.

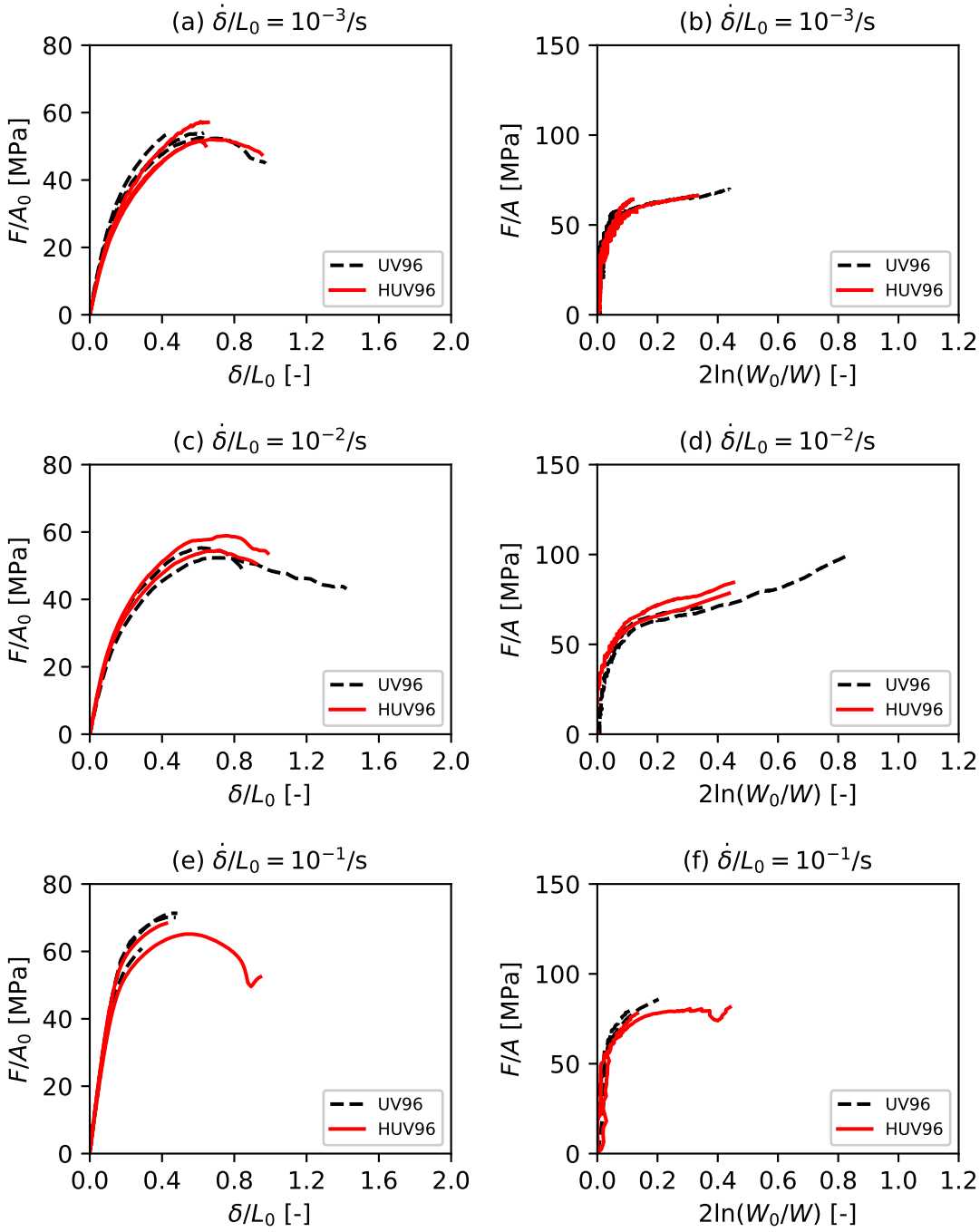

Figure F.7: The mechanical response of PA-6 films subjected to UV96 and HUV96 aging. The nominal mechanical response is shown in the left column (a,c,e) and the true mechanical response is shown in the right column (b,d,f). Results are grouped in rows by nominal strain rate: (a,b) $\dot{\delta}/L_0 = 10^{-3}$ /s, (c,d) $\dot{\delta}/L_0 = 10^{-2}$ /s, (e,f) $\dot{\delta}/L_0 = 10^{-1}$ /s.

an apparent strength significantly lower than other tests using the same conditions. This does not reflect a reduction in intrinsic strength. Instead, these specimens fractured before reaching the load at which structural softening begins.

The failure strain is investigated for UV48 and HUV48 aged films in Fig. F.10 and for UV96 and HUV96 aged films in Fig. F.11. Although a large scatter is observed in the failure strain, no consistent trends emerge when comparing UV and HUV conditions. As with the bulk bars, any chemical aging induced or accelerated by the hygrothermal aging is insignificant compared to the chemical aging induced by UV radiation.

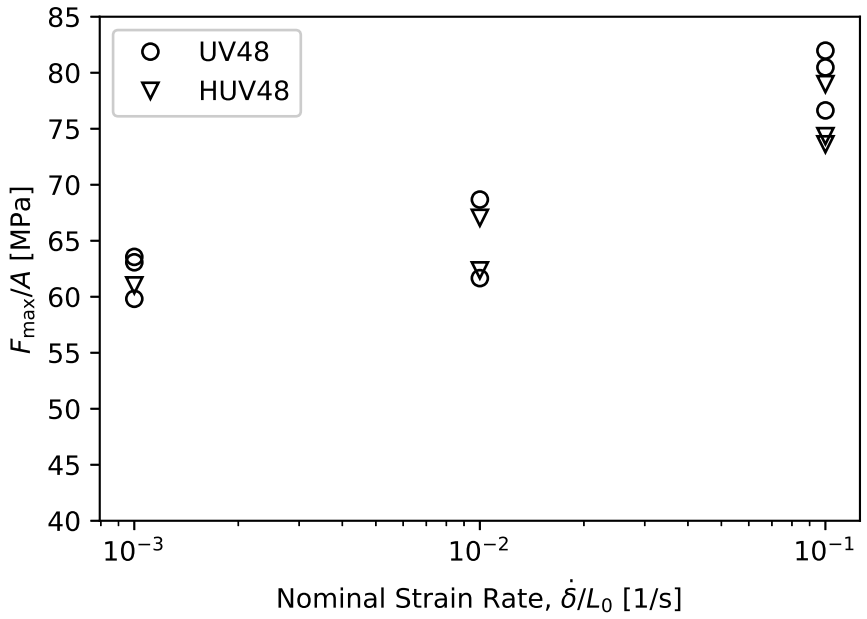

Figure F.8: The true stress at the maximum force versus strain rate for PA-6 films subjected to UV48 and HUV48 aging.

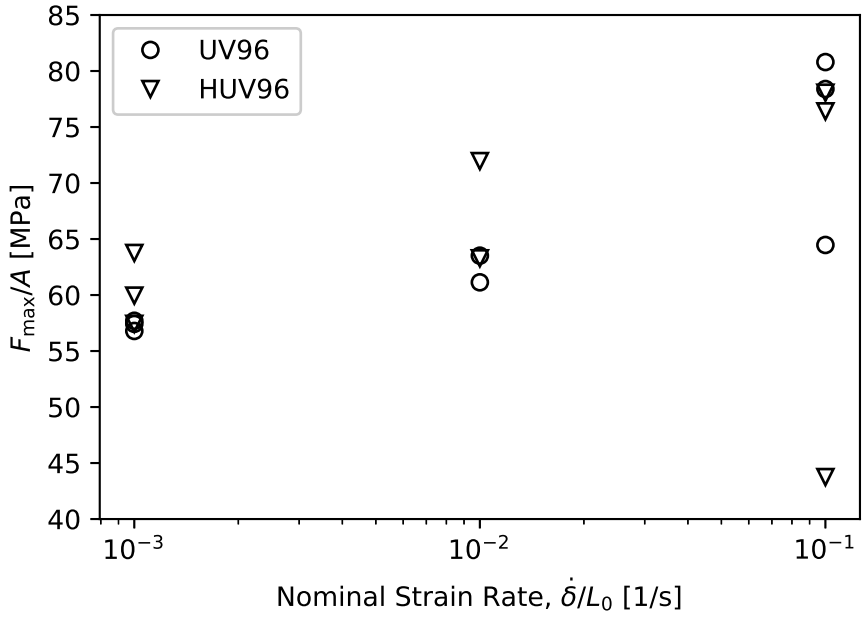

Figure F.9: The true stress at the maximum force versus strain rate for PA-6 films subjected to UV96 and HUV96 aging.

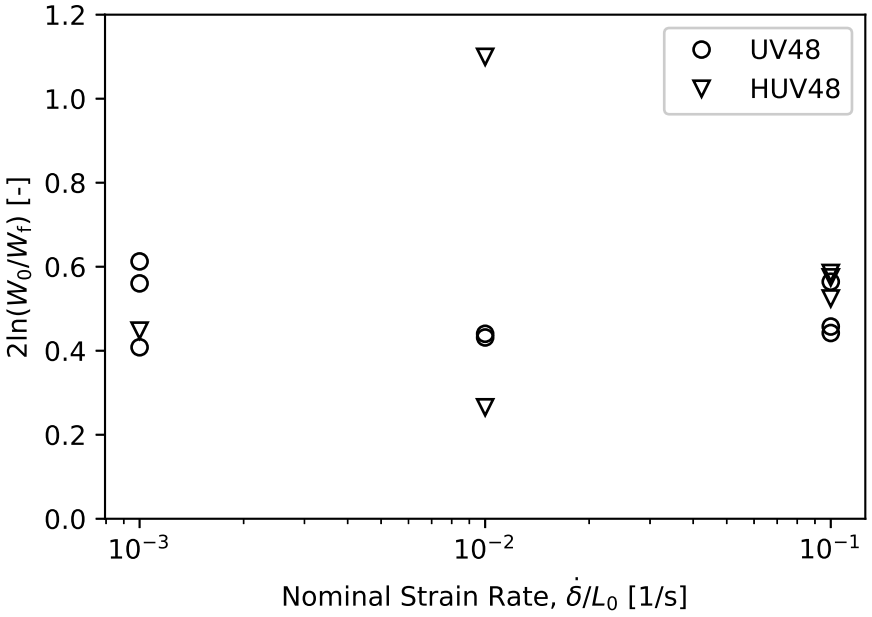

Figure F.10: The true failure strain versus strain rate for PA-6 films subjected to UV48 and HUV48 aging.

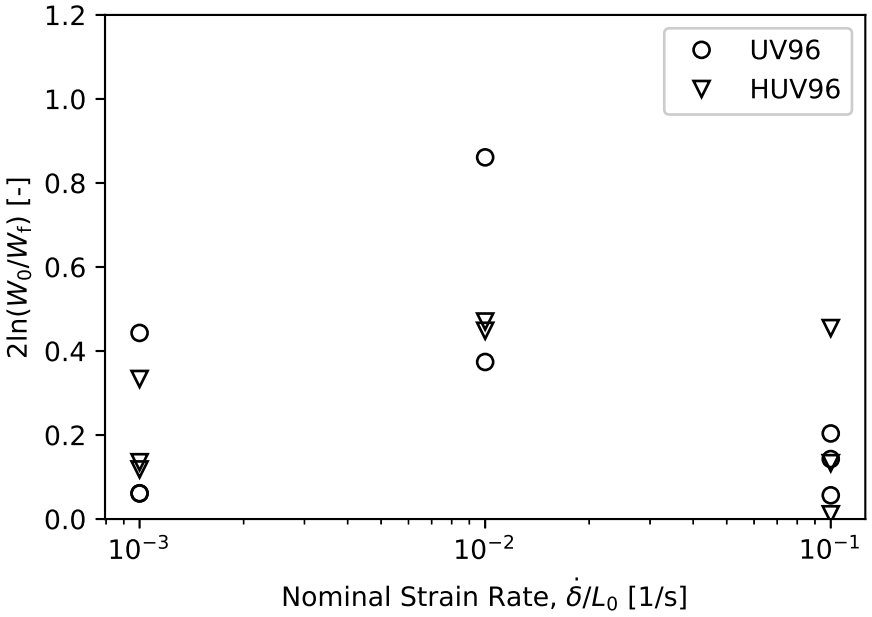

Figure F.11: The true failure strain versus strain rate for PA-6 films subjected to UV96 and HUV96 aging.

F.5 Conclusion

Mechanical tests were conducted on bulk and film PA-6 specimens that were subjected to UV and HUV aging. Special attention was given to comparing UV and HUV conditions that used the same amount of UV exposure time. In this way, the effect of hygrothermal aging could be investigated. In bulk specimens, hygrothermal aging resulted in a decrease in strength, but this was a result of the hygroscopic nature of PA-6 and the role of water as a plasticizer in PA-6. It was not an effect of chemical changes caused by hydrolysis. The original conditioning treatment used to dry the PA-6 bulk specimens was too short to remove all the moisture absorbed during hygrothermal aging, since the elevated temperature and humidity increased moisture absorption. When the conditioning treatment was extended from 72 hours to 144 hours, HUV aging had no effect on the strength of bulk specimens.

For the film specimens, no loss of strength was observed with HUV aging, even using the standard conditioning treatment. Even though the films also absorb additional moisture during hygrothermal aging, they are thin enough that all moisture is removed during the standard length (72 hour) conditioning treatment.

For both the bulk and film specimens, hygrothermal aging had no effect on the failure strain.

For the aging conditions studied here, chemical aging induced by hygrothermal aging is insignificant compared to chemical aging induced by UV radiation. For this reason, the main text of this dissertation avoids discussion of hygrothermal aging. These findings do not indicate that hygrothermal aging is not an important factor for chemical aging. All that can be said is that the specific doses of hygrothermal aging applied here have no significant impact on the chemical aging of the materials studied here.

APPENDIX G. ANISOTROPIC BEHAVIOR OF UV-AGED LOW DENSITY POLYETHYLENE FILMS

G.1 Introduction

In UV-aged low-density polyethylene (LDPE) films, chemical cracks have been observed parallel to the transverse direction of the film [99]. Presumably, the preferred orientation of the cracks is related to the processing-induced orientation of the films. In this case, UV-aging may have a more detrimental effect on the fracture strain along the molding direction than along the transverse direction. In this short study, UV-aged LDPE films are loaded along the molding direction and the transverse direction to characterize their anisotropic mechanical behavior. This study was done in collaboration with Ana K. Rodriguez [148].

G.2 Experimental

Low density polyethylene (LDPE) films of thickness 50 µm were used in this study. The films were aged by exposure to UV radiation for 96 h. After aging, the specimens were cut from the film using a punch. Some films were cut parallel to the molding direction (MD) of the film, while others were cut parallel to the transverse direction (TD). The specimens had an initial gauge length of $L_0 = 6\,\text{mm}$, and used the same geometry as the 0.060 mm thick PA-6 films used elsewhere in this dissertation, see Fig. A.2. For full details regarding the material, aging procedure, and specimen fabrication, see Ref. [99].

Mechanical tests were carried out on an MTS Insight electro-mechanical test frame in displacement control mode. A 1 kN load cell was used. The films were loaded at a constant displacement rate of $\dot{\delta} = 3.600\,\text{mm/min}$, which corresponds to a constant nominal strain rate of $\dot{\delta}/L_0 = 10^{-2}\,/\text{s}$. The mechanical behavior is reported using the nominal stress, F/A_0, and the nominal strain, δ/L_0, where F is the force measured by the load cell, A_0 is the initial cross-sectional area of the specimen, δ is the crosshead displacement, and L_0 is the initial gauge length of the specimen.

G.3 Results

Fig. G.1 shows the effect of the specimen orientation (MD or TD) on the nominal stress–strain curves for UV-aged LDPE films. Initially, the nominal stress gradually increases to a peak, defined here as the nominal yield stress, $\sigma_{\mathrm{y}} = F_{\mathrm{y}}/A_0$. Afterwards the stress decreases slightly before a stress plateau is observed. In some cases, the stress begins to increase very slightly after the plateau. Eventually, the films fracture, which is marked by an immediate reduction of the stress to zero. The displacement at which the film fractures is used to define the nominal fracture strain, $\varepsilon_{\mathrm{f}} = \delta_{\mathrm{f}}/L_0$.

Fig. G.2a shows the effects of orientation on the nominal yield stress. Both MD and TD-oriented films have a yield stress of approximately 10 MPa. However, a single MD-oriented film has a slightly higher yield stress of 12 MPa. In Ref. [99], unaged LDPE films formed under the same processing conditions were tested along the MD and TD. In those films, the yield stress along the MD is also approximately 10 MPa, but the yield stress along the TD is approximately 8 MPa. Therefore, the yield stress is affected differently by UV aging along the MD and the TD.

Aging also alters the post-peak hardening behavior. In the unaged films [99], the MD-oriented film shows significant post-peak hardening, while the hardening in the TD-oriented film is relatively low. Here, the UV-aged LDPE films show very low strain hardening along both the MD and TD direction, although the hardening is slightly greater along the MD, see Fig. G.1.

Fig. G.2b shows the effects of orientation on the nominal fracture strain. The MD-oriented films typically have a greater fracture strain than the TD-oriented films. This is in contrast with the results on the unaged films in Ref. [99], where the unaged MD-oriented film has a much lower fracture strain than the unaged TD-oriented film. Therefore, UV aging has had a greater impact on the fracture strain along the TD than along the MD. Given that cracks are observed parallel to the TD in Ref. [99], this result is counterintuitive.

Fig. G.3 shows images from LDPE films immediately prior to fracture. Fig. G.3a shows

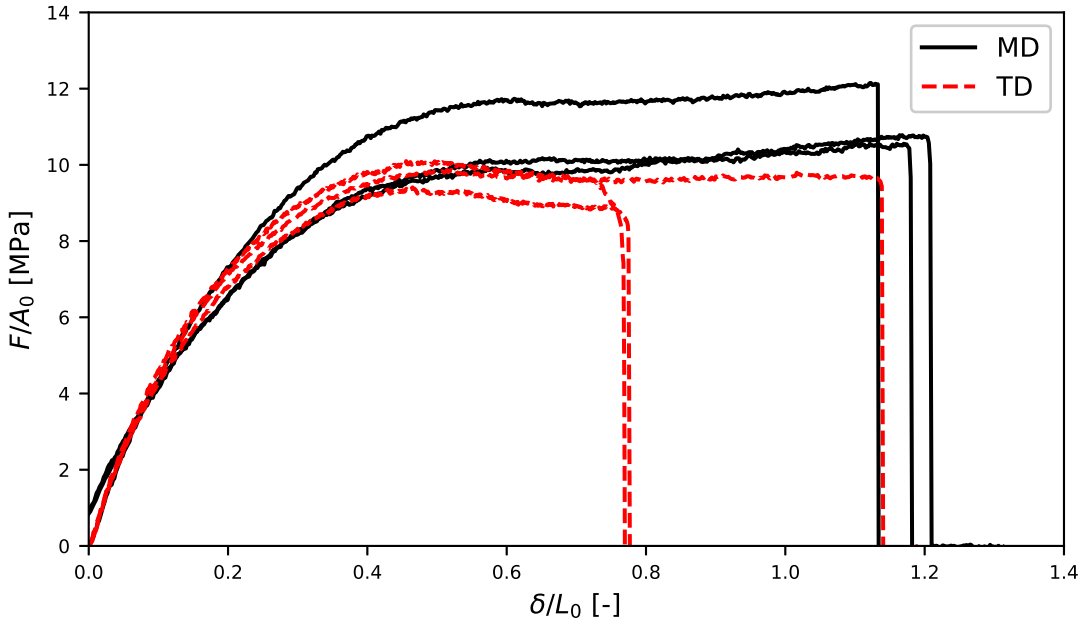

Figure G.1: Nominal stress–strain curves for UV-aged LDPE films. Some specimens were cut parallel to the molding direction (MD), while others were cut parallel to the transverse direction (TD).

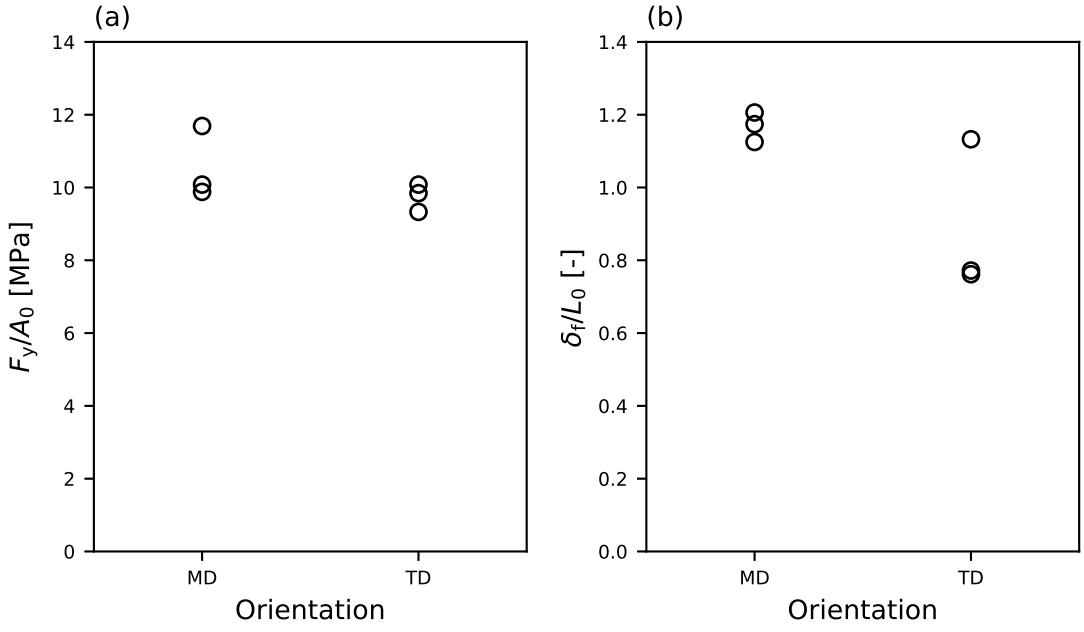

Figure G.2: The effect of orientation on the (a) nominal yield stress and (b) nominal fracture strain of UV-aged LDPE films.

(a) MD

(b) TD

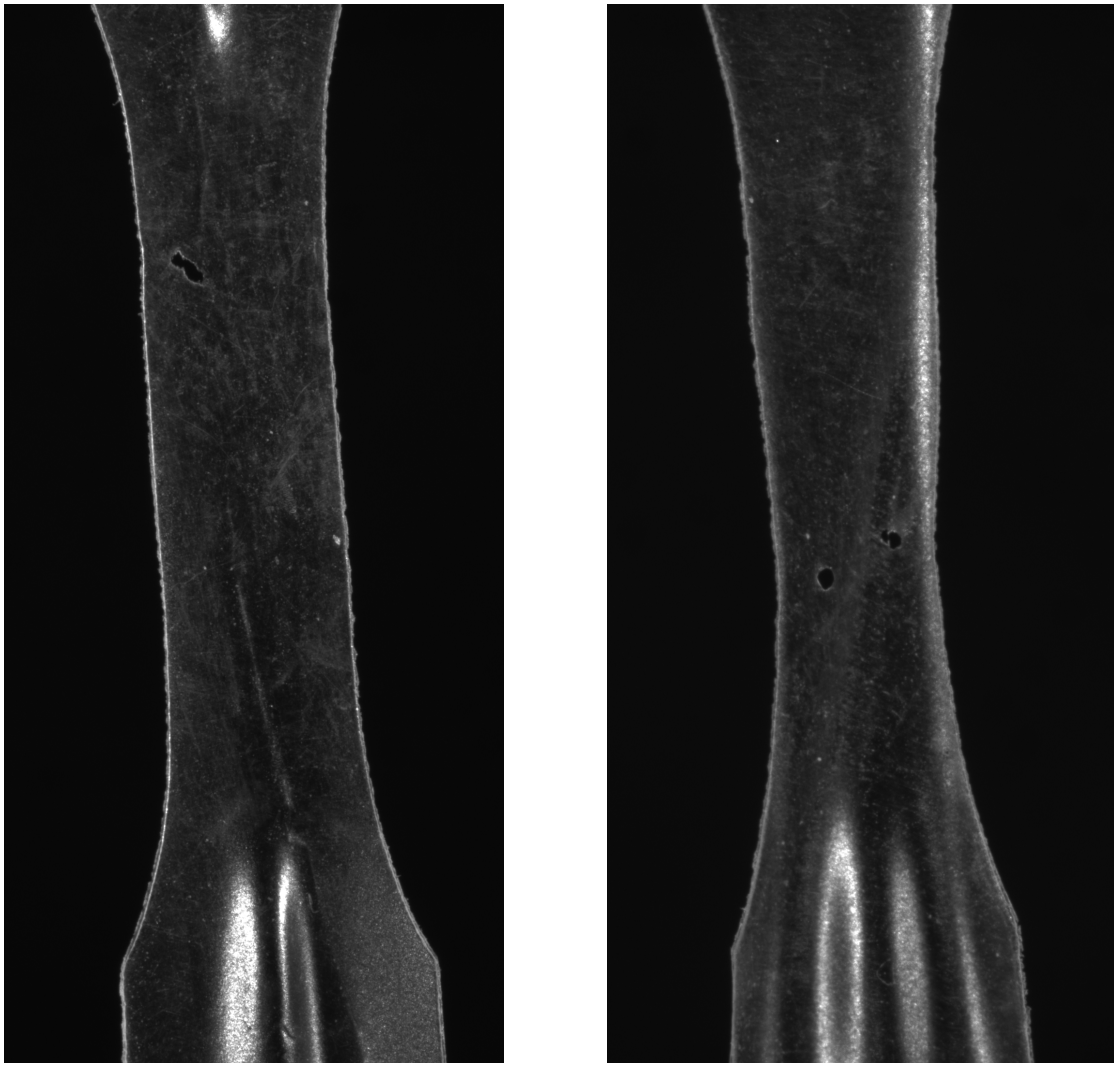

Figure G.3: Images of UV-aged LDPE films immediately prior to fracture. (a) A specimen cut parallel to the molding direction (MD) of the film. (b) A specimen cut parallel to the transverse direction (TD) of the film.

an MD-oriented film, and Fig. G.3b shows a TD-oriented film. In both cases, voids open up within the gauge section and cause fracture. The shape of some voids suggest that coalescence with neighboring voids has occurred. Vids. G.1–G.6 show the deformation and fracture of the LDPE films.[1] Vids. G.1, G.2, and G.3 show experiments on MD-oriented films. Vids. G.4, G.5, and G.6 show experiments on TD-oriented films.

G.4 Conclusion

The anisotropy of UV-aged LDPE was investigated by mechanical tests. Specimens were either cut along the molding direction (MD) or the transverse direction (TD) of the film. In both MD and TD-oriented films, the yield stress and strain hardening were approximately equal. This is in contrast to the unaged films, where the MD-oriented films showed greater yield stress and strain hardening than the TD-oriented films [99]. The MD-oriented films also had a larger fracture strain than the TD-oriented films, which is also contrary to the results from unaged films, where the TD-oriented films had a larger fracture strain. This result is in opposition to the hypothesis that the fracture strain along the MD should be more severely reduced by UV radiation due to cracks oriented parallel to the TD.

[1] Email `kncundiff.dissertationquestions@gmail.com` to request video files.

APPENDIX H. EXPERIMENTAL DATABASE: CYLINDRICAL BARS

H.1 Introduction

Results from mechanical tests are discussed throughout the body of this text, but the presentation of every experiment was not necessary to support the primary narrative. This appendix is the first in a series that provides a complete set of data from mechanical tests on a single specimen type. In some cases, data is repeated from the main text in order to create a single location where all data is presented. The present appendix documents all results from mechanical tests on cylindrical bars.[1]

An extensive experimental campaign on bulk specimens was carried out while conducting research for this dissertation. The bulk experimental campaign had two goals. The first goal was to investigate the effects of UV aging on PA-6 specimens loaded under a variety of stress states. To this end, four different specimen geometries were subjected to a variety of aging conditions. The second goal was to produce a robust experimental database useful for calibration and validation a viscoplastic polymer model. For this goal, tests were carried out in tension and compression at a variety of strain rates and temperatures.

The experiments presented here investigate the effects of UV aging, drawing temperature, and strain rate on the mechanical behavior of PA-6 in tension. Results from a single realization may be repeated across multiple figures to facilitate visualizing the effects of the aforementioned conditions. Severe strain localization in the form of necking is seen in the cylindrical bars studied here. Strain localization poses challenges for accurately measuring strain. For this reason, a variety of extensometry methods were explored. The results in this chapter are grouped by extensometry method. Results from a single experiment may appear in multiple figures but with different measures of deformation presented.

The outline of this chapter is as follows. The methodology and test matrix are presented

[1] The mechanical behavior of cylindrical bars subjected to HUV aging are not discussed in this appendix. All experiments on HUV aged specimens are presented in Appendix F.

in Section H.2. The results are presented in Section H.3. The results are grouped by extensometry methods. Measurements using the crosshead displacement, a laser extensometer, digital image correlation (DIC), and contour tracking are presented in Subsections H.3.1, H.3.2, H.3.3, and H.3.4, respectively. Each of these subsections begin with a description of that extensometry method, including its strengths and weaknesses. The DIC and contour tracking methodologies are video based methods. The videos from these tests are available from the author upon request.[2] A table of available videos is presented in Section H.4.

H.2 Experimental

H.2.1 Procedure

The procedure for conducting mechanical tests on the cylindrical bars was already presented in detail in Section 3.2. A brief overview is reiterated here. A cast plate of PA-6 was purchased from Plastics International. The crystal mass fraction of the plate was measured as 38 % using differential scanning calorimetry. Cylindrical bars were machined from the plate using a lathe. See Fig. A.1 for a detailed drawing of the cylindrical bars. Some bars were aged by UV exposure in an accelerated weathering machine. Aging conditions are referred to by the hours of exposure prepended by "UV", e.g. UV48, UV96, UV192 refer to 48, 96, and 192 hours of UV exposure. To control the moisture content of the PA-6 bars, they were dried in a vacuum oven at 80 °C for 72 hours prior to testing. The mechanical tests were carried out an an electro-mechanical test frame in displacement control mode. A 30 kN load cell was used.

The procedure presented in Section 3.2 only considers tests at a nominal strain rate of 10^{-3} /s and at room temperature (24 °C). Here, multiple strain rates and temperatures were explored. The nominal strain rate was calculated using the rate of crosshead displacement, $\dot{\delta}$, divided by the initial length of the gauge section, L_0. The temperature was controlled using a custom temperature chamber mounted to the test frame. The chamber functions as an oven when the temperature needs to be increased, and uses liquid nitrogen for cooling.

[2] Email `kncundiff.dissertationquestions@gmail.com` to request video files.

Various methods for measuring the specimen deformation were employed. The different methods are discussed in context with the results produced from those methods.

H.2.2 Test Matrix

Tables H.1 and H.2 constitute the complete test matrix of conditions studied using cylindrical bars of PA-6 tested in tension. Table H.1 lists realizations of unaged bars, where the effects of temperature and strain rate were investigated. Table H.2 lists realizations of aged bars. Footnotes indicate which realizations used a particular extensometry method.

Table H.1: Test matrix for unaged PA-6 cylindrical bars.

Unaged Realizations		Temperature, $T < T_g$			$T > T_g$
		$-30\,°C$	$0\,°C$	$24\,°C$	$60\,°C$
$\left\|\dot{\delta}\right\| / L_0$	$10^{-1}\,/s$		$1^{\|}$	$1^{\|} + 1^{\dagger} + 1^{\ddagger}$	$1^{\|}$
	$10^{-3}\,/s$		$1^{\|}$	$2^{\|} + 1^{\dagger} + 3^{\ddagger}$	
	$10^{-5}\,/s$			1^{*}	

Table H.2: Test matrix for aged PA-6 cylindrical bars.

Aged, $24\,°C$ Realizations		Aging Condition		
		UV48	UV96	UV192
$\left\|\dot{\delta}\right\| / L_0$	$10^{-1}\,/s$			$1^{\dagger} + 1^{\ddagger}$
	$10^{-3}\,/s$	$1^{\dagger} + 1^{\ddagger}$	$1^{\dagger} + 1^{\ddagger}$	$1^{\dagger} + 1^{\ddagger}$
	$10^{-3}\,/s$			

$^{\|}$Laser extensometer
†Contour tracking
‡DIC and contour tracking
*Crosshead only. Not tested to fracture

H.3 Results

H.3.1 Crosshead displacement

The crosshead displacement is the simplest extensometry employed. It provides an approximation of the nominal strain by normalizing the motion of the test frame's crosshead, δ by the initial length of the gauge section L_0, i.e.

$$\varepsilon^{\text{nom}} \approx \frac{\delta}{L_0}. \tag{H.1}$$

When presenting strain data using crosshead displacement, the nominal stress is also presented,

$$\sigma^{\text{nom}} = \frac{F}{A_0}, \tag{H.2}$$

where F is the force measured by the load cell and A_0 is the initial cross-sectional area of the gauge section.

The strength of this method is its simplicity. Since it requires no additional equipment, all realizations have data using the crosshead displacement. However, this method is not very accurate. The crosshead displacement also includes deformation of the specimen outside the gauge section (i.e. deformation of the grips) as well as deformation from compliance in the test frame. For this reason, it is only an approximation of the nominal strain. Since the crosshead measures an axial elongation, this method cannot resolve strain localization.

Since the test frame drives deformation by the motion of the crosshead, the nominal strain rate is defined using the rate of crosshead displacement. For this reason, the nominal strain rate is denoted as $\dot{\delta}/L_0$.

Figures presenting data from the crosshead displacement are listed below.

- Fig. H.1; Temperature effects, $\dot{\delta}/L_0 = 10^{-3}$ /s, unaged
- Fig. H.2; Temperature effects, $\dot{\delta}/L_0 = 10^{-1}$ /s, unaged
- Fig. H.3; Rate effects, $T = 24\,^{\circ}\mathrm{C}$, unaged
- Fig. H.4; Rate effects, $T = 0\,^{\circ}\mathrm{C}$, unaged
- Fig. H.5; Rate effects, $T = 24\,^{\circ}\mathrm{C}$, UV192
- Fig. H.6; Aging effects, $T = 24\,^{\circ}\mathrm{C}$, $\dot{\delta}/L_0 = 10^{-3}$ /s
  - Data from this figure is discussed at length in Section 3.3.
- Fig. H.7; Aging effects, $T = 24\,^{\circ}\mathrm{C}$, $\dot{\delta}/L_0 = 10^{-1}$ /s

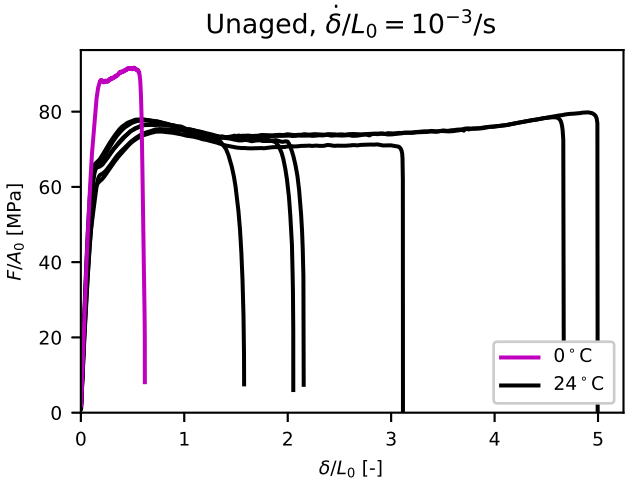

Figure H.1: The effects of temperature on the mechanical response of PA-6. The material is unaged and the nominal displacement rate is $\dot{\delta}/L_0 = 10^{-3}$ /s. The strain is measured using the crosshead displacement.

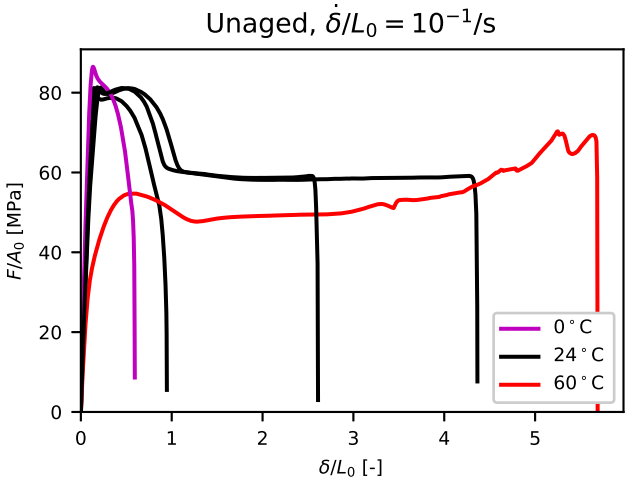

Figure H.2: The effects of temperature on the mechanical response of PA-6. The material is unaged and the nominal displacement rate is $\dot{\delta}/L_0 = 10^{-1}$ /s. The strain is measured using the crosshead displacement.

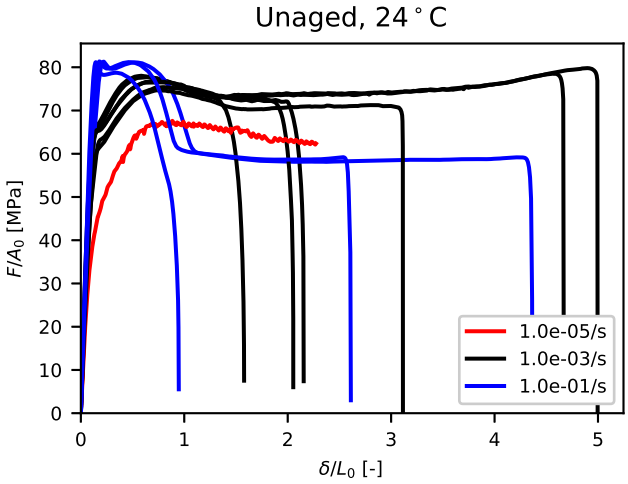

Figure H.3: The effects of nominal strain rate on the mechanical response of PA-6. The material is unaged and the test temperature is $T = 24\,°\text{C}$. The strain is measured using the crosshead displacement.

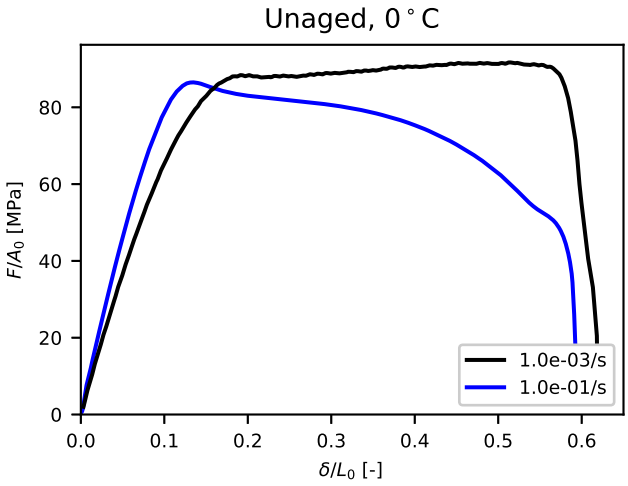

Figure H.4: The effects of nominal strain rate on the mechanical response of PA-6. The material is unaged and the test temperature is $T = 0\,°\text{C}$. The strain is measured using the crosshead displacement.

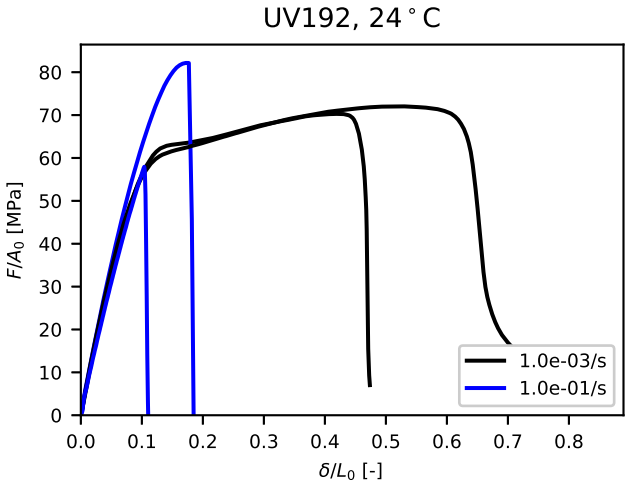

Figure H.5: The effects of nominal strain rate on the mechanical response of PA-6. UV192 aged bars are used and the test temperature is $T = 24\,°\text{C}$. The strain is measured using the crosshead displacement.

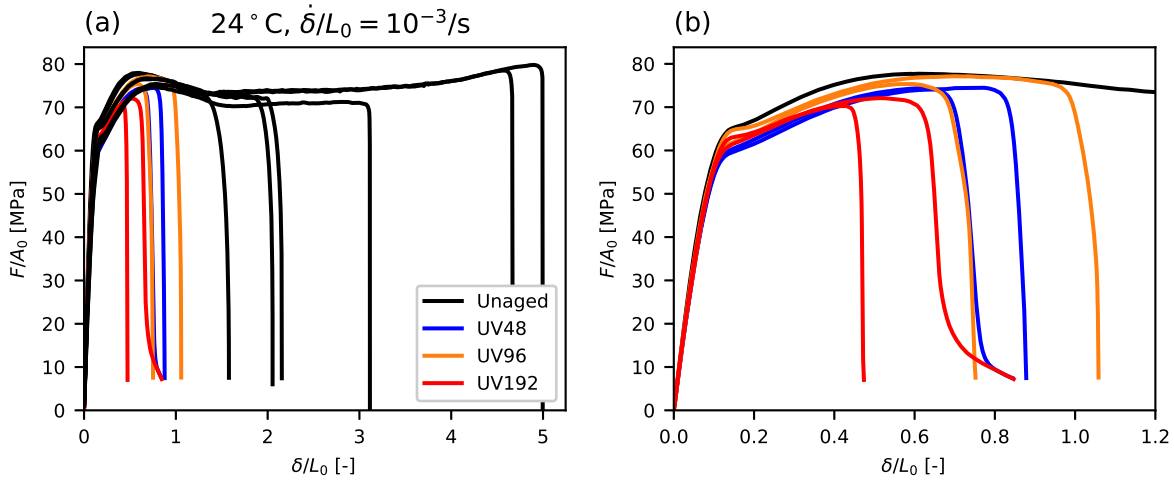

Figure H.6: The effects of photo-oxidation on the mechanical response of PA-6. The test temperature is $T = 24\,°\text{C}$ and the nominal strain rate is $\dot{\delta}/L_0 = 10^{-3}\,/\text{s}$. The strain is measured using the crosshead displacement. (a) All realizations. (b) Aged realizations with only one unaged realization for reference.

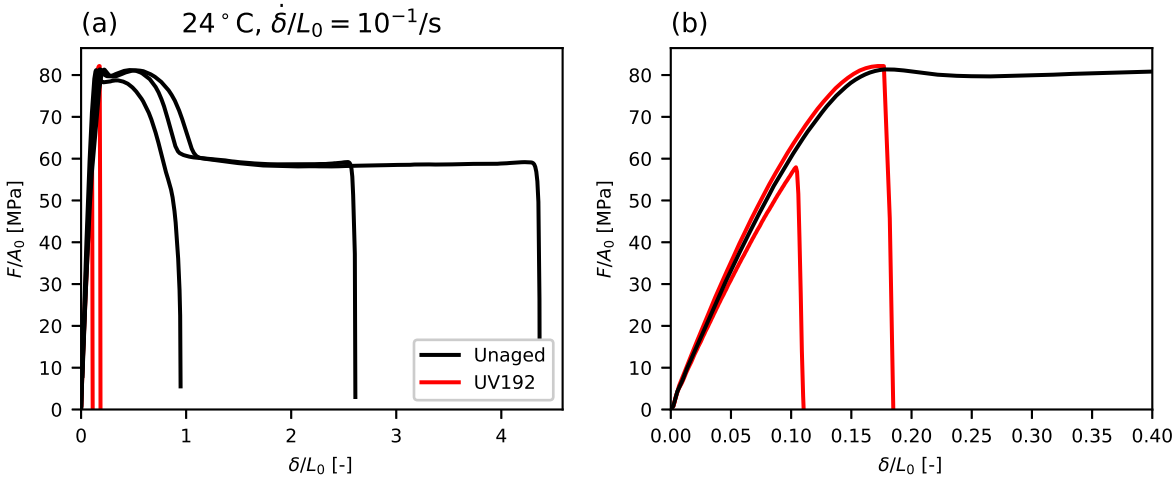

Figure H.7: The effects of photo-oxidation on the mechanical response of PA-6. The test temperature is $T = 24\,°\text{C}$ and the nominal strain rate is $\dot{\delta}/L_0 = 10^{-1}\,/\text{s}$. The strain is measured using the crosshead displacement. (a) All realizations. (b) Aged realizations with only one unaged realization for reference.

H.3.2 Laser extensometer

In some tests, an MTS LX1500 laser extensometer was used to obtain accurate measurements of the nominal strain. To use the laser extensometer, two pieces of reflective tape are placed at the top and bottom of the specimen gauge section. The laser extensometer then tracks the deformation of the gauge section by measuring the distance between the reflective tape. When using a laser extensometer, the nominal strain is calculated by

$$\varepsilon^{\text{nom}} = \frac{\Delta L}{L_0}, \tag{H.3}$$

where ΔL is the deformation of the gauge section measured by the laser extensometer and L_0 is the initial gauge length. When presenting strain data measured by the laser extensometer, the nominal stress is used,

$$\sigma^{\text{nom}} = \frac{F}{A_0}. \tag{H.4}$$

Laser extensometer measurements are superior to the crosshead displacement since measurements from the former do not include deformation outside the gauge section or from compliance of the test frame. Additionally, the laser extensometer could be used through the window of the temperature chamber, making it the preferred method of extensometry for tests not at room temperature. However, it is still an axial measurement of deformation and therefore not ideal for measuring strain after the onset of necking.

Figures presenting data from the laser extensometer are listed below.

- Fig. H.8; Temperature effects, $\dot{\delta}/L_0 = 10^{-3}\,/\text{s}$, unaged
- Fig. H.9; Temperature effects, $\dot{\delta}/L_0 = 10^{-1}\,/\text{s}$, unaged
- Fig. H.10; Rate effects, $T = 24\,^{\circ}\text{C}$, unaged
- Fig. H.11; Rate effects, $T = 0\,^{\circ}\text{C}$, unaged

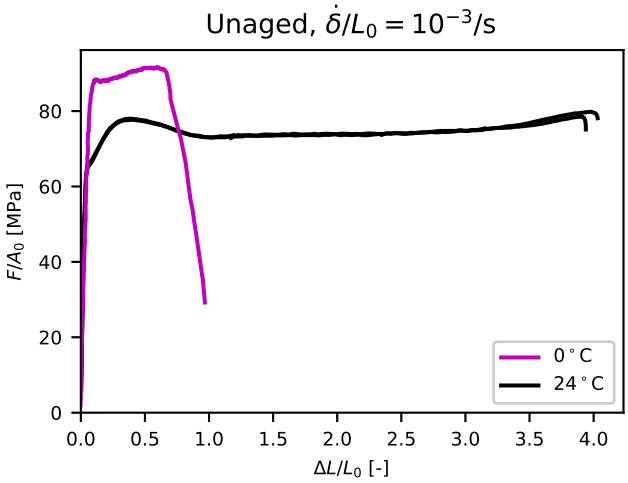

Figure H.8: The effects of temperature on the mechanical response of PA-6. The material is unaged and the nominal strain rate is $\dot{\delta}/L_0 = 10^{-3}$ /s. The strain is measured using a laser extensometer.

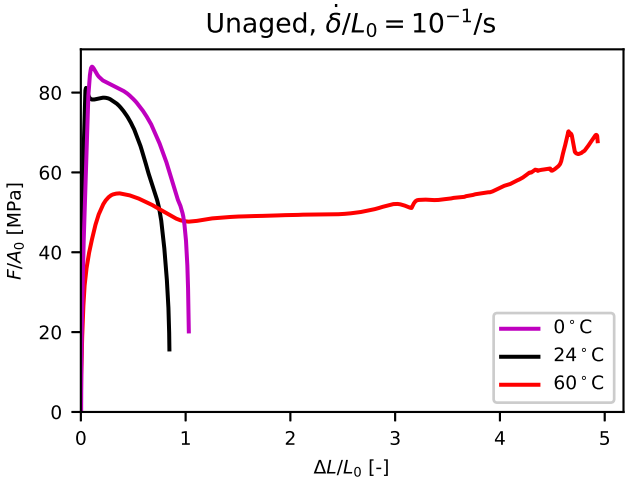

Figure H.9: The effects of temperature on the mechanical response of PA-6. The material is unaged and the nominal strain rate is $\dot{\delta}/L_0 = 10^{-1}$ /s. The strain is measured using a laser extensometer.

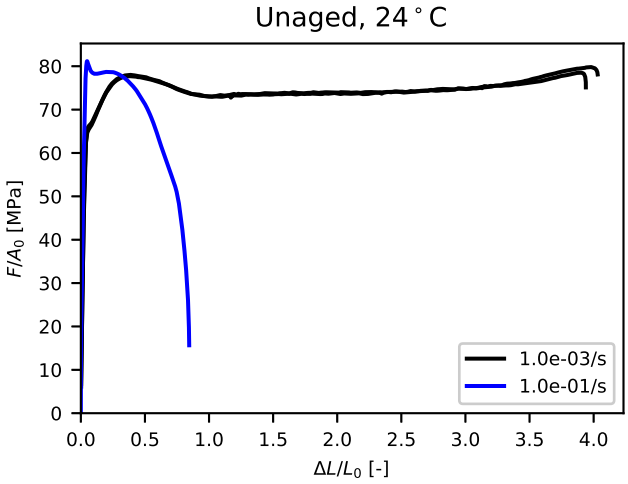

Figure H.10: The effects of nominal strain rate on the mechanical response of PA-6. The material is unaged and the test temperature is $T = 24\,°\text{C}$. The strain is measured using a laser extensometer.

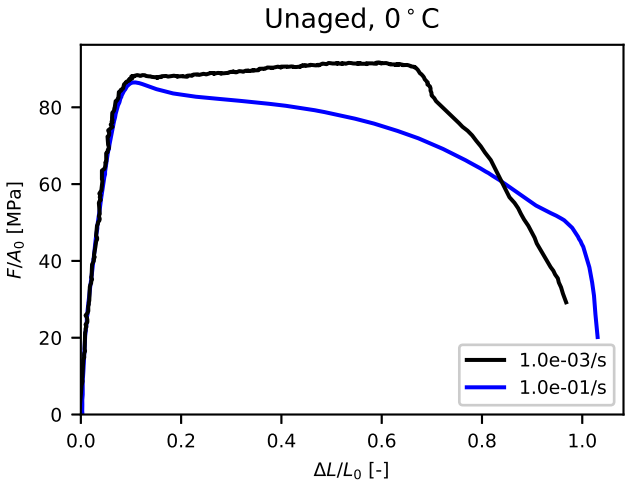

Figure H.11: The effects of nominal strain rate on the mechanical response of PA-6. The material is unaged and the test temperature is $T = 0\,°\text{C}$. The strain is measured using a laser extensometer.

H.3.3 Digital image correlation

A small number of tests utilized digital image correlation (DIC). In DIC, full strain fields of the specimen surface are generated from videos of the test by tracking the deformation of a speckle pattern painted onto the specimen. Here, it was necessary to use 3D-DIC in order to accurately analyze the surface of the curved specimen. In 3D-DIC, two cameras are used to record the videos. Each camera views the specimen from a slightly different angle. In this case, the cameras were placed at approximately 15° apart from each other. Videos were recorded using two Grasshopper Express Point Grey digital CCD cameras (Part number: GX-FW-60S6M-C) equipped with Tokina Macro 100 F2.8 D lenses. The resolution of the cameras was 2.8 megapixels. The software VIC-Snap from Correlated Solutions was used to control the cameras. VIC-3D, also from Correlated Solutions, was used to perform the DIC analysis. After analyzing the images using 3D-DIC, the maximum Hencky strain was extracted from a vertical line down the center of the specimen. The true stress is then approximated by

$$\sigma^{\text{true}} = \left(\frac{F}{A_0}\right) \exp\left(\varepsilon^{\text{DIC}}\right), \tag{H.5}$$

where F is the force measured by the load cell, A_0 is the initial cross-sectional area, and ε^{DIC} is the maximum Hencky strain along the centerline of the specimen. Because DIC generates a strain field over the entire field of view, strain localizations are easily measured. However, DIC requires that the specimen surface be painted. In tests on photo-oxidized specimens, the paint obscured growing surface cracks from view. Additionally, after large deformations, the speckle pattern becomes too deformed to be tracked, so strain measurements become unreliable before fracture. This is only an issue in the unaged bars. It should be emphasized that DIC measures the strain at a point on the surface of the specimen.

Figures presenting data from DIC are listed below.

- Fig. H.12; Aging effects, $T = 24\,^{\circ}\mathrm{C}$, $\dot{\delta}/L_0 = 10^{-3}\,/\mathrm{s}$
- Fig. H.13; Aging effects, $T = 24\,^{\circ}\mathrm{C}$, $\dot{\delta}/L_0 = 10^{-1}\,/\mathrm{s}$

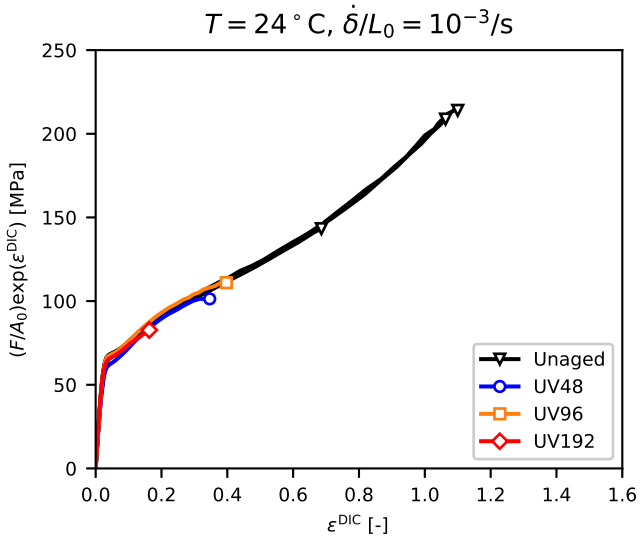

Figure H.12: The effects of photo-oxidation on the mechanical response of PA-6. The test temperature is $T = 24\,^\circ$C and the nominal strain rate is $\dot{\delta}/L_0 = 10^{-3}$ /s. The true stress and strain are approximated using DIC.

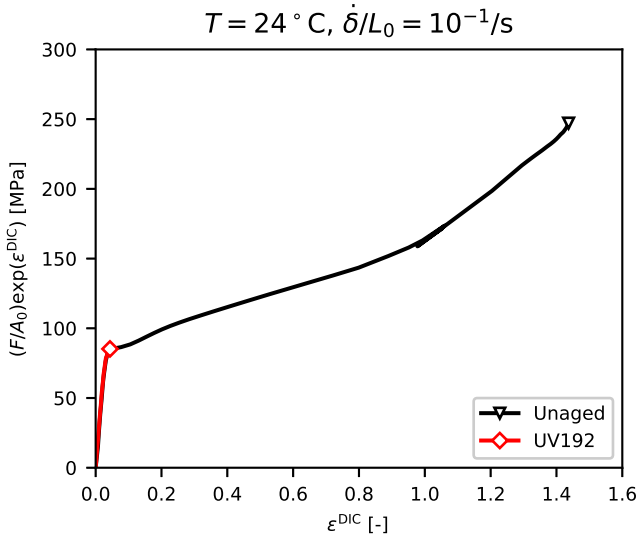

Figure H.13: The effects of photo-oxidation on the mechanical response of PA-6. The test temperature is $T = 24\,^\circ$C and the nominal strain rate is $\dot{\delta}/L_0 = 10^{-1}$ /s. The true stress and strain are approximated using DIC.

H.3.4 Contour tracking

Contour tracking was first introduced in Section 3.2.6. It is used in this dissertation as the primary method of measuring the true stress and strain from a mechanical test. Contour tracking analyzes test images to measure lateral deformations. Test images are processed by a script that identifies specimen contours and finds the minimum distance between them. For a circular specimen, the minimum distance corresponds to the minimum diameter of the cross-section. Assuming the cross-section remains circular, the true strain is calculated using

$$\varepsilon^{\text{true}} = 2 \ln \frac{\Phi_0}{\Phi}, \tag{H.6}$$

where Φ is the minimum diameter of the specimen for the current image and Φ_0 is the diameter of the specimen prior to deformation. This equation for strain assumes that the deformation is incompressible, the deformation is homogenous in the radial direction, and also that the material is transversely isotropic. The true stress is calculated using

$$\sigma^{\text{true}} = \frac{4F}{\pi \Phi^2}, \tag{H.7}$$

where F is the force measured by the load cell. To be consistent in how videos were recorded between contour tracking and DIC methodologies, the same video setup was used as described in Section H.3.3. However, only one camera is really necessary to perform contour tracking measurements. Results from either camera provided similar results, but using both cameras had the added benefit of providing two points of view on the formation of the final crack leading to fracture.

Contour tracking measures lateral deformations at the narrowest point on the specimen. This allows it to accurately measure strain when strong strain localizations occur. Contour tracking requires no painting, which is useful as paint may obscure surface cracks. For example, the cracks shown in Fig. 3.10 would not have been visible using DIC. Contour

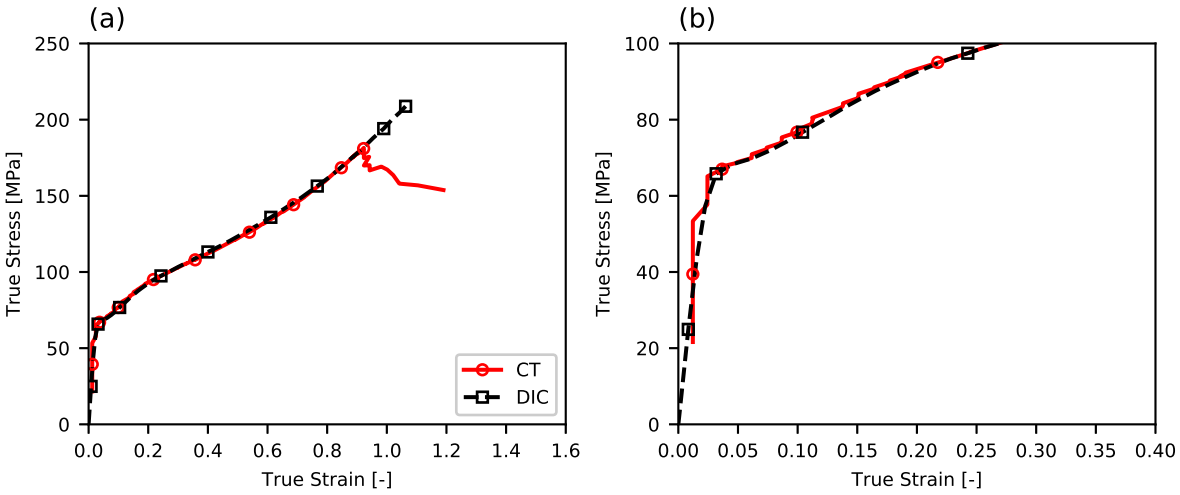

Figure H.14: A comparison of the true stress-strain curves produced by contour tracking (CT) and DIC.

tracking requires no proprietary software and can also be used to retroactively process a sequence of images initially used for DIC. Contour tracking is a global measure of the lateral deformation, i.e. it is an average strain over the entire cross-section. This is in contrast to DIC, which is a local measure of deformation.

One weakness of contour tracking is that it only measures the true axial stress. When necking initiates, a triaxial stress state is induced. During this time, F/A will overestimate the true stress. Once the neck fronts have propagated away form the minimum section, the local geometry becomes cylindrical again and the local stress state returns to uniaxial. Therefore, this weakness is only transient. This issue is discussed in more detail in Chapter 3 and 6. An improved contour tracking method could be developed that measured local curvature and accounted for this effect.

Fig. H.14 compares the true stress-strain curves generated from contour tracking and DIC. Data from nine images are highlighted by plotting the data from those images with large markers. This permits the comparison of contour tracking and DIC for a single image. Although the stress-strain curves produced by contour tracking are nearly identical, DIC

predicts a higher final strain, as can be seen by comparing the final two emphasized points. However, at small to medium strains, results are nearly identical for a given image, as can be seen from the nearly overlapping points at early stages of deformation. Fig. H.14b reveals that DIC produces more accurate measurements at small strains. The noise in the contour tracking data could be reduced by using a higher resolution camera. Fig. H.14 can be used as a "sanity check" for the accuracy of contour tracking. Overall, the comparison between the two methods is good.

Figures presenting data from contour tracking are listed below.

- Fig. H.15; Aging effects, $T = 24\,^{\circ}\mathrm{C}$, $\dot{\delta}/L_0 = 10^{-3}\,/\mathrm{s}$
  - Data from this figure is discussed at length in Section 3.3.
- Fig. H.16; Aging effects, $T = 24\,^{\circ}\mathrm{C}$, $\dot{\delta}/L_0 = 10^{-1}\,/\mathrm{s}$
- Fig. H.17; Rate effects, $T = 24\,^{\circ}\mathrm{C}$, unaged
- Fig. H.18; Rate effects, $T = 24\,^{\circ}\mathrm{C}$, UV192

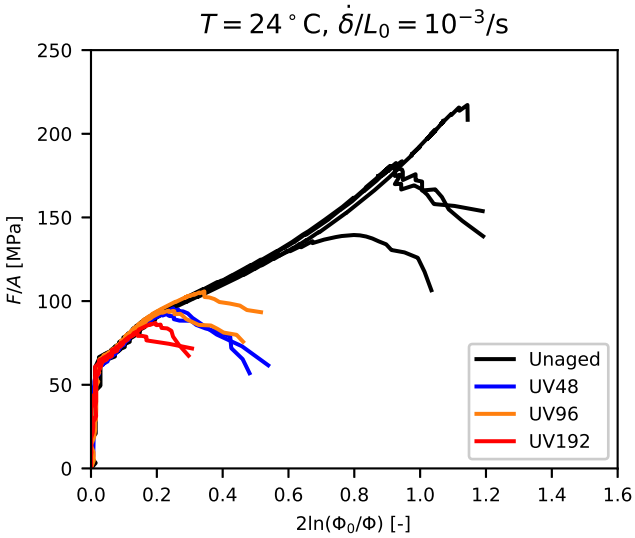

Figure H.15: The effects of photo-oxidation on the mechanical response of PA-6. The test temperature is $T = 24\,^\circ$C and the nominal strain rate is $\dot{\delta}/L_0 = 10^{-3}$ /s. The true stress and strain are approximated using contour tracking.

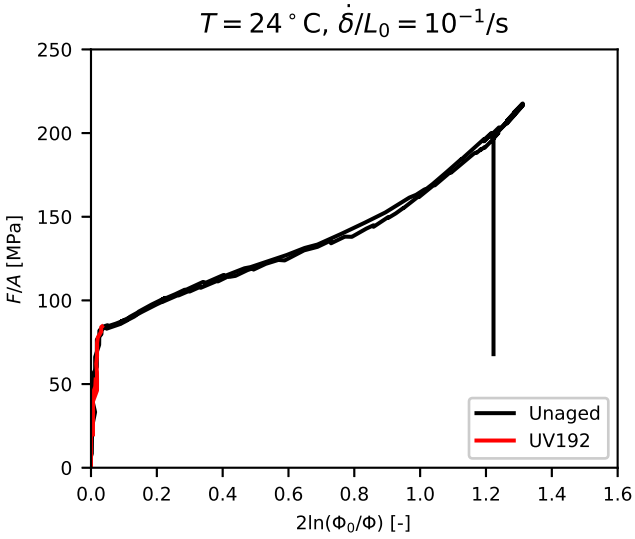

Figure H.16: The effects of photo-oxidation on the mechanical response of PA-6. The test temperature is $T = 24\,^\circ$C and the nominal strain rate is $\dot{\delta}/L_0 = 10^{-1}$ /s. The true stress and strain are approximated using contour tracking.

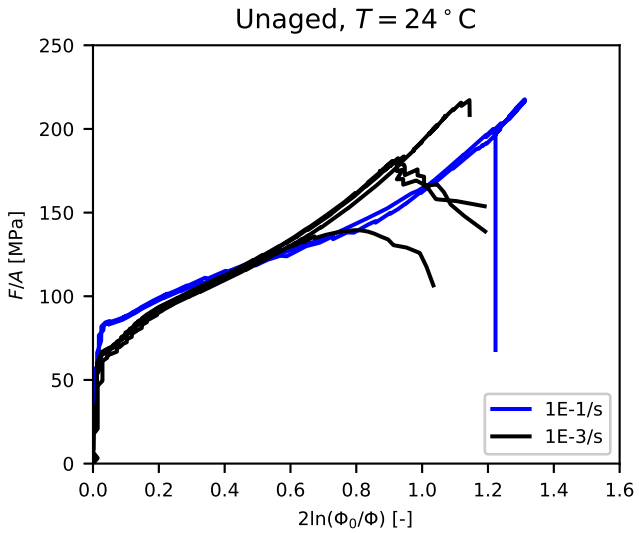

Figure H.17: The effects of nominal strain rate on the mechanical response of PA-6. The material is unaged and the test temperature is $T = 24\,^\circ$C. The true stress and strain are approximated using contour tracking.

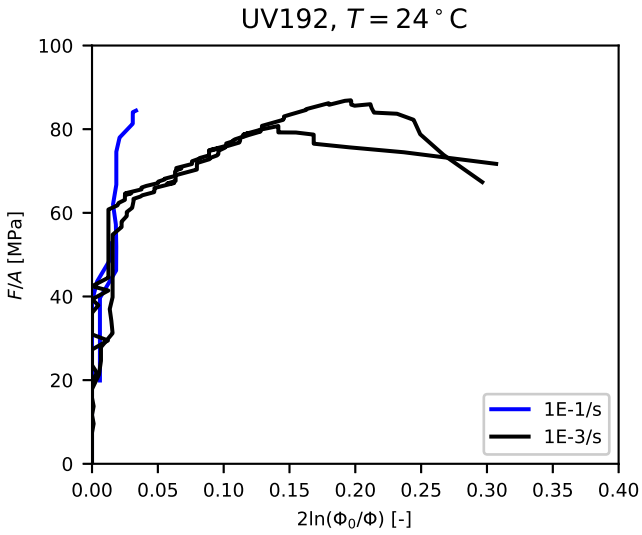

Figure H.18: The effects of nominal strain rate on the mechanical response of PA-6. UV192 aged bars are used and the test temperature is $T = 24\,^\circ$C. The true stress and strain are approximated using contour tracking.

H.4 Videos of Mechanical Tests

Table H.3 lists all available videos of mechanical tests on cylindrical bars.[4] Fig. H.19 shows the information provided in each videos by providing a single frame from Vid. H.4. Each video (1) provides information about the test conditions, (2) shows images of the test specimen during deformation, (3) shows the nominal stress-strain curve as measured by crosshead displacement, (3) shows the true stress-strain curve as measured by contour tracking. A point moves along each stress-strain curve to indicate the stress and strain for the current test image.

Table H.3: List of videos of mechanical tests on cylindrical bars of PA-6. Videos also show animated nominal and true stress-strain plots.

Aging Condition	$\dot{\delta}/L_0$	Test Temperature	Videos
Unaged	10^{-3} /s	24 °C	Vids. H.1, H.2, H.3, H.4
UV48	10^{-3} /s	24 °C	Vids. H.5, H.6
UV96	10^{-3} /s	24 °C	Vids. H.7, H.8
UV192	10^{-3} /s	24 °C	Vids. H.9, H.10
Unaged	10^{-1} /s	24 °C	Vids. H.11, H.12
UV192	10^{-1} /s	24 °C	Vids. H.13, H.14

[4] Email `kncundiff.dissertationquestions@gmail.com` to request video files.

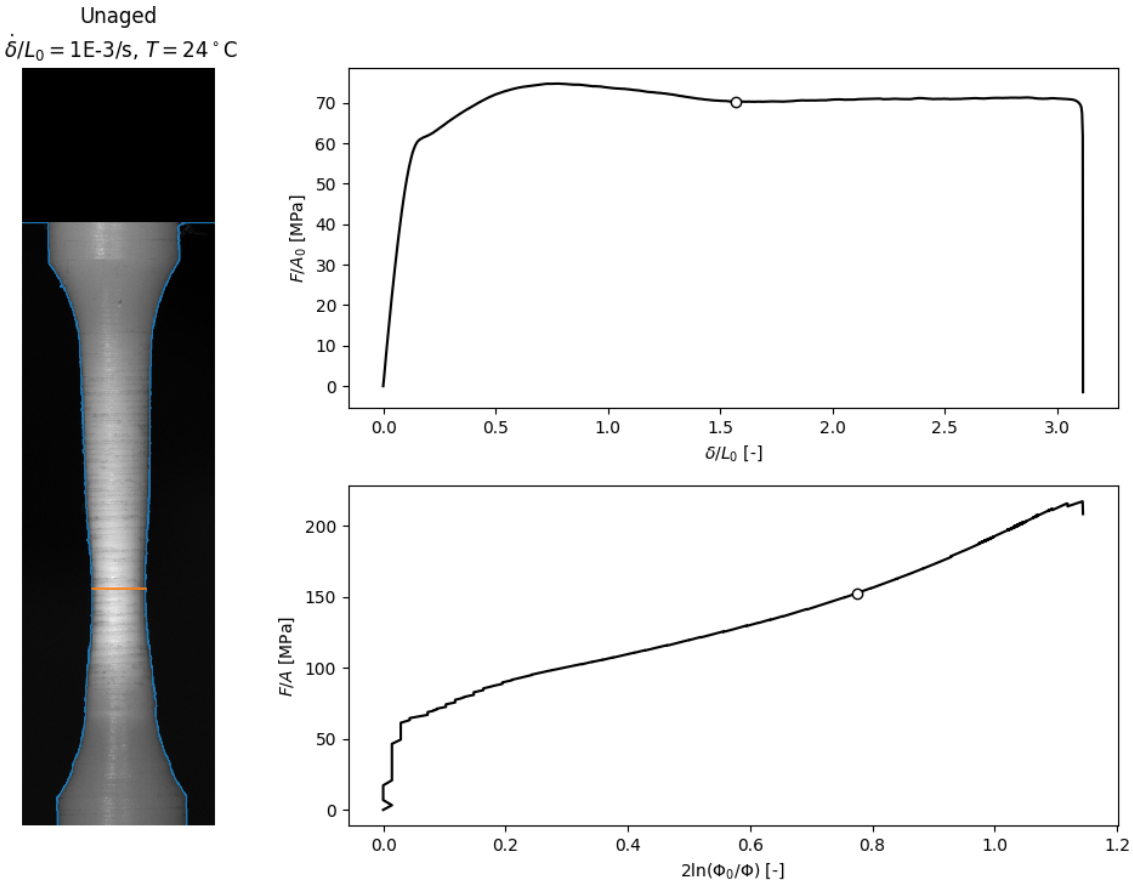

Figure H.19: A single frame from Vid. H.4 to show the information provided by the test videos.

APPENDIX I. EXPERIMENTAL DATABASE: COMPRESSION PINS

I.1 Introduction

Results from mechanical tests are discussed throughout the body of this text, but the presentation of every experiment was not necessary to support the primary narrative. This appendix is the second in a series that provides a complete set of data from mechanical tests on a single specimen type. In some cases, data is repeated from the main text in order to create a single location where all data is presented. The present appendix documents all results from mechanical tests on compression pins.

An extensive experimental campaign on bulk specimens was carried out while conducting research for this dissertation. The bulk experimental campaign had two goals. The first goal was to investigate the effects of UV aging on PA-6 specimens loaded under a variety of stress states. To this end, four different specimen geometries were subjected to a variety of aging conditions. The second goal was to produce a robust experimental database useful for calibration and validation a viscoplastic polymer model. For this goal, tests were carried out in tension and compression at a variety of strain rates and temperatures.

The experiments presented here investigate the effects of UV aging, testing temperature, and strain rate on the mechanical behavior of PA-6 in compression. Results from a single realization may be repeated across multiple figures to facilitate visualizing the effects of each test condition.

The outline of this chapter is as follows. In Section I.2, the experimental procedure is described, including how the true stress and strain are calculated and a test matrix of the conditions studied. The results are presented in Section I.3. In Subsection I.3.1, results are organized to highlight the effects of UV aging and temperature. In Subsection I.3.2, results are organized to highlight the effects of strain rate. Some concluding remarks are made in Section I.4.

I.2 Experimental

I.2.1 Material and specimen geometry

A cast plate of additive-free PA-6 with thickness 0.5 in (12.7 mm) was obtained from Plastics International. The crystallinity of the as-received material was measured to be $38\,\% \pm 1\,\%$ using a TA instruments Q20 DSC. The determination of the crystallinity assumes that the melting enthalpy of 100 % crystalline PA-6 is 190 J/g, which is an approximation that assumes multiple crystalline forms are present [94, 95]. The T_g of the material was measured as 47 °C, also using a TA instruments Q20 DSC. In the as-received material, no glass transition is apparent, as the presence of the crystalline phase suppresses the appearance of the transition. By heating the material above the crystal melting temperature ($\approx 220\,°C$) and then rapidly quenching, the crystallinity is reduced and the glass transition can then be measured by DSC.

Compression pins were machined from the plate using a lathe. The pins had a height and diameter of 0.375 in (9.53 mm). A drawing of the compression pin can be found in Fig. A.1. The pins were machined from the same plate used to create the cylindrical bars in Chapter 3 and the round notched bars in Chapter 4.

I.2.2 Aging

The compression pins were aged in a QUV Accelerated Weathering Tester by exposure to UV radiation for 192 hours. The aging took place at a temperature of 60 °C in ambient humidity. The accelerated aging used UVA lamps with a spectral irradiance of $1.55\,W/m^2/nm$ and an approximate wavelength of 340 nm. To evenly irradiate the pins, they were periodically rotated by 120°. Each 120° section of the lateral surface was aged for 192 hours. Throughout this dissertation, aging conditions are referred to by the nominal duration of UV exposure in hours appended to "UV" (e.g. UV48, UV96, UV192 for 48, 96, and 192 hours of UV exposure). Only the unaged and UV192 conditions are investigated using compression pins.

I.2.3 Conditioning

Since PA-6 is a hygroscopic material [92], the specimens were conditioned for 72 hours in a Napco model 5831 vacuum oven fitted with a Welch-Ilmvac Duoseal 1400B-01 pump. The conditioning took place at 80 °C. This procedure removes moisture from the specimen, which acts as a plasticizer and therefore increases the ductility [93] and reduces the strength [111]. The conditioning procedure is carried out in a vacuum oven to prevent additional thermal-oxidation. More information about the effects of absorbed moisture on PA-6 can be found in Appendix E.

I.2.4 Mechanical testing

The specimens were tested on an MTS Insight Electromechanical Testing System that was operated in displacement control mode. A 30 kN load cell was used to measure the force. The tests were carried out at nominal strain rates of $\left|\dot{\delta}\right| / L_0 = 10^{-3}$ /s and $\left|\dot{\delta}\right| / L_0 = 10^{-1}$ /s, where δ is the motion of the MTS crosshead and L_0 is the initial height of the compression pin. Polytetrafluoroethylene (PTFE) tape was used to lubricate the contact between the pins and the platens. To study the temperature dependence of PA-6, tests were carried out at temperatures of −30 °C, 0 °C, 24 °C, and 60 °C. For tests not at room temperature (24 °C), a custom designed temperature chamber was mounted on the test frame. The chamber acted as a oven to maintain temperatures above room temperature and used liquid nitrogen to maintain temperatures below room temperature.

I.2.5 Extensometry

Unlike many mechanical tests presented elsewhere in this dissertation, deformation in the compression pins did not require sophisticated extensometry. The compression pins exhibited a low degree of barreling, allowing the assumption of homogeneous deformation, thereby eliminating the need for video-based extensometry. Using the assumptions of homogenous and incompressible deformation, the true stress-strain curves were approximated from the

nominal stress-strain data using

$$\varepsilon = \left| \ln\left(1 - \frac{|\delta|}{L_0}\right) \right| \tag{I.1}$$

and

$$\sigma = \frac{|F|}{A_0}\left(1 - \frac{|\delta|}{L_0}\right), \tag{I.2}$$

where δ is the crosshead displacement, L_0 is the initial height of the pin, A_0 is the initial cross-sectional area of the pin, and F is the force measured by the load cell.

I.2.6 Test Matrix

The number of experimental realizations at different drawing temperatures (T) and nominal strain rates ($\left|\dot{\delta}/L_0\right|$) are presented for unaged PA-6 compression pins in Table I.1. The number of experimental realizations for UV192 PA-6 compression pins are shown in Table I.2. The data in Section I.3 is organized so that the effects of strain rate, temperature, and aging are easily visualized, which means data from a single realization may be shown in multiple figures.

Table I.1: Test matrix for unaged PA-6 compression pins.

Unaged Realizations		Temperature, $T < T_g$			$T > T_g$
		$-30\,°C$	$0\,°C$	$24\,°C$	$60\,°C$
$\left\|\dot{\delta}\right\|/L_0$	$10^{-1}\,/s$	3		1	
	$10^{-3}\,/s$	3	2	3	2
	$10^{-5}\,/s$				

I.3 Results

I.3.1 Effects of photo-oxidation and drawing temperature

Fig. I.1a shows the nominal stress-strain curves for photo-oxidized and unaged PA-6 pins loaded in compression. The pins do not fracture, but instead continuously flatten until the

Table I.2: Test matrix for UV192 PA-6 compression pins.

UV192 Realizations		Temperature, $T < T_g$ $-30\,°C$	$0\,°C$	$24\,°C$	$T > T_g$ $60\,°C$
$\left\|\dot{\delta}\right\|/L_0$	10^{-1} /s	2	2	2	1
	10^{-3} /s				
	10^{-5} /s				

load cell limit is reached, which is apparent by observing that each compression test ends at approximately 300 MPa of nominal stress (21.4 kN of force).

The true stress-strain curves are calculated using Eqs. (I.1) and (I.2) and are plotted in Fig. I.1b. The initial region of the true stress-strain response exhibits an approximately proportional relationship between stress and strain. Here, as with the other bulk specimens, the yield stress is defined as the limit of proportionality. Immediately after yield, there is a short plateau in the stress, quickly followed by hardening. The rate of hardening declines until a second stress plateau is reached, which is sometimes followed by a small amount of softening. The load cell employed in this study was insufficient to probe the mechanical behavior beyond this, as the specimens flattened without fracture until the load cell limit was reached. The compression pins tested at 60 °C behave slightly differently, which is unsurprising considering that this is above the glass transition temperature of the amorphous domains. When compressed at 60 °C, there is no clear yield point and the stress-strain curve exhibits a gradual rollover from a proportional response to flow.

Fig. I.1 depicts the compressive response at test temperatures of −30 °C, 24 °C, and 60 °C. However, testing was also conducted at 0 °C, but these results have been omitted from Fig. I.1 for clarity. The mechanical response of photo-oxidized and unaged pins tested at 0 °C is depicted in Fig. I.2, alongside unaged pins tested at −30 °C for reference.

Fig. I.3 shows the effect of temperature and photo-oxidation on the yield stress of PA-6 pins loaded in compression. The expected effect of temperature on the strength is observed.

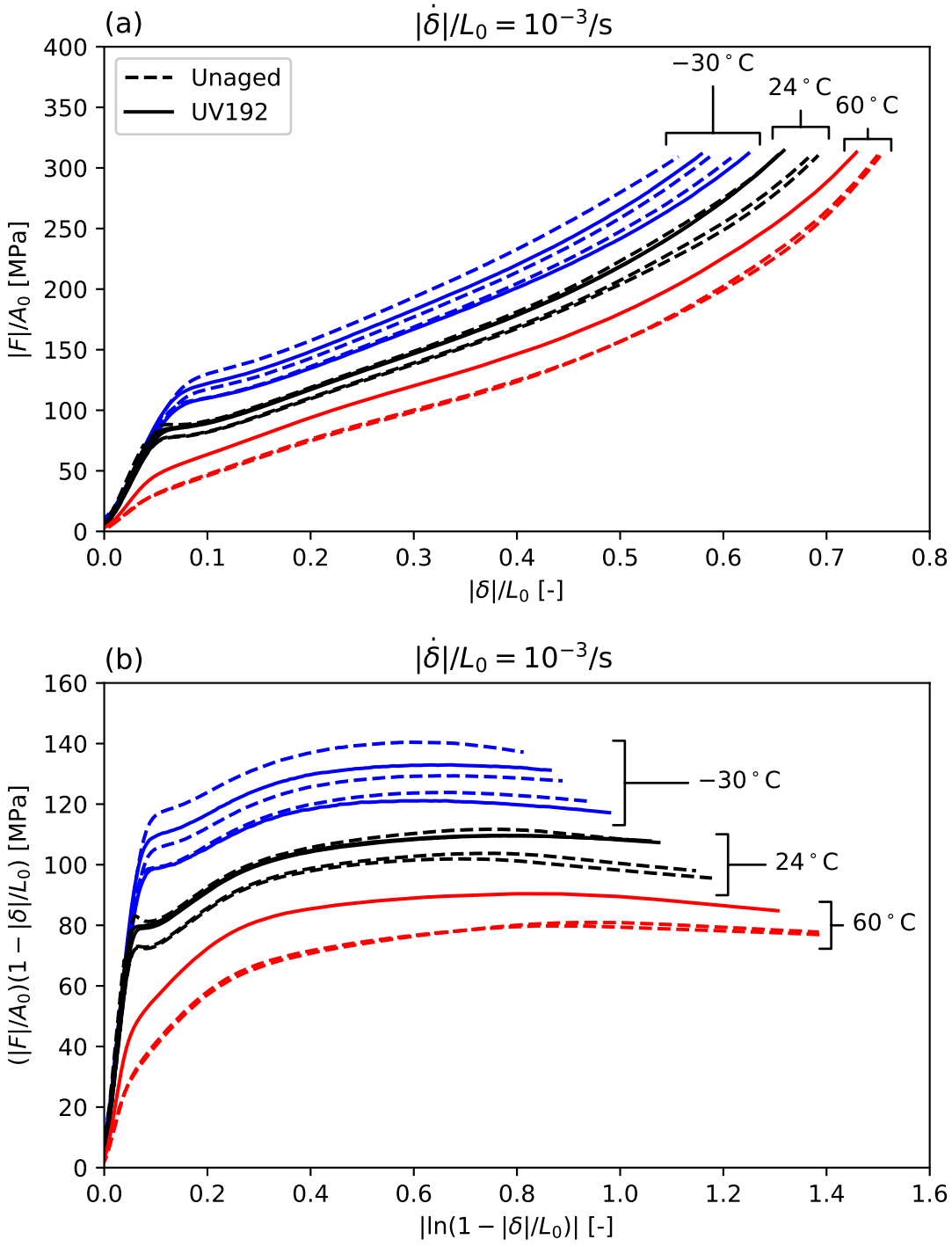

Figure I.1: Mechanical response of photo-oxidized and unaged PA-6 pins loaded in compression at a nominal strain rate of 10^{-3} /s under various test temperatures. (a) Nominal stress-strain response. (b) True stress-strain response assuming incompressible and homogeneous deformation.

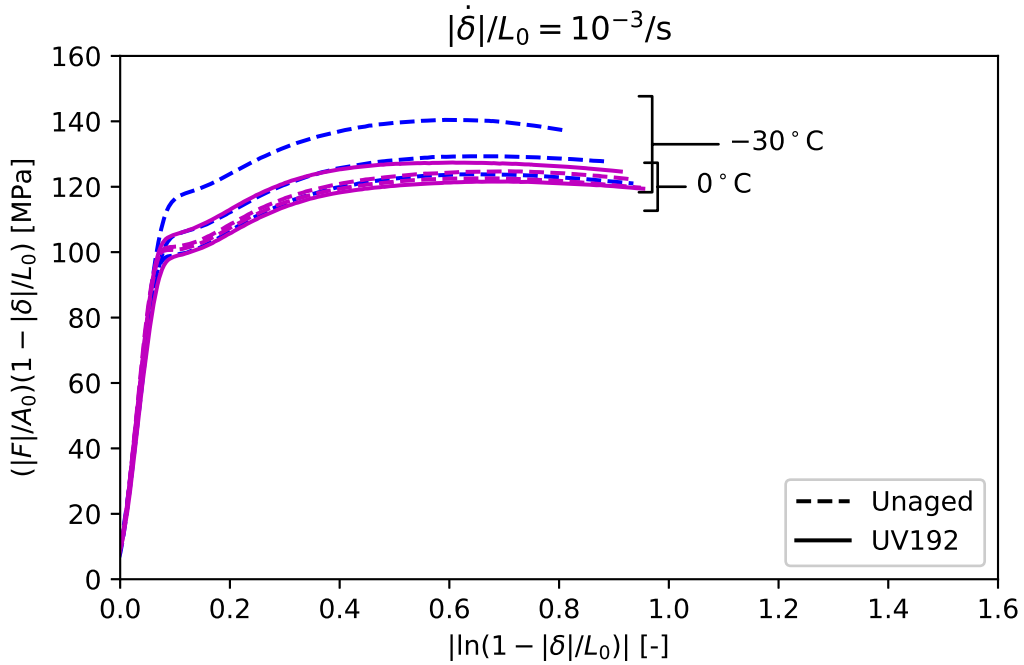

Figure I.2: True stress-strain response of photo-oxidized and unaged PA-6 pins loaded in compression at a nominal strain rate of 10^{-3} /s under test temperatures of −30 °C and 0 °C.

Between 0 °C to 60 °C, the yield stress decreases with increasing temperature. From −30 °C to 0 °C, the yield stress is less sensitive to the temperature, which may indicate that the amorphous domains are cooled deep into the glassy state at 0 °C and below.

No effect of photo-oxidation is observed on the yield stress in compression. As with the cylindrical bars tested in tension in Chapter 3, the yield stress is insensitive UV aging, since only a limited thickness of the specimen is oxidized. The depth of the damage can be limited by the diffusion of oxygen (DLO) or by attenuation of the UV radiation, but the oxidative damage in thermoplastics is typically limited to a depth on the order of 100 µm [16, 27]. Only a superficial layer of the specimen is degraded, leaving the average strength of the volume effectively unchanged. In the photo-oxidized cylindrical bars, surface damage caused by aging reduces the failure strain even though the strength of the volume is unaffected (see Chapter 3). The compression pins do not fracture in either the aged or the unaged condition,

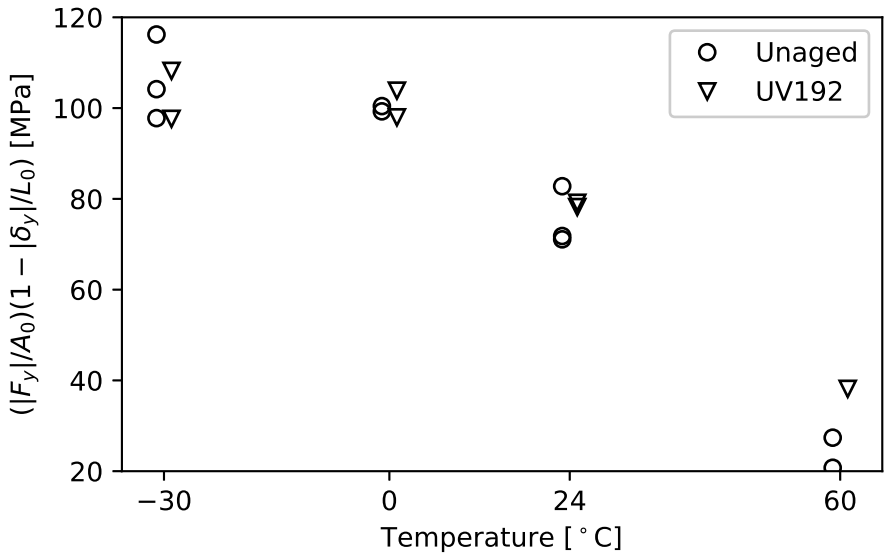

Figure I.3: The effect of test temperature on the true yield stress, defined as the limit of proportionality, for unaged and photo-oxidized PA-6 pins loaded in compression.

so photo-oxidation has no apparent effect on their mechanical behavior. Although oxidation may induce micromechanical damage in the surface of the material [151], a compressive stress state will not activate any such damage. However, the compression pins still show evidence of oxidation-induced damage on the surface of the specimen. Fig. I.4 shows two pins, one unaged and one photo-oxidized, after compressive loading up to the load cell maximum. The unaged specimen (left) exhibits a smooth lateral surface, while the lateral surface of the photo-oxidized specimen (right) is spalling. This is clear evidence that a superficial layer of the specimen is embrittled during aging and then breaks during compressive loading, even though the depth of the damaged layer is insufficient to impact the specimen-level response.

Fig. I.5 presents the effects of the test temperature on the mechanical response of PA-6 pins loaded in compression at $\left|\dot{\delta}\right|/L_0 = 10^{-1}$ /s. The effect of temperature on the yield stress for all unaged pins is presented in Fig. I.6.

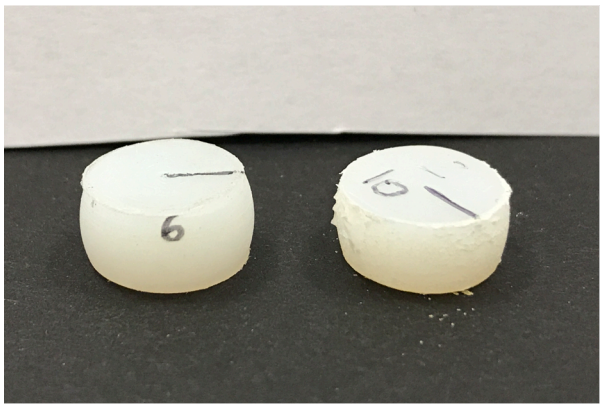

Figure I.4: (Left) An unaged PA-6 pin and (Right) a photo-oxidized PA-6 pin after compressive loading. Notice the material flaking off of the oxidized specimen while the unaged specimen remains smooth after loading.

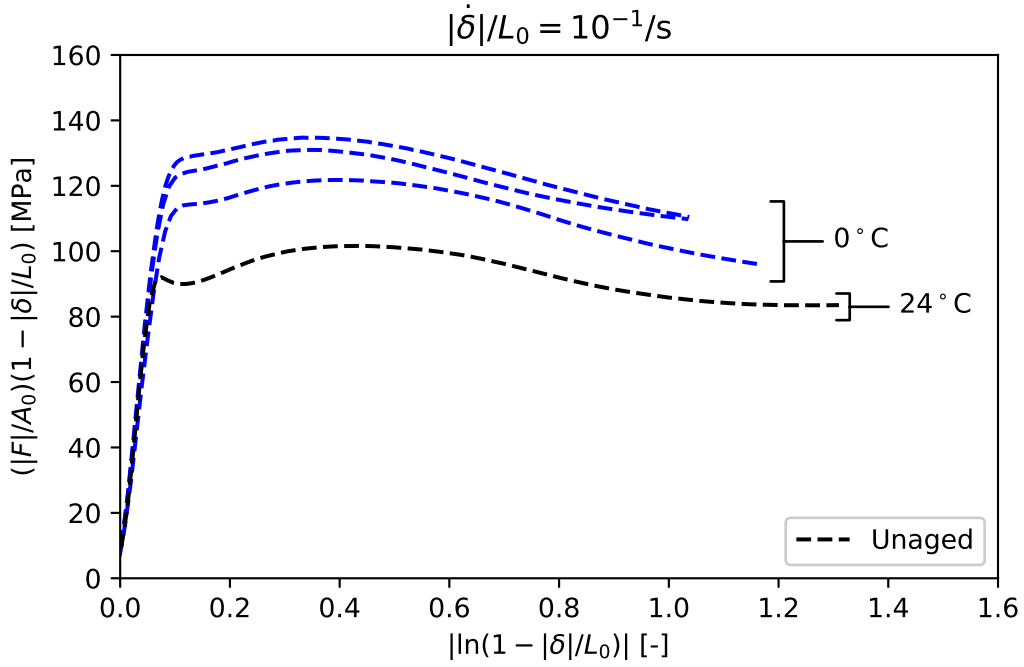

Figure I.5: True stress-strain response of unaged PA-6 pins loaded in compression at a nominal strain rate of 10^{-1} /s under test temperatures of 0 °C and 24 °C.

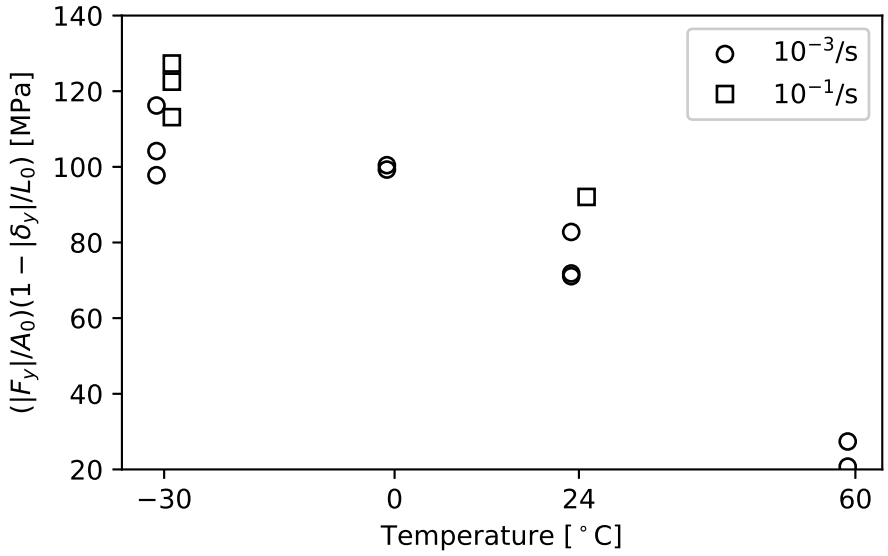

Figure I.6: The effect of test temperature on the true yield stress, defined as the limit of proportionality, for unaged PA-6 pins loaded in compression at nominal strain rates of 10^{-1} /s and 10^{-3} /s.

I.3.2 Effects of strain rate on the mechanical response

Fig. I.7 compares the mechanical response of PA-6 pins loaded in compression at different nominal strain rates. As expected, increasing the strain rate increases the yield stress of the material. However, the pins tested at $\left|\dot{\delta}\right| / L_0 = 10^{-1}$ /s show much higher softening than pins tested at $\left|\dot{\delta}\right| / L_0 = 10^{-3}$ /s. In fact, softening is so high that the two stress-strain curves cross. The extreme softening observed at the higher strain rate is most likely an effect of self-heating. At high strain rates, heat is generated in the material faster than it diffuses into the surrounding environment. Therefore, the temperature in the specimen increases as the test progresses, which decreases the strength.

The effects of strain rate on the true yield stress is presented in Fig. I.8.

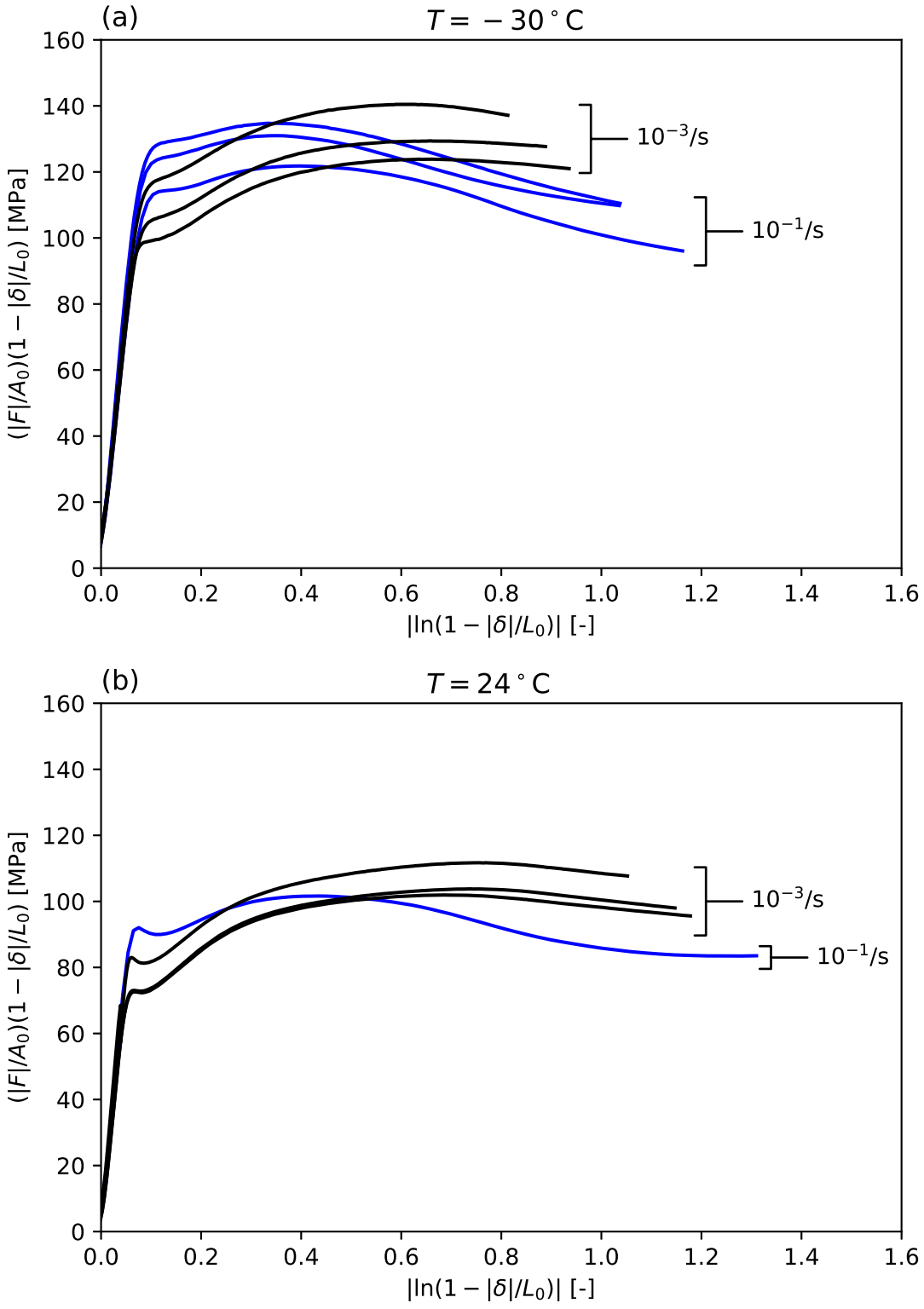

Figure I.7: True stress-strain response of unaged PA-6 pins loaded in compression at nominal strain rates of 10^{-1} /s and 10^{-3} /s and under test temperatures of (a) $-30\,^\circ$C and (b) $24\,^\circ$C.

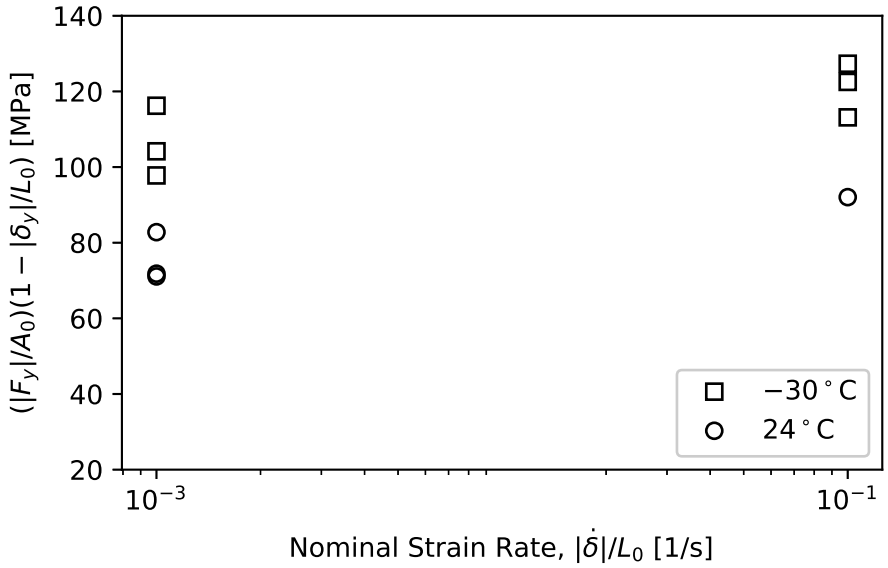

Figure I.8: The effect of nominal strain rate on the true yield stress, defined as the limit of proportionality, for unaged PA-6 pins loaded in compression at testing temperatures of −30 °C and 24 °C.

I.4 Conclusion

No effect of photo-oxidation is observed on the mechanical behavior of PA-6 loaded in compression. The strength is not affected because the depth of oxidative damage in thermoplastics is on the order of 100 µm, which is insufficient to affect the average behavior of the volume. The fracture behavior is unaffected because the cracks induced by oxidative aging are not activated by a compressive stress state. The unaged pins never fracture, but simply flatten until the load cell limit is reached. Similarly, the photo-oxidized pins never fracture, but spalling of the damaged surface is observed after loading.

The expected effect of temperature on the mechanical behavior is observed; increasing the temperature decreases the strength. Between the two coldest testing conditions, $T = -30\,^{\circ}\mathrm{C}$ and $T = 0\,^{\circ}\mathrm{C}$, the sensitivity of strength to temperature is reduced. At $T = 60\,^{\circ}\mathrm{C} > T_{\mathrm{g}}$, the clear yield point observed at the other temperatures disappears.

The expected effect of strain rate on the mechanical behavior is observed; increasing the strain rate increases the strength. However, at the higher strain rate ($\left|\dot{\delta}\right| / L_0 = 10^{-1}\,/\mathrm{s}$), the mechanical response softens until is softer than tests at the lower strain rate ($\left|\dot{\delta}\right| / L_0 = 10^{-3}\,/\mathrm{s}$). This effect is most likely due to self-heating at high strain rates. Therefore, results from tests carried out at $\left|\dot{\delta}\right| / L_0 = 10^{-1}\,/\mathrm{s}$ should be interpreted cautiously, as the temperature of the material may be significantly different from the intended test temperature.

APPENDIX J. EXPERIMENTAL DATABASE: THIN FILM SPECIMENS

J.1 Introduction

Results from mechanical tests are discussed throughout the body of this text, but the presentation of every experiment was not necessary to support the primary narrative. This appendix is the third in a series that provides a complete set of data from mechanical tests on a single specimen type. In some cases, data is repeated from the main text in order to create a single location where all data is presented. The present appendix documents all results from mechanical tests on the thin film specimens ($t_0 = 0.060\,\text{mm}$).[1]

In a semicrystalline thermoplastic, the diffusion of oxygen is limited to a depth of approximately $100\,\mu\text{m}$ [16, 28]. This limits the depth of oxidative aging in bulk specimens, creating an aged surface layered over an unaged substrate. This creates structural effects in mechanical tests on aged bulk specimens, which obfuscates the effects of aging on the intrinsic mechanical behavior. In the film specimens studied here, the thickness ($t_0 = 0.060\,\text{mm}$) is less than the nominal depth of oxidation ($100\,\mu\text{m}$). Therefore, the films are suitable for studying the effects of aging on the mechanical behavior. The film specimens are referred to here as "thin film" specimens to distinguish them from the film specimens used for *in situ* synchrotron tomography, which used a thicker film grade and a different specimen geometry.

In this appendix, the results from mechanical tests on thin film specimens ($t_0 = 0.060\,\text{mm}$) are presented. The tests explore the effects of UV aging and the (nominal) strain rate. Results from a single realization may be repeated across multiple figures to facilitate visualizing the effects of the different testing conditions. The mechanical behavior is presented using both the nominal stress–strain data and the true stress–strain data measured by contour tracking [88].

The outline of this appendix is as follows. In Section J.2, the methodology is presented,

[1] The mechanical behavior of films subjected to HUV aging are not discussed in this appendix. All experiments on HUV aged specimens are presented in Appendix F.

including a test matrix of experimental realizations. In Section J.3, the results are presented. In Section J.4, interesting videos of mechanical tests are described.

J.2 Experimental

The procedure for conducting mechanical tests on the thin films is already presented in detail in Section 3.2. A brief overview is reiterated here. PA-6 films with thickness $t_0 = 0.060\,\text{mm}$ were obtained from Goodfellow. Some films were aged by UV exposure in an accelerated weathering machine. Aging conditions are referred to by the hours of exposure prepended by "UV", e.g. UV48, UV96, UV192, and UV240 refer to 48, 96, 196, and 240 hours of UV exposure. Since the films are thinner than the nominal depth of oxidative aging, they were not flipped during aging. To control the moisture content of the PA-6 films, they were dried in a vacuum oven at 80 °C for 72 h prior to testing.

Specimens with an initial gauge length of $L_0 = 6.0\,\text{mm}$ and an initial gauge width of $W_0 = 4.0\,\text{mm}$ were cut from the films using a punch. The specimens were cut from the films after aging. All thin film specimens used throughout this dissertation used the specimen geometry depicted in Fig. A.2.

Using differential scanning calorimetry (DSC), the initial crystal mass fraction in the unaged film was determined to be $38\,\% \pm 1\,\%$. The DSC procedure is described in Section 3.2.4. DSC was also used to determine the crystallinity in the films after UV48, UV96, and UV192 aging. The crystal mass fraction of the films as a function of the UV exposure time is presented in the inset of Fig. 3.7b.

Mechanical tests were carried out an an electro-mechanical test frame in displacement control mode. A 1 kN load cell was used. The procedure presented in Section 3.2 only considers tests at a nominal strain rate of $\dot{\delta}/L_0 = 10^{-3}\,/\text{s}$. Here, three different nominal strain rates were used, $10^{-3}\,/\text{s}$, $10^{-2}\,/\text{s}$, $10^{-1}\,/\text{s}$, corresponding to crosshead displacement rates, $\dot{\delta}$, of 0.360 mm/min, 3.600 mm/min, and 36.0 mm/min, respectively.

Mechanical results are presented using nominal and true stress–strain curves. The nom-

Table J.1: Test matrix for thin film specimens.

	$\dot{\delta}/L_0$		
Aging Condition	10^{-3} /s	10^{-2} /s	10^{-1} /s
Unaged	2	2	2
UV48	3	2	3
UV96	3	2	3
UV192	2		2
UV240	1	1	

inal strain is calculated as

$$\varepsilon^{\text{nom}} = \frac{\delta}{L_0}, \tag{J.1}$$

where δ is the crosshead displacement and L_0 is the initial gauge length. The nominal stress is calculated as

$$\sigma^{\text{nom}} = \frac{F}{A_0}, \tag{J.2}$$

where F is the force measured by the load cell and A_0 is the initial cross-sectional area. The true stress and strain are calculated using contour tracking. The procedure for contour tracking is described in Section 3.2.6. The true strain is calculated as

$$\varepsilon^{\text{true}} = 2 \ln \left(\frac{W_0}{W} \right), \tag{J.3}$$

where W_0 is the initial width of the specimen and W is the current width of the specimen measured by contour tracking. The true stress is calculated as

$$\sigma^{\text{true}} = \frac{F}{A} = \frac{F}{A_0 \left(\frac{W}{W_0} \right)^2}. \tag{J.4}$$

The test matrix for the thin film specimens is shown in Table J.1. For all unaged, UV48, and UV96 aged films, the mechanical behavior is presented using both nominal and true stress–strain curves. For the UV192 and UV240 aged films, true stress–strain results are not

presented. At these extremely high aging conditions, failure occurs at strains of the same order of magnitude as the resolution of the contour tracking methodology employed here.

J.3 Results

The results from the film tests are replotted in multiple figures to help visualize different trends.

- Fig. J.1 shows the effects of aging of the mechanical behavior.
- Fig. J.2 shows the effects of aging on the mechanical behavior, but unaged films are removed from the plot so the limits of the abscissa are better suited for viewing the aged results.
- Fig. J.3 shows the effects of the nominal strain rate on the mechanical behavior.
- Fig. J.4 shows the effects of the nominal strain rate on UV192 and UV240 films, which are too brittle to been clearly seen on plots with other results. These films undergo almost no deformation before fracture, so contour tracking is unsuitable for measuring their true strain.

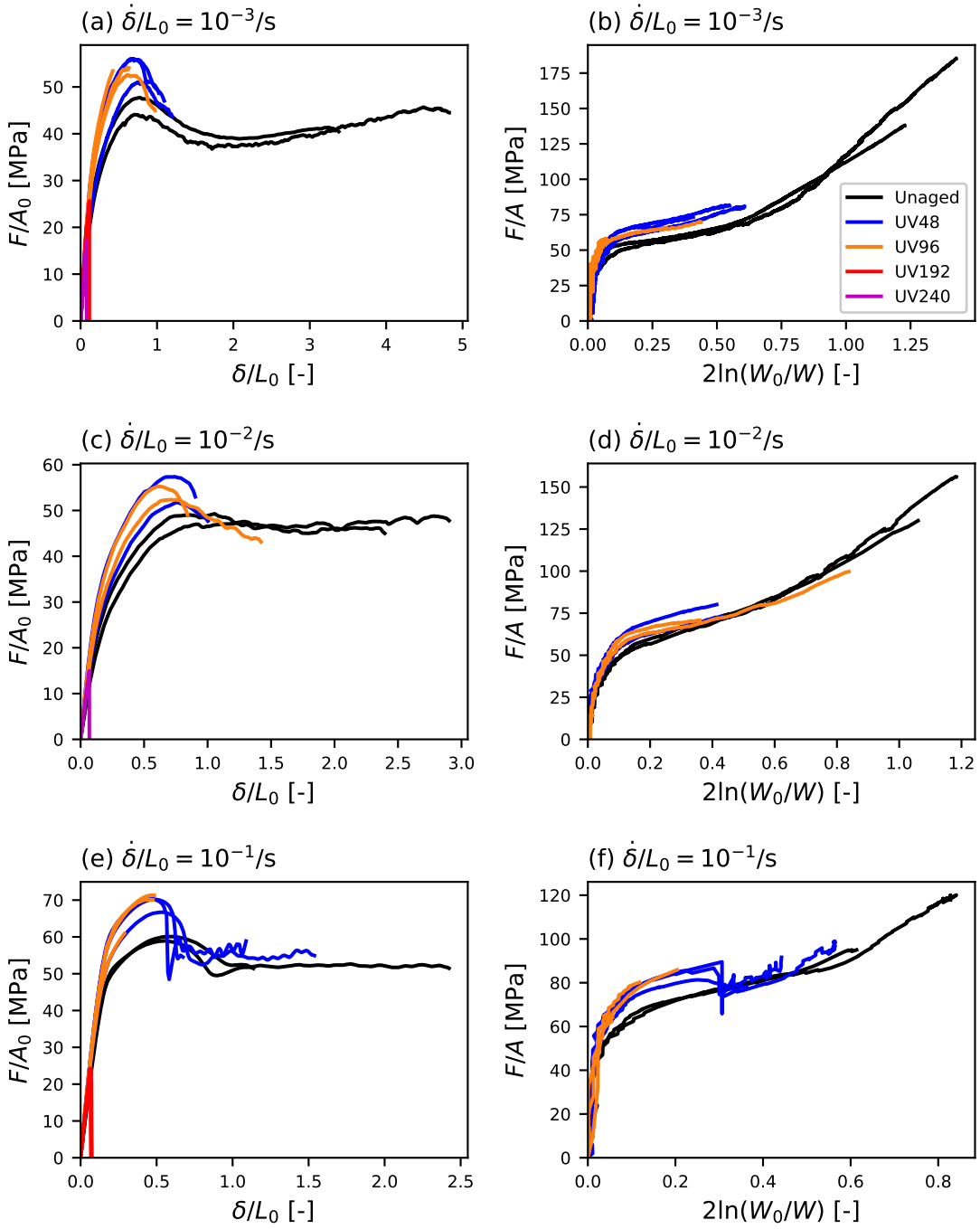

Figure J.1: The (a,c,e) nominal and (b,d,f) true stress–strain curves for PA-6 films of thickness 0.060 mm loaded in tension. Subplots are organized to show the effects of aging. True stress–strain curves for UV192 and UV240 films are not shown. Tests at nominal strain rates of (a,b) $\dot{\delta}/L_0 = 10^{-3}$ /s, (c,d) $\dot{\delta}/L_0 = 10^{-2}$ /s, and (e,f) $\dot{\delta}/L_0 = 10^{-1}$ /s.

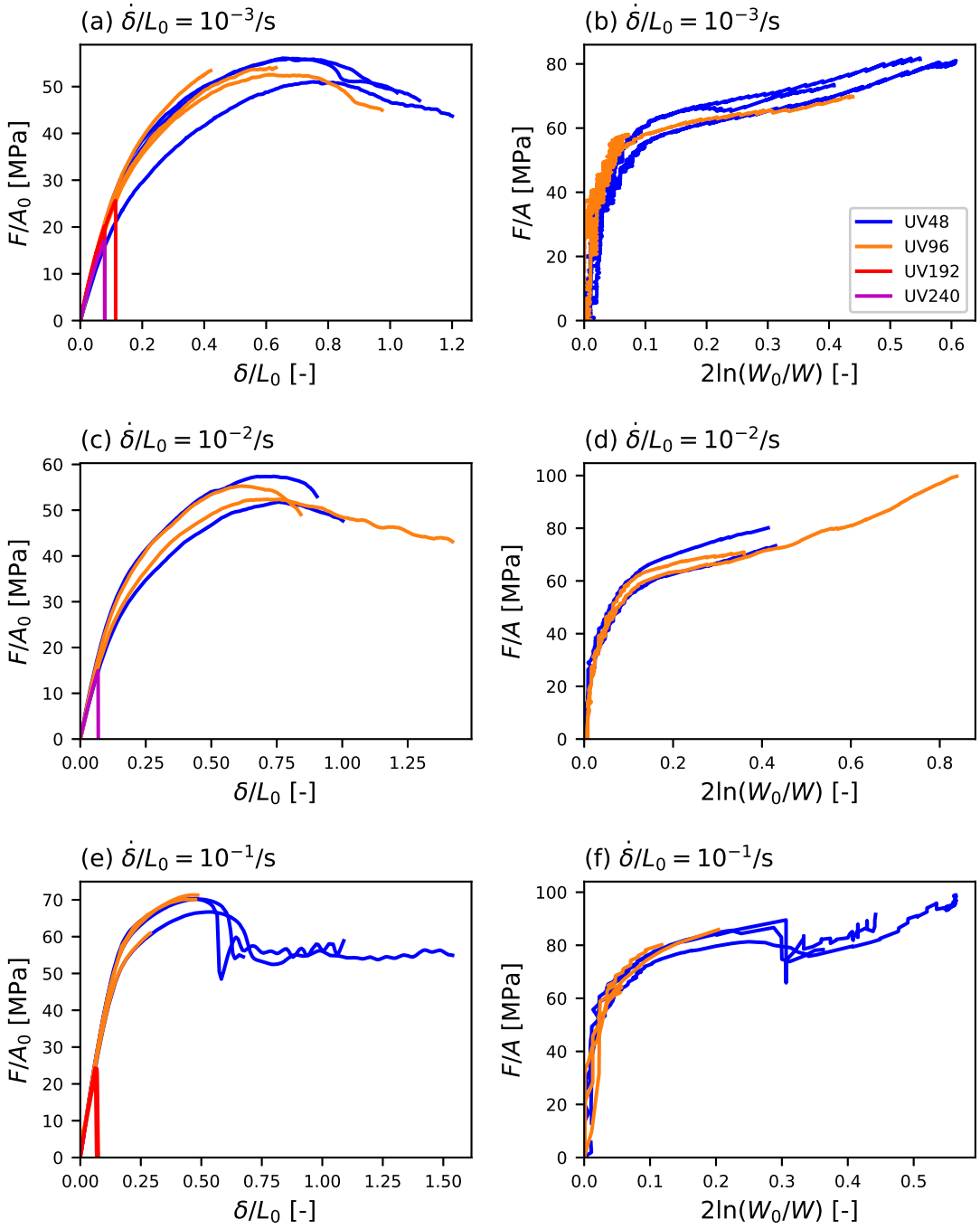

Figure J.2: The (a,c,e) nominal and (b,d,f) true stress–strain curves for PA-6 films of thickness 0.060 mm loaded in tension. Subplots are organized to show the effects of aging. To clearly see results from aged films, results from unaged films are not shown. True stress–strain curves for UV192 and UV240 films are not shown. Tests at nominal strain rates of (a,b) $\dot{\delta}/L_0 = 10^{-3}$ /s, (c,d) $\dot{\delta}/L_0 = 10^{-2}$ /s, and (e,f) $\dot{\delta}/L_0 = 10^{-1}$ /s.

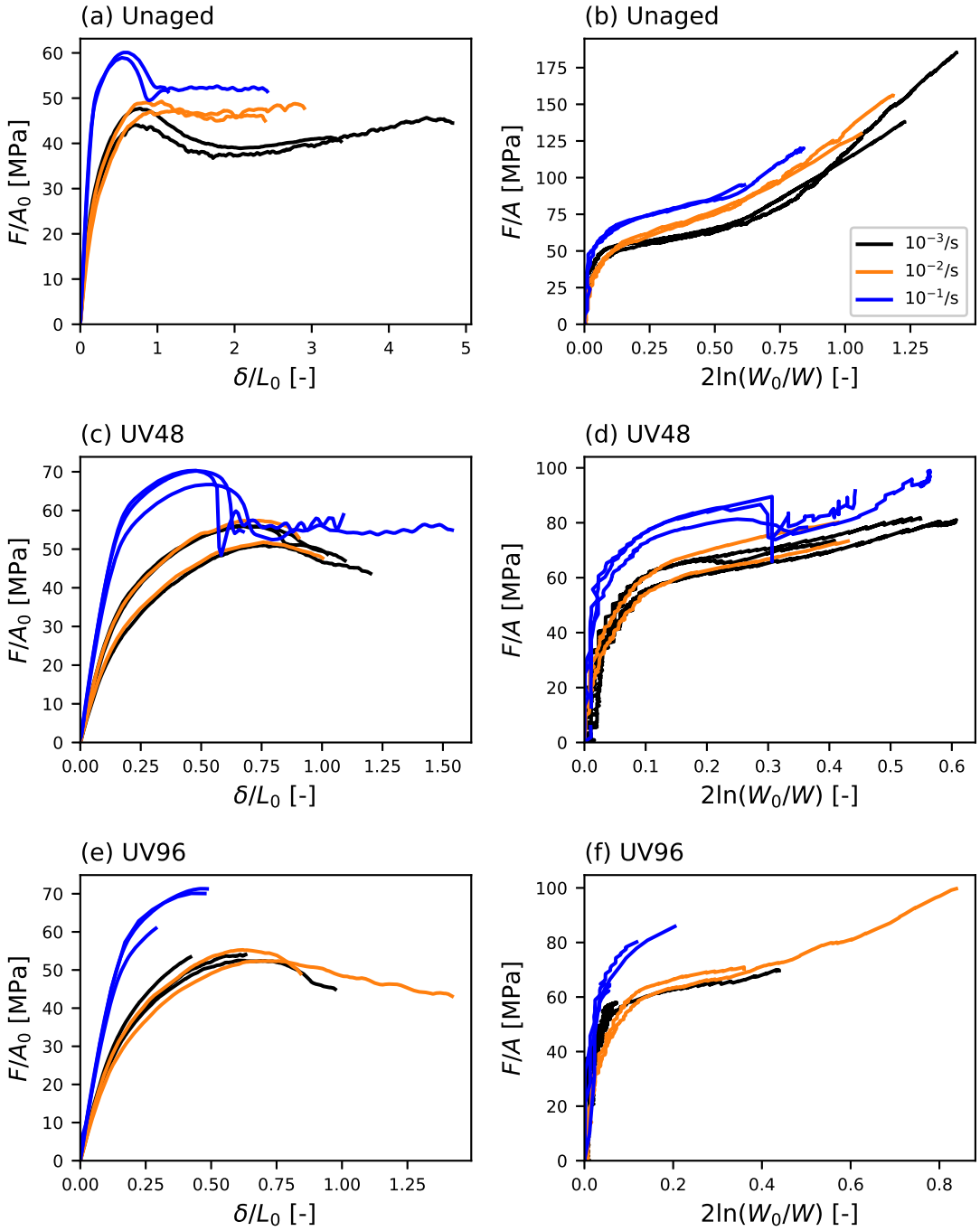

Figure J.3: The (a,c,e) nominal and (b,d,f) true stress–strain curves for PA-6 films of thickness 0.060 mm loaded in tension. Subplots are organized to show the effects of the nominal strain rate. True stress–strain curves for UV192 and UV240 films are not shown. Results from tests on (a,b) unaged films, (c,d) UV48 films, and (e,f) UV96 films.

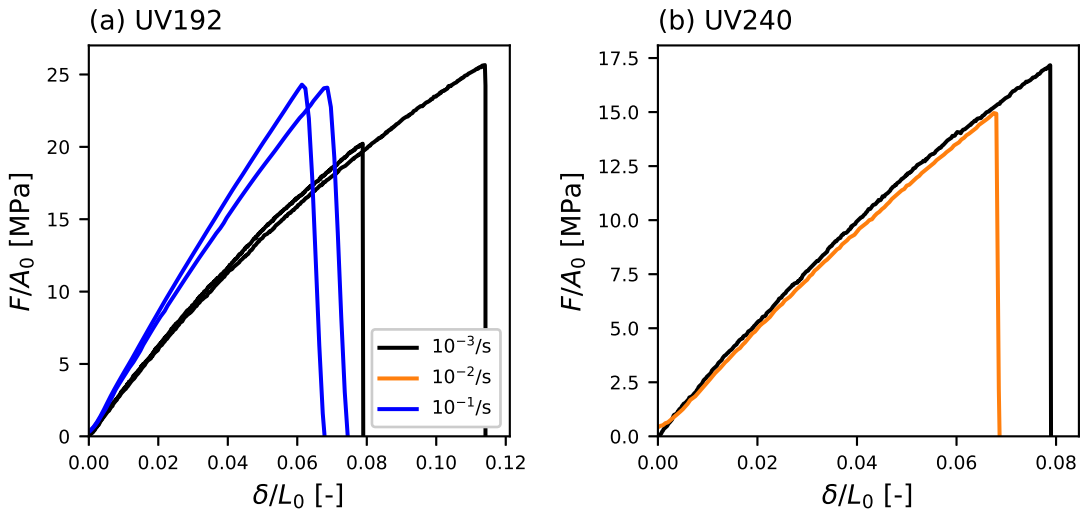

Figure J.4: The nominal stress–strain curves for PA-6 films of thickness 0.060 mm loaded in tension. (a) UV192 films and (b) UV240 films.

J.4 Videos of mechanical tests

Test videos of the films reveal different damage mechanism leading to fracture. A curated set of test videos are listed in Table J.2. Unaged and UV48 films most commonly fracture from tearing that initiates at the edges of the film. UV96 films most commonly fracture from small cracks. Whitening around the cracks is also sometimes visible. UV192 and UV240 films are extremely brittle and fracture nearly immediately after loading.

An interesting phenomenon occurs uniquely in UV48 films tested at $\dot{\delta}/L_0 = 10^{-1}$ /s. During loading, white bands appear on the film. The bands appear one after another, and the appearance of each band causes a rapid load oscillation, see Fig. J.3c.

Sample images from videos are shown in Fig. J.5.

- Fig. J.5a shows tearing in an unaged film.
- Fig. J.5b shows white bands appearing in a UV48 film tested at $\dot{\delta}/L_0 = 10^{-1}$ /s.
- Fig. J.5c shows a crack appearing in the center of an HUV96 film. Although stress–strain curves from HUV-aged are not presented here, this was the best image of a

crack captured in the experiments on the thin film specimens. Stress–strain curves for HUV-aged films are presented in Appendix F, where it is shown that HUV96 films and UV96 films are indistinguishable.

- Fig. J.5d shows a fractured UV192 film. At this aging condition, fracture occurs nearly immediately after loading. In the video frame immediately before this image, no damage is visible. For this test, the camera was set to take an image every 100 ms.

Table J.2: Curated list of test videos from films of thickness 0.060 mm.

Video	Age	$\dot{\delta}/L_0$	Description
Vid. J.1	Unaged	10^{-3} /s	Multiple tears initiate from the edges.
Vid. J.2	Unaged	10^{-1} /s	Tear initiates near the neck front.
Vid. J.3	UV48	10^{-1} /s	White bands appear near tear.
Vid. J.4	UV48	10^{-1} /s	White bands appear neck front and tear.
Vid. J.5	HUV96	10^{-3} /s	Crack appears in center of film.
Vid. J.6	UV96	10^{-3} /s	Crack appears at edge of film.
Vid. J.7	UV96	10^{-1} /s	Crack appears at edge of film.
Vid. J.8	UV192	10^{-3} /s	Film is extremely brittle.
Vid. J.9	UV192	10^{-1} /s	Film is extremely brittle.

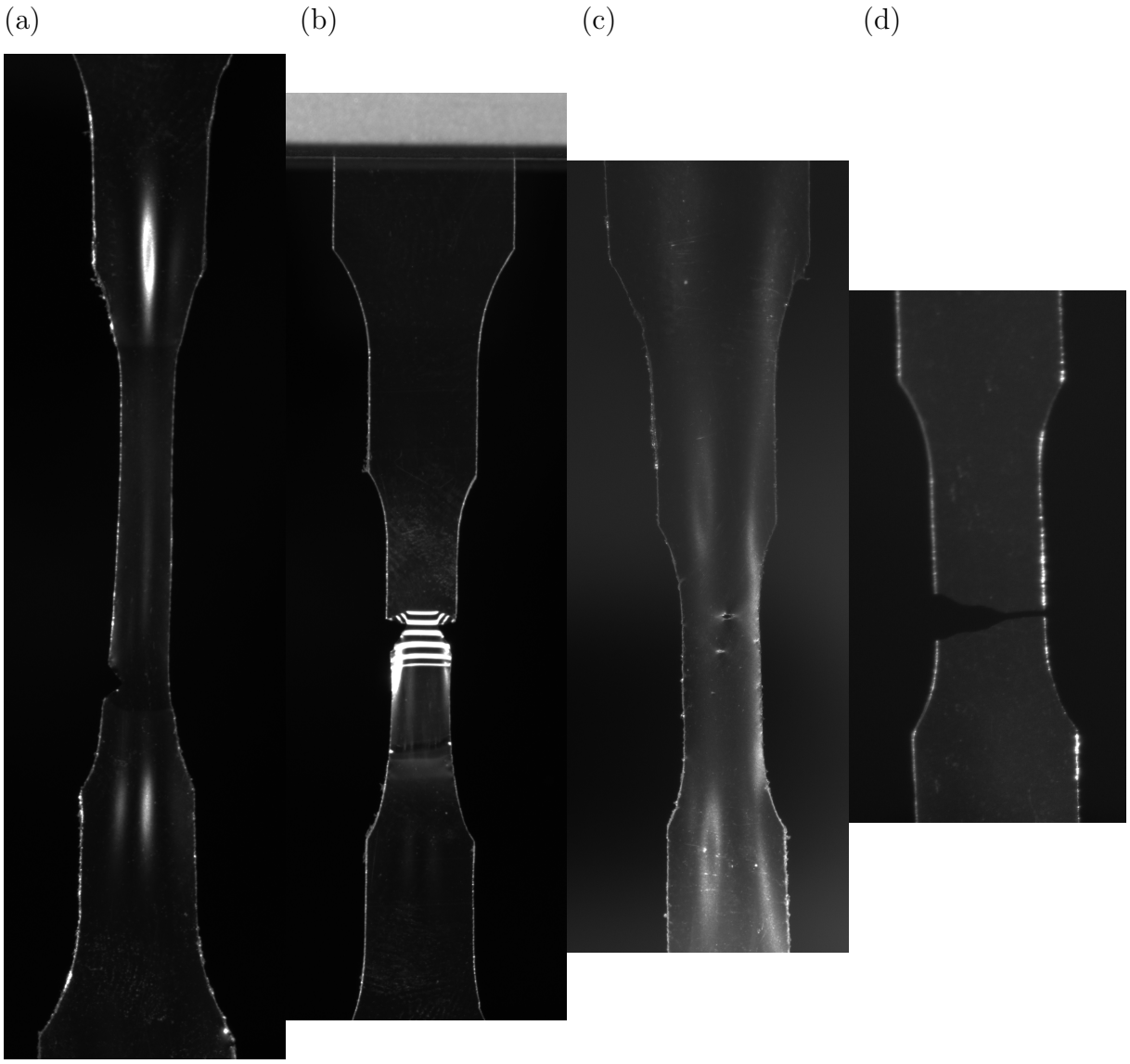

Figure J.5: Images from videos of mechanical tests on PA-6 films of thickness 0.060 mm. (a) Unaged film tested at $\dot{\delta}/L_0 = 10^{-1}$ /s, see Vid. J.2. (b) UV48 film tested at $\dot{\delta}/L_0 = 10^{-1}$ /s, see Vid. J.4. (c) HUV96 film tested at $\dot{\delta}/L_0 = 10^{-3}$ /s, see Vid. J.5. (d) UV192 film tested at $\dot{\delta}/L_0 = 10^{-3}$ /s, see Vid. J.8.

APPENDIX K. EXPERIMENTAL DATABASE: THICK FILM SPECIMENS

K.1 Introduction

Results from mechanical tests are discussed throughout the body of this text, but the presentation of every experiment was not necessary to support the primary narrative. This appendix is the fourth, and final, in a series that provides a complete set of data from mechanical tests on a single specimen type. In some cases, data is repeated from the main text in order to create a single location where all data is presented. The present appendix documents all results from mechanical tests on the thick film specimens ($t_0 = 0.1\,\text{mm}$).

These film specimens were used for *in situ* tomography in Chapter 5. Originally, films with a thickness of 0.060 mm were chosen for all experiments on PA-6 films. However, technical difficulties were encountered when using films of thickness 0.060 mm with the custom test frame designed for *in situ* synchrotron tomography. Therefore, films of thickness 0.1 mm were used instead. The specimens made from the 0.1 mm films are referred to as "thick film" specimens to distinguish them from the original 0.060 mm film specimens used in Chapter 3 and Appendix J. Also, the thick film specimens use a different geometry than the thin film specimens. The different geometry was chosen to accommodate the custom test frame used for *in situ* synchrotron tomography.

Prior to the conducting the *in situ* synchrotron tomography experiments on the thick films, a series of mechanical tests were performed to characterize their mechanical behavior. This appendix presents the results from this preliminary characterization. The mechanical tests explore the effects of UV aging and the displacement rate, $\dot{\delta}$. Results from a single experiment may be repeated across multiple figures to facilitate visualizing the effects of the different testing conditions. The mechanical behavior is primarily presented using the nominal stress, F/A_0, and crosshead displacement, δ. Contour tracking was applied to some films to measure the true strain and true axial stress [88].

The outline of this appendix is as follows. In Section K.2, the methodology is presented, including a test matrix of experimental realizations. In Section K.3, the results are presented.

K.2 Experimental

PA-6 films with thickness $t_0 = 0.1\,\text{mm}$ were obtained from Goodfellow. Some films were aged by UV exposure in an accelerated weathering machine. Aging conditions are referred to by the hours of UV exposure prepended by "UV". The films are aged for 12 h, 24 h, and 48 h, and are therefore referred to as UV12, UV24, and UV48 films, respectively. Since the films are approximately the same thickness as the nominal depth of oxidative aging [16,27,28], they were periodically flipped during aging. Each face of the film was exposed to UV radiation for the full nominal aging time, e.g. both faces of a UV12 film are aged for 12 h. To control the moisture content of the PA-6 films, they were dried in a vacuum oven at 80 °C for at least 24 h prior to testing.

After aging and conditioning, specimens were cut from the films using a custom punch. The specimen geometry was designed to be compatible with a custom test frame used for *in situ* synchrotron tomography [29]. The specimens had a gauge length of 23 mm with two 5 mm tabs used for gripping. The gauge section had a very shallow notch of radius 30 mm to help localize the deformation and damage. At the minimum cross-section, the width of the specimen was 1.3 mm. A drawing of the specimen geometry is shown in Fig. A.3.

Since the test frame for *in situ* tomography fully encloses the specimen, no video-based extensometry was possible. Therefore, two test frames were used. The first test frame allowed for the use of video-based extensometry to determine the true axial stress and true strain. The second frame was the custom test frame for *in situ* tomography, which is nicknamed *Bulky* [29]. Preliminary tests were conducted on *Bulky* as practice before conducting experiments at the synchrotron. In order to compare results from both test frames, mechanical data is reported using the nominal stress, F/A_0, and the crosshead displacement, δ.

On the first test frame, displacement rates of $\dot{\delta} = 1.800\,\text{mm/s}$ and $\dot{\delta} = 0.047\,\text{mm/s}$ were

used.[1] On this test frame, a camera was used to capture videos of the specimens. Test videos were analyzed using contour tracking, where the true strain is calculated using

$$\varepsilon = 2 \ln \left(\frac{W_0}{W} \right), \tag{K.1}$$

and the true axial stress is calculated using

$$\sigma = \frac{F}{A} = \frac{F}{A_0 \left(\frac{W}{W_0} \right)^2}, \tag{K.2}$$

where W_0 is the initial width of the film, W is the current width, A_0 is the initial cross-sectional area, A is the current cross-sectional area, and F is the force measured by the load cell. For more details on using contour tracking with film specimens, see Section 5.2.4. For experiments on the test frame *Bulky*, three different displacement rates were used, $\dot{\delta} = 0.010\,\text{mm/s}$, $\dot{\delta} = 0.005\,\text{mm/s}$, and $\dot{\delta} = 0.001\,\text{mm/s}$. A test matrix for the thick film specimens is shown in Table K.1.

Table K.1: Test matrix for thick film specimens.

	Displacement rate, $\dot{\delta}$				
Aging Condition	1.800 mm/s	0.047 mm/s	0.010 mm/s	0.005 mm/s	0.001 mm/s
Unaged		1			
UV12		1	1		1
UV24	1	3	2	1	2
UV48		3	1		1

[1] The single test using $\dot{\delta} = 1.800\,\text{mm/s}$ was initiated on accident, but the results were recorded nonetheless.

K.3 Results

Results from mechanical tests on thick films are shown in Figs. K.1–K.3. Unaged and UV12 films did not fracture, even when loaded to the maximum crosshead displacement. Some UV12 films on bulky were interrupted before the maximum displacement. All UV24 and UV48 films were loaded to fracture.

- Fig. K.1 shows the effects of aging on the mechanical behavior from tests using a displacement rate of $\dot{\delta} = 0.047\,\text{mm/s}$. Nominal stress–displacement curves are shown in Fig. K.1a. The true axial stress–true strain curves from the same tests are shown in Fig. K.1b. For videos of the mechanical tests and animated stress–strain plots, see Vids. 5.1–5.4.[2]

- Fig. K.2 shows the effects of aging on the mechanical behavior from tests conducted on *Bulky*. Fig. K.2a shows results from tests using a displacement rate of $\dot{\delta} = 0.010\,\text{mm/s}$. Fig. K.2b shows results from tests using a displacement rate of $\dot{\delta} = 0.001\,\text{mm/s}$.

- Fig. K.3 shows the effects of the displacement rate on the mechanical behavior of aged films. UV12 films are shown in Fig. K.3a, UV24 films are shown in Fig. K.3b, and UV48 films are shown in Fig. K.3c.

[2] Email `kncundiff.dissertationquestions@gmail.com` to request video files.

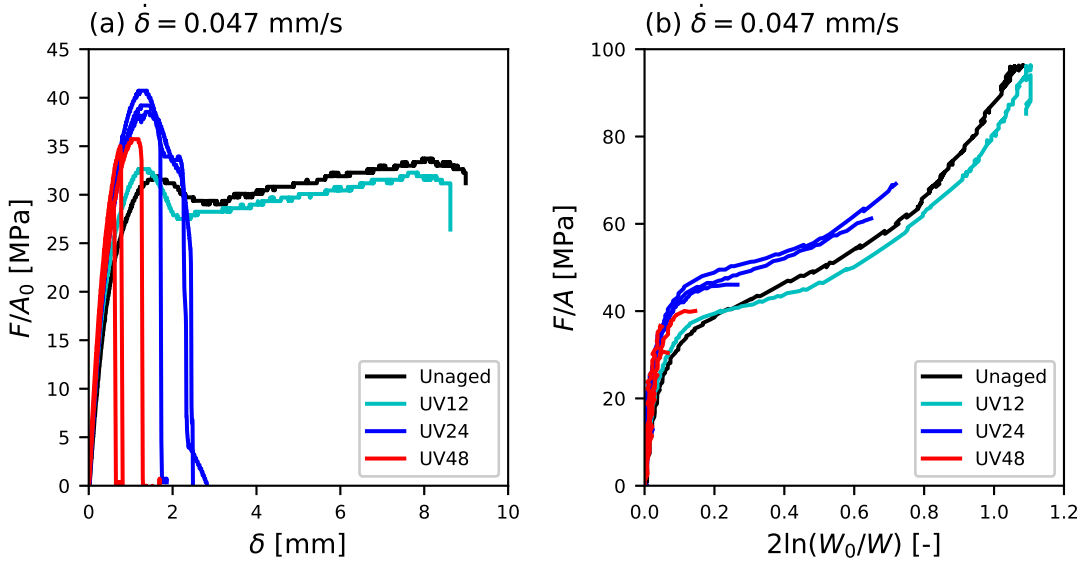

Figure K.1: The effects of aging on the mechanical behavior of PA-6 films with thickness 0.1 mm. Test were conducted using a displacement rate of $\dot{\delta} = 0.047$ mm/s. Unaged and UV12 films did not fracture, even when loaded to the maximum crosshead displacement. All other films were loaded to fracture. (a) Nominal stress–displacement curves. (b) True axial stress–true strain curves.

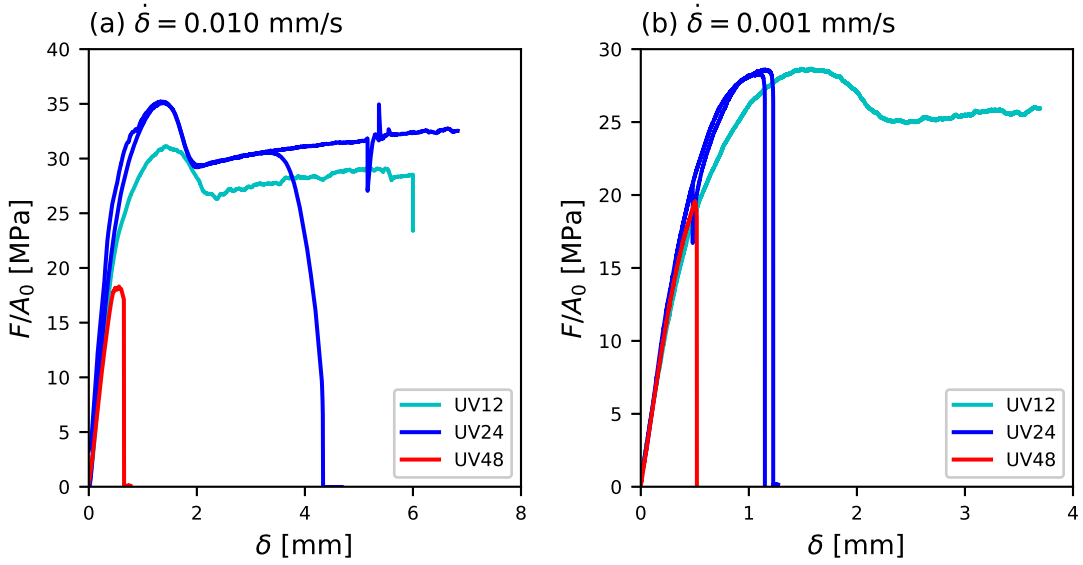

Figure K.2: The effects of aging the mechanical behavior of PA-6 films with thickness 0.1 mm. Nominal stress–displacement curves are shown. UV12 films did not fracture, even when loaded to the maximum crosshead displacement. All other films were loaded to fracture. Tests using a displacement rate of (a) $\dot{\delta} = 0.010$ mm/s and (b) $\dot{\delta} = 0.001$ mm/s.

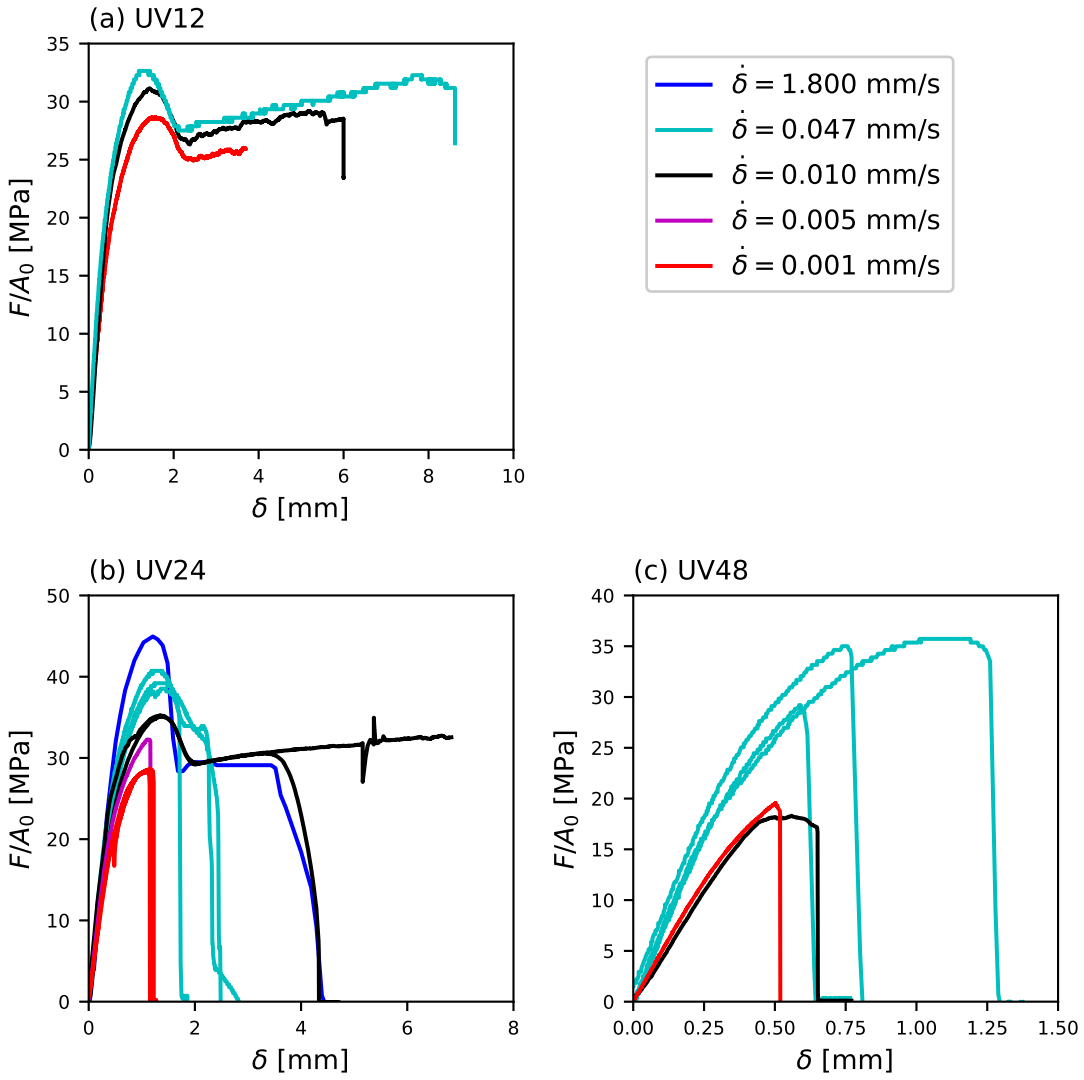

Figure K.3: The effects of the displacement rate on the mechanical behavior of aged PA-6 films with thickness 0.1 mm. Nominal stress–displacement curves are shown. UV12 films did not fracture, even when loaded to the maximum crosshead displacement. All other films were loaded to fracture. (a) UV12 films, (b) UV24 films, and (c) UV48 films.